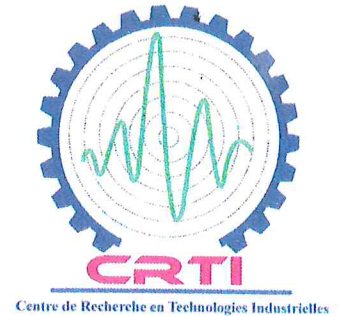




الجمهورية الجزائرية الديمقراطية الشعبية  
وزارة التعليم العالي والبحث العلمي  
جامعة فرحات عباس سطيف 1. معهد البصريات وميكانيك الدقة  
مركز البحث في التكنولوجيات الصناعية  
People's Democratic Republic of Algeria  
Ministry of Higher Education and Scientific Research.  
Ferhat Abbas, University Setif 1 Institute of Optics and Precision Mechanics  
Research Center in Industrial technologies



## ATTENDANCE CERTIFICATE

This certificate is attributed to:

**“Leila BECHANE”**

For her participation to the Fourth International Conference on Mechanics and Materials ICMM'23. Held in Setif 1 University, Algeria. November 6-7<sup>th</sup>, 2023, and gave the following poster presentation:

**“Numerical optimization of (FTO/ZnO/Cs<sub>2</sub>AgBiBr<sub>6</sub>/P3HT/MO) perovskite solar cell”**

Co-authors: SLIMANI Wahiba

This certificate is issued for whatever legal purpose it may serve. November 7<sup>th</sup>, 2023

On behalf of the Scientific committee  
Pr. Boualem KESKES

Professor  
KESKES Boualem

On behalf of the Organizing committee  
Pr. Kamel LOUCIF, ICMM'23 Chairman



Chairman  
Pr. LOUCIF Kamel

People's Democratic Republic of  
Algeria

Ministry of Higher Education and  
Scientific Research

Ferhat Abbas, Setif 1 University  
Institute of Optics and Precision  
Mechanics



الجمهورية الجزائرية الديمقراطية  
الشعبية

وزارة التعليم العالي والبحث العلمي

جامعة فرحات عباس سطيف 1  
معهد البصريات و ميكانيك الدقة

October 31, 2023

## Acceptance letter

4<sup>th</sup> International Conference of Mechanics and Materials  
ICMM'2023. 6-7 November 2023, Setif, Algeria

To Whom It May Concern

Dear LEILA BECHANE

Your abstract entitled "Numerical optimization of (FTO/ZnO/Cs<sub>2</sub>AgBiBr<sub>6</sub>/P3HT/MO) perovskite solar cell", was accepted as a **poster** presentation for the 4<sup>th</sup> International Conference on Mechanics and Materials "ICMM2023" which will take place in Setif, Algeria, on November 6-7, 2023.

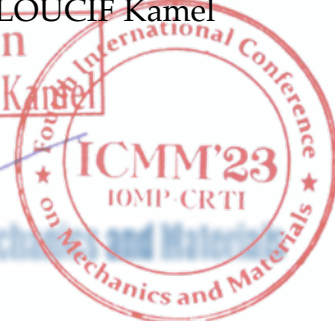
Best regards

For the Organizing Committee of the  
4<sup>th</sup> International Conference of Mechanics and Materials

Conference Chairman:

Pr. LOUCIF Kamel

Chairman  
Pr. LOUCIF Kamel



e-mail: [icmm.setif.23@gmail.com](mailto:icmm.setif.23@gmail.com)

**CONFERENCE LOCATION:** AUDITORIUM Nait BELKACEM, SETIF 1 UNIVERSITY, ELBEZ CAMPUS, SETIF



الجمهورية الجزائرية الديمقراطية الشعبية  
وزارة التعليم العالي و البحث العلمي  
تحت الرعاية السامية للسيد وزير التعليم العالي  
و البحث العلمي والسيد والي ولاية سطيف  
ينظم  
معهد البصريات وميكانيك الدقة  
بالتعاون مع :  
مركز البحث في التكنولوجيات الصناعية

تاريخ المؤتمر

6-7

نوفمبر 2023

# المؤتمر الدولي الرابع للميكانيك والمواد



# ICMM ' 23



نظم من قبل



برعاية



المكان : قاعة المحاضرات الدكتور صالح كرمي  
بمجمع المعبودة



# PREFACE

The fourth edition of the International Conference on Mechanics and Materials **ICMM'23**, will be held in **Setif, Algeria**. Organized by **Ferhat Abbas University Setif 1 (UFAS 1)** with the cooperation of the **Research Center in Industrial Technologies (CRTI)**, from **November 6th to 7th, 2023**.

This fourth conference will bring together academics and industrials from all over the world. The aim of the conference is to provide an international forum for experts to promote, share, and discuss various issues and development in the field.





# **HONORY COMITEE**

## **Honorary President:**

**Pr. Mohamed El Hadi, LATRECHE**

President of the University

## **Vice honorary President:**

**Pr. Nabil, BELKHIR**

Director of the Institute of Optics and Precision Mechanics, IOMP

## **Vice honorary President:**

**Pr. Riadh, BADJI**

Director of the Research center in Industrial Technologies, CRTI

# **ORGANIZING COMMITTEE**

**Chairman: Pr. Kamel, LOUCIF**

**Vice Chairwoman: Dr. Fatiha, KERAGHEL**

**Vice Chairman: Pr. Halim, MERABTI**

## **Members:**

- **Dr. Semchedine FEDALA**
- **Dr. Abla GUECHI**
- **Dr. Akram ZEGADI**
- **Dr. Bousaha BOUCHOUL**
- **Dr. Boubekeur Mohammed Bilel MERTANI**
- **Dr. Hamza FERHAT**
- **Dr. Farouk LAIDOUDI**
- **Mr. Nacim BENACHOUR**

## **SCIENTIFIC COMMITTEE**

**President : Pr. Boualem, KESKES**

**Vice President : Pr. Redouane, DERAJ**

**Vice President: Pr. El Hadj, OUAKDI**

### **Members:**

1. **Hocine, OSMANI**
2. **Rachid, LOUAHDI**
3. **Sabira, MOUHOUBI**
4. **Ferhat, DJEDDOU**
5. **Mohamed, HAMIDOUCHE**
6. **Azzedine, SOUALEM**
7. **Mostafa, KOLLI**
8. **Nafissa, KHANAFI**
9. **Ahmed, FELKAOUI**
10. **Zahra, MALOU**
11. **Said, BOUZID**
12. **Saad, ABEDESSALEM**
13. **Farouk, BENALI**
14. **Abdelghani, MERDAS**
15. **Dalila, BENMAHDI**
16. **Fouad, ROUMILI**
17. **Abdelaziz, FACI**
18. **Yazid, FIZI**
19. **Hind, LAOUAMRI**
20. **Layachi, BOUSSOUAR**
21. **Mourad, DEMOUCHE**
22. **Ismail, BENTERKI**
23. **Elhadi, BOURAHLI**
24. **Mourad, BOUTLIKHT**
25. **Mohamed, RAHMANI**
26. **Abdessalam, BENAMMAR**
27. **Nacer, TALA**
28. **Bilel, CHENITI**
29. **Latifa, ALIMI**
30. **Yamina, MEBDOUA**
31. **Mohamed, OUCHABANE**
32. **BOUSAID, OUZINE**
33. **Kamel, CHAOUI**
34. **Mabrouk, BOUABDALLAH**
35. **Ammar, HAIAHEM**
36. **Rachid, TIBERKAK**
37. **Samir, LACHEHEB**
38. **Djamel, MIROUD**
39. **Abdellah, HADJ**



40. Ammar, AMOURI
41. Zakaria, BOUMERZOUG
42. Nedjmedine, BOUNAR
43. Kamel, BOUDEGHDAGH
44. Ammar, GUEDRI
45. Ahmed, MAATI
46. Omar ALLAOUI
47. Ali, DEBIH
48. Hocine, BELHOUCHE
49. Naceredine, BENSAID
50. Fethi, BENKHENAFOU
51. Mustapha, ALLOUTI

### ***FOREIGNERS :***

- |                          |                 |
|--------------------------|-----------------|
| 1. Fakher, CHAARI        | (Tunisia)       |
| 2. Mohamed, HADDAR       | (Tunisia)       |
| 3. Rafael, M. BOUGMA     | (Burkina Fasso) |
| 4. Nouredine, FENINECHE  | (France)        |
| 5. Abdelkarim, REDJAIMIA | (France)        |
| 6. Hacene, ZAHOUANI      | (France)        |
| 7. Alexandre, MAITRE     | ( France)       |
| 8. Alexandre, VALENCE    | (France)        |
| 9. Tarek, MERZOUKI       | (France)        |
| 10. Tomas, DONEAU        | (Belgium)       |
| 11. Claudine, B. HERMAN  | (Belgium)       |
| 12. Cecile, MOUCHERON    | (Belgium)       |
| 13. Hakan, KALELI        | (Turkey)        |
| 14. Mahmut, ALTINER      | (Turkey)        |
| 15. Akram, TOFSKI        | (Turkey)        |
| 16. Moataz, ATALLAH      | (UK)            |
| 17. Giorgio, BIZARI      | (UK)            |
| 18. Rau, GIULIETTA       | (Italy)         |
| 19. Ridlin, IDDA         | (Germany)       |

# 4th International Conference on Mechanics and Materials (ICMM'23)

## PROGRAM

Monday 06/11/2023	
8h-9h00	<b>Welcome-Registration</b>
9h00-10h30	<b>Opening Ceremony</b>
10h30-11.00h	<p><b>Plenary Session 1</b>  “Additive Manufacturing to process soft magnetic lattice structures for aeronautical applications ”</p> <p><b>Pr. NOUREDINE FENINECHE</b>  <i>ICB UMR 6303, CNRS, Univ. Bourgogne Franche-Comté, UTBM, F-90010 Belfort, France</i></p> <p>Introduced by: <b>Pr. A.S. Benammar &amp; Pr. B. Keskes</b></p>
11h00-11h30	<p>Poster Session 1 &amp; Coffee break  <b>A. Zegadi &amp; F. Laidoudi</b></p>
11h30-12.00h	<p><b>Plenary Session2</b>  “Design of A Light Weight Refractory High Entropy Alloy For Industrial Applications ”</p> <p><b>Pr. ABDELKRIM REDJAÏMIA</b>  <i>Institut Jean Lamour, Université de Lorraine, UMR CNRS 7198, Nancy, F-54042, France</i>  <a href="mailto:Abdelkrim.redjaimia@univ-Lorraine.fr">Abdelkrim.redjaimia@univ-Lorraine.fr</a></p> <p>Introduced by: <b>Pr. E.H. Ouakdi &amp; Pr. R. Draï</b></p>
12h00-12h15	<p><b>Oral Session1</b>  (Chairs: <b>Pr. N. Fenineche &amp; Pr. S. Mouhoubi</b>)</p>
12h00-12h15	<b>B. Bouchoul</b> Étude des propriétés mécaniques des composites à base d'une résine photosensible/TiO <sub>2</sub> pour l'impression 3D par DLP
12h15-12h30	<b>Aimen Aouni</b> Analyzing Friction Models for Predicting Pressure and Shear Stress Distributions in Rolling Processes
12h30-12h45	<b>Djamel Batache</b> Effect of pore shape irregularity on the compressive strength of cellular materials
12h45-13h00	<b>Badis Ouahab</b> Novel Robust Fast Terminal Sliding Mode Controller for Distributed 3-DOF Hover Quadrotor



13h00-13h15	<b>Alrifai Hazem</b> Navigating Roller Bearing Lubrication Regimes with Emphasis on Elastohydrodynamic Lubrication
13h15-13h30	<b>Merabet Safia</b> Effet de la trempe libre du polypropylene isotactic sur les propriétés thermiques
<b>13h30-14h30</b>	<b>Lunch</b>
14h30-15h00	<p><b>Plenary Session 3</b> “Intergranular Stress Corrosion Cracking Mitigation of Piping Systems”</p> <p><b>Pr. ABDELMOUMENE GUEDRI</b> <i>Infra-Res Laboratory, Department of Mechanical Engineering, University of Souk Ahras, Algeria</i> <i>a.guedri@univ-soukahras.dz</i></p> <p>Introduced by : <b>Pr. A.K. Redjaimia &amp; Pr. A. Felkaoui</b></p>
15h00-15h15	<p><b>Oral Session 2</b> Chairs : <b>Pr. Smata &amp; Pr. F. Keraghel</b></p>
15h00-15h15	<b>Samir ADJEL</b> Fatigue and Corrosion-Fatigue Defects of Aluminum 1050A
15h15-15h30	<b>Mohamed Hamidouche</b> Effect of welding current on the properties of stainless-steel parts produced by the WAAM-CMT additive manufacturing technique
15h30-15h45	<b>S. DJOUADI</b> Morphological, structural, and magnetic properties of the mechanically alloyed Co63Cr35Mo2 mixture
15h45-16h.00	<b>Mustapha Dahak</b> Experimental and numerical study on free vibration of cracked composite cantilever beam
16h00-16h15	<b>Toufik Bensana</b> The role of vibration analysis in diagnosing rotating machinery failures
16h15-16h30	<b>Lasmi Sofiane</b> Mechanical and thermal properties of poly (ethylene-co-vinyl acetate)/mesoporous silica nanocomposites
16h30-16h45	<b>Amine Hamdi</b> Machinability assessment of unreinforced polypropylene (PP) in turning: study of roughness, temperature, and specific cutting energy
16h45-17h30	<p>Poster Session 2 &amp; Coffee break <b>H. Ferhat &amp; B. Bouchoul</b></p>

## Tuesday 07 / 11 / 2023

8h30-9h30	<p style="text-align: center;"><b>Plenary Session 3</b></p> <p style="text-align: center;"><b>“Start-up: ideas and achievements”</b></p> <p style="text-align: center;"><b>M<sup>me</sup> K. BENCHOUFI</b>, Incubateur &amp; Chargée du design, société Brandt Samha Sétif</p> <p style="text-align: center;">Introduced by: <b>Pr. A.L. Hamouda &amp; Pr. M. Kolli</b></p>
	<p style="text-align: center;"><b>Oral Session 3</b></p> <p style="text-align: center;">Chairs : <b>Pr. R. Ziani &amp; Pr. F. Djeddou</b></p>
9h30-9h45	<b>Abderrahmane BEN YAGOUR</b> Suivi cyclique de la durée de vie résiduelle RUL pour le pronostic des défauts de roulements
9h45 – 10h00	<b>Ferhat Hamza</b> Optimization of machining parameters for multi-pass milling processes
10h00 – 10h15	<b>M. Demouche</b> Application of design of experiments method and ANOVA to study the effect of process parameters on kerf width in plasma arc cutting of mild steel
10h30 – 10h15	<b>Ounissa Cherrad</b> Effect of thickness on the physical properties of evaporated Permalloy/GaAs(100) thin films
10h45 – 11h00	<b>Brahimi Abdelkhalek</b> Elaboration of Kaolin-Bound Porous SiC-Al <sub>2</sub> O <sub>3</sub> Composites
11h00 – 11h15	<b>Abdelkader Tamrabet</b> Effect of porosity on the mechanical buckling of functionally graded ceramic and metal sandwich plate containing a metallic foam core using high quasi-3d theory
11h15 – 12h00	<p style="text-align: center;">Poster Session 3 &amp; Coffee break</p> <p style="text-align: center;"><b>D. Benmahdi &amp; Kh. Ariane</b></p>
12h00 – 13h00	Closing ceremony
13h00 – 14h00	<b>Lunch</b>



## PLENARY SESSION

Authors	Article title
Pr. NOUREDINE FENINECHE	Additive Manufacturing to process soft magnetic lattice structures for aeronautical applications
Pr. ABDELKRIM REDJAÏMIA	Design of A Light Weight Refractory High Entropy Alloy For Industrial Applications
Pr. ABDELMOUMENE GUEDRI	Intergranular Stress Corrosion Cracking Mitigation of Piping Systems
Mme K. BENCHOUFI	Start-up: ideas and achievements

## POSTER SESSION

### Session1

**Monday 6 / 11 / 2023**  
**11h00-11h30**

Authors	Article title
A. BOUZIANE	Conception of vibrating table to isolate copper from plastic
SMAHAT Amine	Harmonic structural analysis of Satellite Separation Mechanism
Okba Abid CHAREF	Enhancement of Vibration Attenuation in Damped Mechanical Systems using a Novel Non-Traditional Tuned Mass Damper with Negative Stiffness
F. MATOUK	Dynamic characterization of a composite material Glass/Epoxy
AOUFI Djalila	Effect of Plasticizer Content on the Properties of Biodegradable coating based on Starch/ Microcrystalline Cellulose Blend
Lahcene FELLAH	Effect of barium doping on the properties of NiO thin films
BOUCHAREB Samir	PROTHESES PAR FABRICATION ADDITIVE (IMPRESSION 3D)
CHADI Kamel	The effect of the Geometry and Material Type of Heat Sink on the Cooling of the Electronic Chip
CHADI Kamel	Impact of the Diameter Dimension of Multi-Channel Cooler on the Flow and Temperature Distribution
Leila LAMIRI	Effect of printing direction on 3D printed 3 DM ABS black reins specimens by Stereolithography SLA

FOURAR Issam	A numerical analysis of the mixing effect caused by internal helical fins inside an additively manufactured tube
FOURAR Issam	Effect of pores geometry on the heat transfer for longitudinal pores.
KATIB Hamlaoui	Study the effect of 3D printing parameters on the cross-linking rate of stereolithography.
BOUHANK Antar	Reduce Porosity in CMTed Aluminium Parts (Walls and Massive Parts)
BENCID Abdeslam	Effect of the Free Quenching Residual Stresses on the Thermophysical and Morphological Properties of Acrylonitrile-Butadiene-Styrene (ABS).
CHADI kamel	The Effect of Micro-channels Geometry on the Fluid Flow Characteristics
KAHLOUCHE Abdesalem	Caractérisation microstructurale et mécanique d'une couronne élaborée par fabrication additive
Ammar HABOUSSI	Evaluation of the Effect of Infill Patterns and Orientations on Mechanical Properties of 3D-printed samples
TALANTIKITE Massil	SIMULATION AND STUDY OF STRUCTURE AND HARDNESS OF STEEL SHEET AFTER ECAP
ZIANI.B	Modeling the path of the cutting tool for the 5-axis CNC machine
Abderrazak KEDADRIA	Topology Optimization of Customized Fixation Plate for Treating Middle One-Third Clavicle Fracture
Houari AOUED	Low-Cost Inertial Measurement Unit, Application to: Tilt-Ducted-Fan Unmanned Aerial Vehicle
DJILI Abderrahmane	Global and Local Strain Evaluation in Tensile Test of AL2017-T4 Friction Stir Welded Joint Using Digital Image Correlation
Khouloud BAALI	Effect of varying submerged arc welding speeds on the metallurgical structure of steel for LPG cylinder manufacture
BELAID Hichem	Bending analysis of sandwich plates with different face sheet materials and functionally graded
H. BALIT	Influence of fibers on the thermal conductivity of the composite materials
Zeyneb CHERMAT	Effet de l'oxyde de fer sur l'élaboration d'une céramique chamotte carbone
Soufyane AOUNALLAH	Study of friction and wear of polystyrene crystal using Taguchi technique
Soufyane AOUNALLAH	Tribology of polystyrene sliding against steel
Abdelhakim DJALAB	Effet des contaminants du sable sur l'usure des contacts élastohydrodynamiques
KESKES Boualem	Quasi-static indentation and low-velocity impact response of an aluminium honeycomb sandwich structure
KESKES Boualem	Experimental investigation of flexural static and fatigue behavior of Nomex Honeycomb Sandwich Panels and modelling



Malika Saidi	Fabrication et caractérisation de composites flexibles à matrice silicone renforcées par des nanoparticules céramiques KNN
Abla GUECHI	Structural and mechanical properties of the ternary silicide $Gd_2Re_3Si_5$
Abla GUECHI	Etude numérique de cellules solaires à double absorbeur à base de tellure de cadmium (CdTe) et de disiliciure de fer ( $FeSi_2$ )
Aissa BOUDILMI	Determination of the relation between the pressures, young's modulus and poisson's ratio from continuous conical indentation testing
Abdelhafid RAHMANE	Effect of the location added mass on natural vibration of laminate composite structure during measurement
KHELLAF IKRAM	Recycled polystyrene used as a binder for optical glass finishing pellets

## Session 2

**Monday 06 / 11 / 2023**

**16h45-17h30**

Author	Title
Imane RADJA	Spray-Coated assisted synthesise of Cu: SnS <sub>2</sub> thin films for antibacterial activities and photocatalytic properties
TOUNSI Assia	Elaboration, Design, characterization and Mechanisms of PANI-MnO <sub>2</sub>
D. EMBAREK	Influence of quenching temperature on the characteristics of a high strength material: 42CrMo4
Djamel DJEGHADER	Mechanical behavior under static, dynamic and cyclic loading test of jute reinforced polyester composite material
A. BOUKELLOUD	Statistical modelling of the fracture resistance of brittle materials: case of concrete
A. BEKHOUCHE	Effect of solution treatment on the martensitic transformation in NiMnSn Heusler alloy
A. BOUZIANE	Improvement of cementitious materials by using artificial aggregates
C. DJIDJELI	Elaboration and characterization of ZnO and AZO thin films by Sol-Gel method, the effect of incorporating Ag nanoparticles
S. ATTAF	Synthesis and characterization of $Y_{1-x}Ca_xBa_2Cu_3O_y$ superconductor ceramics
A. MANGOUCI	Effect of Temperature and Humidity on the Mechanical Behavior of a Cotton Yarn
LACHACHE Rafika	Strength and Mechanical Behavior of Fiber Reinforced Clayey Soil: Experimental Study

**November 6-7<sup>th</sup>, 2023 Setif, Algeria**

DERGHOUM Romayssa	Tribological and Morphological properties of films deposit on metallic prostheses
Ikram KADRI	Effect of variation in stiffener shape on panel behavior under dynamic loading
N. MEZIANE	Simulation of vehicle behavior when passing an obstacle. Optimization of the suspension
TRADKHODJA Boutheina	Study on Vibration Analysis of Hybrid Laminated Bio-Composites
Mohammed Amine ZAFRANE	Acoustic Environment Analysis for Launch Vehicles and Satellite Impacts
Mohamed-Said CHEBBAH	Numerical modelling of the preheating temperature on cast IN-738 Ni Superalloy TIG welding
ATEF CHIBANI	A numerical analysis of the melting process of Phase change material-metal foam-based latent thermal energy storage.
DJENDARA Abdelhakim Amine	Comparison of the two Fluid Ostwald with Newtonian Fluid Effect in Hydrodynamic Lubrication Slid Bearing Film
Keltoum MOKRANI	Optimisation des paramètres influençant la qualité d'un produit en emboutissage de tôles
ATOUI Anfel	Caractérisation chimiques, géométriques et mécaniques des aciers destinés à la mise en forme par déformation plastique
C. DJIDJELI	Elaboration and characterization of ZnO and AZO thin films by Sol-Gel method, the effect of incorporating Ag nanoparticles.
Fayssal BOUFELGHA	Development of ZnO nanoparticles for polymer reinforcement
Leila BECHANE	Numerical optimization of (FTO/ZnO/Cs <sub>2</sub> AgBiBr <sub>6</sub> /P3HT/MO) perovskite solar cell
ZELLAGUI Rahima	Characterization of fiber of palm for reinforced polymer
MOHAMMED AMINE BELYAMNA	the Effect of Welding Current and Speed on The Thermal and Residual Stress Distributions of A 100% Austenitic Pipes Butt Weld
Abdelhalim ALLAOUI	Numerical Simulation of Fatigue Crack Propagation In 304L Stainless Steel
Chouaib ZEGHIDA	Intergranular Stress Corrosion Cracking Mitigation Using Mechanical Stress Improvement Process
Ismail GHEMRAS	Exalted dual-scale surface roughening in laser ablated aluminum capped with a transparent thin fim: Wetting and anti-icing behavior
SALIMA ABERKANE	Micromechanical behavior study of delta phase of the different morphologies of 316L alloy elaborated by WAAM
S. FEDALA	Nouvelle Approche D'estimation De La Durée De Vie Résiduelle Des Roulements
S. FEDALA	Contribution Au Diagnostic Intelligent Des Défauts Des Arbres Tournants

# Session3

**Tuesday 7 / 11 / 2023**  
**11h15-12h00**

Author	Title
BECHANE Kawther	Electron-impact ionization of Argon 3p
Asma ABCHI	Spreading coefficient effect of thin films on the optical glass
GAIDI Fayçal	Les problèmes liés à l'exploitation des circuits de refroidissement de la Raffinerie de condensât RA2K-SONATRACH- SKIKDA
F.Z. MESSAGIER	Effect of graphene oxide nanosheets on the microstructure and morphology of the electrodeposited Ni-Co coatings
Imene ABDEDAIM	Effet de la cémentation sur le retour élastique dans l'essai d'étréage pliage en U
BELKADI Noufel	A new algorithm to optimize the effect of manufacturing errors on the kinematic and dynamic performances of a planar mechanism
HOSNA Abdenour	PSO-JAYA hybrid algorithm to optimize the design of a constrained mixed variable speed reducer
KOUACHI Mohamed	Simulation of temperature distribution during the butt-joint friction stir welding of stainless steel 304L
Tallal HAKMI	Mathematical modeling of surface roughness in polyoxymethylene (POM-C) turning
GASMI Khalid	An Enhanced African vulture's optimization algorithm for mechanical design problems
Dalila BENMAHDI	Détection Automatique de Défauts Mécaniques par Méta-Heuristiques
Ikram DAKHOUCHE	Study of the effectiveness with mechanical and optical profilometer of organic inhibitors against corrosion wear in HCl acid of XC48 steel's surface
Sofiane BLILITA	Electronic properties of MAX phase materials (Ti <sub>2</sub> AlC and Ti <sub>2</sub> AlB)
KRIM Samah	Characterization of wear resistance and adhesion of Ni-Al surface alloy produced by electrodeposition on aluminum alloy
BOUCHELOUCHE Fatima	Comportement mécanique d'une soudure par friction malaxage avant et après un traitement de vieillissement post-soudage
Kahina TAIEB	Parametric Study of the polishing process of ceramic scintillator used as radiation detector in Positron emission tomography
ARIANE Khalissa	Kinetic study of transparent fluormica glass-ceramic
YOUNES Leyla	Effet du temps de traitement sur quelques paramètres de l'échange ionique d'un verre silico-sodo calcique

MOUNIR Hassena	Study of technological parameters of polishing animated by a vibratory movement
Badra BOUCHAREB	Elaboration and Characterization of Nanocomposites with PVC Matrix Reinforced by Nanoclays: Case of Montmorillonites
Samira FOUDI	Elaboration and characterization of perovskite oxide for photocatalyse application
Imene ABID	Elaboration et Characterization des couches minces d'Oxyde de Cuivre Préparées par Electrodeposition
Samira KEROUANI	Efficacité des stéarates de Cobalt dans l'amélioration de l'oxo-biodégradation des films de polyéthylène
S. KHELFI	Optimization of the aluminum dross washing for subsequent use in the synthesis of the spinel ( $MgAl_2O_4$ )
Abdelaziz GAHMOUSSE	Elaboration Processes of $Fe_2O_3$ -Aluminosilicate Glass for Energy-Efficient Coatings
Nada BOUMAZZA	NiP Thin Films Synthesis with Desired Properties Via Electrodeposition
Ahlem MELLOUL	Investigation of magnetic and structural properties of $CoxFe_{100-x}$ thin films thermally evaporated onto amorphous silicon and Si(111) substrates
RIZI Hadje	Évaluation de l'effet pouzzolanique à l'aide d'une méthode basé sur la conductivité électrique
Wissem BOUGHOUICHE	Ni-W Thin Films: Elaboration and Characterization
Soumia Hamdani	Nano-indentation of bcc Vanadium: Atomistic simulation of plastic deformation
H. LAOUAMRI	Investigation on solid particle erosion behavior of jute fiber reinforced polyester composite
ARIANE khalissa	Damage behaviour of polyurethane foam-cored sandwich panel subjected to localized indentation
Mahdi Zakaria BELAÏB	Etude du comportement mécanique en compression des matériaux cellulaire en fibres de verre
Abderrahmane ABDESSELAM	Influence of elevated temperatures on the bond between CFRP and concrete
Ahcene OUBOUZID	Validation of a mathematical model for fatigue-induced damage in composite sandwich structures
Fahima ARAB	Investigation of new surface acoustic wave modes in IDTs/ $ZnO$ / $Al_2O_3$ micromechanical pillar resonators
BECHANE Kawther	Electron-impact ionization of Argon 3p
Belkadi Noufel	A new algorithm to optimize the effect of manufacturing errors on the kinematic and dynamic performances of a planar mechanism
BELAIB Mahdi Zakaria	Optimisation de la conception des multiplicateurs de vitesse des éoliennes



Zeyneb CHERMAT	Effet de l'oxyde de fer sur l'élaboration d'une céramique chamotte carbone
YOUNES Leyla,	Effet du temps de traitement sur quelques paramètres de l'échange ionique d'un verre silico-sodo calcique
BELAIB Mahdi Zakaria	Etude du comportement mécanique en compression des matériaux cellulaire en fibres de verre
KHIRANI Dalel	Investigation of progression failure of sandwich structure loading in monotonic 3-points bending test using acoustic emission
KHIRANI Dalel	Polyurethane foam sandwich structures collapse modes under three-point bending
MOUHOUBI. S	Investigation of local plant fibers "Diss" in the development of plaster matrix composite
BALI.T	Optimization of a copper-coat composite coating
CHOUITER Adel	Conception et réalisation d'un dispositif de cisaillement pour les panneaux sandwich
CHOUITER Adel	Optimisation du choix des outils de coupe pour l'usinage des poches quadrilatères en 2D1/2
Ahcene OUBOUZID	Numerical study with FEA of honeycomb cellular materials subjected to buckling
El hadj OUAKDI	Étude du retour élastique des panneaux sandwich métal-polyuréthane
BARBERIS Marwa	Determination of the Mechanical Properties of Thermal Sprayed NiCrAlY Coatings using Experimental and Numerical Simulations
Wahiba SLIMANI	Study of efficiency of the heterogeneous cell CdTe/ CdS/ SnS
LAMECHE Norelhou	Synthèse de couches minces d'oxyde de cuivre par sol gel
Yasmine NASRI	L'étude de l'effet de la forme et du taux de remplissage sur les propriétés mécaniques des pièces réalisées avec l'impression 3D
Fatiha KERAGHEL	Characterization of enameled steel sheets
MERTANI Boubekeur Mohammed Bilel	Comportement mécanique des structures en nid d'abeille soumises à la compression rapide
M.L. BELLA	Effect of the addition of aluminum hydroxide Al (oh) 3 on the sintering of djebel Debagh kaolin
MERTANI Boubekeur Mohammed Bilel	Etude du comportement mécanique d'un composite sandwich en mousse soumis à l'impact dynamique
HAKIMI Nesrine	Étude des caractéristiques mécaniques du polymère cellulose dans l'alfa et le coton
LOUCIF Maroua	Simulation of Hetero-junction ZnO/NiO by "SCAPS 1D" Calculation
Lamine TABERKANI	Structural, magnetic and electrical properties of thermally evaporated NixFe1-x thin films

Lamine TABERKANI	Investigations of the structural, magnetic and electrical properties of thermally evaporated $\text{Ni}_x\text{Fe}_{1-x}$ thin films
Zegadi. A	improvement of surface state of a transparent $\text{MgAl}_2\text{O}_4$ spinel by deposition of a metal oxide layer
Zegadi. A	Mechanical behavior of 3D printed bamboo-inspired cellular structures
Fatiha KERAGHEL	Etudes des fissures dans les tôles embouties fabriquées par l'entreprise nationales SONARIC.

***" Plenary session "***

# Additive Manufacturing to process soft magnetic lattice structures for aeronautical applications

NOUREDINE FENINECHE<sup>1</sup>, SHUOHONG GAO<sup>2</sup>, MEHER ZAIED<sup>1</sup>

<sup>1</sup>ICB UMR 6303, CNRS, Univ. Bourgogne Franche-Comté, UTBM, F-90010 Belfort, France

<sup>2</sup>National Engineering Laboratory for Modern Materials Surface Engineering Technology, Guangdong Academy of Sciences, Guangzhou 510651, P.R. China

## ABSTRACT (1,000 characters)

*Most of the studies on the Additive Manufacturing metallic materials are focused on the development of the mechanical properties of the parts obtained and only a limited number of the studies has been devoted to the manufacturing of parts with other remarkable properties (thermal, electrical, magnetic). Studies on the manufacturing of ferromagnetic materials (the most common type of magnetic material used in electrotechnical applications) are still few. The manufacture of parts in iron-silicon alloys (FeSi) by AM process having relevant magnetic properties for electrical engineering applications must allow to reach properties close to those obtained from traditional processes and using standard magnetic alloys (FeSi, FeNi, FeCo, etc) which have a high saturation induction ( $B > 1.6$  T) and low coercivity ( $H_c < 100$  A/m); Among the soft ferromagnetic materials targeted in this work, the iron-silicon "FeSi" with Si contents  $> 6\%$  by mass, presents intrinsically interesting magnetic properties. Nevertheless, the interest of working with a Si content higher than the classical materials ( $> 3\%$  in mass) can improve magnetic characteristics especially magnetic losses, however this increase involves a reduction of its ductility. The aim of this research is to achieve the manufacturing of samples or work pieces (by the LBM metal additive manufacturing technologies) starting from a ferromagnetic powder electrical silicon steel with a Fe-3wt.%Si and Fe6.5wt Si composition.*

## KEY WORDS (3 to 6 key words)

SLM process; magnetic materials; FeSi alloys; LBM

## I. INTRODUCTION

Electrical machines (EMs) are a key role in modern industry. EMs are applied in ranging scales from small mW or medium kW scale to large MW scale [1]. They are widely used for domestic daily life, propulsion, electrical power generation and more specialized industries. They produce virtually all the electric power in the world through electro-mechanical conversion [1,2]. As EMs are heavily utilized, the

research community is continuously seeking further development of EM designs [3]. Especially, the development of new materials and their industrial integration through next-generation production methods, which has been regarded as the most significant route for improving the performance of the EMs overall [1]. The practical applications of the machines are limited significantly by the characteristics of materials, whereas the machine performance and their special application could be achieved fine-tuning via design and optimization [1, 3]. Therefore, it is necessary to develop some ingenious processing routes for EMs to meet the above requirements [4]. At present, a potential solution had been proposed in novel additive manufacturing (AM) technologies that can obtain the EM design of previously unfeasible part topologies [5-8]. Selective laser melting (SLM) technology is one of the most versatile AM technologies. Due to the commercial maturity and capacity for fusing high-density, low porosity parts, the SLM technique was the most widely encountered AM method for the study of manufacturing EM materials so far, such as Fe-Ni, Fe-Si (iron steel), Fe-Co alloys and soft magnetic composites [1, 6-8].

## 1 Materials and methods

### 1.1. Powders characterization

In this work, Fe-3% and 6.5%wt.Si alloys powder were used as the raw material. The powder was purchased from POCO Holding CO., LTD (Shenzhen, China). Shape, morphology, and chemical composition of the powder were characterized by a scanning electron microscopy (SEM JEOL-5900 LV, Japan) equipped with an energy dispersive spectroscopy (EDS) unit. The particle size distribution of the powder was measured by a laser diffraction powder sizer (Mastersizer 2000, Malvern Instruments Ltd., UK). Besides, the overview and representative magnified

morphology of the used metallurgical powder are presented in **Erreur ! Source du renvoi introuvable.**(a). The powder particles were mainly spherical and near-spherical in shape, without satellite particles on the surface. That is an important characteristic of excellent flowability which meets exactly the requirement during the SLM process.

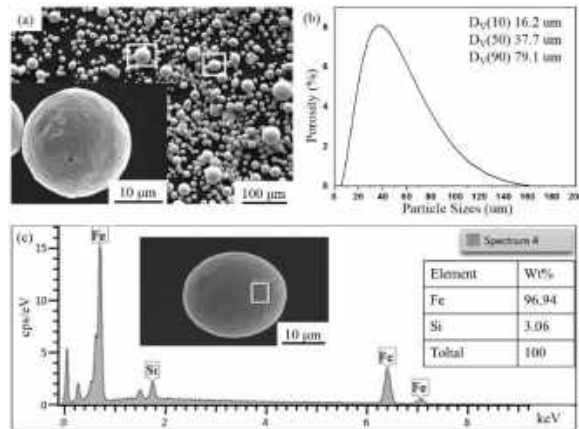


Fig. 1 (a) Macroscopic morphology of the feedstock powder; (b) particle size distribution; (c) chemical composition of powder by EDS.

The abstract contains a summary of approximately 1,000 signs, followed by key words (from 3 to 6 maximum). This short introduction presents the purpose of the text and places it in the scientific context of the authors. It will be organized around sections that will present the main results and the contributions of the communication to the theme to which it relates. The bibliographic references of the text are placed at the end of the text; they should not exceed thirty references.

### 1.2. SLM SAMPLES PREPARATION

A series of cubic specimens with dimensions of 8 mm × 8 mm × 8 mm were prepared using a selective laser melting machine MCP Realizer SLM 250 system (MCP-HEK Tooling GmbH, Germany). It was equipped with an Nd-YAG fiber laser, an adjustable focal length, and a maximum power of 400 W. As described in **Erreur ! Source du renvoi introuvable.**, a zigzag scanning pattern with the neighboring laser track rotation of 90° was utilized during the SLM process. Five different laser powers (P, W) with 50W, 70W, 100W, 140W, 180W were used to prepare a series of SLM cubic samples.

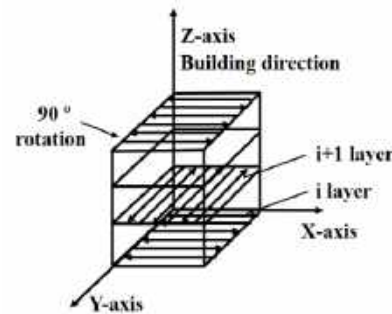


Fig. 2. SLM scanning strategy used to process samples.

## II. CONCLUSION

In this work, a series of Fe-Si alloys were successfully prepared by SLM technology using metallurgical powder. The impact of laser energy density on the surface morphology, surface roughness, microstructure of the selective laser melted Fe-Si alloys was analyzed and described in details.

## REFERENCES

- [1] H. Tiismus, A. Kallaste, T. Vaimann, A. Rassõlkin, State of the Art of Additively Manufactured Electromagnetic Materials for Topology Optimized Electrical Machines, Additive Manufacturing, (2022) 102778.
- [2] G. Ouyang, B. Jensen, W. Tang, J. Schlager, B. Hilliard, C. Pan, B. Cui, K. Dennis, D. Jiles, T. Monson, Near net shape fabrication of anisotropic Fe-6.5% Si soft magnetic materials, Acta Materialia, 201 (2020) 209-216.
- [3] M.U. Naseer, A. Kallaste, B. Asad, T. Vaimann, A. Rassõlkin, A review on additive manufacturing possibilities for electrical machines, Energies, 14 (2021) 1940.
- [4] C. Zhang, X. Li, L. Jiang, D. Tang, H. Xu, P. Zhao, J. Fu, Q. Zhou, Y. Chen, 3D printing of functional magnetic materials: from design to applications, Advanced Functional Materials, 31 (2021) 2102777.
- [5] B. Zhang, N.-E. Fenineche, H. Liao, C. Coddet, Magnetic properties of in-situ synthesized FeNi<sub>3</sub> by selective laser melting Fe-80% Ni powders, Journal of Magnetism and Magnetic Materials, 336 (2013) 49-54.
- [6] B. Zhang, N.-E. Fenineche, H. Liao, C. Coddet, Microstructure and magnetic properties of Fe-Ni alloy fabricated by selective laser melting Fe/Ni mixed powders, Journal of Materials Science & Technology, 29 (2013) 757-760.
- [7] A. Mazeeva, M. Staritsyn, V. Bobyr, S. Manninen, Magnetic properties of Fe-Ni permalloy produced by selective laser melting, Journal of Alloys and Compounds, 814 (2020) 152315.
- [8] J. Zou, Y. Gaber, G. Voulazeris, S. Li, L. Vazquez, Controlling the grain orientation during laser powder bed fusion to tailor the magnetic characteristics in a Ni-Fe based soft magnet, Acta Mater., 158 (2018) 230-238



*TiTaNiVAL*,  
Design of A Light Weight Refractory High Entropy Alloy  
For Industrial Applications

**ABDELKRIM REDJAÏMIA\***

JAÂFAR GHANBAJA, HIBA KABBARA, GHOUTI MEDJAHI,  
SYLVIE MIGOT, JÉRÔME HILDENBRAND

Institut Jean Lamour, Université de Lorraine, UMR CNRS 7198, Nancy, F-54042, France

\* [Abdelkrim.redjaimia@univ-Lorraine.fr](mailto:Abdelkrim.redjaimia@univ-Lorraine.fr)

## ABSTRACT

*The concept of high entropy alloy (HEA) opens a vast unexplored composition range for alloy design. Thermodynamic approach, Crystal structure, Microstructure and Mechanical properties of the Titanival, a quinary equimolar Refractory High Entropy Alloy (LW-RHEA) will be presented. The selected Titanival including light (Al, Ti) and refractory (Ta) constituent metallic elements is expected to bring the values of the mechanical properties (ductility, tensile strength, etc.) of industrial components, to a high level while keeping a low density.*

**KEY WORDS:**

HEA; Refractory; Phase diagram; Crystal structure; Microstructure; Nano-indentation.

## I. INTRODUCTION

High Entropy Alloys (HEA) is a new class of material [1,2] that has many favorable mechanical and thermal properties, making them a perfect candidate for structural uses in the transportation and energy industries. Basically, the HEA is a mixture of, at least, five metallic elements. This combination has first to answer to the fundamental parameter of the high entropy of mixing  $\Delta S_{mix} \geq 13.38 (mol.K)^{-1}$  (Fig.1a) and to obey to the thermodynamic ( $\Omega$ ), steric ( $\delta r$ ), electronic ( $VEC$ ) and chemical (PSFE) empiric parameters [3, 4] (Fig.1b).

In this study, we are intended to manufacture a new alloy which first posses a high entropy alloy of mixing, responds as much as possible to the phase formation empirical criteria (Fig. 1b) to finally establish the parallel between the experimental results (structural and microstructural) and the theoretical equilibrium phases diagram (Fig. 2).

The selected HEA, is, in fact, a quinary equimolar alloy (Ti, Ta, Ni, V, and Al). This alloy, qualified as Light Weight Refractory HEA is labelled LW-RHEA or, for convenience, *Titanival*. In addition to Ni and V, it includes light (Al, Ti) and refractory (Ta) metallic elements. *Titanival* is expected to bring the values of the mechanical properties (ductility,

tensile strength, *etc.*) of industrial components, to a high level while keeping a low density.

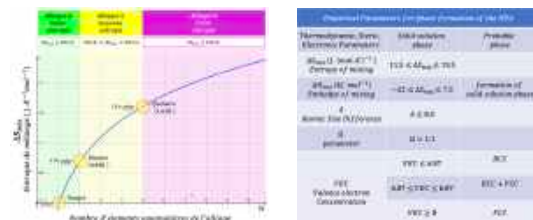


**Fig. 1 a)** Mixing entropy of the alloys versus the equimolar element number, **b)** Phase formation Criteria of the HEA.

The *Titanival* characteristic parameters are gathered in [Tab. 1]. The solidification path of the *Titanival* ( $L$ ,  $\alpha$ ,  $\gamma$  and  $\alpha'$ ) is well illustrated in [Fig. 2a]. One can notice that the melting temperature is about 1600 °C and the freezing domain extends between 1600 °C and 690 °C. A quasi-binary phase diagram is also presented in Fig. 2b, where the chemical composition (20 at % Al) of the studied alloy is indicated by the isopleth in black color vertical dashed line. The volume fraction of each phase and the amount of the alloying elements in the Liquid (L),  $\alpha$ ,  $\gamma$  and  $\alpha'$  (BCC-ordered of  $\alpha$ -phase) phases, are calculated with ThermoCalc™ software using SSOL4: SGTE data base.

System (Alloy)	$T_m$ K	$\alpha_L$ weight $\mu\text{mol}^{-1}$	$\beta$ $\mu\text{cm}^{-1}$	$r$ $\mu\text{m}$	$VEC$	$\delta r$ %	$\Delta H^m$ kJ mol $^{-1}$	$\Delta S^m$ J (mol K) $^{-1}$	$\Delta$	PSEF %
(TiTaNiWAl) $_{125}$	2015	7309	7.78	137.7	5.4	5.98	-27.36	13.38	0.99	80

**Tab. 1.** HEA parameters of the *Titanival* alloy.

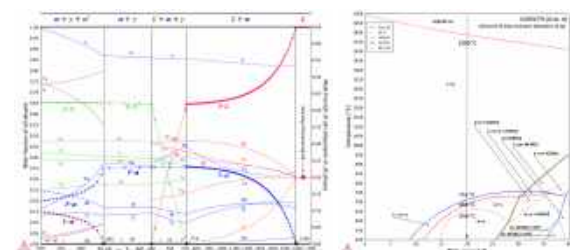


**Fig. 2. a)** Theoretical Phase Diagram of the *TiTaNiAl* alloy  
**b)** Calculated quasi-binary phase diagram for *Titanival* alloy. The chemical composition (20 at % Al) of the studied alloy is indicated by the isopleth in black color vertical dashed line.

## II. MATERIAL AND EXPERIMENTAL PROCEDURE:

A quinary equimolar alloy was prepared with the nominal composition  $Ti_{20}Ta_{20}Ni_{20}V_{20}Al_{20}$ , hereinafter labelled the *Titanival* or LW-RHEA (Light Weight Refractory High Entropy Alloy).

Based on metallic powder elements, with at least 99.9 wt.% purity, the *Titanival* alloy was synthesised by VAC (Vacuum Arc Melting) in Argon atmosphere as pellets. The latter were re-melted at least 5 times to ensure homogeneity and then dropped in water.

Various techniques, including, XRD, Electron Diffraction, Scanning electron microscopy (SE and BSE modes), Transmission electron Microscopy imaging (TEM, STEM, HAADF), Spectroscopy (EDS), FIB (Focused Ion Beam), were employed to characterise the crystal structure and the microstructure of the as-cast *Titanival* alloy. The experimental results are related and confronted to the thermodynamic predictions.

## III. RESULTTS AND DISCUSSION

### IIIa. Microstructure of the as-cast *Titanival* alloy

The SEM-BSE (Fig.3) points out that the microstructure of the as-cast *Titanival* is compound of two solid solutions, two phases ( $\alpha + \gamma$ ), and a lamellar aggregate. The BF-TEM image (Fig. 4) shows that the  $\alpha$  phase is located in between the equiaxed  $\gamma$  grains. When based on Fig. 2, the lamellar aggregate could be identified as a peritectic.

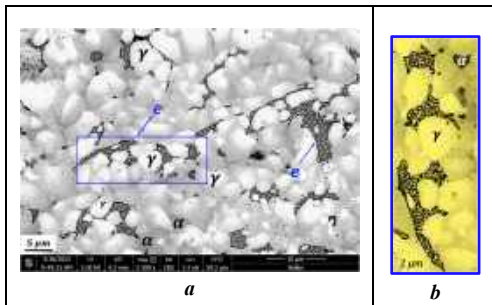


Fig. 3. a) SEM-BSE images of the as-cast *TiTaNiVAl* alloy: two solid solution ( $\alpha + \gamma$ ) and b) lamellar aggregates.

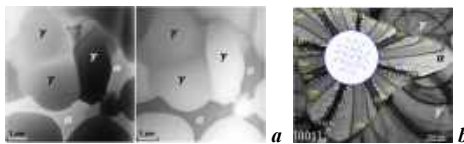


Fig. 4. a) BF-STEM / HAADF images pointing out the brighter and darker phases in relation with the high and low atomic number, respectively. b) BF-TEM image of  $\alpha$ -phase seen along  $\langle 001 \rangle$ .

The BF-STEM image and its corresponding HAADF show the distribution of the alloying element in the two solid solution  $\alpha$  and  $\gamma$  phases (Fig. 4). One can notice that the  $\gamma$ -phase appear brighter than  $\alpha$ -phase indicating that  $\gamma$ -phase is rich in element with higher atomic number (notably Ta) while  $\alpha$ -phase is rich in Ti (Fig. 5a). This result is confirmed by the the EDS profile along  $\gamma/\alpha/\gamma$  grains (Fig. 5b).

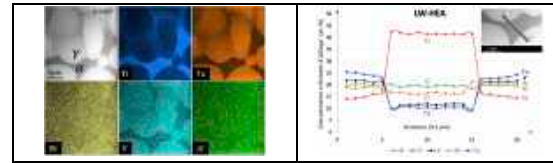


Fig. 5. a) EDS X maps of the alloy elements across  $\alpha$  and  $\gamma$  phases. One can notice that Ti and Ta segregate in  $\alpha$  and  $\gamma$ , respectively. b) EDS line-profiles of the elements across  $\gamma/\alpha/\gamma$  phases (insert).

### IIIb. Crystal structure of the *Titanival* phases, $\alpha$ -pahse

The crystal structure is focused only on the  $\alpha$ -phase.

The Fig. 6 points out SAED patterns recorded along  $\langle 001 \rangle$ ,  $\langle 111 \rangle$  and  $\langle 110 \rangle$  zone axes pointing out the  $(4mm)$ ,  $(6mm)$  and  $(2mm)$  ideal symmetries leading to  $m\bar{3}m$  point group. The dashed circles, as drawn, lead to the centred Bravais lattice and  $Im\bar{3}m$  or  $Ia\bar{3}m$  space group. Taking into account the reflection extinctions due to the glide plane  $a$ , the space group is in fact  $Im\bar{3}m$ .

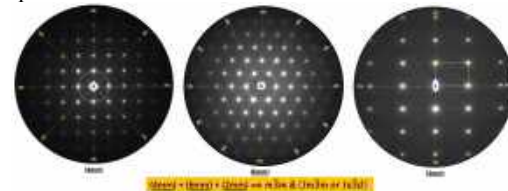


Fig. 6. SAED patterns recorded along  $\langle 001 \rangle$ ,  $\langle 111 \rangle$  and  $\langle 110 \rangle$  zone axes pointing out the  $(4mm)$ ,  $(6mm)$   $(2mm)$  ideal symmetries.

### IIIc. Mechanical properties, nanoindentation

Nanoindentation measurements were performed using a Berkovich indenter. Indentation maps (7x7) were performed at an applied load of 10 mN. Hardness and Youngs modulus were evaluated using the well-known Oliver & Pharr methodology. The results are gathered in Tab. 2.

Indentation number	1	2	3	4	5	6	7	8	9	10	11	12	13	14	15
$E^*$ (GPa)	228	343	231	224	209	242	222	310	380	218	307	332	214	220	237
HV <sub>0.05</sub> (Vickers)	1099	1009	1096	1275	968	1182	1250	1662	1276	1319	1496	1170	1576	2420	1660

Tab. 2. Elastic modulus and hardness of the *Titanival* alloy derived from nanoindentation mapping.

## IV. CONCLUSION

The *Titanival* is a dual phase alloy. Although certain discrepancies exist between the theoretical calculations and the experimental results, the fact remains that the contribution of the latter is valuable. These divergences would be less if the study was conducted on equilibrium states of and not resulting from quenching states: tempering heat treatments with long periods are necessary to reach equilibrium, especially at lower temperatures. Calculated isopleth provides useful guidelines to explain the origin of the lamellar aggregate developed in the *Titanival* alloy.

## REFERENCES

- [1] J.W. Yeh *et al.*, Adv. Eng. Mater., 6, 299-303 (2004)
- [2] B. Cantor *et al.*, Mater. Sci. Eng. A, 375-377, 213-218 (2004)
- [3] M.H. Tsai *et al.*, Mater. Res. Lett., 4 : 2 90-95 (2016)
- [4] D.B. Miracle *et al.*, Acta Mater., 122, 448-511 (2017)

# Intergranular Stress Corrosion Cracking Mitigation of Piping Systems

ABDELMOUMENE GUEDRI <sup>\*1</sup>, CHOUAIB ZEGHIDA <sup>1</sup>, ABDELHALIM ALLAOUI <sup>2</sup>  
AND MOHAMMED AMINE BELYAMNA <sup>1</sup>

1. Infra-Res Laboratory, Department of Mechanical Engineering, University of Souk Ahras, Algeria; E-Mails: [a.guedri@univ-soukahras.dz](mailto:a.guedri@univ-soukahras.dz); [c.zeghida@univ-soukahras.dz](mailto:c.zeghida@univ-soukahras.dz); [m.belyamna@univ-soukahras.dz](mailto:m.belyamna@univ-soukahras.dz)

2. Department. of Mechanical Engineering, University of Khenchela, Algeria; E-Mail: [allaoui.abdelhalim@univ-khenchela.dz](mailto:allaoui.abdelhalim@univ-khenchela.dz)

## ABSTRACT

*The purpose of this paper is to review the influence of residual stresses on the reliability of piping under IGSCC. A procedure such as induction heating stress improvement (IHSI) is a means of altering the residual stress pattern in a pipe. Examples of the use of this technique for the initiation and growth of stress corrosion cracks in pipes are presented for various pipe sizes and residual stress distributions. The effectiveness of IHSI as an eternal countermeasure for IGSCC depends upon the level of service stress as well as the crack size and its large benefit is immediately apparent.*

**KEYWORDS** : Probabilistic fracture mechanics, crack initiation and growth, residual stresses, structural reliability, intergranular stress corrosion cracking, pressured pipes.

## I. INTRODUCTION

Remedies for IGSCC are based on the observation that all three factors are required simultaneously for cracking to occur. Thus, the absence of any one of these factors should contribute to alleviating cracking. The focus of this paper is on removing tensile stresses in the areas of observed cracking. Although residual stresses as well as thermal and mechanical loading can contribute to the tensile state of stress, the welding residual stresses are of primary concern here [1-5].

The purpose of this paper is to apply probabilistic fracture mechanics to the analysis of the influence of remedial actions on structural reliability limited to IHSI. The increased need for high performance or very high degrees of reliability or both has led to an increased interest in probabilistic analysis of structural reliability.

This paper describes the stress corrosion cracking model used in the pc-PRAISE [6] for simulating the initiation and growth of IGSCC cracks. This model is

based on laboratory data from IGSCC tests in combination with the calibration of the model using field data from pipe-cracking experience. [2-5] have improved on the prior calibrations by adjusting the modeling of plant loading/unloading cycles in addition to adjustments to residual stress levels, and [3] concluded that equations used in PRAISE to calculate the stress intensity factors to simulate crack propagation need modification. The computational analysis for welding and IHSI treatment has four steps: (1) temperature analysis for welding, (2) residual stress analysis for welding, (3) temperature analysis for IHSI, and (4) residual stress analysis for IHSI. These steps are outlined in the following sections.

## II. CONCEPT OF INDUCTION HEATING STRESS IMPROVEMENT (IHSI)

Before considering ways of removing weld-induced residual tensile stresses, it is worthwhile to review the factors that cause residual stresses. Briefly, welding produces high temperature gradients in a pipe. These gradients cause thermal stresses that exceed the temperature-dependent yield stress of the material and result in residual stresses upon cooling. Certain temperature histories result in inside surface residual tensile stresses, while other thermal histories can produce compressive residual stresses.

In the case of girth-welded pipes, temperature gradients, which cause compressive residual stresses on the inner surface, arise from heating the pipe exterior while the inside is cooled. IHSI uses this concept for improving stresses. That is, as illustrated in Fig.1, the welded pipe is inductively heated from the outside while water flows through the pipe to remove heat from the interior surface.

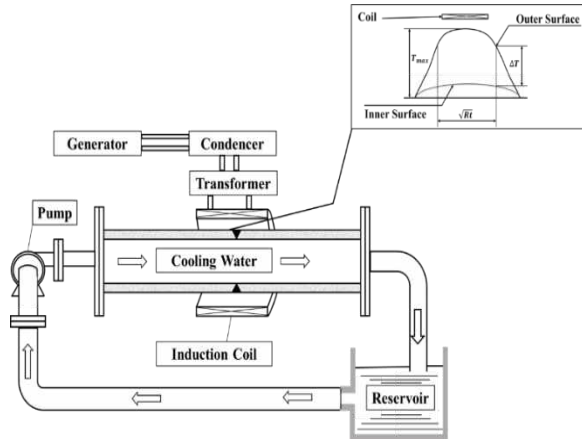


Fig. 1. Concept of the IHSI Method.

### III. RESULTS AND DISCUSSION

#### A. Results without IHSI

In this section, a finite element residual stress analysis of IAS304 stainless steel pipe (interior diameter of 300 mm, a wall thickness of 30 mm) was conducted for girth welding and welding plus IHSI treatment in the next section using ANSYS 20R2. Material constants used in the analyses are obtained from [7]. The same material constants are used for the weld material and the heat-affected zone. After completing the simulation of the pipe butt-welding, residual stresses are established.

The polynomial fitted residual stresses data can be used to calculate cumulative leak probability using M-PRAISE are shown in Fig.2.

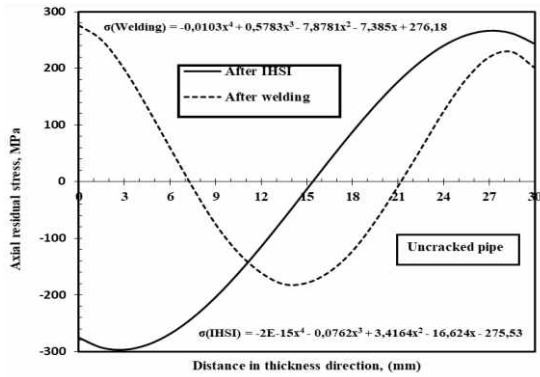


Fig. 2. Axial residual stress distribution versus the wall thickness after welding and IHSI for Uncracked pipe.

Fig.3 compares the field cumulative leak probability given by [2]. In this case, the adjusted residual stress level used to limit the disagreement between predicted and observed leak probabilities was set at 75% of their original values. The resulting predictions had a much more rational basis and were in very good agreement with operational conditions.

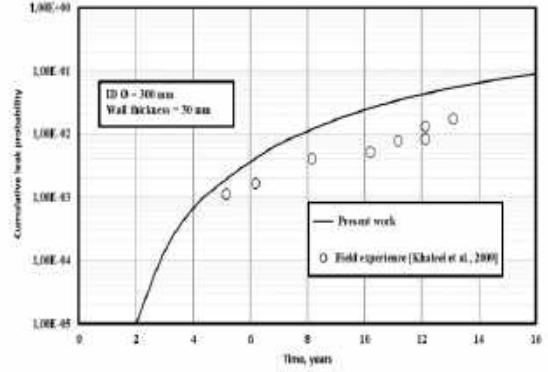


Fig. 3. Field observations of leak probabilities compared with M-PRAISE results for various values of the residual stress adjustment factors and plant cycles.

#### B. Effect of Changing Residual Stresses after IHSI

An analysis of IHSI treatment after welding was then performed. The IHSI coil was modeled as being 152 mm long. The maximum outer surface temperature was 550 °C and the inner surface temperature was 100 °C. A region of nearly constant heat generation density was modeled over the central 76 mm of the coil. The heating decayed parabolically to zero heat generation density at the edge of the coil. These conditions are consistent with the conditions being used and observed in the experimental studies of IHSI [8]. To induce the IHSI treatment the Ansoft Maxwell program simulation tools are linked within the ANSYS Workbench interface.

The residual stress distributions used in this paper were obtained from a computational model for predicting welding-induced residual stresses. The model consists of a thermo-elastic-plastic finite element model. The temperature histories resulting from the thermal model serve as input to the finite element analysis. IHSI treatment after welding can convert the tensile weld residual stresses to compressive values (Fig.2). The computational representation for the IHSI process is identical to that for conventional welding, except that the temperature history is extended to include the temperature history of the IHSI process.

In Fig.4 the calculation of K factors for various crack sizes was performed making use of the influence function implemented in PRAISE code for complete circumferential interior surface cracks. The stress intensity factors are calculated as a function of crack depth for sections with known residual stress distributions and the effectiveness of IHSI as a permanent countermeasure for IGSCC depends upon the level of service stress in the operating condition as well as on the crack depth. A long circumferential crack will be prevented from further extension by IHSI



if the depth is under 30% of the thickness and the service stress is under 75% of membrane stress, which seems to be likely in normal circumstances. For the nominal membrane stress, IHSI cannot keep the crack tip stress in compression. But the level of stress is well below the other case in which no IHSI was applied.

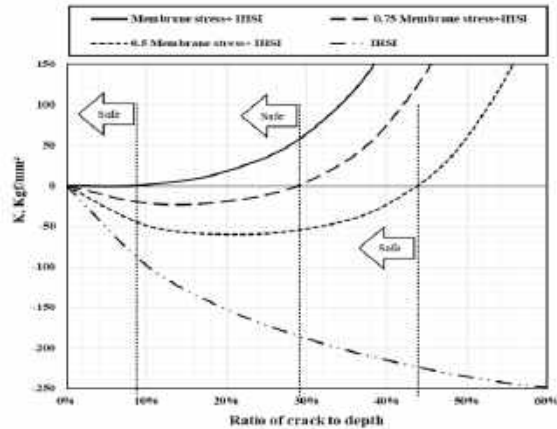


Fig. 4. Observed effect of the applied total stress on the contribution of IHSI.

#### IV. CONCLUSION

From both numerical and analytical evaluations, several key conclusions emerge. First, after the IHSI process, the residual stress can be compressive at the crack tip. This phenomenon significantly mitigates the sensitivity to IGSCC, enhancing the overall integrity of the material. Additionally, a streamlined method for gauging the effectiveness of IHSI on pre-flawed pipes has been proposed. This approach capitalizes on the calculation of stress intensity factors by adhering to the superposition principle. Notably, the computational modeling studies underscored the potential in predicting the impact of the IHSI procedure on weld-induced residual stresses. It also highlighted the utility of these computational models in comprehending the ramifications when the recommended guidelines for IHSI parameters are not strictly followed. Lastly, for those aiming to alter the residual stress during the mid-life phase, employing the M-PRAISE code can prove invaluable. There is a pronounced effect in diminishing leak probabilities after the IHSI treatment, ensuring a longer, more stable operational life.

#### REFERENCES

- [1] Rybicki, E. F., McGuire, P. A., The Effects of Induction Heating Conditions on Controlling Residual Stresses in Welded Pipes. *Journal of Engineering Materials and Technology*, 1982, Vol. 104/267. DOI:10.1115/1.3225075
- [2] Khaleel, MA, Simonen, FA., Evaluations of Structural Failure Probabilities and Candidate In-service Inspection Programs. NUREG/CR-6986; PNNL-13810, Pacific Northwest National Laboratory, Richland, WA. 2009.
- [3] Guedri, A., Zeghloul, A., Merzoug, B., 2009. Reliability analysis of BWR piping including the effect of residual stresses. *International Review of Mechanical Engineering (I.R.E.M.E.)*, pp. 640–645, Vol. 3, n. 5.
- [4] Guedri, A., Djebbar, Y., Khaleel, M., and Zeghloul, A., Structural Reliability Improvement Using In-Service Inspection for Intergranular Stress Corrosion of Large Stainless Steel Piping, in *Applied Fracture Mechanics*. London, UK: IntechOpen, 2012. DOI: 10.5772/48521.
- [5] Guedri, A., 2013a. Reliability analysis of stainless steel piping using a single stress corrosion cracking damage parameter, *Int. J. Press. Vessel. Pip.*, 111–112, pp. 1–11, DOI: 10.1016/j.ijpvp.2013.03.011.
- [6] Guedri, A., 2013b. Effects of remedial actions on small piping reliability, *Proc. Inst. Mech. Eng. Part O J. Risk Reliab.*, 227(2), pp. 144–161, DOI: 10.1177/1748006X13477798.
- [7] Liu, Y., Wang, P., Fang, H., Ma, N., 2021. Mitigation of residual stress and deformation induced by TIG welding in thin-walled pipes through external constraint, *Journal of Materials Research and Technology*, Vol.15, 4636–4651, DOI: 10.1016/j.jmrt.2021.10.035.
- [8] Tanaka, S., Umemoto, T., Residual Stress Improvement by Means of Induction Heating, presented at Session 3 of the Seminar and Countermeasures for BWR Pipe Cracking, EPRI, Palo Alto, Calif., Jan. 22-24, 1980.



***Session T1: Vibration  
and acoustic in  
mechanical system  
and structure***

# Conception of vibrating table to isolate copper from plastic.

A. BOUZIANE<sup>1\*</sup>, F. BOUKHOULDA<sup>2</sup>, AND A. TILMATINE<sup>2</sup>

Laboratory of Mechanics of structures and solids

University of Djillali Liabes, Sidi Bel Abbès, Algeria.

\*bouzi20nouri@gmail.ocm

## ABSTRACT

*Electrical cables are mainly composed of metal and plastic. The core of the cable contains metallic wires, mainly made of copper, but can also be composed of other metals such as lead, tin, aluminium, iron, nickel, zinc and phosphorus.*

*The recycling of electrical cables begins with the separation of the plastic elements from the metal elements. These elements are then crushed into granules or chips to be reused. In order to achieve this goal, we are developing a machine that would separate the metal from the plastic with a vibratory system.*

## KEY WORDS

Vibration, density table, recycling, electrical cables.

## I. INTRODUCTION

Vibratory separation of metal and plastic represents an economically viable technology for environmental preservation, as it offers high quality recycled plastic and better metal recovery than conventional waste treatment methods. Vibratory separation is nowadays an efficient technology for recycling used materials from industrial waste and is considered an innovative method to use the separation of a mixture of insulation-metal granules.

## II. SEPARATION OF "METAL/PLASTIC" PARTICLES BY DENSIMETRIC VIBRATION TABLE)

the densimetric vibratory table is a machine to separate the copper from the plastic of electrical cables, to achieve this result we have done several research to

model prototypes, this machine consists of an electric motor and a crank rod system that pushes the table being attached to the blade that allows it to vibrate (fig.1).

Then we calculated the different forces and stresses acting on the machine and we checked the resistance conditions to guarantee the good functioning of the machine.

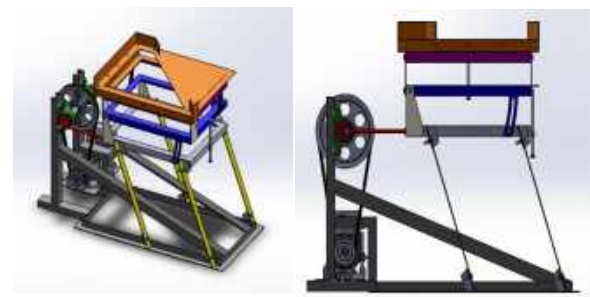


Fig. 1. Modeling of the machine.

- The motor and motion transmission system is in light gray.
- The yellow blades allow to vibrate the table.
- The purple and blue tables allow to tilt the system.
- The orange table allows to separate the particles using a grid.

### III. VIBRATING BLADES

This part concerns the calculation of the max bending moment, the max deflection as well as the resistance conditions of the vibrating plates of our machine (Fig.2).

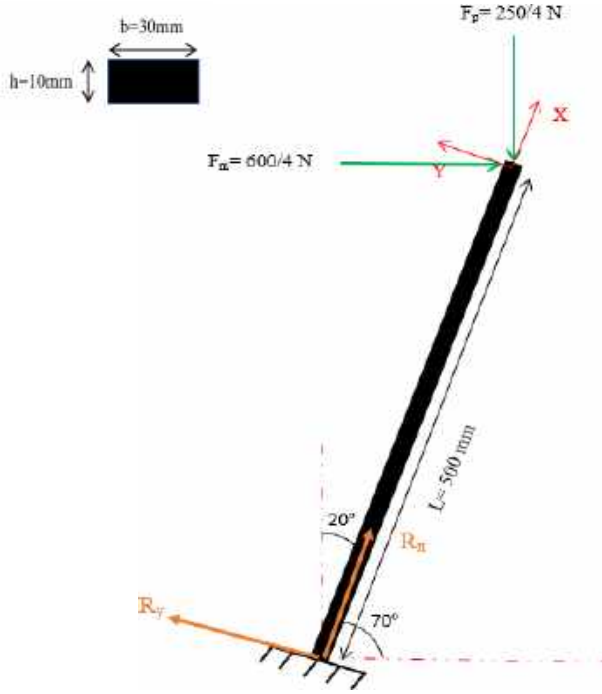


Fig. 2. Representation of the forces acting on the vibrating blade.

#### A. Calculation of the reactions at the level of the vibrating blade

$\Sigma F_{ext}$ : along the X axis:

$$\begin{aligned} F_p \cos(20) + F_m \cos(70) + R_x &= 0 \\ R_x &= F_p \cos(20) - F_m \cos(70) \\ R_x &= 7.43 \text{ N} \end{aligned} \quad (1)$$

$\Sigma F_{ext}$ : along the Y axis:

$$\begin{aligned} -F_p \sin(20) - F_m \sin(70) + R_y &= 0 \\ R_y &= F_p \sin(20) + F_m \sin(70) \\ R_y &= 162.3 \text{ N} \end{aligned} \quad (2)$$

#### B. Calculation of the maximum bending moment for a blade

$$\begin{aligned} M_{f \max} &= (F_p \sin(20) + F_m \sin(70)) * L \\ M_{f \max} &= 162.5 * 500 = 81250 \text{ N.mm} \end{aligned} \quad (3)$$

#### C. Calculation of the moment of inertia

$$I_{GZ} = \frac{bh^3}{12} = \frac{30 * 10^3}{12} = 2500 \text{ mm}^4 \quad (4)$$

#### D. Calculation of the maximum deflection

We have  $E = 210000 \text{ Mpa}$

$$F_e = F_p \sin(20) + F_m \sin(70) = -650 \text{ N} \quad (5)$$

$$Y_{\max} = -\frac{F_e * L^3}{3EI_{GZ}}$$

$$Y_{\max} = -\frac{-162.5 * 500^3}{3 * 210000 * 2500} = 12.9 \text{ mm}$$

#### E. Condition of resistance

$$\sigma \leq \frac{R_e}{S} \quad (6)$$

With  $R_e = 235 \text{ Mpa}$ ,  $\sigma = \frac{M_{f \max}}{I_{GZ}} \rho$  and  $S = 4/3$

$$\frac{M_{f \max}}{I_{GZ}} \rho \leq \frac{R_e}{S}$$

$$\frac{81250}{2500} * 5 \leq \frac{235}{4} * 3 = 176.25$$

$$162.5 \text{ Mpa} \leq 176.25 \text{ Mpa}$$

Resistance condition Check.

#### F. Calculation of the force required to obtain a maximum deflection of 10 mm

We want to take a maximum deflection of the vibrating blade which is equal to 10 mm.

$$Y_{\max} = 10 \text{ mm}$$

$$F = \frac{3Y_{\max} E I_{GZ}}{L^3} \quad (7)$$

$$F = \frac{3 * 10 * 210000 * 2500}{500^3} = 126 \text{ N}$$

$$M_{f \max} = 126 * 500 = 63000 \text{ N.mm}$$

$$\sigma \leq \frac{R_e}{S}$$

$$\frac{M_{f \max}}{I_{GZ}} \rho \leq \frac{R_e}{S} \quad (8)$$

$$\frac{63000}{2500} * 5 \leq 176.25$$

$$126 \leq 176.25 \text{ Mpa}$$

Resistance condition Check.

### IV. CONCLUSION

After modeling several prototypes we have concluded that the use of vibrating blades and the crank rod system gives better results in the metal/plastic separation process.

Based on these results, a prototype is being made with a vibratory system that allows to control the path of the metal and plastic particles.

Moreover, the prototype has been designed with a system that allows it to incline the upper part with some degree, which gives a better control of the particles path.

# The role of vibration analysis in diagnosing rotating machinery failures

TOUFIK BENSANA <sup>1,2,\*</sup>, MEDKOUR MIHOUB <sup>2</sup>, MOHAMED FNIDES <sup>2</sup>

1. The Higher School of Technological Education in Skikda, Azzaba Skikda, Algeria, E-mail: tbensana@gmail.com
2. Tissemsilt University, Tissemsilt, Algeria
3. The Higher School of Technological Education in Skikda, Azzaba Skikda, Algeria

## ABSTRACT

*The high security requirements, reducing operating costs and control of equipment availability provide to maintenance of systems a major role. It should minimize the repair time, and provide a reliable and easily interpretable diagnosis despite the complexity of the equipment. Consequently vibration signals collected from defective ball bearings which are generally non-stationary, nonlinear and with strong noise interference, so it is essential to obtain the characteristics of the defects accurately. As well a combined approach is proposed and applied for vibration diagnosis. This method uses the combination of singular value decomposition (SVD) and local mean decomposition (LMD). The results show the excellent performance of the proposed technique in the diagnosis of defects of ball bearings.*

## KEY WORDS

Vibration analysis; fault diagnosis; rolling element bearing; local mean decomposition; singular value decomposition.

## I. INTRODUCTION

The Vibration based time–frequency analysis to the mechanical vibration signals has become a most successful and effective technique in recent years. Empirical mode decomposition (EMD) has been recently developed in fault diagnosis of rotating machinery. EMD is based on the local characteristic time scales of a signal and could decompose the complicated signal into a set of complete and almost orthogonal intrinsic mode functions (IMFs). EMD is a selfadaptive signal processing method that can be applied to non-linear and non-stationary process perfectly. However, one of the major drawbacks of EMD is the mode mixing problem.

This paper proposes a hybrid approach for the fault detection of rolling element bearing which combine Singular value decomposition (SVD) with LMD algorithm and the results show the excellent performance of the proposed technique in revealing the rolling element bearing fault

## 4. Experiment data analysis

To verify the effectiveness of the proposed approach. In this paper all the roller bearing vibration data analyzed are from the website of Case Western Reserve University Bearing Data Center [29], motor power of the test is 14.7 KW, and 6205-2RS SKF bearing was selected, motor speed of test is 1680 tr/min, the sampling frequency is 12000 HZ, the test had simulated inner and outer rings fault of the bearing.

## 4. Results and discussion

Fig. 1 shows the raw vibration signal collected from bearing with an outer race fault. Consequently, we combine LMD with other techniques to bearing fault diagnosis

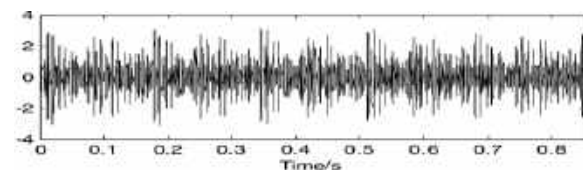


Fig. 1 The raw vibration signal collected from bearing with an outer race fault

Applying the proposed method which combines SVD denoising and LMD algorithm. The ambient noises are effectively suppressed, meanwhile, the

periodicity impacts features are well reserved, PFs components are obtained shown in Fig. 2. Meantime instantaneous amplitude and instantaneous frequency of each PF component can be calculated then fault feature can be extracted accurately by applying spectrum analysis to the instantaneous amplitude of PF component including dominant feature information. The FFT spectrum of the instantaneous amplitude of PF1 From Fig. 7, it can be seen clearly PF1 is modulated, so the fault feature of vibration signals would be extracted effectively by applying FFT transform to the instantaneous amplitude of the first PF component. The calculated frequency of the roller bearing with outtrace fault (107.57 Hz) and its harmonic frequencies could be found in the amplitude spectrum shown in (Fig. 3), it is clear that the proposed method can achieve better results compared with the use of LMD alone.

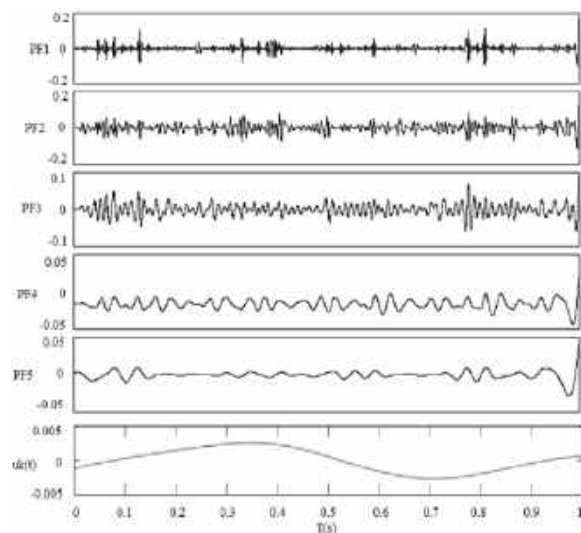


Fig. 2 PFs of tested bearing with outtrace fault using hybrid SVD and LMD

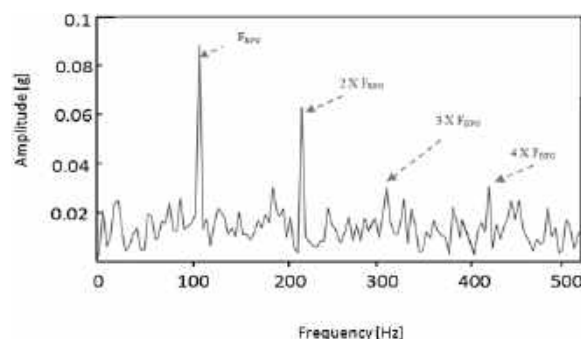


Fig. 3 The FFT spectrum of the instantaneous amplitude of PF1

## 5. Conclusions

LMD is very suitable for the analysis and feature extraction for non-stationary modulation signals. SVD is taken as the as prefilter to denoise and enhance the impulsive features, then the fault characteristic frequency of the roller bearing can be extracted by applying spectrum analysis to the instantaneous amplitude of PF component containing dominant fault information. Finally the results demonstrate that the proposed approach is successful for rolling bearing fault detection and diagnosis.

## References

1. **Dong, Y.B.; Liao, M.F.; Zhang, X.L.** 2011. Faults diagnosis of rolling element bearings based on modified morphological method, *Mech. Syst. Signal Process* 25(4): 1276-1286. <http://dx.doi.org/10.1016/j.ymssp.2010.10.008>.
2. **Lei, Y.G.; Lin, J.; He, Z.J.** 2011. Application of an improved kurtogram method for fault diagnosis of rolling element bearings, *Mech. Syst. Signal Process* 25(1): 1738-1749. <http://dx.doi.org/10.1016/j.ymssp.2010.12.011>.
3. **Zhu Fulei; Peng Zhike; Feng Zhipeng** 2009. *Mechanical fault diagnosis of modern signal processing methods*, Beijing Science Press 41(4): 1-130.
4. **Fan, X.; Liang, M.; Yeap, T.H.; Kind, B.** 2007. A joint wavelet lifting and independent component analysis approach to fault detection of rolling element bearing, *Smart Mater. Struct.* 16(5): 1973-1987. <http://dx.doi.org/10.1088/0964-1726/16/5/056>.
5. **He, W.; Jiang, Z.N.; Qin, Q.** 2010. A joint adaptive wavelet filter and morphological signal processing method for weak mechanical impulse extraction, *J. Mech. Sci. Technol.* 24(8): 1709-1716. <http://dx.doi.org/10.1007/s12206-010-0511-4>.
6. **Amarnath, M.; Krishna, I. P.** 2012. Empirical mode decomposition of acoustic signals for diagnosis offaults in gears and rolling element bearings, *IET. Sci. Mea. Technol* 6:279-287. <https://DOI:10.1049/iet-smt.2011.0082>.
7. **Smith, J. S.** 2005. The local mean decomposition and its application to EEG perception date, *JR Soc interface* 2(5):443454. <https://doi.org/10.1098/rsif.2005.0058>.



# Electron-impact ionization of Argon 3p

BECHANE KAWTHER<sup>1</sup>

1. LPQSD, Department of Physics, Faculty of Sciences, University Sétif1, Sétif 19000, Algeria,  
bechanekawther34@gmail.com

## ABSTRACT

*Ionization of atoms by electron impact is part of basic research which enables to study the importance of fundamental interactions. Triple differential cross sections (TDCSs) are presented for the electron impact ionization of a 3p shell of argon, using a new model called (3CWZ). Within this model, the projectile as well as the ejected electrons are represented by variable charges  $Z(r)$  instead of an effective charge, the post collision interaction (PCI) is also included. Our results are compared with recent experiments and other theoretical predictions in a range of several kinematics.*

**KEY WORDS** (Ionization, electron, cross section, post collision interaction, variable charge)

## I. INTRODUCTION

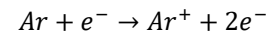
Electron impact ionization of atoms and molecules represent theoretically a few body problems. The triple differential cross section (TDCS) represents a rigorous test for the most efficient models, the (TDCS) measured in (e,2e) experiments provides the probability that the scattered and ejected electrons are selected in energy and direction and detected in coincidence. In the present work we introduce an improved theoretical approach to describe the (e,2e) reaction for atoms, it is in fact an extension of our earlier studies which provided rather good agreement between experiment and theory, The present theoretical description is a fully quantum mechanical approach, it is actually a kind of (BBK). We present a new model to study the dynamics of electron impact ionization of atoms called (3CWZ).

## II. THEORY

In the (BBK) model the ejected and the scattered electrons are both represented by Coulomb waves with an effective charge ( $Z=1$ ), the post collision interaction (PCI) is introduced and treated exactly

to all orders, while the incident electron is described by a plane wave.

In the (3CWZ) model the three electrons ejected, scattered and incident are described by Coulomb wave with a variable charge  $Z(r)$ , in this work we take into account the exchange effects. The electron impact ionization of argon atoms in its ground state is schematized as:



### A. OBJECTIVES

The object of this work concerns the use of this variable charge scheme, which somehow represents a full approximate distorted wave model (a kind of a (3DW) model), and check how this will affect the (TDCS) in the (e,2e) reaction of argon 3p. The model is called (3CWZ), the obtained results within this model are compared with experiments and other theories like the (BBK2CWZ) model [3] (BBK2CWZ) model is improved by representing both outgoing electrons with a Coulomb wave with a variable charge, while the incident electron is described by a plane wave).

### B. RESULT

(TDCS) for the ionization of Ar 3p as a function of the ejection angle at fixed scattering and ejected energies  $E_a = 500$  ev and  $E_b = 205$ ev. The projectile is scattered at a fixed scattering angle  $\theta_1=3^\circ$ . Theoretical results are blue solid line (3CWZ), red solid line (BBK2CWZ). The experimental data are black squares taken from [1], as shown in Fig1.

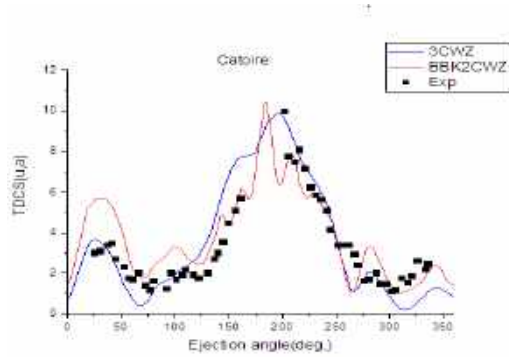


Fig. 1.(TDCS) for the ionization of Ar 3p as a function of the ejection angle.

### C. RESULT2

Absolute (TDCS) for the ionization of Ar 3p as a function of the ejection angle at fixed scattering angle  $\theta_1=15^\circ$ . The incident and ejected electrons have respective energies  $E_0=200\text{ev}$  and  $E_b=10\text{ev}$ . Theoretical results are blue solid line (3CWZ), red dash line (3DW). The experimental data are black squares taken from [3], as shown in Fig2.

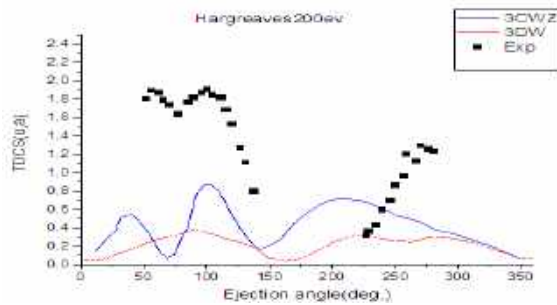


Fig. 2. (TDCS) for the ionization of Ar 3p as a function of the ejection angle.

## III. CONCLUSION

In this work, an (e,2e) theoretical study of Ar 3p has been used to investigate the (e,2e) ionization reaction in several kinematics.

-In a first step (3CWZ) results turned out to be in good agreement with the experimental data better than (BBK2CWZ).

-In a second step we can state that (3CWZ) model doesn't describe correctly the experimental data but reproduces qualitatively the shape of the (TDCS), while (3DW) predict nearly the same shape.

## REFERENCES

- [1] F. Catoire, E. M. Staicu-Casagrande, M. Nekkab, C. Dal Cappello, K. Bartschat and A. Lahmam-Bennani, J. Phys. B 39, 2827 (2006).
- [2] R. L. Hargreaves, M. A. Stevenson and B Lohmann, J. Phys.B 43, 205202 (2010).
- [3] Attia M, Houamer S, Khatir T, Bechane K and Dal Cappello C J.phys.B 56 075201 (2023).

# Harmonic structural analysis of Satellite Separation Mechanism

SMAHAT AMINE<sup>1\*</sup>, MANKOUR ABDELJELIL<sup>1</sup>, BENDINE KOUIDER<sup>2</sup> AND BENSIKADDOUR EL HABIB<sup>1</sup>

1. Department of Research in Space Mechanics. Satellite Development Center  
Oran, Algeria, aminesba13@hotmail.fr
2. Mechanics of Structures and Solids Laboratory, Faculty of technologys, Djillali Liabès University  
Sidi Bel-Abbès, Algeria

## ABSTRACT

*Separation mechanisms play a crucial role in the field of astronautics, ensuring the precise and reliable deployment of satellites into orbit. A thorough understanding of the vibrational response of these mechanisms is essential to ensure their proper functioning. This paper presents a harmonic analysis of the structure of the separation mechanism of a microsatellite using the finite element method. We begin with detailed modelling of the structure of the separation mechanism, taking into account the material properties, bonds, and charges associated with microsatellite separation. harmonic analysis is performed to evaluate the vibration response of the structure under typical separation loads. This analysis makes it possible to determine the natural frequencies, vibration modes and harmonic excitation levels in the structure.*

## KEY WORDS (3 to 6 key words)

Harmonic analysis; Structural modeling; Dynamic response; Vibration Modes; finite elements

## I. INTRODUCTION

In the field of astronautics, the success of a space mission often depends on a multitude of factors, ranging from propulsion to navigation and communication. One of these crucial factors is the separation mechanism, a discrete but vital element that helps ensure the precise and reliable deployment of microsatellites and payloads into orbit. Poor design or insufficient understanding of the vibrational response of these mechanisms can have disastrous consequences, ranging from mission failure to loss of valuable hardware. The objective of this paper is to explore in depth the harmonic analysis of the structure of a microsatellite separation mechanism, using the finite element method. Harmonic analysis is essential for evaluating the structure's vibrational response to typical separation loads, by identifying natural frequencies, vibration modes, and harmonic excitation

levels. This information is crucial for the design, optimization, and reliability of separation mechanisms, thus helping to guarantee the success of space missions. In the following section, we will present in detail the methodology used to carry out this harmonic analysis, with emphasis on the modeling of the structure, the discretization by the finite element method, the separation loads considered, and the aspects linked to harmonic simulation. The obtained results, discussed later, offer key perspectives for engineers and researchers in the space domain, emphasizing the importance of this analysis for the design of microsatellite separation mechanisms.

## II. MATERIALS AND METHODS

### A. SEPARATION SYSTEM MODELING

The first step consists of the detailed modeling of the structure of the separation mechanism. This involves the geometric representation of the mechanism, considering its components, its dimensions and its general configuration. Additionally, the properties of the materials used in the construction of the structure are specified, including stiffness, mass, and damping coefficients. The quality of this modeling has a significant impact on the precision of the harmonic analysis results.

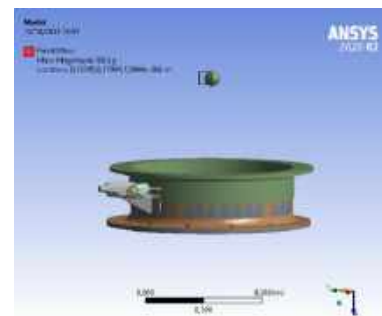


Fig. 1. Geometrical model.

### B. ANALYSIS PROCESS

Harmonic analysis is carried out by decomposing the separation loads into harmonic components. A frequency discretization is carried out to evaluate the vibration response of the structure at each harmonic frequency of interest. Harmonic excitation levels indicate how the structure responds to separation loads at different frequencies. We assessed harmonic excitation levels across the entire structure, identifying areas sensitive to specific excitations. Harmonic excitation levels are presented in tabular form, highlighting the vibration amplitudes at each harmonic frequency.

Frequency [Hz]	Amplitude[m/s <sup>2</sup> ]
5	1.3 g
8	2.5 g
100	4.5 g

Table 1. Natural Sine qualification levels X, Y and Z.

### III. RESULTS AND DISCUSSION

Modal analysis results reveal the natural frequencies of the separation mechanism structure. These natural frequencies correspond to the structure's natural modes of vibration, and they are essential for understanding how the structure will respond to separation loads. The natural frequencies identified are as follows:

Mode	Frequency [Hz]
1	129,19
2	129,66
3	255,52
4	344,8
5	500,22
6	556,5

Table 2. Natural frequencies.

Figures 2-3 shows the analysis results from harmonic input. The generated values of Von mises stresses and acceleration output indicated the structure is safe to withstand the requirements .

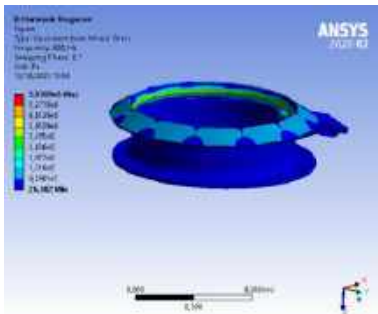


Fig. 2. Von mises stress-along Z axis

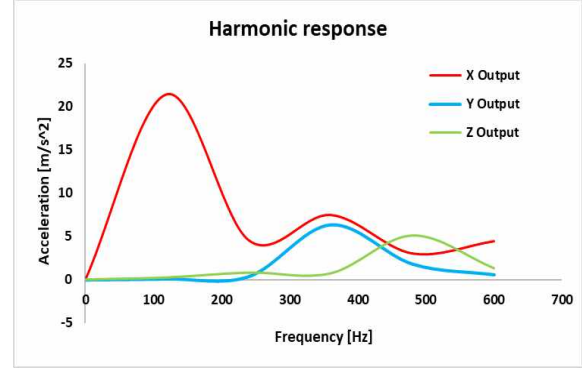


Fig. 3. Harmonic loads response Vs. Frequency.

### IV. CONCLUSION

The harmonic analysis of the structure of the separation mechanism of a microsatellite using the finite element method provided essential information for the design, optimization and reliability of these systems. The main conclusions of our study are as follows:

- The natural frequencies and vibration modes of the structure were identified, allowing an in-depth understanding of the structure's vibrational response to separation loads.
- Harmonic excitation levels were evaluated, highlighting vibration amplitudes at different frequencies. This information is crucial for evaluating the stresses experienced by the components of the separation mechanism.
- Critical frequencies have been identified, highlighting the importance of monitoring and controlling vibrations at these frequencies to ensure the reliability of the separation mechanism.

### REFERENCES

- [1] J Ding, H Zhao, J Wang, Yi Sun, Z Chen "Numerical and experimental investigation on the shock mitigation of satellite-rocket separation" Aerospace Science and Technology Volume 96, January (2020).
- [2] Honghao YUE, Yifei YANG, Yifan LU, Fei YANG, Jun WU, Qi RUAN, Zongquan DENG. Research progress of space non-pyrotechnic low-shock connection and separation technology. Chinese Journal of Aeronautics. (2021).
- [3] Xiangyu Zhao, Chunjuan Zhao, Jiale Li, Yongliang Guan, Shanbo Chen and Lei Zhang. Research on Design, "Simulation, and Experiment of Separation Mechanism for Micro-Nano Satellites." Applied Science (2022).

# Enhancement of Vibration Attenuation in Damped Mechanical Systems using a Novel Non-Traditional Tuned Mass Damper with Negative Stiffness

OKBA ABID CHAREF<sup>1,\*</sup>, AND MAYADA BOUAOUN<sup>2</sup>

1. Ecole Nationale Polytechnique de Constantine, Mechanical Engineering Department  
Constantine, Algeria, okba3c@gmail.com
2. University of CONSTANTINE3 SALAH BOUBNIDER, Process Engineering Department  
Constantine, Algeria, mayadaok13@gmail.com

## ABSTRACT

*In this paper, a min-max optimum design of a non-traditional tuned mass damper with negative stiffness (NTNS-TMD) for a damped primary system is investigated to reduce high amplitudes in the resonant range of vibrations. The formulation of optimal parameters of TMD is a very complicated task when the primary structure is damped. A closed-form solution of optimum tuning coefficient can be reached by using the fixed-point approach and an average damping of the primary system must be considered. Then the optimum damping ratio and negative stiffness coefficient can be obtained by solving a set of nonlinear equations developed by Chebyshev's equioscillation theorem. Finally, the control performance of the proposed optimal design is compared with those of two existing typical TMDs, which were presented by Pennestri and Liu, respectively. Extended simulations were performed to examine the performance of the proposed non-traditional TMD with negative stiffness and the sensitivity of the optimal parameters. The simulation results show that the presented NTNS-TMD in this paper provides the highest suppression of the resonant vibration of the damped primary structure.*

## KEY WORDS

Non-Traditional Tuned Mass Damper; Vibration control performance; Damped primary system; Min-Max optimization; Negative stiffness

## REFERENCES

- [1] H. Frahm, "Device for damping vibrations of bodies," US Patent 0989958, (1909)
- [2] J. P. Den Hartog, Mechanical Vibrations. New York: Mc Graw-Hill, (1985).
- [3] J. E. Brock, "A note on the damped vibration absorber," (1946).
- [4] M. Z. Ren, "a Variant Design of the Dynamic Vibration Absorber," Journal of Sound Vibration, vol. 245, no. 4, pp.

762–770, (2001).

- [5] O. Abid Charef and S. Khalfallah, "Closed-Form Solution to H-Infinity Optimization of Pre-Tensioned Tuned Mass Damper," International Review of Mechanical Engineering (IREME), vol. 15, no. 3, pp. 157–164, (2021).
- [6] E. Pennestri, "An application of Chebyshev's min-max criterion to the optimal design of a damped dynamic vibration absorber," Journal of Sound and Vibration, vol. 217, no. 4, pp. 757–765, (1998).
- [7] A. Ghosh and B. Basu, "A closed-form optimal tuning criterion for TMD in damped structures," Structural Control and Health Monitoring, vol. 14, no. 4, pp. 681–692, (2006).
- [8] K. Liu and G. Coppola, "Optimal design of damped dynamic vibration absorber for damped primary systems," Transactions of the Canadian Society for Mechanical Engineering, vol. 34, no. 1, pp. 119–135, (2010).

# Titre : Suivi cyclique de la durée de vie résiduelle RUL pour le pronostic des défauts de roulements

ABDERRAHMANE BEN YAGOUB <sup>1\*</sup>, RIDHA ZIANI <sup>2</sup>

1. LMPA, Laboratoire de Mécanique de Précision Appliquée, Institut d'Optique et Mécanique de Précision, Université Setif-1-, 19000 Sétif, Algérie, benyagoub.abde@univ-setif.dz
2. LMPA, Laboratoire de Mécanique de Précision Appliquée, Institut d'Optique et Mécanique de Précision, Université Setif-1-, 19000 Sétif, Algérie, ziani\_lmpa@yahoo.fr

## RESUME :

*L'étude propose l'utilisation de la méthode de prédiction cyclique pour exploiter pleinement l'approche des "données de seuil" pour les défauts de roulements. L'objectif est de démontrer que le suivi cyclique peut estimer avec précision la durée de vie résiduelle (RUL) des défauts de roulements en utilisant la totalité des données disponibles.*

*Notre travail comporte plusieurs sections, notamment une description de la base de données, une méthodologie comprenant la comparaison des filtres et la prédiction de la RUL à travers l'analyse en composantes principales (ACP) et le montage d'un modèle de dégradation. En conclusion, cette recherche met en avant une approche prometteuse pour le pronostic des défauts de roulements, en mettant en lumière l'efficacité du suivi cyclique et des méthodes utilisées pour estimer avec précision la RUL des roulements.*

**MOTS CLES :** pronostic, maintenance préventive, durée de vie résiduelle (RUL)

## I- INTRODUCTION :

Ces dernières décennies, le pronostic à occuper une place prépondérante dans la maintenance préventive en industrie. Il est généralement question d'estimer la durée de vie résiduelle (RUL) ou TTF (Time to Failure) des systèmes mécaniques. Cette maintenance nécessite un travail qui combine des connaissances en traitement de signal, et des connaissances en mécanique appliquée.

Souvent, en pronostic, l'analyse peut être purement guidée par des données (analyse de tendance), elle nécessite un grand nombre de données pour estimer avec précision l'état de dégradation du système, elle présente le double avantage d'être applicable à un nombre suffisant de systèmes et d'être relativement précis. Cependant, cette approche du pronostic n'est possible que sur des systèmes dont la dégradation est progressive et passe par des états de dégradation différents et identifiables. L'analyse de tendance est l'une des méthodes les plus utilisées dans les publications concernant le pronostic en général, mais également concernant les roulements. Plusieurs travaux qui

traitent du pronostic des défauts de roulement en vue le jour appliquant des techniques d'apprentissage comme les réseaux bayésiens, les réseaux de neurones ou le Support Vector Machine (SVM) [1], afin d'estimer l'évolution de la dégradation donnant ainsi le temps exact de la défaillance en heures et minutes.

Dans ce travail nous avons voulu suivre l'approche des « données de seuil » car on dispose d'une quantité limitée de données d'exécution jusqu'à l'échec [2] et les caractéristiques des roulements conviennent pour créer un modèle de dégradation, parallèlement nous avons voulu mettre en lumière la méthode de prédiction cyclique afin de ne pas négliger les données, Il est question de prouver que le suivi cyclique peut également estimer la durée de vie résiduelle des défauts de roulement avec la totalité des données et avec un suivi précis. Nous avons tout d'abord comparé différents filtres: simple moving average (SMA), Cumulative Moving Average (CMA) et Exponentiel Moving Average (EMA) pour apporter le meilleur lissage possible, ensuite nous avons appliqué une analyse en composantes principales (ACP) et un ajustement de courbe (Model Fitting) afin de construire un modèle de décodage et d'ajuster la fonction exponentielle aux n dernières données. Enfin nous avons, à l'aide d'indicateurs sélectionnés, estimé la durée de vie résiduelle RUL d'un roulement de manière cyclique exhibant ainsi les prédictions exactes dans chaque phase de vie du roulement jusqu'à la défaillance.

## II-BASE DE DONNEES IMS :

Les données ont été générées par le NSF I/UCR Center for Intelligent Maintenance Systems (IMS – www.imscenter.net) avec le soutien de Rexnord Corp. à Milwaukee, au Wisconsin. [2].

## II-1-DESCRIPTION DU BANC D'ESSAI

La configuration expérimentale consistait à installer quatre (4) roulements à double rangée Rexnord ZA-2115 sur un arbre, comme le montre la figure 1. Pour assurer une vitesse de rotation



constante de 2000 tours par minute, un moteur à courant alternatif était connecté à l'arbre par des courroies de frottement. Un mécanisme à ressort a été utilisé pour appliquer une charge radiale de 6000 livres à l'arbre et aux roulements. Notamment, tous les roulements ont été lubrifiés à l'aide d'une lubrification par force pour une performance optimale [1].

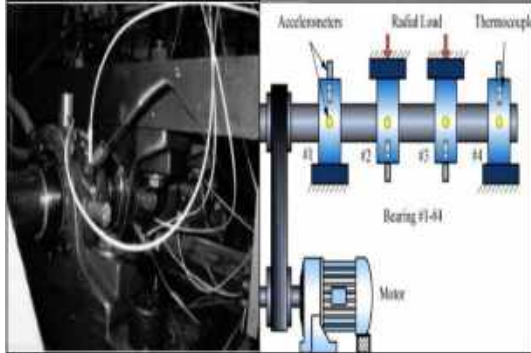


Figure 1 : Disposition du banc d'essai de l'IMS [1].

## II.2 DESCRIPTION DES DONNEES

Le paquet de données, IMS-Rexnord Bearing Data.zip, comprend trois (3) ensembles de données qui représentent des expériences de test à échec. Chaque ensemble de données comprend plusieurs fichiers individuels qui représentent des signaux de vibration d'une seconde enregistrés à des intervalles spécifiques. Ces fichiers comprennent 20 480 points de données avec un taux d'échantillonnage de 20 kHz. Les noms des fichiers indiquent les heures de collecte respectives. Dans les fichiers de données, chaque enregistrement (ligne) représente un point de données. Aussi, des intervalles de temps plus importants indiqués dans les noms de fichiers signifient la poursuite de l'expérience le jour ouvrable suivant.

Dataset	Dégâts annoncés à la fin	Nombre de fichiers	Nombre de canaux	Durée d'endurance/Signal enregistré
1	Roulement 3 : bague intérieure Roulement 4: élément roulant	2156	8	49680 min 34 jours 12h / 36 min
2	Roulement 1 : bague extérieure	984	4	9840 min 6 jours 20h /16 min
3	Roulement 3 : bague extérieure	4448	4	44480 min 31 jours 10h /74 min

Tableau 1 : Description des ensembles de données.

## III- METHODOLOGIE

### III.1 ÉVALUATION COMPARATIVE DES FILTRES

Dans cette étude, nous avons choisi d'étudier un type spécifique de défaut de la base de données dans le but d'appliquer notre stratégie d'estimation cyclique pour la durée de vie résiduelle RUL. Notre sélection s'est concentrée sur le roulement trois (3) de l'ensemble de données 1, qui présente un défaut de bague intérieure.

Après avoir effectué une analyse des caractéristiques statistiques extraites des données (en calculant des indicateurs temporels), nous avons estimé qu'une évaluation comparative de trois itérations distinctes du filtre de moyenne mobile doit être établie. Cette évaluation vise à déterminer le filtre optimal qui capture avec précision la dynamique authentique inhérente aux données. Aussi, le filtre de moyenne mobile, qui englobe les méthodologies de moyenne mobile simple (SMA), moyenne mobile cumulative (CMA) et moyenne mobile exponentielle (EMA), est utilisé pour réaliser le lissage des données dans le contexte temporel.

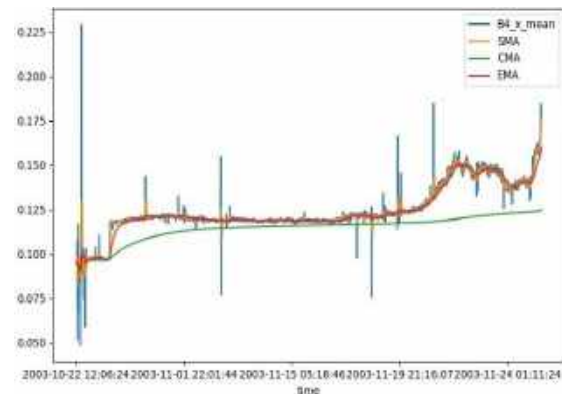


Figure 2 : Comparaison des filtres à moyenne mobile

Après une analyse approfondie des représentations graphiques et une évaluation comparative, nous pouvons conclure que l'EMA apparaît comme le choix le plus viable pour le filtrage des données. Cette détermination est fondée sur sa capacité supérieure à capturer et à refléter avec précision les mouvements réels observés dans l'ensemble des données réel.

### III.2 PREDICTION DE LA RUL

a) L'analyse en composantes principales (ACP) est utilisée pour construire un modèle de dégradation en extrayant une caractéristique représentative qui encapsule l'information contenue dans les caractéristiques de base. Cette technique identifie la composante principale avec la plus grande variance. Grâce à ACP, la redondance de dimensionnalité inhérente aux données est effectivement réduite, ce qui entraîne l'acquisition d'une caractéristique

primaire qui capture les caractéristiques essentielles. Nous avons constaté que la variance expliquée de la composante principale 1 s'élève à **0,9955862512721826 (99,56%)**, ce qui indique sa contribution substantielle à la représentation de l'ensemble de données original.

b) Ajustement du modèle : En ce qui concerne la prédiction des séries temporelles, on suppose généralement que les dégradations suivent un modèle exponentiel dans de nombreux phénomènes naturels. Par conséquent, une fonction représentant un modèle exponentiel avec une pente constamment positive est construite et ajustée en utilisant la bibliothèque **scipy.optimize**. Pour assurer l'inclusion de mouvements spécifiques qui pourraient aider à prévoir les résultats futurs, le modèle exponentiel n'est pas adapté à l'ensemble des données disponibles, en revanche cette fonction exponentielle est adaptée spécifiquement aux points de données « n » les plus récents.

c) Nous avons appliqué notre prédiction cyclique en supposant que les 650 premiers cycles sont sains. Les figures ci-dessous illustrent certaines prédictions des cycles.

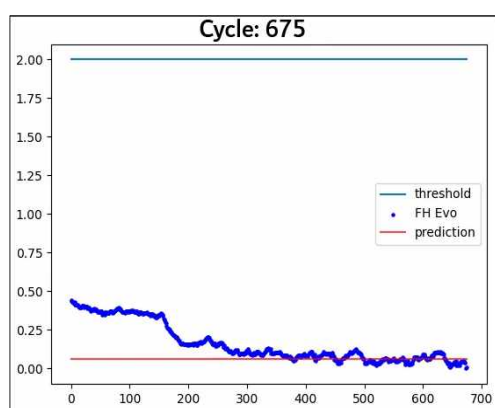


Figure 03. Cycle sans défauts

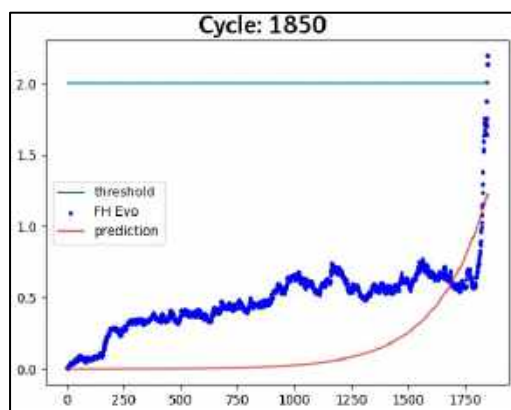


Figure 04. Cycle suspect

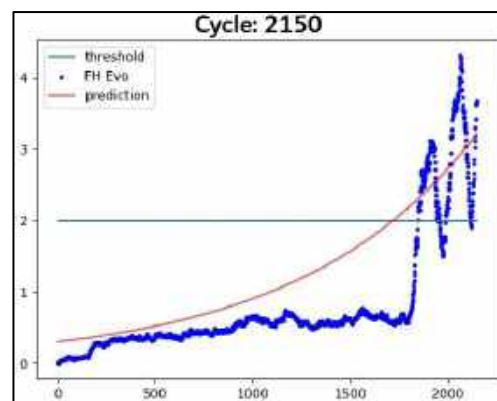


Figure 05. Cycle avec défauts

Nous avons trouvé que la prédiction de la défaillance est de **1717,9009275180667**. Le tableau reprend la prédiction cyclique du roulement 03 :

Cycle	temps	Prédiction	isvalid	reel
<b>675</b>	2003-11-09 00:51:44	6.218055e+10	faux	normal
975	2003-11-15 01:08:46	7.432427e+11	faux	normal
1350	2003-11-18 05:12:30	1.987825e+03	Vrai	normal
1625	2003-11-21 01:24:03	5.951757e+10	faux	normal
1775	2003-11-22 06:56:56	2.547281e+03	faux	normal
1800	2003-11-22 11:06:56	2.567900e+03	faux	suspect
<b>1850</b>	2003-11-22 19:26:56	1.959186e+03	Vrai	<b>suspect</b>
1975	2003-11-23 21:01:24	1.895768e+03	Vrai	suspect
2100	2003-11-24 20:57:32	1.804905e+03	Vrai	suspect
2125	2003-11-25 11:47:32	1.659149e+03	Vrai	Défaut bague intérieure
<b>2150</b>	<b>2003-11-25 15:57:32</b>	<b>1.717901e+03</b>	Vrai	Défaut bague intérieure

Tableau 2. Prédiction cyclique

## VI-CONCLUSION:

Les résultats obtenus dans cette étude montrent que la méthode de suivi cyclique combinée aux bons choix de filtres et à l'application de l'ACP permettent d'estimer avec précision la durée de vie résiduelle (RUL) des défauts de roulements : Le choix de l'EMA comme filtre de lissage est justifié par sa capacité à capturer précisément les mouvements réels observés dans les données, cela permet d'éliminer les variations indésirables et de mettre en évidence les tendances de dégradation. L'ACP appliquée aux données a permis de réduire leur dimensionnalité tout en conservant l'essentiel de l'information, la composante principale 1 explique près de 99,56% de la variance totale, ce qui montre son importance dans la représentation de l'ensemble des données. Enfin, l'estimation de la durée de vie résiduelle (RUL) d'un roulement par la prédiction cyclique a donné un résultat de 1717,9009275180667. Cela signifie que l'on peut prédire avec précision le moment de défaillance du roulement en se basant sur les données disponibles.

Ces résultats ouvrent des perspectives intéressantes pour l'amélioration de la maintenance préventive et la réduction des coûts liés aux défaillances des roulements. Il serait intéressant de poursuivre cette recherche en appliquant ces méthodes à d'autres types de systèmes mécaniques.

## REFERENCES

- [1] D. Lixiang, F. Zhao, W. Jinjiang, W. Ning et Z. Jiwang, An Integrated Cumulative Transformation and Feature Fusion Approach for Bearing Degradation Prognostics, Hindawi, 2018.
- [2] J. Lee, H. Qiu, G. Yu, J. Lin, and Rexnord Technical Services, IMS, "Bearing Data Set", NASA Prognostics Data Repository, NASA Ames Research Center, Moffett Field, CA, University of Cincinnati, 2007.
- [3] Q. Hai, L. Jay, L. Jing, Wavelet Filter-based Weak Signature Detection Method and its Application on Roller Bearing Prognostics. Journal of Sound and Vibration, 2006, 289, pp.1066-1090.

# Experimental and numerical study on free vibration of cracked composite cantilever beam

Mustapha DAHAK<sup>1,\*</sup>, Nouredine TOUAT<sup>1</sup> AND Tarak BENKEDJOUH<sup>2</sup>

1. Department of Mechanical Construction and Production, Faculty of Mechanical Engineering and Process Engineering, University of Science and Technology Houari Boumediene, 16111 Algiers, Algeria;
  2. Mechanical Structures Laboratory, Ecole Militaire Polytechnique, Bordj El Bahri, 16046, Algiers,
- \* Correspondence: mustapha.dahak@usthb.edu.dz;

## ABSTRACT

*The objective of this work is to study the free vibration of a cracked composite beam. First, a finite element model is presented. Then, the effect of the crack on the natural frequencies of a unidirectional glass-fiber-reinforced epoxy beam is illustrated. Finally, it is shown that the shape given by the change in the natural frequencies is only a function of the damage position. So, the crack can be located by the correlation between the shape of the measured frequencies and those obtained by the finite elements, where the position that gives the calculated shape, which is the most similar to the measured one, indicates the crack position. Finally, an experimental application is presented to confirm the numerical study.*

## KEY WORDS

free vibration, modal analysis, natural frequency, composite beam, finite element method, crack.

## I. INTRODUCTION

Over the past decade, the applications of composite structures have become very attractive, mainly in various engineering applications. However, in order to avoid possible catastrophic defects, techniques that can detect the damage at an early stage must be developed. Detecting damage through visual inspections can be laborious and costly. Other traditional non-destructive testing methods, such as X-ray and ultrasonic imaging, are frequently expensive. The vibration-based damage-detection methods present a potential alternative. They are based on the idea that damage can modify the mechanical characteristics of a structure, especially mass and stiffness, which results in changes in dynamic parameters [1]. These changes are frequently employed for damage identification. In this work, the free vibration of a cracked composite cantilever beam is studied for use in damage detection.

## II. FINITE ELEMENT FORMULATION

Consider a fiber-reinforced composite beam with unidirectional plies and an edge surface crack (Fig 1).

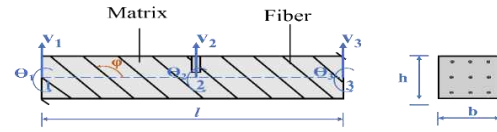


Figure 1. composite beam element

The elemental mass matrix (M) and stiffness matrix (K) are given by [2]. The additional local flexibility matrix  $[C_a]_{4 \times 4}$  can be calculated as:

$$C_{11}^a = C_{13}^a = C_{33}^a = \frac{2B_2\pi}{b} \int_0^{\bar{a}} \bar{a} (F_{II})^2 d\bar{a}$$

$$C_{22}^a = C_{24}^a = C_{44}^a = \frac{72B_1\pi}{bh^2} \int_0^{\bar{a}} \bar{a} (F_I Y)^2 d\bar{a}$$

$$C_{12}^a = C_{14}^a = C_{23}^a = C_{34}^a = \frac{6B_{12}\pi}{bh} \int_0^{\bar{a}} \bar{a} F_{II} d\bar{a}$$

where,  $F_I$ ,  $F_{II}$  and  $Y$  are the correction factors defined by Krawczuk [2] and  $\bar{a}$  is the normalized crack depth.

## III. CRACK EFFECT

Consider the cantilever beam in Figure 1 with a unidirectional glass-fiber-reinforced epoxy beam. The geometric properties of the beam are:  $l = 600\text{mm}$  length,  $h = 0.035\text{m}$  height, and  $w = 0.0075\text{m}$  width. The material properties are given in [3].

Figure 2 represents the variation of the first four normalized frequency reductions (df) as a function of the crack position and depth. It can be seen that the frequency reduction is influenced by the crack position and depth. So, for each mode of vibration, the same crack gives various frequency reductions if it occurs in a different position. Additionally, the same crack in the same position and depth produces different frequency reductions for each mode.

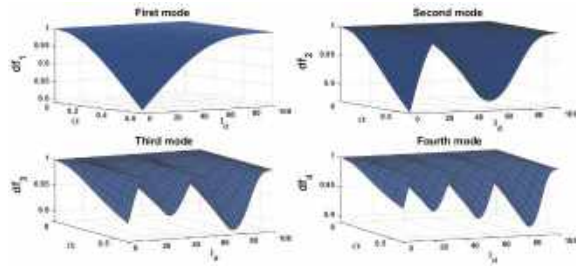


Figure 2. Variation of the first four frequency ratios as a function of the crack position and depth.

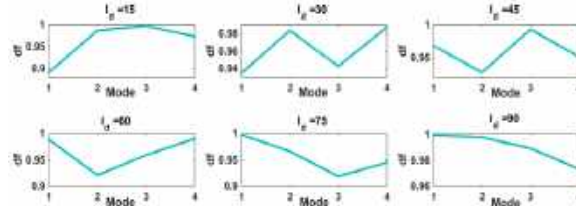


Figure 3. The shape of the first four normalized frequencies for different crack positions.

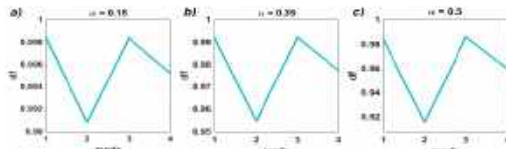


Figure 4. The shape of the first four normalized frequencies for different crack depths.

Figure 3 shows the shape of the first four normalized frequencies ( $df$ ) for different crack positions (for a fixed depth of 50%). We can notice that the forms given by  $df$  change according to the crack position, where each position gives a specific shape. According to Dahak et al [4], the presence of cracks produces a loss of stored strain energy, and this loss changes as a function of the mode shape. In summary, each frequency changes according to its mode shape displacement at the position of the crack, which explains why each crack position gives different forms of  $df$ . Thus, the shape given by the frequencies is characterized by the crack position, and the crack depth just amplifies it. For example, Figure 4 shows the shape of the first four normalized frequencies for different crack depths (at the fixed position  $l_d=55\%$ ). We can notice that the shape given by  $df$  is the same for each crack depth. Consequently, the damage can be located by the correlation between the measured shape and the calculated one.

#### IV. EXPERIMENTAL VALIDATION

An experimental modal analysis was performed employing an impact hammer, an accelerometer vibration analyzer, and a laptop to measure the vibration response (Figure 5). First, the frequencies of the intact beam were measured. Then, a crack with a depth of 5 mm at position  $l_{d1} = 50\text{mm}$  was created

using a saw. Finally, for the second and third cases, we increased the crack depth to 10mm and 16mm.

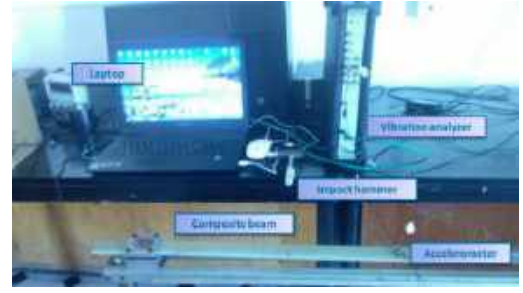


Figure 5. Experimental setup

Figure 6 shows that, by changing the crack depth, the frequency shape does not change. This confirms that frequency shapes can be used for damage localization in real structures.

Table 6. Experimental natural frequencies

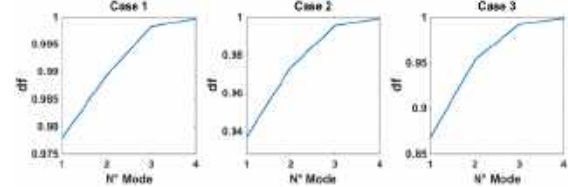


Figure 6. Experimental Frequencies shape

#### V. CONCLUSION

In this study, the free vibration of a cracked composite beam is studied. It is shown that the shape given by the change in the natural frequencies is only a function of the damage position. So, the crack can be located by the correlation between the shape of the measured frequencies and those obtained by the finite elements, where the position that gives the calculated shape, which is the most similar to the measured one, indicates the crack position. Finally, an experimental application is presented to confirm the numerical study.

#### REFERENCES

- [1] M. Dahak et al., "On the classification of normalized natural frequencies for damage detection in cantilever beam," J. Sound Vib, 402, (2017).
- [2] Krawczuk M., (1994) "A new finite element for the static and dynamic analysis of cracked composite beams", Comput Struct, 52, (1994).
- [3] M. Dahak et al., "Crack localization in composite cantilever beams using natural frequency measurements", Nondestruct. Test. Evaluation, Accepted, 2023
- [4] M. Dahak et al., "Damage detection in beam through change in measured frequency and undamaged curvature mode shape," Inverse Probl Sci Eng, 27, (2018).



# Title: Study on Vibration Analysis of Hybrid Laminated Bio-Composites

TRADKHODJA BOUTHEINA <sup>1,2,\*</sup>, BENZIDAIN RACHID <sup>2</sup>, AND BENNEGADI MOHAMMED EL LARBI<sup>2</sup>,BOUKHARI AHMED,BOUSSOUFI AICHA

1. Affiliation (Author): Laboratory member: Composite Structures and Innovative Materials (LSCMI)  
University of Science and Technology of Oran Mohamed Boudiaf. BP 1505 El M'naouar, Oran, Algeria

Faculty of Mechanical Engineering Department of Maritime Engineering

2. Affiliation (Author): Trad khodja Boutheina [boutheina.tradkhodja@univ-usto.dz](mailto:boutheina.tradkhodja@univ-usto.dz)

## ABSTRACT

*The growing interest in the proper use of natural fibers, alongside glass, is mainly due to their advantages; light weight, biodegradability... Bio composite materials are applicable to the aerospace, automotive and shipbuilding industries. The present work aims to study the mechanical and dynamic behaviour of hybrid bio-source materials. Then, hybrid bio-source composites have been developed based on jute fabrics and a polyester resin. Experimental vibration tests under Free-Free boundary condition were performed to determine the dynamic properties (eigenfrequencies and eigenmodes) for each material.*

**KEY WORDS:** hybrid, jute, bio-composites, dynamic

## I. INTRODUCTION

Scientists in academia and industry are increasingly turning to greener materials from biological sources to blend natural and synthetic fibers. One reason for this growing interest is that natural fibers have higher specific strength and similar specific moduli to glass fiber. [1]

Natural fibers are obtained from the outer stems of the respective plant, have very good mechanical properties and are used as reinforcing materials in polymer composites. [2]

The goal of composite materials is to combine two or more materials, creating a synergistic effect between these different materials.

An experimental modal analysis was carried out to determine the dynamic properties (frequency and eigenmode) of the bio source hybrid plate under free-

free boundary conditions.

## II. ANALYSE VIBRATOIRE

### A. TECHNIQUE DE TEST

Experimental modal analysis of vibrations due to shock excitation has the advantage of being very simple to make. These natural frequencies are determined using the following measurement chain:

- An accelerometer is fixed on the structure; the accelerometer is linked to an electronic chassis (NI acquisition device) which is linked to a desktop computer via an Ethernet connection.
- An impact hammer instrumented with a connected force sensor also to the electronic chassis.
- SO Analyzer software from m+p INTERNATIONAL. We excite the structure with the impact hammer, the sensor measures the force transmitted to the structure as a function of frequency, the accelerometer receives the response from the system based on frequency. The data is processed by the software and obtains among other things the FRF.

### B. Modal analysis of bio-composite plates

In this part we are interested in the analysis of the



free oscillation of a plate is carried out by shock excitation. The dynamic properties (frequencies and natural modes) under conditions at free-free limits are determined from a measurement chain consisting of an accelerometer on stage, a percussion hammer and SO analysis software m+p. Experimental modal analysis of the plate is carried out by shock excitation. The dynamic properties (frequencies and natural modes) under conditions.

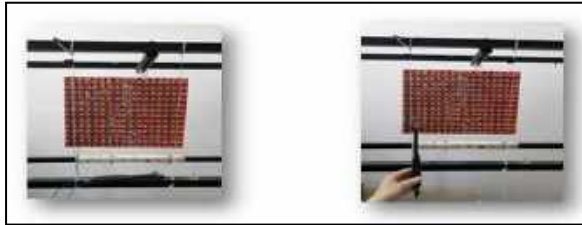


**Fig. 1.** Vibration analysis of free-free plates.

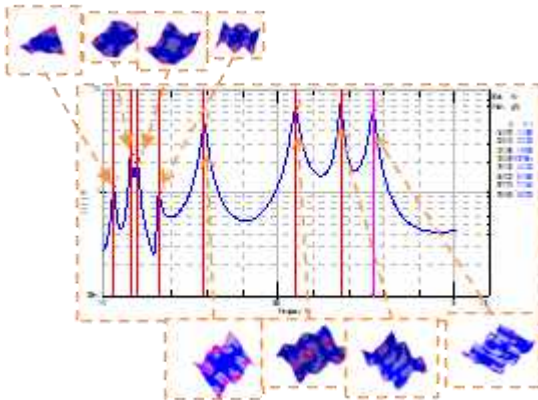


**Fig. II.** The dynamic response with the natural modes of the material plate.

Figure II represents the dynamic response (amplitude as a function of natural frequency) with the natural modes associated with each frequency, of the bio-source hybrid plate using the material to compare the vibration results carried out experimentally on the bio-source hybrid plates; three natural frequencies for each case representing the different hybrid materials are given in Fig.III

Frequency [Hz] Thickness [mm]	Materail 01 3.325	Materail 02 3.4428	Materail 03 2.678	Materail 04 2.0785
Fr 1	34,375	41,406	28,125	25
Fr 2	82,813	114,84	76,953	57,422
Fr 3	101,58	193,75	153,52	77,734

**Fig.III.** The first deformation frequencies of a plate.

### III. CONCLUSION

This work is part of a research project on the development of natural resources, jute. This study gives us, for the first time, an overview of new construction materials (biogenic sources), their advantages, particularly ecological, and their disadvantages

The type of jute fabric used in the production of the plates has an effect on the natural frequencies of the bio-source hybrid plates. It is evident that the increase in thickness has a positive effect on the vibrational behavior of the bio-source hybrid plates. We note that a relative (proportional) relationship between the natural frequencies and the natural modes depending on the thicknesses of the bio-source hybrid plates.

### REFERENCES

- [1] Laurent , G, ' Généralités sur les Matériaux Composites, (École Centrale de Nantes, 2011).
- [2] Edgars, S., « Propriétés mécaniques des fibres de lin et de leurs composites », thèse de licence (Université de technologie de Luleå, Suède, 2006).

# Dynamic characterization of a composite material Glass/Epoxy

F. MATOUK <sup>1,2,\*</sup>, L.ABDELHAKEM KORIDAK <sup>2</sup>, A.SEMMANI <sup>1</sup>, A.BOUSSOUFI <sup>1</sup>

<sup>1</sup>Affiliation (Auteur) : Laboratoire Structure des Composites et Matériaux Innovants (LSCMI) University of Science and Technology of Oran Mohamed Boudiaf. BP 1505 El M'naouar, Oran.

Email: fadhila.maatouk@univ-usto.dz

## ABSTRACT

This paper presents the dynamic characterization of a beam made of two configurations of composite, short glass fiber/epoxy and glass fiber Mat/epoxy. The first part is devoted to preparing the composite specimens and identifying their vibratory responses by an experimental setup. Using an impact hammer, the natural frequencies of the beams are predicted. The second part is used to determine the dynamic Young's modulus of the composites using the Euler-Bernoulli theory.

**KEY WORDS** : Free Vibration, Composite, Glass/epoxy, Dynamic Young modulus, Natural Frequency

## I. INTRODUCTION

Experimental modal analysis was carried out to determine the vibration characteristics of the composite beams under the free-free boundary conditions. The dynamic characteristic (Young's modulus) of the glass/epoxy composite beams is obtained using theoretical formulations based on the Euler-Bernoulli beam theory.

## II. ANALYSIS OF VIBRATION BEHAVIOUR

### A. development of glass/epoxy composite beams

The composites were produced using the contact method, with molds prepared by a manual method (Fig. 1). Two categories of the composite were made, the first one is made from a Médapoxy STR resin matrix reinforced with short glass fibers. The second one is a laminate made of Médapoxy STR resin/mat of glass fiber.



**Fig. 1.** Production of glass/epoxy composite specimens.

### B. Free vibration test of the composite beams

The experimental modal analysis was carried out to determine the natural frequencies of glass/epoxy composite beams under the free-free boundary condition.



**Fig. 2.** Vibration analysis of free-floating beams.

Experimental modal analysis of vibrations due to shock excitation has the advantage of being very simple to make. These natural frequencies are determined using the following measurement chain:

- An accelerometer is fixed on the structure; the accelerometer is linked to an electronic chassis (NI acquisition device) which is linked to a desktop computer via an Ethernet

connection.

- An impact hammer instrumented with a connected force sensor also to the electronic chassis.
- SO Analyzer software from m+p INTERNATIONAL. We excite the structure with the impact hammer, the sensor measures the force transmitted to the structure as a function of frequency, the accelerometer receives the response from the system based on frequency. The data is processed by the software and obtains among other things the FRF.

### C. Determination of young's modulus of composite from beam natural frequencies :

According to the Euler-Bernoulli beam theory, the natural frequencies are given by the following relationship :

$$f_i = \frac{X_i^2}{2 \cdot \pi \cdot l^2} \sqrt{\frac{Eh^2}{12 \cdot \rho}}$$

### C. Results and discussion

The dynamic response of the composite beam:

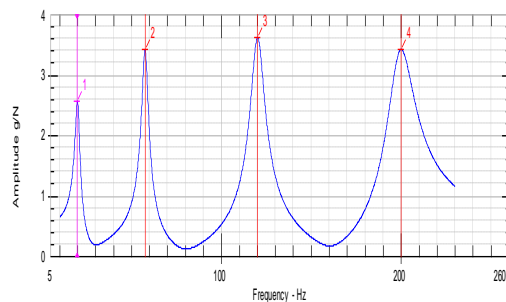


**Fig. 3.** The dynamic response of a short glass fiber-reinforced composite beam.

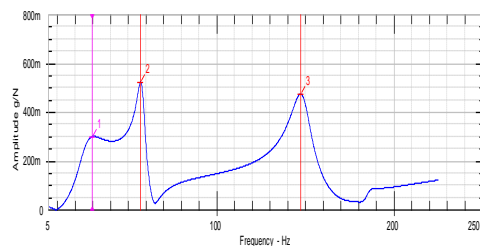


**Fig. 4.** The dynamic response of a composite beam reinforced with glass mat fabric

**Table.1.** The dynamic Young's modulus obtained from natural

frequencies of glass/epoxy composite.

	Short glass-fibre reinforced beam	Beams reinforced with Mat glass fabric
<b>Young's modulus [Pa]</b>	4.1731 <sup>E9</sup>	3.022 <sup>E9</sup>

### III. CONCLUSION

The orientation of the fibers has a very important role in the beam's mechanical strength and vibration behavior (weight and rigidity). To this end, two composites have been proposed: a mat and a shorts glass fiber layer. It was found that the composite reinforced with fibers mat has lower values of the natural frequencies than the composite reinforced with short fibers.

A comparison of the dynamic Young's modulus of the short glass fiber-reinforced composite beam and the laminated beam revealed the effect of the fibers on the rigidity of the composite structures .

### LES RÉFÉRENCES

- [1] MEMOIRE BOUSSALIH « modelisation du comportement vibratoire transverse des plaques sous différentes configurations » 2013 thèse de magister
- [2] Fairouz BOUROUIS, "étude de comportement mécanique des structures sandwichs à différents matériaux de revêtements", Université Mentouri-Constantine, Faculté des sciences de l'ingénieur.
- [3] Laurent Gornet, 19 May 2011, "Généralités sur les matériaux composites".
- [4] Laurent Gornet. Généralités sur les matériaux composites. Ecole d'ingénieur. 2008. <cel-00470296v2> HAL Id: cel-00470296 <https://cel.archives-ouvertes.fr/cel-00470296v2>.

# Simulation of vehicle behavior when passing an obstacle. Optimization of the suspension

N.MEZIANE<sup>1</sup>, N.DAHAK<sup>2</sup>, AND N.TOUAT<sup>2</sup>

1. Nedjmeddine MEZIANE: Faculty of Mechanical and Process Engineering University of Science and Technology Houari Boumediene, BP 32 Bab Ezzouar, 16111, Algiers, Algeria, nedjmeddine.meziane@etu.usthb.dz
2. Moustapha DAHAK, Noureddine TOUAT: Faculty of Mechanical and Process Engineering University of Science and Technology Houari Boumediene, BP 32 EL Alia, 16111, Algiers, Algeria, mdahak@usthb.dz, ntouat@usthb.dz

## ABSTRACT

*The main function of vehicle suspension is to ensure good stability and passenger comfort, whatever the road conditions. These requirements are contradictory. This article aims to show the possibilities offered by modelling in a virtual environment to solve this problem. The mathematical model of a complete vehicle was developed in Matlab/Simulink. The behaviour of the vehicle when passing an obstacle was analysed and the passive suspension parameters were optimised using the RMS criterion. The results of the simulations with the original and optimised parameters were compared.*

## KEY WORDS

Suspension; Optimisation of suspension parameters; Obstacle simulation.

## I. INTRODUCTION

When analysing the dynamic behaviour of vehicles, the most commonly used models are the quarter-vehicle or half-vehicle [1]. As the characterisation using these models is not sufficiently detailed, it is essential to refine the modelling. Although the current trend is towards semi-active and active suspension control schemes, controlled by parametric laws [2] and [3], neural networks, fuzzy or neuro-fuzzy logic, passive suspensions are still the most widespread due to their low cost and mechanical design. However, in terms of performance, these systems have reached their limits, as they require a compromise between comfort and road holding, one of which cannot be optimised without degrading the other.

## II. DYNAMIC MODEL OF THE VEHICLE

Fig. 1 shows the dynamic model of the vehicle with

seven degrees of freedom.

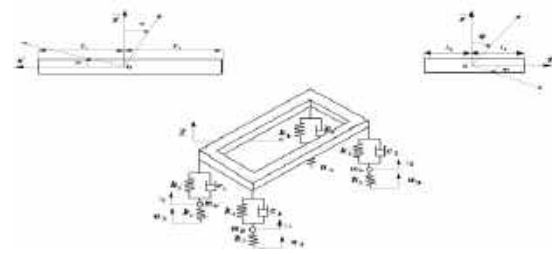


Fig. 1. Parameterization and Dynamic Model.

$k_1/k_2$ : front axle suspension stiffness, left/right respectively.  $k_3/k_4$ : rear axle suspension stiffness, left/right respectively.  $k_p$ : pneumatic stiffness.  $c_1/c_2$ : Damping coefficients of the front axle suspensions respectively, left/right.  $c_3/c_4$ : damping coefficients of the rear axle suspensions respectively, left/right.  $m_{av}/m_{ar}$ : unsprung masses of the wheels, left and right of the rear axle and those of the front respectively.  $G$ : centre of gravity,  $E$ : the wheelbase,  $Z$ : vertical displacement of centre of gravity.

$z_1, z_2$ : vertical displacements of the front axle respectively the left and right wheel.  $z_3, z_4$ : Vertical displacements of the rear axle respectively the left and right wheel.  $u_{1,2,3,4}$ : input function, each wheel 1,2,3 and 4 respectively.  $l$ : vehicle width.

Differential equations of motion of the 7 degrees of freedom system

$$[M] \times \{\ddot{q}\} + [C] \times \{\dot{q}\} + [K] \times \{q\} = \{Q\} \quad (1)$$

$[M]$ ,  $[C]$ ,  $[K]$ : inertia, damping and stiffness matrices  $\{q\}$ : generalized coordinate vector.  $\{Q\}$ : generalized force vector.

The transient responses of the vehicle are calculated for a harmonic type excitation Equation. 2.

$$u(x)_i = h \cos\left(\frac{\pi}{2p}x\right) \quad (2)$$

$u(x)$ : excitation function,  $h$ : height of the obstacle  $p$ : half width of the obstacle

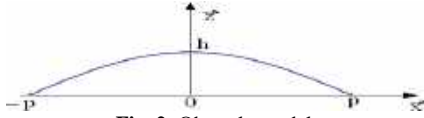


Fig. 2. Obstacle model.

The vehicle speed being assumed constant, the excitation function takes the form Equation. 3, and satisfies the conditions Equation. 4 and (5).

$$u(t)_i = h \cos\left(\frac{\pi}{2p}(d_j + p - V_0 \cdot t)\right) \quad (3)$$

$V_0$ : Vehicle speed

$d_j$ : distance between the axle and the obstacle  $j=1,2$

For the front axle  $i=1,2$  and  $j=1$

$$\begin{cases} t < \frac{d_1}{V_0} \dots \dots \dots u(t)_{1,2} = 0 \\ \frac{d_1}{V_0} \leq t \leq \frac{d_1 + 2p}{V_0}; u(t)_{1,2} = h \cos\left(\frac{\pi}{2p}(d_1 + p - V_0 \cdot t)\right) \\ t > \frac{d_1 + 2p}{V_0} \dots \dots \dots u(t)_{1,2} = 0 \end{cases} \quad (4)$$

For the rear axle  $i=3,4$  and  $j=2$

$$\begin{cases} t < \frac{d_2}{V_0} \dots \dots \dots u(t)_{3,4} = 0 \\ \frac{d_2}{V_0} \leq t \leq \frac{d_2 + 2p}{V_0}; u(t)_{3,4} = h \cos\left(\frac{\pi}{2p}(d_2 + p - V_0 \cdot t)\right) \\ t > \frac{d_2 + 2p}{V_0} \dots \dots \dots u(t)_{3,4} = 0 \end{cases} \quad (5)$$

### III. SIMULATION

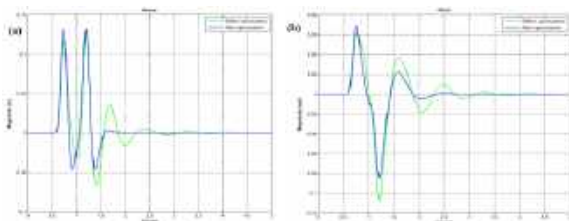


Fig. 3. Vehicle responses a- Heave; b- Pitch

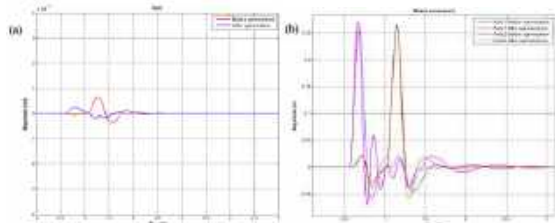


Fig. 4. Vehicle responses a-Roll; b-Wheel movement.

After optimization the performance in terms of road, holding and comfort are clearly improved.

### IV. OPTIMIZATION OF THE SUSPENSION

The objective is to develop a performing tool allowing designers to determine graphically the parameters of the optimal suspension from a preselection of the constraint defining the working conditions, Fig.4. The optimization criterion by RMS, is based on the performance index as an objective function.

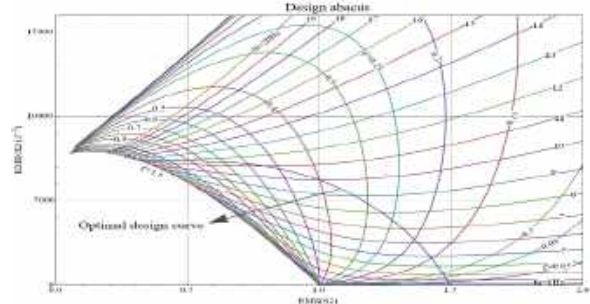


Fig. 5. Design Abacus

### V. CONCLUSIONS

The results of the simulation with optimized parameters show a significant reduction of the amplitudes and a faster stabilization compared to the behavior of the vehicle when passing the obstacle with its original parameters. Generally, vibrations in any vehicle are unpredictable and difficult to control. Thanks to the optimized suspension, we can ensure an improvement of the behavior both in terms of comfort and handling.

### VI. REFERENCES

- [1] Hakan Yazici : Design of a Parameter-Dependent Optimal Vibration Control of a Non-Linear Vehicle Suspension System, Math. Comput. Appl. 2016, 21, 13
- [2] Koona Ramji, V. K. Goel , Kusum Deep, Optimum design of suspension system of three wheeled motor vehicles, World Journal of Modelling and Simulation Vol. 3 (2007) No. 1, pp. 36-44
- [3] Wael Abbas, Ashraf Emam, Saeed Badran : Optimal Seat and Suspension Design for a Half-Car with Driver Model Using Genetic Algorithm. Intelligent Control and Automation, 2013, 4, 199-205. Scientific Research.

# effect of the location added mass on natural vibration of laminate composite structure during measurement

ABDELHAFID RAHMANE<sup>1</sup>, SOUFYANE AOUNALLAH<sup>2</sup>

<sup>1</sup>Dept Mechanical engineering, University Center Morsli Abdallah Tipaza, Tipaza, Algeria [abdelhafid.rahmane@cu-tipaza.dz](mailto:abdelhafid.rahmane@cu-tipaza.dz)

<sup>2</sup>Dept. physic University of Science and Technology HouariBoumediene, USTHB Alger, Algeria, [Aounallahs@univ-setif.dz](mailto:Aounallahs@univ-setif.dz)

## ABSTRACT

A low mass accelerometer is used to measure the vibration response on machines and structure, though, it is proved that the accelerometer mass affects the measurements. The present study addresses the effect of attached mass by accelerometer on natural frequencies of symmetric angle play laminate composite. The considered factors parameters are: attached mass of accelerometer locations from the clamped edge, staking sequences and boundary conditions. The results of this study indicate that the natural frequencies of the laminate composite plates is sensitive to the attached accelerometer mass during measurement, where it is found to be proportional to the locations of the attached accelerometer mass. The findings of this study indicate that the attached mass decreases frequency parameter, if it is inserted at a point other than a nodal line.

**KEY WORDS:** Laminate composite, Stacking sequence, Carbon-epoxy, accelerometer mass.

## I. INTRODUCTION

With regard to the vibration behavior of the composite structures, many studies were carried out to control and determine the dynamic characteristics of those materials. Several authors have performed vibration analysis of laminated composite under various conditions of reinforcement and configuration. Tsai and chang [1] developed two-dimensional analytical model for the characterization of the damping ratio which was validated experimentally and compared with the results of Ni and Adams [2], Adams and Maheri [3]. Adams and Bacon [4] developed a damping process in which the energy dissipation can be described as separable energy dissipations associated to the individual stress components. The numerical simulations and

experiments of free vibration behaviours of carbon fibre reinforced composite lattice-core sandwich cylinder (LSC) were studied under different boundary conditions, including end-free constraints by Yongshuai Han et al. [5] the results revealed that the attached masses affect the vibration modes and decrease the fundamental frequency. S.M.R. Khalili et al. [6] investigated the free vibrations of a cross-ply composite shell with and without regularly distributed attached mass, under a diversity of conditions such as the thickness of the shell and the thickness of the distributed attached mass using higher order shell theory. Therefore, the aim of this work is to fill this gap by studying the effects of the accelerometer attached mass as a function of accelerometer locations and stacking sequences). Furthermore, the paper presents a finite element model (FEM) carried out by using ANSYS software and validated experimentally.

## II. EXPERIMENTAL SET-UP

The experimental tests have been carried out with the aim of understanding the physical behavior of carbon/Epoxy (IM7/8552) laminate composite and validating the numerical models constructed using ANSYS software. The dimensions of the specimens are:  $a = 270$  mm (along x direction),  $b = 300$  mm (along y direction). They are consisted from 8 layers of unidirectional fiber carbon / epoxy. The thickness of each layer is 0.125 mm.

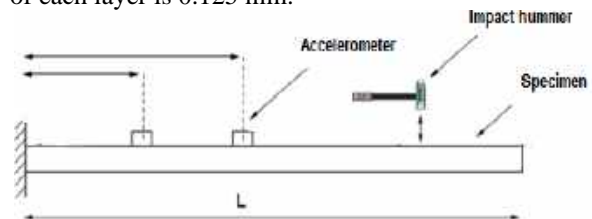


Fig. 1 Accelerometer positions variation on the laminate composite



Three laminated composites with the symmetrical stacking sequences of  $[\pm 20]_2s$ ,  $[\pm 25]_2s$ ,  $[\pm 30]_2s$ , are excited in free vibration.

In order to analyze the effect of the accelerometer mass on the natural frequencies of the laminated FRP composite, the relative positions of the attached accelerometer are shown in figure 1.

### III. FINITE ELEMENT SIMULATION

The FEM simulation is realized by using ANSYS software. Figure 3 illustrates Fundamental numerical mode shapes of  $[\pm 20]_2s$  plate with 30g (M/4) attached mass on the composite laminate plates

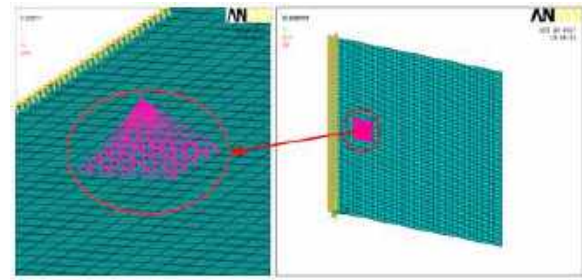


**Fig. 2** Finite element model of composite laminate plates with mass loading

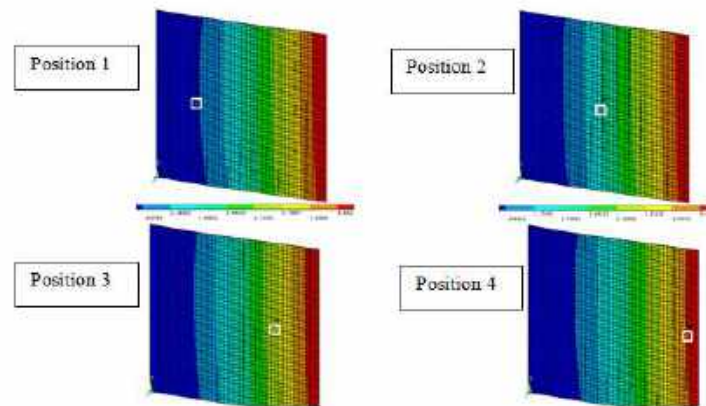


**Fig. 3** Fundamental numerical mode shapes of  $[\pm 20]_2s$  plate with 30g (M/4) attached mass

### IV. RESULTATS DISCUTION

The Tables 1-3 the experimental results of the fundamental natural frequencies of plates composite with attached accelerometer mass are compared with the finite element method (FEM). The percentage differences between FEM results and the experimental results are less than 7.6 % ,12.06 % and 6.25% for  $[\pm 20]_2s$ ,  $[\pm 25]_2s$ ,  $[\pm 30]_2s$  laminated composites plates respectively. Generally, it is seen that a good agreement exists between experimental numerical and numerical results.

**Tab. 1** Fundamental natural frequencies with attached accelerometer mass of the specimen  $[\pm 20]_2s$ .

Locations of attached masses	Fundamental frequency (Hz)		
	Exp	FEM	Error (%)
L1	5.6	6.084	2.6
L2	5.2	5.683	7.6
L3	4.8	4.993	1.25
L4	4.4	4.393	4.5

**Tab.2** Fundamental natural frequencies with attached accelerometer mass of the specimen  $[\pm 25]_2s$ .

Locations of attached masses	Fundamental frequency (Hz)		
	Exp	FEM	Error (%)
L1	5.8	6.595	12.06
L2	5.4	6.038	11.1
L3	5.1	5.1985	1.9
L4	4.8	4.6506	3.1

**Tab.3** Fundamental natural frequencies with attached accelerometer mass of the specimen [ $\pm 30$ ]2s.

Locations of attached masses	Fundamental frequency (Hz)		
	Exp	FEM	Error (%)
L1	6.8	7.2254	5.8
L2	6.4	6.7913	4.7
L3	5.9	5.8178	0.2
L4	5.6	5.2503	6.25

The Tabs. 1- 3 the experimental results of the fundamental natural frequencies of plates composite with attached accelerometer mass are compared with the finite element method (FEM). The percentage differences between FEM results and the experimental results are less than 7.6 % ,12.06 % and 6.25% for [ $\pm 20$ ]2s, [ $\pm 25$ ]2s, [ $\pm 30$ ]2s laminated composites plates respectively. Generally, it is seen that a good agreement exists between experimental numerical and numerical results.

The present result in the tabs.1-3 are compared with that in the fig. 3 and shows variation of fundamental frequencies between plates. Generally, the fundamental frequency decreases as the location of the attached mass (L1, L2, L3, and L4) is closer to the clamped edge (Fig. 3). The differences are probable due to the geometric imperfections in the structure of plate's composite, where the difficult to define a perfect clamped edges in experimental tests (due to possible flexibility of the clamping apparatus, neglecting shear deformation), uniform variations in ply thickness and the effect of misalignments in ply orientation, that have not been considered in the numerical model. These error parameters affect the stiffness, by consequently on the frequencies and damping ratio of the plates.

## V. CONCLUSION

This paper presents the findings of an experimental investigation into the effect of staking sequences on the dynamic behavior of the carbon-epoxy laminate composite under flexural vibration for two boundary conditions. Through the results obtained above, the following conclusions could be drawn:

By changing staking sequences the accelerometer mass changes the position and shape of nodal lines.

The accelerometer mass decreases frequency parameter of the composite plate if it is inserted at a

point other than a nodal line. This change is more pronounced if the accelerometer is attached farther from the nodal lines of the mode shapes.

- This result is important from the point of view of the location of the sensor and accelerometer on the machines and the improvement of vibratory measurements by the optimization of emplacement. And can be used to eliminate the mass of accelerometers used in the experimental tests for detection of defects in plates and machines by vibration methods.

## REFERENCES

- [1] J.L Tsai, N.R Chang. "2-D analytical model for characterizing flexural damping responses of composite laminates". *Compos Struct.* Vol.89 pp.443-447, 2009.
- [2] R. G Ni, R.D. Adams, "The damping and dynamic moduli of symmetric laminated composite beams theoretical and experimental results". *J Compos Mater* Vol.18 (2) pp.10-21,1984.
- [3] R. D. Adams, M. R Maheri. "Dynamic flexural properties of anisotropic fibrous composite beams". *Compos Sci Technol.* Vol.50(4) pp.497-514,1994.
- [4] R. D. Adams, D.G. C Bacon. "Effect of fibre orientation and laminate geometry on the dynamic properties of CFRP", *J Compos Mater*, vol.7, N.4, 1973.
- [5] Y.W. Han, P. plang, H. Fan , F. Sun, L. Chen, D. Fang. "Free vibration of CFRC lattice-core sandwich cylinder with attached mass", *Composites Science and Technology*, Vol.118, pp. 226-235, 2015.
- [6] S.M.R. Khalili, Tafazoli, S. Malekzadeh, K. Fard. "Free vibrations of laminated composite shells with uniformly distributed attached mass using higher order shell theory including stiffness effect", *Journal of Sound and Vibration*, Vol. 330, pp. 6355-6371, 2011.

# Investigation of new surface acoustic wave modes in IDTs/ZnO/ $\text{Al}_2\text{O}_3$ micromechanical pillar resonators

FAHIMA ARAB<sup>1,\*</sup> AND FARES KANOUNI<sup>1</sup>

1. Photonic Crystals Team, Research Unit in Optics and Photonics UROP, Center for Development of Advanced Technologies? University of Setif 1, El-Bez, Setif,19000, Algeria. [farab@cdta.dz](mailto:farab@cdta.dz)

**ABSTRACT** *Phononic crystals (PnC) are artificial materials able to inhibit the propagation of mechanical waves at certain frequencies called phononic band gaps. Surface acoustic wave (SAW) devices are one of the most attractive candidates for use in modern electronic devices, owing to their low cost, low losses, high sensitivity and ease of integration. In recent studies, it has been demonstrated that phononic crystals (PnC) are of particular interest for surface acoustic wave (SAW) devices. In this study, we focus on the relationship between pillars and love and Rayleigh waves. Micro-pillars are constructed in nickel or aluminum (Ni/Al) and incorporated into the design of single-port saw resonators. The simulation was performed with the finite element method in COMSOL Multiphysics software. The results of the calculation show that the frequency response of a two-port IDT/ZnO/sapphire SAW resonator (445 MHz) is in excellent agreement with the experimental data (440 MHz). We have also observed that by introducing Ni (Al) pillars, new Love and Rayleigh modes appeared at low frequencies, namely 1.48 MHz and 2.28 MHz (1.90 MHz and 3.26 MHz), respectively. In comparison with aluminum pillars, nickel pillars have a significantly greater effect on Love and Rayleigh waves resonance frequencies. Based on our findings, the IDTs/ZnO/Sapphire SAW resonators with Ni pillars that we have described, are a promising structure for Love wave-based sensing devices.*

**KEY WORDS** SAW resonators; Finite Element Method (FEM); ZnO; Phononic Crystal; Sensor

## I. INTRODUCTION

Surface acoustic waves (SAW) are acoustic waves propagating on the surface of an elastic solid with amplitude decaying into the solid [1]. Saw resonators could provide a number of benefits in various applications, near-surface confinement and gigahertz resonant frequency [2]. Phononic crystals (PCs) are a novel physical concept analogous to photonic crystals in the field of condensed matter physics. Recently, the modulation of acoustic wave propagation properties

using surface phononic crystals (SPCs) has attracted considerable interest [3]. As an example, in comparison with the on-port AlN/Sapphire SAW resonator, a new resonance mode is observed using crystals (SPCs) [4]. Xiao-qing LIU et al, presented a method for designing and fabricating a Love wave resonator utilizing Ni pillars on ZnO/sapphire structure [5]. In this paper, we will investigate the characteristics of the SAW ZnO/sapphire resonator coupled with Ni (Al) micro-pillars. Eigen frequency analysis and frequency domains based on COMSOL Multiphysics software used to investigate the effects of pillars on Rayleigh and Love wave propagation.

## II. MATERIALS AND METHOD

The 3D geometry of the Ni (Al)/ZnO/ $\text{Al}_2\text{O}_3$  structure used for simulation is shown in **Fig. 1(a)**. In the present study, the width of the electrode Al is  $\lambda/4$ , where  $\lambda$  is IDT period equal to 11.2  $\mu\text{m}$ . 1.45  $\mu\text{m}$  ZnO thin film is deposited above  $5\lambda$  of  $\text{Al}_2\text{O}_3$  as substrate.

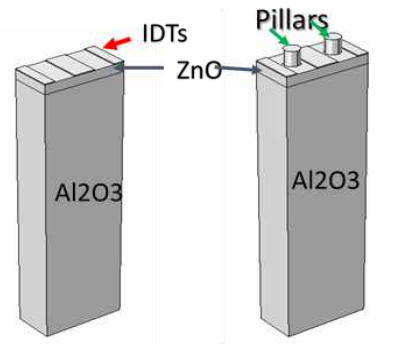


**Fig. 1.** Geometry of Ni(Al)/ ZnO / $\text{Al}_2\text{O}_3$  structure used in the simulation ( $h_{\text{pillar}} = 2.2 \mu\text{m}$ ,  $r_{\text{pillar}} = 1 \mu\text{m}$ ).

### III. RESULTS AND DISCUSSIONS

In this study, eigenfrequency analysis was employed to examine the deformation profile of the surface of total displacement of Rayleigh and Love waves of the geometry defined by Fig. 1. The obtained results are shown in **Fig.2**. We noted that by adding Ni(Al) pillars, the new Love and Rayleigh modes appeared at low frequencies, i.e. 1.48 MHz and 2.28 MHz (1.90 MHz and 3.26 MHz), respectively.

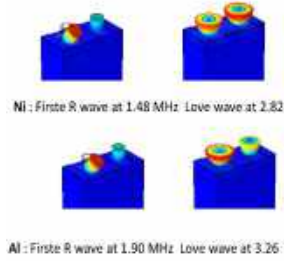


**Fig. 2.** Deformation profile of total displacement for Rayleigh and Love waves.

The frequency domain used to find the frequency response for SAW resonators in the selected bandwidth. Ground and terminal were both applied to the two electrodes (0 and 1V) to calculate the frequency response and S-parameters. The finding resultants were presented by Figs. 3, 4, and 5.

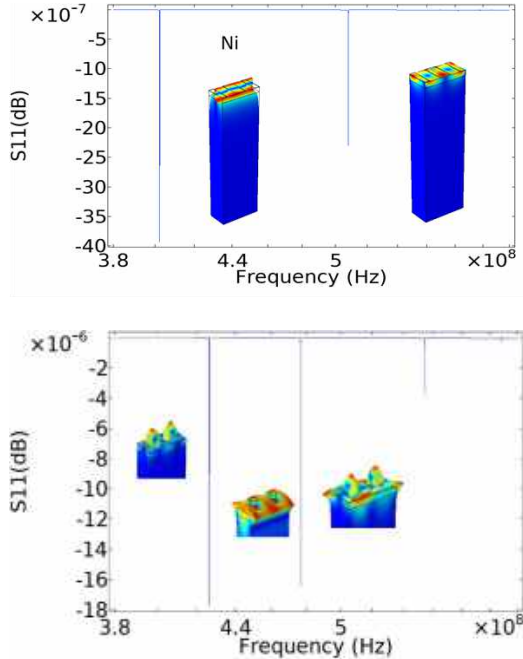


**Fig. 3.** Reflection coefficient S11 (dB) with, and without Ni pillars ( $h = 2.2 \mu\text{m}$ ,  $r = 1 \mu\text{m}$ ).

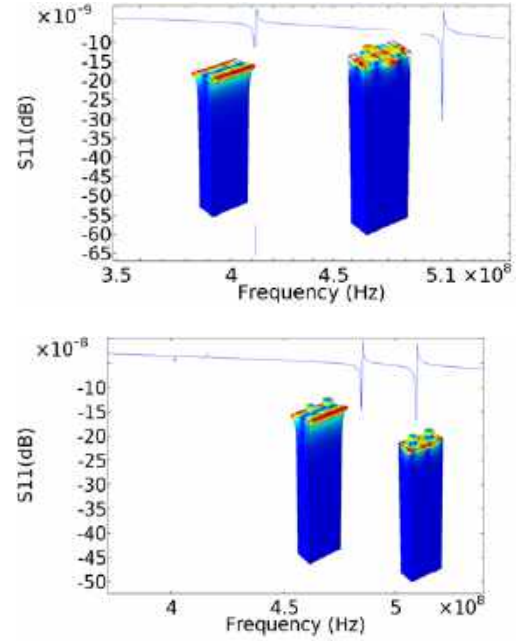


**Fig. 4.** Reflection coefficient S11 (dB) with, and without Al pillars ( $h = 2.2 \mu\text{m}$ ,  $r = 1 \mu\text{m}$ ).

It can be seen that as Al (Ni) pillars introduce the central frequency increase. This is mainly owing to the Aluminium (Al)/Nickel (Ni) mass loading. In addition, new waves of love type are created when Nickel pillars are introduced.

Finally, the simulated insertion loss (S21) of a two-port IDT/ZnO/Al<sub>2</sub>O<sub>3</sub> is in good agreement with the theoretical and the measured one (see Fig.5) [6].

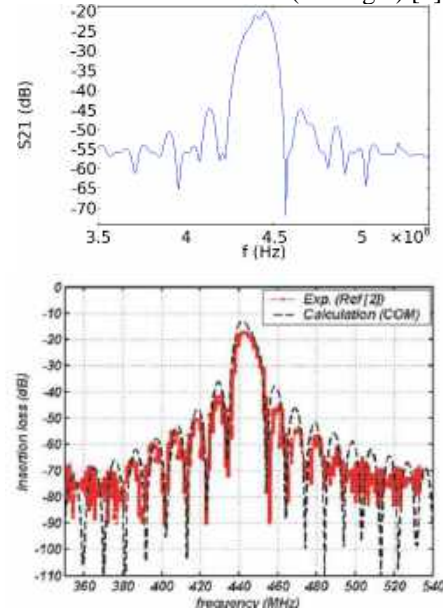


**Fig.5.** Comparing the calculated and the measured insertion loss (S21).

## I. CONCLUSION

According to the simulation results, we can observed that at low frequencies, new Love and Rayleigh modes appeared by introducing of Ni pillars. micromechanical pillar resonators IDT/ZnO/sapphire, is a promising structure for Love wave-based sensing devices. In summary, the simulation findings are consistent with previous theoretical and experimental data.

## REFERENCES

- [1] C. Campbell, Surface Acoustic Wave Devices and their Signal Processing Applications (Academic Press, San Diego,CA, 1989).
- [2] Shao, Linbo, et al. "Phononic band structure engineering for high-Q gigahertz surface acoustic wave resonators on lithium niobate." *Physical Review Applied* 12.1 (2019): 014022.
- [3] Yudistira D, Pennec Y, Djafari Rouhani B, Dupont S and Laude V 2012 Non-radiative complete surface acoustic wave bandgap for finite-depth holey phononic crystal in lithium niobate *Appl. Phys. Lett.* 100 061912.
- [4] Dong, W., Ji, X., Huang, J., Zhou, T., Li, T., Fan, Y., & Xu, K. (2019). Sensitivity enhanced temperature sensor: one-port 2D surface phononic crystal resonator based on AlN/sapphire. *Semiconductor Science and Technology*, 34(5), 055005.
- [5] LIU, X. Q., SHANG, S. L., Yan, W. A. N. G., & LIANG, S. P. (2019, November). Characteristics of Love Wave Device with Ni Pillars on ZnO/R-Sapphire Structure. In 2019 14th Symposium on Piezoelectricity, Acoustic Waves and Device Applications (SPAWDA) (pp. 1-5). IEEE.
- [6] Chen, Y. Y., Wu, T. T., & Chou, T. T. (2003). Analysis of the frequency response of a dispersive IDT/ZnO/sapphire SAW filter using effective permittivity and the coupling of modes model. *Journal of Physics D: Applied Physics*, 37(1), 120.



# Contribution au diagnostic intelligent des défauts des arbres tournants

FEDALA SEMCHEDINE<sup>1\*</sup>

1. Laboratoire de Mécanique de précision Appliquée (LMPA), Institut d'Optique et Mécanique de Précision, Université Sétif 1, Algérie, e-mail: fedala.semchedine@univ-setif.dz

## ABSTRACT

*Dans cette étude, nous proposons d'utiliser l'intégration numérique des signaux d'accélération pour obtenir les signaux de vitesse et de déplacement. Les signaux obtenus sont comparés par les techniques de traitement du signal et les réseaux de neurones artificiels du type perceptron multicouches (MLP) pour détecter et d'identifier les défauts des arbres tournants, tels que le balourd et les désalignements.*

**KEY WORDS** défauts d'arbres, Accélération, Vitesse, déplacement, Diagnostic, Perceptron multicouches MLP

## I. INTRODUCTION

Les déséquilibres de masses (balourd) et les désalignements font partie des causes majeures des défauts prématurés et des vibrations excessives dans les machines tournantes. Ces défauts pourraient mener à la réduction de la durée de vie des machines, aux arrêts de production et à l'augmentation des coûts d'entretien. Le diagnostic peut être abordé selon deux approches principales avec ou sans connaissance préalable. La première approche est basée sur la modélisation des systèmes tandis que la seconde repose sur les principes de l'intelligence artificielle. Les méthodes sans connaissance préalable présentent plusieurs avantages, en particulier le fait qu'il n'est pas nécessaire d'utiliser le modèle du système à surveiller. Cette catégorie repose sur les méthodes de la reconnaissance de formes (RdF) qui exploitent les mesures prélevées sur le système surveillé. Les signaux d'accélération représentent la grandeur la plus utilisée dans le domaine de diagnostic des machines tournantes. Cependant, pour les composantes relativement basses fréquences, comme celles des défauts d'arbres, il est recommandé d'utiliser soit le signal de vitesse ou de déplacement. Ces derniers sont délivrés généralement par des

capteurs appropriés ou bien générés synthétiquement à partir des données numériques d'accélération. Dans ce travail, nous proposons premièrement de générer numériquement les signaux de déplacement et de vitesse à partir des signaux d'accélération délivrée par la base de données des défauts d'arbres tournants (Machines Fault Database MaFaulDa) [1]. Ensuite, de comparer ces trois grandeurs pour la détection et l'identification automatisé des défauts d'arbres tournants en utilisant les réseaux de neurones artificiels du type perceptron multicouches (MLP).

## II. PARTIE EXPERIMENTALE

### A. BASE DE DONNÉES MAFAULDA

Cette base de données est composée de séries temporelles multivariées acquises par des capteurs sur un simulateur de pannes de machines (Machinery Fault Simulator, MFS) [1]. Cet équipement est composé d'un moteur, de deux paliers supportant l'arbre et il permet l'étude de multiples défauts tels que le balourd, le désalignement d'arbres et les défauts de roulements. Le dispositif expérimental est illustré sur la figure 1.

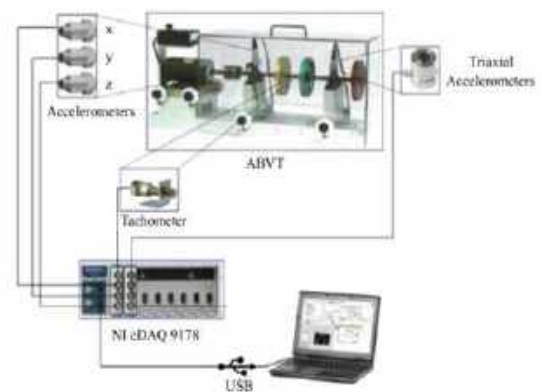


**Fig. 1.** Configuration expérimentale de la base de données



Le système est équipé d'un accéléromètre triaxial sur un palier et de trois accéléromètres sur l'autre palier (dans les directions axiale, radiale et tangentielle), un tachymètre pour mesurer la fréquence de rotation et un microphone pour capturer le son. Une fréquence d'échantillonnage de 50 kHz est utilisée pour tous les signaux. Cette base de données contient des signaux enregistrés pour différents état de fonctionnement :

- Fonctionnement normal (sans défaut), comprend un ensemble de 49 scénarios distincts, chacun avec une vitesse de rotation constante dans la plage allant de 737 tr/min à 3686 tr/min avec un pas d'environ 60 tr/min.
- Fonctionnement déséquilibré, des valeurs de charge distinctes de 6g, 10g, 15g, 20g, 25g, 30g et 35g sont rajoutées au rotor. Le nombre de total de séquences est de 333 mesures.
- Désalignement parallèle horizontal: l'arbre du moteur est déplacé horizontalement de 0,5 mm, 1,0 mm, 1,5 mm et 2,0 mm. En utilisant les mêmes fréquences de rotation qu'en fonctionnement normal pour chaque décalage. Un total de 197 scénarios différents.
- Désalignement parallèle vertical: l'arbre du moteur est décalé verticalement de 0,51 mm, 0,63 mm, 1,27 mm, 1,40 mm, 17,8 mm et 1,90 mm. Au total 301 scénarios différents ont été réalisés.

Un nombre total de 880 enregistrements pour les différents états de fonctionnement : normal, balourd, désalignement vertical et horizontal.).

## B. INTEGRATION DES SIGNAUX

Les signaux d'accélération sont exprimés soit en [g], soit en [m/s<sup>2</sup>]. La première unité provient directement des caractéristiques électriques des accéléromètres, qui sont décrites par la "sensibilité" - exprimée en [mV/g]. La seconde, en revanche, est la seule unité "légale" incluse dans le Système international d'unités (SI). Le signal de vitesse est exprimé en [mm/s].

Le calcul du signal de vitesse à partir de l'accélération après la mise à l'échelle (accélération-vitesse) implique les étapes suivantes :

- Filtrage passe haut avec élimination a priori de la composante continue.
- Intégration numérique
- Affichage du signal de vitesse
- Calcul des amplitudes spectrales (Hz)
- Affichage du spectre de vitesse.

Les mêmes étapes sont nécessaires pour le calcul du signal de déplacement à partir de la vitesse.

Le signal d'accélération (Fig. 2.) a été enregistré avec une fréquence de rotation nominale de 56.7296 Hz et un défaut de balourd de 35 grammes. La figure illustre les trois formes d'ondes temporelles. Le graphique du haut illustre le signal d'accélération original avec une composante de balourd claire (environ 0.018s, soit 55 Hz). Les graphiques du bas montrent les signaux de vitesse et de déplacement calculés par simple et double intégration respectivement de l'accélération en utilisant un filtrage passe haut de fréquence de coupure ne dépassant pas 10 Hz et une intégration numérique.

Comme on peut le voir, les formes d'onde de vitesse et de déplacement présentent la composante générée par le balourd plus clairement que le signal d'accélération, ce qui est un phénomène fondamental utilisé dans les diagnostics basés sur les vibrations.

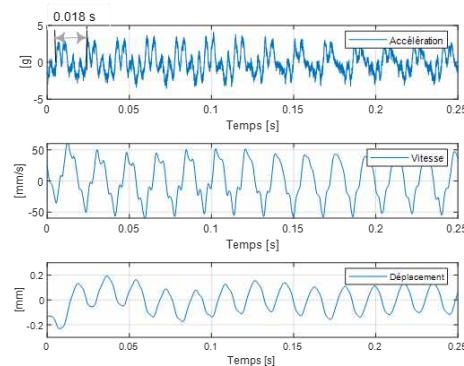


Fig. 1. Signaux temporels pour le défaut du balourd : accélération, vitesse et déplacement

La figure 2 illustre les trois spectres. Le graphique du haut illustre le spectre de l'accélération original. Le graphique central montre le spectre du signal de vitesse et enfin le graphique du bas montre le spectre généré à partir du signal de déplacement.

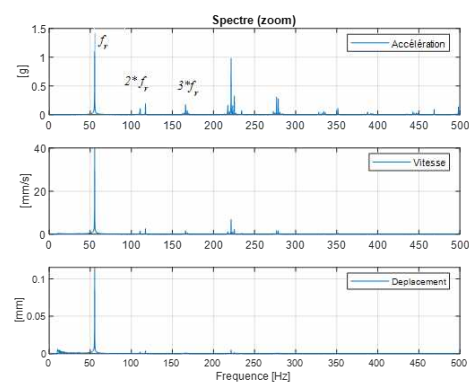


Fig. 2. Spectres d'accélération, vitesse et déplacement pour le défaut du balourd

Par analogie avec la forme d'onde temporelle, les

spectres de vitesse et de déplacement présentent la composante fréquentielle du défaut de balourd plus clairement que le spectre d'accélération.

### C. VECTEUR FORME (VF)

Pour les indicateurs temporels, on a choisi les indicateurs kurtosis et RMS. Tandis que pour les indicateurs fréquentiels, on a prélevé le pic qui représente la fréquence de rotation, ainsi que ses deux premiers harmoniques (2fr et 3fr) et le dernier indicateur c'est la somme de la fréquence de rotation et ses deux premiers harmoniques ( $fr + 2*fr + 3*fr$ ). Étant donné que chaque acquisition comprend 6 signaux et que 6 indicateurs ont été calculés pour chaque signal, cela signifie que le vecteur de forme complet (VF) est constitué de 36 indicateurs au total pour chaque grandeur.

$$VF = \{ \text{Kutosisi, RMSi, } fr, 2*fr, 3*fr, fr+2*fr+3*fr \}$$

Où  $i = 2 \text{ à } 7$  : représente le nombre de la voie d'acquisition.

### D. Classification par MLP

Les étapes suivantes ont été appliquées pour les trois grandeurs (accélération, vitesse et déplacement) :

- Lors de la classification par les réseaux de neurones MLP, la base de données de 880 acquisitions a été divisée en deux ensembles distincts, chacun avec un pourcentage différent pour l'apprentissage 60%, la validation 10% et le test 30% pour chaque grandeur.
- Un classifieur utilisant des réseaux de neurones MLP est conçu avec une couche d'entrée comportant 36 neurones, ce nombre étant égal à la taille du vecteur de forme. Le nombre de neurones dans la couche cachée dépend généralement du problème à résoudre et ne peut être fixé à l'avance. Il doit être ajusté jusqu'à obtenir le nombre optimal. Le nombre de neurones dans la couche de sortie est égal au nombre de classes.
- Initialement, nous avons attribué des étiquettes en système binaire à chaque vecteur de forme afin de pouvoir comparer les sorties générées par la méthode de classification avec les sorties réelles. Ces étiquettes indiquent la répartition des classes, à savoir : normale, défaut de balourd, défaut de désalignement vertical et défaut de désalignement horizontal. Nous avons donc varié nos choix afin de détecter et identifier distinctement ces différents types de défauts. Par conséquent, nous avons effectué deux classifications distinctes en fonction des cas existants :

- 1ère classification (détection du défaut) : seulement deux classes ont été utilisées dans ce

cas, la première classe présente l'état normal sans défaut comprenant 49 acquisitions et la deuxième c'est le cas avec défaut comprend 831 acquisitions (la somme des différents défauts)

- 2ème classification (identification du défaut) : dans ce cas l'état sans défaut est éliminé, il reste les cas avec défaut (balourd, désalignement horizontal, désalignement vertical). Cette phase comprend au total 831 acquisitions.

#### - Phase de détection

Les tableaux suivants présentent la moyenne des résultats de classification par le réseau MLP pour chaque grandeur, dont l'architecture ci-dessous est 36 neurones dans la couche d'entrée, 10 dans la couche cachée et 2 dans la couche de sortie

##### - Signaux d'accélération

Classes	Target	
	Sans défaut	Avec défaut
Sans défaut	49/49	0/49
Avec défaut	0/831	831/831
Total (%)	<b>96.65±1.4</b>	

##### - Signaux de vitesse

Classes	Target	
	Sans défaut	Avec défaut
Sans défaut	49/49	0/49
Avec défaut	0/831	831/831
Total (%)	<b>97.29±0.9</b>	

##### - Signaux de déplacement

Classes	Target	
	Sans défaut	Avec défaut
Sans défaut	49/49	0/49
Avec défaut	0/831	831/831
Total (%)	<b>96.65±1.4</b>	

Le système est capable de détecter de manière précise la présence d'un défaut quel que soit la grandeur utilisée.

#### - Phase d'identification

Les tableaux suivants indiquent les résultats moyens de classification obtenus par le réseau MLP pour chaque grandeur. L'architecture du réseau est configurée avec 36 neurones dans la couche d'entrée, 10 neurones dans la couche cachée et 3 neurones dans la couche de sortie.

##### - Signaux d'accélération

Classes	Target		
	Balourd	D. Horizontal	D. Vertical
Balourd	333/333	0/333	0/333
D. Horizontal	0/197	197/197	0/197
D. Vertical	0/301	0/301	301/301
Total (%)	<b>97.2±1.0121</b>		

## - Signaux de vitesse

Classes	Target		
	Balourd	D. Horizontal	D. Vertical
Balourd	333/333	0/333	0/333
D. Horizontal	0/197	197/197	0/197
D. Vertical	0/301	0/301	301/301
Total (%)	<b>96.79±0.48</b>		

## - Signaux de déplacement

Classes	Target		
	Balourd	D. Horizontal	D. Vertical
Balourd	333/333	0/333	0/333
D. Horizontal	0/197	197/197	0/197
D. Vertical	0/301	0/301	301/301
Total (%)	<b>96.52±0.53</b>		

Ces résultats indiquent que le système est capable d'identifier avec précision le défaut par l'utilisation d'un des grandeurs précédentes.

Ces résultats sont supérieurs à ceux trouvées dans la littérature pour la même base de données avec des algorithmes de traitement du signal plus complexes [2-4].

### III. CONCLUSION

Les résultats des phases de détection et d'identification des défauts des arbres tournants indiquent que les trois grandeurs vibratoires à savoir l'accélération, la vitesse et le déplacement sont capables de détecter et d'identifier n'importe quel défaut d'arbre et ce, quel que soit la vitesse de rotation, avec une précision qui dépassent 96.5%. Donc on peut dire qu'on présence d'autre type de défauts, comme les défauts d'engrenage ou des roulements, il est fortement recommandé de travailler en plus avec les signaux de vitesses et/ou de déplacement en effectuant une ou double intégration numérique de l'accélération.

### REFERENCES

- [1] MaFaulDa - Machinery Fault Database, <http://www02.smt.ufrj.br/682~offshore/mfs/>
- [2] M.A. Ali, et al., "The Influence of Handling Imbalance Classes on the Classification of Mechanical Faults Using Neural Networks". The 8th International Conference on Modeling Simulation and Applied Optimization (2019) (ICMSAO), Bahrain, 15–17 April 2019
- [3] D. Saidani et al. "Faults Detection and Classification under Variable Condition Using Intrinsic Time–Scale Decomposition and Neural Network". Journal Européen des Systèmes Automatisés Vol. 54, No. 5, pp. 777-782, (2021)
- [4] A. A. de Lima, et al. "On Fault Classification in Rotating Machines using Fourier Domain Features and Neural Networks", Federal Center of Tech. Edu. Celso Suckow da Fonseca (CEFET-RJ) - Nova Iguac, U. Brazil. pp1-4

***Session T2: Computer  
Aided Design/  
Manufacturing  
CAD/CAM***

# A new algorithm to optimize the effect of manufacturing errors on the kinematic and dynamic performances of a planar mechanism

Belkadi Noufel<sup>1</sup>, Hosna Abdenour<sup>1</sup>, Djeddou Ferhat<sup>1</sup>, Smata Lakhdar<sup>1</sup>.

<sup>1</sup>Applied Precision Mechanics Laboratory, Institute of Optics and Precision Mechanics, University Setif1, 19000 Setif, Algeria

## ABSTRACT

*Optimization is essential in mechanical engineering problems that mostly are non-linear, depend on mixed decision variables and usually subject to constraints. In real life, the design parameters differ from their theoretical values. This difference is due to the manufacturing errors of mechanism parts. In this paper, a new hybrid approach is proposed to study the effect of manufacturing errors on the kinematic and dynamic performances of a planar mechanism. Furthermore, an analytical method based on the partial derivatives is used to study to determine the mathematical equation representing the kinematic errors of the mechanism. The Lagrangian equation is adopted to define the mathematical expression of the mechanism motion. Two objectives are considered regarding the acceleration error and dynamic performance. In the optimization process, a new hybrid algorithm between Particle Swarm Optimization and JAYA is used to achieve better kinematic and dynamic performances of the planar mechanism. Moreover, the obtained results reveal really that the developed algorithm is a promising approach to optimize the effect of manufacturing errors and the used methodology was found to be helpful to achieve optimal kinematic and dynamic behaviour for a planar mechanism.*

## KEY WORDS

Manufacturing errors ; optimization ; PSO algorithm ; JAYA algorithm ; Planar mechanism

## I. INTRODUCTION

The word optimization in mechanical engineering refers to the pursuit of a better solution or better design to certain products or system. On the other hand, there are always difference in values between real and theoretical counterpart's values of mechanism. This difference is mainly due to the manufacturing errors. In many mechanisms, the variation of link dimensions and joint clearance due to manufacturing errors affects the dynamic and kinematic performance of mechanisms. On the other hand, there is a huge need to develop new methods to tackle the synthesis of mechanisms since it has a significant effect on their performances. In the present work, the kinematic errors (position, velocity and acceleration) due to the error manufacturing of dimension links are

investigated using an analytical method. This technique is based on the partial derivatives of the motion constraint equations. In the first step, the acceleration error is considered as the first objective to minimize the kinematic error and to determine the direction of clearance joints. Secondly, the results obtained from the first step are used to optimize the design parameters of slider-crank mechanism. The second objective is to minimize the effect of manufacturing errors and clearance joints on the dynamic performance of this mechanism. In this step, the Lagrangian function is adopted for modeling the motion of mechanism and optimize the mass distribution of the links in order to reduce the effect of manufacturing errors [1,3]. A new hybrid PSO and JAYA algorithm is used to solve this problem [2].

## II. THE MODEL OF JOINT CLEARANCE

Throughout this study, links of mechanism are assumed to be connected with each other by revolute joints with clearance. This clearance can be defined as the radii difference between the pin and socket (as shown in Fig.1). when considering the assumption of the continuous contact model between pin and socket at the joint, the clearance may be modeled as vectors corresponding to mass-less virtual connection with lengths equal to joint clearance [2]. The virtual joint clearance  $r_c$  (Fig.1) is determined as:  $r_c = r_B - r_j$

## III. CASE STUDY: SLIDER-CRANK MECHANISM WITH JOINT CLEARANCES

In this work, the slider-crank mechanism with two joint clearance ( $\gamma_2, \gamma_3$ ) is taken as a case study (Fig.2).

### A. Optimization of the acceleration error

In this study, the acceleration error of the slider is formulated as an optimization problem and is defined as follows:

$$\text{Minimize } F_1(X_1) = \delta \ddot{x}_{G4} = (C_1 \tan \theta_3 + D_1) \delta l_2 + (C_2 \tan \theta_3 + D_2) \delta l_3$$

### B. Optimization of the dynamic performance of the mechanism

In this section, the dynamic performance of the mechanism is optimized. The mechanism links are assumed to be rigid; as a result, the direction of the clearance vector can be derived using Lagrange's equation [2,3] which is may be given in the following expression:

$$\begin{aligned} \text{Minimize } F_2(X_2) = & \sum_{i=2}^4 \left( I_i \ddot{\theta}_i \frac{\partial \theta_i}{\partial \gamma_j} \right. \\ & + m_i \left( \ddot{x}_{Gi} \frac{\partial x_{Gi}}{\partial \gamma_j} + \ddot{y}_{Gi} \frac{\partial y_{Gi}}{\partial \gamma_j} \right) \\ & \left. + m_i g \frac{\partial y_{Gi}}{\partial \gamma_j} + C_{\theta i} \dot{\theta}_i \frac{\partial \theta_i}{\partial \gamma_j} \right) + C_\gamma \dot{\gamma}_j = 0 \end{aligned}$$

### C. The proposed hybrid method

The hybridization proposed in this method uses both the velocity changing particles of PSO and the best and worst changing population concept of JAYA. One can also say it is an introduction of JAYA rules into PSO in order to help stabilize the optimization algorithm and to avoid falling into local optimum which is a problem we can face using PSO.

## IV. RESULTS AND DISCUSSION

Kinematic and dynamic optimization performances of slider mass center are illustrated in Fig.3 and Fig.4.

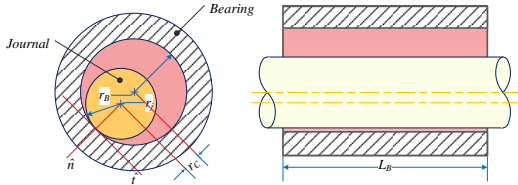


Fig. 1. The model of revolute joint with clearance.

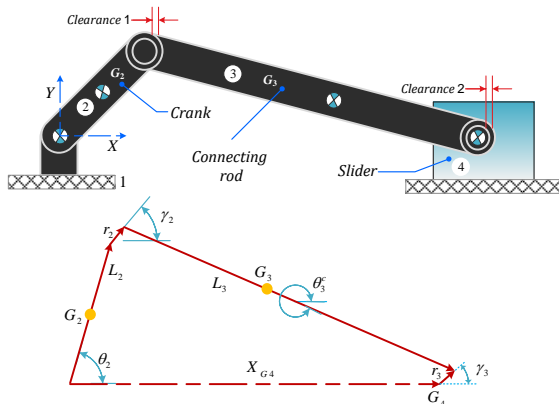


Fig. 2. Slider-crank mechanism with joint clearances.

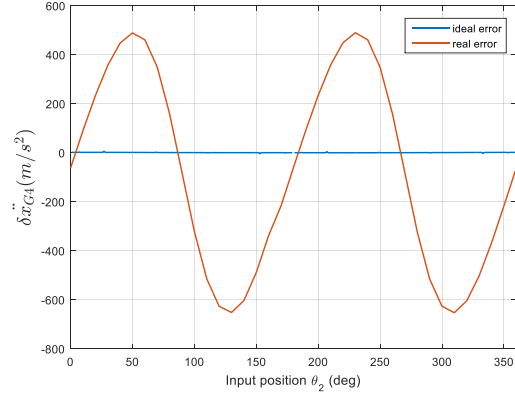


Fig. 3. Ideal and real linear acceleration error of slider.

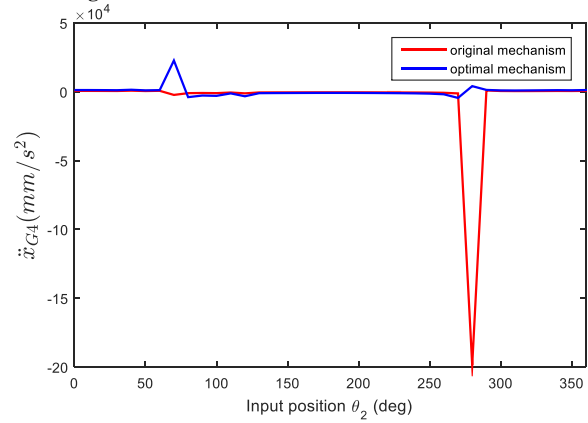


Fig. 4. Angular acceleration of connecting rod.

## V. CONCLUSION

In this study, the effect of manufacturing errors in the kinematic and dynamic performances of a planar mechanism are studied and optimized. furthermore, a new hybrid PSO-JAYA algorithm is developed and used to solve this problem. Finally, the results showed that the optimal parameters of the mechanism offer better kinematical and dynamical performances than the original mechanism.

## REFERENCES

- [1] Belkadi.N et al (2022) Optimization Study of the Effect of Manufacturing Tolerances on the Kinematic and Dynamic Performances of a Planar Mechanism. SAE. Int. J. Mater. Manuf. volume 16, issue1,2023. <https://doi.10.4271/05-16-02-00011>
- [2] Hosna.A et al (2023) A New Hybrid Particle Swarm Optimization and Jaya Algorithm for Optimal Weight Design of a Gear Train. SAE. Int. J. Mater. Manuf. volume 16, issue2,2023. <https://doi.10.4271/05-16-01-0005>
- [3] A.Sardashti, H.M.Daniali, S.M.Varedi(2013) Optimal free-defect synthesis of four-bar linkage with joint clearance using PSO algorithm. Meccanica 48:1681-1693. <https://DOI.10.1007/s11012-013-9699-6>



# Effect of pore shape irregularity on the compressive strength of cellular materials

DJAMEL BATACHE, ABDELGHANI KHENNAB \*, ABDENNOUR BENHIZIA, AND ILYAS BENSALEM

Mechanics of Structures and Materials Laboratory, University of Batna 2, Algeria  
a.khennab@univ-batna2.dz

## ABSTRACT (1,000 characters)

*The pore structure of cellular material is usually modeled as a circle. However, in natural cellular material, the shape of pores is arbitrary and irregular. This can affect the mechanical properties if it is included. This study examines the effect of pore shape irregularity on the compressive strength of cellular material. The Abaqus software is used to simulate the compression test. Comprehensive deformation mode and compressive properties were presented. The numerical findings demonstrated that the compressive characteristics were considerably influenced by the geometry of the void. Compared to shapes with non-equal radius ratios, those with near-equal ratios exhibit stronger compression properties.*

## KEY WORDS

Void shape, Cellular material, Force-displacement, Compressive properties

## I. INTRODUCTION

The increasing interest in the safety and crashworthiness of structures has led to the study of different materials and geometrical aspects of structures. Therefore, many studies have investigated the effects of various geometric shapes such as circular, square, and hexagonal on the energy absorption capability. Lightweight materials, such as foams, and honeycombs have the advantages of adjustable density and strength [1], outstanding performance [2], and convenience for construction in-place [3]. Therefore, they have been increasingly used in engineering applications, such as embankments [4], bridge approaches, precast walls [5], aircraft arresting systems [6], and insulation floor/roof screeds [7]. In most numerical studies of cellular material, the pore structure is modeled as a circle. However, in natural cellular material, the shape of pores is arbitrary and irregular. This indicates that the pore parameters could be a primary factor influencing the material properties

of cellular materials. Therefore, a comparative study is necessary to illustrate the effect of void shapes on mechanical properties. In the present study, the shape of the pores in the structure was investigated by comparing the mechanical response and force-displacement curves of two types of 3D models: nearly equal radius ratio of the pores with non-equal radius ratios.

## II. MATERIALS AND METHODS

### A. SAMPLE DESIGN

The analyzed pores shapes in this study are designed in SolidWorks and included in the structure as randomly dispersed pores using the DIGIMAT software as shown in Fig. 1.

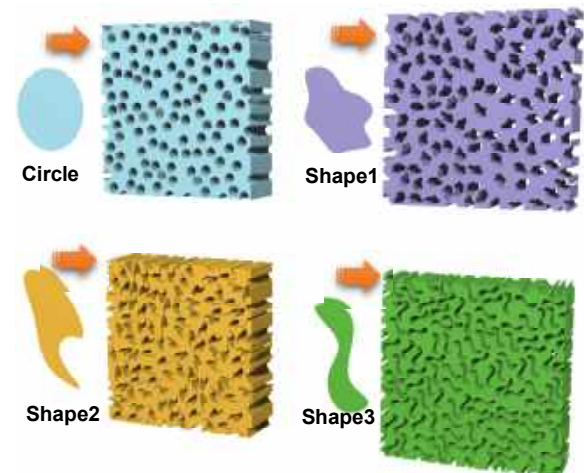


Fig. 1. Geometrical illustrations of the analyzed structures with different pore shape irregularity.

### B. FINITE ELEMENT ANALYSIS

The studied structures are made from PLA material. The axial compression test is simulated using the FE code ABAQUS/Explicit. To allow a meaningful comparison of the results, the dimensions of the shapes

of the pores were kept the same, which gives the same porosity in the four models. The developed 3D finite element (FE) models were supported by a rigid fixed lower plate and loaded by a rigid moving upper plate at a constant velocity of 15.2 m/s [9] as shown in Fig. 2.

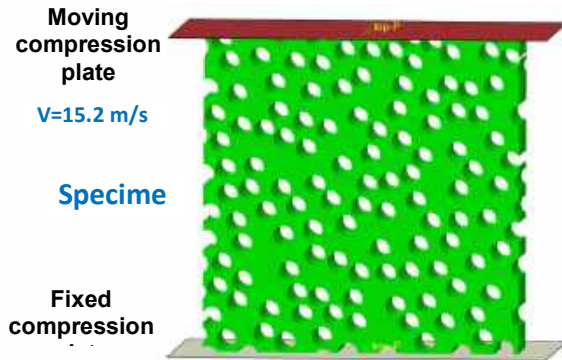


Fig. 2. Numerical model with boundary conditions.

### C. RESULTS

The results of the numerical simulations presented below show the deformation modes and reaction force-displacement curves for different pore shapes.

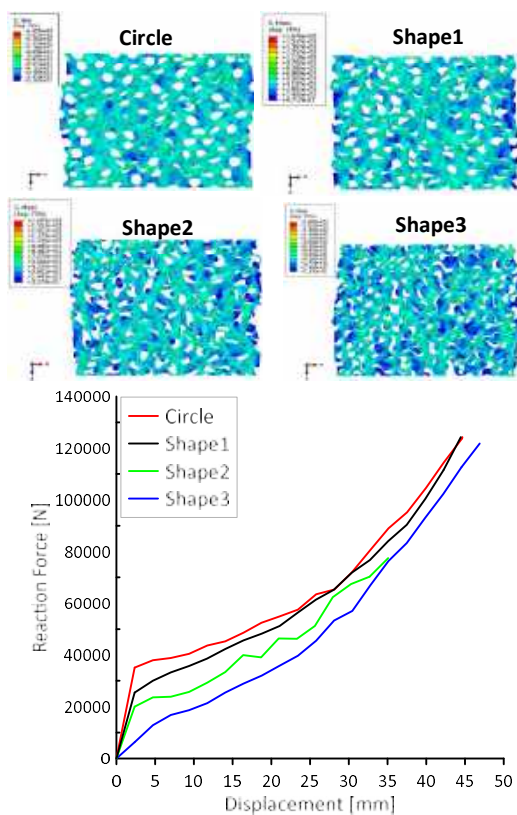


Fig. 2. Deformation modes and reaction force-displacement curves.

### III. CONCLUSION

To quantify the effect of pores' shape irregularity in cellular materials, a comparative study was conducted in a quasi-static compression test. The numerical results showed that the mechanical response of the compressed structures can be divided into three stages: elastic deformation limited by peak force, plateau stage represented by an average plateau force, and densification stage characterized by a rapid increase of stress with a small strain value. The irregularity of the shape of the pores significantly affects the compressive properties of the structure. The lowest crashworthiness performance is recorded in the structure with non-equal ratios of shape radius. Structures with almost equal ratios showed higher strength and can be considered the best energy-absorbing device.

### REFERENCES

- [1] Khennab Abdelghani and Benhizia, Abdennour. Design and evaluation of compressive properties of 3D-printed PLA stochastic open-cell foam. *International Journal of Crashworthiness*. (2023).
- [2] Ilyas Bensalem, Abdennour Benhizia, Novel design of irregular closed-cell foams structures based on spherical particle inflation and evaluation of its compressive performance, *Thin-Walled Structures*, Volume 181, (2022).
- [3] Zhong, R., X. Ren, et al, Mechanical properties of concrete composites with auxetic single and layered honeycomb structures, *Construction and Building Materials* 322: 126453, (2022).
- [4] Dai, Z., M. Zhang, et al. Model Tests on Performance of Embankment Reinforced with Geocell Under Static and Cyclic Loading, *Proceedings of GeoShanghai International Conference: Ground Improvement and Geosynthetics*, Singapore, Springer Singapore, (2018).
- [5] Hussain, M., N. Abbas, et al. Investigating the performance of GFRP/wood-based honeycomb sandwich panels for sustainable prefab building construction, *SN Applied Sciences* 1: 1-8, (2019).
- [6] Xing, Y., X. Yang, et al, A theoretical model of honeycomb material arresting system for aircrafts, *Applied Mathematical Modelling* 48: 316-337, (2017).
- [7] Almutairi, M. M., M. Osman, et al. Thermal Behavior of Auxetic Honeycomb Structure: An Experimental and Modeling Investigation, *Journal of Energy Resources Technology* 140(12), (2018).

# PSO-JAYA hybrid algorithm to optimize the design of a constrained mixed variable speed reducer

Hosna Abdenour<sup>1</sup>. Djeddou Ferhat<sup>1</sup>. Hamouda abdelatif<sup>2</sup>.

<sup>1</sup>Applied Precision Mechanics Laboratory, Institute of Optics and Precision Mechanics, University Setif1, 19000 Setif, Algeria

<sup>2</sup>QU.E.R.E Laboratory , University Setif1, 19000 Setif, Algeria

## Abstract

Optimization is a necessary tool used by mechanical engineers for improvement of a design. These designs usually contain mixed variables are subject to constraints. Meta-heuristic methods can tackle the optimization problem containing mixed variables easily, PSO and JAYA are two of these algorithms. The hybridization of these two algorithms aim to improve upon the achieved result and performance. In this work we have applied the proposed method to a constrained mixed variable problem. The problem is the reduction of weight of a speed reducer. This problem was treated before by other algorithms which gave us the chance to compare our result with that of other authors. The hybrid algorithm between Particle Swarm Optimization and JAYA has achieved better results than PSO and all the other algorithms used before on the problem while satisfying constraints.

The PSO-JAYA hybrid proved to be very useful method to deal with discrete and normalized variables in an optimization problem.

## Key words

Optimal design, gear design, optimization, particle swarm optimization, JAYA, speed reducer

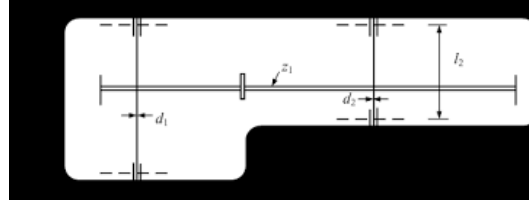
## Introduction

In engineering the effects of the pricing approach provoked the creation of what we call optimal design that has become a branch of engineering. The goal of optimizing the product varies from correcting its defects and problems to maximizing or minimizing its characteristics. The concept of optimization has taken a place in applied mathematics level, whether the methods are classic optimization methods or meta-heuristic methods like the one used in this work.

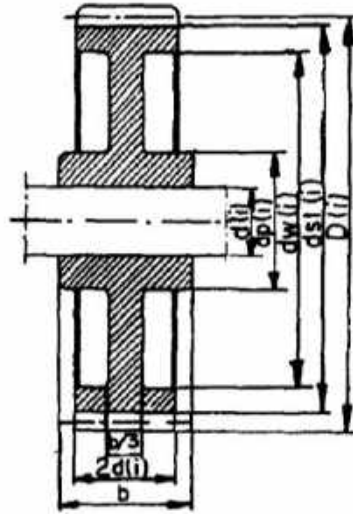
In the pursuit of improvement hybridization of meta-heuristics is adopted. The reason behind it is to improve on existing algorithms performance and accuracy. In this work we aim to test the hybrid algorithm PSO-JAYA for the weight reaction of a speed reducer. The problem contains mixed variable and is subject to constraints.

## Case study

Dr. Jan Golinski wrote his article [1] about solving optimal problems using nonlinear programming. The author has applied several nonlinear methods to solve different optimization problems. We have chosen the speed reducer for the application of the hybrid algorithm. The results we find will be compared to his results. We also will compare the obtained results to those of other authors [2] [3] [4] having worked on the example. The minimization of the weight of a speed reducer given is the objective function. The speed reducer is shown by Fig 1.

**Fig1**

In order to minimize the weight of a gear we must reduce its volume. Therefore, when trying to minimize the weight of the speed reducer, the expression must be established not for the weight but for the volume. We must mention also both gears have the following form as shown in Fig 2.

**-Fig 2** cutting view of the gear used in the speed reducer-

The expression for volume will be the sum of both gears and both shafts volume. The volume of each gear is given as following:

$$V = (d_{st}^2 - d_w^2) \times \frac{\pi b}{4} + (d_w^2 - d_p^2) \times \frac{\pi}{12} + (d_p^2 - d_i^2) \times 2b$$

Out of the objective function we extract the design variables. As we can notice there are 7 parameters not defined in the objective function and those are our design variables.

$$f(x) = V = f(m, z, b, l_1, l_2, d_1, d_2) = f(x_1, x_2, x_3, x_4, x_5, x_6, x_7,)$$

The optimization problem is also subject to 11 constraints.

### Proposed method

The hybridization of PSO and JAYA[5] utilizes the characteristics of both algorithms to achieve

a result. From PSO it borrows the velocity changing particles and from JAYA its dependence on the best and worst solution achieved by iteration. The introduction of both rules in one algorithm aims to add stability and accuracy to the performance. It also aims to search for better solution the other algorithms haven't found yet.

## Results and discussion

The results as shown in Fig 3 show that the hybrid algorithm is fast at arriving to the optimal solution. The program also managed to satisfy all design constraints in the process.

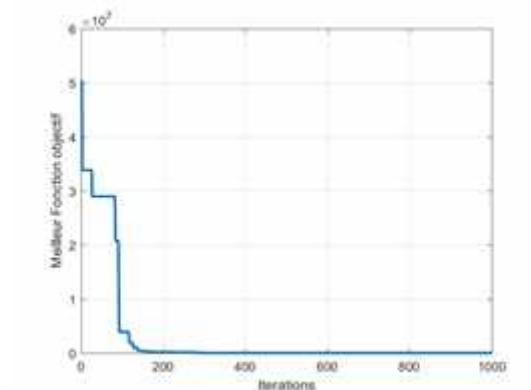


**Fig 3** objective function variation

In Table 1 the result the algorithm found is shown and compared to other algorithms. The result found in this works proved to be the best as shown in the table below.

**Table 1** comparative results between different algorithms

	the proposed PSO method	Kuang et al (Taguchi method)[4]	Oluwole ,A and Green,P (GDE)[3]	Rashid et al (GA)[2]
<b>Objective function (<math>cm^3</math>)</b>	2994.43	2876.12	2996.34	3087

## Conclusion

In the case of mechanical optimization problems, PSO-JAYA has shown capability of treating constrained problems with both discrete and continuous variables. The obtained results have respected the constraints applied on the mechanical devices.

## References

[1] Golinski, J., Optimal synthesis problems solved by means of nonlinear programming and random methods., Journal of Mechanisms, volume 5. pp. 287-309, 1969

- [2] Rashid, M, Muhammad, H, Q, Huneza, A, Rohail, Z., Glowinski's speed reducer problem revisited., American scientific research journal for engineering, technology, and sciences (ASRJETS), volume16, pp.55-65, 2016
- [3] Oluwole, A, Green, P., Conceptual comparison of population based metaheuristics for engineering problems., The Scientific World Journal, 2015
- [4] Kuang, J, K, Rao, S, S, Chen, L., Taguchi-aided search method for design optimization of engineering systems, Eng. Opt., volume 30, pp1-23, 1998
- [5] Hosna.A , Djedou.F , Hmouada.A , (2023) A New Hybrid Particle Swarm Optimization and Jaya Algorithm for Optimal Weight Design of a Gear Train. SAE. Int. J. Mater. Manuf. volume 16, issue2,2023. <https://doi.10.4271/05-16-01-0005>



# Mathematical modeling of surface roughness in polyoxymethylene (POM-C) turning

TALLAL HAKMI\*, AMINE HAMDI

Laboratory of Mechanical Engineering, Materials and Structures, Tissemsilt University, Tissemsilt 38000, Algeria, \*Corresponding author: [tallal.hakmi@univ-tissemsilt.dz](mailto:tallal.hakmi@univ-tissemsilt.dz)

## ABSTRACT

*Polymers are materials increasingly used in the mechanical industry. The main objective of this work is to study the effect of cutting conditions (cutting speed  $V_c$ , feed rate  $f$ , depth of cut  $ap$ , tool nose radius  $r_e$ , and principal cutting edge angle  $X_r$ ) on surface roughness ( $R_a$ ) in the turning of polyoxymethylene (POM-C). To achieve this goal, two carbide inserts, SPMR 120304 and SPMR 120308, are used to perform cutting operations according to a selected method based on a minimum of Taguchi  $L_{16}$  experiments ( $4^3 \times 2^2$ ). In this regard, analysis of variance (ANOVA) was employed to assess the significance of input parameters on the two response variables. Additionally, an artificial neural network (ANN) is implemented to obtain a mathematical modeling of the responses.*

**KEY WORDS** : Polyacetal POM-C; turning; ANN; artificial intelligence; mathematical modeling

## I. INTRODUCTION

Polymeric materials have become increasingly prevalent in mechanical engineering applications, such as automotive, aerospace, optics, robotics, and machinery [1, 2]. In the field of automotive mechanics, this technical material is used to manufacture complex parts, including gears, racks, wheels, bearings, transmission pinions, valve seats, and more [3]. These organic materials generally offer several advantages in the aforementioned applications, including excellent formability and molding capability, good mechanical properties, low cost and weight, high resistance to corrosion and wear, resilience to various aggressive environments, the ability to operate quietly and without lubrication, as well as dimensional stability and high rigidity [3, 4, 5].

As a result, they provide an interesting alternative to traditional metals in a wide range of applications aimed at reducing production costs. In plastic

processing, the extrusion method is often the most commonly used for both thermoplastic and thermosetting polymers. Consequently, various molding techniques serve as production processes for technical plastics in the case of mass production. However, parts manufactured through forming processes (molding, shaping, etc.) often require additional machining operations before being put into service. Thus, material removal machining of small batch mechanical parts is necessary when dimensional precision and surface quality are demanded by the industry [1, 3, 6, 7].

The main objective of this work was to study the effect of cutting parameters ( $V_c$ ,  $f$ ,  $ap$ ,  $r_e$ , and  $X_r$ ) on the quality of machined parts ( $R_a$ ) in the turning of polyacetal POM-C. The measured response values were used to determine the mathematical model using the ANN approach.

## II. EXPERIMENTAL PROCEDURE

Polyoxymethylene POM-C is a semi-crystalline thermoplastic known for its excellent corrosion resistance, low moisture absorption, and high resistance to abrasion. The cutting condition ranges were selected within the manufacturer's recommended intervals for Dormer Pramet cutting tools. To establish and reduce the number of experiments compared to a full factorial design (FFD), the Taguchi multifactorial method ( $L_{16} = 4^3 \times 2^2$ ) was chosen.

## III. RESULTS AND DISCUSSION

The mathematical model obtained for  $R_a$  as a function of the input parameters ( $V_c$ ,  $f$ ,  $ap$ ,  $r_e$ , and  $X_r$ ) and their coefficient of determination ( $R^2$ ) is presented by equation 1. The value of  $R^2$  is very close to unity ( $R^2 = 0.99$ ), indicating that the model developed using the ANN technique is statistically significant, demonstrating a strong correlation

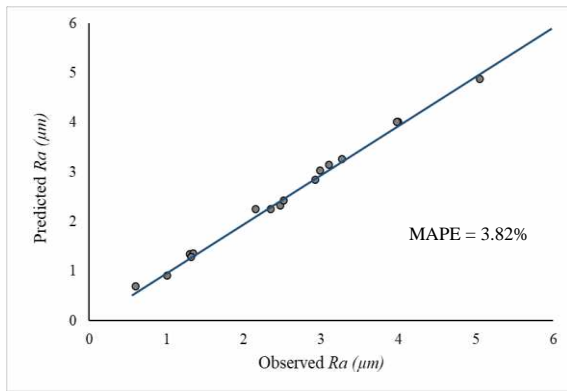
between the experimental data and the prediction results.

$$\begin{aligned} R_a &= 0.80328H_1 - 0.86417H_2 + 3.42147H_3 \\ &+ 3.35752 \\ R_{Ra}^2 &= 0.99986 \end{aligned} \quad (1)$$

Where :

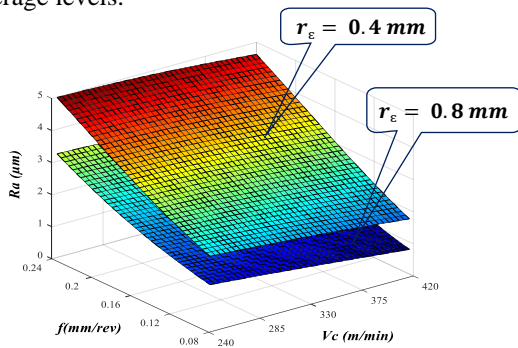
$$\begin{aligned} H_1 &= \tanh(0.5(-0.00768V_c + 3.7979f - 0.651ap \\ &\quad - 1.3423r_\epsilon + 0.03102X_r \\ &\quad + 2.6805)) \\ H_2 &= \tanh(0.5(0.0072V_c + 1.16324f - 0.3428ap \\ &\quad - 1.3113r_\epsilon + 0.0654X_r \\ &\quad - 5.84277)) \\ H_3 &= \tanh(0.5(0.00154V_c + 10.791f + 0.04807ap \\ &\quad - 2.5646r_\epsilon - 0.0034X_r \\ &\quad - 1.58929)) \end{aligned}$$

Figure 1 shows the comparison between the experimental response values ( $R_a$ ) and the results predicted by the ANN mathematical model.



**Fig. 1.** Comparison between experimental response values ( $R_a$ ) and results predicted by the ANN model.

3D plots were created for the most significant explanatory variables ( $V_c$ ,  $f$ ,  $ap$ , and  $r_\epsilon$ ) with the factors not represented in Figure 2 maintained at their average levels.



**Fig. 2.** 3D plots of  $R_a$  as a function of the most significant explanatory variables.

#### IV. CONCLUSION

This study aimed to assess the impact of cutting conditions ( $V_c$ ,  $f$ ,  $ap$ ,  $r_\epsilon$ , and  $X_r$ ) on the arithmetic mean roughness ( $R_a$ ) during the turning process of polyacetal POM-C. The ANOVA analysis identified the feed rate ( $f$ ) as the most influential factor, contributing over 50%, followed by  $r_\epsilon$ ,  $X_r$ , and  $V_c$  at 32.25%, 3.86%, and 2.40%, respectively. Additionally, the use of cutting inserts with a larger nose radius ( $r_\epsilon$ ) and a greater principal cutting edge angle ( $X_r$ ) was found to enhance surface roughness. The roughness model ( $R_a$ ) developed using the ANN method was proven reliable and consistent with experimental results, making it a valuable tool for predicting outcomes within a range of cutting condition variations.

#### REFERENCES

- [1] J. Paulo Davim, L.R. Silva, A. Festas, A.M. Abrão: Machinability study on precision turning of PA66 polyamide with and without glass fiber reinforcing. *Materials and Design* 30, 228–234 (2009).
- [2] J. Paulo Davim, F. Mata : A comparative evaluation of the turning of reinforced and unreinforced polyamide. *Int J Adv Manuf Technol* 33, 911–914 (2007).
- [3] T.U. Jagtap, H.A. Mandave : Machining of Plastics: A Review. *Int J Eng Res Gen Sci*, 3 (2), 577–581 (2015).
- [4] F. Mata, P. Reis, J. Paulo Davim : Physical Cutting Model of Polyamide Composites (PA66 GF30). *Materials Science Forum* Vols 514-516, 643–647 (2006).
- [5] J. Paulo Davim, P. Reis, V. Lapa, C. Conceição António : Machinability study on polyetheretherketone (PEEK) unreinforced and reinforced (GF30) for applications in structural components. *Composite Structures* 62, 67–73 (2003).
- [6] R. Keresztes, G. Kalácska, L. Zsidai, Z. Dobrocsi : Machinability of engineering polymers. *Sustainable Construction and Design*, 2(1):106-114(2011).
- [7] R. Bertolinia, S. Bruschi, A. Ghiotti : Enhanced Surface Integrity of a Biomedical Grade Polyetheretherketone through Cryogenic Machining. *Procedia CIRP*, 102, (488–493) 2021.

# Simulation of temperature distribution during the butt-joint friction stir welding of stainless steel 304L

KOUACHI MOHAMED<sup>1</sup>, RAOUACHE ELHADJ<sup>2</sup>

1. Department of Mechanical Engineering, Mohamed El Bachir El Ibrahimi University of Bordj Bou Arréridj BBA, Algeria, mohamed.kouachi@univ-bba.dz
2. Department of Mechanical Engineering, Mohamed El Bachir El Ibrahimi University of Bordj Bou Arréridj BBA, Algeria, elhadj.raouache@univ-bba.dz

## ABSTRACT

*Friction stir welding is a solid-state joining process. It has several advantages over other welding processes. The welding of the stainless steels and the aluminium alloys is of particular interest for applications in aviation, automotive, and other industries. This allows you to determine the welding thermal field and dangerous areas.*

*The purpose of this study is to contribute to the understanding of the thermal behaviour of welded stainless metal plates. The seat is made of the metals mentioned above. The thermal problem was modelled by a stationary heat equation. Finite element methods are used to discretize and solve equations in mathematical models. Results are determined using COMSOL® software. Based on these results, it was possible to determine the influence of thermal energy on the temperature field and identify the dangerous areas of the welded plates.*

**KEY WORDS:** Friction Stir Welding, stainless steel, COMSOL, HAZ, rotational speed, feed speed.

## I. INTRODUCTION

Friction stir welding (FSW) is considered as a modern manufacturing technique, allows to assemble alloys difficult to weld by conventional methods, this process was invented by the Welding Institute (TWI, Cambridge in 1991 [1]).

In this work, we focused on welding of two steel plates 304 L. Our work is divided into two parts, the first part is devoted to the COMSOL® software, we approached the analytical development of the heat equation with a modeling of the welding thermal source. In the second part all 2D thermal simulation results applied to 304L stainless steel are presented and interpreted.

R. Padmanaban, V. Ratna Kishore, V. Balusamy. [2] developed a numerical model using computational

fluid dynamics (CFD) to predict the temperature distribution and material flow during friction stir welding (FSW) of different aluminum alloys AA2024 and AA7075. The results showed that the peak temperature of the welded plate increased as the temperature increased. The tool rotation speed and shoulder diameter increase, but decrease as the welding speed increases. Furthermore, increasing the tool rotation speed and shoulder diameter increases the material flow, while increasing the welding speed decreases the material flow in the stirring zone.

Atharifar, H., D. Lin, and R. Kovacevic [3] Implemented a computational fluid dynamics model (CFD) to simulate material flow and heat transfer in friction stir welding (FSW) of aluminum alloy 6061-T6. The objective is to analyze the viscous and inertial loads on the FSW tool by varying the welding parameters. The numerical results are in good agreement with experimental studies.

Nikola Sibalic and Milan Vukcevic [4] investigated the effects of friction for welding aluminum alloy AA6082-T6, with the aim of determining the reliability of these simulations in capturing large deformations and various geometric and kinematic parameters. A numerical simulation of the stirred welding (FSW) process was performed. The simulations were based on his experimental studies using a five-phase quadrature design, and the measured force and temperature fields were compared with experimental results.

## II. FRICTION STIR WELDING

### A. DEFINITION

Friction stir welding (FSW) is a solid-state joining process (i.e., no metal melts during the process). Friction stir welding also creates plasticized regions of

the material, but in a different way. The first step is to push the non-consumable rotary tool into the material to be welded, then bring the central pin or probe, followed by the shoulder, into contact with his two parts to be joined. As the tool rotates, the material it contacts heats and plasticizes. As the tool moves along the bond line, material from the front side of the tool is forced backwards around this plasticizing ring, removing the interface [5].

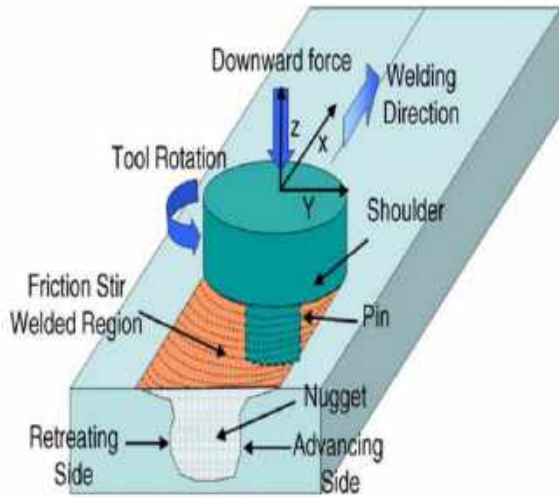


Fig. 1. The schematic view of the FSW process [6].

It excites a several types of FSW, the figure 2 shows some of them:

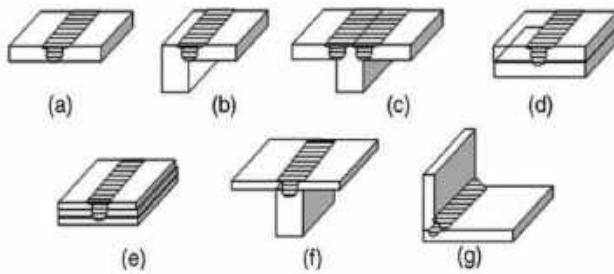


Fig. 2. Various FSW joint configurations (a) Butt joint, (b) angle t-welding, (c) double t-welding, (d) double lap-welding, (e) triple lap-welding, (f) t-welding, (g) angle welding [2].

### B. THE PARAMETERS OF FSW

The friction stir welding has several parameters like process parameters, tool parameters, type of welding and the plate to weld, the following figure 3 show you:

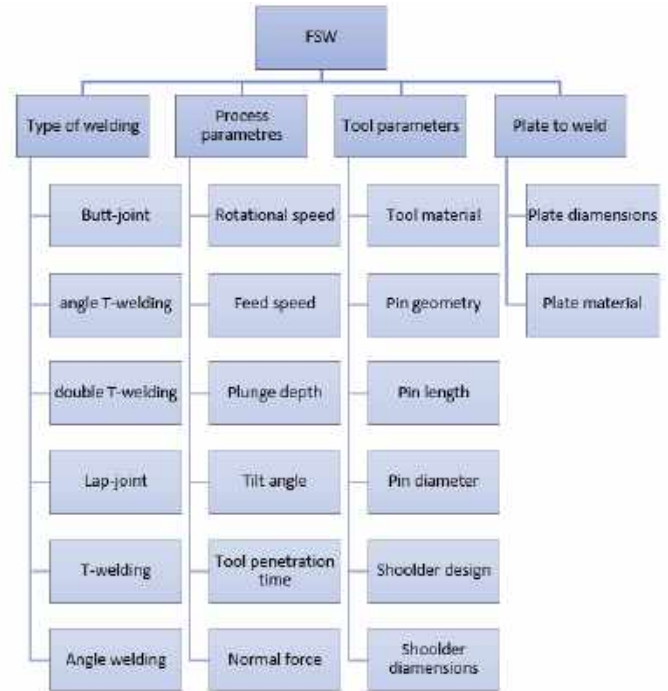


Fig. 3. FSW parameters

## III. NUMIRICAL STUDY :

### A. COMSOL® SOFTWARE

COMSOL Multiphysics is a numerical simulation software based on the finite element method. This software allows you to simulate a large number of technical phenomena, especially in combination with Multiphysics simulation. Users define couplings or select predefined interfaces. The various phases of the modeling process are integrated into one interface. Optional application modules include linear and nonlinear mechanics, acoustics, fluid flow, heat transfer, chemical engineering, geophysics, low and high frequency electromagnetism, corrosion, plasma, particle tracking, optimization, MEMS, CAD and MATLAB software Provides a special interface containing only.

### B. METHOD & STEPS OF STUDY

In this study, we used the structural calculation code COMSOL Multiphysics 5.5, which is calculation software that implements the finite element method, to solve the discretized model.

The general flowchart for solving a problem with COMSOL Multiphysics is as follows:

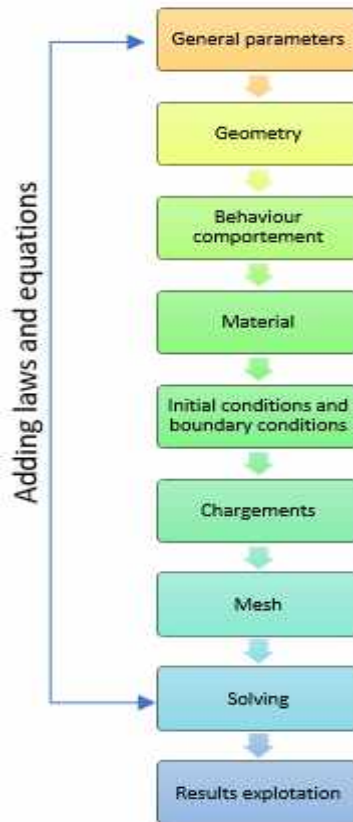


**Fig. 4.** General flowchart for resolving a problem with COMSOL Multiphysics [7]

The main steps are [7]:

- Definition of geometry
- Specifying the physics
- Selection of material properties
- Selection of initial conditions and boundary conditions
- Mesh
- Problem resolution
- Post-processing of results

### C. MATERIAL & GEOMETRY TO WELD

The material used in our study for the plate to weld is the stainless steel 304L how is hard to weld by the conventional method.

The following table 1 show the chemical composition of the stainless steel 304L.

The figures 5 & 6 shows the geometry and the dimensions of the welded plates and the welding tool modelled by SolidWorks.

Element	%
Fe	69.9
Cr	17.7
Ni	7.9
Mn	1.75
Mo	0.32
Si	0.015
S	0.006
C	0.025
P	0.03
Cu	0.84
Co	0.17
N	0.07
V	0.1

**Tab. 1.** Chemical composition of 304L stainless steel [8]

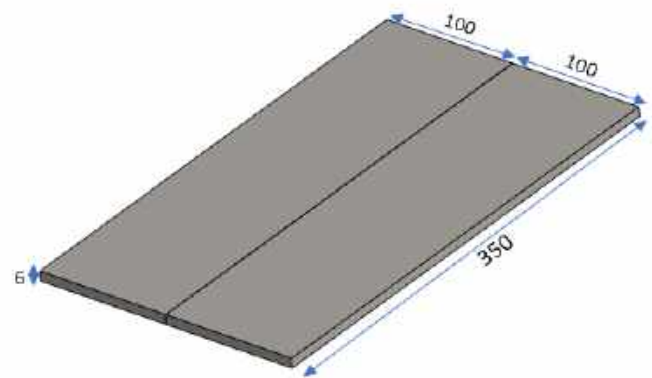


**Fig. 5.** Geometry and dimensions of plates to weld modelled by SolidWorks (unit of measurement is: mm)

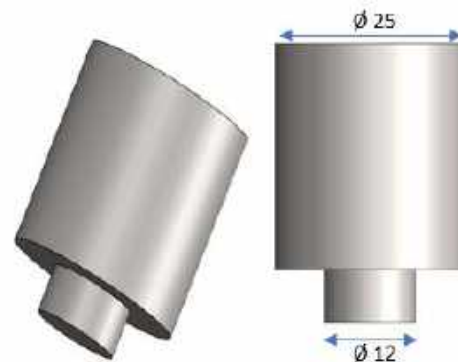


**Fig. 6.** Geometry and dimensions of welding tool modelled by SolidWorks (unit of measurement is: mm)



#### IV. RESULTS & DISCUSSION:

##### A. EFFECT OF ROTATIONAL SPEED ON TEMPERATURE DISTRIBUTION

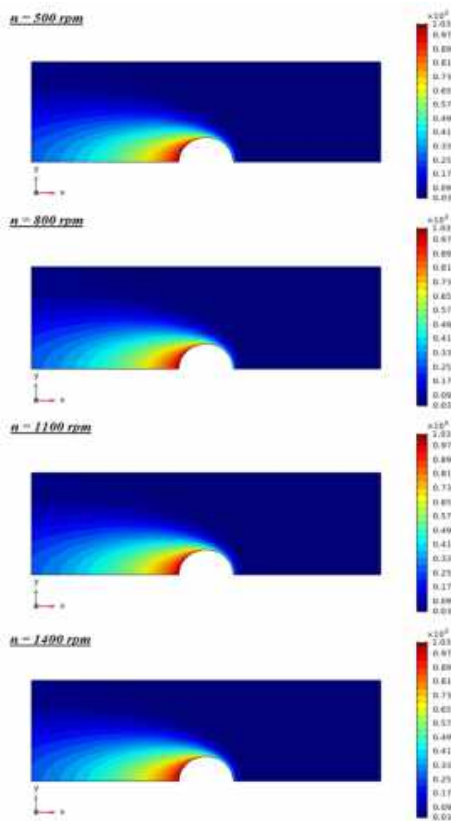
In this first side of simulation, we studied the effect of rotational speed on temperature distribution in the welded plates.

We used these parameters by fixing the feed speed and varying the rotational speed, as indicated in the following table:

	Rotational speed (rpm)	Feed speed (mm/s)	Normal force (KN)
1	500	1	10
2	800		
3	1100		
4	1400		

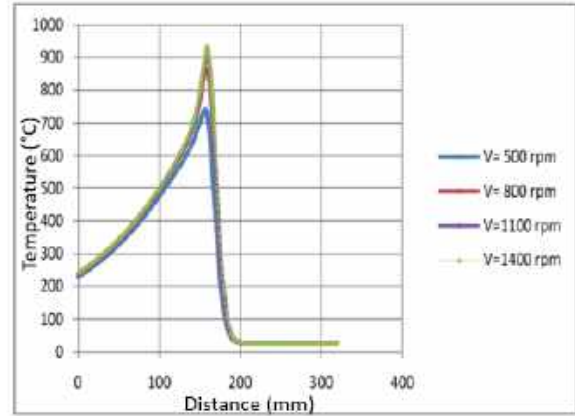
**Tab. 2.** Parameters used in study of effect of rotational speed on temperature distribution

Figure 7 shows the temperature distribution on the plate surface. The highest temperature is reached in the kneading zone, moving slightly to the rear of the center of the tool. This is interpreted by the movement and the effect of softened material ejected behind the tool.



**Fig. 7.** Temperature distribution on the upper surface of the plate with different rotational speed

Figure 8 shows the temperature variation along the line shown in Figure 7. Depending on the conditions applied, an increase in rotational speed will increase the maximum temperature. This increase is clearly visible during the tool penetration time.



**Fig. 8.** Temperature variations along a straight line parallel to the weld line for different rotation speeds.

##### B. EFFECT OF FEED SPEED ON TEMPERATURE DISTRIBUTION

In this second side of simulation, we studied the effect of feed speed (speed of welding) on temperature distribution in the welded plates.

We used these parameters by fixing the rotational speed and varying the feed speed, as indicated in the following table:

	Rotational speed (rpm)	Feed speed (mm/s)	Normal force (KN)
1	637	0.5	10
2		1	
3		1.5	
4		2	
5		2.5	
6		3	

**Tab. 3.** Parameters used in study of effect of feed speed on temperature distribution

Figure 9 shows the temperature distribution on the plate surface during welding. Depending on the operating conditions, the temperature gradient in front of the tool can be very high as the plate is cooled by exchange with the external environment.



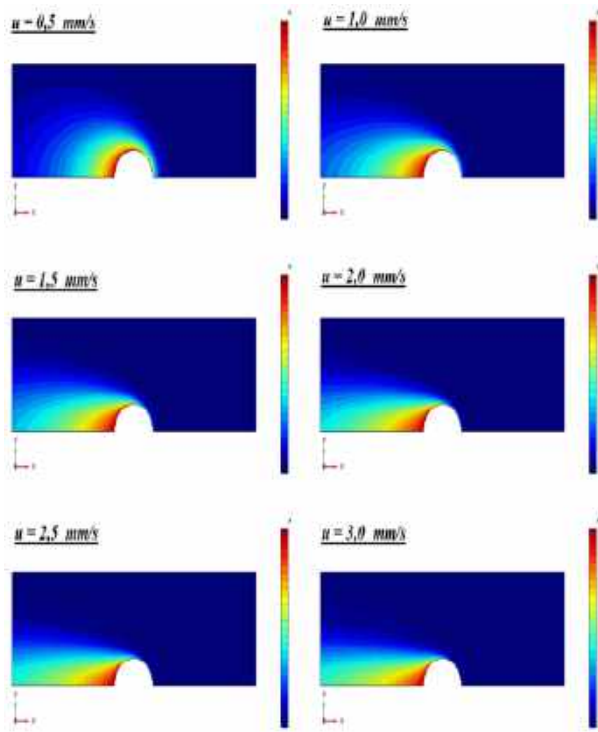


Fig. 9. Temperature distribution on the upper surface of the plate with different feed speed

Figure 10 shows the temperature variation along the center line of the assembled sample. Therefore, an increase in feed rate leads to a decrease in maximum temperature.

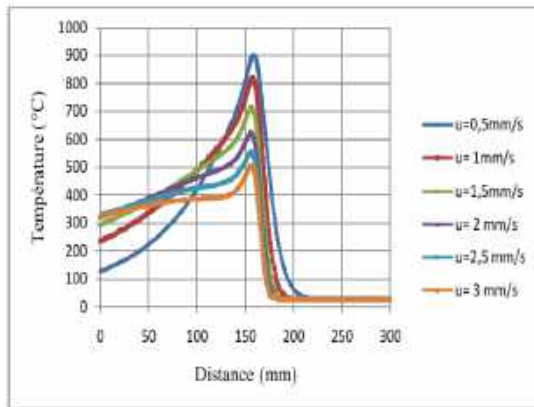


Fig. 10. Temperature variations along a straight line located in the weld line for the different feed speed

### C. CONCLUSION

The main objective of this work was to model friction stir welding (FSW) of 304L stainless steel. The type of analysis used is stationary.

COMSOL software used a moving coordinate system in the numerical simulations.

The results thus obtained regarding heat transfer

phenomena during friction stir welding FSW can be cited as follows.

1. The friction stir welding process causes large deformations plastics and significant temperature increases. This results in an evolution of microstructure of the material which influences its properties. It is then necessary to understand changes in the mechanical and thermal properties of materials studied to optimize welding parameters and weld strength.
2. In the first simulation we can see that when we increase the rotational speed, the maximum temperature increase (figure 8)
3. In the second simulation, we can see that when we increase the feed speed, the maximum temperature decrease (figure 10).
4. A slight influence of the feed speed is observed on the distribution of the temperature, in the area located just behind the shoulder of the tool.

### REFERENCES

- [1] Thomas, W.M., et al, "Friction Stir Butt Welding", The Welding Institute of Cambridge UK, 1991.
- [2] R. Padmanaban, V. Ratna Kishore, and V. Balusamyc, "Numerical Simulation of Temperature Distribution and Material Flow During Friction Stir Welding of Dissimilar Aluminum Alloys", *Procedia Engineering* 97 (2014) 854 – 863.
- [3] Atharifar, H., D. Lin, and R. Kovacevic, "Numerical and Experimental Investigations on the Loads Carried by the Tool During Friction Stir Welding", *Journal of Materials Engineering and Performance*, 2009.
- [4] Nikola.Sibalic, Milan.Vukcevic, "Numerical Simulation for FSW Process at Welding Aluminium Alloy AA6082-T6", *MDPI Metals*, 2019.
- [5] Dhanesh G Mohan and S Gopi, "Study on The Mechanical Behavior of Friction Stir Welded Aluminum Alloys 6061 With 5052", In *Proceedings of the 2017 8th Annual Industrial Automation and Electromechanical Engineering Conference (IEMECON)*, Bangkok, Thailand, 16–18 August 2017.
- [6] Rishikesh Arun Gite, Praveen Kumar Loharkar and Rajendra Shimpi, "Friction stir welding parameters and application", A review. *Mater. Today Proc.*, 2019.
- [7] Hassane MOUSTABCHIR, "Étude des défauts présents dans des tuyaux soumis à une pression interne", Mémoire de thèse de doctorat, Université Paul Verlaine de Metz. (Mars 2008).
- [8] W. Pacquentin, N. Caron and R. Oltra, "Effect of microstructure and chemical composition on localized corrosion resistance of a AISI 304L stainless steel after nanopulsed-laser surface melting", *Applied Surface Science* 356 (2015) 561–573

# Optimisation de la conception des multiplicateurs de vitesse des éoliennes

BELAIB MAHDI ZAKARIA<sup>1</sup>, SMATA LAKHDAR<sup>1</sup>, ETDJEDDOU FERHAT<sup>1</sup>

1. Laboratoire de mécanique de précision appliqué (LMPA). (IOMP). UFAS- SETIF 1 ALGERIE.

## RESUME

*L'optimisation de la conception des multiplicateurs d'éoliennes est un processus complexe qui implique de multiples facteurs et considérations. Cependant, voici quelques lignes directrices générales qui pourraient être suivies pour améliorer la conception des multiplicateurs d'éoliennes :*

*Sélection des matériaux, géométrie des engrenages, lubrification, conception structurelle, tolérances de fabrication. En résumé, l'optimisation de la conception des multiplicateurs d'éoliennes implique une approche multidisciplinaire qui nécessite un examen attentif de la sélection des matériaux, de la géométrie des engrenages, de la lubrification, de la conception structurelle et des tolérances de fabrication. En optimisant ces facteurs, les multiplicateurs d'éoliennes peuvent être conçus pour atteindre une efficacité, une fiabilité et une durabilité élevées.*

## I. MOTS CLES :

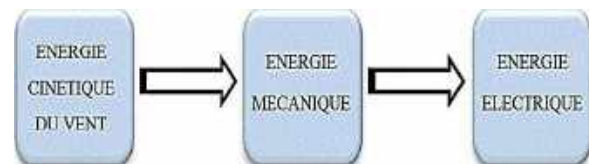
Les multiplicateurs de vitesse , engrenages, éoliennes, énergie éolienne , optimisation.

## I. INTRODUCTION

LA UTILISATION DU VENT PAR L'HOMME NE DATE PAS D'AUJOURD'HUI, ELLE EST TRES ANCIENNE. DE NOS JOURS L'ENERGIE MECANIQUE DU VENT PRODUIT L'ELECTRICITE. LE PRINCIPE DES EOLIENNES S'INSPIRE DE CELUI DES MOULINS A VENT ET A EAU AUTREFOIS UTILISE POUR MOUDRE LE GRAIN OU POMPER L'EAU. L'EOLIEN EST L'UNE DES ENERGIES RENOUVELABLES LES PLUS «PROMETTEUSES» A DEVELOPPER. ELLE EST INTERESSANTE D'UN POINT DE VUE ECONOMIQUE ET ENVIRONNEMENTAL. PENDANT CES DERNIERES ANNEES L'EOLIEN

C'EST TRES FORTEMENT DEVELOPPE, DANS LE MONDE ET PLUS PARTICULIEREMENT EN EUROPE. LES AVANCEMENTS TECHNOLOGIQUES DANS CE DOMAINE, NE CESSENT DE PROGRESSER.[1,2]

L'ENERGIE EOLIENNE EST UTILISEE DE TROIS MANIERES



## II. LES DIFFÉRENTS TYPES D'ÉOLIENNES [3,4,5]



FIG. 1. EOLIENNE VERTICAL

FIG. 2. EOLIENNE HORIZONTALE

## III. LES COMPOSANTES ET LE FONCTIONNEMENT D'UNE ÉOLIENNE

Il existe plusieurs configurations possibles d'aérogénérateurs qui peuvent avoir des différents importants. Néanmoins, une éolienne "classique" est généralement constituée de trois éléments principaux : la mat, la nacelle et le rotor.

Le rotor des aérogénérateurs est composé en général de 3 pales tournant à une vitesse maximum de 30 tours par minute et fixés sur un moyeu qui fait tourner le multiplicateur. Il fait tourner l'arbre rapide à une vitesse 75 fois supérieur à celle de l'arbre lent, ce qui fait tourner un générateur électrique qui transforme l'énergie mécanique du vent en électricité. [2,5,6]

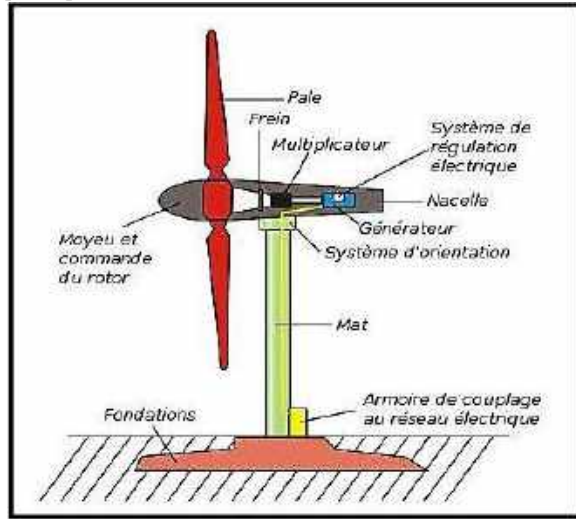


Fig .3 . Principe d'éolienne

#### IV. Optimisation de la conception des systèmes

L'optimisation de la conception des systèmes mécaniques vise à améliorer l'efficacité, les performances et la fiabilité des systèmes mécaniques. Cela peut inclure des machines, des mécanismes, des composants ou des dispositifs utilisés dans divers domaines tels que l'ingénierie mécanique, l'automobile, l'aérospatiale, etc. Voici les étapes clés pour optimiser la conception des systèmes mécaniques : [7,8]

**Définition des objectifs :** Identifiez les objectifs spécifiques de conception, tels que la réduction des coûts de fabrication, l'augmentation de la résistance ou de la durabilité, l'amélioration des performances ou l'optimisation des caractéristiques fonctionnelles. Assurez-vous de prendre en compte les contraintes techniques, les exigences opérationnelles et les réglementations applicables. [8]

**Modélisation et analyse :** Utilisez des outils de modélisation et d'analyse, tels que les logiciels de conception assistée par ordinateur (CAO) et les logiciels de simulation par éléments finis (FEA), pour représenter et évaluer le système mécanique. Créez des modèles virtuels du système et analysez-les pour évaluer leur comportement sous différentes conditions de charge, de vibration, de température, etc. [9]

**Exploration des concepts :** Générez différentes

configurations ou concepts de conception pour le système mécanique. Cela peut inclure la variation de paramètres tels que la géométrie, les matériaux, les liaisons, les dimensions, etc. Utilisez des techniques d'exploration, telles que la conception paramétrique ou l'optimisation générative, pour générer automatiquement des alternatives de conception. [7]

**Analyse et évaluation des concepts :** Évaluez chaque concept de conception généré en utilisant des critères tels que les performances, la fiabilité, le poids, le coût, la facilité de fabrication, etc. Effectuez des simulations numériques, des tests physiques ou des analyses de sensibilité pour quantifier les performances de chaque concept.

**Sélection de la meilleure conception :** Comparez les résultats de l'évaluation et sélectionnez la conception qui répond le mieux aux objectifs spécifiques. Tenez compte des compromis nécessaires entre les différentes caractéristiques du système et des contraintes de fabrication, de coût et de performance. [10]

**Optimisation fine :** Affinez la conception sélectionnée en ajustant les détails pour améliorer les performances ou répondre aux exigences spécifiques. Cela peut inclure l'optimisation des dimensions, la sélection des matériaux, l'amélioration de la fluidité des mouvements, la réduction des contraintes, etc.

**Validation et itération :** Validez la conception optimisée en effectuant des tests, des simulations ou des prototypes physiques. Identifiez les éventuels problèmes ou limitations et apportez les modifications nécessaires. Répétez le processus d'optimisation et de validation jusqu'à ce que les performances et les objectifs souhaités soient atteints.

L'utilisation de logiciels de CAO, de FEA et d'outils d'optimisation spécifiques peut grandement faciliter le processus d'optimisation de la conception des systèmes mécaniques. Cela permet de réduire les coûts, d'optimiser les performances et de raccourcir les délais de développement des systèmes mécaniques. [10]

#### V. Optimisation de la conception des engrenages en fonction de durée de vie en fatigue



## VI. Resultats et discussion

### a) Effet de la contrainte sur la durée de vie en fatigue

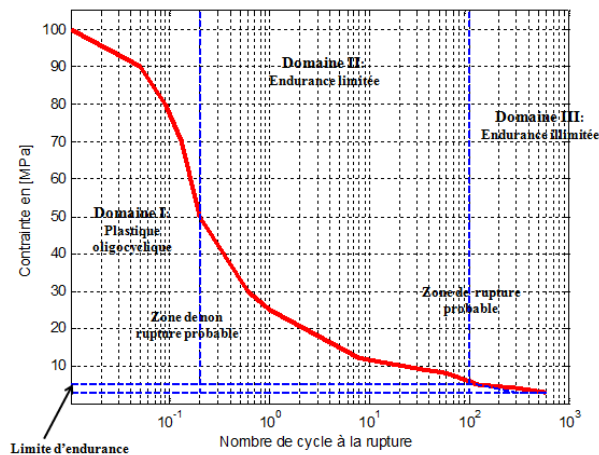


Fig. 4 : Courbe contrainte/ Durée de vie

## VII. CONCLUSION

L'optimisation est un processus crucial dans nombreux domaines, visant à améliorer l'efficacité, la performance et les résultats.

La contrainte maximale appliquée sur les engrenages a influencé la durée de vie des engrenages.

La courbe contrainte / durée de vie se divise en trois parties :

**DOMAINE I: PLASTIQUE OLIGOCYCLIQUE**

**DOMAINE II: ENDURANCE LIMITEE**

**DOMAINE II: ENDURANCE LIMITEE**

## REFERENCES

- [1] AL ghossini, H. Contributions to the Study of Control for Small-Scale Wind Turbine Connected to Electrical Microgrid with and without Sensor. Thèse Doctorat. UNIVERSITE DE TECHNOLOGIE DE COMPIEGNE, COMPIEGNE, France, 2016.
- [2] Ashglaf, M. O. Development of Hybridization Concept for Horizontal Axis Wind / Tidal Systems Using Functional Similarities and Advanced Real-Time Emulation Methods. Thèse Doctorat. Université du Havre, Havre, France, 2019.
- [3] Sørensen, J. N. General Momentum Theory for Horizontal Axis Wind Turbines. Springer International Publishing : Imprint: Springer, Cham, 2016.

Publishing : Imprint: Springer, Cham, 2016.

[4] Fortmann, J. Modeling of Wind Turbines with Doubly [5] Schaffarczyk, A. Introduction to Wind Turbine Aerodynamics. 2020.

[6] Li, Q., Cai, C., Maeda, T., Kamada, Y., Shimizu, K., Dong, Y., Zhang, F., and Xu, J. "Visualization of Aerodynamic Forces and Flow Field on a Straight-Bladed Vertical Axis Wind Turbine by Wind Tunnel Experiments and Panel Method." Energy, Vol. 225, 2021, p. 120274.

[7] GUILLOT J. "Assemblages par éléments filetés" Technique de l'ingénieur n° B 5560 - 1987

[8] GUILLOT J. "Méthodologie de définition des ensembles mécaniques en conception assistée par ordinateur, recherche des solutions optimales." Thèse d'état, n° d'ordre 1343, Université Paul Sabatier, TOULOUSE (1987)

[9] MANGASARIAN O. L. "Nonlinear Programming" Edition Mac Graw Hill 1969

[10] Lafon, P., Conception optimale de systèmes mécaniques: Optimisation en variables mixtes, 1994, Institut National des Sciences Appliquées de Toulouse.

***Session T3:  
Reliability,  
mechanical design  
and condition  
monitoring***

# Application of design of experiments method and ANOVA to study the effect of process parameters on kerf width in plasma arc cutting of mild steel

M.DEMOUCHE<sup>1</sup>, F.BETTINE<sup>2</sup>, I.N.TEBIB<sup>1</sup>

1. Laboratory of physics and mechanics of metallic materials, IOMP Sétif; ALGERIA

[mdemouche14@gmail.com](mailto:mdemouche14@gmail.com)

2. Laboratory of non metallic materials , IOMP, Sétif, ALGERIA

## ABSTRACT-

*In plasma arc cutting, the kerf width is an important indicator of characteristics of response quality. In the present study, we attempt to optimize the cutting conditions in plasma arc cutting of a mild steel to obtain a cut with minimum kerf width using Taguchi method. With the aim of determining the optimal values of Current, Cutting speed and stand off distance, the signal to noise S/N ratio ,ANOVA and regression analysis were used. It was find that the cutting speed has a major influence on the Kerf width. A confirmation test with optimum parameters has been carried out with predicted values to validate the obtained model.*

**KEY WORDS:** Plasma arc cutting, Taguchi method, ANOVA, regression model.

## I. INTRODUCTION

Plasma arc cutting is a non-traditional cutting process used to produce complex shapes. Utilizing this process allows for greater precision and quality of cut. In plasma arc cutting, an electric arc is generated from a nozzle, creating a plasma that melts the metal with the heat needed for cutting. The quality of plasma arc cutting can be assessed by the following indicators: surface finish, kerf width, bevel angle, drag lines, dross...etc. These indicators are influenced by various parameters such as cutting speed, gas pressure, current, torch-work piece distance (stand off),work piece thickness, ..etc. The kerf width shown in Fig. 2,is one of the most important indicators for assessing the quality of the plasma arc cutting process. The aim of this study is to experimentally find out the effect of process parameters on kerf width using Design Of Experiments methods such as Taguchi method. Finally, a model describing the dependence of the kerf width on the input parameters (cutting speed, current and stand off) was developed.

## II. MATERIALS AND METHODS

The experiments were conducted using a CNC plasma cutting machine. The material of workpiece experiments is mild steel (0.096% C, 0.65 % Mn, 0.50% Cr) with a thickness of cut 5 mm. For the kerf width measurement, five measurements were taken

along each cut and the average value of these five measurements was considered as the result.

### • Design of Experiments

In order to optimize the process parameters, the Taguchi method was utilized for designing Experiments (DOE). A taguchi Array L8 (2<sup>3</sup>) was considered. The control factors and their associated levels were defined (Tab 1).

**Table 1** Factors and Levels

factor	Levels	
	1	2
Current (A)	80	110
Cutting Speed (mm/min)	1000	2000
Stand off Distance (mm)	1,5	2,5

## III. RESULTS AND DISCUSSION

The evaluation of cut quality was based on the measurement of kerf width (Fig 2.).

**Table 2.** Runs and results

Run	Current (A)	Cutting Speed (mm/mn)	Stand off (mm)	Kerf Width (mm)
1	80	1000	1.5	2.5
2	80	1000	2.5	3.00
3	80	2000	1.5	2.5
4	80	2000	2.5	3.2
5	110	1000	1.5	2.40
6	110	1000	2.5	2.85
7	110	2000	1.5	3.50
8	110	2000	2.5	3.75

### • S/N RATIO ANALYSIS

In this work, we aim to minimize the cutting width, which leads us to choose the type criterion: smaller is better, which is calculated by the following formula:





Figure 1 Plasma arc cut specimens

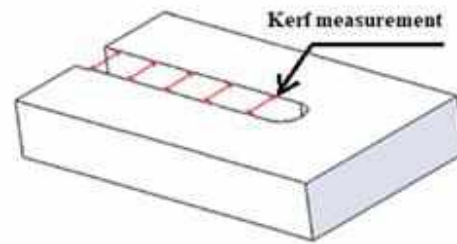


Figure 2 Kerf width measurement

$$\left[ \frac{S}{N} \right]_i = -10 \log_{10} \left( \frac{\sum y_i^2}{n} \right)$$

$y_i$ : Observed value for each experiment  
and  $n_i$ : Number of repeated experiments

- **OPTIMAL SETTINGS FOR MINIMUM KERF** (fig 3)

Current = 80 A

Cutting Speed = 1000 mm/min

Stand off Distance = 1.5 mm

- **MATHEMATECAL MODEL**

Kerf Width (mm) = 0,158

+ 0,01083 Current (A)

+ 0,000550 Cutting Speed (mm/min)

+ 0,475 Stand off Distance (mm)

#### IV. CONCLUSION

In this work, an experimental study was carried out to study the effect of process parameters on the kerf width during plasma arc cutting of mild steel. Three parameters were considered, the cutting speed, current intensity and stand off distance. Using the Taguchi method for designing of experiments, S/N ratio and ANOVA analysis, it was found that the parameter cutting speed has got the greatest effect on kerf width. In addition, it was found that the error caused by the effect of noise factors has got a contribution rate of 26.47%. A regression analysis made it possible to establish a model representative of the combined effect of process parameters on cutting width.

#### REFERENCES

[1] H.M. Magid, “Experimental study of mild steel cutting process by using the plasma arc method”, Journal of Achievements in Materials and

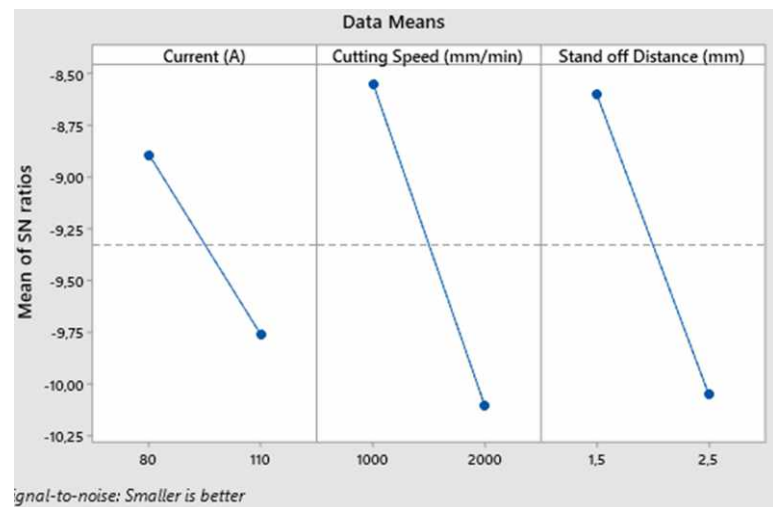


Figure 3 Main Effects plot for S/N ratios

Manufacturing Engineering, Volume 108 ,Issue 2,October 2021, DOI: 10.5604/01.3001.0015.5066

[2] K. Salonitis, S. Vatosianos “Experimental Investigation of the Plasma Arc Cutting Process”, Procedia CIRP 3 ( 2012 ) 287 – 292.

[3] A. Suresh, G. Diwakar, “Optimization of process parameters in plasma arc cutting for TWIP steel plates”, Materials Today: Proceedings 38 (2021) 2417–2424

[4] Nicolas Godinaud & al, “Development of a new OpenFOAM solver for plasma cutting modeling”, Computers and Fluids 241 (2022) 105479.

[5] Parthkumar Patel & al, “Study the effect of process parameters in plasma arc cutting on Quard-400 material using analysis of variance”, Materials Today: Proceedings 5 (2018) 6023–6029.

[6] Andjela Lazarevic et al, “Effects of plasma arc cutting process parameters on the cutting speed optimization based on the required cut quality”, CIRP Journal of Manufacturing Science and Technology 38 (2022) 836–843

[7] R. Bini & al, “Experimental study of the features of the kerf generated by a 200A high tolerance plasma arc cutting system”, journal of materials processing technology 196 ( 2008 ) 345–355

# An Enhanced African vulture's optimization algorithm for mechanical design problems

GASMI KHALID<sup>1\*</sup>, FERHAT HAMZA<sup>1</sup>, DJEDDOU FERHAT<sup>1</sup>, AND SMATA LAKHDAR<sup>2</sup>

1. Applied Precision Mechanics Laboratory, Institute of Optics and Precision Mechanics, Setif-1-University, 19000 Setif, Algeria, gasmikhalidfr@gmail.com
2. Physics and Mechanics of Metallic Materials Laboratory, Institute of Optics and Precision Mechanics, Setif-1-University, 19000 Setif, Algeria

## ABSTRACT

*As meta-heuristics play a crucial role in solving optimization problems, there is a significant orientation towards nature, especially its mechanisms of animal collective intelligence. In the past, well-established algorithms such as Genetic Algorithm (GA), Differential Evolution (DE), Particle Swarm Optimization (PSO), Ant Colony Optimization (ACO), Whale Optimization Algorithm (WOA), and Harmony Search Algorithm (HSA) have proven to be powerful. However, a recently effective optimizer, named the African Vultures Optimization Algorithm (AVOA), has been introduced. In this research, we propose an enhanced version of the African Vulture's Optimization, termed EAVOA, in response to the necessity for solving complex mechanical problems. We test the proposed EAVOA on four benchmark mechanical problems from the literature. The results obtained indicate that this research contributes a novel promising approach for optimization of mechanical systems.*

## KEY WORDS

Optimization; Enhanced AVOA; Circle chaotic map; Mechanical design.

## I. INTRODUCTION

To achieve optimal cost-effectiveness, metaheuristic approaches emerge as a superior choice over classical programming, each harboring its own set of limitations. Metaheuristics can be classified into evolution-based, swarm intelligence-based, physics-based, and human behavior-related categories. Some examples include the Genetic Algorithm (GA) by Holland (1992), Harmony Search (HS) proposed by Gim et al. (Geem, Kim, & Logana-than, 2001), Bee Colony Optimization (ABC) by Karaboga & Basturk (2007), Firefly Algorithm (FA) by Yang (2008), Bat Algorithm (BA) by (Yang, 2010), and Particle Swarm Optimization (PSO) by Kennedy and Eberhart (1997).

The latest addition to this repertoire, proposed by Mirjalili and collaborators in August 2021, introduces a new nature-inspired metaheuristic algorithm called AVOA. In addressing inherent limitations, this research integrates the Circle Chaotic Map (CCM) technique into AVOA to reinforce dynamism and mitigate issues like local optimum trapping. This integration improves the solution accuracy and convergence rates, highlighting the efficacy of our enhanced algorithm.

## II. Enhanced AVOA

### A. BASIC AFRICAN VULTURE'S OPTIMIZATION ALGORITHM

AVOA initializes a population, assesses fitness through an objective function, and emulates the foraging behavior of African vultures to iteratively adjust solution positions. Through a balance of exploration and exploitation, AVOA aims for optimal convergence in solving optimization problems. The accompanying flowchart visually depicts the sequential steps of AVOA's algorithmic process.

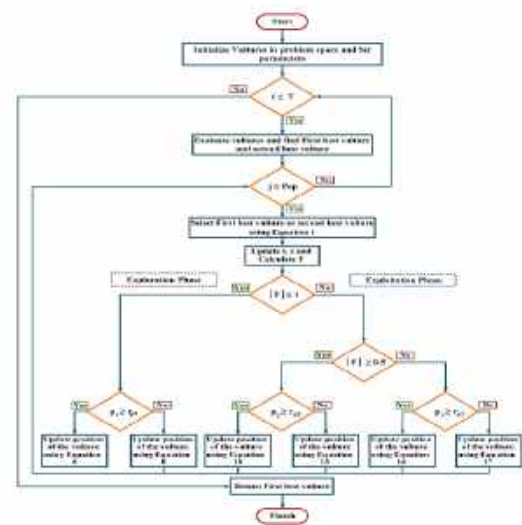


fig. 1. AVO flowchart.[2]

### B. IMPROVED AVOA BASED ON THE CIRCLE MAP

Chaos theory finds widespread applications in group intelligence algorithms, leveraging its capacity for introducing randomness and non-repetition to enhance the diversity of initialized populations. This technique significantly improves the optimization performance of algorithms. In contrast to the classical random search methods, chaos theory enables a more thorough exploration of the search space. The mathematical model of the chaotic map employed in the population initialization process is presented as follows [1]:

$$x_{-}(k+1) = x_{-}k + a - \text{mod}(\frac{b}{2\pi} * \sin(2\pi x_{-}k), 1) \dots \dots \dots (1)$$

where  $x$  is design variable at  $k$  iteration,  $a = 0.5$ , and  $b = 2.2$ .

### III. Numerical examples and test problems

In this section, we conduct experiments and tests for EAVOA. To evaluate its performance, we use four well-known mechanical design problems which are the Welded Beam Problem, Speed Gear Reducer, Pressure Vessel, and Helical Spring Parameter. The setting parameters selected in this study are  $N_p=100$  and  $G_{\max}=200$ . The optimal result obtained by EAVOA and other optimization methods from the literature are presented for the four problems in the following tables.

Vs	WCA	WOA	PSO	DE	AVOA	EAVOA <sup>†</sup>
x1	0.20572	0.21492	0.20572	0.20573	0.20573	<b>0.20538</b>
x2	3.47052	3.65920	3.47049	3.47048	3.47047	<b>3.47801</b>
x3	9.03662	8.81560	17.0000	9.03661	9.03662	<b>9.03652</b>
x4	0.20572	0.21618	9.03662	0.20573	0.20573	<b>0.20573</b>
f	1.72485	1.80578	1.72489	1.72485	1.72486	<b>1.724858</b>

Tab. 1. Results for the Welded beam problem.

Vs	WCA	ABC	DE	NSGA2	AVOA	EAVOA*
x1	3.5	3.4999	3.5000	3.5003	3.50007	<b>3.500005</b>
x2	0.7	0.7	3.5000	0.7000	0.70001	<b>0.7</b>
x3	17	17	17	17.000	17.0000	<b>17</b>
x4	7.3	7.3	7.3000	7.3000	7.59616	<b>7.356929</b>
x5	7.715	3.8	7.7140	7.7139	7.72712	<b>7.749078</b>
x6	3.350	3.3502	3.3461	3.3463	3.34743	<b>3.346201</b>
x7	5.286	5.2878	5.2853	5.2853	5.28635	<b>5.285356</b>
f	2994.4	2997.0	2992.4	2992.6	2996.4	<b>2993.74</b>

Tab. 2. Results the speed gear reducer.

Vs	DE	PSO	WCA	NSGA2	AVOA	EAVOA*
x1	0.778169	0.81730	0.7781	0.828949	0.77895	<b>0.778445</b>
x2	0.384649	0.40577	0.3846	0.409691	0.38503	<b>0.384785</b>
x3	40.31963	42.3186	40.3196	42.94157	40.3603	<b>40.33394</b>
x4	199.999	174.383	200	166.4617	199.434	<b>199.8006</b>
f	5885.33	5975.76	5888.33	5978.86	5886.67	<b>5885.80</b>

Vs	GWO	ICS	WC A	DE	PSO	NSG A2	AVOA	EAVO A*
x1	0.0523	0.0517	0.0516	0.052249	0.050627	0.05167	0.05446	<b>0.322019</b>
x2	0.3722	0.3570	0.3562	0.370246	0.331701	0.35625	0.42734	<b>0.322019</b>
x3	10.4141	11.2699	11.3004	10.54305	12.92229	11.3170	8.09923	<b>13.65599</b>
f(x)	0.0128	0.01269	0.01266	0.012678	0.012686	0.012666	0.01280	<b>0.012706</b>

Tab. 4. Results for the helical spring

### IV. Discussion

From the comparison results, EAVOA outperforms AVOA and other metaheuristic optimization algorithms for the four benchmarks, demonstrating its superior performance. The results indicate that EAVOA has not only better convergence rate but also good stability, compared to other algorithms, thanks to the implemented CCM. This improvement helps the basic AVOA to be able and effective in solving a large variety of engineering problems

### V. Conclusion

In this paper, we introduce an Enhanced African Vulture's Optimization Algorithm EAVOA that employs the Circle Chaotic Mapping to increase the randomness of population initialization, which leads to improving the performance of search process. Future works will focus on coupling the EAVOA with other methods, making it adaptable to complex problems and real engineering applications.

### REFERENCES

- [1] Y. Wang, T. Wang, S. Dong, and C. Yao, "An Improved Grey-Wolf Optimization Algorithm Based on Circle Map," J. Phys. Conf. Ser., vol. 1682, no. 1, p. 012020, (Nov. 2020).
- [2] B. Abdollahzadeh, F. S. Gharehchopogh, et S. Mirjalili, "African vultures optimization algorithm: A new nature-inspired metaheuristic algorithm for global optimization problems," Comput. Ind. Eng., vol. 158, p. 107408, (août 2021).
- [3] Saremi S, Mirjalili S, Lewis A, "Grasshopper Optimisation Algorithm: Theory and application. Advances in Engineering Software,"; 105: 30 47,( 2017).
- [4] Mirjalili S, Lewis A. The Whale Optimization Algorithm. Advances in Engineering Software,"; 95: 51–67,( 2016).

# Détection Automatique de Défauts Mécaniques par Méta-Heuristiques

DALILA BENMAHDI

Laboratoire de mécanique de précision appliquée, Institut d'optique et de mécanique de précision, Université Ferhat Abbas de Sétif1, Sétif, Algérie.  
Email: dalilabenmahdi@gmail.com

## ABSTRACT

*Le présent article présente une contribution significative dans le domaine de la maintenance préventive des systèmes mécaniques. L'étude applique des méta-heuristiques innovantes à la détection de défauts de roulement et offre des résultats prometteurs.*

*La contribution principale de l'article réside dans l'application réussie des méta-heuristiques pour améliorer la fiabilité des systèmes mécaniques. En utilisant ces techniques, il a été possible de détecter des défauts potentiels plus rapidement et avec une précision accrue par rapport aux méthodes traditionnelles d'analyse vibratoire. Cette avancée revêt une importance cruciale pour les industries où la fiabilité des systèmes mécaniques est critique.*

## KEY WORDS

Diagnostic; métha heuristiques; roulement; défaut; Détection précoce.

## I. INTRODUCTION

La détection automatique des défauts de roulement est un domaine essentiel de la maintenance préventive dans diverses industries. Les défauts de roulement peuvent entraîner des dysfonctionnements coûteux, des temps d'arrêt inattendus et une usure prématurée des équipements.

Les méta-heuristiques sont des méthodes de recherche efficaces qui s'inspirent de phénomènes naturels et de comportements d'animaux pour résoudre des problèmes d'optimisation complexes. Parmi les méta-heuristiques les plus influentes, on trouve l'algorithme inspiré des chauves-souris de Yang [1] et la recherche des coucous basée sur les mouvements de Lévy [2]. Ces techniques ont ouvert de nouvelles perspectives pour la détection des défauts de roulement en combinant des stratégies d'exploration et d'exploitation pour trouver les solutions optimales.

Les algorithmes génétiques, les algorithmes à évolution différentielle et le PSO sont des méta-heuristiques qui imitent le processus d'évolution

naturelle pour résoudre des problèmes d'optimisation. Les algorithmes génétiques [4], par exemple, utilisent des opérateurs de sélection, de croisement et de mutation pour faire évoluer une population de solutions vers des solutions de meilleure qualité. Les algorithmes à évolution différentielle [4] se concentrent sur la différence entre les solutions actuelles pour améliorer la recherche. Le PSO [6], quant à lui, simule le comportement social des oiseaux en faisant converger un essaim vers la meilleure solution.

Dans cet article, nous explorerons en détail comment ces méta-heuristiques, y compris les algorithmes génétiques, les algorithmes à évolution différentielle et le PSO, sont appliqués à la détection automatique des défauts de roulement. Nous examinerons leurs avantages, leurs limitations et leurs domaines d'application. Nous discuterons également de recherches antérieures pertinentes, telles que l'automatisation de la surveillance des machines électriques rotatives [5], l'analyse des vibrations pour la détection de défauts [6], et les méthodes de classification en temps réel pour la surveillance des roulements [7].

Les méta-heuristiques, y compris les algorithmes génétiques GA, les algorithmes à évolution différentielle DE et l'Optimisation par Essaim Particulaire PSO, sont des techniques d'optimisation qui peuvent être adaptées à la détection de défauts mécaniques. Validation expérimentale

Les données utilisées dans cette étude sont extraites des signaux de roulement à galet utilisés dans l'étude de Benmahdi et al. (2017). Dans cette étude, nous avons calculé un seul indicateur temporel, à savoir la valeur efficace RMS, pour les signaux provenant des deux capteurs. Les nuages de points caractérisant les différents états de défaut sont présentés en utilisant le RMS du premier capteur en fonction du RMS du deuxième capteur.

## II. RÉSULTATS ET DISCUSSIONS

Les résultats obtenus montrent que l'application de ces trois méthodes de méta-heuristiques à la détection précoce de défauts mécaniques a nettement amélioré la performance par rapport aux méthodes classiques d'analyse vibratoire.

Cette approche proactive a entraîné une réduction significative des coûts de maintenance, car les réparations ont pu être effectuées avant que les défauts ne deviennent critiques. De plus, elle a permis de minimiser les temps d'arrêt des équipements.

On peut remarquer que les méthodes appliquées ont réussi à détecter presque 90 % des différents clusters caractérisant les différents stades de défaillance des roulements surveillés. L'erreur de classification, en particulier pour les clusters en couleur rouge et en marron, est due à la proximité des tailles de défauts.

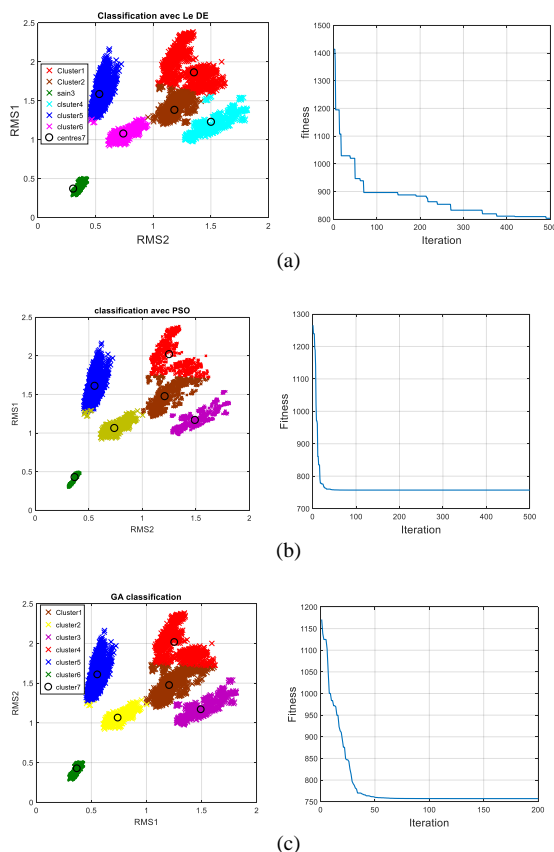


**Fig. 1.** Résultats de détection de défaut de roulement et l'évolution de la fonction objectif par:

- (a) Algorithme à évolutions différentielle DE;
- (b) Algorithme génétique GA;
- (c) Optimisation par essaim des particules PSO.

Un défaut notable lors de l'application de ces méthodes réside dans leur sensibilité à la forme des clusters. Cela a été remarqué dans le cas des tailles de défauts plus proches les unes des autres. En particulier, ces

méthodes sont efficaces pour détecter des clusters de forme sphérique en raison de l'utilisation de la distance euclidienne comme mesure de base entre les points caractérisant chaque signal. Cette sensibilité à la forme des clusters peut entraîner des limitations dans la détection de défauts lorsque les clusters ont des formes non sphériques ou complexes. Pour surmonter cette limitation, l'utilisation de métriques de distance plus adaptées aux structures de clusters non sphériques ou l'exploration de méta-heuristiques spécifiquement conçues pour gérer cette variabilité de forme des clusters.

On remarque ainsi une différence de convergence des trois méthodes vers la solution dite optimale de classification des données. Pour l'algorithme DE, on ne remarque pas une convergence claire de la classification. En revanche, pour le PSO, on observe une convergence vers un optimum global dès la 45ème itération. De même, pour l'algorithme génétique, la convergence a été atteinte à la 100ème itération.

## III. CONCLUSION

l'article propose une contribution importante en montrant comment les méta-heuristiques peuvent être appliquées avec succès à la détection de défauts mécaniques, conduisant à une optimisation significative de la fiabilité des systèmes mécaniques. Les résultats obtenus soulignent l'impact positif de cette approche sur l'efficacité opérationnelle et la réduction des coûts pour les industries concernées.

## REFERENCES

- [1] Yang, X. S. (2010). A new metaheuristic bat-inspired algorithm. In *Nature inspired cooperative strategies for optimization (NICSO 2010)* (pp. 65-74). Springer.
- [2] Yang, X. S., & Deb, S. (2009). Cuckoo search via Lévy flights. In *World Congress on Nature & Biologically Inspired Computing (NaBIC 2009)* (pp. 210-214). IEEE.
- [2] Yang, X.S. (2010). "A New Metaheuristic Bat-Inspired Algorithm." In: *Nature Inspired Cooperative Strategies for Optimization (NICSO 2010)*, Springer, pp. 65-74.
- [3] Yang, X.S., Deb, S. (2009). "Cuckoo Search via Lévy Flights." In: *World Congress on Nature & Biologically Inspired Computing, 2009. NaBIC 2009, IEEE*, pp. 210-214.
- [4] J. F. Cuttino, A. C. Miller, and D. E. Schinstock, "Performance optimization of a fast tool servo for single-point diamond turning
- [5] Kande, Mallikarjun, Alf J. Isaksson, Rajeev Thottappillil, and Nathaniel Taylor. 2017. "Rotating Electrical Machine Condition Monitoring Automation—A Review" *Machines* 5, no. 4: 24.
- [6] Park, You-Jin, Shu-Kai S. Fan, and Chia-Yu Hsu. 2020. "A Review on Fault Detection and Process Diagnostics in Industrial Processes" *Processes* 8, no. 9: 1123.
- [7] Benmahdi D. et al. (2017). RT-OPTICS: Real-Time Classification Based on OPTICS Method to Monitor Bearings Faults. *J. Intell. Manuf.* 2019, 30, 2157–2170.

***Session T4:***  
***Mechatronic and***  
***robotics***



# Novel Robust Fast Terminal Sliding Mode Controller for Distributed 3-DOF Hover Quadrotor

Badis Ouahab<sup>a</sup>, Mohamed Amine Alouane<sup>a</sup>, Fares Boudjema<sup>b</sup> and Nasreddin Saadallah<sup>b</sup>

<sup>a</sup>Ecole Militaire Polytechnique

<sup>b</sup>Ecole Supérieure Ali Chabati

**Abstract**—In this paper, a new robust fast terminal sliding mode control (FTSMC) strategy is designed to control and stabilize a 3-DOF hover system in the presence of external disturbances. The suggested approach provides an assurance of achieving pre-determined performance levels. The fast terminal sliding manifold is considered to produce the new hyperplane sliding variable for attitude of a 3-DOF hover quadrotor. The proposed FT sliding surface allow attitude tracking errors to converge towards zero in a finite-time. Moreover, the stability analysis by using Lyapunov theory is proposed as a means of demonstrating the finite time convergence and the achievement of zero attitude tracking errors through the suggested FTSMC scheme. Finally, in order to highlight its effectiveness and superiority, a comparative analysis is conducted between the suggested control strategy and an fast terminal sliding mode controller. The results of this analysis demonstrate the proposed strategy's superiority.

**Index Terms**—3-DOF Hover Quadrotor, Fast Terminal Sliding Mode Control, Attitude Control, External Disturbances

## I. INTRODUCTION

Over the past few years, there has been a significant increase in research and development related to Unmanned Aerial Vehicles (UAVs). This growth is evident in both civilian and military sectors [2]. UAVs, also known as drones, have become increasingly popular due to their ability to perform various tasks such as surveillance, inspection, delivery, and aerial photography, among others. They have also been employed in military operations as they can perform tasks that are deemed too dangerous or difficult for humans.

To achieve accurate and stable control of quadrotors, numerous control techniques have been developed and applied in closed-loop control systems. These techniques include backstepping control [15], which involves designing a series of feedback controllers that stabilize the system in a stepwise manner; fuzzy logic control based on intelligent control [13], which uses fuzzy sets and rules to handle uncertain and nonlinear systems; sliding mode control [8], which utilizes a sliding surface to regulate the system to a desired state; adaptive control approaches [6, 21], which adjust control parameters online based on system states to handle parametric uncertainties; neural network methods [10], which utilize artificial neural networks to model the system and predict control signals; intelligent fuzzy logic control [5], which combines fuzzy logic and artificial intelligence to achieve accurate and robust control; and model predictive control [3, 9, 20], which predicts the system behavior over a future time horizon and calculates the control signal accordingly.

In recent years, researchers have focused on developing control methods for systems that are affected by uncertainties and disturbances [4, 19, 22]. This is particularly relevant for quadrotors, which are highly sensitive to external disturbances and uncertainties in their dynamics.

Sliding mode control (SMC) has been a topic of significant interest among researchers due to its conceptual simplicity, ease of implementation, and robustness to external disturbances and model uncertainties when compared to other control methods [7, 23]. SMC is a nonlinear control strategy that aims to bring the closed-loop trajectories to the switching manifold within a finite-time interval by utilizing a discontinuous feedback control action.

With aim to achieve the desired trajectory and improve the attitude performance of a 3-DOF hover quadrotor, in [16], an Active Disturbance Rejection Controller (ADRC) is implemented to handle parametric uncertainties of the system and also external perturbations into the system. In [12], an application of sliding mode controllers obtained via amplified linear quadratic regulator (ALQR) strategy is designed to a 3DOF hover. The approach in [14] combines a disturbance observer with a SMC for a 3-DOF hover system in the presence of electrical and physical constraints.

In this paper, a robust fast terminal sliding mode control scheme is designed on the Matlab simulation platform to control the disturbed 3-DOF hover quadrotor with input saturation and ensures accurate tracking under the effect of disturbances. The proposed manifolds for 3-DOF hover system are designed to obtain robust, accurate tracking performance, and fast convergence of the state variables.

The significant contributions of this research paper can be highlighted in the following manner:

- The proposed approach offers superior tracking accuracy, faster convergence, reduced steady-state error, and increased robustness against disturbances.
- The 3-DOF hover quadrotor state variables are converged in their desired attitude in short finite-time.
- The performances of the FTSMC proposed in this work is compared with fast terminal sliding mode controller(FTSMC) designed in [17].
- To augment the system's robustness, we introduce the Power Rate Reaching Law (PRRL) as a proposed approach.

The paper is structured in the following manner. The 3-

DOF hover system description and its dynamic model under the external disturbances are given in section III. The controller design procedure and stability analysis are presented in section III. The simulation results are presented in section IV to verify the superiority of the proposed control strategy and finally the conclusion and future works are given in the last section.

## II. SYSTEM DESCRIPTION AND MATHEMATICAL MODELING OF A 3-DOF HOVER QUADROTOR

### A. Model Description

The schematic representation of the 3-DOF hover, shown in Figure 1, consists of a helicopter model mounted on a fixed base with two propellers that are driven by DC motors. The symbols used in the 3-DOF hover system are in the following.  $[X, Y, Z]^T$  denotes the position in earth coordinate (m).  $[x, y, z]^T$  denotes the position in body coordinate (m).  $L$  is the distance between pivot to each motor.  $J$  is the rotor inertia.  $J_y, J_p, J_r$  denotes moments of inertia about yaw, pitch, and roll axis respectively.  $K_f$  is the force-thrust constant of motor.  $K_t$  is the torque thrust constant of motor.  $V_f, V_b, V_r, V_l$  denotes front, back, right, and left motor voltage input, respectively.

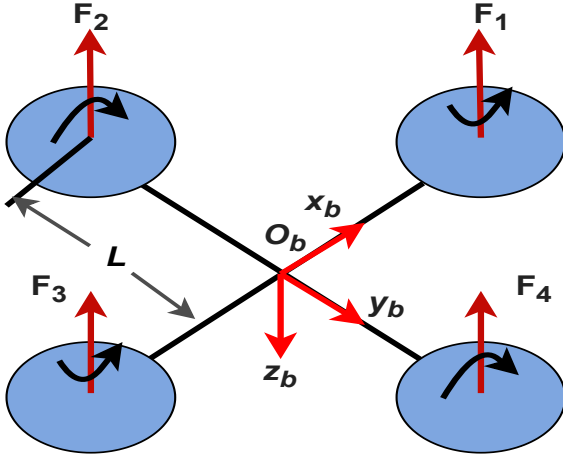


Figure 1. The 3-DOF hover quadrotor configuration.

Using the previous work presented in [11], the dynamic model of the 3-DOF hover quadrotor can be formulated as:

$$\begin{cases} \ddot{\phi} = (\frac{J_p - J_y}{J_r})\dot{\theta}\dot{\psi} + \frac{u_\phi}{J_r} + d_\phi \\ \ddot{\theta} = (\frac{J_y - J_r}{J_p})\dot{\phi}\dot{\psi} + \frac{u_\theta}{J_p} + d_\theta \\ \ddot{\psi} = (\frac{J_r - J_p}{J_y})\dot{\phi}\dot{\theta} + \frac{u_\psi}{J_y} + d_\psi \end{cases} \quad (1)$$

Where  $d_i \in \mathbb{R}$  for  $i = (\phi, \theta, \psi)$  represents the time-varying external disturbances. The term  $\tau_f^B = [u_\phi, u_\theta, u_\psi]^T \in \mathbb{R}^3$  presents the motors torque (control inputs) given by the following equations:

$$u_\phi = LK_f(V_r - V_l) \quad (2)$$

$$u_\theta = LK_f(V_f - V_b) \quad (3)$$

$$u_\psi = K_t(V_r - V_f + V_l - V_b) \quad (4)$$

The control design will incorporate the utilization of the following model:

$$\begin{cases} \dot{x}_1(t) = x_2(t) \\ \dot{x}_2(t) = f_\eta(x, t) + g_\eta(x, t)u_\eta(t) + d_\eta \end{cases} \quad (5)$$

where  $x = [x_1, x_2]^T$  denotes the measurable state of the system,  $x_1 = \eta = [\phi, \theta, \psi]^T \in \mathbb{R}^3$ ,  $x_2 = [\dot{\phi}, \dot{\theta}, \dot{\psi}]^T \in \mathbb{R}^3$ ,  $f_\eta(x, t)$  and  $g_\eta(x, t)$  are nonlinear differentiable functions defined by:

$$\begin{cases} f_\phi(x, t) = (\frac{J_p - J_y}{J_r})\dot{\theta}\dot{\psi}, & g_\phi = \frac{1}{J_r} \\ f_\theta(x, t) = (\frac{J_y - J_r}{J_p})\dot{\phi}\dot{\psi}, & g_\theta = \frac{1}{J_p} \\ f_\psi(x, t) = (\frac{J_r - J_p}{J_y})\dot{\phi}\dot{\theta}, & g_\psi = \frac{1}{J_y} \end{cases} \quad (6)$$

**Assumption 1:** The total disturbance  $d_\eta(t) \in \mathbb{R}^3$  in [5] satisfies  $\|\ddot{d}_\eta(t)\| \leq \zeta$  for a bounded Lipschitz constant.

**Assumption 2:** Assuming that complete state feedback is available, it is required that the following conditions are met:  $-\frac{\pi}{2} < \phi < \frac{\pi}{2}$ ,  $-\frac{\pi}{2} < \theta < \frac{\pi}{2}$ , and  $-\pi < \psi \leq \pi$ .

### B. Preliminaries

Consider the following system subjected to time-varying disturbances, depicted by:

$$\begin{cases} \dot{z}(t) = f(z(t), d(t)), & z(0) = z_0 \\ y(t) = z(t) \end{cases} \quad (7)$$

Where  $z \in \mathbb{R}^n$ , the nonlinear function  $f : \mathbb{R}^n \rightarrow \mathbb{R}^n$  is continuous with respect to  $y$ , the initial state is represented by  $z(0) = z_0 \in \mathbb{R}^n$ . Suppose that the origin is an equilibrium point.

**Definition 1 [18]:** The system [7] is deemed to have a globally finite-time stable origin if it is globally asymptotically stable, and for any solution  $z(t, z_0)$  of [7], the equilibrium is reached at some finite time. The origin of system [7] is classified as finite-time stable if it is globally finite-time stable and the settling time is uniformly bounded, i.e., there exists a fixed upper bound  $T_{max} > 0$  such that  $T(z_0) \leq T_{max}$  for all initial conditions  $z_0 \in \mathbb{R}^n$ .

**Lemma 1:** [24] Consider the following scalar system:

$$\dot{y} = -\nu y^{a/b} - \xi y^{r/s} \quad (8)$$

Where  $a, b, r, s$  are positive odd integers satisfying  $a > b$ ,  $r < s$ , and  $\nu, \xi > 0$ . Then, the equilibrium of system [8] is globally finite-time stable and the settling time is bounded by:

$$T < \frac{b}{\nu(a-b)} + \frac{s}{\xi(s-r)} \quad (9)$$

**Lemma 2:** Consider the system described in [7]. Suppose there exists a continuous positive definite function  $V(z) :$

$\mathbb{R}^n \rightarrow \mathbb{R}$ . This refers to the condition that there are real numbers  $\iota > 0$  and  $\kappa \in (0, 1)$  such that:

$$\dot{V}(z(t)) \leq \iota(V(z(t)))^\kappa \quad (10)$$

Then, the origin is a globally finite-time stable equilibrium of system (7) and the settling time is:

$$T(z_0) \leq \frac{1}{\iota(1-\kappa)} V(z_0)^{1-\kappa} \quad (11)$$

### III. CONTROLLER DESIGN

In this section, we present a novel control scheme designed for achieving finite-time tracking control of a 3-DOF hover quadrotor system, even in the presence of external disturbances. The structure block of the proposed finite-time control for the 3-DOF hover system is depicted in Figure 2.

#### A. Design of Novel Sliding Surface

The desired attitude trajectory is defined as:  $\eta_d = [\phi_d, \theta_d, \psi_d]^T \in \mathbb{R}^3$ , and the angle tracking error is defined as  $e_\eta = \eta_d - \eta = [e_\phi, e_\theta, e_\psi]^T \in \mathbb{R}^3$ ,  $\dot{e}_\eta = \dot{\eta}_d - \dot{\eta}$ ,  $\ddot{e}_\eta = \ddot{\eta}_d - \ddot{\eta}$ . In order to obtain the fast terminal convergence of the state variables, nonlinear fast terminal sliding variable is proposed as:

$$\Xi_\eta = \dot{e}_\eta + \alpha_\eta e_\eta^{m/n} + \beta_\eta |e_\eta|^{p/q} \text{sign}(e_\eta) \quad (12)$$

Where  $\alpha_\eta > 0$ ,  $\beta_\eta > 0$ ,  $m$ ,  $n$ ,  $p$  and  $q$  are positive odd numbers, with  $n < m$  and  $p < q$ .

##### 1) Stability Analysis and Finite Time Convergence

For (12), letting the sliding hyperplane  $\Xi_\eta = 0$ , we get:

$$\dot{e}_\eta + \alpha_\eta e_\eta^{m/n} + \beta_\eta |e_\eta|^{p/q} \text{sign}(e_\eta) = 0 \quad (13)$$

From (13), we have:

$$\dot{e}_\eta = -\alpha_\eta e_\eta^{m/n} - \beta_\eta |e_\eta|^{p/q} \text{sign}(e_\eta) \quad (14)$$

**Theorem 1:** Under the presence of uncertain limited disturbance in the system, the variables  $e_\eta$  and  $\dot{e}_\eta$ , as defined in equation (12), exhibit the capability to converge to a neighborhood surrounding the equilibrium point (0, 0) within a finite time.

**Proof 1:** Choose a function  $V_\eta(e_\eta) \geq 0$  as:  $V_\eta(e_\eta) = e_\eta^2$ , then by differentiating  $V_\eta(e_\eta)$  with respect to time, we get:

$$\begin{aligned} \dot{V}_\eta(e_\eta) &= e_\eta \dot{e}_\eta = -2\alpha_\eta e_\eta^{(m+n)/n} - 2\beta_\eta |e_\eta|^{(p+q)/q} \\ &= -2(\alpha_\eta V_\eta^{\frac{m+n}{2n}} |V_\eta|^{\frac{-p-q}{2q}} + \beta_\eta) |V_\eta|^{(p+q)/2q} \end{aligned} \quad (15)$$

The fact  $\alpha_\eta V_\eta^{\frac{m+n}{2n}} |V_\eta|^{\frac{-p-q}{2q}} > 0$  implies that  $\dot{V}_\eta(e_\eta) \leq -2\beta_\eta |V_\eta|^{(p+q)/2q}$ . In view of  $0 < \frac{p+q}{2q} < 1$ , the system in (12) is globally finite-time stable due to the Lemma 2. Thus, the variables  $e_\eta$  and  $\dot{e}_\eta$  can be stabilized in the vicinity of the equilibrium point.

Assuming that  $e_\eta(0) > 1$ , the transition from the initial state to the equilibrium point may be separated into two stages.

**Stage 1:** from the initial state of the system to  $e_\eta(t) = 1$ : In this first stage, the importance of the first term in (14)

surpasses that of the second term, thereby allowing for the disregard of the latter. Then:

$$\dot{e}_\eta = -\alpha_\eta e_\eta^{\frac{m}{n}} \quad (16)$$

We integrate Equation (16) as:

$$\int_{e_\eta(t_0)}^{e_\eta(t_{r1})} \frac{de_\eta}{-\alpha_\eta e_\eta^{\frac{m}{n}}} = \int_{t_0}^{t_{r1}} dt \quad (17)$$

Lastly, the formulas of  $t_{r1}$  is obtained as follows:

$$t_{r1} = \frac{1 - (e_\eta(t_0))^{\frac{n-m}{n}}}{\alpha(\frac{m}{n} - 1)} \quad (18)$$

**Stage 2:** from the system state  $e_\eta(t) = 1$  to the equilibrium point:

In this stage, the significance of the second term in (14) outweighs that of the first term, making it possible to ignore the latter. Then:

$$\dot{e}_\eta = -\beta_\eta |e_\eta|^{\frac{p}{q}} \text{sign}(e_\eta) \quad (19)$$

The time required for the system to reach the equilibrium point from its initial state can be obtained by integrating equation (19).

$$dt_{r2} = \frac{1}{\beta_\eta} \int_0^{e_\eta(t_0)} \frac{1}{|e_\eta|^{p/q} \text{sign}(e_\eta)} de_\eta \quad (20)$$

When  $e_\eta < 0$ , we have:

$$t_{r2} = \frac{1}{\beta_\eta} \int_0^{-e_\eta(t_0)} \frac{1}{|e_\eta|^{p/q}} de_\eta \quad (21)$$

When  $e_\eta > 0$ , we have:

$$t_{r2} = \frac{1}{\beta_\eta} \int_0^{e_\eta(t_0)} \frac{1}{|e_\eta|^{p/q}} de_\eta \quad (22)$$

Based on (21) and (22):

$$t_{r2} = \frac{1}{\beta_\eta} \int_0^{|e_\eta(t_0)|} \frac{1}{|e_\eta|^{-p/q}} de_\eta \quad (23)$$

From (23), we have:

$$t_{r2} = \frac{1}{\beta_\eta} \int_0^{|e_\eta(t_0)|} |e_\eta|^{p/q} de_\eta \quad (24)$$

Finally, we get:

$$t_{r2} = \frac{1}{\beta_\eta(1 - \frac{p}{q})} |e_\eta(t_0)|^{1 - \frac{p}{q}} \quad (25)$$

Let  $T_f$  be the time taken by the system from the initial state to reach the equilibrium point, then:

$$T_f < t_{r1} + t_{r2} = \frac{1 - (e_\eta(t_0))^{\frac{n-m}{n}}}{\alpha(\frac{m}{n} - 1)} + \frac{1}{\beta_\eta(1 - \frac{p}{q})} |e_\eta(t_0)|^{1 - \frac{p}{q}} \quad (26)$$

According to (26) we can notice that the system state converges in a finite time.

### B. Design of Control Law and Combinatorial Reaching Law

The tracking error shall be defined as:

$$e_\eta = \eta_d - \eta \quad (27)$$

**Assumption 3** The assumed desired attitude trajectory denoted by  $\phi_d, \theta_d, \psi_d$ , are both feasible and characterized by a smooth variation.

Consider the FTSM surface function of the 3DOF hover quadrotor attitude as:

$$\begin{cases} \Xi_\phi = \dot{e}_\phi + \alpha_\phi e_\phi^{m/n} + \beta_\phi |e_\phi|^{p/q} \text{sign}(e_\phi), \\ \Xi_\theta = \dot{e}_\theta + \alpha_\theta e_\theta^{m/n} + \beta_\theta |e_\theta|^{p/q} \text{sign}(e_\theta), \\ \Xi_\psi = \dot{e}_\psi + \alpha_\psi e_\psi^{m/n} + \beta_\psi |e_\psi|^{p/q} \text{sign}(e_\psi). \end{cases} \quad (28)$$

The surface dynamics are given by:

$$\begin{cases} \dot{\Xi}_\phi = \ddot{e}_\phi + \alpha_\phi \frac{m}{n} e_\phi^{(m-n)/n} \dot{e}_\phi + \beta_\phi \frac{p}{q} |e_\phi|^{(p-q)/q} \dot{e}_\phi, \\ \dot{\Xi}_\theta = \ddot{e}_\theta + \alpha_\theta \frac{m}{n} e_\theta^{(m-n)/n} \dot{e}_\theta + \beta_\theta \frac{p}{q} |e_\theta|^{(p-q)/q} \dot{e}_\theta, \\ \dot{\Xi}_\psi = \ddot{e}_\psi + \alpha_\psi \frac{m}{n} e_\psi^{(m-n)/n} \dot{e}_\psi + \beta_\psi \frac{p}{q} |e_\psi|^{(p-q)/q} \dot{e}_\psi. \end{cases} \quad (29)$$

To increase the robustness of the system, the Power Rate Reaching Law (PRRL) is proposed as:

$$\begin{cases} \dot{\Xi}_\eta = -K_{1\eta} |\Xi_\eta|^\gamma \text{sign}(\Xi_\eta) - K_{2\eta} H(\Xi_\eta), \\ H(\Xi_\eta) = \left( \frac{1 - \exp(-\mu \Xi_\eta)}{1 + \exp(-\mu \Xi_\eta)} \right). \end{cases} \quad (30)$$

Where  $K_{1\eta} > 0$ ,  $K_{2\eta} > 0$  are strictly positive constants and  $0 < \gamma < 1$ , and  $\mu \in \mathbb{R}_+$  is a positive constant.

From equation (29) and equation (30), the control laws of the attitude system are given as:

$$u_\eta = \frac{1}{g_\eta} \left( \ddot{\eta}_d - \ddot{f}_\eta - \ddot{d}_\eta + \alpha_\eta \frac{m}{n} e_\eta^{(m-n)/n} \dot{e}_\eta + \beta_\eta \frac{p}{q} |e_\eta|^{(p-q)/q} \dot{e}_\eta + K_{1\eta} |\Xi_\eta|^\gamma \text{sign}(\Xi_\eta) + K_{2\eta} H(\Xi_\eta) \right). \quad (31)$$

**Theorem 2:** Considering the system (5) with the designed controller (31), thus the asymptotic stability is guaranteed using the Lyapunov function.

**Proof 2:** The Lyapunov function for the system (5) is considered as:

$$\Gamma_\eta = \frac{1}{2} \Xi_\eta^2 \quad (32)$$

We can acquire the time derivative of  $\Gamma_\eta$  as follows:

$$\dot{\Gamma}_\eta = \Xi_\eta \dot{\Xi}_\eta \quad (33)$$

By combining (31) and (29) with (33), we can obtain:

$$\dot{\Gamma}_\eta = -K_{1\eta} |\Xi_\eta|^{\gamma+1} - K_{2\eta} \Xi_\eta H(\Xi_\eta) \leq 0 \quad (34)$$

From (34), it is obvious that the asymptotic stability is guaranteed.

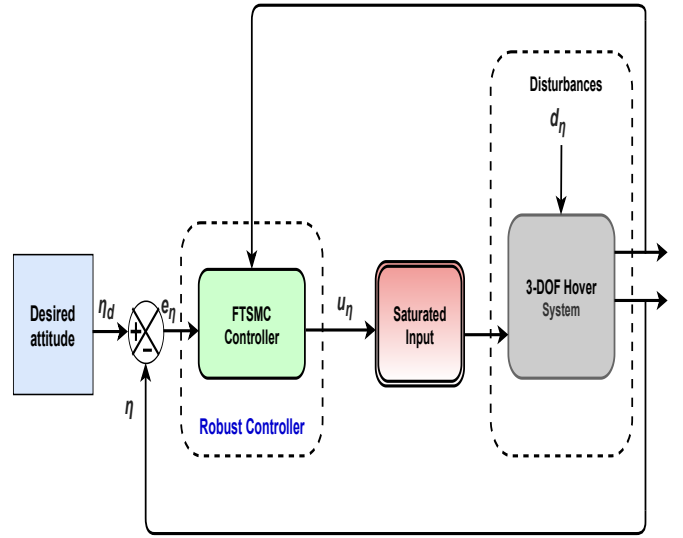


**Figure 2.** The schematic diagram of the proposed control strategy.

### IV. SIMULATION RESULT AND DISCUSSION

The simulation-based implementation of the suggested controller follows the schematic diagram illustrated in Figure 2. Table I provides the specific physical parameters for the 3-DOF hover system, while Table II outlines the coefficients associated with the proposed controller.

**Table I.** 3-DOF hover parameters [11]

Parameter	Value	Parameter	Value
$L$	0.197	$J_r$	0.0552
$J$	6e-5	$K_f$	0.1188
$J_y$	0.110	$K_t$	0.0036
$J_p$	0.0552	$K_v$	54.945

**Table II.** The control strategy parameters

Parameter	Value	Parameter	Value
$m$	5	$\mu$	25
$n$	4	$K_{1\phi, 1\theta, 1\psi}$	0.8
$p$	3	$\beta_{\phi, \theta, \psi}$	2.3
$q$	5	$\alpha_{\phi, \theta, \psi}$	1.8
$K_{2\phi, 2\theta, 2\psi}$	30	/	/
$\gamma$	0.18	/	/

In order to replicate the effects of external disturbances, we incorporate a time-varying disturbance into the model of the 3-DOF hover system. This is represented mathematically by the following equations:

$$\begin{cases} d_\phi(t) = 0.2 \cos(\frac{\pi}{2}t) \text{ (rad/s}^2\text{)}, t > 10s \\ d_\theta(t) = 0.4 \sin(\pi t) \text{ (rad/s}^2\text{)}, t > 20s \\ d_\psi(t) = 0.4 \sin(\pi t) \text{ (rad/s}^2\text{)}, t > 30s \end{cases} \quad (35)$$

Figures 3 to 5 illustrate the attitude tracking performance

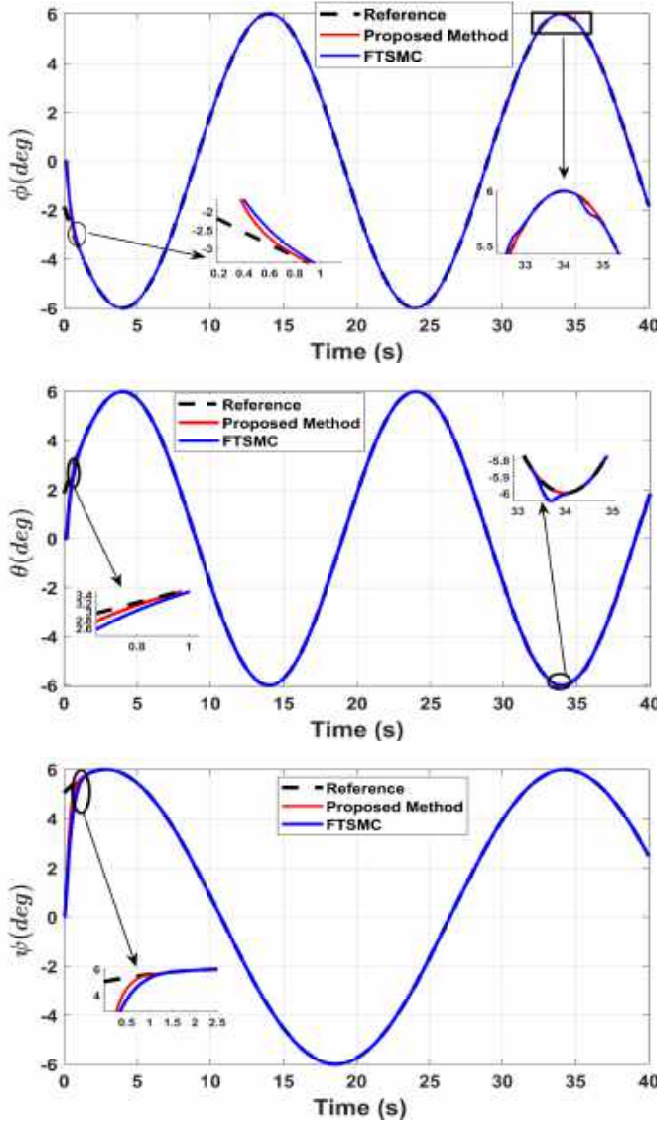


**Figure 3.** Time response of attitude tracking under time-varying disturbances.

using the control approach proposed in this paper, and FTSMC proposed in [17]. From Figure 3, it can be observed that the proposed controller ensures that the 3-DOF hover system follows the desired attitude trajectory with great precision, even when disturbances are present. The roll, pitch, and yaw angles converge to their intended angles in a short finite time, as shown in Figure 3. Besides, the attitude of the FTSMC method has oscillations and overshoots during the disturbed period of the desired attitude. The vehicle is more stable under the proposed controller under the disturbed flight. Then, the suggested controller produced faster attitude responses than the FSMC approach. Moreover, The Figures 4 shows the convergence of tracking errors in finite time.

Finally, the findings demonstrate that in the presence of external disturbances, the suggested control method offers

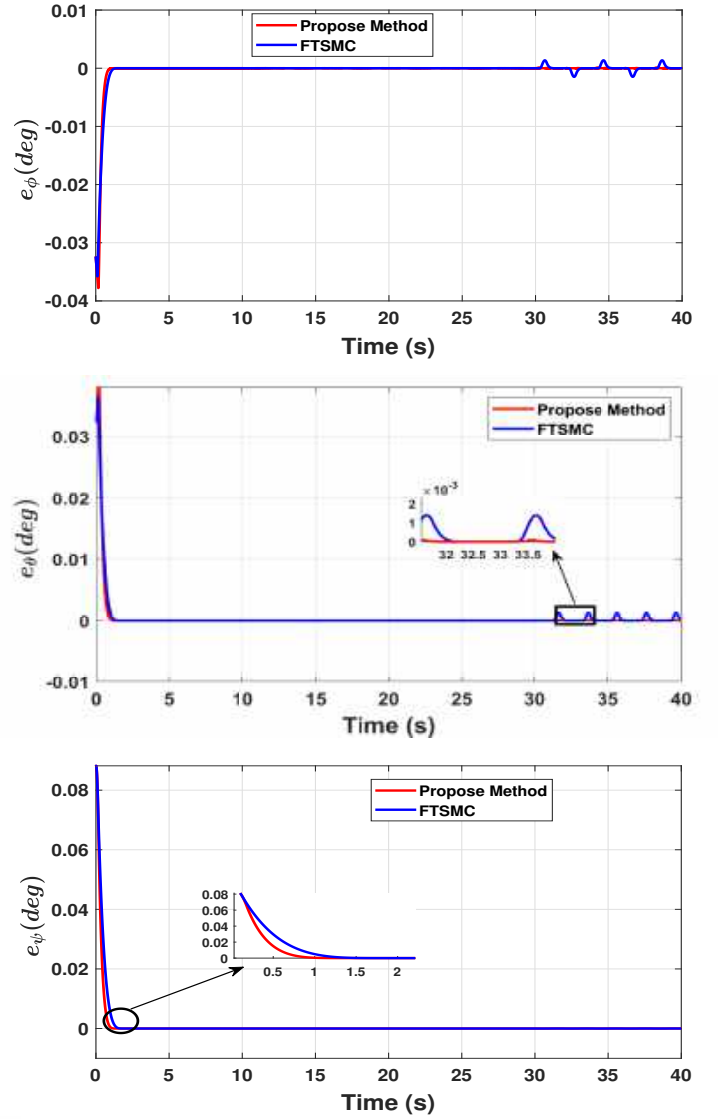


**Figure 4.** Time response of attitude errors under time-varying disturbances.

greater stability for the 3-DOF hover system compared to the FTSC controller.

**Robustness Analysis** We conduct a quantitative analysis to compare the proposed control strategy and FTSMC method. The comparison is based on the integral square error (ISE) performance indexes, as defined in [11]:

$$ISE = \int_{t_i}^{t_f} e(t)^2 dt. \quad (36)$$

Where  $t_i$  and  $t_f$  denote the initial and final instants, respectively and  $e$  represents the tracking errors. To make the results more meaningful, a representation in bar graph can be seen in Figure 6. Compared to FTSMC, the proposed controller demonstrates that the ISE index is less important and has an excellent tracking of the attitude trajectory.



## V. CONCLUSION

In this study, a novel fast terminal sliding mode control is proposed for the attitude tracking of the 3-DOF hover quadrotor. The Lyapunov function is used to analyse the stability of the proposed control strategy. The effectiveness of the proposed control scheme is presented by the results of comparative simulation.

For further works, the propose strategy will be validated by experiment.

## REFERENCES

- [1] Yasser Bouzid, Houria Siguerdidjane, and Yasmina Bestaoui. Nonlinear internal model control applied to vtol multi-rotors uav. *Mechatronics*, 47:49–66, 2017.
- [2] Zhaobi Chu, Songgang Zhou, Min Zhu, and Hua Li. Finite-time trajectory control for a quadrotor aircraft using disturbance observer. *International Journal of Advanced Robotic Systems*, 17(2):1729881420903847, 2020.
- [3] Alexandre Didier, Anilkumar Parsi, Jeremy Coulson, and Roy S Smith. Robust adaptive model predictive control of quadrotors. In *2021 European Control Conference (ECC)*, pages 657–662. IEEE, 2021.
- [4] Shihong Ding, Wen-Hua Chen, Keqi Mei, and David J Murray-Smith. Disturbance observer design for nonlinear systems represented by input–output models. *IEEE Transactions on Industrial Electronics*, 67(2):1222–1232, 2019.
- [5] Khadija El Hamidi, Mostafa Mjahed, Abdeljalil El Kari, and Hassan Ayad. Neural network and fuzzy-logic-based self-tuning pid control for quadcopter path tracking. *Studies in Informatics and Control*, 28(4):401–412, 2019.
- [6] Kanishke Gamagedara and Taeyoung Lee. Geometric adaptive controls of a quadrotor unmanned aerial vehicle with decoupled attitude dynamics. *Journal of Dynamic Systems, Measurement, and Control*, 144(3), 2022.
- [7] Chong-yi Gao, Jun Dai, Jing Li, Jian-xiong Li, et al. Finite-time convergence eso-based nonsingular fast terminal sliding mode control for pmsm with unknown parameters and time-varying load. *Mathematical Problems in Engineering*, 2022, 2022.
- [8] Mingyuan Hu, Hyeongki Ahn, and Kwanho You. Finite-time rapid global sliding-mode control for quadrotor trajectory tracking. *IEEE Access*, 11:22364–22375, 2023.
- [9] Guanrui Li, Alex Tunchez, and Giuseppe Loianno. Learning model predictive control for quadrotors. In *2022 International Conference on Robotics and Automation (ICRA)*, pages 5872–5878. IEEE, 2022.
- [10] Xumei Lin, Yulu Wang, and Yunfei Liu. Neural-network-based robust terminal sliding-mode control of quadrotor. *Asian Journal of Control*, 24(1):427–438, 2022.
- [11] Badis Ouahab, Mohamed Amine Alouane, and Fares Boudjema. Robust sliding mode control design for a 3-dof hover system. In *2022 International Conference of Advanced Technology in Electronic and Electrical Engineering (ICATEEE)*, pages 1–6. IEEE, 2022.

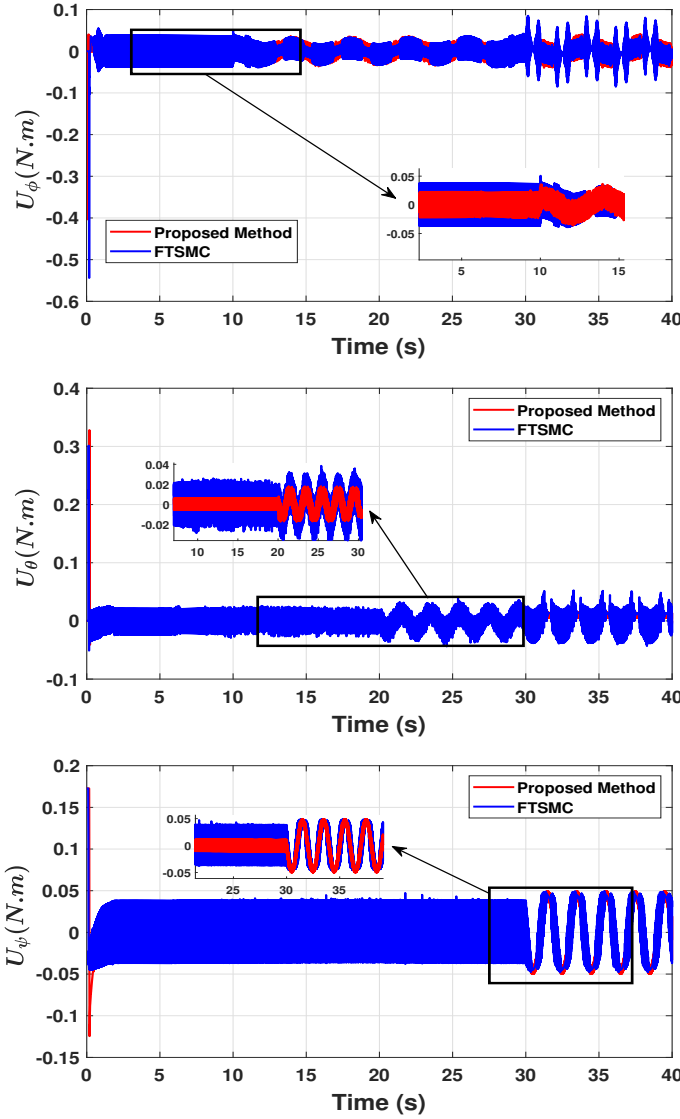


**Figure 5.** Time response of control inputs under time-varying disturbances.

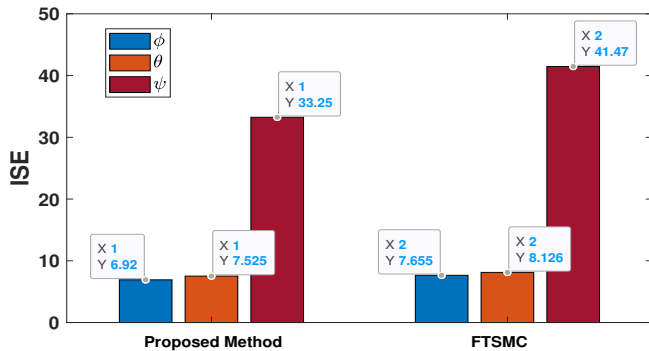


**Figure 6.** Properties of the performance index ISE: Comparison under disturbances.



- [12] Renan Lima Pereira and Karl Heinz Kienitz. Experimental investigation of nonlinear controllers applied to a 3dof hover: Smc via alqr approach. In *2015 23rd Mediterranean Conference on Control and Automation (MED)*, pages 520–524. IEEE, 2015.
- [13] Safeena Qadir, Shahida Khatoon, and Mohammad Shahid. Comparison of conventional, modern and intelligent control techniques on uav control. In *2023 International Conference on Power, Instrumentation, Energy and Control (PIECON)*, pages 1–6. IEEE, 2023.
- [14] Mahmut Reyhanoglu, Remon Damen, and William MacKunis. Observer-based sliding mode control of a 3-dof hover system. In *2016 14th International Conference on Control, Automation, Robotics and Vision (ICARCV)*, pages 1–6. IEEE, 2016.
- [15] Ali Saibi, Razika Boushaki, and Hadjira Belaidi. Backstepping control of drone. *Engineering Proceedings*, 14(1):4, 2022.
- [16] Ricardo Sanz, Pedro Garcia, and Pedro Albertos. Active disturbance rejection by state feedback: Experimental validation in a 3-dof quadrotor platform. In *2015 54th Annual Conference of the Society of Instrument and Control Engineers of Japan (SICE)*, pages 794–799. IEEE, 2015.
- [17] Xiaoyu Shi and Yuhua Cheng. Adaptive fast terminal sliding mode (ftsm) control design for quadrotor uav under external windy disturbances. In *2020 International Conference on Unmanned Aircraft Systems (ICUAS)*, pages 512–516. IEEE, 2020.
- [18] Xiaodong Sun, Jiangling Wu, Gang Lei, Youguang Guo, and Jianguo Zhu. Torque ripple reduction of srm drive using improved direct torque control with sliding mode controller and observer. *IEEE Transactions on Industrial Electronics*, 68(10):9334–9345, 2020.
- [19] Bo Wang, Mohamed Derbeli, Oscar Barambones, Amin Yousefpour, Hadi Jahanshahi, Stelios Bekiros, Ayman A Aly, and Mosleh M Alharthi. Experimental validation of disturbance observer-based adaptive terminal sliding mode control subject to control input limitations for siso and mimo systems. *European Journal of Control*, 63:151–163, 2022.
- [20] Dong Wang, Quan Pan, Yang Shi, Jinwen Hu, and Chunhui Zhao. Efficient nonlinear model predictive control for quadrotor trajectory tracking: Algorithms and experiment. *IEEE Transactions on Cybernetics*, 51(10):5057–5068, 2021.
- [21] Zhuohuan Wu, Sheng Cheng, Kasey A Ackerman, Aditya Gahlawat, Arun Lakshmanan, Pan Zhao, and Naira Hovakimyan. L 1 adaptive augmentation for geometric tracking control of quadrotors. In *2022 International Conference on Robotics and Automation (ICRA)*, pages 1329–1336. IEEE, 2022.
- [22] Yuanqing Xia, Jinhui Zhang, Kunfeng Lu, Ning Zhou, Yuanqing Xia, Jinhui Zhang, Kunfeng Lu, and Ning Zhou. Attitude control of multiple rigid bodies with uncertainties and disturbances. *Finite Time and Cooperative Control of Flight Vehicles*, pages 195–213, 2019.
- [23] Jun Yang, Shihua Li, Jinya Su, and Xinghuo Yu. Continuous nonsingular terminal sliding mode control for systems with mismatched disturbances. *Automatica*, 49(7):2287–2291, 2013.
- [24] Zongyu Zuo and Lin Tie. Distributed robust finite-time nonlinear consensus protocols for multi-agent systems. *International Journal of Systems Science*, 47(6):1366–1375, 2016.

# Low Cost Inertial Measurement Unit, Application to: Tilt-Ducted-Fan Unmanned Aerial Vehicle

HOUARI AOUED<sup>1\*</sup>, MEDJADJI ILHAM<sup>2</sup>, MEDJAHDI RAWDA<sup>3</sup> AND YOUSSEF MEDDAHI<sup>4</sup>

1. Department of Electronics, UHBC University at Chlef-Algeria  
[h.aoued@univ-chlef.dz](mailto:h.aoued@univ-chlef.dz)
2. Department of Electronics, UHBC University at Chlef-Algeria  
[hilinn3000@gmail.com](mailto:hilinn3000@gmail.com)
3. Department of Electronics, UHBC University at Chlef-Algeria  
[rrowda044@gmail.com](mailto:rrowda044@gmail.com)
4. Department of Electronics, UHBC University at Chlef-Algeria  
[y.meddahi@univ-chlef.dz](mailto:y.meddahi@univ-chlef.dz)

## ABSTRACT

*The aim of this work was to design and develop a drone control unit with an integrated Inertial Measurement Unit (IMU) using the fourth generation GSM network at the lowest cost, this unit is subject to validation tests to have the capacity to determine the exact position and movements of our drone for stable automatic flight while avoiding obstacles in its environment.*

*This implementation is associated with an in-depth aerodynamic, mechanic and math modelling study of the design of a Tilt Ducted-Fan unmanned aerial vehicle.*

*A graphical interface for the ground station (control station) developed in Python language which aims to monitor the drone in real time, it uses the 4G GSM network to receive/transmit data/commands from the ground station to the drone and vice versa. This portable application can be installed on all Android devices giving users more freedom of movement as well as control of the drone from any location.*

## KEY WORDS

Inertial measurement unit, GSM, Tilt, Ducted-Fan, Unmanned Aerial Vehicle, ground station.

## I. INTRODUCTION

Drones, commonly known as Unmanned Aerial Vehicles (UAVs), are autonomous aircraft that are independent of human control. These duties require

intrinsic control and instruction, contemporary ground control computers, locally available efficient navigation systems with data collection capabilities, and a plethora of other features.

Fast technological advancements together with advancements in flight controls, battery life, and other crucial components have all contributed to the explosive growth that has allowed for the rise of numerous drone manufacturers. The emergence of what is known as an inertial measurement unit has been instrumental in the transmission of drones to advanced stages of maneuvering and control.

IMUs are gadgets that have a variety of sensors, such as magnetometers, gyroscopes, and accelerometers. It offers a wealth of crucial information regarding the direction, speed, acceleration, and position of the drone, which is crucial for efficient flight control and navigation and enables aircraft to do aggressive manoeuvres and fly at high speeds.

## II. PROBLEMATIC:

Getting all the necessary parameters of flight for a drone is crucial and need attention in order to ensure high stability and security of the flying engine. Different open source control board are developed in recent years specially for the unmanned aerial vehicles in order to facilitate the control of this flying machines and give to users the possibility to develop

more this boards, our innovative design of a tilt ducted fan UAV needs some special functions to be integrated in the control board because of its special design and flying modes (helicopter mode, transition mode, cruise mode), in this context our research paper will invest.

### III. PROPOSED IMU-CONTROL BOARD SYSTEM:

The purpose of this section is to describe the instrumentation platform used to develop and design an inertial measurement unit and in order to obtain the physical quantities to be measured depending on the sensors that make up the unit.

Our IMU-Control Board is composed of an Arduino Mega microcontroller, a developed shield for the superposed board, MPU6050, Neo6M GPS Module, 4G Receiver/transmitter network modules and Radar for obstacle detection

From a mathematical point of view, a complete description of acceleration and angular rates over time is sufficient to determine the trajectory of any movement. However, errors due to bias, nonlinearity, hysteresis, etc., of the inertial sensor results render them useless if not combined with the lack of drift information about orientation and position. In order to integrate data from accelerometers and gyroscopes



**Fig. 1.** The Developed IMU-Control Board.

(sensor fusion techniques), we decide to implement the Kalman filtering algorithms to estimate direction, angular velocity and displacement from sensor data, reducing errors as using GPS to correct for altitude drift. This integrated approach helps overcome the

limitations and drift associated with inertial sensors alone, resulting in improved accuracy and reliability in determining trajectories and motions. The developed IMU-Control Board is depicted in Fig. 1

As mentioned in the beginning of this paper, this developed board will be subject of some validation tests in order to ensure its correct functionality, the Fig. 2 demonstrate the acquired data from our control board.

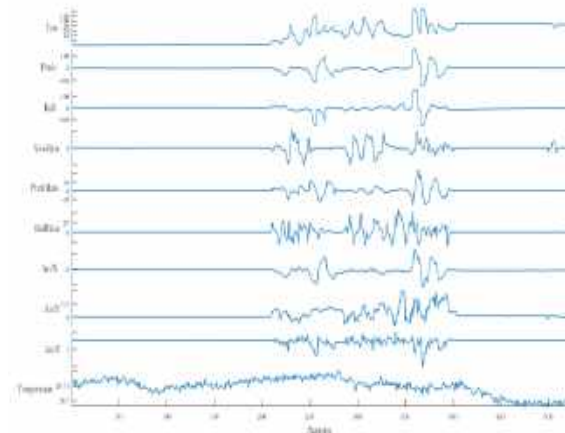


**Fig. 2.** Measured data in real time from IMU-Control Board.

### IV. CONCLUSION

The goal of this research paper is achieved by creating an inertial measurement unit (IMU) using fourth generation technology. Despite the difficult conditions, we obtained satisfactory results. Huge relevant information related to the IMU operating system was covered.

### REFERENCES

- [1] C. Jekeli, Inertial Navigation Systems with Geodetic Applications, De Gruyter, 2012.
- [2] D. L. Sun Yi, «Design and experimental study of a new flapping wing rotor micro aerial vehicle» International Conference on Unmanned Systems (ICUS), China, 2017.
- [3] J. L. Junkins, Inertial Navigation Systems, Wiley Encyclopedia of Electrical and Electronics Engineering, 2018.
- [4] S. B. a. R. Kammar, «4G TECHNOLOGY» International Journal of Scientific Research and Modern Education 2016
- [5] P. Promrit, S. Chokchaitam et M. Ikura, «In-Vehicle MEMS IMU Calibration Using Accelerometer,», International Conference on Smart Instrumentation, Measurement and Application, Thailand, 2019

# ***Session T5: Metallic materials for engineering***

# Electronic properties of MAX phase materials ( $\text{Ti}_2\text{AlC}$ and $\text{Ti}_2\text{AlB}$ )

SOFIANE BLILITA <sup>1</sup>, KAMEL KASSALI <sup>1</sup>, ABDELMADJID BOUHEMADOU <sup>1</sup>

1. University of Ferhat Abbas Setif1, Setif, Algeria

## ABSTRACT

*Electronic structure of the hexagonal MAX phase  $\text{Ti}_2\text{AlC}$  and  $\text{Ti}_2\text{AlB}$  calculated with VASP code using the DFT calculation are presented. Structural optimization of the unit cell is in good agreement with experimental data. We found that the intensity of the total density of state at Fermi level is higher for  $\text{Ti}_2\text{AlB}$  that has also a higher electrical conductivity.*

**KEY WORDS:** DFT, VASP,  $\text{Ti}_2\text{AlC}$ ,  $\text{Ti}_2\text{AlB}$

## I. INTRODUCTION

Advances in technology have made the demand for a larger library of materials more apparent than ever before. MAX phases have  $\text{M}(\text{n}+1)\text{AX}_\text{n}$  formula with  $\text{n}=1,2$  and 3 where M is a transition metal, A is an A group element and X is Carbon and/or Nitrogen [1]. The MAX phases crystallize in P63/mmc hexagonal structure and their ionic, metallic and covalent bonding give them unique properties [2]. The MAX phases have both metallic and ceramic properties that lead to good damage

## II. CALCULATION DETAILS

The DFT calculations are performed using the Vienna Ab initio Simulation Package (VASP) [3]. The pseudopotentials are chosen according to Perdew-Burke-Ernzerhof (PBE) parametrization of the generalized gradient approximation (GGA) for the exchange and correlation terms of the electron-electron interaction [3]. For the electron-ion interaction, Projector Augmented Wave (PAW) method [4] has been implemented and the kinetic energy cut off is chosen 400 eV. The  $12 \times 12 \times 12$  k-point mesh has been generated which is centered at the  $\Gamma$ - point.

## III. RESULTS

### IV.III.1 $\text{Ti}_2\text{AlC}$

We analyze the electronic properties of  $\text{Ti}_2\text{AlC}$  by calculating the density of states (DOS) and the electronic band structure

Figure.1 and 2 shows the total density of states and the total band structure of  $\text{Ti}_2\text{AlC}$ .

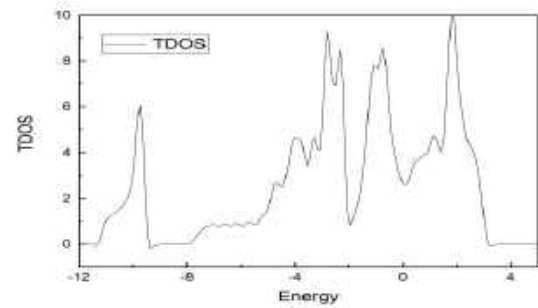


Figure.1: total density of states of  $\text{Ti}_2\text{AlC}$ .

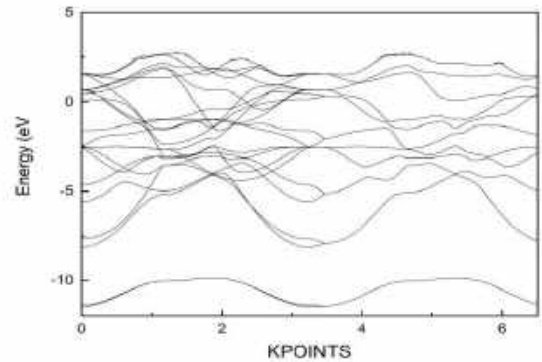


Figure.2: total band structure of  $\text{Ti}_2\text{AlC}$ .

### III.2 Ti<sub>2</sub>AlB

We analyze the electronic properties of Ti<sub>2</sub>AlB. Figure.3 and 4 shows the total density of states and the total band structure of Ti<sub>2</sub>AlB.

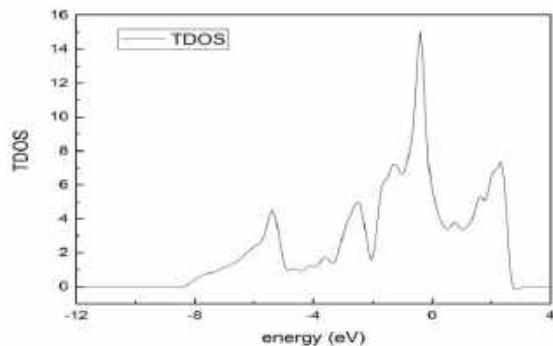


Figure.3: total density of states of Ti<sub>2</sub>AlB

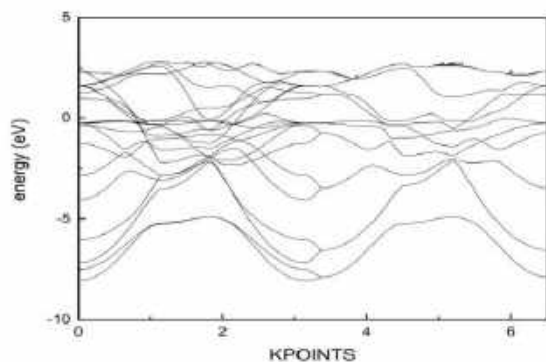


Figure 4 : total band structure of Ti<sub>2</sub>AlB

### IV. Conclusion

The calculations for the two crystallographic structures Ti<sub>2</sub>AlC and Ti<sub>2</sub>AlB (1 and 2) under consideration show that the total energy is always higher for structure 2. This energy difference is to be attributed to the “AA” metallic stacking in structure 2. The calculations predict also that the electric conductivity should be higher in Ti<sub>2</sub>AlB than in Ti<sub>2</sub>AlC in agreement with previous results. [5] [6]

### References

- [1] M.W. Barsoum, The Mn +1AX<sub>n</sub> Phases and their Properties, in Ceramics Science and Technology, Wiley-VCH Verlag GmbH & Co. KGaA, Weinheim, Germany, 2014, pp. 299–347
- [2] M. Magnuson and M. Mattesini, Chemical bonding and electronic-structure in MAX phases as viewed by X-ray spectroscopy and density functional theory, Thin Solid Films 621 (2017), pp. 108–130.
- [3] G. Kresse and J. Furthmüller, Efficiency of ab-initio total energy calculations for metals and semiconductors using a plane-wave basis set, Comput. Mater. Sci. 6 (1996), pp. 15–50
- [4] G. Kresse and D. Joubert, From ultrasoft pseudopotentials to the projector augmented-wave method, Phys. Rev. B 59 (1999), pp. 1758–1775.
- [5] G.Hug and E. Fries, Full-potential electronic structure of Ti<sub>2</sub>AlC and Ti<sub>2</sub>AlN 2002DOI:10.1103/PhysRevB.65.11310
- [6] A.Gencer and G. Surucu Electronic and Lattice Dynamical Properties of Ti<sub>2</sub>SiB, MAX Phase 2018 AUTHOR SUBMITTED MANUSCRIPT - MRX-108420.R



# Characterization of wear resistance and adhesion of Ni-Al surface alloy produced by electrodeposition on aluminum alloy

KRIM SAMAH<sup>1,2,\*</sup>, LOUCIF KAMEL<sup>1,2</sup>, HAMIDOUCHE MOHAMED<sup>2</sup> AND CHERIFI ACHRAF<sup>2</sup>

1. University Ferhat Abbas Sétif 1, Non-Metallic Materials Laboratory, IOMP, 19000 Sétif, Algeria

2. Research Center in Industrial Technologies CRTI-URFA, ZI 15A, Sétif, Algeria

Corresponding author\*: krim.sameh40@gmail.com

## ABSTRACT (1,000 characters)

*Aluminum alloys exhibit mediocre mechanical and tribological characteristics linked to their surface properties, with very low wear resistance and susceptibility to contact stresses. To enhance these properties, optimization of surface characteristics is imperative. In this study, we improved the tribological behavior of an aluminum-magnesium alloy by developing a Ni-Al surface alloy using the electrodeposition technique. This process unfolded in two stages: an initial phase of nickel electrodeposition on the aluminum substrate, followed by a second phase involving diffusion of the deposited nickel into the aluminum substrate through annealing at 450°C for 24 and 40 hours, resulting in the formation of a surface alloy. Various techniques were employed to characterize the material's mechanical and tribological behavior, including friction tests at different forces and sliding speeds, adhesion tests, and scanning electron microscopy. The surface alloy obtained through nickel diffusion into aluminum at 450°C for 24 and 40 hours exhibited the presence of  $Al_3Ni$  and  $Al_3Ni_2$  phases in the form of intermediate layers at the deposit/substrate interface. The results reveal that the coated and annealed aluminum substrates exhibited lower friction coefficients than the original  $Al_{0.95}Mg_{0.05}$  aluminum substrates, attributed to the formation of the Ni-Al surface alloy. Notably, the friction coefficient of the surface alloy developed at 450°C for 40 hours was lower than that developed for 24 hours, even with an increase in applied force or sliding speed. Additionally, the wear behavior indicates an abrasion with adhesion mechanism for the nickel deposit treated at 450°C for 40 hours, and an abrasion mechanism for that treated at 24 hours. The untreated nickel deposit and the thermally treated deposit demonstrated good scratch resistance over the entire trace, with only a few small detached areas observed at the end of the scratch, without significant damage.*

**KEY WORDS** Aluminum alloy, Surface alloy Ni-Al, friction coefficient, adhesion, abrasion.

## I. INTRODUCTION

Due to their interesting properties, such as high specific strength, high thermal and electrical

conductivity, good formability, excellent corrosion resistance, and good machinability, aluminum alloys are widely used in various engineering applications, including the automotive industry, electronics applications, aerospace, and other fields. Compared to steel, their excellent weight and ductility ratio combination makes them promising materials for industrial applications [1]. However, the main drawbacks of aluminum alloys are their poor tribological and mechanical properties due to their low hardness and wear resistance. They affect their surface performance and limit their applications [2]. Various techniques have been used to improve the mechanical surface properties of these alloys [3]. Among the techniques used, the electrodeposition technique is considered the most efficient. It offers many interesting advantages in the field of surface coatings, such as low production costs, good reproducibility with uniform deposition, the possibility of coating surfaces with complex shapes and a high deposition rate [4]. Nickel aluminide compounds such as  $Al_3Ni$ ,  $Al_3Ni_2$ ,  $AlNi$ , and  $AlNi_3$  in binary Ni-Al systems [5] are widely adopted for protective surface coatings in many applications requiring good tribological and mechanical properties [6]. They are widely used in a variety of industries, including chemical, aerospace, and automotive manufacturing [4], due to their attractive combination of low density, excellent corrosion resistance, high oxidation resistance at high temperatures, outstanding wear resistance and hardness [7]. In this work, we carried out a nickel deposition through electrodeposition on  $Al_{0.95}Mg_{0.05}$  substrates, followed by annealing at 450°C for 24 and 40 hours. The main objective is to study the tribological behavior of the Ni-Al surface alloy formed on the aluminum substrate. Friction and adhesion tests were conducted to understand the effects of time and temperature in the treatments. Wear tracks and scratch tracks were analyzed using scanning electron microscopy (SEM).

## II. EXPERIMENTAL

A DC Watts bath was used to deposit nickel layers on  $\text{Al}_{0.95}\text{Mg}_{0.05}$  substrates using a 309N Autolab galvanostat-potentiostat piloted by a computer. Cathodes were made of 14 mm alloy discs with a thickness of 4 mm. As an anode, a pure nickel electrode was used. Mechanical polishing with various abrasive papers up to paper grade 4000 was followed by polishing with 3 m diamond paste. They were then degreased in an ultrasonic bath for 10 min with an alkaline solution before being rinsed with distilled water. Before electroplating, the Al substrates were dipped in a zincate bath for 30s followed by an acidic cleaning during 5s. Then, after cleaning the surface, the specimens were again dipped in a second zincate bath for 60s and rinsed with distilled water, and immediately introduced in the electrolytic Watt's. Heat treatments at 450°C during 24 and 40h was then performed to improve coating adhesion and surface mechanical properties. After heat treatment, an alumina ball with a diameter of 6 mm was used to perform wear tests on aluminum substrate and nickel coatings. At room temperature, wear tests were performed with different applied loads of 5N, 10N and 15N with reciprocating motion at different sliding velocities of 20, 30 and 40 mm.min<sup>-1</sup>. The total sliding distance was 1m, corresponding to 500 friction cycles on a 1mm track. Each sample was subjected to at least three tests to ensure reproducibility. To assess the adhesion of our coatings to the substrates, scratch tests were conducted with a progressively increasing and continuous load ranging from 0.1 to 10N. The loading rate was 1.56mm/N, while the sliding speed was 2 mm/min over a distance of 5mm. The morphology of the wear tracks and scratches of the heat-treated coatings and the composition of the worn surface were studied by SEM and EDS.

## III. CONCLUSION

In this study, uniform and adherent ni coatings were produced on  $\text{Al}_{0.95}\text{Mg}_{0.05}$  substrates by electrodeposition and followed by a heat treatment at 450°C to improve mechanic properties by forming the intermetallic phases  $\text{Al}_3\text{Ni}$  and  $\text{Al}_3\text{Ni}_2$ . The hardness, wear resistance, and adhesion of the coatings to the substrate were studied. The highest hardness and the lowest friction coefficient were obtained after annealing at 450°C for 40 h due to the formation of the surface alloy. Compared to the short-treated coating (10/450\_24), the friction coefficients of the long-treated coating (10/450\_40) were lower for all normal forces, and sliding velocities were applied. The coatings demonstrated good scratch resistance over the entire trace, without significant damage.

## REFERENCES

- [1] G. Çam et G. İpekoğlu, "Recent developments in joining of aluminum alloys," *Int. J. Adv. Manuf. Technol.* 91,1851-1866 (2017).
- [2] J. M. Wheeler, J. A. Curran, et S. Shrestha, "Microstructure and multi-scale mechanical behavior of hard anodized and plasma electrolytic oxidation (PEO) coatings on aluminum alloy 5052," *Surf. Coat. Technol.* 207, 480-488 (2012).
- [3] A. Kumar Das et O. Verma, "Development of Ni + TiB<sub>2</sub> metal matrix composite coating on AA6061 aluminium alloy substrate by gas tungsten arc cladding process," *Mater. Today Proc.* (2021)
- [4] A. Bigos *et al.*, "Citrate-based baths for electrodeposition of nanocrystalline nickel coatings with enhanced hardness," *J. Alloys Compd.* 850, 156857 (2021).
- [5] T. B. Massalski, "*Binary Alloy Phase Diagrams*". American Society for Metals, (1987).
- [6] Y. Yu, J. Zhou, S. Ren, L. Wang, B. Xin, et S. Cao, "Tribological properties of laser cladding NiAl intermetallic compound coatings at elevated temperatures," *Tribol. Int.* 104, 321-327 (2016).
- [7] H. S. Maharana, B. Bishoyi, et A. Basu, "Current density dependent microstructure and texture evolution and related effects on properties of electrodeposited Ni-Al coating," *J. Alloys Compd.* 787, 483-494 (2019).

# Comportement mécanique d'une soudure par friction malaxage avant et après un traitement de vieillissement post-soudage

BOUCHELOUCHE FATIMA<sup>1,\*</sup>, DEBIH ALI<sup>1, 2</sup> et OUKADI ELHADJ<sup>1</sup>

1. LPMMP, Institut d'Optique et Mécanique de Précision, IOMP, Université Ferhat Abbas de Setif1, Algerie, e-mail: fatima.bouchelouche@gmail.com
2. Département de mécanique, Université Mohamed Boudiaf de M'sila

## RESUME

*Le procédé de soudage par friction malaxage FSW peut offrir une solution pour l'assemblage plus rapide et plus économique des alliages d'aluminium. Dans ce travail, nous avons étudié le comportement mécanique et métallographique des soudures FSW des plaques d'alliage d'aluminium 6061 d'épaisseur de 5 mm, soudée bout à bout par une vitesse de rotation 1400tr/min. Des traitements thermiques de vieillissement post- soudage ont été aussi effectués afin de connaître son effet sur les caractéristiques mécaniques. Plusieurs méthodes de caractérisation sont utilisées, tel que l'essai de traction, de résilience, la microscopie optique et enfin des essais de la microdureté.*

## MOTS CLÉS

AL6061, Soudage par friction malaxage, métallographie, ZAT, ZATM, microdureté

## I. INTRODUCTION

De nos jours, les alliages d'aluminium sont largement utilisés dans l'industrie. Ils ont remplacé les métaux ferreux dans plusieurs domaines industriels en raison de leur légèreté et, surtout, de leur rapport résistance/poids plus élevé [1]. Ces alliages étaient autrefois difficiles à souder avec des techniques conventionnelles telles que le TIG et le MIG-MAG....). Le procédé de soudage par friction malaxage (Friction Stir Welding FSW) intéresse particulièrement les utilisateurs d'alliages d'aluminium car le succès de ce procédé est basé sur le principe que le soudage se fait à froid, c'est-à-dire que le matériau n'atteint pas le point de fusion.

Le soudage par friction malaxage(FSW) consiste à assembler des plaques par déformation plastique à chaud. La chaleur générée par le frottement entre l'outil en rotation et les deux pièces ramollit le matériau à souder. Ce métal plastifié subit de forte déformation plastique et s'écoule lorsque l'outil est déplacé dans le sens du soudage[2]. Les plaques sont

fortement bridées afin d'éliminer tout mouvement lors du malaxage.

## II. PROCÉDURE EXPERIMENTAL

### A. MATERIELE ET METHODE

Le matériau que nous avons étudié est l'alliage AL 6061 laminié (ep=5mm), l'élément majeur est l'Al de l'ordre de 96%, il se caractérise par la présence de Mg et Si. Les soudures ont été réalisées à l'aide d'un outil de malaxage, en acier rapide (HSS Co5). Sa géométrie est composée d'un pion cylindrique d'une longueur 4.8 mm avec un épaulement cylindrique de diamètre 20 mm. Les paramètres utilisés pour les soudures par procédé FSW sont:  $v_r=1400\text{tr/min}$  et  $V_a=31.5\text{mm/min}$ . Après l'obtention des plaques soudées, nous avons prélevé plusieurs échantillons pour les tests avec des dimensions spécifiques(fig.1) à l'aide d'une machine d'électroérosion à fil, ou nous avons divisé ces échantillons en deux parties, Les premiers sont réservés à la caractérisation directe après soudage les autres échantillons prélevés ont subi des traitements thermiques T6 qui est un traitement de durcissement par précipitation

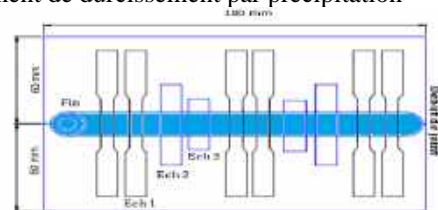


Fig. 1.Découpe des échantillons sur les plaques soudées.

### B. RÉSULTAT ET DÉSCUTION

Essai de traction:L'opération de soudage FSW a été réalisée pour but d'obtenir des soudures de haute qualité, solides et fiables entre des pièces soudées. Le processus de friction a fortement influencé les propriétés mécaniques d'alliage en fonction des paramètres cinématiques du processus de soudage qui provoque une diminution totale en propriétés

mécaniques pour l'ensemble des éprouvettes soudées. D'après les courbes de traction, Les éprouvettes du métal de base sont appariées clairement avec une diminution dans la résistance ( $\sigma = 198 \text{ MPa}$ ) causée par l'effet de traitement thermique (TT), Fig.2. Les TT ont restauré la structure de l'alliage, fortement laminé à l'état initial. Une diminution de ductilité est aussi observé dans le métal traité qui pourrait être liée à une recristallisation secondaire.

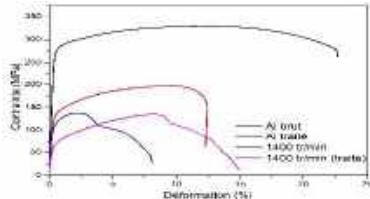


Fig.2. courbe de traction (cotrainte-déformation)

Essai de résilience : L'énergie absorbée par le choc est plus élevée dans le métal de base traitée ou non traité comparativement à celles mesurées durant les essais sur les éprouvettes soudées (traitées et non traitées), Fig.3 Cela est expliqué par l'absence des défauts, Cette énergie s'accroît légèrement à cause de la précipitation produite après un recuit de mise en solution solide ( $50 \text{ J/cm}^2$  au lieu de  $40 \text{ J/cm}^2$ )

L'énergie absorbée par le choc devient plus faible pour les échantillons soudés et elle devient encore très très faible en faisant un traitement thermique sur les joints soudés quel que soit la vitesse de rotation de soudage. Cela laisse dire que les défauts tunnels. En plus de cela, un recuit de mise en solution solide très long ( $535^\circ\text{C}$ ,  $t = 1\text{h}$ ) conduit à une recristallisation secondaire et à la migration des atomes de soluté vers l'extérieur

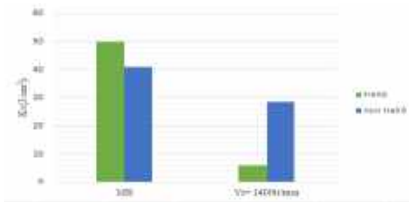


Fig.3. Variation de l'énergie absorbée

Pour ce qui est de microdureté, on constate que les courbes de microdureté ont un profil typique en w, on observe une chute de micro-dureté au niveau du noyau la plage de chute de dureté est très limitée. En réalité l'absence d'un bon malaxage laisse exister des pores dans le métal conduisant à une faible dureté, Pour les échantillons traités on observe une augmentation de dureté au niveau du joint de soudure dû à la présence des précipités.

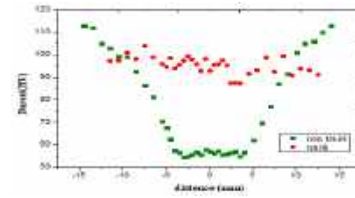


Fig.4. Profil de microdureté

L'analyse macrographique nous permet de mettre en évidence la morphologie des différentes zones des joints soudés (MB, ZAT, ZATM et Noyau). La figure.5 montre une structure fine au niveau du noyau, et la ZATM est plus nette du côté entrant du joint que du côté sortant

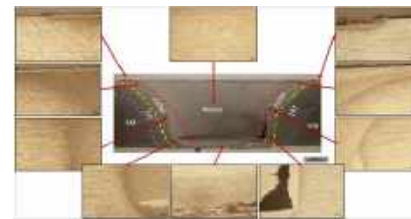


Fig.5. Observation microscopique des différentes zones

### III. CONCLUSION

- La présence de défauts dans les échantillons soudés est le responsable d'affaiblissement de la résistance en général et de l'énergie absorbée par le choc comparativement à celle de métal de base.
- Le profil de microdureté de la soudure brut a montré une chute importante de dureté dans le joint de soudure, plus précisément dans la zone affectée thermiquement et le noyau (jusqu'à 50% de la dureté initiale).
- Une structure est plus fine au niveau du noyau et de la zone ZATM à cause d'une recristallisation dynamique.
- Le traitement thermique conduit à l'apparition du trois phénomènes métallurgiques : la restauration, la recristallisation secondaire et la précipitation.

### REFERENCES

- [1] V. Jaiganesh and P. Sevel, « Effect of Process Parameters during Friction Stir Welding of Al 6063 Alloy », *AMR*, vol. 984-985, p.604-607, juill.2014, doi:10.4028/www.scientific.net/AMR.984-985.604.
- [2] R. Nandan, T. Debroy, and H. Bhadeshia, « recent advances in friction-stir welding – process, weldment structure and properties », *progress in materials science*, vol. 53, n° 6, p. 980-1023, août 2008, doi: 10.1016/j.pmatsci.2008.05.001.

# Global and Local Strain Evaluation in Tensile Test of AA2017-T4 Friction Stir Welded Joint Using Digital Image Correlation

DJILI ABDERRAHMANE<sup>1,2,\*</sup>, BEZZAZI BOUDJEMAA<sup>1</sup>

1. Unité de Recherche Matériaux Procédés et Environnement- UR MPE Université M'hamed Bougara, Boumerdès, Algérie
2. Génie mécanique et productique, Ecole Nationale Supérieure de Technologie Avancé, Alger, Algérie

## ABSTRACT (1,000 characters)

*Tensile tests under digital image correlation (3D) were performed on 4 mm thick friction stir welded joints of Al2024-T3 aluminium alloy sheets to assess global and local deformation. The results presented show that the 2017-T4 aluminium alloy welded joint has a significant loss of mechanical properties in comparison with the base metal. The overall strain (in the loading direction) recorded is 4.5%. The largest strain occurs at the joint, with the strain concentrated near the interfaces (ZATM/ZAT), which can be explained by the heterogeneities generated by the welding process.*

## KEY

FSW; Tensile test; DIC; Local strain

## I. INTRODUCTION

Friction stir welding, first introduced in the early 1990s [1], is a joining technique that makes it possible to weld without reaching the fusion temperature. It allows the welding of aluminium alloys that are notoriously difficult to weld [2]. Like all conventional welding processes, friction stir welding produces a heterogeneous microstructure and, as a result, a heterogeneous mechanical behavior [2]. To understand the mechanical behaviour of FSW welds, digital image correlation techniques can be used to measure local deformation fields [3]. In this paper, digital image correlation has been used for the measurement of local and global strain fields during uniaxial tensile tests. The tensile tests have been carried out at room temperature. Tensile samples used are standardised, cut from welded and un-welded AA2017-T4 sheets, normal to the direction of welding, with the joint in the centre of the sample..

## II. EXPERIMENTAL

Tensile tests were performed on standardised tensile specimens at imposed displacement (0.1 mm/s) and at room temperature. Five specimens taken from the seamless plates, and five others from the welded plates of 2017-T4 aluminum alloys were subjected to tensile tests. The digital image correlation technique was used to measure the strain fields. In addition to a computer and image processing software, the experimental apparatus used for digital image correlation consists of two cameras and appropriate lighting.

## II. RESULTS AND DISCUSSION

The results presented in Figures 1 and 2 show that the welded joint of the 2017-T4 aluminium alloy shows a significant loss of mechanical properties compared to the base metal, namely yield strength, resistance to tensile stress at break (UTS) and elongation at break (UE). These losses are explained by the inhomogeneities and geometric changes caused by welding. This heterogeneity is highlighted by comparing the distribution of strain fields. For the base metal, the distribution of the strain fields is homogeneous up to the appearance of the fracture zone in a single location. On the other hand, for the welded specimens, a rather heterogeneous distribution is observed, we can see at the level of the elastic limit three levels of strain fields, strong at the core level, less strong on the base metal and weak at the interface between ZAT and ZATM. In the plastic part we see that the deformation is weak on the base metal, strong on the core and stronger at the ZAT/ZATM interface and it is in this region that fracture occurs.

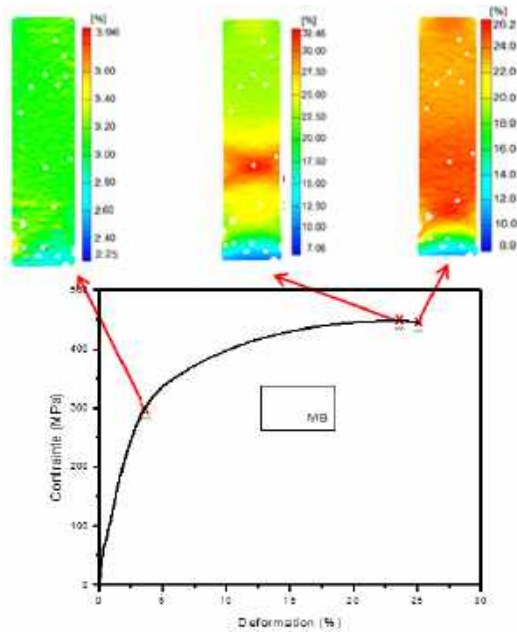


**Fig. 1.** Tensile curve, 2017-T4 base metal and field measurement images..

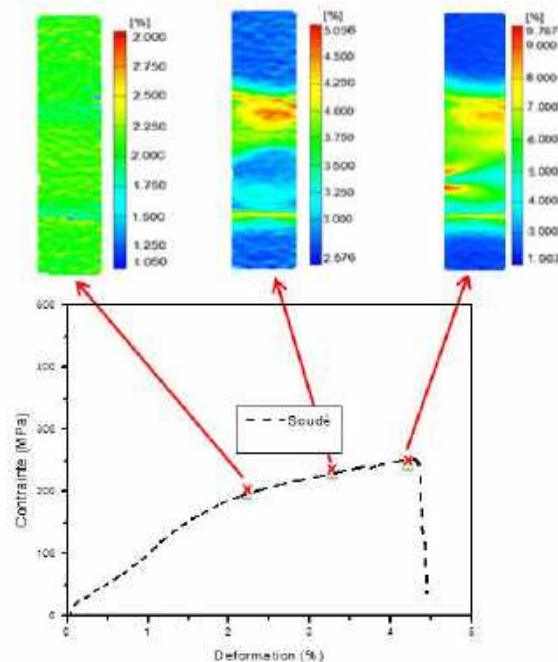


**Fig. 2.** Tensile curve of AA2017-T4 welds with strain field images.

### III. CONCLUSION

In this work, 2 mm thick aluminium alloy AA2017-T4 sheets were welded using the FSW technique on a conventional milling machine. The AA2017-T4 FSW weld was tested under uniaxial loading in the tensile test. The weld showed an efficiency of 60% and 18% compared to the base metal in terms of strength and deformation respectively. In contrast to the base metal, the strain fields across the welds measured by digital image correlation show heterogeneous behaviour.

### REFERENCES

- [1] W.M. Thomas, E.D. Nicholas, J.C. Needham, M.G. Murch, P. Temple-Smith, C.J. Dawes, "Friction stir butt welding". International patent application No. PCT/GB92/02203, 1991.GB Patent No. 9125978.8
- [2] M.M.Z. Ahmed, S. Ataya, M.M. El-Sayed Seleman, H.R. Ammar, E. Ahmed, "Friction stir welding of similar and dissimilar AA7075 and AA5083". J. Mater. Process. Technol., 242, 77–91, (2017).
- [3] C. Leitão, I. Galvão, R.M. Leal, D.M. Rodrigues, "Determination of local constitutive properties of aluminium friction stir welds using digital image correlation", Mater. Des, 33, 69-74 (2012).



# Title: Effect of varying submerged arc welding speeds on the metallurgical structure of steel for LPG cylinder manufacture

KHOULOUDD BAALI <sup>1,\*</sup>, ABDELLAH BOURIH <sup>2</sup>

1.2 Mechanics of Structures and Materials Laboratory , Mechanical Engineering Department, Faculty of Technology, BATNA 2 University, Batna, ALGERIA

1. [khoulouddbaali@gmail.com](mailto:khoulouddbaali@gmail.com)

## ABSTRACT

*This work presents the significance of the effect of varying the speed of the submerged arc welding operation on the metallurgical structure of BS2 steel for transportable and refillable liquefied petroleum gas (LPG) cylinders. The variation of the welding speeds on the BS2 steel may make it difference to improve its structure. Optical microscope test was applied on specimens. It should be noted that involvement in this study required in-depth knowledge in metallurgical fields , particularly relating to the phenomenon of phase transformation, which occurs during welding and the proposed speed changes. The results were found satisfactory.*

## KEY WORDS

Steel; SAW; Structure; Welding speeds; Optical microscope

## I. INTRODUCTION

Welding is most widely used in the manufacturing industry; submerged arc welding is one of the predominantly used joining processes to join materials with a higher thickness to reduce the defects during welding [1]. This welding process is preferred in the gas cylinder industry, preferable due to ease of automation, high production rate and high efficiency. However, during cylinders manufacturing; the quality of the joint is influenced by several factors. This experimental study was conducted to evaluate the effects of varying welding speeds on the metallurgical structure of steel.

### A. STEEL USED

To carry out this study we have chosen the steel of grade BS2 (P265NB), the thickness of material  $3 \pm 0.1$  mm, in accordance with the EN 10120. It used in the industry of LPG gas cylinders, in the enterprise (BAG) Batna

### B. WELDING PROCESS USED: SUBMERGED ARC WELDING (SAW)

Longitudinal welding of the gas cylinder shell is carried out in an automatic process, the arc created between the wire and the workpiece is protected by a flux layer. This flux layer protects the molten pool from contamination and concentrates the energy input into the joint. The flux melts, mixes intimately with the molten metal, with a de-oxidising, purifying and enriching action on the molten metal, then rises to the surface of the metal bath to form the slag. The following figure shows the type of welding used for the LPG cylinder [2].



Fig. 1. Submerged arc welding

1. Schematic presentation of the gas cylinder and the sampling areas of the samples studied.

The following figure shows the view of the cylinder using Solidworks software and clearly shows the sampling area in the bottle of our samples.



Fig. 2. Model of the cylinder specifying the sampling area

2. The areas affected

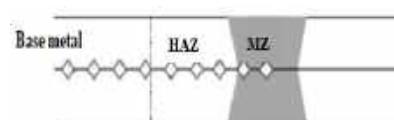


Fig.3. Main affected areas

### C. WELDING SPEED

The influence of welding speed can be assessed by its effect on linear welding heat input. Heat input is related to welding speed by the relationship:

$$H = U \cdot I / S$$

With: H : Heat input (Kj/cm), I: Current (A).

U: Voltage (V), S: Welding speed (cm/min).

An increase in welding speed reduces the amount of heat per unit length of weld, resulting in a reduction in the cross-section of the molten zone. However, several authors [3] have found that arc yield is higher when welding speed is relatively high. Notes that reducing welding speed promotes penetration. He points out, however, that this reduction must be very significant if the increase in penetration is to be achieved. [4] In the absence of surfactants, found that the P/L ratio increased slightly with increasing speed.

### D. OPTICAL MICROSCOPE

The use of an optical microscope enabled us to follow the evolution of the microstructure of the samples. Metallographic observations are made using a microscope (Fig.4). This technique allows us to observe the phases and comment on their respective morphologies.



Fig.4. Optical microscope type OLYMPUS CX40

### E. RESULTS AND INTERPRETATION

The aim of this characterization is to study the effect of varying welding speeds on the microstructure of welded joints. For this experimental study we used two submerged arc welding speeds ( $S_1 = 16\text{mm/s}$ ,  $S_2 = 8\text{mm/s}$ )

#### 1. Optical microscope examination of BS2 steel and welded joint

Microscopic observation of BS2 steel at its reception point showed the existence of a Ferrite and Pearlite structure.

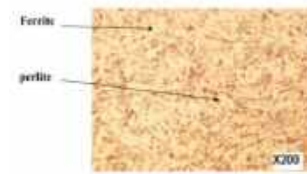


Fig.5. BS2 steel sheet microstructure

#### 1.1 Examination of base metal

Figure 6 illustrates the base metal structure of sheet metal welded at a speed of 16mm/s, the structure showing fine grains of Equiaxed Ferrite and Pearlite.

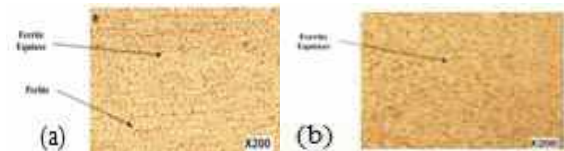


Fig.6. Base metal microstructure of welded sheet metal at speeds (a) 16mm/s and (b) 8 mm/s GX200

#### 1.2 Melt zone (MZ) examination

The microstructures of the molten zones of welded sheets for different speed values are shown below, bearing in mind that a microstructure can be controlled by balancing the effects of filler metal composition and welding speed and by taking into account the cooling conditions of the welded joint [5]. Microscopic observation Figure .7 (a) of the molten zone of the sheet welded at a speed of 16mm/s shows the following phases: - Aliotriomorphic ferrite FG. - Polygonal ferrite FP.

The microstructure of the molten weld zone at a speed of 8mm/s is shown in Figure 7 (b). Following the solidification process, shows a structure of Acicular Ferrite FA and Polygonal Ferrite FP [5]. The molten zone of the sheet welded at a speed of 8mm/s clearly shows a structure of Polygonal Ferrite FP.



Fig.7. melt zone microstructure of welded sheet metal at speeds (a) 16mm/s and (b) 8 mm/s GX200

### 1.3 Examination of heat-affected zones (HAZ)

Figure 8 shows the microstructures of the heat-affected zone at different welding speeds (8 and 16 mm/s). Microscopic observation of the heat-affected zone of welded sheets at different welding speeds shows both Polygonal Ferrite FP and Widmenstätten Ferrite FW and Aliotriomorphic Ferrite FG [5].



**Fig.8.** Heat-affected zones (HAZ) microstructure of welded sheet metal at speeds (a) 16mm/s and (b) 8 mm/s GX200

## I. CONCLUSION

Optical microscope examination of the BS2 steel after welding shows that the steel has the same ferritic structure as that observed before welding. The observed metallurgical structure shows the formation of Equiaxial ferrite when welding is carried out at a speed of 8 mm/s, and the formation of aliotriomorphic ferrite FG, with polygonal ferrite FP when welding is carried out at a speed of 16 mm/s.

## REFERENCES

- [1] K. Kumara, P.V.Gopal Krishnab, K.Kishorec, Study of Metallurgical and Mechanical Properties in Submerged Arc Welding With Different Composition of Fluxes-A Review. Sci.Vol. 22 (2020) pp.1.
- [2] Technical documents for the manufacture of the LPG gas cylinder, SNS BAG Batna.
- [3] NILES R.W. and JACKSON C.E. Wei thermal efficiency of the GTAW process. Welding Journal, January 1975, res. supp. pp. 25s-32s.
- [4] SUNDELL R.E., SOLOMON H.D., HARRIS L.D., WOJCIK L.A., SAVAGE W.F et WALSH O. W. Miner element affects or gas tungsten arc weld penetration. Contract No MEA-8208950, December 1983. General Electric Company, Shenectady, New York 12301.
- [5] D. CHEMS-EDDINE. Thèse Doctorat "Effet de la soudure sur la structure de l'acier", Université Mohamed Khieder– Biskra. 2011.

# Numerical modelling of the preheating temperature on cast IN-738 Ni Superalloy TIG welding

MOHAMED-SAID CHEBBAH<sup>1\*</sup>, CHERIF SAIB<sup>2</sup>, AND ABDELHAKIM BEGAR<sup>3</sup>

1. Mechanical Engineering Department of University Mohamed Khider of Biskra, UMKB, Biskra, Algeria, [ms.chebbah@univ-biskra.dz](mailto:ms.chebbah@univ-biskra.dz)
2. Mechanical Engineering Department, University Mohamed Boudiaf of M'sila, UMBM, M'sila, Algeria, [cherif.saib@univ-msila.dz](mailto:cherif.saib@univ-msila.dz)
3. Mechanical Engineering Department of University Mohamed Khider of Biskra, UMKB, Biskra, Algeria, [a.begar@univ-biskra.dz](mailto:a.begar@univ-biskra.dz)

## ABSTRACT

*The present paper deals with numerical simulations of the effect of preheating temperature on the thermal and mechanical phenomena occurring during welding. The numerical solution of the transient heat transfer equation by using ABAQUS/Standard<sup>®</sup> solver as finite element method. We use the volumetric Goldak's heat source as moving heat input. We use a DFLUX subroutine for application of the movable welding heat source on the butt-welded plates for welding simulation with respect to the welding conditions. In computer simulation, we consider the thermophysical properties of the Ni superalloy INC 738 LC. The transversal residual stresses and the distortions (strains) of the welded plates were calculated.*

## KEY WORDS (3 to 6 key words)

Distortion, preheating, residual stresses, TIG welding.

## I. INTRODUCTION

The Ni superalloy, INC 738 LC, used particularly in hot parts of gas turbine engines, subject to high temperatures varying between 900 and 1200 °C. Its high mechanical properties and very good resistance at high temperatures are due principally to the presence of a large fraction of  $\gamma'$  nano intermetallic particles of Ni<sub>3</sub> (Ti-Al) type controlled by precipitation hardening. Some researchers found that the solution to the hot cracking may occur by optimization of the welding current and low welding speed [3] and others stand that we can vanish the hot crack during welding and post welding heat treatment in the welded by using a preheating between 750°C [1] to 1050°C [4]. In order to predict the quality and state of residual stresses of the welded parts in connection with the welding

operating parameters (current, voltage, speed), we have developed a digital model which is based on a fully coupled thermal mechanical 3D analysis which was performed with the commercial software ABAQUS/Standard<sup>®</sup>. In order to simulate the welding torch movement with the specified speed.

## II. MATERIALS AND METHODS

The welding process of butt-weld joint of Ni superalloy INC 738 LC was simulated using a rectangular plate with 50mm x 60mm x 3 mm as dimensions. Since the welded plate taken for investigation was symmetrical, the symmetry axis was at the plate center. The plate meshing (Fig.1) was composed of 44 400 continua solid three-dimensional linear standard elements (C3D8RT). A fine mesh of 0.5mm x 0.5mm x 0.5mm is used in the welding area to insure an accurate application of heat flux.

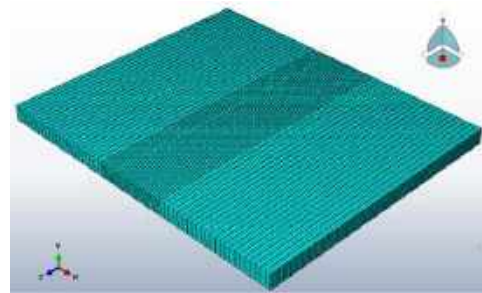


Fig. 1. Mesh model used for analysis.

Table 1. TIG welding process parameters

Current (A)	Voltage (V)	Arc efficiency	The net heat input per time unit Q(W)	Speed (m/s)	The net heat input per length unit Q(J/m)	Argon flux (l/min.)
40	10	0.8	320	0.004	80×10 <sup>3</sup>	8

Table 1 show the TIG welding process parameters supposed constant for both the surface distribution and volumetric heat input, for the current study. The Refs [1, 14 and 16] gives the temperature dependent properties, specific heat, thermal conductivity and thermomechanical properties of cast INC 738LC alloy.

The total strain (distortion) next welding is the total of elastic, plastic and thermal strain. The elastic strain is modeled using the isotropic Hooke's law with temperature-dependent Young's modulus and Poisson's ratio. For the plastic strain component, a plastic model is employed with the following features: The Von Mises yield surface and temperature-dependent material properties. The use of an elastoplastic behavior model (EP) allows obtaining better results regarding the estimation of the residual strains compared to an elasto-visco-plastic (EVP) model

### III. RESULTS AND DISCUSSIONS

Fig. 2 and Fig. 3 show the heat flux and the temperature distributions of the Goldak's input at 8.121 s respectively.

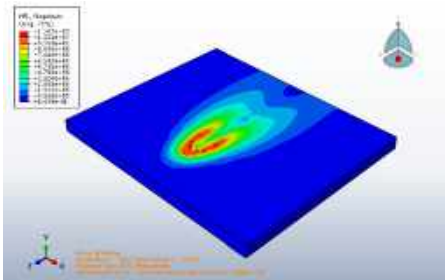


Fig. 2. Isometric view of the Goldak's heat flux at 8.121 s.

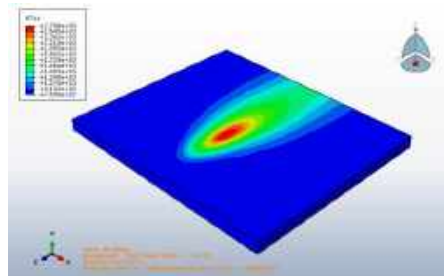


Fig. 3. Isometric view of temperature distribution of Goldak's heat input at 8.121 s.

By using the Goldak's heat input, Fig.4 show the transverse residual stresses in a point at 8.10 s from the welding line. The residual stress curve raises from base metal to attain a maximum value 0.7 GPa in the Fusion zone at 750°C, attain 0.46 GPa in the Fusion zone at

950°C and reaches the 0.2 GPa at the 1050°C as maximum stresses. When the preheating raises the transverse residual stresses in fusion, zone enlargement is narrower and less.

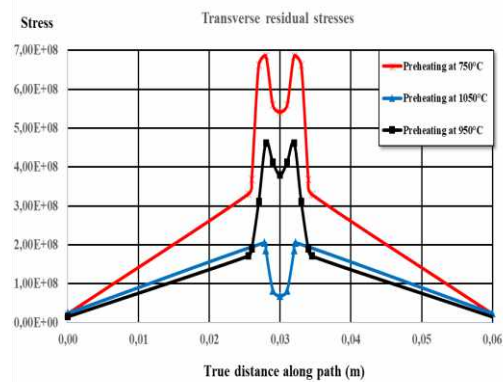


Fig. 7. The transverse stresses superposition for the three preheating temperatures.

### IV. CONCLUSION

This paper present resolution of a transient heat transfer on a solid body equation as welding simulation of the Ni superalloy INC 738 LC plate for three preheating temperatures (750°C, 950°C and 1050°C) by the element finite method using Abaqus solver, the following conclusions can be drawn:

- A volumetric heat input is used as moving torch welding simulation,
- The thermal fields and heat flux were established for the Goldak's heat source,
- The residual stresses level reaches the lowest value 0.2 GPa with preheating at 1050°C and without enlargement in fusion zone.
- With the preheating at 1050°C, The smallest distortions (strains) were unregistered in the welded plates.

### REFERENCES

- [1] Y. Danis, E. Lacoste and C. Arvieu, "Numerical modeling of inconel 738LC deposition welding: Prediction of residual stress induced cracking", Journal of Materials Processing Technology, vol. 210, pp. 2053–2061, 2010.
- [4] J. Xu, X. Lin, "The effect of preheating on microstructure and mechanical properties of laser solid forming IN-738LC alloy", Materials Science & Engineering A, vol. 691, pp. 71–80, 2017.
- [14] ALLOY IN-738 Technical data, INCO, The International Nickel Company INC. N.Y.10004, U.S.A.
- [16] D. Deng and H. Murakawa, "Prediction of welding distortion and residual stress in a thin plate butt-welded joint", Computational Materials Science, vol. 43, pp. 353–365, 2008.



# A numerical analysis of the melting process of Phase change material-metal foam-based latent thermal energy storage.

ATEF CHIBANI<sup>\*1</sup>, SLIMANE MEROUANI<sup>2</sup>, LEILA LAMIRI<sup>1</sup>, ISSAM FOURAR<sup>1</sup>, ASSIA TOUNSI<sup>1</sup>, BOUSSAHA BOUCHOUL<sup>1</sup>

1. Research Center in Industrial Technologies, CRTI, P.O.Box 64, Cheraga 16014 Algiers, Algeria

2. Laboratory of Environmental Process Engineering, Department of Chemical Engineering, Faculty of Process Engineering, University Salah Boubnider Constantine 3, P.O. Box 72, 25000 Constantine, Algeria

[chibaniatef@gmail.com](mailto:chibaniatef@gmail.com)

## ABSTRACT

*In the current work, a large-scale shell-and-tube based latent thermal energy storage unit (LTES) has had its phase change material (PCM) melting process embedded with nanoparticles and metal foams (MF) examined numerically. At first, experimental data was used to validate the constructed model. Next, based on temperature and liquid fraction measurements made during the melting operation, the effects of adding  $Al_2O_3$  (5%) nanoparticles and various MFs, such as aluminium (Al), copper (Cu), nickel (Ni), and titanium (Ti), with varying porosities (96–99%), on the performance of the melting process have been compared.*

## KEY WORDS

MF-PCM; Metal Foam; Heat transfer.

## I. INTRODUCTION

The latent heat thermal energy storage (LHTES) using phase change materials (PCMs) attracts scientist and researchers in recent years, due to its advantages of high energy storage capacity and its isothermal operation mode, in which thermal energy is stored during melting whereas it is released during solidification of the PCM [1–3]. Initially, when PCMs absorb heat, their temperature rises from its ambient temperature to that of the phase change. In this period, the PCMs store energy primarily by sensible heat. Then, the thermal energy is transferred when the solid PCMs change to liquid PCMs. In this second period, the thermal energy is mainly charged by latent heat. The PCMs absorb heat in a very small temperature interval. At the third period, the PCM temperature starts to increase again, until reaches its maximum value. During this period, the energy is charged only by sensible heat under a fusion form [4,5]. Therefore, the principal objective of the present work is to numerically investigate the melting process of paraffin-PCM embedded with various metal foams,

i.e. of different porosities, in a large scale shell-and-tube heat exchanger. Four different cases are adopted to study the effects of foam material (Cooper, Aluminum, Nickel and Titanium) on the variation of the temperature and liquid fraction of the paraffin

## II. MODEL DESCRIPTION

The PCM selected in this study is the paraffin. The latent thermal energy storage unit considered in the present study is a shell-and-tube type heat exchanger ( $\varnothing = 0.4$  m) with multi-tubes, where heat transfer fluid (HTF) flows through the twenty-five inner hexagonal tubes and exchange heat with PCM (Fig. 1). The PCM is filled in the annular space of the storage system. The cross section of a horizontal unit is shown in Fig. 1.

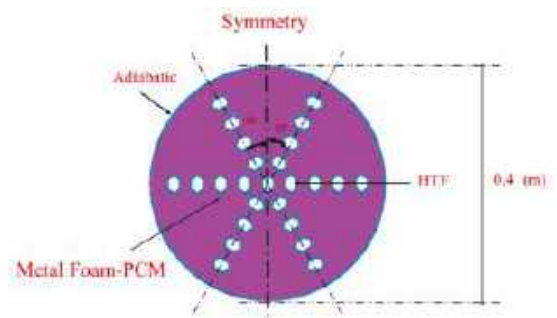


**Fig.1.** Schematic illustration of the metal Foam-PCM heat exchanger.

## III. RESULTS

In this case, we conducted a 3D simulation for a tube without the fins and with 4 internal fins. The height of the fins is always the same (10 mm) while the pitch  $P$  changes from 300, 60, and 30 mm. Fig. 3. shows the



variation between the maximum and the minimum temperatures in the outlet.

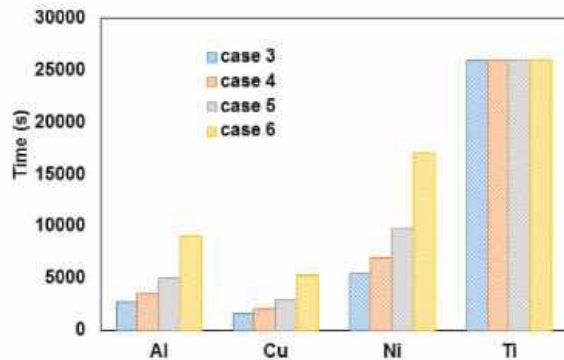


**Fig. 2.** Variation of time required for reaching complete melting, for different MF-PCM systems. Case 3 to 6 correspond to  $\varepsilon = 96$  to 99% (by step of 1%), respectively.

Fig. 2. Shows the time required for total melting (liquid fraction  $f = 96$  to 99%). Overall, the beneficial effect of MF for the melting process followed the order  $\text{Cu} > \text{Al} > \text{Ni} > \text{Ti}$ , which is the same order of the thermal conductivity. Moreover, relatively lower MF porosity facilitates the heat transfer and accelerates the PCM fusion. By reducing the porosity of the metal foam and as a result increasing the amount of the metal in the system, a higher rate of heat transfer is achieved as expected. Therefore, the PCM melts in a shorter time. However, it is not recommended to work with low porosity due to the consequent loss of the PCM mass in the system which is the main volume of heat storage. By increasing the portion of metal foams from porosity of 0.99 to 0.98 and 0.96, the melting time was reduced by 44% and 69%, respectively, for Cu, Al and Ni based MFs.

#### IV. CONCLUSION

In this study, the effect of nanomaterial addition and metal foams embedded into the PCM has been investigated on the heat transfer performance including the liquid fraction and PCM-temperature in multi-pipes energy storage-heat exchanger of large scale. The model was firstly validated by experimental data. The MF-PCM systems showed the best performance over the nano- and pure PCMs, with a huge reduction in the melting time. The porosity of the MF play an important role particularly when the selected MF is of lower thermal conductivity, i.e. like Titanium as compared to Copper and Aluminum.

Temperatures and liquid fractions profiles have been established for different cases of MF nature and porosity. The special distribution of the liquid fraction has also been stated. The results of this study may furnished guidelines to develop more effective LHS unit for the practical application of a high-performance unit at large scale.

#### REFERENCES

- [1] F. Agyenim et al., "A review of materials, heat transfer and phase change problem formulation for latent heat thermal energy storage systems (LHTESS)" *Renew. Sustain. Energy Rev.* 14, 615–628 (2010).
- [2] D. Zhou et al., "Review on thermal energy storage with phase change materials (PCMs) in building applications" *Appl. Energy*. 92, 593–605 (2012).
- [3] Z. Zhang et al., "Preparation and thermal energy storage properties of paraffin/expanded graphite composite phase change material" *Appl. Energy* 91, 426–431 (2012).
- [4] F. Benmoussa et al., "Thermal behavior of latent thermal energy storage unit using two phase change materials: effects of HTF inlet temperature" *Case Stud, Therm. Eng.* 10, 475–483 (2017).
- [5] F. Benmoussa et al., "Numerical analysis of concentric double pipe latent thermal energy storage unit using two phase change materials for solar water heating applications, Comput" *Therm. Sci.* 10, 355–374 (2018).

# Quasi-static indentation and low-velocity impact response of an aluminium honeycomb sandwich structure

KESKES BOUALEM

LABORATOIRE DE MÉCANIQUE DE PRÉCISION APPLIQUÉE LMPA.

INSTITUT D'OPTIQUE ET MÉCANIQUE DE PRÉCISION, UNIVERSITÉ DE SÉTIF-1. ALGÉRIE.

E-MAIL: BKK@UNIV-SETIF.DZ, B\_KESKES@YAHOO.FR

1. Affiliation (Author): dept. name of organization name of organization, acronyms acceptable  
City, Country, e-mail address
2. Affiliation (Author): dept. name of organization name of organization, acronyms acceptable  
City, Country, e-mail address

## ABSTRACT (1,000 characters)

*The honeycomb sandwiches are widely used in the transportation engineering for the realization of lightweight and crashworthy structures. However their application requires a better understanding of their impact response.*

*In this present article we aim to investigate experimentally and theoretically the behavior of honeycomb sandwiches panels subjected to quasi-static and low-velocity impact loading. The parameters which influence the static and dynamic response of AHS and their capacity of energy absorption such the cell size, impact energy and indenter geometry were analysed. Quasi-static indentation tests were carried out and the effect of indenter shape has been investigated. The indentation resistance depends on the indenter geometry and is strongly influenced by the cell diameter of the AHS. Otherwise, a series of low-velocity impact tests were carried out and a different collapse mechanism was observed: generally, the collapse of honeycomb sandwiches occurred for the buckling of the cells and is strongly influenced by the cell size. It was found that these factors have large influence on the indentation response of the sandwich panels in terms of absorbed energy, indentation at failure and damage area.*

## .KEY WORDS (3 to 6 key words)

Sandwiches structures, honeycomb core, low-velocity impact and indentation.

## I. INTRODUCTION

In this study we aim to investigate experimentally and theoretically the behavior of honeycomb sandwiches panels subjected to quasi-static and low-velocity impact loading. The parameters which influence the static and dynamic response of AHS and their capacity of energy absorption such the cell size, impact energy and indenter geometry were analysed. Quasi-static indentation tests were carried out and the effect of indenter shape has been investigated. The indentation resistance depends on the indenter geometry and is strongly influenced by the cell diameter of the AHS. Otherwise, a series of low-velocity impact tests were carried out and a different collapse mechanism was observed: generally, the collapse of honeycomb sandwiches occurred for the buckling of the cells and is strongly influenced by the cell size. It was found that these factors have large influence on the indentation response of the sandwich panels in terms of absorbed energy, indentation at failure and damage area.

## 2- Experimental procedures

### 2-1- Materials

For different types of HexWeb® hexagonal aluminium honeycombs with varying cell size, cell wall thickness and nominal density were used in both the indentation and low-velocity impact tests. The honeycombs were

manufactured by bonding together sheets of aluminium foil, then by expanding these sheets to form a cellular honeycomb configuration. During the experiment, the aluminium honeycombs were varied in terms of honeycomb cell size and foil thickness. The cell size is defined as the distance between the two vertical walls of the hexagonal cell. All specimens were carefully prepared to prevent deformation during cutting process. The properties of the honeycombs, which are provided by the manufacturer, are shown in Table 1.



**Fig.1:** Honeycomb sandwich structure with face-sheet and the honeycomb core



**Fig. 2:** The test system used in the quasi-static indentation tests (Zwick/Roell).

### 3- Results and Discussion

#### 3-1-Quasi-static indentation

A typical load/displacement curve obtained from indentation tests on AHS panel is shown in Fig. 5. It is possible to identify three regions on the above reported curve:

- An elastic region for low values of indentation;
- The curve became non-linear and, at increasing displacement, a series of small drops appears due to the local cracks formation on the upper skin with buckling of the honeycomb core. When loaded to the peak value, buckling of the wall leads to an abrupt load drop.
- At higher displacement the indented zone becomes thinner as the densification of damage increases and the sample shows a residual strength until the complete perforation of the upper skin happens.

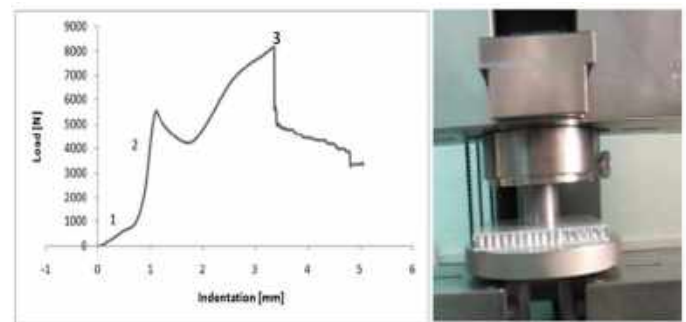


**Fig. 3 :** Load/displacement curve for a static indentation test (Aluminium honeycomb sandwich panel, Flat indenter)

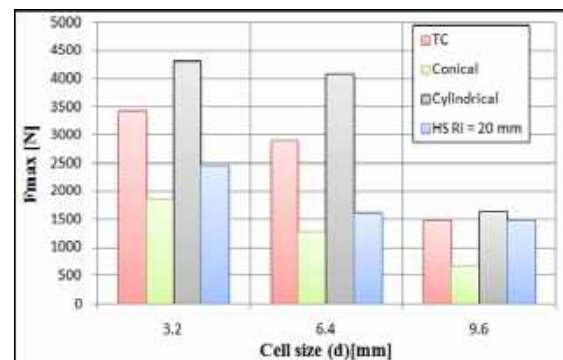


**Figure 5 :** Max indentation load at varying the cell size of AHS for each indenter



**Figure 6 :** Failure modes observed during indentation: failure of face: (skin/core debonding, fracture of the

face, core shear)

### 3.2. Low-velocity impact

The impact response of the honeycomb sandwiches was investigated in Crupi and al. [14] using a theoretical approach, based on the energy balance model and the model parameters were obtained by the tomographic analyses of the impacted panels. The vertical displacement  $w_b$  of the core at bottom face sheet interface and the striker displacement  $w_i$  were measured by analyzing the CT images of the panels (Figure 7) impacted at velocities lower than 5 m/s, that did not produce penetration of the panels.

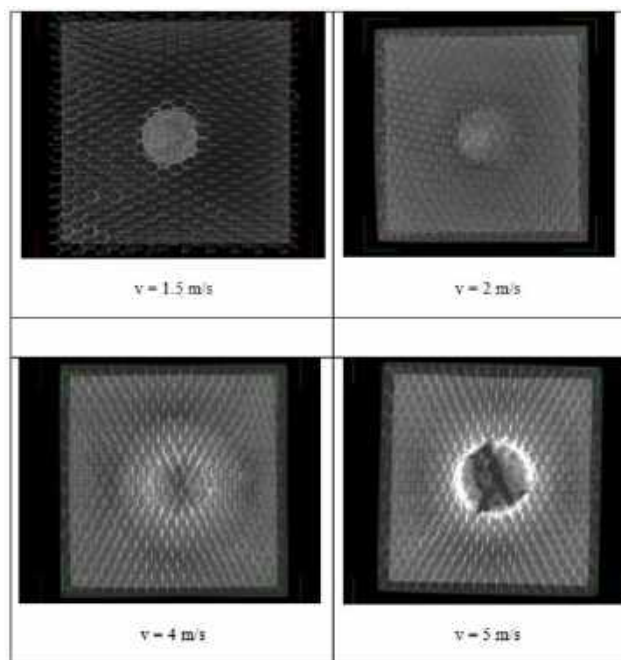


Fig. 7. Analysis of Fock states at one of the inputs of the Interferometer.

## 4. CONCLUSION

The conclusions of the present work are: - It was observed that the load-indentation curve showed a linear behaviour for low values of indentation, followed by a non-linear regime with a quick decrease in the sandwich panel stiffness caused by the extensive core crushing in the area under the indenter.

- It was found that the indentation load increases with the increase of the density of the core and the load is increased when the diameter of the indenter increases.

- Indenter nose shape has great influence on the indentation and impact resistance of sandwich panels, the failure mechanisms depend on the indenter nose shape.

- The sandwich with high density is much suitable for working conditions in which localised load resistance is necessary.

- The damage for a sandwich structure under static indentation test is dependent on the support kind, the indenter shape and the skins thickness.

- The pin geometry influences the shape of the damaged area on the sandwich. In fact, failure can be radial for a conical indenter (a crack starts at the pin/material interface with a petals shape during the penetration) or it can be circumferential if the indenter is cylindrical/ spherical (the material under the pin undergoes compressive stress and the strain interests the whole sample)

## REFERENCES

- [1] Jae-Youl Lee, Kwang-Bok Shin and Jong-Cheol Jeong. Experimental and Numerical Simulation Studies of Low-Velocity Impact Responses on Sandwich Panels for a BIMODAL Tram. *Advanced Composite Materials* 18 (2009) 1–20
- 13 et 14 Windsurf-Board Sandwich Panels Under Static Indentation C. Borsellino & L. Calabrese & G. Di Bella *Appl Compos Mater* (2008) 15:75–86.
- [2] Abrate, S. *Impact on composite structures*, 1998 (Cambridge University Press, Cambridge).
- [3] C C Foo, G B Chai, and L K Seah *Proc. Quasi-static and low-velocity impact failure of aluminium honeycomb sandwich panels. IMechE Vol. 220 Part L: J. Materials: Design and Applications* B2006.
- [3]. Nettles AT, Douglas MJ. A comparison of quasi-static testing to low velocity impact testing. In: Zureick A, Nettles AT, editors. *Composites Materials: Testing, Design, and Acceptance Criteria*, ASTM STP 1416. West Conshohocken, PA: American Society for Testing and Materials International, 2002. p. 116-130.
- [4]. Flores-Johnson EA. Quasi-static indentation and low velocity impact on polymeric foams and CFRP sandwich panels with polymeric foam cores. PhD thesis. School of Mechanical, Aerospace and Civil Engineering, the University of Manchester: Manchester, 2009.
- [5]. Lolive E, Berthelot J-M. Non-linear behaviour of foam cores and sandwich materials, part 2: indentation and three-point bending. *J Sandw Struct Mater* 2002; 4(4):297-352.
- [6]. Sun CT, Wu CL. Low velocity



# Experimental investigation of flexural static and fatigue behavior of Nomex Honeycomb Sandwich Panels and modelling

KESKES BOUALEM

Laboratoire de mécanique de précision appliquée, Institut d'Optique et Mécanique de Précision,  
Université Ferhat Abbas de Sétif, Algérie.

[b\\_keskes@yahoo.fr](mailto:b_keskes@yahoo.fr), [bkeskes@univ-setif.dz](mailto:bkeskes@univ-setif.dz)

## ABSTRACT

Composite sandwich structures have received a considerable attention because of their superior flexural rigidity, corrosion resistance, lower density, impact energy absorption and sound absorption. They are being increasingly used in high-performance structural applications, for instance: aircraft industry, satellites, bridge construction, ships, automobiles, rail cars, and other transportation applications. In order to use these materials in different applications, the knowledge of simply their static properties alone is not sufficient but additional information on their fatigue properties and durability are required. In this paper static and fatigue behaviours of Nomex honeycomb sandwich composites, made of aramid fiber core, are investigated through four-point flexural tests. The fatigue test was conducted at cyclic stress levels of 100%, 90%, 80%, 70%, 65% and 60% of the static flexural maximum strength of the sandwich beam. Effects of core densities and the cell orientation (L or W) on the maximum static load and on the damage processes are also investigated. The objectives of the investigated tests were to obtain basic knowledge on the fatigue behaviour of Nomex honeycomb sandwich composites as the standard stress-life, S-N diagrams and fatigue damage modes.

The fatigue model used for this study is based on the shear fatigue modulus concept (degradation of stiffness by core shearing) which is proposed for core-dominated behaviour and for transverse direction cells (W) of honeycomb. Two non-linear cumulative damage models derived from the chosen stiffness degradation equation are examined in context with the linear Miner's damage summation and compared with available experimental results. The application of the exponential model gave a good result when the cells are in W direction. Furthermore, the non-linear damage model, which is based on the stiffness

*degradation of the core sandwich specimens, provides better prediction of the remaining fatigue lives than the traditional linear damage model.*

**Keywords:** *Fatigue behaviour; honeycomb Sandwich; Stiffness degradation; damage models*

## 1- INTRODUCTION

Due to advantages of light weight, high stiffness and strength ration [Vinson, 1999], high impact strength and the high corrosion resistance, design flexibility, etc, honeycomb sandwich structures are attractive structural components and are therefore widely used in aerospace, satellite, shipbuilding, automobile, civil engineering and other areas. The sandwich composites are multi-layered materials made by bonding stiff, high strength skins facings to low density core material. Although large numbers of research projects have been performed by various authors, the design of structural elements made from sandwich composites is often a difficult task. In order to use these sandwich structures in different applications, the knowledge of their static and fatigue behaviours are required and a better understanding of the various failure mechanisms under static and fatigue loadings conditions is necessary [Qinghua, 2013]. From phenomenological point of view, fatigue damage can be evaluated, in the global sense by stiffness, residual strength or other mechanical properties. Fatigue modulus concept for fatigue life prediction of composite materials is proposed by [Hwang, 1986]. It is suggested that the changes in stiffness might be an appropriate measure of fatigue damage. The degradation behaviour and to predict the fatigue life is selected by [Wen-Fang, 1996]. There is an interesting feature in stiffness degradation approach that only limited amount of data is needed for obtaining reasonable results [Kin, 1999] reports that the reduction of bending strength of foam

cored sandwich specimen is caused by the stiffness reduction of foam due to ageing of polyurethane foam during fatigue cycles. [Shenoi, 1995] investigate the static and flexural fatigue characteristics of foam core polymer composite sandwich beams. Failure modes relate to both core shear and skin failure. The results of the stiffness degradation correlated well with the mechanical properties of the sandwich panels. The aim of this study is to develop analytical models describing the flexural behaviour of sandwich composite panels under cyclic fatigue. The stiffness degradation approach allows the assessment of the fatigue damage. Two non-linear cumulative damage models derived from the chosen stiffness degradation equations are examined assuming linear Miner's damage summation. Predicted results are compared to the available experimental data

### 3. Materials and experimental method

#### 3.1. Materials specimen

The honeycomb sandwich panels used in this study (Fig.1) have been provided by Euro-Composites S.A. (Luxembourg) and are intended for the aircraft industry. The sandwich panels are made from Nomex (aramid fiber) honeycomb core and pure aluminium (AlMg<sub>3</sub>) face sheet. The honeycomb core is an opened cell with various densities of 48, 80, 128 and 144 kg/m<sup>3</sup>. The geometrical dimensions of the specimen are shown in Table 1. The mechanical properties of the sandwich panels are depicted in Tables 2.

#### 3.2. Experimental Method

Both static and fatigue tests were carried out through a four-point bending testing fixture device schematically shown in Fig. 2. Static and fatigue tests were carried out in a servo-hydraulic Instron model 8800 testing machine with 10 kN capacity of loading cell (Fig.3). The INSTRON electronic unit performs the test control and the data acquisition. Static tests were carried out on all configurations samples, using a loading rate of 2 mm/min, according to the military standards: MIL-STD-401 DIN53291.

Cyclic flexural tests were performed on a minimum of three replicate sandwich beams of the same dimension as in static tests. The tests were achieved under load control at a load ratio  $R=0.1$  using a sinusoidal wave form. The beams were cycled at frequencies of 2 Hz. Fatigue data were generated at load levels of 100%, 90%, 80%, 70% and 60% of the static ultimate load. The fatigue life of the specimens is characterized as the number of cycles to ultimate failure. The normalised

applied load is plotted against the number of cycles on log-log scale.

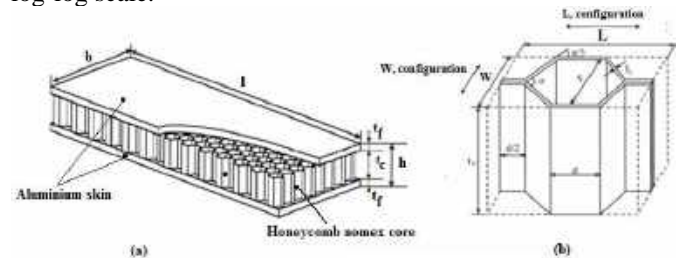


Figure 1. Description of the honeycomb sandwich

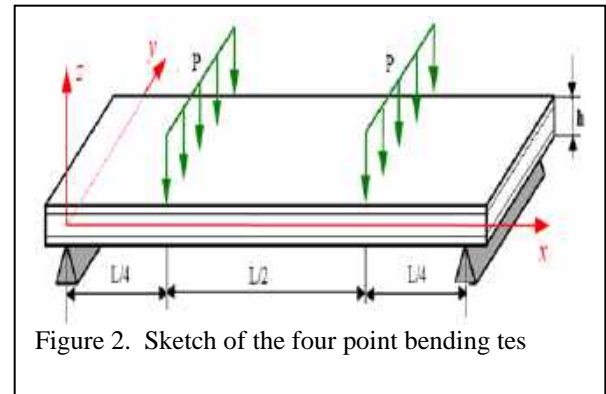


Figure 2. Sketch of the four point bending test

structure and Cells configuration (L and W)

### 4. Results and discussion

#### a) static four bending results

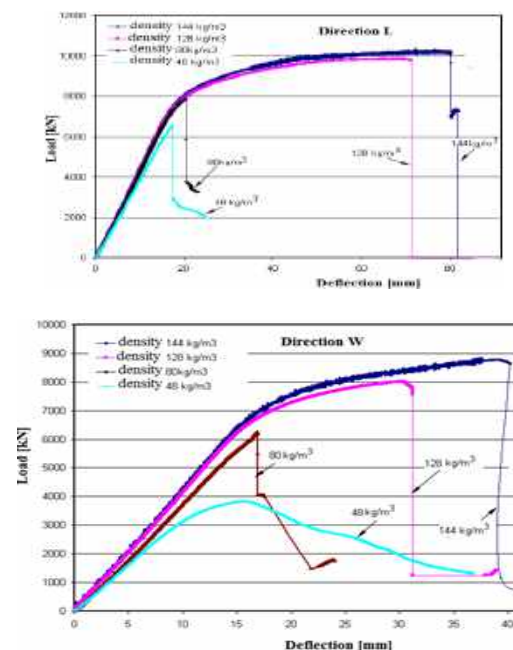


Fig. 3. Load/deflection curve for both cell directions (L and W) aluminium-Nomex sandwich panel.



## b) fatigue results

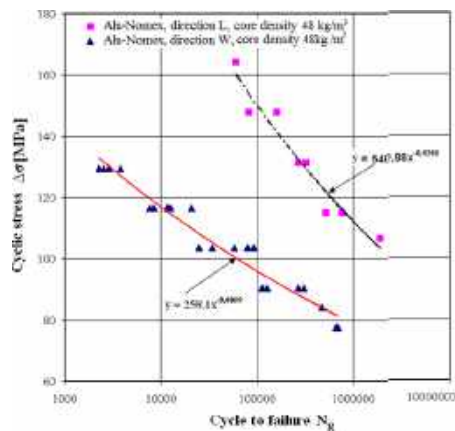


Fig. 4. Log-log representation of S-N fatigue curve nomex sandwich for 48 kg/m<sup>3</sup> core density

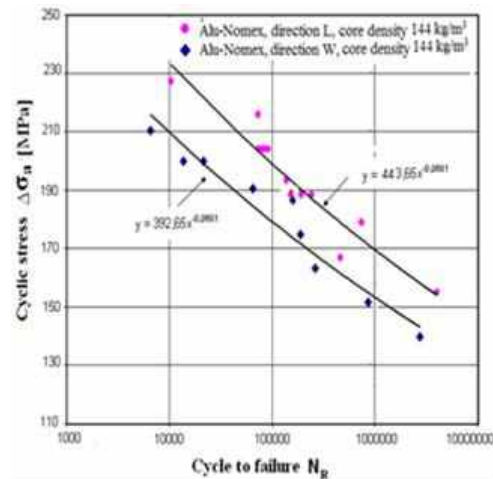


Fig. 5. Log-log representation of S-N fatigue curve nomex sandwich for 144 kg/m<sup>3</sup> core density in the W and L directions

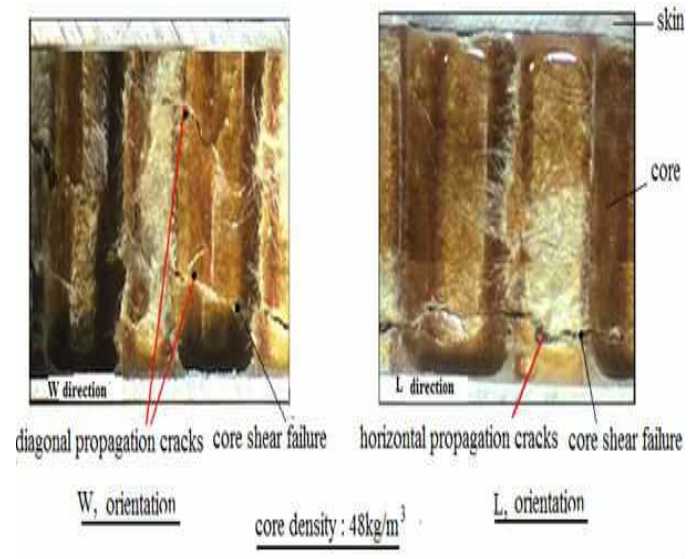
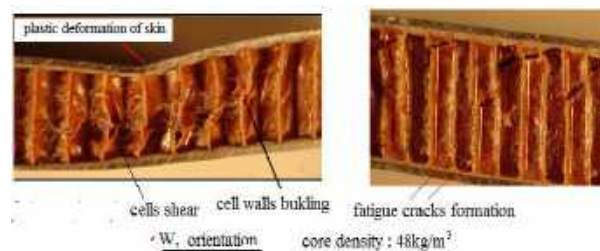
c) Failure mode for 48kg/m<sup>3</sup> and 144 kg/m<sup>3</sup> core density

Fig.6. Fatigue failure modes of sandwich panel with nomex honeycomb core of 48 kg/m<sup>3</sup> density , in the W and L-orientations

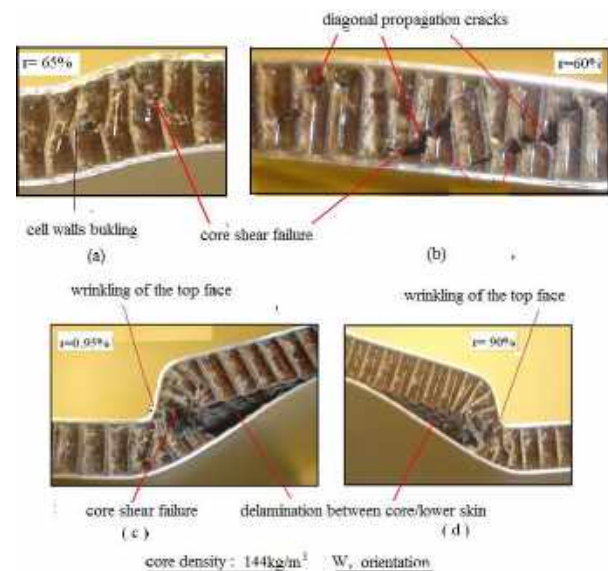


Fig. 7. Fatigue failure modes of sandwich panel with nomex honeycomb core of 144 kg/m<sup>3</sup> density in W orientation of cells

# Study of the effectiveness with optical profilometer of organic inhibitors against corrosion wear in HCl acid of XC48 steel's surface

IKRAM DAKHOUCHE<sup>1,2</sup>, NAFISSA KHENNAFI-BENGHALEM<sup>1</sup>, NADJIB CHAFAÏ<sup>2</sup>, RACHIDA KERKOUR<sup>2</sup>, MOURAD LATOUT<sup>3</sup>, MOHAMED HAMIDOUCHE<sup>4</sup>.

1. Emerging Materials Research Unit (URME), Institute of Optics and Precision Mechanics, University Ferhat Abbas-Setif 1.
2. Laboratory of Electrochemistry of Molecular and Complex Materials (LEMMC), Department of Process Engineering, Faculty of Technology, University Ferhat Abbas Setif 1, 19000 Setif, Algeria.
3. Laboratory of Electrochemistry, Molecular Engineering and Redox Catalysis, Faculty of Technology, Ferhat Abbas University, Setif 19137, Algeria.
4. URFA-CRTI additive manufacturing research unit, Setif, Algeria.

roughness, metallic engineering.

## ABSTRACT

*The corrosion wear of metals leads to many disasters and problems in industrial installations, and also causes environmental pollution, in particular the pollution of industrial waters by the metal oxides formed. From a chemical point of view, corrosion is an electrochemical reaction that occurs on the surface of a metal and leads to a modification of the mechanical, physicochemical and electromagnetic properties. To avoid the aforementioned issues and to provide a long life for the metals used in industrial installations, corrosion protection must be addressed in this context. Generally, the solution chosen must be compliant with the guidelines for environmental protection and enable the recycling or elimination of the individual components upon completion of their useful lives. In order to protect metals from corrosion, a number of methods have been utilized. Among these, corrosion inhibitors have been described. It's fascinating how a corrosion inhibitor is applied. This kind of substance slows or stops the corrosion process of a metal when introduced in few doses to the corrosive medium. Corrosion inhibitors made of organic compounds are now frequently employed to shield metals from rust in a variety of conditions. This work evaluates the corrosion inhibiting activity of two different organic inhibitors using the profilometer (mechanical and optical profilometer), which have been shown in our experimental studies to be very effective corrosion inhibitors against the corrosion wear of XC48 steel in acidic solution, and in the same time a study of steel's surface roughness.*

## KEY WORDS

Corrosion wear, Inhibitors, Protection, steel's

## I. INTRODUCTION

A solid surface, or more exactly a solid–gas or solid–liquid interface, has a complex structure and complex properties depending on the nature of the solids, the method of surface preparation, and the interaction between the surface and the environment. Properties of solid surfaces are crucial to surface interaction because surface properties affect real area of contact, friction, wear, and lubrication. In addition to tribological functions, surface properties are important in other applications, such as optical, electrical and thermal performance, painting, and appearance.[1] The study of metallic materials involves the study of their intrinsic properties which are very often also properties of use. In particular, understanding the behavior of metals and their alloys with respect to different forms of corrosion, and in particular stress corrosion, requires knowledge of some fundamental bases on the crystal structure of metals. Within the meaning of the ISO 8044 standard, corrosion is defined as the physicochemical interaction between a metal and its surrounding environment leading to modifications in the metal's properties and often a functional degradation of the metal itself, its environment or the technical system constituted by the two factors [2]. There are many different ways to apply chemical inhibitors to slow down the rate of corrosion processes. Inhibitors have long been regarded as the first line of defense against corrosion in the extraction and processing of oil. The topic of corrosion inhibitors has

been the subject of numerous scientific investigations. The majority of what is understood, nevertheless, has developed through trial-and-error research in labs and on the ground. There are very few guidelines, formulas, or hypotheses to direct the creation or application of inhibitors. A chemical compound that successfully slows the rate of corrosion when applied to an environment in a tiny quantity is known as a corrosion inhibitor.

## II. EXPERIMENTAL

### A. MATERIALS

First of all, we used a metallic sample ( $\Phi$  20mm\*10mm) which is carbon steel XC48 with the following chemical composition (wt.%): C = 0.418%, Mn = 0.730%, Mo = 0.012%, P = 0.016%, S = 0.019%, Si = 0.245%, Ni = 0.079%, F = 0.777% and Fe = 98.09873%. They are well polished, dried, and we putted every single one on each solution. Solution: the first solution was preparing on laboratory hydrochloric acid, then in two different solution we put a few concentrations from two our synthesis inhibitors. The inhibitors used: the two inhibitors used in our study had synthesized on our Laboratory of Electrochemistry of Molecular and Complex Materials (LEMMC).

### B. SURFACE CHARACTERIZATION

The Optical Profilometer images of the polished mild steel surface with and without immersion in the 1 M HCl solution in the absence and presence of a concentration of  $10^{-3}$  M of the inhibitors were taken in 2D and 3D after keeping them for 24h to demonstrate the effectiveness of these inhibitors in protecting the surface of carbon steel. The results are shown in Figures from 1.1 which is the result of the verge sample, to 4.2

### C. RESULTS

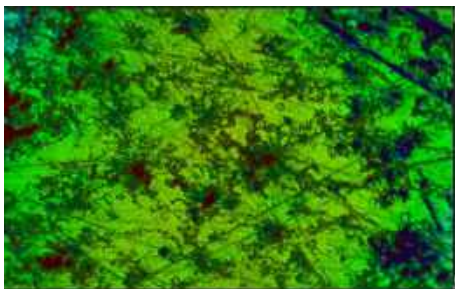


Fig1.1: the optical profilometer image 2D of verge sample XC48.

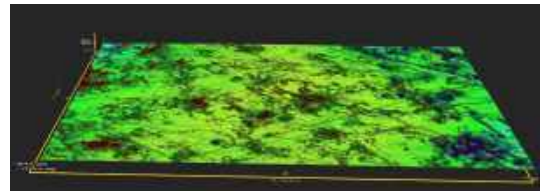


Fig1.2: The Optical Profilometer Image 3D Of verge sample XC48.

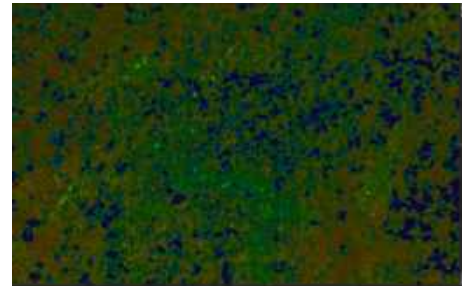


Fig 2.1: The 2D image of XC48 sample inside HCl solution acid.

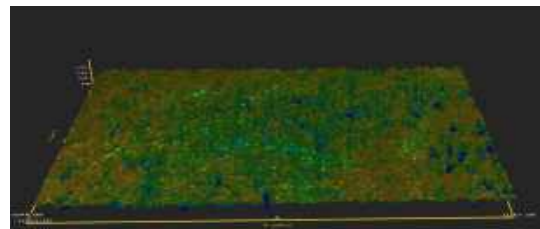


Fig2.2: The 3D image of XC48 sample inside HCl solution acid.

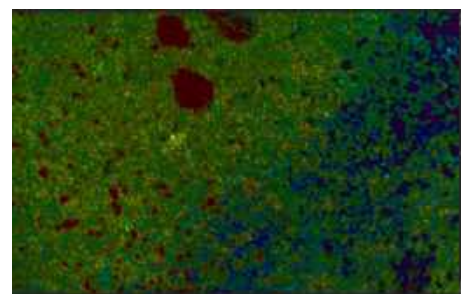


Fig 3.1: The 2D image of XC48 sample inside HCl+  $10^{-3}$ M inhibitor 1.

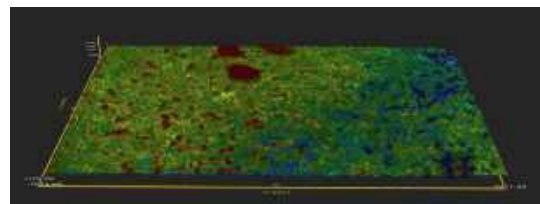


Fig 3.2: The 3D image of XC48 sample inside HCl+  $10^{-3}$  M inhibitor 1.



Fig 4.1: The 2D image of XC48 sample inside HCl+ 10-3M inhibitor 2.

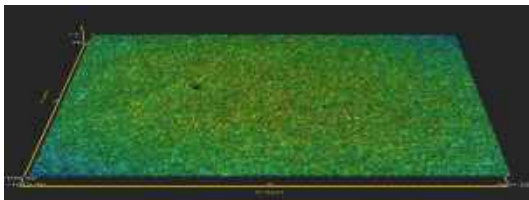


Fig 4.2: The 3D image of XC48 sample inside HCl+ 10-3M inhibitor2.

### III. CONCLUSION

- The corrosion is the most finding obstacle in industry and the most terrible problem investigated in scientific studies.
- The development of corrosion inhibitors, which come in a variety of forms, marked a major shift in the history of the fight against rust.
- Our both inhibitors seem a great protection against corrosion, that they improve the surface's roughness.
- The inhibitors used in our work are synthesis in lab of chemistry by Mm. KERKOUR.

### REFERENCES

- [1] Bharat BHUSHAN; « Modern Tribology Handbook »; Boca Raton; December 2000.
- [2] Max HELIE ; « Corrosion des matériaux métalliques »; ellipses; La France; Mars 2015.

***Session T6: Glass,  
ceramics and  
composite***



# Parametric Study of the polishing process of ceramic scintillator used as radiation detector in Positron emission tomography

KAHINA TAIEB<sup>1,\*</sup>, NABIL BELKHIR<sup>1</sup>, AND GREGORY BIZARRI<sup>2</sup>

1. Institute of optics and precision mechanics, Ferhat Abbas University, Setif, 1900, Algeria
2. Cranfield University, Bedfordshire, MK43 0AL, England, United Kingdom.

## ABSTRACT

*Scintillation is a material used in the Positron Emission Tomography imaging, many parameters influence the performance of this type of imaging as the impact on the light output. One of the materials used in this technic is a single crystal scintillator. In this paper, we worked on the Bismuth Germanate scintillator. We have started by a different parametric study on the scintillation, where the purpose is to achieve an optimal roughness depending on the given parameters using the Polishing process. The results have shown a difference depending on the variation of parameters under the found optimal parameters, we were able to arrive at a roughness of:  $Ra=3.3\pm0.5$  nm.*

## KEY WORDS

PET Imaging ; BGO scintillator ; CMP Process ; Surface finishing.

## I. INTRODUCTION

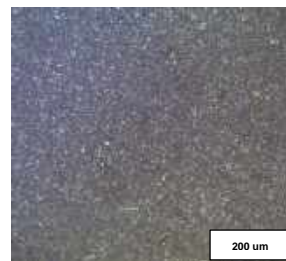
One of the requirements to achieve high performance of scintillators in the Positron emission tomography imaging is the quality of the finish surface, it has a direct impact on the light output in (PET) detectors. To optimize the surface finish and improve the performance of the detectors, the polishing abrasive finishing process is an important step [1-4]. We will look for an ultra-precise surface with less damage and compare the light output and the transmission to improve the performance of the material. A parametric study will be done comparing different polishing parameters and their influence on the performance of BGO.

## II. MATERIALS AND METHODS

### A. SAMPLES PREPARATION FOR POLISHING PROCESS

We have chosen to work on the rough BGO, starting by cutting it to small pieces of (3x3x4) mm<sup>3</sup> (0.49 um), using a precision machining process which is the wire cutting saw (Princeton scientific corp, precision wire saw, Tungsten 0.05mm, Twelve BGO samples of same dimensions will be used for the experimental tests. Cleaning the samples after finishing the cutting step by using an Ultrasonic cleaner, a microscopic view of the surface quality is shown in Fig.1, Roughness measurements were done and shown in Tab. 1.

A Grinding process was done to remove defects using different grits paper all the steps are shown in Tab. 2. The final surface roughness after the grinding process is  $Ra = 70.264$  nm.



Ra	1.002 um
Rt	6.378 um
Rv	3.233 um
Rp	2.68 um

**Tab. 1.** Roughness measurements after cutting the BGO Sample.

**Fig. 1.** Microscopic view of the Rough BGO surface.

Grinding parameters	
<b>Workpiece</b>	
Type	BGO
Mounted	Transparent Resin
Diameter	30 mm
Samples Number	6
<b>Grinding Wheel</b>	
Diameter	200 mm
Grains type	SiC (Silicon carbide): P800, P1200, P2500
<b>Process Parameters</b>	
Rotation speed	80 RPM
Applied Load	100 N
Time	5 min for each paper

**Tab. 2.** Grinding parameters.



### B. PARAMETRIC STUDY OF THE POLISHING PROCESS

The polishing process was applied on the twelve samples where each test has a changed parameter, the different polishing parameters studied are :

Polishing Parameters	Rotation Speed (RPM)	Applied Pressure (MPa)	Cloth Type	Grains Size and Type
(1)	50	15	ChemiCloth M	1 um Diamond
(2)	80	15	ChemiCloth M	0.3 um Alumina
(3)	80	10	ChemiCloth M	1 um Alumina
(4)	50	10	ChemiCloth M	0.3 um Alumina
(5)	50	10	MD Chem. Cloth	0.25 um Diamond
(6)	50	20	ChemiCloth M	0.3 um Alumina
(7)	80	10	ChemiCloth M	1 um Alumina
(8)	120	15	ChemiCloth M	0.3 um Alumina
(9)	50	15	ChemiCloth M	0.3 um Alumina
(10)	80	10	ChemiCloth M	0.25 um Diamond
(11)	80	10	ChemiCloth M	0.3 um Alumina
(12)	50	10	ChemiCloth M	0.25 um Diamond

Tab. 3. Polishing parameters.

### III. RESULTS AND DISCUSSION

The different results obtained for all the samples are :  
By applying the same parameters: Rotation Speed 50 RPM, Applied Load 10 N, Suspension 0.25 um Diamond. And by varying the type of Cloth we obtained the following roughness values for each type:

**ChemiCloth M :  $R_a = 5.03 \pm 0.5$  nm**

MD Chem Cloth :  $R_a = 5.58 \pm 0.5$  nm

Rotation Speed 80 RPM, Applied Load 10 N, ChemiCloth M. And by varying the type and size of the grains suspension we obtained the following roughness values for each type:

**1 um Alumina:  $R_a = 7.01 \pm 0.5$  nm**

1 um Diamond:  $R_a = 11.03 \pm 0.5$  nm

We can conclude that there is not a big influence by changing the type of grains between diamond and alumina because the hardness of the two grains is (10 Mohs for diamond and 9 Mohs for the alumina), and by the shape of the grains which also almost similar (angular attack).

**0.3 um Alumina:  $R_a = 4.13 \pm 0.5$  nm**

0,25 um Diamond:  $R_a = 4.48 \pm 0.5$  nm

The small grains size gives better roughness results.

By varying the applied load we obtained the following roughness values for each load:

10N:  $R_a = 4.7 \pm 0.5$  nm.

**15N:  $R_a = 4.08 \pm 0.5$  nm.**

20N:  $R_a = 5.74 \pm 0.5$  nm.

From the results obtained, by increasing the applied load to 20 N during the finishing of our BGO samples the surface quality decreases while using the 0.3 um Alumina.

By varying the speed of rotation we obtained the following roughness values for each speed:

50 RPM:  $R_a = 4.08 \pm 0.5$  nm.

80 RPM:  $R_a = 3.9 \pm 0.5$  nm

**120 RPM:  $R_a = 3.3 \pm 0.5$  nm.**

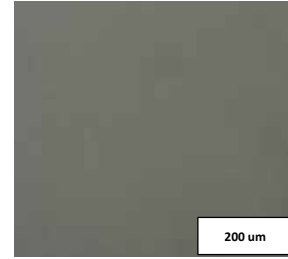


Fig. 2. Microscopic view of the final optimal surface.

### IV. CONCLUSION

Despite the constraints present and the difficulty of polishing such an assembly, the novel technique has given very good results. This technique and the optimal parameters combined can be applied for the finishing of the BGO used for PET imaging, where the roughness has a direct influence on the optical and scintillator properties.

The final optimal parameters found for this kind of polishing process of BGO are: **ChemiCloth M, 0.3 um Alumina, 15N, 120 RPM**

### REFERENCES

- [1] Ishibashi, H., S. Akiyama, and M. Ishii, Effect of surface roughness and crystal shape on performance of bismuth germanate scintillators. Japanese journal of applied physics, 1986. 25(9R): p. 1435.
- [2] Ishibashi, H., S. Akiyama, and M. Ishii, Influence of surface roughness and crystal shape on scintillation performance of bismuth germanates. 1982.
- [3] Valenciaga, Y., D. Prout, and A. Chatzioannou. Investigation of the effects of scintillator pixel shape, surface treatment and optical coupling on the performance of Si-PM based BGO detectors. in 2013 IEEE Nuclear Science Symposium and Medical Imaging Conference (2013 NSS/MIC). 2013. IEEE.
- [4] Rinaldi, D., et al. Influence of a surface finishing method on light collection behaviour of PWO scintillator crystals. in Photonics. 2018. MDPI.

# Elaboration and Characterization of Nanocomposites with PVC Matrix Reinforced by Nanoclays: Case of Montmorillonites

BADRA BOUCHAREB<sup>1,2</sup>, NACEREDDINE HADDAOUI<sup>1</sup>

1. Department of Process Engineering Ferhat Abbas Setif University 1 Sétif, Algeria.  
[badrabouchareb4@gmail.com](mailto:badrabouchareb4@gmail.com)
2. Research center in Industrial Technologies URFA-CRTI setif, Algeria.

## ABSTRACT

*The poly(vinyl chloride)/montmorillonite nanocomposites were prepared by melt mixing. Three types of montmorillonite were used: raw montmorillonite (MMT-Brt), sodium montmorillonite (MMT-Na<sup>+</sup>), and montmorillonite modified with hexadecylammonium chloride ions (MMT-O). These montmorillonites were incorporated at different contents (1, 3, 5, 7, and 9 phr) in the presence of dioctyl phthalate (DOP). The thermal, Fourier transform infrared spectroscopy (FTIR), and morphological properties were studied using different techniques such as X-ray diffraction (XRD) and Atomic Force Microscopy (AFM). The XRD results show that the PVC chains can be exfoliated and intercalated in the gallery of MMT-O and MMT-Na<sup>+</sup>, respectively. An immiscible structure is formed in PVC/MMT-Brt composites when the MMT-Brt content is incorporated from 1 to 9 phr. However, FTIR analysis identified a small shoulder at 1667 cm<sup>-1</sup> in all nanocomposites. This peak is attributed to the vibrations of the double bond (C=C), which suggests that the nanocomposite films have undergone coloring. The glass transition temperature (T<sub>g</sub>) of PVC/MMT-O nanocomposites is lower than that of nanocomposites containing MMT-Brt and MMT-Na<sup>+</sup>, suggesting that MMT-O acts as a plasticizer by increasing the distance between the polymer chains. This increase reduces interactions between chains, resulting in a decrease in T<sub>g</sub>. AFM analysis revealed that the surface roughness of the nanocomposites (PVC/MMT-O) is reduced under the effect of the modification of raw montmorillonite, and particularly at 1 phr of MMT-O.*

**KEY WORDS:** PVC, unmodified montmorillonite, modified montmorillonite, nanocomposites, physical properties.

## I. INTRODUCTION

Traditionally, composite materials are developed by adding conventional fillers, such as glass fibers, mica, or calcium carbonate, with the primary aim of enhancing mechanical performance and/or reducing production costs [1].

In recent years, a new class of filled polymer has emerged, known as "nanocomposites." This category of materials has the unique feature of exhibiting improved properties of the host matrix at low concentrations of nano-fillers (1-5%) compared to conventional polymers. These properties include increased stiffness, toughness, chemical resistance, barrier properties, and thermal stability. Various mineral and organic fillers have been used to create

these nanocomposites, including silica nanoparticles, carbon nanotubes, and metallic particles [2]. However, clays remain by far the most widely used materials to create these composites. This widely available and cost-effective mineral significantly enhances mechanical, thermal, barrier, and flame-retardant properties of nanocomposites (polymer/clay) without increasing their density or reducing their transparency compared to the original materials. Low loading levels, typically in the range of 1-5% by weight relative to the base matrix, are sufficient to achieve the desired performance enhancements [3].

The main objective of this study is to elaborate on and characterize a new nanocomposite material based on polyvinyl chloride (PVC) reinforced with montmorillonite-type (modified and unmodified) at various concentrations (0, 1, 3, 5, 7, and 9 pcr).

## A. EXPERIMENTAL

The nanocomposites (PVC/Montmorillonite) were prepared using a two-roll mill mixer of the Rodolfo Busto Arsizio type. The PVC resin, along with additives such as plasticizer, stabilizers, lubricant, and nano-fillers, was manually mixed in containers. Subsequently, they were introduced into the two-roll mill mixer at a temperature of 160°C and a cylinder rotation speed of 30 rpm to ensure complete homogenization between the resin and additives. This process yielded nanocomposite films with a thickness of (0.5 ± 0.1) mm, which were removed after a period of 8 minutes. Finally, these films were air-cooled.

## B. RESULTS

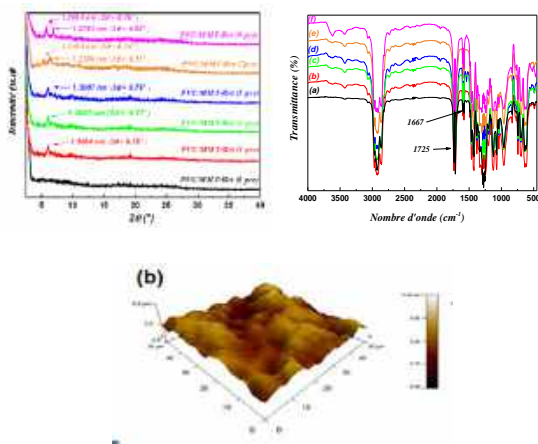


**Figure I.** X-ray diffractograms, FTIR spectra and AFM micrographs (3phr) of nanocomposites (PVC/MMT-Brt).

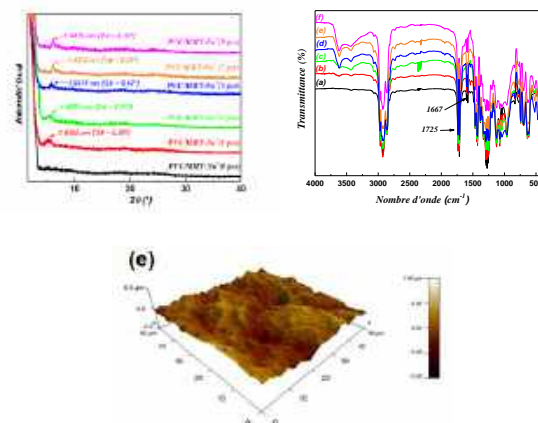


**Figure II.** X-ray diffractograms, FTIR spectra and AFM micrographs (3phr) of nanocomposites (PVC/MMT-Na<sup>+</sup>).

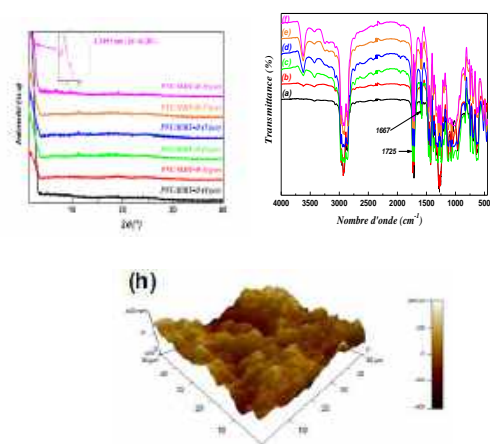


**Figure III.** X-ray diffractograms, FTIR spectra and AFM micrographs (3phr) of nanocomposites (PVC/MMT-O).

## I. CONCLUSION

From the results obtained, we can state the following conclusions:

- The XRD results show that the PVC chains can be exfoliated and intercalated in the gallery of MMT-O and MMT-Na<sup>+</sup>. An immiscible structure is formed in PVC/MMT-Brt composites when the MMT-Brt content is incorporated from 1 to 9 phr.
- FTIR analysis identified a small peak at 1667 cm<sup>-1</sup> in all nanocomposites, attributed to vibrations of the double bond (C=C), suggesting coloration of the nanocomposite films.
- The results of atomic force microscopy (AFM) showed that the nanocomposites (PVC/MMT-O) presented a reduction in the surface roughness under the effect of the modification of montmorillonite, particularly at a content of 1 phr of MMT-O.

## REFERENCES

- [1] CD.Armitt et al. "Particulate Fillers, Selection, and Use in Polymer Composites," *Encycl. Poly. Compos.*,1-9,(2017).
- [2] L. Flandin et al., "New nanocomposite materials made of an insulating matrix and conducting fillers: Processing and properties," *Poly. Compos.* 21, 165-174 (2000).
- [3] D.E. Kheoub et al. "Nylon 6/clay nanocomposites prepared with Algerian modified clay (12-maghnite)," *Res. Chem. Interme.*, 41, 5217-5228, (2015).

# Bending analysis of sandwich plates with different face sheet materials and functionally graded

BELAID HICHEM <sup>1</sup>, HIMEUR MOHAMMED <sup>2</sup>, ZIOU HASSINA <sup>3</sup> AND CHABANE SI AHMED <sup>4</sup>

<sup>1,2</sup> May 8, 1945, Guelma University, Civil Engineering Department, Guelma, Algeria,

<sup>1</sup> [belaid.hichem@univ-guelma.dz](mailto:belaid.hichem@univ-guelma.dz)

<sup>2</sup> [bet\\_himeur@yahoo.fr](mailto:bet_himeur@yahoo.fr)

<sup>3</sup> National Centre for Studies and Integrated Research on Building (CNERIB), Souidania, Algeria,

<sup>3</sup> [hassina.geniecivil@gmail.com](mailto:hassina.geniecivil@gmail.com)

<sup>4</sup> Abderahmane mira, Bejaia University, Civil Engineering Department, Bejaia, Algeria,

[chabane.siahmed@univ-bejaia.dz](mailto:chabane.siahmed@univ-bejaia.dz)

## ABSTRACT

*This paper presents a study on the bending of sandwich plates made of functionally graded materials (FGM) under distributed transverse loads. A new FGM sandwich plate model is developed. The top and bottom sheets have different material properties. The material properties of the functionally graded soft core are assumed to be graduated according to the volume fractions of the constituents in the thickness direction. Comparisons of reference solutions of the new model with solutions of several other theories to verify the effectiveness of the proposed method. The influences of volume fraction distribution, thickness/side ratio and thickness/layer ratio on the bending characteristics of the plate are studied in detail.*

**KEY WORDS** Functionally graded, Sandwich plate, Bending behavior, Finite element method.

## I. INTRODUCTION

The formulation of finite elements using the deformation approach has been of interest to many researchers to develop efficient elements in which the displacement shape functions can be obtained by integration from assumed deformations and not directly from assumed displacements. Much research has been done to extend the deformation approach to Reissner-Mindlin plate elements ([1]; [2]), Khirchof plate elements [4] and [3], and cylindrical shells ([5], [6], [7]) for nonlinear and dynamic geometric behavior.

Due to their unique properties, such as high specific

rigidity and strength, as well as energy absorption capacity, sandwich structures have been widely used in the aerospace and construction industries. However, the sudden change in material properties across the interfaces between face sheets and core can result in significant interlaminar damage, often leading to delamination, which is a major problem in sandwich structures. Exploring functionally graded materials (FGMs) in sandwich design is one solution to this problem. The properties of functionally graded materials vary continuously and evenly. This eliminates the abrupt changes mentioned above [8,9]. To date, several studies have investigated the bending of FGM sandwich plates. A sinusoidal shear deformation theory was proposed by Zenkour [10] to study the bending of a simply supported FGM type-A sandwich plate. A two-stage perturbation technique was used to analyze the nonlinear bending of an type-A sandwich plate resting on an elastic foundation by Wang and Shen [11].

## II. FORMULATION

### A . STRAIN AND DISPLACEMENT FIELDS

We Consider A Finite Element Of A Quadrilateral Plate Of Planar Elasticity, Which Has Three Degrees Of Freedom ( $W_i$ ,  $\Theta_{xi}$  And  $\Theta_{yi}$ ) The Formulation Of The Element Is Based On The Deformation Approach.

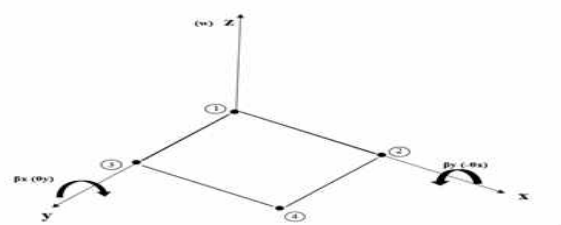


**Fig. 1** the developed element and coordinate system

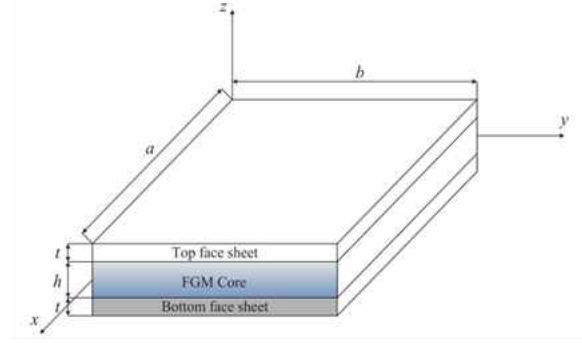


**Fig. 2-** Sandwich plate with FGM core and isotropic homogeneous face sheets

The equilibrium conditions are given by the following equation:

$$\begin{bmatrix} \frac{\partial}{\partial x} & 0 & \frac{\partial}{\partial y} \\ 0 & \frac{\partial}{\partial y} & \frac{\partial}{\partial x} \end{bmatrix} \cdot \begin{Bmatrix} \sigma_x \\ \sigma_y \\ \tau_{xy} \end{Bmatrix} + \begin{Bmatrix} f_x \\ f_y \end{Bmatrix} = \begin{Bmatrix} 0 \\ 0 \end{Bmatrix} \quad (1)$$

For zero value of volume forces, Airy functions are introduced to reduce the problem of the equilibrium condition of relation (1) to the bi-harmonic equation:

$$\nabla^4 F(x, y) = 0 \quad (2)$$

$$\text{where : } \begin{cases} \sigma_x = \frac{\partial^2 F(x, y)}{\partial y^2} \\ \sigma_y = \frac{\partial^2 F(x, y)}{\partial x^2} \\ \tau_{xy} = \frac{\partial^2 F(x, y)}{\partial x \partial y} \end{cases} \quad (3)$$

For the plane stress state and isotropic materials, the relations (Hooke's law) that relate strain to stress are as follows:

$$\begin{Bmatrix} \sigma_x \\ \sigma_y \\ \tau_{xy} \end{Bmatrix} = \frac{E}{1-\nu^2} \begin{bmatrix} 1 & \nu & 0 \\ \nu & 1 & 0 \\ 0 & 0 & \frac{1-\nu}{2} \end{bmatrix} \cdot \begin{Bmatrix} \varepsilon_x \\ \varepsilon_y \\ \gamma_{xy} \end{Bmatrix}$$

$$\Rightarrow \begin{Bmatrix} \varepsilon_x \\ \varepsilon_y \\ \gamma_{xy} \end{Bmatrix} = \frac{1}{E} \begin{bmatrix} 1 & -\nu & 0 \\ -\nu & 1 & 0 \\ 0 & 0 & 2(1+\nu) \end{bmatrix} \cdot \begin{Bmatrix} \sigma_x \\ \sigma_y \\ \tau_{xy} \end{Bmatrix} \quad (4)$$

### III. Numerical results and discussions:

In this section, various numerical examples are presented and discussed to validate the proposed solution of the present work and investigate the effects of the power law index, the thickness to side ratio and the layer thickness ratio on the bending behavior of the sandwich plate.

#### Example 1

In this example, the new model for FGM sandwich plate is to be compared with a similar model reported by Li et al. [12], in which a simply supported square sandwich plate ( $a=b$ ) consists of a FGM core and homogeneous face sheets made of same materials. Li et al.'s model can be considered as a special case of the new model. It is subjected to a bi-sinusoidal load  $q = q_0 \sin(\pi x/a) \sin(\pi y/b)$

The following material properties are adopted for the face sheets and the core:

<b>Young's modulus</b>	$E_t^+ = E_t^- = 70 \text{ GPa}$
<b>Poisson's ratio</b>	$\nu_t^+ = \nu_t^- = 0.3$

For the FGM core, the Young's modulus of the core varies through the thickness with a power law distribution, which is given below:

$$E(z) = (E_t - E_b) \left( \frac{z}{h} + \frac{1}{2} \right)^p + E_b$$

$$-\frac{h}{2} \leq z \leq \frac{h}{2}$$

In this example,  $E_t = 3.8 \text{ GPa}$ ,  $E_b = 0.7 \text{ GPa}$ ,  $\nu = 0.3$ , and  $h = a/10$ . The non-dimensional deflection is defined

$$\bar{w} = w(x, y) \frac{100(h + 2t)^3 E_t}{q_0 a^4}$$

Table 1 shows the results of non-dimensional deflection for various values of the thickness ratio of the face sheet to the core layer  $t/h = \{2, 1, 0.5, 0.1, 0.01\}$  and the power index  $p = \{0, 0.5, 1, 2, 4, 10\}$ . These results are compared with the solutions in Ref. [12]. It can be noticed from this table that the non-dimensional deflection  $w$  in Ref. [12] is greater than that of the present research. The reason is that the face sheets in Ref. [12] are assumed to be in membrane-stress state while the face sheets in present research are assumed to be thin plates which have bending stiffness and shear stiffness. The difference decreases as the thickness ratio of the face sheet to the core layer reduces, because the stress states of thin face sheet are close to those of membranes.



$t/h$	Theory	$P = 0$	$P = 0.5$	$P = 1$	$P = 2$	$P = 4$	$P = 10$
<b>2</b>	Ref. [12]	2.0055	2.9479	3.9697	5.4955	7.0959	8.6506
	Dongdong Li and [al]	0.7363	0.8471	0.9147	0.9147	1.0181	1.0450
	<b>Present</b>	<b>1.7450</b>	<b>1.9440</b>	<b>2.3595</b>	<b>3.7845</b>	<b>5.2356</b>	<b>6.1250</b>
<b>1</b>	Ref. [12]	1.0603	1.5182	2.0148	2.7564	3.5342	4.2898
	Dongdong Li and [al]	0.6993	0.8730	1.0171	1.1769	1.2990	1.3889
	<b>Present</b>	<b>0.8934</b>	<b>1.2435</b>	<b>1.7840</b>	<b>2.0105</b>	<b>2.7525</b>	<b>3.0030</b>
<b>0.5</b>	Ref. [12]	0.6486	0.8899	1.1515	1.5421	1.9518	2.3498
	Dongdong Li and [al]	0.5724	0.7524	0.9312	1.1711	1.3932	1.5849
	<b>Present</b>	<b>0.6115</b>	<b>0.8020</b>	<b>1.0035</b>	<b>1.3450</b>	<b>1.7280</b>	<b>2.0750</b>
<b>0.1</b>	Ref. [12]	0.5502	0.6471	0.7522	0.9091	1.0736	1.2335
	Dongdong Li and [al]	0.5479	0.6440	0.7479	0.9028	1.0649	1.2220
	<b>Present</b>	<b>0.5497</b>	<b>0.6454</b>	<b>0.7490</b>	<b>0.9053</b>	<b>1.0679</b>	<b>1.2230</b>
<b>0.01</b>	Ref. [12]	2.7749	2.8455	2.9220	3.0363	3.1562	3.2726
	Dongdong Li and [al]	2.7748	2.8454	2.9219	3.0362	3.1561	3.2725
	<b>Present</b>	<b>2.7750</b>	<b>2.8456</b>	<b>2.9221</b>	<b>3.0365</b>	<b>3.1565</b>	<b>3.2728</b>

**Table 1.** Dimensionless deflection  $w$  of FGM sandwich square plates with same face sheet materials under bi-sinusoidal loads

#### IV. Conclusion

This paper presents a bending analysis of simply supported FGM sandwich plates with different face sheet materials and a FGM core subjected to transverse distributed loadings. The face sheets are considered to be thin plates and the core is assumed to be a FG soft core. The governing equations are deduced based on the static equilibrium method. In the present method, the number of unknowns is only three, significantly facilitating engineering analysis. The results of the proposed solution in this study show rationality compared with those of several theories existing in the literature. Furthermore the proposed method is much more concise, and the corresponding computation is much more efficient in bending analysis of FGM sandwich plates with different face sheet materials and a FG soft core. Parameter studies are conducted to determine the influences of power law index, thickness to side ratio and layer thickness ratio on the non-dimensional deflection  $w$ .

#### V. References

- [1]. Robinson J. (Oct. 1978). "Element evaluation. A set of assessment points and standards tests Proc.", Element method in the commercial environment, vol. 1, p. 217-248.
- [2]. Belounar L., and Guenfoud M. (2005). A new rectangular finite element based on the strain approach for plate bending, Thin-Walled Structures, Vol. 43, pp. 47-63.
- [3]. Boussem F., Belounar A., and Belounar L. (2021). Assumed Strain Finite Element for Natural Frequencies of Bending Plates, World Journal of Engineering.
- [4]. Boussem F., and Belounar L. (2020). A Plate Bending Kirchhoff Element Based on Assumed Strain Functions, Journal of Solid Mechanics, Vol. 12(4), pp. 935-952.
- [5]. Himeur M., and Guenfoud M. (2011). Bending triangular finite element with a fictitious fourth node based on the strain approach, European Journal of Computational Mechanics, Vol.20 (7-8), pp.455-485.
- [6]. Guenfoud H., Humeur M., Ziou H. and Guenfoud M. (2018). A consistent triangular thin flat shell finite element with drilling rotation based on the strain approach. International Journal of Structural Engineering, Vol.9, No. 3, pp.191-223.
- [7]. Djoudi M.S., and Bahai H. (2003). A shallow shell finite element for the linear and nonlinear analysis of cylindrical shells, Engineering Structures, Vol. 25, pp. 769-778.
- [8]. V. Birman, T. Keil, S. Hosder, Functionally graded materials in engineering, in: S. Thomopoulos, V. Birman, G.M. Genin (Eds.), Structural Interfaces and Attachments in Biology, Springer, New York, 2013, pp. 19-41.
- [9]. H.L. Dai, Y.N. Rao, T. Dai, A review of recent researches on FGM cylindrical structures under coupled physical interactions, 2000-2015, Compos. Struct. 152 (2016) 199-225.
- [10]. A.M. Zenkour, A comprehensive analysis of functionally graded sandwich plates: Part 1—deflection and stresses, Int. J. Solids Struct. 42 (18-19) (2005) 5224-5242.
- [11]. Z.X. Wang, H.S. Shen, Nonlinear analysis of sandwich plates with FGM face sheets resting on



elastic foundations, *Compos. Struct.* 93 (10) (2011) 2521–2532.

[12]. H. Li, X. Zhu, Z. Mei, J. Qiu, Y. Zhang, Bending of orthotropic sandwich plates with a functionally graded core subjected to distributed loadings, *Acta Mech. Solid. Sin.* 26 (3) (2013) 292–301.

# Influence of fibers on the thermal conductivity of the composite materials

H. BALIT<sup>1,\*</sup>, M. S. BOUTAANI<sup>1</sup>, Y. KHELFAOUI<sup>1</sup>

1. Department of Mechanical Engineering, Laboratory of Mechanics, Materials & Energy (L2ME), University Abderrahmane Mira of Bejaia, 06000. Algeria, [balit.hadjila1996@gmail.com](mailto:balit.hadjila1996@gmail.com).

## ABSTRACT

*This work presents an in-depth numerical modeling study aimed at characterizing the effective thermal behavior of a composite material based on High-Density Polyethylene (HDPE) and wood fibers. The digital homogenization technique was used, employing a representative volume element (RVE) adapted to each reinforcement fraction. The analysis of the results was justified using the analytical models of Maxwell and parallel. The results showed that the higher the percentage of wood fibers, the lower the temperature of the composite.*

**KEYWORDS :** Thermal conductivity; RVE ; HDPE/wood fiber composite; Volume fraction.

## I. INTRODUCTION

Composite materials with synthetic polymer matrices reinforced with wood fibers are internationally known by the acronym WPC for Wood Plastic Composites [1]. Natural fibers have recently garnered the attention of scientists due to their properties of low cost, low density, renewability, biodegradability, and non-abrasiveness [2]. In this study, our primary objective is to determine the influence of the fiber volume fraction on the thermal conductivity of high-density polyethylene (HDPE) reinforced with wood fibers using the digital homogenization technique [3].

## II. NUMERICAL & ANALYTICAL MODELING

The classic thermal conduction equation applies to a (RVE) of a composite material (uses Fourier's law):

$$\vec{q} = -\lambda \cdot \nabla T \quad (1)$$

Or:  $\vec{q}$ : designates the heat flux density (W/m<sup>2</sup>),  $\lambda$ : the thermal conductivity,  $\nabla$ : the gradient operator and  $T$ : the temperature (K).

In the context of our study, the composite material

consisted of polypropylene reinforced with cylindrical wood fibers, using cubic-shaped unit cells. The volume fractions of fibers varied from 10%, 15%, to 20% of the total composite volume.

**Table. 1.** The physical properties of the high-density polyethylene composite with wood fibers [2-3].

Composite	Thermal conductivity (W/m.K)	Heat capacity (kJ/m <sup>3</sup> .K)	Density (kg/m <sup>3</sup> )
HDPE	0.48	1550	965
Wood fibers	0.22	350	1100

### A. NUMERICAL MODELING

The concept of RVE is defined as a model that minimizes the introduction of heterogeneities to obtain effective properties [4]. In our case, we employed the COMSOL Multiphysics software to implement this approach.

### B. ANALYTICAL APPROACHES

The evaluation of the numerical results was conducted using two analytical models, Maxwell and parallel. These models played a key role in ensuring the reliability and accuracy of our conclusions.

#### • MAXWELL'S AND PARALLEL METHODS

The equivalent thermal conductivities of the Parallel models are given by equations (2 and 3).

$$\lambda^{Max} = \lambda_m \frac{\lambda_f + 2\lambda_m + 2P_f(\lambda_f - \lambda_m)}{\lambda_f + 2\lambda_m + P_f(\lambda_f - \lambda_m)} \quad (2)$$

$$\lambda^{Par} = (1 - P_f)\lambda_m + P_f\lambda_f \quad (3)$$

Where,  $\lambda_m$  et  $\lambda_f$  are the thermal conductivities of the matrix and fibers, respectively.  $P_f$  is the volume fraction of fibers.

### III. RESULTS AND DISCUSSION

#### A. MICROSTRUCTURE GENERATION AND MESHING

The generation of the microstructure containing cylindrical particles is achieved using a Matlab script.

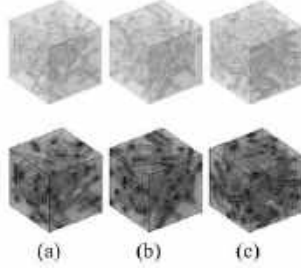


**Fig. 1.** Examples of microstructures at different volume fractions, namely a) 10%, b) 15%, and c) 20%.

The applied periodic boundary conditions for our model are referred to as the "Uniform Linear Temperature Boundary Condition" (Fig. 2). This equation is defined as follows:

$$\langle T \rangle = \frac{G \cdot x}{L}, \quad x \in \partial V \quad (4)$$

Where  $G$  is a constant vector independent of the position  $x$ .  $G$  is the volumetric integral of a gradient.

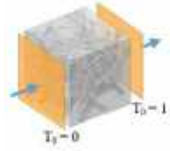


**Fig. 2.** Periodic boundary condition of RVE

#### B. DISTRIBUTION OF TEMPERATURE GRADIENTS

We recorded the distribution of temperature gradients across the RVEs (Fig. 3) illustrates the distribution of temperature gradients for different volume fractions.

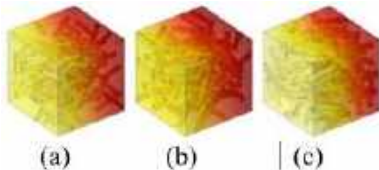


**Fig. 3.** Distribution of temperature gradients for different volume fractions, a) 10%, b) 15%, and c) 20%.

The curve above represents the variation of temperature with respect to the size of the RVE for the

three different fraction cases.

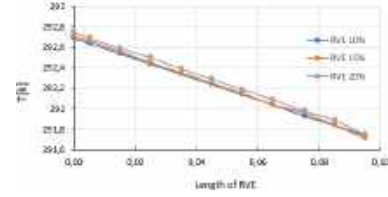


**Fig. 4.** Effect of thermal conductivity as a function of volume (%).

#### C. INFLUENCE OF FIBRE PERCENTAGE ON THERMAL CONDUCTIVITY

The effect of the thermal conductivity of the composite as a function of the volume fraction of fibers is shown in (fig. 5). The results closely match the Maxwell model.

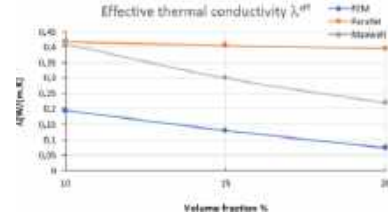


**Fig. 5.** Thermal conductivity curve as a function of volume fraction.

### CONCLUSION

In conclusion, this study thoroughly examined the influence of fiber percentage on the thermal conductivity of high-density polyethylene (HDPE) reinforced with wood fibers. RVE models were generated using an algorithm implemented with Matlab code. The results demonstrated that an increase in the volume fraction of wood fibers led to a reduction in the thermal conductivity of the composite.

### REFERENCES

- [1] M. Laurent Augier, "Study of the development of PVC/wood composite materials from carpentry waste: formulation, characterization, durability and recyclability," (2007).
- [2] M.S. Sukiman, T. Kanit, F. N'Guyen, A. Imad, A. El Moumen, F. Erchiqui, "Effective thermal and mechanical properties of randomly oriented short and long fiber composites," *Mechanics of Materials*. 107, 56-70 (2017).
- [3] J. C. Maxwell. "A treatise on electricity and magnetism," V. 1. Clarendon Press Oxford. (1873).
- [4] A. El Moumen, T. Kanit, A. Imad, H. El Minor. "Effect of overlapping inclusions on effective elastic properties of composites," *Mechanics Research Communications* 53, 24-30 (2013).

# Effet de l'oxyde de fer sur l'élaboration d'une céramique chamotte carbone

Zeyneb CHERMAT<sup>1</sup>, Thiziri AOURAGH<sup>1</sup>, Kamel LOUCIF<sup>1</sup>

1. Laboratoire des Matériaux Non Métalliques,

IOMP. Université F.A.Sétif 1, Algérie

Email : zyneb.chermat@gmail.com

## ABSTRACT

*L'ampleur des céramiques thermiques prend de plus en plus de l'élan, étant donné le recours à l'énergie non fossile avec le défi du stockage d'énergie. Le stockage d'énergie par des matériaux particuliers représente une opportunité simple et efficace compte tenu leurs propriétés exceptionnelles.*

*Le but du présent travail consiste à contrôler la réactivité du kaolin par ajout de de l'oxyde de fer sur le mélange de la chamotte du kaolin DD3 de djebel debbagh et 15% du carbone. Le frittage a été réalisé sous une atmosphère riche en carbone afin d'empêcher l'évacuation du carbone de l'échantillon et par conséquent éviter le changement de composition à la température de 1300°C. L'étude a été suivie par mesure de densité, la porosité ; la résistance mécanique à compression, la diffraction des rayons X, microscopie électronique à balayage, du mélange fritté pendant 2, 6 et 10 heures à 1300°C. Les résultats de cet étude ont montré que :*

*- l'évolution des retraits, la perte de masse, la densité et la porosité se déroulent en majeure partie entre 2 et 6 heures de frittage.*

*- la résistance mécanique est liée à l'état microstructural du matériau. Les réactions qui contrôlent le frittage sont fortement conditionnées par le comportement de la phase vitreuse.*

*- la cristobalite perd sa structure cristalline à la température de frittage utilisée.*

*Nous avons mis en évidence que l'ajout de l'oxyde de fer a joué un rôle significatif dans la réactivité de la silice résiduelle avec le carbone ajouté. D'autre part, la silice contenue dans la mullite est consommée par le carbone est traduit par l'apparition de l'alumine.*

## KEYWORDS

Carbothermique, SiC, Al<sub>2</sub>O<sub>3</sub>, Céramique thermique, Réfractaire

## I. INTRODUCTION

En raison de l'épuisement progressif des énergies non renouvelables telles que le charbon et le pétrole, l'utilisation efficace de l'énergie solaire et d'autres sources d'énergie renouvelables ont attiré beaucoup l'attention des chercheurs. Pour l'énergie solaire, le caractère intermittent conduit à une fluctuation de la production d'énergie électrique. À supprimer la fluctuation du réseau électrique, les systèmes de stockage thermique sont appliqués pour convertir l'énergie solaire à l'énergie thermique pendant les heures d'ensoleillement et libérer l'énergie lorsque la lumière du soleil n'est pas disponible [1,2].

Les matériaux utilisés pour le stockage thermique doivent être choisis en fonction de la capacité de stockage thermique et de la stabilité des propriétés. L'utilisation large des céramiques à base d'Al<sub>2</sub>O<sub>3</sub>-SiC revient aux

propriétés : haute densité de stockage thermique, haute conductivité thermique et meilleure résistance au fluage.

D'autre part, la réduction carbothermique des aluminosilicates est considérée comme une méthode simple et moins coûteuse pour l'élaboration des céramique composite Al<sub>2</sub>O<sub>3</sub>-SiC. Elle permet d'éliminer les effets négatifs de la silice sur les propriétés thermiques des céramiques [3-7].

## II. PARTIE EXPERIMENTALE

La poudre de chamotte est soigneusement broyée dans pendant 3 heures pour atteindre une taille de l'ordre de quelques micromètres. Ensuite, la poudre est étuvée à 100°C pendant 2 heures pour un séchage complet, suivie d'un tamisage. Après le dosage de carbone et d'oxyde de fer, les trois poudres sont mélangées avec des billes en alumine et malaxées pendant 24 heures. Les échantillons sont formés par pressage uniaxial avec un liant organique, puis soumis à des traitements thermiques comprenant le déliantage à 650°C, le préfrittage à 1000°C et le frittage à 1300°C. La caractérisation physique et microstructurale est réalisée par la mesure de la perte en masse, le retrait, la densité, la porosité et de la résistance à la compression. Les essais de compression ont été réalisés sur une machine de traction universelle de type Zwick 100. La microstructure a été étudiée par DRX en utilisant Bruker D2 Phaser et par MEB.

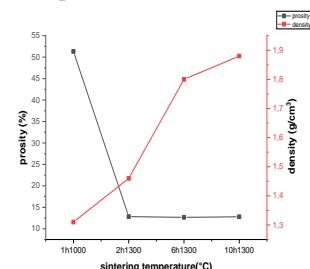
## III. RESULTATS ET DISCUSSION

### A. CARACTERISATION PHYSIQUE

La figure montre la variation de la densité et la porosité du mélange en fonction du temps à 1300°C.

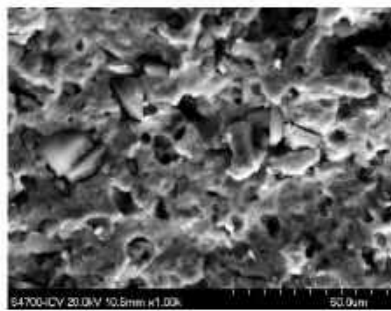
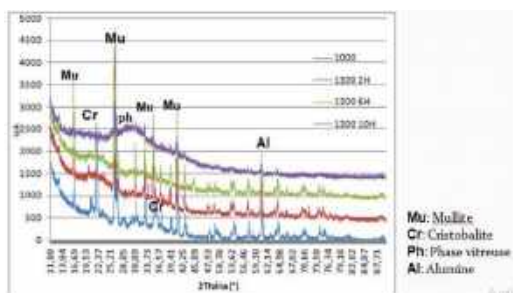
Cette allure montre que la densité augmente et la porosité diminue au cours des premières heures de frittage. Pour les longues durées de frittage, les deux caractéristiques tendent vers une stabilisation. Ces

évolutions montrent un redéploiement de matériaux et non une transformation microstructurale. La diminution de la porosité peut être expliquée par la fermeture des pores par l'écoulement de silice par effet de l'oxyde de fer. La stabilité de la porosité est le résultat de concours de deux phénomènes contradictoires. Le premier est la carboréduction de la silice visant à faire évacuer du matériau. Le second est l'écoulement de la silice fondue et le colmatage des pores [1-2].



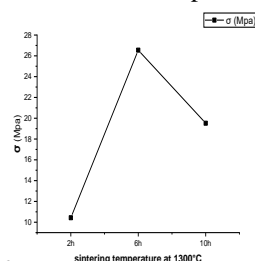
### B. CARACTERISATION MICROSTRUCTURALE

Le diffractogramme montre la présence de la cristobalite et la mullite à l'état initial puis le matériau cours une transformation prouvée par la diminution des intensités des pics de la mullite et la disparition de ceux de la cristobalite. Pour une durée de 10 heures, seuls les pics de la mullite persistent dans une matrice amorphe générale. Cette amorphisation est due à l'effet fondant de l'oxyde de fer qui dissout la cristobalite [5]. Cette constatation explique l'augmentation de la densité au cours des premières durées (2 et 6 heures) de frittage. La microscopie électronique prouve l'état vitreux généralisé après 10 heures de frittage qui noie la phase cristalline ; la mullite [8-9]. Celle-ci voit ses pics de diffraction s'affaiblir.



### C. CARACTERISATION MECANIQUE

La figure montre que la résistance à la compression significativement entre 2h et 6h puis chute après 10h de frittage. Cela prouve qu'après 6h de frittage un redéploiement de matériau s'effectue [7]. Après 10h de frittage, la réaction carbothermique se déclenche et conduit à la perte de masse sous forme de monoxyde de silicium  $\text{SiO}$  et monoxyde de carbone  $\text{CO}$  [10-11]. Cette perte de masse s'accompagne d'un appauvrissement de la phase vitreuse consolidant le matériau. Au fur et à mesure que la phase consolidante diminue, le matériau devient de plus en plus fragile.



## IV. CONCLUSION

A partir de ce travail, nous pouvons conclure les points suivants :

- La perte de masse augmente significativement avec la durée de frittage, indiquant des réactions chimiques prédominantes au début du processus.
- Le retrait du matériau augmente également avec la durée de frittage, montrant une variation plus marquée entre 2 et 6 heures, signe d'une consolidation progressive.
- L'analyse par diffraction des rayons X (DRX) révèle des réactions chimiques majeures, y compris la réduction de la cristobalite et la formation de nouvelles phases telles que l'alumine.
- Les observations en microscopie électronique à balayage (MEB) montrent une évolution de la structure poreuse du matériau avec le temps de frittage, confirmant une consolidation progressive.
- La résistance à la compression du matériau augmente considérablement après 6 heures de frittage en raison de la consolidation et de la formation de nouvelles phases.
- Le matériau présente un comportement mécanique fragile, probablement lié à la porosité et à la perte de masse par carboréduction.

## V. REFERENCES

- [1] X. Lao and X. Xu et al., "Effect of silicon on properties of  $\text{Al}_2\text{O}_3$ -SiCw composite ceramics in-situ synthesized by aluminium-assisted carbothermal reduction of coal series kaolin for solar thermal storage", *Journal of Alloys and Compounds*, Vol. 692, (2017) pp. 825-832
- [2] X. Lao and X. Xu et al., "Synthesis and characterization of  $\text{Al}_2\text{O}_3$ /SiC composite ceramics via carbothermal reduction of aluminosilicate precursor for solar sensible thermal storage", *Journal of Alloys and Compounds*, 2016, 662: 126-137.
- [3] E. Kurovics and Kotova et al., "Preparation of particle-reinforced mullite composite ceramic materials using kaolin and IG-017 bio-origin additives Épitô anyag – *Journal of Silicate Based and Composite Materials*", 4 - 2019, 114–119. p.
- [4] H. Wu and Ma B, et al., "Recycling of silicon kerf waste for preparation of porous SiCw/SiC membrane supports by in situ synthesis", *journal of Appl Ceram Technol.* 06-2019;1–9p.
- [5] S. Sembiring and W. Simanjuntak, et al. "structure and microstructure properties of a refractory cordierite prepared from amorphous rice husk silica resulting from periclase introduction " *journal of Chemical Technology and Metallurgy.* 2-2019, 721-726p.
- [6] F. J. Narciso-Romero and F. Rodriguez-Reinoso, "Synthesis of SiC from rice husks catalysed by iron, cobalt or nickel " *journal of materials science* 31 1-1996 ;779-784p.
- [7] A.C.D. Chaklader and C.A. Das Gupta, E.C.Y. Lin, B. Gutowski, " *Journal of the American Ceramic Society* "75 (1992) 2283±2285.
- [8] O. San and C. Özgür, "Investigation of a high stable-cristobalite ceramic powder from  $\text{CaO-Al}_2\text{O}_3\text{-SiO}_2$  system", *Journal of the European Ceramic Society* 29 (2009) 2945–2949
- [9] A.S.Charles., " *Refractories Handbook* ", Edition : Marcel Dekker, Inc., 2004.
- [10] R. Naghizadeh and F. Golestani-Fard, "H.R. Rezaie, Stability and phase evolution of mullite in reducing atmosphere, *Mater. Charact*", 62 (5) (2011) 540-544.
- [11] J.Rösler and H. Harders et al., " *Mechanical Behaviour of Engineering Materials* ",



# Kinetic study of transparent fluormica glass-ceramic

ARIANE KHALISSA<sup>1\*</sup>, CHORFA ABDELLAH<sup>2</sup>

1. Applied Precision Mechanics Laboratory, Institute of Optics and Precision Mechanics, Ferhat Abbas University Setif 1, Setif, Algeria  
[khalissa.ariane@univ-setif.dz](mailto:khalissa.ariane@univ-setif.dz)
2. Laboratory of applied optics, Institute of Optics and Precision Mechanics, Ferhat Abbas University Setif 1, Setif, Algeria

## ABSTRACT

*The crystallization behaviour of  $K_2O-MgO-Al_2O_3-B_2O_3-SiO_2-MgF_2$  glass-ceramic system without and with  $P_2O_5$  as nucleating agent are studied. The crystallization mechanism without  $P_2O_5$  oxide represented one-dimensional surface crystallization with a fixed number of nuclei, and with the addition of  $P_2O_5$ , the mechanism tends to two-dimensional bulk crystallization with a constant nucleation rate. The base glasses had the spinodal phase separation, which coarsened considerably by increasing  $P_2O_5$  content.  $P_2O_5$  had a strong influence on the microstructure and morphology of this type of glass-ceramic*

## KEY WORDS

Glass-ceramic; Kinetic; Fluor-mica;  $P_2O_5$

## I. INTRODUCTION

Glass-ceramics (GC) are a kind of polycrystalline material formed by controlled crystallization of the parent glasses. They demonstrate the ability to combine various remarkable properties in one material based on variability in chemical composition, microstructure and heat-treatment conditions. Their properties could be inherent to the glass itself, or could be a result of modifications in structure and microstructure arising from processing techniques [1]. An important group of these materials are the mica-containing GC which received wider attention due to their high machinability and thermal shock resistance [2]. Crystallization process is generally affected by nucleating agents, which either accumulate in a specific microphase of the phase separated base glass

or support the phase separation.

GC with  $MgF_2$  as the source of fluorine exhibits uniform bulk crystallization but on contrary, if  $NaF$  is incorporated as nucleating agent only surface crystallization occurs [3].

In the present work, we focus on the preparation of transparent  $K_2O-MgO-Al_2O_3-B_2O_3-SiO_2-MgF_2$  GC where kinetics are tailored through the addition of  $P_2O_5$  as nucleating agent.

## II. PREPARATION OF MATERIALS AND CHARACTERIZATION

The system  $K_2O-MgO-Al_2O_3-B_2O_3-SiO_2$  plus  $MgF_2$  as nucleating agent has been studied in the present work. The nominal composition of the original glass (MP0) is given in Table 1.  $P_2O_5$  (purity>98%) has been also added to MP0 in 1.0 (MP1), 2.0 (MP2) and 3.0 (MP3) mol% as the double nucleating agent. Each 100 g batch was well mixed, calcined in a platinum crucible using an electric furnace for 3 h at a temperature of 900 °C (heating rate of 10 °C/min), and then melted at about 1600 °C (10 °C/min) and held for 3 h till complete homogenization. Then, the molten charge was poured to a preheated copper molds. The as-prepared samples were further annealed at 550 °C (10 °C/min) for 4 h and cooled to room temperature (2 °C/min).

**Table 1.** Nominal composition (wt.%) of MP0

	SiO <sub>2</sub>	Al <sub>2</sub> O <sub>3</sub>	K <sub>2</sub> CO <sub>3</sub>	MgO	B <sub>2</sub> O <sub>3</sub>	MgF <sub>2</sub>	P <sub>2</sub> O <sub>5</sub>
MP0	41	15	14	18	0.2	10	00



Crystallization kinetic parameters were analyzed by differential thermal analysis (DTA, TA Instruments, SDT Q600, USA) using glass powders sieved below 50  $\mu\text{m}$  and heated from 25 to 1300  $^{\circ}\text{C}$  at different heating rates (5, 10 and 15  $^{\circ}\text{C}.\text{min}^{-1}$ ) in air atmosphere.

### III. RESULTS AND DISCUSSIONS

Peak positions,  $T_{c1}$  and  $T_{c2}$ , full-width of the exothermic peak at half-maximum intensity ( $\Delta w$ ) and intensities of the peaks were obtained from a deconvolution procedure of different DTA curves assuming that every peak presents a mixed Gaussian-Lorentzian (50 %-50 %) shape.

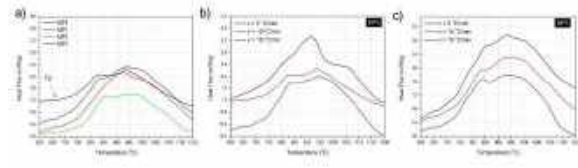


**Fig. 1.** DTA of the glasses a) heat treated at 10  $^{\circ}\text{C}/\text{min}$ , b) DTA of MP0 glass and c) DTA of the MP3 glass.

The variation of the crystallization peaks  $T_{c1}$  and  $T_{c2}$  with different DTA heating rates ( $\nu$ ) is used to calculate activation energy for crystallization and allows identifying the most plausible crystallization mechanism. The Kissinger [4] equation is one of the most common methods to calculate the crystallization activation energy by plotting the inverse of the crystallization temperature,  $1/T_c$  versus  $\ln(\nu/T_c^2)$ . Matusita-Sakka [5] stated that the Kissinger equation must be only used if crystal growth occurs on a fixed number of nuclei and have suggested a modified form of the Kissinger equation as:

$$\ln\left(\frac{\nu^n}{T_c^2}\right) = -m \frac{E_c}{R T_c} + \text{constant} \quad (1)$$

where  $m$  refers to the crystal growth dimensionality and the Avrami parameter  $n$ :

$$n = \frac{2.5 R T_c^2}{\Delta w E_c} \quad (2)$$

The DTA curves present two peaks at different heating rates  $T_{c1}$  and  $T_{c2}$  and the values of  $E_c$  for crystallization calculated by the Matusita-Sakka method, the values of Avrami exponent  $n$  and the  $m$  parameter of the two exothermic peaks are given in Table 2.

**Table 2:** Activation energies ( $\text{kJ}.\text{mol}^{-1}$ ),  $n$  and  $m$  parameters of each exothermic peak (Pk) for the studied specimens.

		Activation energy ( $\text{kJ}/\text{mol}$ )	$n$	$m$
MP0	<b>Pk1</b>	346.22	1.07	1.05
	<b>Pk2</b>	403.85	0.87	0.89
MP1	<b>Pk1</b>	361.83	1.12	0.95
	<b>Pk2</b>	485.82	1.93	1.86

MP2	<b>Pk1</b>	291.88	1.02	0.94
	<b>Pk2</b>	439.45	1.89	1.92
MP3	<b>Pk1</b>	177.16	1.29	0.82
	<b>Pk2</b>	231.63	1.82	1.73

Using the  $E_c$  values, the Avrami constants corresponding to the crystallization mechanism were determined. The values of  $m$  in this work are approximately equal to the values of  $n$ , i.e. the nuclei formed in the first heat-treatment before the thermal analysis run are dominant (crystallization occurs on a fixed number of nuclei). A surface crystallization mechanism occurred in free- $\text{P}_2\text{O}_5$  specimen ( $n = m = 1$ ) whereas by incorporating small amount of  $\text{P}_2\text{O}_5$ , the second crystallization peak evolves to a bulk crystallization.

The data collected in Table 2 regarding the  $n$  and  $m$  values indicate that the incorporation of  $\text{P}_2\text{O}_5$  leads to a homogeneous crystallization mechanism for both exothermic peaks and mainly with one- and two-dimensional growth of crystals. The incorporation of  $\text{P}_2\text{O}_5$  to the base glasses restrains the surface crystallization and promotes bulk crystallization.

### IV. CONCLUSION

Form these results, it can be concluded that  $\text{P}_2\text{O}_5$  additive performs better than free- $\text{P}_2\text{O}_5$  for improving crystallization ability (lowering the activation energy of crystallization), which also could promote crystallization at lower temperatures because of the decrease in the viscosity of the glasses. Consequently, the base glasses have the spinodal phase separation, which coarsened considerably by increasing  $\text{P}_2\text{O}_5$  content.

### REFERENCES

- [1] W. Höland, E. Apel, C. van't Hoen, V. Rheinberger, "Studies of crystal phase formations in high-strength lithium disilicate glass-ceramics", *Journal of Non-Crystalline Solids*, 352, 4041-4050, (2006).
- [2] S. Roy, B. Basu, "Microstructure development in machinable mica based dental glass ceramics", *Trends Biomater Artif Organs*, 20, 90-100 (2006).
- [3] K. Cheng, J. Wan, K. Liang, Crystallization of  $\text{R}_2\text{O}-\text{MgO}-\text{Al}_2\text{O}_3-\text{B}_2\text{O}_3-\text{SiO}_2-\text{F}$  ( $\text{R} = \text{K}^+, \text{Na}^+$ ) glasses with different fluorine source, *Materials Letters*, 47, 1-6, (2001).
- [4] H.E. Kissinger, "Reaction kinetics in differential thermal analysis, *Analytical chemistry*", 29, 1702-1706 (1957).
- [5] K. Matusita, S. Sakka, "Kinetic study of crystallization of glass by differential thermal analysis—criterion on application of Kissinger plot", *Journal of Non-Crystalline Solids*, 38, 741-746 (1980).

# EFFECT OF POROSITY ON THE MECHANICAL BUCKLING OF FUNCTIONALLY GRADED CERAMIC AND METAL SANDWICH PLATE CONTAINING A METALLIC FOAM CORE USING HIGH QUASI-3D THEORY

ABDELKADER TAMRABET<sup>1,2,\*</sup>, ABDELHAKIM BOUHADRA<sup>3</sup>, ABDERRAHMANE MENASRIA<sup>3</sup>

1. Department of Civil Engineering, University of Ferhat Abbas-Setif1, Faculty of Technology, Algeria.

2. Research Unit of Emerging Materials, University of Ferhat Abbas-Setif1, Algeria.

Kader40tamrabet@gmail.com

3. Department of Civil Engineering, University of Abbes Laghrour Khenchela, Faculty of Science and Technology, Algeria. bouhadrahako@gmail.com

## ABSTRACT

*This paper aims to study the effect of porosity on the buckling of functionally graded sandwich plate containing metallic foam core and FGM face sheets resting on various boundary conditions. The mathematical development is illustrated for a sandwich plate using new power law function for three different configurations. The displacement field based on quasi - three D theory is using here by introduced six variables. The governing equations are obtained by Hamilton's principal then solved by Navier-type method for simply supported plate and Galerkin Vlasov's solution for different boundary conditions. the present model validated with those from the literature, then the influence of many parameters: porosities parameters, boundary conditions, power law index, ration aspect on the variation of the buckling behaviour are demonstrated.*

**Keywords:** functionally graded materials, sandwich plate, metal foam, porosity, mechanical buckling;

## I. INTRODUCTION

The result of scientific development in materials area, have given a rise to the continual demand for advanced materials that can provide the necessary advanced properties and qualities[1]. Functionally graded materials are an advanced engineering materials that are able to retains the strengths and eliminates the problems existing in composite materials as the concentration of the stress between discrete materials, specifically in the high thermal environment.[2].Functionally Graded Materials (FGMs) are inhomogeneous material usually made from two different material constituents, ceramic and metal, to combine the best properties of these materials in which change gradually across the thickness.

FGM sandwich structures is usually found in many structural applications in civil engineering as well as to strengthen concrete materials in bridges because these

reinforced materials enhance the resistance of the steel in corrosion attacks, and the FGM structures also found in mechanical engineering including thermal systems such as aerospace, automotive Aerotech, Polyurethane Pipe, medical and many other filed where the combination of various characteristics is crucial to achieving optimal performance[3].

To study the effect of porosity on the behavior of sandwich plate, many analytical models are proposed. Singh et al. analyzed the effect of different porosity shapes on buckling and vibration of thick FGM sandwich plate using Galerkin Vlasov's method resting to various boundary conditions[4]. Long et al. analyzed the effect of porosity on the buckling behavior of thick FGM shell under thermo-mechanical load using on HSDT theory[5]. Mekerbi et al Studied the effect of porosity on the buckling behavior of FGM plate under thermal environment using quasi 3D theory [6]. Furthermore the FGM sandwich plate containing foams core is analyzing for bending and buckling behavior using Chebyshev-Ritz method by Chen et al [7]. Garg et al. analyzed the effect of three different types of the metal foam core in the buckling and free vibration of sandwich FGM plate basing finite element method using zigzag theory[8].

The literature review has completed above, focusing on the important work on effect of porosity, higher order shear deformation theory, behavior of structure containing metallic foam. One can confirm that there is no prior work on the application of higher order shear deformation theory with the consideration of the thickness stretching effect. However, in this paper quasi-3D high deformation theory is using to examine the impact of three deferent shapes of micro voids of metal foam core on the mechanical buckling of sandwich FG plates when the metal foam core surrounding by two FG face sheets rested to various boundary condition under axial in-plane load. Based on Hamilton's principal, the stability equations are derived and then solved by Galerkin Vlasov's method. The results obtained are verified with those existing in the literature, then the effect of geometrics parameters metal foam coefficient,

different boundaries condition on the mechanical buckling of the sandwich plate are thoroughly illustrated.

## II. MATHEMATICAL NOTATIONS AND EQUATIONS

Sandwich plate is considered in this work with uniform thickness  $h$ , two skins in the bottom and the top cover the metallic foam core in the middle layer. The distribution of the modulus young for sandwich plate with metal foam core is described in three models below [8, 9]:

$$\begin{aligned} E1(z) &= E_f + (E_c - E_f) * \left( \frac{z - h_1}{h_0 - h_1} \right)^k \quad z \in [h_0 \dots h_1] \\ E2(z) &= E_f * \lambda_i \quad z \in [h_1 \dots h_2] \\ E3(z) &= E_f + (E_c - E_f) * \left( \frac{z - h_2}{h_3 - h_2} \right)^k \quad z \in [h_2 \dots h_3] \end{aligned} \quad (01)$$

With  $E_f$  is the young modulus of metal foam,  $E_c$  is the young modulus of ceramic,  $\lambda_{I,II,III}$  is Foam I, II and III distributions,

$\eta, \eta^*$  and  $\gamma$  are the metal foam coefficients

### A. DISPLACEMENT FIELD

$$\begin{aligned} u(x, y, z) &= u_0(x, y, t) - z \frac{dw_0(x, y, t)}{dx} + \\ &\quad f(z) K_1 \int \theta_1(x, y, t) dx \\ v(x, y, z) &= v_0(x, y, t) - z \frac{dw_0(x, y, t)}{dy} + \\ &\quad f(z) K_2 \int \theta_2(x, y, t) dy \\ w(x, y, z) &= w_0(x, y, t) + H(z) \varphi((x, y, t)) \end{aligned} \quad (02)$$

### B. THE STABILITY EQUATIONS

$$\delta u_0 : \frac{\partial N_{11}}{\partial x} + \frac{\partial N_{12}}{\partial y} = 0, \quad \delta v_0 : \frac{\partial N_{12}}{\partial x} + \frac{\partial N_{22}}{\partial y} = 0 \quad (06.a)$$

$$\delta w_0 : \frac{\partial^2 M_{11}}{\partial x^2} + 2 \frac{\partial^2 M_{12}}{\partial x \partial y} + \frac{\partial^2 M_{22}}{\partial y^2} + N_{cr} = 0 \quad (06.b)$$

$$\delta \theta_x : -K_1 A \frac{\partial^2 R_{11}}{\partial x^2} - K_1 A \frac{\partial^2 R_{12}}{\partial x \partial y} + K_1 A \frac{\partial S_{13}}{\partial x} = 0, \quad (06.c)$$

$$\delta \theta_y : K_2 B \frac{\partial^2 R_{22}}{\partial y^2} - K_2 B \frac{\partial^2 R_{12}}{\partial x \partial y} + K_2 B \frac{\partial S_{23}}{\partial y} = 0 \quad (06.d)$$

$$\delta \varphi : \frac{\partial Q_{13}}{\partial x} + \frac{\partial Q_{23}}{\partial y} - N_{33} + g(z)^2 N_{cr} = 0$$

### C. RESULTS

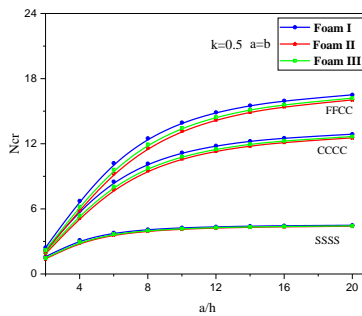


Figure 1: non-dimensional critical buckling load versus  $a/h$  of FG sandwich plate subjected on different boundary conditions

## III. CONCLUSION

Overall, functionally graded materials provide a versatile platform for tailoring material properties to specific requirements, enabling the development of innovative and advanced solutions in engineering and manufacturing. In this work the analysis of the influence of porosity on the critical buckling of two FGM face layers containing metal foam core using new quasi-3D theory are presented by including indeterminate integral terms. The stability equations are given by Hamilton's principal then solved with numerical solution. The effect of the aspect ratio  $a/b$ , side-to-thickness ratio  $a/h$  foam coefficient and various boundary conditions are discussed in the results, so the increasing of  $a/h$  increase the critical buckling, wears the two boundaries condition FFCC and CCCC has the highest critical buckling, in the other hand the increasing of foam parameters decreased the critical buckling

## REFERENCES

- [1].Bever, M. and P. Duwez, *Gradients in composite materials*. Materials Science and Engineering, 1972. **10**: p. 1-8.
- [2].Daikh, A.A. and A.M. Zenkour, *Free vibration and buckling of porous power-law and sigmoid functionally graded sandwich plates using a simple higher-order shear deformation theory*. Materials Research Express, 2019. **6**(11): p. 115707.
- [3].Gong, X., et al., *Improved Four-channel PBTDPA control strategy using force feedback bilateral teleoperation system*. International Journal of Control, Automation and Systems, 2022. **20**(3): p. 1002-1017.
- [4].Singh, S. and S. Harsha, *Analysis of porosity effect on free vibration and buckling responses for sandwich sigmoid function based functionally graded material plate resting on Pasternak foundation using Galerkin Vlasov's method*. Journal of Sandwich Structures & Materials, 2021. **23**(5): p. 1717-1760.
- [5].Long, V.T. and H.V. Tung, *Mechanical buckling analysis of thick FGM toroidal shell segments with porosities using Reddy's higher order shear deformation theory*. Mechanics of Advanced Materials and Structures, 2021: p. 1-10.
- [6].Mekerbi, M., et al., *Investigation on thermal buckling of porous FG plate resting on elastic foundation via quasi 3D solution*. Structural Engineering and Mechanics, 2019. **72**(4): p. 513-524.
- [7].Chen, D., J. Yang, and S. Kitipornchai, *Buckling and bending analyses of a novel functionally graded porous plate using Chebyshev-Ritz method*. Archives of Civil and Mechanical Engineering, 2019. **19**(1): p. 157-170.
- [8].Garg, A., et al., *Vibration and Buckling Analyses of Sandwich Plates Containing Functionally Graded Metal Foam Core*. Acta Mechanica Solida Sinica, 2022: p. 1-16.
- [9].Wang, Y.Q. and Z.Y. Zhang, *Bending and buckling of three-dimensional graphene foam plates*. Results in Physics, 2019. **13**: p. 102136.

# Effet du temps de traitement sur quelques paramètres de l'échange ionique d'un verre silico-sodo calcique

YOUNES LEYLA<sup>1,2,3\*</sup>, HAMIDOUCHE MOHAMED<sup>1,2</sup>, AND MALOU HAMIDOUCHE ZAHRA<sup>1,2</sup>

1. Institut d'optique et mécanique de précision, UFAS1, Sétif, 19000, Algérie.

2. Unité de recherche des matériaux émergents. UFAS1, Sétif, 19000, Algérie.

3. Laboratoire des Matériaux Non Métalliques UFAS1, Sétif, 19000, Algérie.

## ABSTRACT

*Le verre est probablement la matière synthétique la plus ancienne de l'humanité. Les applications du verre sont toujours limitées par sa fragilité ainsi sa faible résistance mécanique.*

*Dans ce travail, nous avons étudié l'effet du temps de traitement sur quelques paramètres de l'échange ionique d'un verre silico-sodo-calcique dans un bain de  $KNO_3$ .*

## KEY WORDS

Verre, échange ionique, temps d'immersion, diffusion.

## I. INTRODUCTION

Le verre est l'un des matériaux les plus utiles et les plus utilisés. Il présente des propriétés très intéressantes, mais son comportement fragile le rend très sensible aux microfissures superficielles qui agissent comme des sites de concentration des contraintes.

Pour certains usages, son renforcement est plus que nécessaire. Parmi les différents procédés de renforcement utilisés, on distingue l'échange ionique par sa facilité de mise en œuvre. Ce dernier se base sur l'échange des ions alcalins de gros rayons ioniques tels que le  $K^+$ , provenant du bain de sel fondu comme le  $KNO_3$ , avec des ions alcalins de la surface du verre de rayon ionique plus petit, tels que  $Na^+$ .

Dans ce travail, nous avons traité par échange ionique un verre plat silico-sodo-calcique d'épaisseur 4mm, fabriqué par flottage par l'entreprise MFG. Ce verre a été trempé dans un bain de nitrate de potassium ( $KNO_3$ ) fondu porté à une température de  $480^\circ C$ . L'immersion a été effectuée pour différents temps de maintien (2h, 20h, 30h, 40h et 50h).

En utilisant le décapage chimique avec de l'acide fluorhydrique (HF), nous avons déterminé la concentration du potassium qui diffuse à la surface du verre.

Les résultats obtenus ont montré que la concentration du potassium qui diffuse à la surface du verre augmente avec l'augmentation du temps de traitement. Ce dernier a aussi un effet notable sur le rapport molaire ( $K/Na$ ) surtout au premiers instants de la diffusion de l'ion  $K^+$ . Un autre résultat aussi important que le premier a été constaté lors de la trempe chimique est celui du coefficient de diffusion qui augmente légèrement avec la concentration massique du  $K_2O$  et décroît cependant avec l'augmentation du temps d'immersion.

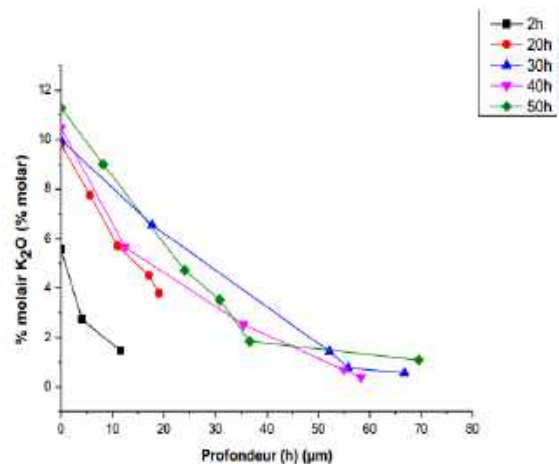


**Fig. 1.** Profils de la concentration molaire du potassium en profondeur des échantillons traités à différents temps d'immersion.

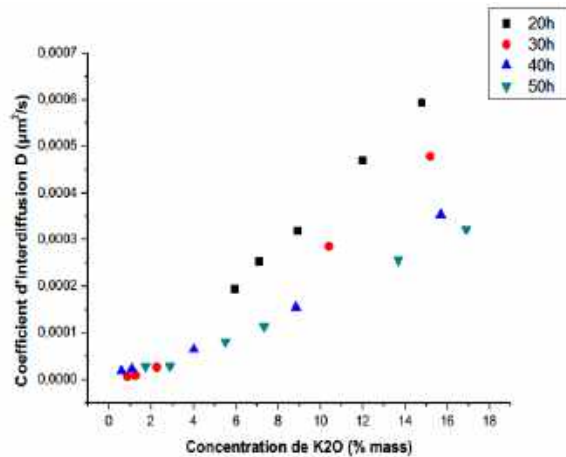


**Fig. 2.** Coefficient d'inter-diffusion dans le verre en fonction de la concentration de K2O à différentes temps d'immersion.

## II. CONCLUSION

Les résultats obtenus montrent que :

- La concentration de potassium incorporé à la surface du verre augmente avec l'augmentation de l'échange ionique.
- Il apparait que l'augmentation du temps de traitement provoque l'augmentation du rapport molaire (K/Na) surtout lors des premiers instants du traitement.
- Le coefficient de diffusion augmente légèrement avec la concentration massique de K2O et décroît avec l'augmentation du temps d'immersion. Les ions K<sup>+</sup> ont de plus en plus de difficultés à diffuser dans le verre, à cause d'un champ électrique interne qui se crée et qui réduit la mobilité des ions.

## REFERENCES

- [1] L. Xiaoyu, L. Jiang, Y. Wang, I. Mohagheghian, J. P. Dear, L. Li, Y. Yan, "Correlation between K<sup>+</sup>-Na<sup>+</sup> diffusion coefficient and flexural strength of chemically tempered aluminosilicate glass", Journal of Non Crystalline Solids, pp. 1-10, (2017).
- [2] S. Karlsson, S. Ali, R. Limbach, M. Strand, L. Wondraczek, Alkali salt vapour deposition and in-line ion exchange on flat glass surfaces, Glass Technology: European Journal of Glass Science and Technology Part A, 56 (6), pp. 203-213, (2015)

# Etude du comportement mécanique en compression des matériaux cellulaire en fibres de verre

BELAIB MAHDI ZAKARIA<sup>1</sup>, MERTANI BOUBEKEUR MOHAMMED BILEL<sup>1</sup>, ET KESKES BOUALEM<sup>1</sup>

1. Laboratoire de mécanique de précision appliqué (LMPA). (IOMP). UFAS- SETIF 1 ALGERIE.

## RESUME

*Ce travail présente une étude du comportement mécanique sous compression différentes vitesses de chargement des âmes nid d'abeilles en fibres de verre utilisées dans les panneaux sandwichs. Une étude expérimentale a été mise en place pour voir l'influence des différentes tailles des échantillons nid d'abeilles en fibres de verre et les différentes vitesses de chargement sur la contrainte maximale .*

## MOTS CLES :

Âme en nid d'abeilles en fibres de verre, Compression dynamique, Compression statique, compression quasi statique, Panneau sandwich.

## I. INTRODUCTION

DANS LE DOMAINE DES MATERIAUX SANDWICHS A AME EN NID D'ABEILLES, LES EXIGENCES DE PERFORMANCES ONT CONDUIT A LA RECHERCHE, ET LE DEVELOPPEMENT DE MATERIAUX PRESENTANT DES PROPRIETES MECANQUES SPECIFIQUES, CAR LES TECHNOLOGIES MODERNES EXIGENT QUE L'ON UTILISE DES MATERIAUX A LA HAUTEUR DE LEUR EMPLOI. POUR CELA, LES MATERIAUX EN NID D'ABEILLES SONT LARGEMENT UTILISES DANS DIVERS DOMAINES STRATEGIQUES TELS QUE L'AERONAUTIQUE, L'AEROSPATIALE, LE NAVAL ET LE FERROVIAIRE. L'UTILISATION FREQUENTE DES AMES EN NID D'ABEILLES EST JUSTIFIEE PAR LEURS FAIBLES DENSITES, LEURS GRANDES RESISTANCES ET UNE RIGIDITE IMPORTANTE ET AUSSI UNE EXCELLENTE DURABILITE. CE PENDANT LA PLUS IMPORTANTE CARACTERISTIQUE DE CES MATERIAUX CONCERNE LEURS CAPACITES D'ABSORPTION D'ENERGIE EN COMPRESSION STATIQUE. [1].



FIG 1. STRUCTURE SANDWICH

FIG 2. DOMAINE D'UTILISATION

## II. COMPORTEMENT EN COMPRESSION DES STRUCTURES SANDWICHS A AMES EN NID D'ABEILLES [2,3].

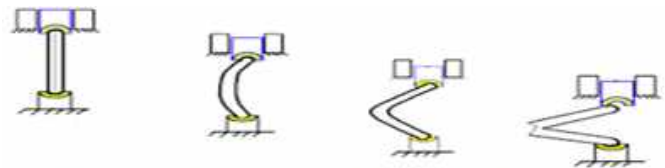


FIG 3. FLAMBEMENT D'UNE REGLE PLATE SOUS UN EFFORT DE COMPRESSION

## III. ETUDE EXPERIMENTALE

### A. Matériau utilisé

Une série d'essais de compression a été effectuée sur des configurations d'âme en nid d'abeilles en fibres de verre fournir par Euro-Composites avec une densité apparente de 74,198 kg/m<sup>3</sup>. Les éprouvettes ont une taille de cellule de 9.6 mm avec une épaisseur de parois de 0.03 mm.

### B. Procédure expérimentale

La procédure expérimentale consiste à varier la vitesse de chargement entre 1 et 150 mm/min et à varier les dimensions des échantillons.



### C. Résultats et discussions

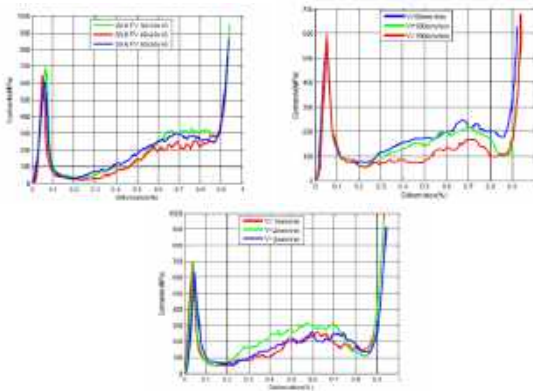


**Fig. 4.** Courbe contrainte - déformation pour différents vitesses de chargement et différents tailles.

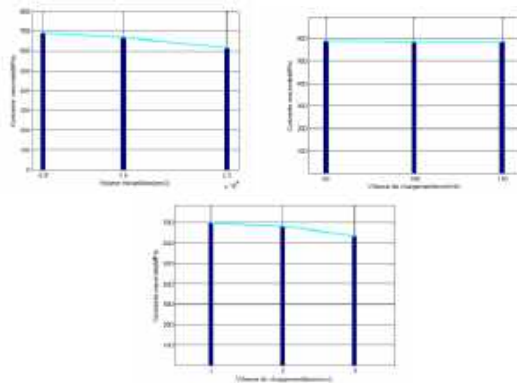


**Fig. 5.** Courbe contrainte maximale en fonction de vitesse de charge et volume d'échantillon

### IV. CONCLUSION

- Les cellules de l'âme en fibres de verre se déforment de manière élastique, ensuite une rupture brutale et totale en petites morceaux de l'échantillon
- La contrainte maximale est influencée par la taille de l'échantillon ; elle est directement proportionnelle aux dimensions d'échantillon.
- La vitesse de chargement n'a aucune influence sur la contrainte maximale de compression.
- Enfin, cette étude nous a permis d'établir une base de données sur la configuration nid d'abeilles en fibres de verre soumis à une compression uniaxiale.

### REFERENCES

- [1] MILLER, W., C. SMITH, AND K. EVANS, *HONEYCOMB CORES WITH ENHANCED BUCKLING STRENGTH*. COMPOSITE STRUCTURES, 2011. 93(3): P. 1072-1077.
- [2] KESKES, B., *COMPORTEMENT EN FATIGUE DES COMPOSITES TYPE SANDWICH EN NIDS D'ABEILLES*, 2007.
- [3] MERTANI, B.-M.-B., *ÉTUDE NUMÉRIQUE ET EXPÉRIMENTALE DU COMPORTEMENT MÉCANIQUE DES PANNEAUX SANDWICH SA AME EN NID D'ABEILLES*, 2021.

# Elaboration of Kaolin-Bound Porous SiC-Al<sub>2</sub>O<sub>3</sub> Composites

BRAHIMI ABDELKHALEK <sup>1,\*</sup>, KERAGHEL FATIHA<sup>1</sup>, LOUCIF KAMEL<sup>1</sup>, MAITRE ALEXANDRE<sup>2</sup>

1. Laboratory of non-metallic materials–IOMP, Ferhat Abbas University Setif 1  
Setif, Algeria, e-mail address: Brahimi-kh@outlook.com
2. IRCER– Institute of research for ceramics University of limoges  
Limoges, France

## ABSTRACT

*The main focus of this research is to control the production parameters of Porous SiC-Al<sub>2</sub>O<sub>3</sub> composites. These composites were successfully synthesized through conventional sintering at temperatures ranging from 1300 to 1500 °C. The utilization of DD3 kaolin served both as a shaping binder and a sintering aid. A systematic exploration was conducted to evaluate the influence of sintering temperature and the kaolin addition rate on the mechanical properties and physical characteristics of the material. The findings highlight that the incorporation of 5% kaolin resulted in the attainment of the most favorable mechanical properties, correlated with an average open porosity level of 28.36%. Notably, the highest compressive strength of 197.17 MPa was achieved at a sintering temperature of 1500 °C, whereas the maximum tensile strength of 32.90 MPa was observed at a sintering temperature of 1300 °C.*

## KEY WORDS

SiC; Al<sub>2</sub>O<sub>3</sub>; Kaolin; PLPS

## I. INTRODUCTION

Porous ceramics have garnered significant attention in diverse industrial applications, serving as catalyst supports, filters for molten metals and hot gases, membranes, heat exchangers [1-9]. In recent years, porous silicon carbide (SiC) ceramics have gained significant attention from researchers and industrialists owing to their exceptional properties such as low thermal expansion coefficient, high thermal conductivity, and excellent mechanical strength, making them an attractive material for high-temperature applications.

However, the challenge of sintering SiC at moderate temperatures due to the strong covalent nature of the Si-C bond [8-9], have sparked significant research interest in exploring to alternative approaches to facilitate their fabrication at lower temperatures,

thereby reducing costs and expanding their applicability.

Kaolin has emerged as a promising technique for bonding SiC particles, owing to its compatibility with SiC and its capability to form mullite a phase known for its close thermal expansion match with SiC and its excellent high-temperature strength and thermal shock resistance [1,8], making it an ideal bonding phase for porous SiC ceramics. The addition of kaolin not only serves as an effective bonding agent but also as binding agent enhancing the mechanical strength of the green bodies. In this context, this current study focuses on the elaboration of porous SiC-Al<sub>2</sub>O<sub>3</sub> bonded by kaolin-based composites with a specific focus on investigating the sintering parameters, porosity, shrinkage, and mechanical strength of the resulting materials. Through a comprehensive analysis, this study seeks to provide valuable insights into the development of cost-effective and high-performance porous ceramic materials tailored for various industrial applications.

## II. EXPERIMENTAL PROCEDURE

### A. RAW MATERIALS

In this study, commercially available black  $\alpha$ -SiC (Silicon Carbide, -400 Mesh particle size,  $\geq 97.5$  wt. % purity, SIGMA-ALDRICH Saint-Louis USA),  $\alpha$ -Al<sub>2</sub>O<sub>3</sub> (Calcined Aluminium Oxide Powder, 1 $\mu$ m particle size,  $\geq 98.14$  wt. % purity, LOGITECH Limited Scotland UK) were used as starting materials. Raw DD3 kaolin ( $\leq 401\mu$ m particle size, Djebel Debbagh site 3 Guelma Algeria) was as binding and bounding aid.

### B. SAMPLES PREPARATION

The raw materials used for this study were mixed accordingly to the compositions shown in table (1). The powders were dry-mixed using  $\leq 3$  mm diameter

alumina balls, with a total volume to ball ratio of 1:3 and ball powder mass ratio of 2:1 for 24 hours at 100 rpm within a polyethylene jar. Using the same parameters to ensure optimal granularity and homogeneity, they were ball-milled in ethanol and dried at 97°C then sieved through a 120-mesh screen.

Sample	SiC	Al <sub>2</sub> O <sub>3</sub>	Kaolin
P1	80 %	15 %	5 %
P2	77 %	15 %	8 %

Tab. 1. Composition of green bodies.

The mixed powders were uniaxially pressed at 75 MPa and 125 MPa in a 12 mm diameter steel die. The green bodies underwent a heat treatment at 600°C in air for 2 hours with heating rate of 2°C/min to remove any organic impurities. Finally the specimens were sintered at 1300-1500°C in air with heating rate of 5°C/min for 2 hours; an Al<sub>2</sub>O<sub>3</sub> powder bed was used.

### C. CHARACTERIZATION

Phase analysis of the starting materials was performed by X-ray diffraction (XRD), and chemical composition was obtained via X-ray fluorescence (XRF). The particle size of the composite powders is determined by laser diffraction particle size analysis, and was subject to a thermogravimetry analysis (TG). Porosity and bulk density were measured by the Archimedes and Arthur method. The diameter and mass of the samples were measured to calculate linear shrinkage and weight loss. Finally the mechanical properties of the sintered samples were investigated through a compression test and diametral compression test.

## III. RESULTS AND DISCUSSION

### A. RAW MATERIALS CHARACTERIZATION

Figure (1) shows the phase analysis and chemical composition of the material used  $\alpha$ -SiC and  $\alpha$ -Al<sub>2</sub>O<sub>3</sub>, it is well known that SiC powder contains free SiO<sub>2</sub> particles. The XRF results shows a 13:12 mass ratio of SiO<sub>2</sub>:Al<sub>2</sub>O<sub>3</sub> as displayed in Table 2.

Oxide	Masse (%)
SiO <sub>2</sub>	52.7
Al <sub>2</sub> O <sub>3</sub>	44.4
F <sub>2</sub> O <sub>3</sub>	0.039
CaO	0.32
Clac.loss	17

Tab. 2. Chemical composition and calcination losses of kaolin

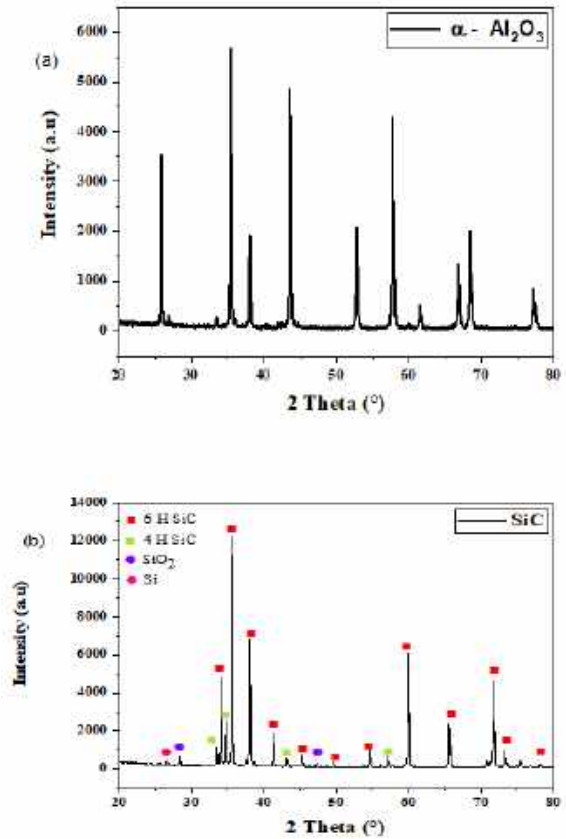


Fig. 1. XRD patterns of the starting materials, (a) Al<sub>2</sub>O<sub>3</sub>, (b) SiC.

The particle size distribution of the mixture P1 varies from 0.389  $\mu$ m to 133  $\mu$ m with an average  $d_{50}$  of 5.95  $\mu$ m, the mixture P2 varies from 0.51  $\mu$ m to 39  $\mu$ m with an average  $d_{50}$  of 9.93  $\mu$ m, as shown in figure (2).

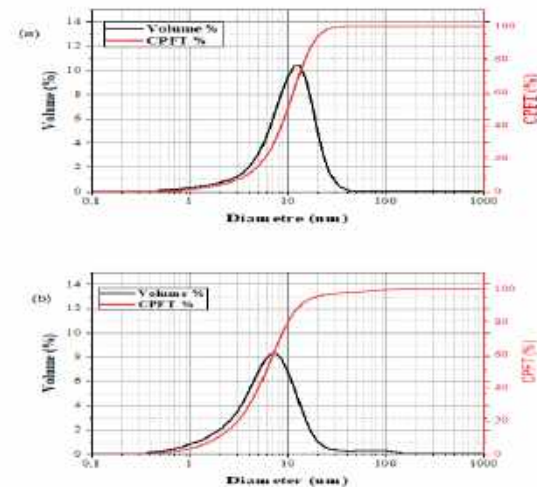


Fig. 2. Cumulative particle size distribution of mixture (a) P1, (b) P2.

### B. SINTERING BEHAVIOR

The sintered ceramics exhibits a mass gain between 4-8% and a recorded dimensional change along length and width of 3-4%, 0.2-1% respectively. Some samples shows signs of crack most likely due the shaping process and white clots formed at the bottom of the samples due to the reaction between the powder bed and the excess released silica witch explain excessive mass gain.

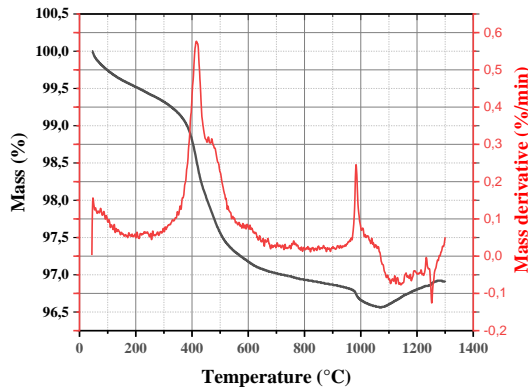
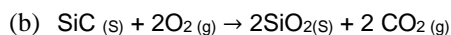
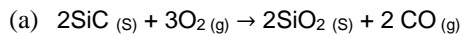


Fig. 3. Analysis of Fock states at one of the inputs of the Interferometer.

A thermogravimetric analysis of the P2 mixture was performed. The results, depicted in Figure (3), illustrate a mass loss of 2.875% over a temperature range of 44 to 600°C. This mass loss corresponds to that measured after debinding, indicating it is attributable to the loss of mass from the kaolin. It is thus deduced that the 0.75% mass loss within the 44-300°C interval arises from the evaporation and dehydration of hygroscopic water, while the 2.5% mass loss in the 300-1000°C range results from the evaporation and dehydration of structural water (kaolin transformation into metakaolin). A 0.25% mass loss is observed within the 1000-1100°C range, followed by a 0.5% mass gain within the 1100-1300°C interval. This behavior is attributed to the oxidation of SiC, as described by the following equations [1-3]:



The release of excess SiO<sub>2</sub> and CO<sub>2</sub> act as pore forming agent, the bulk density and open porosity of the two mixtures measured by the two methods shows the same results about 2% and 25-30% for the apparent density and open porosity respectively. The change of forming pressure from 70 to 125 MPa did not influence

significantly the resulting density and open porosity.

### C. MECHANICAL BEHAVIOR

The study of the compressive behavior (Rc) of the composite as a function of sintering temperature is presented in figure (4). We notice an increase of maximum compressive strength up to 197 MPa at 1500°C for P1 samples, and up to 189.8 MPa at 1400°C for P2 samples.

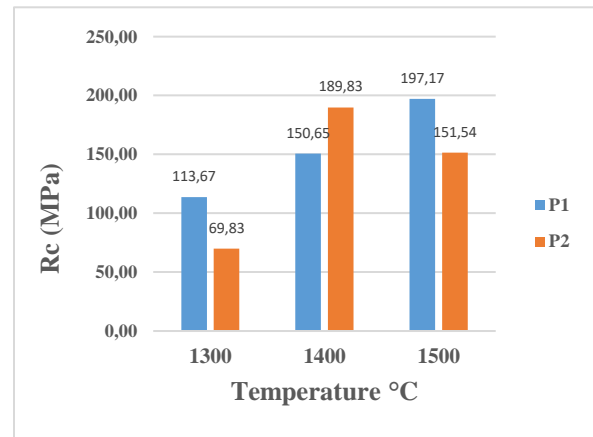


Fig. 4. Compressive behavior as function of sintering temperature.

Figure (5) presents the study of the Diametral compression behavior (Rt). We notice an increase of maximum resistance strength up to 17 MPa at 1500°C for P2 samples, and a decrease up to 17 MPa at 1400°C for P1 samples.

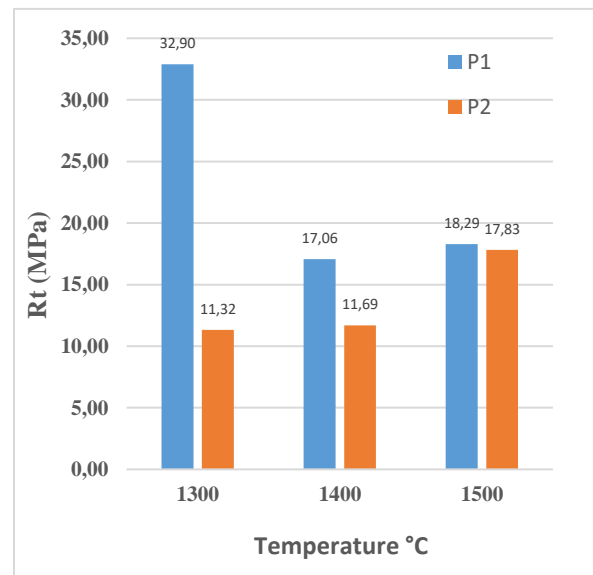


Fig. 5. Diametral compressive behavior as function of sintering temperature.

#### IV. CONCLUSION

In this study, the SiC-Al<sub>2</sub>O<sub>3</sub> porous composite was successfully fabricated at sintering temperatures ranging from 1300 to 1500 °C in open air, with the use of DD3 kaolin as a binder for shaping and as a sintering aid. It was found that an average particle size of 5 to 8 µm and a pressure of 70 to 125 MPa resulted in an average bulk density of 2.09 g/cm<sup>3</sup> either in the green state or after thermal treatment from 600 to 1500 °C, along with an average open porosity of 28.36%, for an addition of 5-8% kaolin. An addition of 5% kaolin led to the attainment of optimal mechanical properties for a porosity rate of 28.36%. With a sintering temperature of 1500 °C, a maximum compressive strength of 197.17 MPa was achieved. A maximum tensile strength of 32.90 MPa was obtained at a sintering temperature of 1300 °C.

#### REFERENCES

- [1] Jing, Y., Deng, X., Li, J., Bai, C., & Jiang, W. (2014). Fabrication and properties of SiC/mullite composite porous ceramics. *Ceramics International*, 40(1 PART B), 1329–1334.
- [2] Ding, S., Zhu, S., Zeng, Y. P., & Jiang, D. (2007). Fabrication of mullite-bonded porous silicon carbide ceramics by in situ reaction bonding. *Journal of the European Ceramic Society*, 27(4), 2095–2102.
- [3] CHI, W., JIANG, D., HUANG, Z., & TAN, S. (2004). SINTERING BEHAVIOR OF POROUS SIC CERAMICS. *CERAMICS INTERNATIONAL*, 30(6), 869–874.
- [4] WANG, Y., LIU, Y., CHEN, Z., LIU, Y., GUO, J., ZHANG, W., RAO, P., & LI, G. (2022). RECENT PROGRESS IN THE PORE SIZE CONTROL OF SILICON CARBIDE CERAMIC MEMBRANES. IN *CERAMICS INTERNATIONAL* (VOL. 48, ISSUE 7, PP. 8960–8971). ELSEVIER LTD.
- [5] EOM, J. H., KIM, Y. W., & RAJU, S. (2013). PROCESSING AND PROPERTIES OF MACROPOROUS SILICON CARBIDE CERAMICS: A REVIEW. IN *JOURNAL OF ASIAN CERAMIC SOCIETIES* (VOL. 1, ISSUE 3, PP. 220–242). TAYLOR AND FRANCIS LTD.
- [6] YUN, S. IL, YOUM, M. R., NAHM, S., & PARK, S. W. (2021). FABRICATION AND PROPERTIES OF MACROPOROUS SIC USING AL<sub>2</sub>O<sub>3</sub>–Y<sub>2</sub>O<sub>3</sub>–SiO<sub>2</sub> AS BONDING ADDITIVES. *CERAMICS INTERNATIONAL*, 47(9), 11979–11988.
- [7] LUO, Z. Y., HAN, W., YU, X. J., AO, W. Q., & LIU, K. Q. (2019). IN-SITU REACTION BONDING TO OBTAIN POROUS SIC MEMBRANE SUPPORTS WITH EXCELLENT MECHANICAL AND PERMEABLE PERFORMANCE. *CERAMICS INTERNATIONAL*, 45(7), 9007–9016.
- [8] BAI, C. Y., DENG, X. Y., LI, J. B., JING, Y. N., & JIANG, W. K. (2014). PREPARATION AND PROPERTIES OF MULLITE-BONDED POROUS SIC CERAMICS USING POROUS ALUMINA AS OXIDE. *MATERIALS CHARACTERIZATION*, 90, 81–87.
- [9] KAYAL, N., DEY, A., & CHAKRABARTI, O. (2012). SYNTHESIS OF MULLITE BONDED POROUS SIC CERAMICS BY A LIQUID PRECURSOR INFILTRATION METHOD: EFFECT OF SINTERING TEMPERATURE ON MATERIAL AND MECHANICAL PROPERTIES. *MATERIALS SCIENCE AND ENGINEERING: A*, 556, 789–795.

# Optimization of a copper-coat composite coating

BALIT<sup>1</sup> AND MOUHOUBI. S<sup>1,2</sup>

1. URME emerging materials research unit, Farhat Abbas university  
Setif, Algérie, [t.bali@univ-setif.dz](mailto:t.bali@univ-setif.dz)

2. Laboratory of no metal materials -LMNM, institute of optics and precision mechanics IOMP, Farhat Abbas university

## ABSTRACT (1,000 characters)

*The main objective of this work; it is the optimization of an antifouling coating based on two types of resin: polyester and acrylic, heavily loaded with copper powder. The development is done in two main stages; where we prepared wooden substrates (oak and beech), and also developed a jute/polyester composite material for use as a substrate and to carry out a study close to maritime reality. Then, we prepared 4 different mixtures of antifouling paint, varying the type of resin and the copper content.*

*In order to identify the different characteristics of the antifouling paint developed, in particular the surface condition, adhesion and hardness of the coating; a comparative study was carried out with different tests: the adhesion test, the wear test, measurement of roughness, observation of the surface condition, measurement of micro-hardness and the study copper grain distributions*

## KEY WORDS

Cooper-coat, Antifouling, Spray, Polyester, Acrylic.

## I. INTRODUCTION

Marine antifouling coatings are multidisciplinary design materials. In addition to preventing marine growth, antifouling coatings also provide a thin undercoat as a protective barrier against corrosion of the metal structure. Traditionally, paints containing biocides have been used to protect metal structures from biofouling. These biocides are slowly released into the environment. The toxic nature of heavy metals used as biocides such as tin, lead, copper, arsenic, mercury and their organic derivatives kills marine organisms and threatens environmental sustainability.

The main objective of this work is the optimization of a copper-based antifouling coating. For this, we chose polyester and acrylic as thermosetting resins. The designated coatings have been applied to different substrates. Regarding these substrates, we have selected materials that can be used for maritime

construction which are: beech and oak wood and a composite material that we have developed. The latter is based on polyester resin and a plant fiber. The application of antifouling paint is carried out by the spraying method.

## II. EXPERIMENTAL METHODS

### A. APPLICATION OF THE ANTIFOULING COATING:

First about 25% of copper powder of 22 $\mu$ m of diameter (the size of the copper grains was determined by HORIBA LA-960 Laser diffusion particle size analyzer), this powder was mixed with deferent ratio of resin, then add the diluent and lastly the hardener. Stir until a homogeneous mixture is obtained, and to keep the copper powder in suspension. A compressed air gun was used for spraying. Each layer must be sprayed on a previous layer that is already dry from where a dryer has been used to avoid dripping of the deposit. For each substrate we made sure to have a deposit of thickness  $\approx$ 1mm.

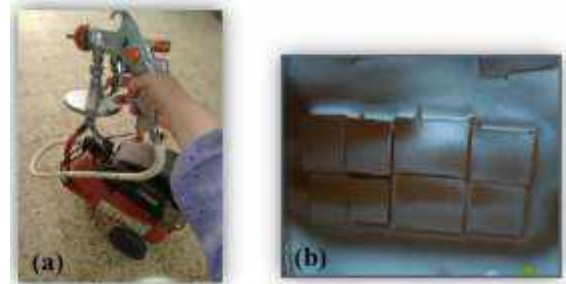


Fig. 1. Preparation of substrates.

Mixture	Resin	Resin volume (ml)	Diluent volume (ml)	Mass of Cu powder (g)	Hardener rate (%)
M1	Polyester	60	60	60	1
M2	Polyester	60	50	30	1
M3	Acrylic	60	50	60	25
M4	Acrylic	60	50	30	25

Tab. 1. Composition of the different mixtures applied



### B. ADHESION TESTS

The tensile-test is carried out on two 23 mm diameter specimens, according to the ASTM C633 standard, at a test speed of 0.05 mm/min at room temperature. Each specimen consists of a substrate bonded with a cross-substrate about a 1mm layer of copper/polyester antifouling coating.

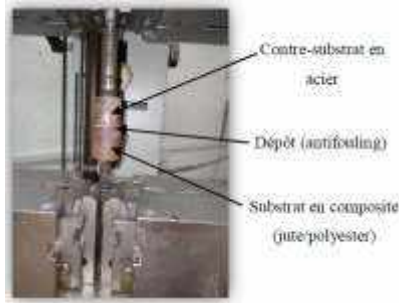


Fig. 3. Tensile specimen for adhesion testing (ASTM C633)

To confirm the results obtained by traction test we have measure hardness subtract/coating interface using a Q30M type micro-durometer from the Qness brand, equipped with a 15 MP resolution camera.

### A. SURFACE CONTROL

To control the surface parameters, we have used a contact profilometer instrumented TAYLOR HOBSON. In addition, we used KLA Tencor' optic profilometer to carry out precise roughness measurements

For studying the wear behavior of different coatings, the device used is based on surface contact under a normal force of 30N and a sliding speed of 35 rpm, between the sample to be tested and a reference ball in hardened 100C6 steel with a diameter of 12 mm.

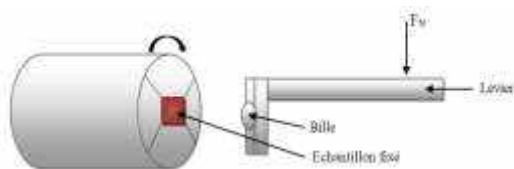


Fig. 4. Demonstrative drawing of the wear device used

### A. RESULTS AND DISCUSSION

Obtaining good mechanical properties requires optimizing the mixing rate. The figures below show the effect of the E/P (Water/plaster) ratio on mechanical properties.

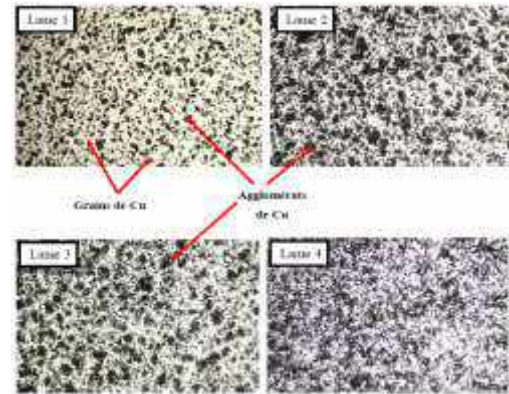


Fig. 5. Micrographs of the distributions of copper grains.

We observe on the 1<sup>st</sup> slid a relatively non-uniform distribution, marked by the dispersion of agglomerations size stuck on the surface. As additional layers are applied, the fine droplets projected by the gun settle. We are witnessing a growth of agglomerates with better dispersion (M4).

The calculated roughness values are presented in the figures below:

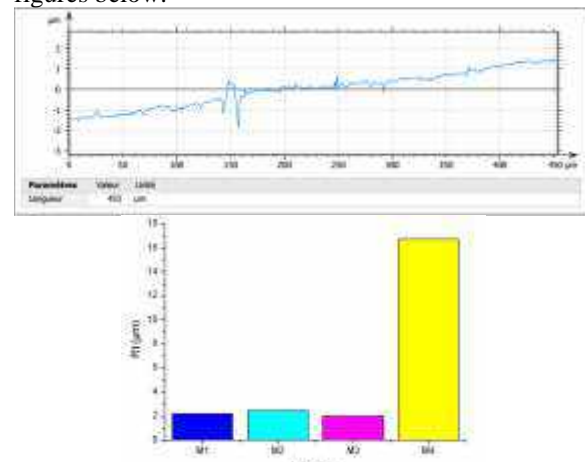


Fig. 6. Average total roughness of each of the 4 antifouling mixtures

The results obtained by the two methods (traction and indentation) coincide and show that the adhesion force is approximately 13MPa.

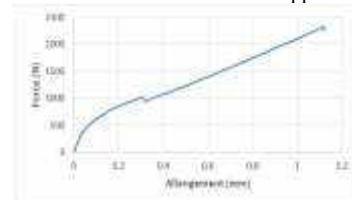
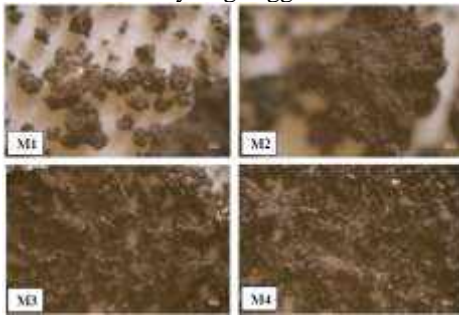


Fig. 7. Evolution of the bending stress of sisal plaster composites



Fig. 6. Micrograph represents the imprint of indenter.

In order to determine the mass loss, the samples were weighed before and after wear. We note that the mass loss is very low, and the debris removed by wear is in the form of a relatively large agglomerate.



**Fig. 5.** Average stress curve as a function of water percentage for composites (plaster/sisal)

The mass loss is very low, and the debris removed by wear from the first two samples (M1 and M2) are represented in the form of large agglomerates (a hardening of the debris has occurred) the ductility of the antifouling coating of these samples is the main reason. Unlike the samples (M3 and M4) where we can say that its antifouling coatings is harder and are in the form of a relatively large agglomerate

### III. CONCLUSION

At the end of the work carried out and the results obtained, we can conclude the following points:

- Spraying under air pressure is the most appropriate. from the point of view of ease and convenience as well as simulation of reality (large boats).
- Acrylic resin mixtures were easier and quicker to spray. This is linked to the difference in viscosity between the two resins.
- Polishing is an important process to improve the surface finish, unify the surface components and reduce the roughness factor.

Finally, and as a perspective, we hope to carry out real biological embedding tests in order to be able to make the optimal and well-founded choice. Consequently, develop another type of antifouling coating, using another type of resin and other biocidal fillers.

### REFERENCES

- [1] JELLALI, Rachid. Elaboration de revêtements antifouling par photo réticulation. Université du Maine. 15 Décembre 2008.
- [2] Banta, George. l'encrassement marin et sa prévention. Naval Institute. Annapolis, Maryland

# Comportement mécanique des structures en nid d'abeille soumises à la compression rapide

Mertani Boubekeur Mohammed Bilel<sup>\*1</sup>, Keskes Boualem<sup>1</sup>, Bouchakour Leila<sup>1</sup>

1- laboratoire de mecanique de precision applique (LMPA). Institut d'optique et de mecanique de precision (IOMP).  
Universite Ferhat Abbas Sétif 1 Algerie.

\* [mertani.bmb@gmail.com](mailto:mertani.bmb@gmail.com)

## RESUME

*Le présent travail se concentre sur une évaluation approfondie des propriétés mécaniques en compression rapide des structures en nid d'abeille hexagonaux. Ce travail vise à explorer les réactions mécaniques de ces structures uniques lorsqu'elles sont soumises à la compression rapide, mettant en évidence leurs comportements, leurs limites et leurs performances dans des conditions de charge particulières. Cette exploration contribue non seulement à la compréhension fondamentale de la dynamique de ces panneaux, mais offre également des perspectives pratiques pour leur utilisation dans des applications réelles.*

## MOTS-CLES

Structure nid d'abeille, Compression dynamique, Impact, Tour de chute.

## INTRODUCTION

L'innovation dans le domaine de l'ingénierie des matériaux a donné lieu à la création de structures novatrices qui répondent aux exigences complexes des applications modernes. Parmi ces structures, les nids d'abeille hexagonaux se démarquent par leur combinaison exceptionnelle de légèreté et de résistance mécanique. En tant que composants essentiels de nombreux secteurs, tels que l'aérospatiale, l'automobile et la construction, ces structures offrent un potentiel considérable pour améliorer l'efficacité, la durabilité et la performance globale des produits finis.

## MONTAGE EXPERIMENTAL

Les essais de compression rapide ont été réalisés à

l'aide d'une tour de chute à masse tombante, en utilisant un impacteur cylindrique plat en acier d'un diamètre de 80 mm, sur des échantillons en nid d'abeille de différentes formes et diamètres avec une masse tombante de 7488g. La Figure 1 présente le schéma montage expérimental. la tour de chute à masse tombante utilisée pour ces essais. Une seule vitesse et une hauteur ont été appliquées. Le signal de la force d'impact a été enregistré à l'aide d'un capteur connecté à une carte d'acquisition. La déformation a été observée à l'aide d'une caméra vidéo. La vitesse de chute de l'impacteur a été mesurée à l'aide d'un dispositif de mesure infrarouge, un photogate.

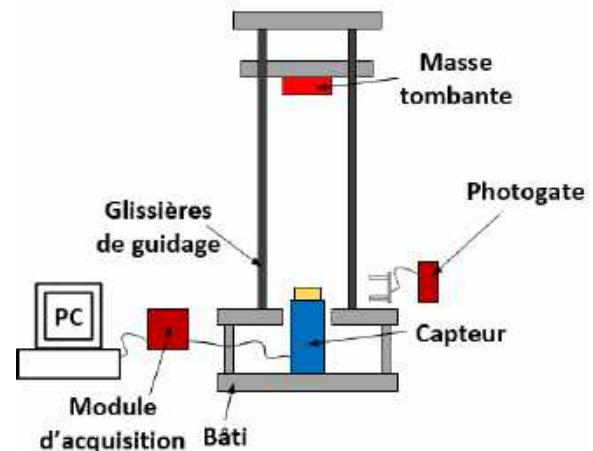


Fig 1. Montage expérimental.

## RESULTATS

Dans cette partie, nous allons présenter les résultats préliminaires obtenus après l'essai de compression rapide et les différentes courbes obtenues qui montrent l'évolution de la force d'impact en fonction du temps pour différentes formes et diamètres des échantillons.

La compression rapide des échantillons motif hexagonal de diamètre 3,2mm est représentée par la figure ci-dessous :

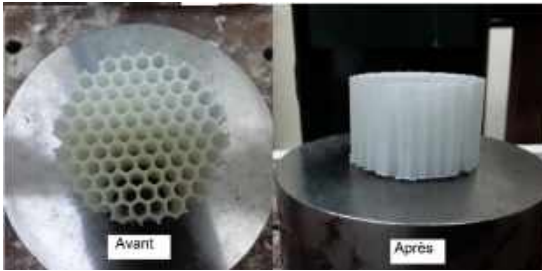


Fig 2. L'échantillon avant et après la compression rapide pour le motif hexagonal de diamètre 3,2mm.

La figure 3 montre la force enregistrée par le capteur en fonction de temps pour 2 échantillons de même diamètre.

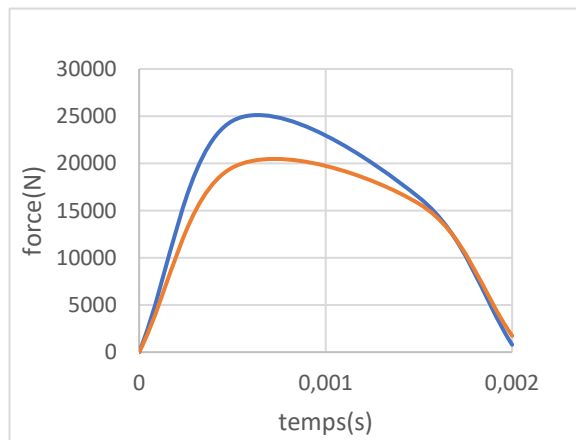


Fig 3. Courbe de force en fonction du temps pour le motif hexagonal de diamètre 3,2 mm.

**Tableau 1.** Tableau des forces maximales des échantillons hexagonaux.

Diamètre (mm)	Essai	Force max (N)
3.2	E1	24500
	E2	19550
	<b>Moyenne</b>	22025
6.4	E1	13400
	E2	13770
	<b>Moyenne</b>	13585
9.6	E1	8857
	E2	9194
	<b>Moyenne</b>	9025
19.2	E1	29760
	E2	25820
	<b>Moyenne</b>	27790

A l'aide du tableau ci-dessus (Tableau 1) on a tracé un histogramme de l'évolution de la force maximale en

fonction du diamètre des échantillons hexagonaux. (Figure 4) :

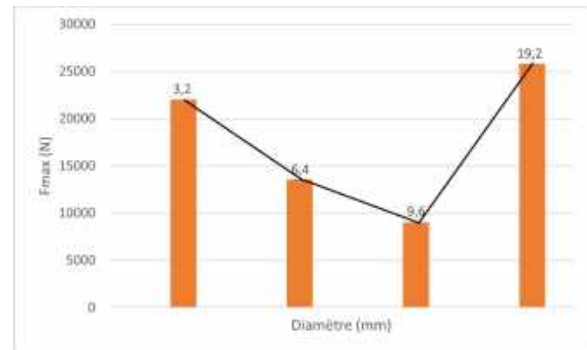


Fig 4. Histogramme de la force maximale en fonction de diamètre des échantillons hexagonaux.

## REFERENCES

- [1] Mertani, B.M.B., B. Keskes, and M. Tarfaoui, Numerical study on the compressive behaviour of an aluminium honeycomb core. *Materiali in tehnologije*, 2019. 53(2): p. 199-206.
- [2] Mertani, B.M.B., B. Keskes, and M. Tarfaoui, Experimental Analysis of the Crushing of Honeycomb Cores Under Compression. *Journal of Materials Engineering and Performance*, 2019. 28(3): p. 1628-1638.
- [3] Bentouhami, A. and B. Keskes, Experimental analysis and modeling of the buckling of a loaded honeycomb sandwich composite. *Materiali in tehnologije*, 2015. 49(2): p. 235-242.

# Investigation of local plant fibers "Diss" in the development of plaster matrix composite

MOUHOUBI. S<sup>1,2</sup>, BALI.T<sup>2</sup>, OSMANI. H<sup>1</sup> AND MIDOUNE. K<sup>1</sup>

1. Laboratory of no metal materials -LMNM, institute of optics and precision mechanics IOMP, Farhat Abbes university  
Setif, Algérie, [s.mouhoubi@univ-setif.dz](mailto:s.mouhoubi@univ-setif.dz)
2. URME emerging materials research unity Farhat Abbes university  
Setif, Algérie

## ABSTRACT (1,000 characters)

*Gypsum is considered the ideal material for use in homes. This is due to its rapid setting, light weight, fire resistance, recyclability and relatively low price. Its main weaknesses, however, are its brittleness, poor mechanical strength and sudden breakage. The addition of plant fibers to gypsum gives it very good mechanical strength, a high degree of toughness that eliminates catastrophic breakage, and above all, this incorporation does not affect its hygrothermal properties and supports its bio-degradability. The main objective of this study is to develop a gypsum matrix composite reinforced with sisal fibers. Consequently, to examine the impact of this incorporation on the behavior of the plaster. On the other hand, we will try to substitute this tropical fiber with one from a local plant, Diss (*ampelodesmos mauritanicus*). The aim is to add value to this fiber, which has never been used in this context. The results obtained are very encouraging.*

## KEY WORDS (3 to 6 key words)

Composite, Gypsum, Plant fiber, Diss, Sisal.

## I. INTRODUCTION

Plaster is considered an ideal material for use in building construction. Definitely, it has interesting properties such as ease of implementation, fire resistance and durability. However, its main weak points are its fragility, its poor mechanical strength and its sudden breakage. The addition of fibers, particularly plant fibers, to the plaster gives it very good mechanical resistance, a very high tenacity which eliminates its catastrophic breakage, and above all this incorporation does not affect these hygrothermal properties and supports its biodegradability. The natural fibers most commonly used for this purpose

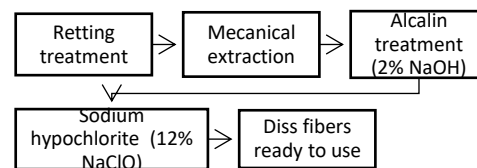
are: hemp fibers, jute fibers and sisal fibers.

The objective of this dissertation is the study of various composite materials with a plaster matrix reinforced by plant fibers (Diss and sisal). More precisely, our approach is based on knowledge of the behavior of hydrated plaster. In order to determine its mechanical behavior with the aim of improving adhesion to the fiber/matrix interface and to study the mechanical behavior of such composites.

## II. EXPERIMENTAL METHODS

### A. EXTRACTION OF LIGNOCELLULOSIC DISS FIBERS:

The flowchart below explains the different steps :



However, sisal fibers, they were used as received.

### B. MANUFACTURING OF MATERIALS

#### B. 1. Preparation of plaster specimens:

In this study, we developed prismatic plaster test specimens with dimensions of 40×40×200 mm<sup>3</sup> for different mixing rates from 0.6 to 0.9 to 0.05. The test pieces thus obtained will be characterized after 14 days.

#### B. 2. Preparation of composites:

Before preparing the plaster slip for the chosen mixing rate, the fibers must be cut according to the 20×200×360 mm<sup>3</sup> mold strips. The plate is unmolded after 24 hours and cut by the band saw to widths of



40mm. All composite materials were developed under the same conditions. Like the plaster specimens, these will be characterized after 14 days.

### C. MECHANICAL TESTS

To determine the mechanical properties of the materials, we carried out a 3-point bending test on a ZWICK-Roell Z100 machine equipped with a 100KN force cell and controlled by TestXpert software.



Fig. 1. Test 3Pts of (a) plaster and (b) composite samples.

### A. RESULTS AND DISCUSSION

Obtaining good mechanical properties requires optimizing the mixing rate. The figures below shows the effect of the E/P (Water/plaster) ratio on mechanical properties.

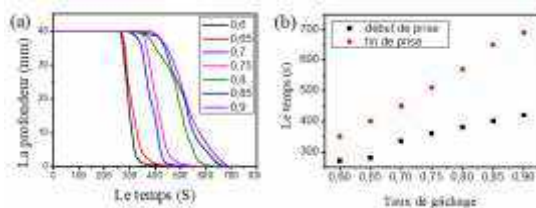


Fig. 2. Effect of E/P ratio.

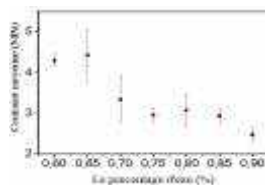


Fig. 3. Average stress curve as a function of E/P.

These results show that the behavior of the composites (plaster/sisal) presents a linear zone up to the maximum stress. The sudden drop is due to the fragile nature of the matrix. Beyond this instability, the reinforcing fibers bridge the matrix crack, hence the stability of crack propagation. The sisal fibers control the propagation of the crack so there is an increase in toughness.

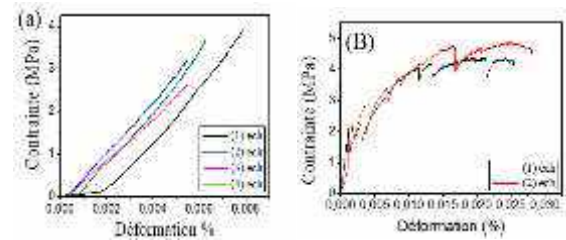


Fig. 4. Evolution of the bending stress of sisal plaster composites

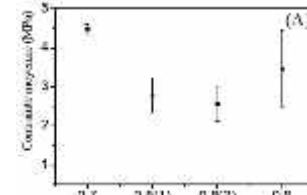


Fig. 5. Average stress curve as a function of water percentage for composites (plaster/sisal)

We see that the sisal fibers increase the breaking stress compared to the raw plaster stress. The E/P=0.7 ratio composite has better mechanical strength with controlled brittle fracture.

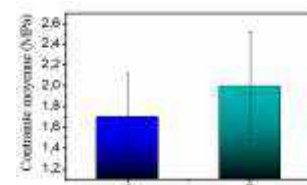


Fig. 6. comparison between the breaking strength of the two composites (a) Diss and (b) sisal.

### III. CONCLUSION

the results show that, the optimal rate is between 60 to 65%. For a rate (E/P = 0.6), the breaking stress in bending is of the order of 4.3MPa, with an elastic modulus of approximately 850 MPa. These properties decrease to reach a resistance value of approximately 2.5 MPa for rate 0.9 with elastic modulus of approximately 367MPa.

When introducing sisal or Diss fibers into the plaster, the mechanical behavior becomes controlled. So, we are seeing an increase in toughness;

In general, the use of plant fibers in the development of a plaster-based material offers an ecological and aesthetic alternative to conventional construction materials. Plaster-plant fiber composite materials offer design versatility, and can be an attractive solution for many applications in the construction and decoration sectors.



# Conception et réalisation d'un dispositif de cisaillement pour les panneaux sandwich

CHOUTER ADEL <sup>1,2,\*</sup>, KESKES BOUALEM<sup>2</sup>, LABANI ABDARRAHMANE<sup>2</sup>.

1. Ferhat Abbas University Setif 1: Institut d'Optique et Mécanique de Précision, Setif, Algeria, achouter25@gmail.com.
2. Ferhat Abbas University Setif 1: Institut d'Optique et Mécanique de Précision, Setif, Algeria, b\_keskes@yahoo.fr.

## ABSTRACT

*La mécanique appliquée, Il est une branche d'ingénierie qui a pour but d'étudier le comportement des dispositifs mécaniques d'intérêt pratique à l'aide de la méthodologie et les résultats de la mécanique théorique.*

*Le but de cette étude est de proposer un moyen de caractérisation des panneaux sandwich à partir d'analyse mécanique. Pour faire une conception et réalisation d'un dispositif de cisaillement pour les panneaux sandwich, le département Mécanique nous a proposé de concevoir et de réaliser selon un cahier des charges prédéfini un dispositif de cisaillement.*

*Après étude et réalisation, ce dispositif sera adapté par la suite sur la machine de traction- (ZWICK) déjà existante, ce qui nous permettra une bonne compréhension du phénomène de sollicitation au cisaillement.*

**LES MOTS CLES :** la méthodologie, panneaux sandwich, un cahier des charges, dispositif de cisaillement

## I. INTRODUCTION

Les panneaux sandwichs à âme nid d'abeilles ou en mousse sont de nouveaux matériaux particulièrement utilisés dans le domaine de l'aéronautique et de l'aérospatial, le secteur des transports, la construction navale et maritime, etc. Leurs avantages résident principalement dans la forte rigidité en flexion, l'excellente résistance à la fatigue, la résistance au feu, bonne isolation thermique et acoustique et le faible poids.

La résistance et la rigidité des panneaux sandwichs dépendent essentiellement de l'adhésif (collage par un film de colle) qui assure la liaison entre les peaux et l'âme. Cet adhésif est un composant important permettant un bon assemblage de la structure sandwich et une bonne transmission des contraintes d'un milieu à l'autre. Sa principale caractéristique est la résistance au cisaillement. Dans cette optique notre travail consiste à faire des essais de cisaillement avec un dispositif réaliser qui nous permettant de caractériser le comportement et la résistance en cisaillement entre les peaux et l'âme des panneaux sandwich. Le dispositif doit être adaptable sur la machine de traction (ZWICK) de notre institut et offre la possibilité de tester le comportement en cisaillement de différentes structures en

panneau sandwich (nid d'abeille, mousse,.. etc) et les assemblages collés.

## II. PROCEDURE EXPERIMENTALE ET MATERIAUX

### A. PROCEDURE EXPERIMENTALE

Cet essai permet de déterminer la résistance maximale en cisaillement et le module de cisaillement, la déformation, etc.

Le dispositif de cisaillement (Figure 1) est fixé directement sur les mors de la machine de traction. Il a été conçu de manière à ce que l'effort de cisaillement soit appliqué sur l'échantillon selon l'axe symétrique de la machine. Cette configuration garantit l'acquisition précise des résultats de l'essai à travers les moyens de mesure de la machine de traction.



Fig. 1. Configuration de l'essai cisaillement.

### B. MATERIAUX ET ÉPROUVETTES

Les échantillons utilisés lors des essais de cisaillement sont de différents matériaux tels que les panneaux sandwichs : l'aluminium- aluminium, aluminium-nomex, métal-polyuréthane en mousse. Les

dimensions géométriques des éprouvettes sont illustrées dans les tableaux (1, 2).

**Table.1** : Dimensions géométriques d'éprouvette en panneaux sandwichs en mousse.

Eprouvette en mousse.	L (longueur) [mm]	b (largeur) [mm]	Epaisseur(d) [mm]
N°1	248	50	50

**Table .2** : Les caractéristiques des panneaux sandwich nid d'abeille en aluminium L et W.

P.S nid d'abeille aluminium-aluminium	l(longueur) [mm]	b (largeur) [mm]	Epaisseur (d) [mm]	Densité [kg/m3]
1 (sens w)	251	52	10	29
2 (sens L)	211	56	10	29

### C. MODE OPERATOIRE DE L'ESSAI DE CISAILLEMENT

- Appliquer l'adhésif (Epoxy steel) sur les deux surfaces peaux de l'éprouvette.
- Placer et coller l'éprouvette entre les deux plaques de chargement du dispositif de cisaillement et attendre au moins dix minutes pour le durcissement de la colle.
- Utiliser les serres joints pour le serrage des deux plaques de chargement avec l'éprouvette pour assurer une bonne adhésion.
- Avant de commencer l'essai, il est nécessaire de régler la vitesse de chargement du dispositif de cisaillement. Pour notre expérience, nous avons choisi une vitesse de déplacement **de 0,5 mm/min.**
- Démarrer l'essai de cisaillement en appliquant la charge progressivement jusqu'à la rupture finale du panneau sandwich
- Pendant l'essai jusqu'à la rupture finale, l'acquisition des résultats sont enregistrés par un micro-ordinateur.
- Après l'essai, les résultats obtenus sont sous formes de courbe (charge ou contrainte de cisaillement en fonction de la déformation) et tableaux de valeurs des caractéristiques mécaniques de l'essai.
- Répétés les mêmes opérations pour les autres éprouvettes.

## III. RESULTATS EXPERIMENTAUX DES ESSAIS DE CISAILLEMENT

les résultats des essais sont illustrées par les figures suivantes :

### A. RESULTATS DES ESSAIS SUR DES EPROUVETTES EN PANNEAUX SANDWICHS EN MOUSSE

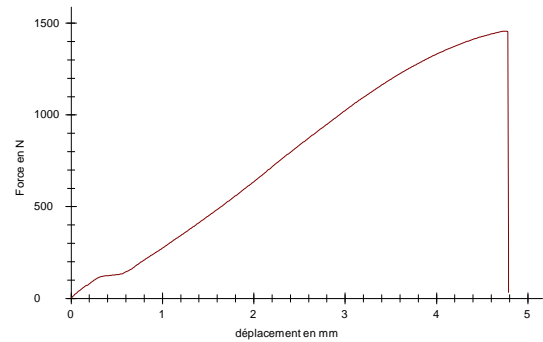


**Fig. 2:** Courbe d'essai représentant la force de cisaillement en fonction du déplacement.

### B. RESULTATS DES ESSAIS SUR DES EPROUVETTES EN PANNEAUX SANDWICHS NID D'ABEILLE : ALUMINIUM-ALUMINIUM, SENS W ET L

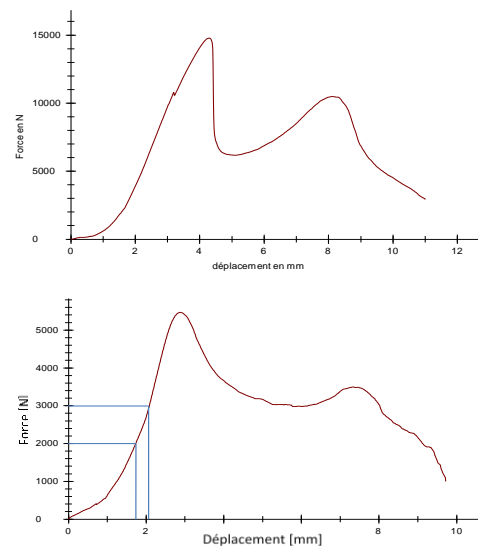


**Figure 3 :** Comparaison entre les résultats d'essai des éprouvettes nid d'abeille en aluminium-aluminium sens (L) et (W).

### C. RESULTATS DE L'ESSAI SUR EPROUVETTE EN PANNEAU SANDWICH NID D'ABEILLE : ALUMINIUM-NOMEX

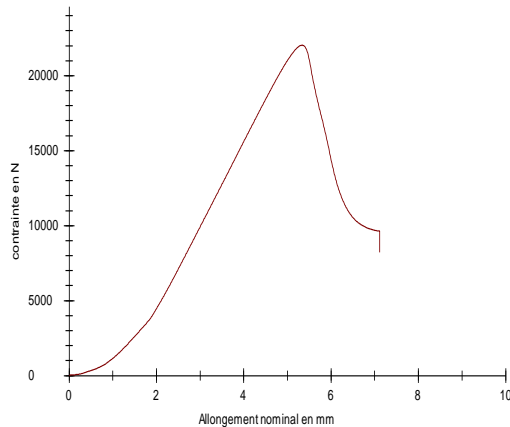


**Figure 4 :** Courbe graphique représentant l'évolution de force (N) en fonction du déformation (mm).

#### IV. CONCLUSION

Afin de valider la fonctionnalité expérimentale du dispositif de cisaillement réalisé, Une partie expérimentale des essais de cisaillement sur des panneaux sandwichs ( en mousse' en nid d'abeilles) a été présentée. Les résultats expérimentaux préliminaires obtenus sont très encourageants et prometteurs.

Nous nous sommes concentrés sur l'essai de cisaillement et son importance dans l'évaluation des propriétés mécaniques des matériaux. Nous avons présenté la fixation de l'éprouvette sur le dispositif de cisaillement que nous avons fabriqué, ainsi que la fixation du dispositif sur la machine de traction. Nous avons décrit les équipements utilisés et les principaux paramètres à prendre en compte. De plus, nous avons effectué des essais sur des panneaux sandwich afin de nous assurer que notre dispositif de cisaillement fonctionnait correctement.

#### REFERENCES

- [1]a. e. guendouz, « conception d'un dispositif d'essai de flambement par compression-flexion et application », p. 72, oct. 2020.
- [2] b. m. b. mertani, « étude numérique et expérimentale du comportement mécanique des panneaux sandwichs à âme en nid d'abeilles », thèse doctorat, ferhat abbas université setif 1, institut d'optique et de mécanique de précision, 2021. [en ligne]. disponible sur: <http://dspace.univ-setif.dz:8888/jspui/handle/123456789/3832>
- [3]y. koutsawa, « caractérisation expérimentale et numérique d'une plaque sandwich à âme nid d'abeilles », mmstp, rapport de stage de dea, 2005.
- [4]l. abdelkarim et a. mohamed, « les matériaux sandwich et

les risques d'instabilités géométriques locales », p. 29, 2014.

[5] l. a, « design of composite sandwich panels for lightweight structures », 2019.

[6] a. s, « flexural behavior of steel face sheet sandwich panels », 2021.

[7] z. j, « thermal and acoustic insulation performances of novel bio-based composite sandwich panel for building applications », 2021.

[8] b. k. benfadel, « élaboration et caractérisation de panneaux sandwichs à matrice cimentaire destinés à la construction », p. 133, 2015 2014.

[9] j. e. arbaoui, « étude comparative et caractérisations mécaniques des structures sandwichs multicouches », thèse doctorat, paul verlaine, metz laboratoire de physique des milieux denses, 2009. [en ligne]. disponible sur: [hal.univ-lorraine.fr/tel-01752670](http://hal.univ-lorraine.fr/tel-01752670)

[10] k. djama, l. michel, a. gabor, et e. ferrier, « comportement en flexion d'un panneau sandwich avec peaux hybrides (gfrp-matrice minérale) liées par une âme gfrp », acad. j. civ. eng., p. 328-331 pages, avr. 2019, doi: 10.26168/ajce.36.1.79.

# Optimisation du choix des outils de coupe pour l'usinage des poches quadrilatères en 2D1/2

CHOUITER ADEL <sup>1,2,\*</sup>, REFFAS SID AHMED<sup>2</sup>, HAMADENE FETHEDDINE<sup>2</sup>.

1. Ferhat Abbas University Setif 1: Institut d'Optique et Mécanique de Précision, Setif, Algeria, achouiter25@gmail.com.
2. Université des Sciences et de la Technologie d'Oran Mohamed-Boudiaf: Génie Mécanique, Oran, Algeria, reffas\_ahmed@yahoo.fr.

## ABSTRACT

*La minimisation du temps de fabrication est un objectif majeur qui doit être pris en compte dès le choix des paramètres d'usinage. Le diamètre de l'outil de coupe est un des paramètres qui influent énormément sur le temps d'usinage des différentes formes géométriques, en particulier les poches. Dans cet article, nous proposons une méthodologie d'optimisation du choix des outils de coupe pour l'usinage des poches quadrilatères en 2D½. Pour ce faire, nous avons développé des modèles analytiques exprimant la longueur des trajets des outils de coupe. Ensuite, nous avons structuré une méthode d'optimisation basée sur la minimisation du temps de coupe. Pour valider notre approche, nous avons traité un exemple d'application pour une poche quadrilatère quelconque en 2D½. Nous avons fait une conception de l'exemple précédent avec une démonstration des opérations d'usinage en utilisant un logiciel de Conception et de Fabrication Assisté par Ordinateur. De cela pour faire une comparaison du temps de coupe de l'optimisation réalisée par l'algorithme et le temps total optimal des opérations d'usinage.*

## KEY WORDS

*Méthodologie d'optimisation; temps de coupe; poche ; CFAO.*

## I. INTRODUCTION

Face à la concurrence internationale et l'accélération du progrès technique, les entreprises doivent continuellement améliorer leur productivité ainsi que la qualité de leurs produits. Les logiciels de conception et de fabrication assistée par ordinateur (CFAO) deviennent des outils indispensables.

Actuellement, plusieurs approches sont développées [1] [2] pour optimiser certains paramètres de coupe (vitesse de coupe, vitesse d'avance, profondeur de passe, etc.), en tenant compte d'un ou de plusieurs critères.

Parmi ces approches on trouve un travail qui décrit une méthode pour déterminer une combinaison optimale des outils de coupe pour l'usinage d'un volume de matière donné

en 3D ou d'un contour en 2D [3]. Le principe de la méthode consiste à rechercher, pour un contour donné, la section accessible par l'outil de coupe ainsi que le volume de matière résiduelle délaissée par le même outil.

Le travail réalisé au cours de cette étude a pour objectif de proposer une méthode d'optimisation du choix des outils de coupe pour l'évidement des poches quadrilatères en 2d ½, dans le cas d'ébauche sur une fraiseuse verticale à commande numérique.

## II. METHODOLOGIE D'OPTIMISATION

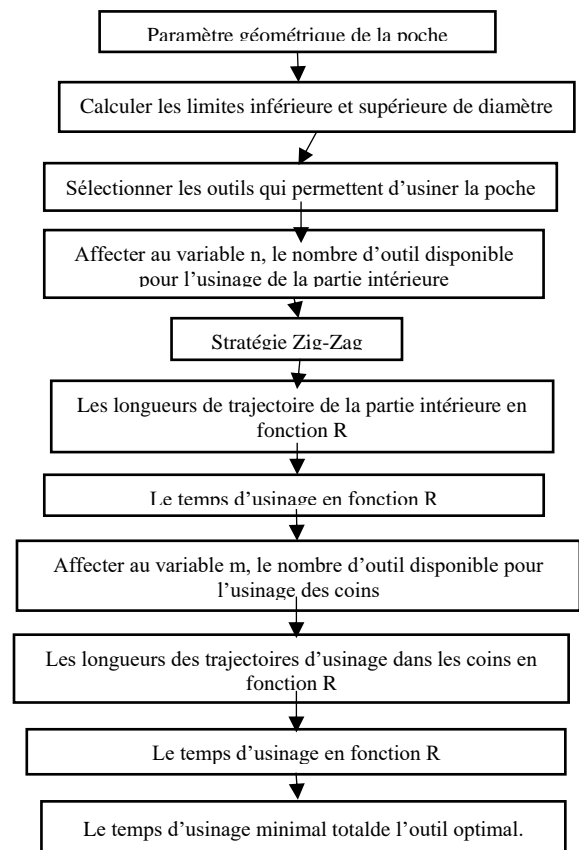


FIG.1 ORGANIGRAMME D'OPTIMISATION DE CHOIX D'OUTIL.

### III. TRAITEMENT D'UN EXEMPLE D'UNE POCHE

#### A. PARAMETRES GEOMETRIQUES DE LA POCHE

Tableau 1. Paramètres de la poche.

Côtés (mm)				Angles °				Raccordements (mm)			
a	b	c	d	a <sub>1</sub>	a <sub>2</sub>	a <sub>3</sub>	a <sub>4</sub>	r <sub>1</sub>	r <sub>2</sub>	r <sub>3</sub>	r <sub>4</sub>
80	38	54	68	72.9	66.8	146.9	73.4	4	4	4	4

Tableau 2. Outils et conditions de coupe.

N°	1	2	3	4	5	6	7	8	9	10	11
D(mm)	8	10	12	14	16	18	20	22	25	28	30
Z	4	4	4	4	4	4	4	4	4	5	5
Fz(10 <sup>-3</sup> mm/dent)	13	20	25	30	35	40	45	50	55	50	50

#### B. RESULTATS NUMERIQUES

Pour notre problème, nous avons développé un programme en langage Matlab.

Qui nous aide à trouver les valeurs de temps d'usinage minimal ainsi que le diamètre de l'outil optimal. Suivant le programme de l'optimisation de la stratégie Zig-zag le temps total est déterminé par la figure 2.

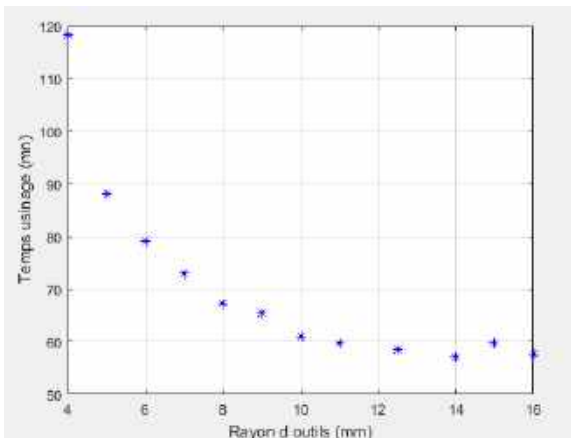


Fig. 2. Variation du temps totale d'usinage en fonction de rayon d'outils.

A partir des résultats obtenus on remarque que le temps d'usinage minimal ne correspond pas à un outil de grand diamètre mais à un outil de diamètre optimal qui prend en considération les deux temps d'usinage « Partie intérieure, coins ».

#### C. SIMULATION EN UTILISANT DES LOGICIELS CFAO

Dans ce travail nous avons choisi le logiciel SolidWorks pour développer les méthodes et techniques proposées. Suivant l'exemple de traitement de la poche proposée dans ce chapitre on fera une

conception pour la poche en tenant compte sur le dimensionnement et les paramètres de la poche. Selon la figure .3. On a dessiné une poche quadrilatère.

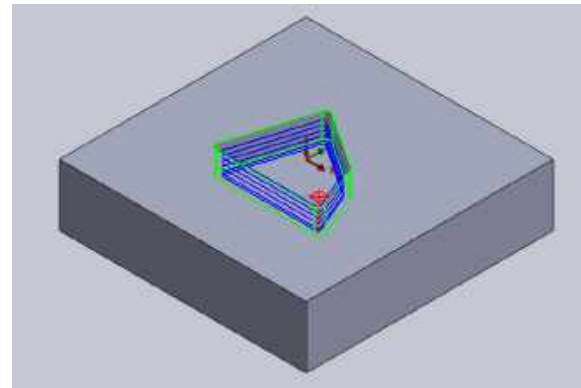


Fig. 3 Trajectoire d'outils de la finition opération contour.

Les résultats obtenus sont représentés dans le tableau suivant :

	Temps total (min)
Ebauchage partie intérieure	18.893
Attaque des coins	19.49
Finition	24.943
L'opération total	63.326

#### D. COMPARAISON DES RESULTATS

Selon les résultats obtenus, nous avons trouvé que le temps total entre l'optimisation Matlab et l'usinage en CamWorks :

Le temps total en utilisant l'optimisation Matlab est plus court que CamWork qui se traduit à un taux de 9%. Cette diminution ce gain de temps est dû notamment aux facteurs suivant les techniques utilisées, la matière de l'outil et le brut, le temps de changement d'outils et la machine...

### IV. CONCLUSION

Selon les résultats obtenus on remarque que le temps d'usinage et le choix des outils de coupe est un facteur important qui affectent la production des pièces et le temps total.

Pour cette étude on a utilisé un programme qui a été développé sous Matlab pour la génération des résultats numériques, ainsi que la simulation des trajectoires de l'outil optimal.

On a traité le même exemple avec CamWorks pour faire une comparaison entre les deux méthodes pour avoir le meilleur temps optimal.

En comparant entre les résultats on remarque que l'optimisation programmé nous donne le temps et l'outil le plus optimal.

**REFERENCES**

- [2] X. yan, k. shirase, m. hirao, et t. yasui, « extraction and optimisation of cutting conditions for 21/2 -axis milling », int. j. adv. manif. technol., vol. 16, no 10, p. 695-699, août 2000, doi: 10.1007/s001700070020.
- [3] Société sandvik-coromant, « fraisage - principes », trav. maté. - assem., janv. 2001, doi: 10.51257/a-v1-bm7082.
- [4] T. lim, h. medellin, r. sung, j. ritchie, et j. corney, « virtual bloxing – assembly rapid prototyping of near net shapes », in asme-afm 2009 world conference on innovative virtual reality, chalon-sur-saône, france, janv. 2009, p. 151-156. doi: 10.1115/winvr2009-723.



# Numerical study with FEA of honeycomb cellular materials subjected to buckling

AHCENE OUBOUZID<sup>1\*</sup>, BOUALEM KESKES<sup>1</sup>,

1. Laboratory of Applied Precision Mechanics (LMPA), Institute of Optics and Precision Mechanics (IOMP),  
Ferhat Abbas University Setif-1, Algeria

## Abstract

Finite component analysis has become the current methodology for analysis of the behaviors of solids, structures and hydraulics. Composite materials and structures are often shapely and with success analyzed in finite component programs. This work discusses the modeling and analyzing the through an experiment tested specimens utilizing numerical ways. Aim of this work is that the numerical study of aluminum honeycomb sandwiches subjected to static and dynamic loading conditions (compression, quasi-static indentation and low-velocity impact tests) victimization ABAQUS package program. The half conferred during this work seeks to predict injury and failure in metal honeycomb sandwich panels specially buckling of honeycomb core. In in the meantime, this program is employed because the answer methodology to numerically calculate the important buckling masses. Otherwise, a three dimensional (3D) reconstructions of the honeycomb panels are meted out so as to accumulate precisely the dimension and therefore the form of the injury (buckling) and to get info concerning pure mathematics and cells defects.

**KEYWORDS:** honeycomb sandwiches, buckling, Finite element analysis,

## INTRODUCTION

Honeycomb sandwich structures are widely used in various industries due to their high strength-to-weight ratio. When these structures are subjected to compressive loads, they can experience buckling, which is a critical failure mode. Finite Element Analysis (FEA) is a powerful numerical method that can be used to study the buckling behavior of honeycomb sandwich structures.

To perform a numerical study with FEA on honeycomb sandwich structures subjected to buckling, you would typically follow these steps:

### GEOMETRY AND MESHING:

Create a 3D model of the honeycomb sandwich structure, including the face sheets and the honeycomb core.

Apply appropriate boundary conditions, such as fixing certain edges or faces to represent the constraints in the real structure.

Generate a mesh that captures the geometric details of the structure. The mesh should have sufficient resolution to accurately capture the buckling behavior.

### MATERIAL PROPERTIES:

Assign appropriate material properties to the face sheets and honeycomb core. These properties may include Young's modulus, Poisson's ratio, and shear modulus.

Consider the material behavior under compression, including any nonlinear effects or failure criteria if necessary. The aluminum honeycomb core materials used in this study are supplied by Euro-Composites and intended for the aeronautical industry. The core structure consists of two-dimensional cells placed in the plane. The density of the honeycomb core is 130 kg / m<sup>3</sup>. The dimensions of the specimens were cut using a diamond disc saw from the sandwich plates. The mechanical properties and dimensions of the core specimens are shown in tables (1, 2).

The specimen had a cell size of 3.2 mm in diameter, with a wall thickness of 0.08 mm,

core material	Aluminum
Ame	ECM
s: Cell size [mm]	3,2
t: Cell wall thickness [mm]	0.08
Densities [Kg / m3]	130
Shear strength (L direction)	5,47
Shear modulus (L direction)	523
Shear strength (W direction)	3.36
Shear modulus (W direction)	311
Compressive strength [MPa]	11.55

Tableau 1: Propriétés mécaniques du nid d'abeille.

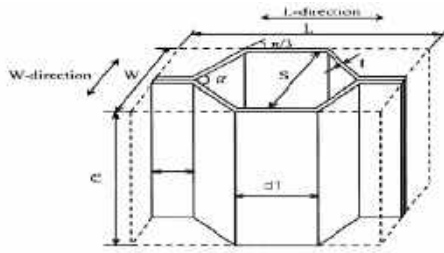


Figure1: Sample size

**LOADING AND CONSTRAINTS:**

Define the loading conditions on the structure, typically applying compressive loads or a combination of loads.

Apply constraints to represent the supports or fixations in the real structure.

**ANALYSIS:**

Perform a linear or nonlinear buckling analysis using an appropriate FEA solver.

For linear buckling analysis, eigenvalue extraction techniques are used to determine the critical buckling load and mode shapes.

For nonlinear buckling analysis, iterative procedures, such as the Risk method or arc-length method, may be employed to capture the post-buckling behavior.

For the skin to be tested, the material characteristics are defined in the "property" module. It is in this module that the coefficients of the behaviour laws are inserted. The Johnson-Cook behaviour law was used. It takes into account the rate of deformation and the deformation itself. The model selected for the study (Eq.1) is in the form:

$$\sigma = [A + B(\epsilon^p)^n] [1 + C \ln \dot{\epsilon}] \left[ 1 - \frac{T - T_0}{T_f - T_0} \right]^m \quad (1)$$

Where:  $\sigma$  is the yield strength defined according to the Von-mises criterion;  $\epsilon$  is the equivalent plastic strain;  $\dot{\epsilon}$  is the equivalent strain rate, and  $\dot{\epsilon}_0$  a reference strain rate;  $T$  is the temperature,  $T_0$  the reference temperature and  $T_f$  the melting temperature. The properties used in the simulations are presented in Table .2

	Al
Density $\rho$ (kg. m <sup>-3</sup> )	2700
Elastic modulus E (GPa)	70
Poisson's ration $\nu$	0.3
Thermal conductivity $\lambda$ (W/m.K)	237.2
Specific heat $C_p$ (J kg <sup>-1</sup> °C <sup>-1</sup> )	898.2
Yield strength A (MPa)	148.4
Hardening Coefficient B (MPa)	345.5
Strain-hardening exponent n	0.183
Strain rate C	0.001
Softening exponent m	0.895
Melting temperature $T_m$ °C	643
Reference temperature $T_r$ °C	25
Reference strain rate (s <sup>-1</sup> )	1

Table .2: Material properties of Aluminium used in this simulation.

The core is modelled with a thickness of 10 mm.

The core was modelled with the properties of Nomex (Fs274/ Fs270). The mechanical properties are: Young's modulus 210GPa, Poisson's ratio 0.29, density 7870 kg/m<sup>3</sup>, yield strength 370 MPa and tensile stress 440 MPa.

**POST-PROCESSING:**

Analyze the results obtained from the FEA solver, including buckling mode shapes, critical buckling loads, and buckling factors.

Evaluate the stress and strain distribution in the structure to identify regions prone to buckling and potential failure mechanisms. Validate the results by comparing them with experimental data or analytical solutions, if available.

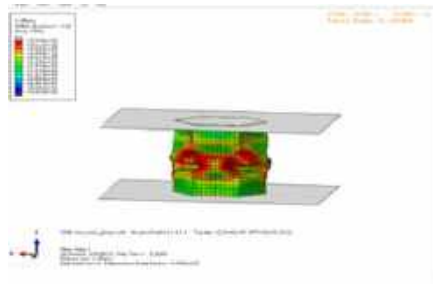


**Figure2.** Sequence from initial buckling to the total crushing configurations corresponding to perfect cell.

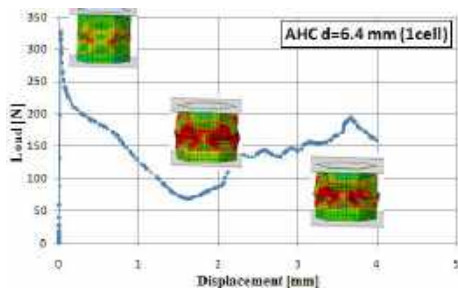


**Figure3.** Computation of buckling response from unit cell.

### OPTIMIZATION AND DESIGN:

Based on the results, you can optimize the honeycomb sandwich structure design to enhance its buckling resistance. This may involve modifying the material properties, geometry, or core configuration.

It's important to note that performing an accurate FEA analysis of honeycomb sandwich structures requires expertise in FEA software and understanding of the underlying physics. Additionally, experimental validation is crucial to ensure the reliability of the numerical results and to account for any limitations or simplifications made in the analysis.

### CONCLUSION

In conclusion, the numerical study using Finite Element Analysis (FEA) of honeycomb sandwich structures subjected to buckling provides a powerful approach to assess and understand the behavior of these structures under compressive loads. FEA allows for detailed analysis of buckling modes, critical loads, buckling factors, as well as stress and strain distribution within the structure.

Through FEA, material properties, loading conditions, and constraints can be accurately considered, enabling the optimization of honeycomb sandwich structure designs to enhance their buckling resistance and prevent potential failures.

However, it is important to note that the numerical analysis results should be experimentally validated to ensure their accuracy and reliability. Additionally, a thorough understanding of FEA software and fundamental concepts of buckling is necessary to successfully conduct this study.

In summary, the FEA numerical study of honeycomb sandwich structures subjected to buckling provides crucial insights into structural behavior and guides the design process to ensure stronger and safer structures.

### REFERENCE

- [1] Jack R. Vinson, (2005). "Sandwich structure: Past, Present, and Future" (2005). Advancing with sandwich structures and materials, Proceeding of the 7th International conference on sandwich structures, Aalborg University, Denmark.
- [2] BERTHELOT, J.-M. (1999). Composite Materials. Mechanical Behaviour and Structural Analysis, SPRINGER-VERLAG, New York, Paris.
- [3] Allen G "Analysis and design of Structural Sandwich Panel" (1969). Pergamon Press Oxford.
- [4] Boualem Keskes, A. Abbadi, Z. Azari, J. Gilgert and N. Bouaouadja (2007) "A FATIGUE CHARACTERIZATION OF HONEYCOMB SANDWICH PANELS WITH A DEFECT" Materials and technology 41 (2007) 4, 157–161 157 (ISSN 1580-294).

# improvement of surface state of a transparent $\text{MgAl}_2\text{O}_4$ spinel by deposition of a metal oxide layer

Zegadi.A<sup>1,2\*</sup>, Ayadi.A<sup>2,3</sup>, Khellaf.F<sup>2,4</sup>, Fontozzi.G<sup>5</sup>, Durán. A<sup>6</sup>, Castro.Y<sup>6</sup>

1. Emerging Materials Research Unit, Ferhat Abbas University Setif 1, Algeria,
2. Optics and Precision Mechanics Institute, Ferhat Abbas University Setif 1, Algeria
3. Laboratoire des Matériaux Non Métalliques, Institut d'Optique et Mécanique de Précision, Université Ferhat Abbas - Setif 1, 19000, Algeria
4. Laboratory of Applied Optics, Institute of Optics and Precision Mechanics, University Ferhat Abbas Setif1, 19000 Setif, Algeria
5. University of Lyon – INSA Lyon, Laboratory MATEIS, Villeurbanne, France
6. Instituto de Cerámica y Vidrio (CSIC), Campus de Cantoblanco, 28049, Madrid, Spain

## ABSTRACT:

Transparent materials in contact with harmful environments are exposed to surface damage. The transparent  $\text{MgAl}_2\text{O}_4$  spinel used as protective window, lens or laser output port etc. is one of these materials affected by these natural attacks Sand impact can cause significant defects on the exposed surface affecting its effectiveness in terms of optical and mechanical properties. The objective of this work is to study the improvement of the surface state of a spinel having a damaged surface by the deposition of a thin layer of  $\text{SiO}_2\text{-ZrO}_2$  produced by sol-gel method. For this, spinel samples of different chemical compositions sintered at different temperatures were sandblasted. Then, coated with thin layers. The results indicated that sandblasting strongly affects the surface morphology and consequently the optical transmission except in the case of samples with very small grain sizes. Also, it has been reported that the deposition of a  $\text{SiO}_2\text{-ZrO}_2$  layer clearly improves the surface condition and the optical properties of the sandblasted samples and even the mechanical properties expressed by hardness.

**KEY WORDS:** transparent spinel, sandblasting,  $\text{SiO}_2$  -  $\text{ZrO}_2$  gel floor coating, transmittance.

## I. INTRODUCTION

Transparent ceramics, particularly spinel  $\text{MgAl}_2\text{O}_4$ , have great potential through their use as transparent shielding ceramics and protective windows for sensors [1] and infrared devices [2] as these types of applications require high levels high optical performance and mechanical. Furthermore, in a

potentially aggressive environment (in the Saharan regions for example), these characteristics must be preserved as long as possible in order to maintain the proper functioning of devices equipped with this type of materials. Unfortunately, there have been only a few studies in the literature addressing the erosion behavior of transparent ceramics [1] and the phenomenon still not understood yet. However, studies on other fragile materials such as glass exist and they are numerous. Indeed, research [3] has shown that the erosion of brittle materials is affected by many factors, including the properties of the incident particles (properties of the target materials (i.e., their hardness, their fracture toughness and their surface condition) and the test conditions (i.e., impact speed, impact angle and temperature). In order to limit the undesirable effects caused by erosion with sand, different reinforcement techniques have been proposed [4] to correct the pre-existing superficial cracks on the surface of the spinel and those created by sandblasting.

## EXPERIMENTAL PROCEDURE:

The  $\text{MgAl}_2\text{O}_4$  spinel used is produced from a pure powder marketed by the company Baikowski (La Balme de Sillingy, France). The powder is supplied in three different batches (S25XRX 12, S25CRX 14, Cr30). Three sintering temperatures 1290, 1310, 1330 °C were chosen in order to obtain different microstructures as well as different physical aspects.

Sandblasting of the spinel samples produced was carried out using a horizontal sandblasting device according to the standards for erosion tests by particles suspended in air (DIN 50 332 and ASTM G76). The deposition solution was prepared by the sol/gel method (solution-gelation) using organic precursors TEOS

(tetraethylorthosilicate)  $\text{Si}(\text{OC}_2\text{H}_5)_4$ , MTES  
(methyltriethoxysilane),  $\text{CH}_3\text{Si}(\text{OC}_2\text{H}_5)_3$  and  
Zirconium n-butoxide  $\text{Zr}(\text{OC}_4\text{H}_9)_4$ .

different sintering temperatures for the different  
chemical compositions: (a) S25CRX12, (b)  
S25CRX14 and (c) S30CR before and after  
sandblasting.

## RESULTS AND DISCUSSION

### 1. Effect of sandblasting on the optical properties of sandblasted samples:

Figure IV.4 shows the optical transmission of transparent spinel as a function of sintering temperatures for  $\lambda=550\text{ nm}$  in the raw and sandblasted state for different compositions a) S25CRX12; b) S25CRX14; c) S30CR, we note that:

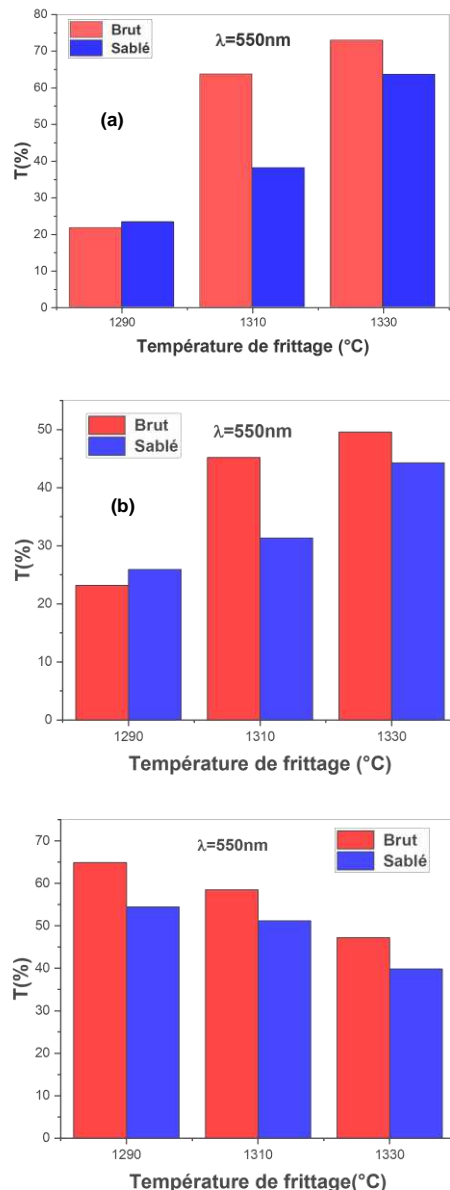


**Figure 2:** The evolution of the transmission of

The results of optical transmission after sandblasting indicate that the values are influenced directly by sandblasting and therefore by the degradation of the surface where we notice all the samples present a reduction in transmission after erosion. This decrease in optical quality, particularly in the case of the S30CR samples, is mainly due to the degradation of the surface condition which led to an increase in the reflection of light on the surface, and a decrease in transmission through the material. This explanation can be better expressed by a characterization of the surface profile.

## II. CONCLUSION

The results obtained allowed us to conclude with the following points: • Optical transmission of the transparent spinel samples decreased after sandblasting the samples regardless of the chemical composition or the sintering temperature. • The coating layer wonderfully corrected the optical properties of the sandblasted samples regardless of the sintering temperature of the sample proven by the increase in optical transmission values. This increase amounts to the correction of surface defects omni present in the surface before sandblasting as well as defects caused by degradation of the surface by erosion. • Correction of optical properties was accompanied by improvement in surface condition investigated by profilometry.

## REFERENCES

- [1] S. von Helden, et al. « Mechanical properties, wear resistance and surface damage of glasses and  $\text{MgAl}_2\text{O}_4$  spinel ceramic after abrasion and scratch exposure », *Ceramics International*, vol. 45, no 8, p. 10765-10775, juin 2019.
- [2] N. Hakmeh, « Elaboration et caractérisation de luminophores et céramiques optiques IR à base d'(oxy)sulfures », thèse de doctorat, Université Rennes 1, 2014.
- [3] B. A. Lindsley et A. R. Marder, « The effect of velocity on the solid particle erosion rate of alloys », *Wear*, vol. 225-229, p. 510-516, avr. 1999, doi: 10.1016/S0043-1648(99)00085-X.
- [4] A. Ayadi « Hybrid  $\text{SiO}_2\text{-ZrO}_2$  coatings for restoring and repairing glasses damaged by sandblasting », *Ceramics International*, vol. 46, no 8, p. 10634-10640, juin 2020, doi: 10.1016/j.ceramint.2020.01.067.

# Etude des caractéristiques mécaniques du polymère Cellulose dans l'alfa et le coton

N.Hakimi<sup>1</sup>, N.Ouslimani<sup>2</sup>

1. Laboratoire de Croissance et Caractérisation de Nouveaux Semi-Conducteurs, Département de Génie des Procédés, Faculté de technologie, Université Sétif 1 (19000) Sétif Algérie.
2. Laboratoire de Traitement et Mise en Forme des Polymères Fibreux. Département Génie des Procédés Industriels, Faculté des Sciences de l'Ingénieur, Université M'hamed Bougara, Avenue de l'Indépendance, (35000) Boumerdes Algérie.

## Résumé

Dans notre travail on essaie d'établir la grande similitude que présente le polymère dans les deux matériaux et ce, en divisant la tâche en deux volets :

1.-Délignification de l'Alfa par un procédé chimique au sulfate pour en séparer la cellulose ; le rendement réalisé est de 52,2% (par rapport au poids sec absolu) ; cette demi pâte est alors blanchie à l'hypochlorite de sodium jusqu'à obtention de 72° de blancheur (par rapport à MgO).

2.-Détermination de la contenance en cellulose pure, des degrés de polymérisation moyen, observations microscopiques des fibres et comparaison avec la fibre de coton.

Le rendement en fibres au blanchiment réalisé est de 43% et la quantité de cellulose pure est de 26,4% ; ces deux résultats permettent d'envisager l'utilisation de la fibre cellulosique contenue dans l'alfa à raison de 80% , en mélange avec 20% de composants biodégradables sans sulfate d'ammonium en pensant combiner et traiter les fibres avec une composition chimique naturelle et non corrosive pour assurer leur longévité ; On pourrait alors envisager de les proposer à la conception d'enveloppes isolantes qui protègent les bâtiments résidentiels et commerciaux de la condensation, du gel et de l'humidité offrant une garantie pour la vie du bâtiment, pour sa résistance thermique et acoustique ; solution permettant de tenir compte à la fois de l'environnement, de la santé et de la qualité de vie tout en réduisant substantiellement les coûts et la consommation d'énergie. On devrait néanmoins évaluer les recettes de collecte du végétal, de son prétraitement (coupage et dépoussiérage) car porteur d'une grande quantité de poussière et sa délignification car on la propose chimique en présence de température.

**Mots CLES :** La cellulose, L'Alfa, Le coton, Valorisation de matériaux

## I. INTRODUCTION

La cellulose est un polysaccharide, de formule  $(C_6H_{10}O_5)_n$  son degrés de polymérisation peut atteindre une valeur de 14000[1]. Principal constituant des végétaux, la cellulose est la matière organique la plus abondante sur Terre (plus de 50 % de la biomasse) [2]. Ce polysaccharide existe à l'état naturel et représente une ressource quasi inépuisable de matière première et renouvelable. [3]. Le coton en est la source la plus importante [4]. Dans le reste des végétaux la cellulose constitue 40 à 50% [5] en dépendance de l'espèce, l'âge et différents autres paramètres. La commercialisation de produits d'origine naturelle, renouvelables et biodégradables permettrait de créer de nouveaux matériaux (et ainsi de nouveaux procédés) et de protéger notre environnement : souci majeure du siècle. De plus, cela dynamiserait des industries dans divers domaines : la papeterie, l'emballage, la santé (pansements, prothèses), le bâtiment (composites) ou encore le transport (pneumatique). [6] Importante matière première industrielle. Elle peut servir soit sous forme de fibres brutes à la fabrication de pâte à papier, soit, après transformation dans l'industrie chimique, à la fabrication de fibres textiles artificielles (acétate de cellulose, viscose, rayonne [7] et divers produits dérivés (acétate de cellulose, cellophane, celluloid, etc...) ou d'explosifs comme les nitrates de cellulose, nitrocellulose.

## II. Matériel et méthodes

Pour les essais on a utilisé l'Alfa, récupéré de l'entreprise CELPAP de Baba Ali servant communément à la fabrication de pâte à papier. Le végétal a été dépoussiéré couper et cuit dans une solution de soude additionnée de sulfure de sodium



(NaOH + Na<sub>2</sub>S), dans des conditions de laboratoire et selon les paramètres résumés dans le tableau suivant :

Tableau 1. Paramètres de cuisson

Sulfidite %	pH	Température au palier	Hidromodule	Palier (mm)
20	13,3	150	8	90

La demi-pâte obtenue a présenté les caractéristiques représentées dans le tableau suivant :

Tableau 2. Propriétés de la pâte obtenue

rendement en fibres %	Contenance en cellulose %	Contenance en lignines %	Degrés de blancheur	Indice de cuisson (Kappa)	Minéraux (%)
52,2	62,2	21,3	72	19,6	4,6

### III. Détermination de la résistance mécanique.

Les propriétés mécaniques sont d'une grande importance lorsqu'il s'agit de fixer le domaine d'utilisation. Dans notre cas, ou le polymère doit être utilisé comme appoint, il doit répondre à la fois à une bonne résistance et surtout à grande souplesse ; caractère généralement acquis après un raffinage, mais parce que coûteux relativement à la destination du produit, on a donc essayé une purification à la soude (17,5%) de façon à obtenir la cellulose à degrés de polymérisation le plus élevé possible : (Cellulose alpha.) ; 24,2% est la contenance obtenue sur notre végétal. Pour mesurer la résistance mécanique de la fibre on a procédé à la confection de formettes de pâte à raison de 91 g/m<sup>2</sup> de cellulose blanchie et épurée pressée par un rouleau de 10 Kg et séchée à l'air pendant 72 heures (dans une salle conditionnée). Cette formette a été transformée en bandes de papier de 200mm de longueur et 15mm de largeur qu'on a soumis par les extrémités à une traction, entre les mâchoires d'un dynamomètre ; on relève alors la résistance à la traction, qui est la force de tension à laquelle la bande se rompt et de là on déduit l'allongement qui caractérise la propriété d'extensibilité. 2,8% pour notre fibre contre un

allongement de 5% sur le coton de Sidi Amer.

### IV. Conclusion

Les résultats réalisés : DPm cellulose Alfa = 360 et P cellulose Coton = 985 et surtout les résistances mécaniques des fibres ( 2390m pour la fibre d'Alfa blanchi et traité à la soude 17,5% ,contre 7200 m pour le coton, encourageraient logiquement l'utilisation de la cellulose de coton ; mais quand on raisonne avec un caractère économique on opte pour l'utilisation de la cellulose d'Alfa , abondante en Algérie et son domaine d'utilisation est restreint à la fabrication de pâte à papier, au fourrage, anarchique d'ailleurs, et quelque peu à l'artisanat. La fibre de coton trouverait plus noble usage dans les domaines de la santé et du textile. Destinée

À la fabrication de panneaux d'isolation une utilisation de cellulose d'Alfa, écru, serait plus indiquée rendement en fibres et les caractéristiques physiques (résistance et souplesse) sont très convenants ; Par contre pour des synthèses ou des nanotechnologies (éthanol, nano composites), les procédés de blanchiment et purification seraient de rigueur, suivis même d'une recristallisation, la destination exigeant un haut degré de pureté. Ce travail permettrait de remettre en question la culture de l'Alfa, végétal endémique répandu en Algérie et véritable source de cellulose et dont l'absence d'intérêt et d'apports sylvicoles menacent de disparition, surtout depuis l'arrêt des entreprises papetières de Baba Ali et Mostaganem.

### References

- [1] GNU, *Free Documentation License Version 1.2*, November 2002
- [2] IMAG-CNR Via De Marini, 6, 16149 Genova, Italie
- [3] J. Baffes: *World Bank Policy Research Working Paper 3218*, February 2004.
- [4] . Soprintendenza per i Beni Culturali ed Architettonici della Liguria Via Balbi.; 10, 16126 Genova, ITALIE
- [5] . Hauchart V., 2005. *Culture du coton et dégradation des sols dans le Mouhoun (Burkina Faso)*, Thèse de géographie, GEGENA (EA3795), Université de Reims-Champagne-Ardenne, 428 p.
- [6] . M.M. Blanco Carmona J.G.Juste Picon S.,Rodriguez Gaston P. et al. *Occupational asthma and contact urticaria caused by mukali wook dust (Anigeria robusta)*. *Journal of investigational allergology and clinical immunology*, 1995, 5 (2) pp. 113-114
- [7] D. Klemm, B. Philipp, T. Heinze, U. Heinze et W. Wagenknecht, *Comprehensive Cellulose Chemistry par éditions Wiley-VCH* 1998.
- [8] La conception bioclimatique - des maisons confortables et économes, Ed. Terre Vivante 2006
- [9] Samuel Courgey et Jean-Pierre Oliva, *Journal of pulp and paper science* ISSN 0826-6220 CODEN JPUSDN

***Session T7: Tribology  
and industrial  
applications***

# Etudes des fissures dans les tôles embouties fabriquées par l'entreprise nationale SONARIC.

FATIHA KERAGHEL<sup>1</sup>, SAMIR TEBBANE<sup>1</sup>

Institute of Optics and Precision Mechanics, Laboratory of Non-Metallic Materials, Ferhat Abbas University Sétif  
1,19000, Algeria, f\_keraghel@univ-setif.dz

## ABSTRACT(1,000 characters)

Les déchirures dans les tôles métalliques embouties sont un problème courant dans l'industrie de la fabrication automobile. Ces déchirures se produisent lorsque la charge appliquée localement est excessive, ce qui entraîne une instabilité locale et fait que la tôle métallique se fissure [1]. Ces déchirures peuvent compromettre la qualité et la fonctionnalité du produit fini, entraînant ainsi des coûts de production plus élevés. Pour mieux comprendre le phénomène des déchirures dans les tôles métalliques embouties, il est nécessaire d'examiner les facteurs qui contribuent à leur occurrence. Ces facteurs comprennent la friction à l'interface entre la tôle et l'outil d'emboutissage, ainsi que l'usure des surfaces de l'outil[2]. L'usure de l'outil peut entraîner des changements dans les conditions aux limites du processus d'emboutissage et influencer considérablement la productivité et la qualité du produit final. En outre, il est important d'étudier l'évolution de la contrainte associée à la diminution de l'épaisseur lors de la déformation de la tôle métallique. Cette connaissance est essentielle pour comprendre les mécanismes de défaillance et de rupture dans le processus d'emboutissage des tôles métalliques. Les déchirures dans les tôles métalliques embouties peuvent être causées par plusieurs facteurs, notamment la superplasticité et la ductilité du matériau, ainsi que la géométrie de la pièce emboutie. Il est donc crucial de mettre en place des méthodes et des procédés appropriés pour prévenir et minimiser les déchirures dans les tôles métalliques embouties. Dans cette optique, différentes méthodes ont été développées et étudiées afin d'améliorer le procédé d'emboutissage des tôles métalliques et de réduire le risque de déchirures. L'objectif de cette étude est d'identifier les causes principales des déchirures, sur les tôles embouties fabriquées par l'entreprise nationale SONARIC.

Les résultats obtenus ont permis de tirer les conclusions suivantes :

- L'analyse chimique a révélé un taux de carbone de 0,05 %, conforme aux exigences pour les aciers destinés à l'emboutissage (0,05-0,08 % de carbone).
- L'essai de dureté a montré une dureté d'environ 62,66 HRB, qui se situe dans la plage requise pour les aciers destinés au formage.
- L'étude de traction a indiqué que la direction 0° (sens de laminage) est la plus adaptée pour le formage.
- Les observations microscopiques ont révélé la présence de la phase ferritique.

Cette étude nous conduit à penser que le problème de la striction des emboutis provient probablement d'un défaut de l'outillage.

## KEY WORDS

Tôles minces, acier, emboutissage, fissures

## REFERENCES

- [1] Huajun W. and al, Friction Shear Stress on the Surface of Iron-Based Coating/HSS during Sliding Wear of Pin Disk, Journal of Applied Mathematics and Physics, 2017
- [2] Bernd-Arno B. and al, Advanced Wear Simulation for Bulk Metal Forming Processes  
Matec Web of Conferences, 2016

# Characterization of enameled steel sheets

FATIHA KERAGHEL<sup>1</sup>, SAMIR TEBBANE<sup>1</sup>

Institute of Optics and Precision Mechanics, Laboratory of Non-Metallic Materials, Ferhat Abbas University Sétif  
1, 19000, Algeria, f\_keraghel@univ-setif.dz

## ABSTRACT

The purpose of this study is to determine the main causes of the so-called chipping defects that occur in the enameled plates produced by the national company Sonarik and intended for the manufacture of gas heaters. Enamel was successfully produced on the plate to be studied in the laboratory. We examined the influence of factors such as cooking temperature, cooking time and water in solution on the performance of enamel deposition. The results showed that at a temperature of 800 ° C, the cooking is not completed and the residue of ferrite powder is still observed, at a temperature of 815 ° C, the vitreous phase begins to appear and at 830 ° C the percentage of the vitreous phase has clearly increased. Regarding the time factor, 6 minutes. Finally it was possible to verify that the increase in the amount of water in the solution is responsible for the formation of hydrogen gas bubbles that are originally causing nail strikes

KEY WORDs (Steel; Silicon; Aluminum oxide; Kaolin; Enamel; defects.)

## I. INTRODUCTION

for several years, humans have been constantly searching for high-quality materials with decorative aspects (presentable appearance, visual appeal, etc.) that are also corrosion-resistant, hence the use of metal surface treatment. surface treatments and coatings are currently essential means of improving the functional properties of metals, including resistance to oxidation and corrosion, fatigue strength in all forms (mechanical, thermal, and surface), friction and wear resistance, covering power, adhesion, impact resistance [1], and not forgetting color and aesthetic appearance [2].

Among these surface coatings, enamel coating on steel sheets is one of the most commonly used. The principle consists of depositing one or more layers of enamel onto a surface of suitable quality steel that has been prepared beforehand. By definition, enamel is a

mixture of natural inorganic materials from the glass family. It is composed of refractory elements, fluxes, and adhesion agents, which in turn constitute opacifiers and various metallic oxides. The latter are responsible for the coloration of the enamel.

The enameling process generally includes several stages: surface preparation, preparation of the enamel slurry, application of the enamel onto the surface, drying, and finally, high-temperature firing, which creates chemical bonds between the enamel and its support, promoting adhesion.

Today, enameling on steel has become a high-tech process that requires the use of highly sophisticated base products combined with modern and highly developed implementation methods. Enameled steel is a material that meets modern standards: longevity, aesthetics, and hygiene [3]. In this work, we carried out the study and microstructural and mechanical characterization of an enamelled steel initially developed by the slip enamel technique. The principle consists of immersing the sheets in the slip, then removing them and letting them dry. After the application of the slip, the sheets are heated at high temperature, usually in an oven, to melt the enamel powder and make it adhere to the surface of the steel. This step is essential to ensure a smooth and uniform finish of the enamel coating. The slip enamel technique is appreciated for its ability to produce durable and aesthetically pleasing enamel coatings on steel sheets, which protects them against corrosion and improves their visual appearance.

## II. GENERAL INFORMATION ON ENAMELING OF STEELS

### A. DEFINITION OF ENAMEL

The enamel is a glass obtained by melting at high temperature between 1000°C and 1300°C. The main constituent is silica. Enamels have variable compositions depending on the type of substrate to be

enamelled. Figure 1 shows a micrograph representing the morphology of an enamelled steel.

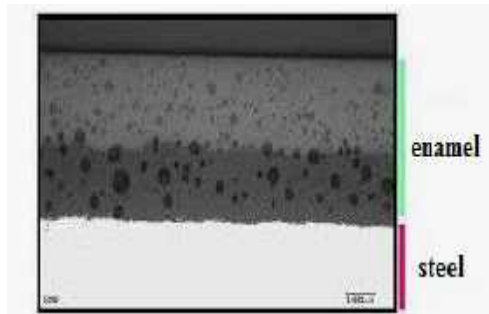


Figure 1- Micrograph of an enameled steel [4]

#### a. omposition of enamel

#### B. COMPOSITION OF ENAMEL

Enamels belong to the family of glasses and are essentially made up of silica oxide ( $\text{SiO}_2$ ). They can be either alkaline borosilicates or complex alkaline-earth. They are composed of refractory materials, fluxes, and additive elements [3].

#### C. CHARACTERISTIC OF ENAMEL

Generally, enameling must have certain characteristics such as:

- Resistance to chemical agents and attack by aqueous media;
- Resistance to thermal shock;
- Resistance to corrosion in the domestic environment; Each characteristic will require a specific study and various controls will be necessary. Some will be specific to a type of enamel, while others will be common [5].

##### -Adhesion

Good adhesion of the enamel to the substrate is essential. In the case of enameling on steel sheet, the European standard EN 10209 defines a measurement method using a shock test machine [6].

##### -Abrasion resistance

Enamel, as a siliceous material, is comparable to glass in terms of hardness. Many methods have been experimented with in order to determine the

resistance of enamel to abrasion and scratching. The Taber apparatus test (which consists of mounting the sample (thickness  $<6\text{mm}$ ) on a horizontal rotating table and subjected to the effect of wear wheels. The test is carried out for a well-determined cycle, then the sample is visually inspected or weighed to determine the layer removed. The mass loss must be a maximum of  $10\text{g}/\text{m}^2$ . The test is not indicative for an evaluation of the loss of shine.

##### -Thermal shock resistance

Classic enamels, as well as ceramic coatings, are chosen materials to solve problems related to sudden temperature variations. Common enamels can withstand sudden temperature variations of over  $100^\circ\text{C}$  without damage (heating appliances, kitchen utensils, exhaust pipes). Thermal shock resistance is influenced by different factors:

- Thickness of the enamel layer;
- Thermal expansion;
- Thermal conductivity of the coating;
- Elasticity and adhesion of the enamel.

##### - Microbial resistance

Food residues pose a risk of microbial proliferation harmful to health in the agri-food industry (collective and household catering). Studies on cleanability and bacterial colonization on various surfaces have shown the excellent performance of smooth enamelled coatings, which, along with shiny stainless steel, provide the highest level of hygiene safety [7].

##### - Corrosion Resistance

Resistance to water, acids, and bases, as well as protection against corrosion by atmospheric agents, have made enamels an effective means of surface protection. There are many types of enamels. Some are resistant to acids (except hydrofluoric acid), others to bases when it is necessary to have enamels resistant to the attack of alkaline solutions. Many products, combined with the initial composition of the frit, tend to improve this resistance. Among them, alumina and silica added during liquid grinding have beneficial effects. The amount of clay, its quality, and the fineness of the enamel play a significant role. Anti-acid enamels are more suitable for household items, sanitary and electrical appliances, and architectural panels. In general, the resistance of an enamel to acids increases with the silica content,

while fluxes such as alkali oxides decrease it. For many years, titanium dioxide has played a key role in the composition of acid-resistant enamels. There is also a range of special enamels designed to resist many chemicals at temperatures above 200°C. These silica-saturated enamels, without any porosity or cracks, are both anti-acid and anti-basic.

### III. CHOICE OF THE SHADE OF THE METAL SUPPORT

The sheets used for the manufacture of enameled articles belong to two families of steels: cold-rolled sheets and hot-rolled sheets [8].

- Cold-rolled sheets:

The most commonly used ones belong to the category of extra soft steels, which have a low mass fraction of carbon and very low mass fractions of impurities, with a typical composition given in Table 1.

**Table 1 - Chemical composition of cold-rolled steel sheets.**

Elements	C %	Mn %	P %	Si %	N %
Mass fraction %	<100	<500	<0,030	<0,040	<0,015

The thickness of these products ranges from 0.5 to 3 mm, and the EN 10209 standard defines seven grades based on their suitability for stamping and enameling.

- DC 01 EK, DC 04 EK and DC 05 EK, carburized steels (about 0.050%) intended for conventional enameling using a mass layer.
- DC 03 ED and DC 04 ED, decarburized steels (less than 0.004%) obtained by decarburizing annealing and intended mainly for direct enameling without a mass layer.
- DC 05 EK and DC 06 ED, interstitial-free steels for very difficult stamping intended respectively for conventional enameling and direct enameling.

- Hot-rolled sheets:

They are generally thicker (at least 1.5 mm) and enameling is usually only guaranteed on one side (to avoid the risk of nail blows). These grades S300 EK and S240 EK have a particular chemical composition and are used for the manufacture of water heaters. For hot-rolled steel sheets as well as for cold-rolled sheets, the transformation from cast iron to steel is carried out using a pure oxygen converter: LD process for top-blowing, LWS process for bottom-blowing [9]. In all cases, it is imperative to choose a grade specifically adapted for enameling to avoid defects called nail blows [10].

### IV. STUDY MATERIALS AND EXPERIMENTAL TECHNIQUES

#### A STUDIED MATERIALS

Our work focuses on mesh defects, therefore the materials used in this study are extra soft low-carbon steel sheets of grades NF EN 10209 DC04 EK. These sheets are cold-rolled and are commonly used for conventional enameling and are intended for the manufacture of household appliances. The chemical composition was determined using the optical emission spectrometer technique. The sheets are used as a substrate for a mesh layer consisting of Clay, Sodium Nitrite, K100, Borax, K91, K12, Quartz.

#### B EXPERIMENTAL TECHNIQUES.

- The Optical Emission Spectrometry

The spectrometric analysis in our case was carried out at BCR Ain-Elkhebra Sétif on a Thermo brand device. The principle of the Optical Emission Spectrometry (OES) analysis method is defined as follows: the atoms in a sample are excited by the energy of ultraviolet (UV) light provided by an electric arc produced between the probe electrode and the sample. This causes the atoms to heat up to very high temperatures, and the excited atoms emit light at a characteristic wavelength. Analysis of this light provides information on the elements contained in the material being studied.

- Measurement of Roughness

The roughness measuring instrument used in our study to analyze the surfaces of the sheets is of PGI Optics type and is available at the Institute of Optics and Precision Mechanics. The operating principle of the roughness meter is as follows: the substrate-carrying stage is beneath the stylus, which consists of



a diamond conical tip with a spherical cap of radius  $10\mu\text{m}$  at its end. An inductive system detects a level variation of  $0.05\mu\text{m}$ . The stylus is mechanically coupled to the core of the coil of a linear differential transformer (L.V.D.T). During the scanning of the stage, the stylus moves over the surface to be measured. The stylus thus moves vertically in response to the surface profile. This movement of the stylus causes the displacement of the L.V.D.T. core, generating analog signals that are then converted into digital signals by a very high precision analog-to-digital converter. We measured the roughness  $R_a$ , which is the arithmetic average that allows for qualitative comparison of various surface conditions.

This movement of the stylus causes the displacement of the L.V.D.T. core, generating analog signals that are then converted into digital signals by a very high precision analog-to-digital converter. We measured the roughness  $R_a$ , which is the arithmetic average that allows for qualitative comparison of various surface conditions.

#### - Measurement of Hardness

The hardness measurement was carried out using a Qness Q30 type microdurometer available at the Institute of Optics and Precision Mechanics. This device is equipped with a camera with a 5 MP resolution connected to a computer that allows the visualization of imprints on a screen. The results are processed using the QPix T2 software, and the magnification ranges from 100 to 1000x. This device allows the measurement of Vickers and Brinell hardness, with a load range varying from 0.25 g to 31.5 kgf.

#### -The tensile test

The tensile test was performed using a Zwick/Roell Z100 universal testing machine, which is available at the Institute of Optics and Precision Mechanics. The test conditions were set as follows: a preload of 2 N and a testing speed of 0.2 mm/min.

#### - Microscopic observation

The microscope used is a universal OXIO microscope from the Euromex brand. It is equipped with an 8 MP resolution camera connected to a computer, allowing for visualization on a screen. The results are processed using "Image Focus alpha"

software, and the magnification ranges from 50 to 1000 times.

#### - Enamel development technique

We carried out the enameling operation as follows:

- We took samples from the treated plate shown in figure 2.A, and samples from the untreated plate shown in figure 2.B

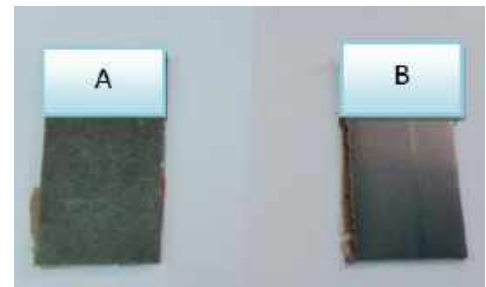


Figure 2- Treated sample (A);  
Untreated sample (B).

- Then, we put them in the oven at a temperature of  $815^{\circ}\text{C}$  for 6 minutes (Figure 3):



Figure 3- Baking oven

- Once the enamel-coated sample (Figure 4) is obtained, we proceed to observe it under the microscope.



Figure 4- Enamelled samples

To study the causes of enamel peeling, we have modified several parameters such as temperature, cooking time, and water proportion.

## V. RESULTS AND DISCUSSION

### A CHARACTERIZATION OF THE STEEL SHEET MATERIAL TO BE STUDIED

-Analysis of the chemical composition of the studied steel sheets

Table 2 represents the chemical composition of the steel sheet used for enameling, determined by optical emission spectrometry.

**Table 2 - The chemical composition of steel sheet**

Elem ents	C	Si	M n	P	S	Cr	Mo
Fract ion %	0,04 4	0,03 3	0,2 95	0,0 14	0,00 2	0,01 2	0,0 05
Elem ents	Al	Co	Cu	Nb	Ti	V	W
Fract ion %	0,07 38	0,00 04	0,0 02	0,0 06	0,00 09	0,00 23	0,0 14
Elem ents	As	Ca	Ce	Se	B	N	Fe
Fract ion %	0,00 9	0,00 01	0,0 00	0,0 00	0,00 19	0,00 33	99, 47

According to the analysis results, it can be observed that the steel sheet used has a low carbon content. Additive elements such as molybdenum are present in trace amounts. These steels belong to the family of ferritic steels.

### B STUDY OF THE ROUGHNESS OF THE SHEETS

The measurement of the roughness of the studied sheet was carried out before and after a chemical treatment involving the successive immersion of the sample in several baths, starting with a bath of soapy water (using industrial soap), followed by a bath of water to remove soap residue, and finally in a bath of

sulfuric acid (at a concentration of 50 kg/m<sup>3</sup> of water).

-Before the surface treatment

The figure 5 shows the scanning directions of the studied surface..



Figure 5- Representation of the scanning direction of the sheet before treatment.

The surface profile scanned in direction 1 is shown in figure 6

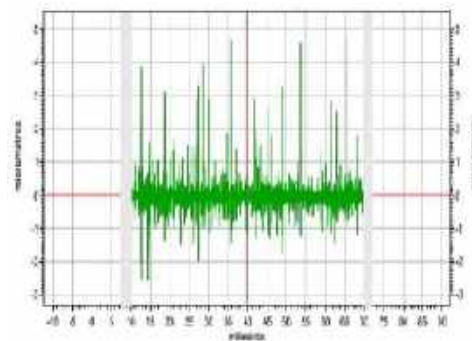


Figure 6- The profile of line 1

The arithmetic roughness  $R_a$  of this profile was found to be 0.2072  $\mu\text{m}$

The surface profile scanned in direction 2 is shown in figure 7

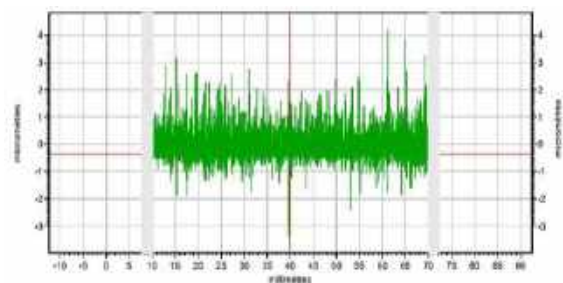


Figure7- The profile of line 2

The arithmetic roughness  $R_a$  for this case is about  $0.3593 \mu\text{m}$ .

-After the surface chemical treatment

The surface profile scanned in direction 1 is shown in figure 8

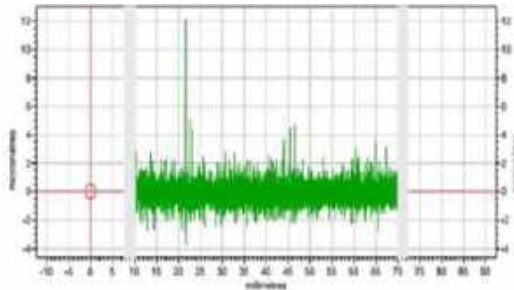


Figure 8- The profile of line 1

The arithmetic roughness  $R_a$  is of the order of  $0.4729 \mu\text{m}$ .

The surface profile scanned in direction 2 is shown in figure 9

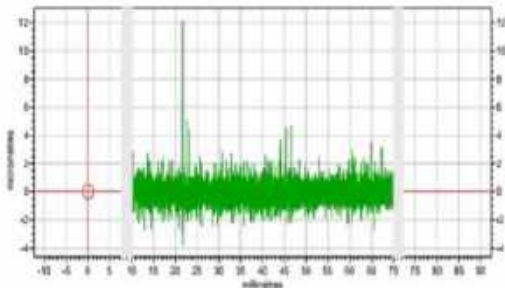


Figure 9- The profile of line 2

The arithmetic roughness  $R_a$  is around  $0.4245 \mu\text{m}$ .

According to the roughness results, an increase in roughness is observed after the surface treatment process, which is desirable as the sheet surface should be rough enough to promote adhesion of the enamel layer.

## B MECHANICAL CHARACTERIZATION

### - Hardness test

The table 3 presents the results of the hardness test, where it can be seen that the average hardness of the sheet is approximately  $(137.75 \pm 0.10)$  HV.

**Table 3- Result of the hardness test**

Test	1	2	3	4	Moyenne numbers
Hardness (HV)	139	130	147	135	$137,75 \pm 10$

### - The tensile test

The tensile test was performed under uniaxial loading, in order to obtain information about the elastic behavior, plastic behavior, and degree of resistance to rupture of the sheet under study. Figure 10 shows an example of a stress-strain curve obtained during the tests carried out on the studied sheet metal

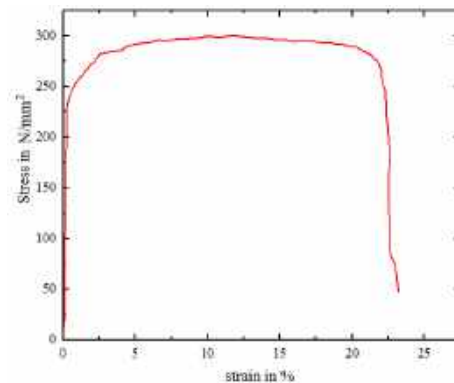


Figure 10 - Tensile curve of the studied sheet metal

In order to verify the reproducibility of the test, we conducted 3 trials. The average values of the mechanical properties are as follows: the Young's modulus is approximately 51.5 GPa, the yield strength is around 238.75 MPa, and the maximum tensile strength is approximately 300 MPa.

## C CHARACTERIZATION OF ENAMELED SHEETS

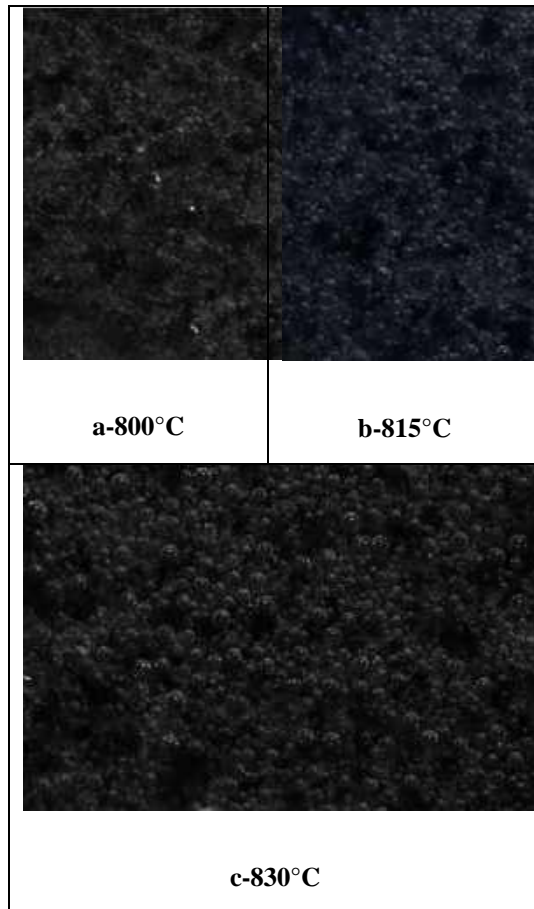
### -Characterization of enameling

#### a- The influence of the baking temperature

To study the influence of the appearance of gas bubbles (hydrogen) on the occurrence of the defect known as "enamel flaking", we varied the cooking temperature from  $800^{\circ}\text{C}$  to  $830^{\circ}\text{C}$  while keeping the cooking time at 6 minutes. We observed that at  $800^{\circ}\text{C}$  (Table 4-a), the cooking was not yet complete, as evidenced by the presence of powder residues, and that fine gas bubbles were appearing. This observation can be explained by the fact that the moisture ( $\text{H}_2\text{O}$ ) and oxygen ( $\text{O}_2$ ) from the furnace

atmosphere penetrate the porous enamel and oxidize the steel. A layer of iron oxide forms at the interface between the enamel and the steel, and atomic hydrogen (derived from  $H_2O$ ) diffuses into the steel and fills the traps present in the steel. At  $815^\circ C$ , the solubility of  $H_2$  in ferrite increased, which explains the increase in the diameter of gas bubbles (Table 4-b). Around  $830^\circ C$  (Table 4-c), we observed an evolution in the morphology of gas bubbles and the beginning of the appearance of the vitreous phase.

Table 4 - Micrographs showing the influence of the baking temperature

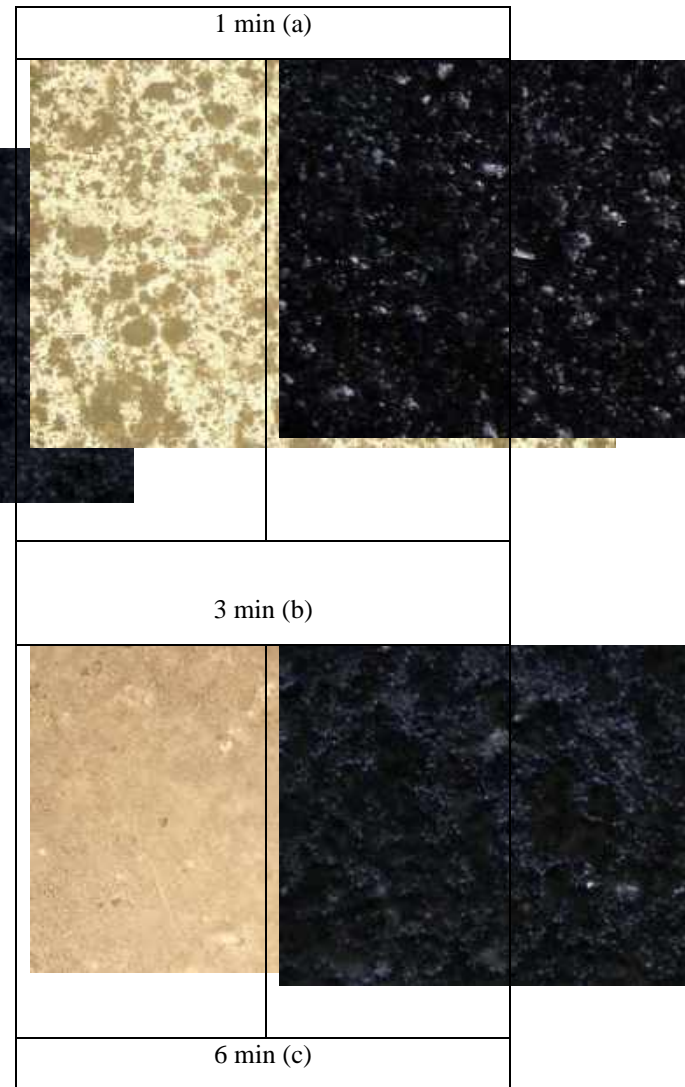


#### b- The influence of cooking time

To study the influence of cooking time on the quality of enamel, we kept the cooking temperature at  $815^\circ C$  while varying the cooking time from 1 minute to 6 minutes according to Table 5. For a duration of one minute, as presented in Table 5-a, we observed that there was almost no fusion of the slurry, and the silica remained practically intact. When we increased the

cooking time to 3 minutes, we observed the appearance of the vitreous phase as well as the beginning of the formation of gas bubbles. For a duration of 6 minutes, we observed an evolution of the vitreous phase and the morphology of hydrogen gas bubbles.

Table 5 - The micrographs showing the influence of cooking time



#### c- The influence of water percentage

##### 1- The influence of the water percentage on the enamel structure

To study the influence of the quantity of water in the slip on the appearance of a defect, we followed the following protocol: we fixed the firing temperature at  $815^\circ C$  and the time at 6 minutes, while varying the amount of water in the slip. Table 6

shows the micrographs for the different water concentrations. For a concentration of 55.70%, the appearance of gas bubbles was activated, leading to a non-homogeneous structure and an increase in bubble size (Table 6-a). For a percentage of 52.84%, we observed an improvement (Table 6-b): the size of gas bubbles decreased, and the structure became more homogeneous. As for the concentration of 36.12% (Table 6-c), the structure was significantly improved.

## 2- The influence of water percentage on enamel thickness

To observe the impact of concentration on the thickness of the enamel layer formed on the surface of the sheet, we followed the following method: We immersed half of the sample in a barbotine solution. After cooking and the formation of an enamel layer, we measured it eight times and calculated the mean and standard deviation. The formula (1) to obtain the mean thickness of the enamel layer is as follows:

$$E_{moy} = \frac{1}{N} \sum E_i \quad (1)$$

N: the number of measurements,

$E_i$ : thickness of the enamel layer

The calculation of the standard deviation is done according to the following formula (2):

$$\Delta E(x) = \frac{1}{N} \sqrt{\sum (E_i - E_{moy})^2} \quad (2)$$

$E_{moy}$ : The mean value

The thickness of the layer is given by the following

$$\text{formula (3): } E = E_{moy} \pm \Delta E \quad (3)$$

Table 6 summarizes the results of thickness measurements as a function of water percentage. The values reported are the means. It can be observed that as the water concentration increases, the thickness of the enamel layer decreases. This can be explained by the relationship between the viscosity of the barbotine and its adherence to the sheet.

Table 6: Thicknesses of enamel layers obtained for different water concentrations

	Sample (55,7% )	Sample (52,8%)	Sample (36,12%)
<b><math>E_{moy}</math> (μm)</b>	94,86	114,2	181,66
<b><math>\Delta E</math> (μm)</b>	1,63	1,04	0,73

## VI. CONCLUSION

In this study, we examined the enameling process on low carbon steel sheets. Generally, enameling of steel sheets aims to impart high mechanical characteristics, such as hardness, excellent resistance to oxidation and corrosion, as well as improved decorative and aesthetic appearance.

The process involves applying a layer of slip with a well-defined composition onto the surface of the treated steel. The results of our study allowed us to draw the following conclusions:

- Chemical composition analysis showed that the studied material is indeed suitable for enameling;
- Surface characterization showed that the roughness of the studied sheets is adequate for the adhesion of the enamel layer;
- Increasing the firing temperature accentuates the formation of hydrogen gas bubbles, which are responsible for defects called "blistering" or "nail marks";
- A firing time of 6 minutes is necessary for the formation of the vitreous phase;
- Increasing the water content in the slip promotes the formation of gas bubbles;
- Lower viscosity results in a thicker enamel layer, while thinner enamel layers show faster occurrence of defects;

Finally, our study confirmed that water concentration is responsible for the occurrence of blistering defects

## REFERENCES

- [1] Robert L'évêque, « traitement et revêtements de surface des métaux », 2013
- [2] Yvette, les Adhérents « Émaillage des métaux », Techniques de l'ingénieur, 10 juin 2010.

- [3] Arcelor Mitral, les aciers pour émaillage et l'acier émaillé .guide d'utilisation.
- [4] Acier –émaillage-Philippe Gousselot.Octobre 2014
- [5] Méthodes d'essai et de mesure en émaillage .Farben fabriken Bayer, p.83
- [6] Million . Thèse sur la nature de l'adhérence email-acier. SOLLAC (1989)
- [7] C. Harf, etude de la decontamination de surface de materiau à usage menager.Larebron Université Louis Pasteur, strasbourg (1991)
- [8] G.Blanchard, Fabrication et caractéristiques des tôles minces pour émaillage.1972
- [9] M. Cagnet, Aciéries de conversion. [M 7 650], Traité Matériaux Métalliques (mars1989)].
- [10] B.Walker, Fischscale formation in enameiled sheet steels (Formation du coup d'ongle dans les tôles d'acier émaillées). Inst. Vitreous Enamellers, vol. 20, 33 fig., n\_1, p. 22-52 (1969)].



# Statistical modelling of the fracture resistance of brittle materials: case of concrete

A. BOUKELLOUDA<sup>1\*</sup>, T. KHEFFACHE<sup>2</sup>, AND N. CHELOUAH<sup>3</sup>

1. Department of Civil Engineering, Faculty of Technology, University of Bejaia, 06000 Bejaia, Algeria, [abdelhafid.boukellouda@univ-bejaia.dz](mailto:abdelhafid.boukellouda@univ-bejaia.dz)
2. Laboratory of Construction Engineering and Architecture (LGCA), Faculty of Technology University of Bejaia, 06000 Bejaia, Algeria, [toufik.kheffache@univ-bejaia.dz](mailto:toufik.kheffache@univ-bejaia.dz)
3. Laboratory of Construction Engineering and Architecture (LGCA), Faculty of Technology University of Bejaia, 06000 Bejaia, Algeria, [nasser.chelouah@univ-bejaia.dz](mailto:nasser.chelouah@univ-bejaia.dz)

## ABSTRACT

*Concrete is a composite material used extensively in the construction industry. The material is characterised by high compressive strength and low tensile strength and also by brittle failure. The average compressive strength of concrete used in construction for design purposes is a deterministic value, but in general it is not sufficient to reliably describe the fracture characteristics of this material due to its fluctuation. In general, this value cannot be a sufficient data to write reliably the characteristics of the failure of this material due to its fluctuation. Hence the need to use approaches based on the notion of probability which allows taking care of the distribution of the variations of the compressive strength. This work presents a statistical study of the variation in compressive strength of made from local materials. The results obtained showed significant differences in strength for all the age classes studied and especially for the youngest age. To arrive at a model that takes into account the quantification of the rate of crushing of the specimens, the Weibull model was used. This model allows the dispersion of the responses measured during the tests to be taken into account.*

**KEY WORDS:** Strength, Dispersion, Weibull, Variation, Concrete, Statistical.

## I. INTRODUCTION

Materials used by in civil engineering practice such as concrete are brittle failure materials and show significant variability in tensile or compressive strength, also variability in failure mechanisms [1]. It becomes necessary to quantify the different variations with adequate statistical descriptors that allow the representation of the results from the experiment. Specimens of similar sizes and from the same materials show different values of strength, which makes it possible to establish a relationship between

compressive strength and specimen size [2] and the amount of existing defects [3-4]. The state of the material prior to loading plays a very important role in the evolution of the crushing and failure of the specimens. Concrete is a heterogeneous material made up of components with very different morphological, mechanical and physico-chemical characteristics. This heterogeneity the presence of defects in the microstructure of the concrete is inevitable and is a source of strength variability. These defects, which take the form of macro-pores and cracks within the material, introduce additional stresses concentrated at geometric singularities [5]. The additional stresses generated vary from one element to another, which leads to variability in the nominal strengths of concrete specimens made and maintained under the same conditions. Also, other defects can be caused during the making of the concrete and its placing in the moulds or formwork because, during the pouring, the bleeding is due to the gravity, which is all the more important when large aggregates are present [6]. The average fracture stress of the specimens used in the sizing and modeling calculations remains a deterministic value which cannot constitute sufficient data to reliably describe their fracture characteristics. This is what justifies the need to use probabilistic statistical approaches to fracture based on the notion of acceptable fracture probability. In this work, we present statistical modeling of the variation in compressive strength of a set of specimens made and kept under the same conditions. The crushing tests were carried out at different ages, 7 days and 28 days. The results obtained showed a significant dispersion of the compressive strength for all ages. The two-parameter Weibull-type statistical model will be used in this work to take into account the heterogeneity of the material, which is assumed to be the source of the

dispersions measured on the stress-at-break values during the tests.

allow efficient reviewing of submissions by the Sc

## II. MATERIALS AND METHODS

### a. Cement

The cement used in this work is high strength class cement, CEM II 42.5 from the AIN KEBIRA (Sétif) cement plant, which meets all specifications of Algerian standard (NA 442).

### b. Aggregates

The aggregates (sand and gravel) used for the making of the concrete come from the quarry of Adrar Oufarnou(Bejaia), the production of the quarry can supply the whole region of Bejaia. These aggregates are crushed products of calcareous nature, are marketed as granular classes: sand (0/3), gravel (3/8), gravel (8/15) and gravel (15/25). The characterisation of these products is necessary, since these aggregates occupy about 70 to 80% of the volume of the concrete.

The physical characteristics of these aggregates are shown in Table 1.

**Table1.** Physical characteristics of the aggregates used

Physical Characteristics	Sand 0/3	Grave 8/15	Grave 15/25
Absolute density (g/cm <sup>3</sup> )	2,45	2,62	2,55
Bulk density (g/cm <sup>3</sup> )	1,51	1,38	1,33
Fineness module (MF)	2,63	-	-
Los Angeles Coefficient (%)	-	30	30
Nature Calcareous	Calcareous	Calcareous	Calcareous

## III. EXPERIMENTAL PROTOCOL

The concerts used in this study were formulated according to the Dreux-Gorisse method to produce a common concrete. The composition for 1 cubic metre of concrete is given in Table 2.

**Table 2.** Composition of concrete according to Dreux

Constituent	% of aggregates	Dosage of constituents (Kg/m <sup>3</sup> )
Gravel 15/25	35	609
Gravel 8/15	31	555
Sand 0/3	34	571
Cement	--	350
Water	--	175

The mixes were prepared and stored in accordance with the specifications of EN 206-1. The concretes

were poured and placed by vibration in cylindrical moulds (diameter = 16 cm and height h = 32 cm). After casting, the cylindrical moulds were stored in a humidity chamber for 24 hours at  $20 \pm 1^\circ\text{C}$  and a relative humidity of over 90%. After 24 hours, the samples were removed from the moulds and placed in a tray filled with water until the age of the test.

Two series of 06 cylindrical concrete specimens were made, i.e. a total of 12 cylindrical specimens, to evaluate the compressive strength according to destructive (crushing) technique at different ages: 7 days and 28 days.

All the specimens tested showed that cracks propagate randomly throughout the specimen volume. These cracks originate on the lateral surface and are due to tensile stresses developed by the fish effect [7]. Radial deformations generate tensile stresses that lead to the appearance of the first cracks. The concrete material may contain heterogeneities that constitute privileged sites for crack initiation [7].

The size, position, shape and orientation of the defects are determined by the manufacturing process [8].

It can be seen that the mode of crack propagation depends on the age of the concrete. For the 7-day old specimens, the majority of the failures are located in the cement matrix, which can be explained by the fact that this is the weakest part where cracks can easily propagate.

The activation of defects and the appearance of cracks will generate tensile stress concentrations in weak areas, firstly the aggregate/cement paste interfaces where micro cracks will initiate, then in the cementitious matrix and finally in the aggregates, especially the coarse grains [9].

The compressive strengths of the specimens at different ages (7 and 28 days) are shown in figures (1 and 2) using destructive technique (crushing).

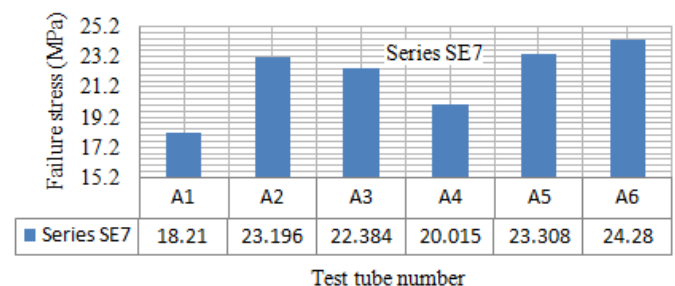


Fig. 1. Variation in compressive strengths from one specimen to another in the SE7 series

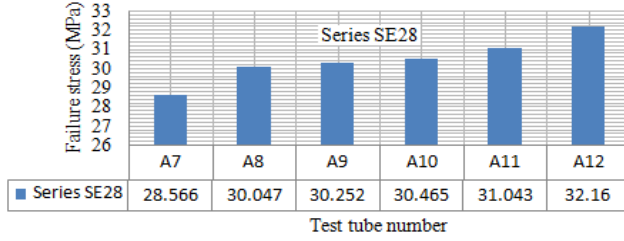


Fig. 2. Variation in compressive strengths from one specimen to another in the SE28 series

In figures (1 and 2), we can see a variation in the compressive strengths of specimens of the same age, made and kept under the same conditions. This variation may depend on several parameters that are difficult to combine, including the presence of possible defects in the volume studied and their distribution [10].

The results of the compressive strength tests are characterised by a high degree of dispersion. This can be explained by the decrease in the number of defects in the specimens as a result of the hardening of the concrete, and also by the variation in their distribution in the specimen volume [10]. The heterogeneous character of this material is probably the cause of the dispersion of the results obtained.

#### IV. STATISTICAL MODELLING

For brittle quayside materials such as concrete, the distribution of defects is the main cause of failure. Experimental results show that statistical analysis is the best way to take defects into account [11]. While the compressive behaviour of concrete can be considered brittle, with the first macro crack leading to failure, the value of the stress at failure varies significantly from sample to sample. As the distribution of defects is random, the maximum stress reached also has this random aspect [12].

The objective of this modelling is to use a statistical model, and to determine a failure criterion more representative of the experimental findings.

The probability of rupture is given by the formula (1) below [13]:

$$P_r = 1 - \exp \left[ - \left( \frac{\sigma}{\sigma_0} \right)^m \right] \quad (1)$$

The identification of the Weibull parameters is based on the experimental dispersion obtained on the fracture strengths of the specimens.

Then using the linear regression method, we obtain formula (2), posing:

$$\begin{aligned} X &= \ln(\sigma_R) \text{ and } Y = \ln [-\ln(1 - P_R)] \\ Y &= mX + B \end{aligned} \quad (2)$$

The resulting regression lines that best describe the trend of the observed cloud are shown in Figures (3 and 4) below:

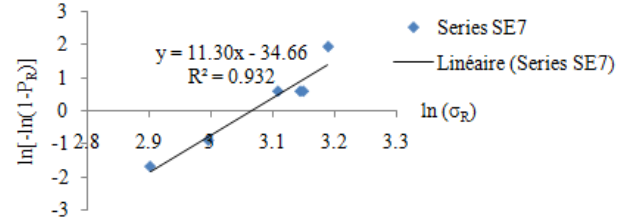


Fig. 3. Weibull diagram for the SE7 series

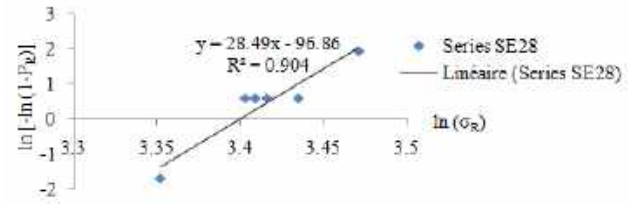


Fig. 4. Weibull diagram for the SE28 series

The Weibull parameters obtained from the modelling for each series of specimens are shown in the following Table 3.

**Table 3.** The Weibull parameters for each set of specimens

Test tubes	Coefficient of Determination R <sup>2</sup>	B	m	σ <sub>0</sub> = exp(-B/m)
S <sub>7</sub>	0,932	-34,66	11,30	21,483
S <sub>28</sub>	0,904	-96,86	28,49	29,958

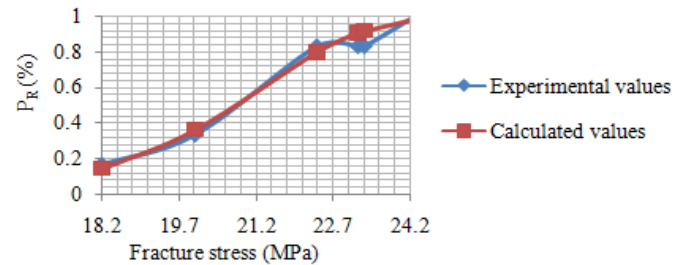


Fig.5. Comparison of the results obtained for the SE7 series

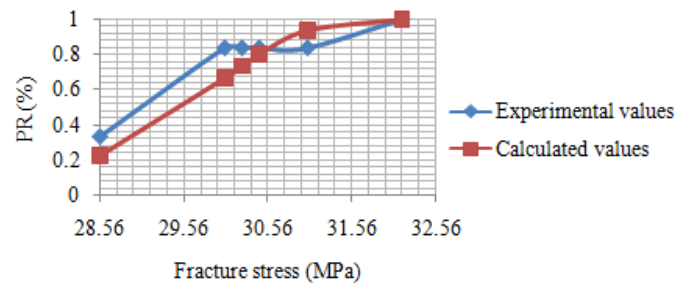


Fig.6. Fig.5. Comparison of the results obtained for the SE28 series

## V. INTERPRETATIONS OF RESULTS

The linearization of the curves shows a linear trend and the Weibull modulus varies with the age of the specimen.

The coefficient of determination  $R^2$  is close to 1, which means that the scatter plot is close to the regression line.

The Weibull modulus is located in the range of concrete [5 -50]. The latter is an indicator of the dispersion.

A low value of  $m$  was recorded for the SE7 series, i.e. the dispersion is greater at younger ages.

The Weibull model is adequate for the SE7 and SE28 series since it explains more 90 % of the variation of  $Y$  in  $X$ .

The results obtained by the two calculations show almost the same pattern with a slight deviation, which means that the formula obtained can represent the failure of the specimens under a given loading.

## VI. CONCLUSION

The study was conducted with the objective of showing the statistical character of the variation of the compressive strength of concrete. The following conclusions can be highlighted:

- The bridge cloud can be represented by  $Y$  regression lines in  $X$ .

- The Weibull modulus is an indicator of the dispersion, it varies with the age of the test tube.

- The coefficient of determination  $R^2$  is close to 1, which means that the scatter plot is close to the regression line.

- The Weibull model is adequate for all the series studied.

- The experimental and calculated results show the same pattern with a slight shift.

- The Weibull model is satisfactorily applicable and appears to be used to describe the behaviour of brittle materials such as concrete.

## REFERENCES

[1] S. Kherris, M. Makhlouf, Dj. Zebbar, and O. Sebbane "Contribution study of the thermodynamics properties of the ammonia-water mixtures". J. Therm. Sci.

Vol.17 N°3. pp.891-902 (2013).

[2] L.E. Kinsler, A. Frey, R. Coppens, A.B. Sander. J.V. "Fundamentals of Acoustics". JohnWiley& Sons, Inc.

Fourth Edition (2000)

[3] D. Aaron, "First Steps toward Automatically Generating Bipedal Robotic Walking from Human Data, in: Krzysztof Kozłowski, Robot Motion and Control 2011". Lecture Notes in Control and Information, Volume 422, Springer. pp. 89-116 (2012).

[4] R.S. Langley, "The dynamic analysis on uncertain structures", in: Proceedings of the Seventh International Conference on Recent Advances in Structural Dynamics, Southampton, pp.1-20 (2000).

[5] D. Zebbar, "Study and elaboration of a methodology of determination of thermal state of cylinder group elements in marine diesel engine", PhD thesis, Astrakhan Technical State University, Astrakhan (20005).

[6] G.Benkechkache, H. Houari, "Étude du comportement différé des bétons autoplaçants : influence des paramètres de composition et de chargement", Mémoire de magister, Université Mentouri Constantine, (2007)

[7] E. Thieulot-Laure, "Méthode probabiliste unifiée pour la prédiction du risque de rupture en fatigue", Thèse, École normale supérieure de Cachan – ENS Cachan, France, NNT: DENS0011, (2008)

[8] X. Regal, "Caractérisation du comportement en traction du béton sous fortes sollicitations : essais de flexion trois points aux barres de Hopkinson, Autre", Thèse, Université d'Orléans, Français, NNT: ORLE2003, (2016)

[9] T. Calais, "Propriétés mécaniques et durabilité d'un béton léger application en régions froides", Thèse, Université Laval Québec, (2013)

[10] A. Boukellouda et al., "Étude statistique de la variation de résistances à la compression du béton", Matériaux & Techniques 108, 406 (2020)

[11] H. Carre, "Étude du comportement à la rupture d'un matériau fragile précontraint : le verre trempé", Thèse, École Nationale des Ponts et Chaussées, France, (1996)

[12] F. Nazaret et al., "Caractérisation et prédiction de la sensibilité à l'effet d'échelle du béton réfractaire renforcé de fibres métalliques (BRRFM), CROMeP", École des mines d'Albi-Carmaux, France, (2006)

[13] W. Weibull, A statistical distribution function of wide applicability, J. Appl. Mech. 18, 293 (1951)

# Effect of solution treatment on the martensitic transformation in NiMnSn Heusler alloy

A.BEKHOUCHE<sup>1,\*</sup>, S. ALLEG<sup>1</sup>, K. DADDA<sup>1</sup> AND J.J. SUÑOL<sup>2</sup>

1. Laboratory of Magnetism and Spectroscopy of Solids (LM2S), Department of Physics, University Badji Mokhtar Annaba, B.P. 12, Annaba 23000, Algeria. [ahlembekhouche46@gmail.com](mailto:ahlembekhouche46@gmail.com)
2. Dept. physics, University of Girona, Campus Montilivi, Girona, 17071, Spain.

## ABSTRACT

*Ni<sub>50</sub>Mn<sub>37.5</sub>Sn<sub>12.5</sub> Heusler alloy was prepared from high-purity elements by arc melting under a protective argon atmosphere. Structure and microstructure have been investigated by X-ray diffraction (XRD), and scanning electron microscopy (SEM). The crystal structure consists of a monoclinic 14 M martensite belonging to space group P21b/m. The disappearance of the martensitic transformation in the alloy might be related to the presence of the dendritic as-cast structure. After annealing at 1173 K for 24 h, the dendritic structure partially disappeared, and the martensitic transformation occurred.*

## KEY WORDS (3 to 6 key words)

Heusler alloys ; Martensitic transition ; SEM ; XRD.

## I. INTRODUCTION

Heusler-based Ni–Mn shape memory alloys have attracted much attention in technological applications due to their diverse multifunctional properties during the martensitic transition (MT). This transition occurs from a cubic austenitic phase at high temperatures to a martensitic phase at low temperatures [1, 2]. Ni–Mn–Sn alloy system is an excellent magnetic shape memory alloy candidate for practical applications due to its nontoxicity and low cost [3, 4]. The present study aims to investigate the effect of the solution treatment on the structural and microstructural properties of NiMnSn Heusler alloy.

## II. MATERIALS AND METHOD

Polycrystalline Ni<sub>50</sub>Mn<sub>37.5</sub>Sn<sub>12.5</sub> alloy (AC-NMS) was prepared by conventional arc-melting from pure starting elements under an argon atmosphere in a water-cooled Cu crucible. A piece of the ingot was annealed in a quartz capsule for 24 h at 1173 K and

quenched in ice water (HT-NMS). The structural, microstructural, and morphological changes of the as-cast and annealed samples were investigated using X-ray diffraction (XRD) in a  $\theta$ -2 $\theta$  Bragg Brentano geometry using Cu-K $\alpha$  radiation ( $\lambda_{Cu} = 1.54056 \text{ \AA}$ ), and scanning electron microscopy (SEM) Zeiss DSM-960A.

## III. RESULTS

The Rietveld refinement of the XRD patterns reveals the formation of a single monoclinic modulated 14M martensite structure belonging to space group P21b/m for both samples.

Figure 1 shows the back-scattered SEM micrographs of the as-cast and annealed samples. The morphology of the as-cast sample (AC-NMS) indicates the existence of black and white regions that can be related to dendritic and martensitic structures, respectively. The heat treatment leads to the disappearance of the dendritic structure. The randomly dispersed black points in the microstructure are probably the shrinkage pores formed during solidification [5].

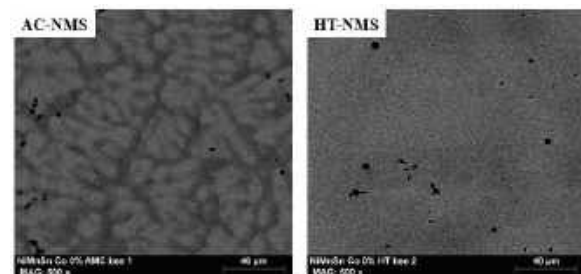


Fig. 1. Fig. 1: Typical SEM micrographs of as-cast (AC-NMS) and heat-treated samples (HT-NMS).

## IV. CONCLUSION

Ni<sub>50</sub>Mn<sub>37.5</sub>Sn<sub>12.5</sub> Heusler alloy was prepared by arc melting. The alloy exhibits a monoclinic 14M martensite structure in the as-cast and heat-treated

samples. A high temperature and long annealing time are essential to obtain the complete homogeneity of the composition of this alloy system.

## REFERENCES

- [1] Krenke, T., Duman, E., Acet, M., Wassermann, E.F., Moya, X., Mañosa, L., et al. Magnetic superelasticity and inverse magnetocaloric effect in Ni-Mn-In. *Physical Review B*. 2007, 75, 104414.
- [2] Bachaga, T., Rekik, H., Krifa, M., Sunol, J., Khitouni, M. Investigation of the enthalpy/entropy variation and structure of Ni-Mn-Sn (Co, In) melt-spun alloys. *Journal of Thermal Analysis and Calorimetry*. 2016, 126, 1463-8.
- [3] Pons, J., Chernenko, V., Santamarta, R., Cesari, E. Crystal structure of martensitic phases in Ni-Mn-Ga shape memory alloys. *Acta Materialia*. 2000, 48, 3027-38.
- [4] Krenke, T., Acet, M., Wassermann, E.F., Moya, X., Mañosa, L., Planes, A. Martensitic transitions and the nature of ferromagnetism in the austenitic and martensitic states of Ni-Mn-Sn alloys. *Physical Review B*. 2005, 72, 014412.
- [5] Wu, Z.-g., Li, H.-y. Effect of solution treatment on the martensitic transformation behavior of a Ni<sub>43</sub>Co<sub>7</sub>Mn<sub>39</sub>Sn<sub>11</sub> polycrystalline alloy. *International Journal of Minerals, Metallurgy, and Materials*. 2015, 22, 620-6.



# Improvement of cementitious materials by using artificial aggregates

H. SLIMANOU<sup>1</sup>|A. BOUZIANE<sup>2</sup>|L. FACI<sup>3</sup>| T. MENDIL<sup>3</sup>| N. BOUZIDI<sup>1</sup>

1. Laboratory of Materials Technology and Process Engineering (LTMGP), University of Bejaia, 06000, Algeria, Houssam.slimanou@univ-bejaia.dz./ nedjmabouzidi@yahoo.fr
2. Laboratory of Construction Engineering and Architecture (LGCA), University of Bejaia, 06000, Algeria, abderrezak.bouziane@univ-bejaia.dz
3. Construction Materials Laboratory, Civil Engineering Department, University of Bejaia, 06000, Algeria, lilialola1357@gmail.com/ mendilkahina50@gmail.com,

## ABSTRACT (1,000 characters)

*In the aim of conserving natural resources and protecting the environment, it is appropriate to study the possibility of recycling wastes generated by various industrial and/or other activities, in the concrete sector. The aim of this work is to contribute to the recovery of artificial aggregates (ie: ceramic wastes) by incorporating them into a cementitious matrix (self-compacting concrete). The behavior of concretes in which natural gravel (8/15 and 3/8) has been substituted by ceramic wastes at different weight contents of 10, 20, 30% has been studied. Based on the results, it was found that compressive strength increased as the addition of artificial gravel was increased, while porosity decreased with the gradual incorporation of artificial gravel. ceramic wastes could be used to produce value-added construction material and solve environmental pollution challenges*

## KEY WORDS

Ceramic, self-compacting concrete, artificial gravel, water absorption, porosity, compressive strength

## I. INTRODUCTION

Waste is any residue from a production, transformation or consumption process, which the owner or holder is obliged to dispose of or eliminate [1]. The disposal of ceramic waste materials presents a number of problems (the space taken up by storage sites, high costs, impact on the environment, etc.), and the construction industry has problems not only at the end of the life cycle of these products, but also at the beginning.

To this end, a number of research projects have been carried out to investigate the possibility of using ceramic waste as an additive in the formulation of

cementitious materials (self-placing concretes) [2]. Waste can be transformed into recycled aggregates to be used, in fill of various kinds, as aggregates for concrete.

This work consists of using ceramic residues after having been crushed, dried and then sieved at fractions 8/15 and 3/8 and incorporated into self-compacting concrete by replacing the volume of gravel (natural) with a fraction of 3/8 and 8/15. by percentages (10%.20% and 30%). Each base material that constitutes these materials is used either to recover local materials or to reuse industrial waste.

## II. MATERIAL AND METHODS

### a. MATERIAL

Two granular classes of gravel are used in this work, a fraction 3/8 and another of 8/15 and a crushed sand of fraction 0/4 coming from the quarry of Bouadjil wilaya of Sétif pet of fraction 0/1 (Sablière Boussaâda). The wastes used in our study come from the valorization of earthenware waste rejected by the SCS factory (Béjaia) in nature after having been recovered, crushed and sieved to fractions of diameter 3/8 and 8/15 (mm).

We used a superplasticizer adjuvant called "Tempo 12" manufactured by SIKA in Eucalyptus - Algiers. It is based on ether polycarboxylates, and the usual range of use is 0.4 to 1.5% of the weight of cement or binder. The cement used to formulate the different concrete compositions is a class 42.5 CPJ CEM II/N cement from the Ain El-Kebira cement plant (wilaya of Sétif). The additions used in our research are elements with dimensions of less than 80µm. calcareous fillers, from ENG d'EIKhroub, noted UF20

## b. METHODS

Particle size analysis N F EN 933-1 [3] is used to determine the size and respective weight percentages of the different families of grains making up the sample. The test consists of classifying the different grains making up the sample using a series of sieves, nested one on top of the other, with openings decreasing in size from top to bottom.

Absolute density is determined in accordance with the standard NF P 18-554 [4], and is the mass per unit volume of the material making up the aggregate, without taking into account any voids that may exist in or between the grains. The test involves measuring the absolute density of aggregates using a pycnometer.

The absorption coefficient of aggregates " NF. P 18-555 [5] for materials can present an internal porosity that is detrimental, in particular, to the frost resistance of concrete! the water in the aggregate causes the concrete to burst when subjected to prolonged low temperatures.

The most important characteristics for the application of BAP are fluidity, viscosity and resistance to segregation. These recommendations have become the reference on-site tests for validating a BAP formula. Sieve stability test according to standard NF EN 12350-11 [6]. It allows to test the segregation of the fresh mixture. The spreading test EN, B. (2010). 206-9 [7] has become the easiest test to perform. It is used to measure the consistency or flow of concrete.

Compressive strength NF P 18-406 [8] is the most important characteristic sought for hardened concrete. Water absorption is determined according to ASTM C373 [9]. The amounts of the raw materials used in this study are presented on Table 1 (BAT is control concrete). The plan of the different mixtures is presented on Fig. 1.

Table 1. Concrete compositions BAT

Raw materials	cement	air	filler	water	sp	0/1	0/4	3/8
BA <sub>t</sub>	435	1	41.76	189.4	4.77	427.6	268	579

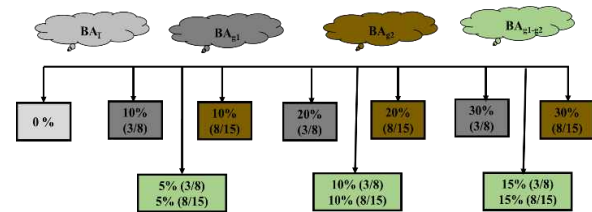


Fig. 1. The plan of the different mixtures.

## III. RESULTS ET DISCUSSION

In order to make the best use of ceramic waste, fresh and hardened tests were carried out at ages of 7 and 28 days, in order to observe the progressive evolution of performance.

### a. Tests on fresh concrete

The results of the particle size analyses of 0/1, 0/4, 3/8, 8/15 sand and artificial gravel are shown in the Fig.2. The fineness modulus of the sand is 3.16, which is  $2.8 < M_f < 3.2$ , i.e. it's a coarse 0/4 sand that needs to be corrected with another 0/1 sand.

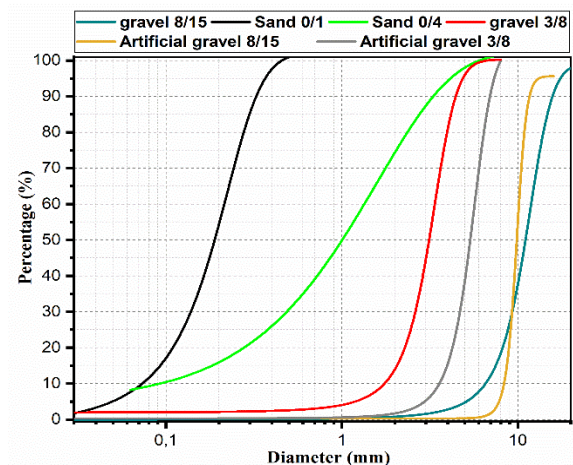


Fig. 2. Particle size analysis

The fineness modulus of the 0/1 sand tested is equal to:  $0.19 < 1$ , i.e. our sand is very fine. 3/8 and 8/15 gravel with a fineness modulus of 2.4 and 0.75 respectively, and artificial gravel gives a fineness modulus of 0.16 and 0.06 for the 3/8 and 8/15 fractions respectively.

Apparent and absolute density values for 0/1, 0/4, 3/8, 8/15 sand and artificial gravel are shown in Table 2. The absolute density is  $3.12 \text{ g/cm}^3$  and the specific surface Blaine  $3715 \text{ cm}^2/\text{g}$ , so the density of limestone filler is  $2.7 \text{ g/cm}^3$ .

The water absorption rate of natural gravel is lower than that of artificial gravel the upper limit of the water absorption coefficient of the aggregate is set at 5%, i.e.

$Ab < 5\%$ . So, in our case, this property is verified for the natural gravel used, but not for the artificial gravel.

**Table 2.** Physical characterization

Granulats	Sand 0/1	Sand 0/4	Gravel 3/8	Gravel 8/15	Ceramic 3/8	Ceramic 8/15
Bulk density (g/cm <sup>3</sup> )	1.62	1.56	.50	1.44	0.79	0.70
Absolute density (g/cm <sup>3</sup> )	2.59	2.67	2.71	2.73	1.96	2.09
Water absorption rate (%)	2.01	1.80	1.66	1.33	12.66	10

#### b. Tests on fresh concrete

The slump flow test is used to characterize concrete fluidity; the results are shown in Fig. 3. According to this figure, it can be seen that all the spread values obtained by all the BAPs are between 65.5 and 72.25 cm, so the specification condition has been correctly met by the various concretes (According to standard (NF EN 206 – 9 [10]), the spread of a self-compacting concrete can vary between (550 and 850 mm)).

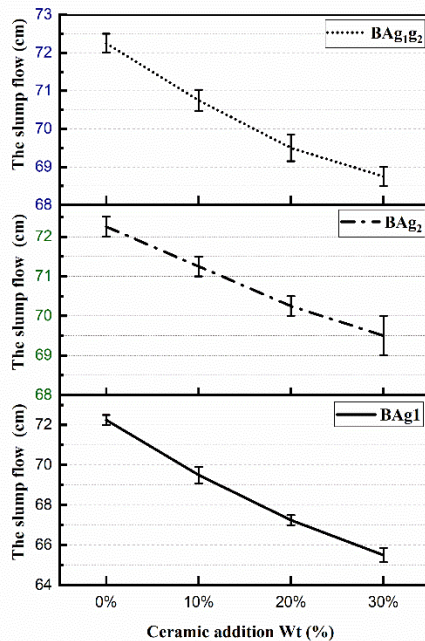


**Fig. 3.** Result of the slump flow

The Fig. 4 shows the sieve stability test values for the various self-compacting concrete formulations studied. The results show that all the ready-mixed BAPs are characterized by stability well below the limit values ( $< 20\%$  or  $< 15\%$ ) recommended by the standard NF EN 206 – 9 [10].

In the general case, ceramic waste reduces the amount of laitance, resulting in improved stability (less bleeding and better resistance to segregation). In fact, the replacement of  $BA_T$  by the quantity of waste (3/8) has no positive influence on segregation resistance, the result being explained by the fact that the grains of the mineral addition improve the granulometry and compactness of the  $BA_P$ , which can result in increased stability [11].

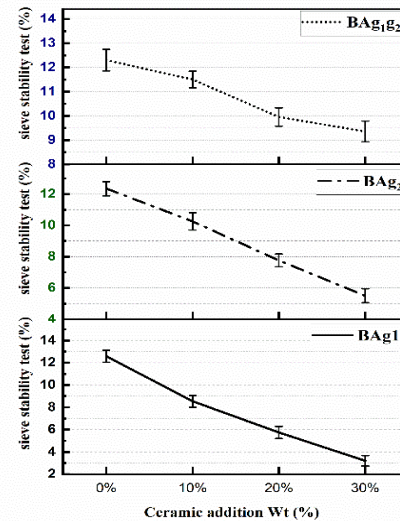


**Fig. 4.** Results of the sieve stability test

#### c. Tests on hardened concrete

In Fig. 5, 6 and 7, the strengths are plotted as a function of time, and it can be seen that the concrete strengths increase with time. Mechanical strength increases proportionally with artificial gravel content, i.e. with class 3/8 and 8/15, so mechanical strengths increase as a function of the age of the composite, whatever the artificial gravel content. The strength of Control concrete gives a value of 41.2 and 49.78 Mpa for 7 and 28 days respectively. Substitution of 30% of the natural gravel fraction (3/8) and 8/15 increases compressive strength to a value of 41.2 and 49.78 Mpa, respectively for 7 and for 28 days. Similar trend is observed for substitution of the two natural gravel fractions 3/8 and 8/15 at the same time which give 56.26 and 56.23 Mpa, respectively for 28 days.

This increase is perhaps linked to the ceramic grains being harder than those of the substituted gravel, so the introduction of artificial gravel improves concrete homogeneity and the pozzolanic reaction decreases porosity. Thus, the hydration of artificial gravel leads to its dissolution and precipitation: C-S-H (gel) [12]. Finally, chemical components and particle size

composition are the main parameters influencing the mechanical behavior of the composite under tests.

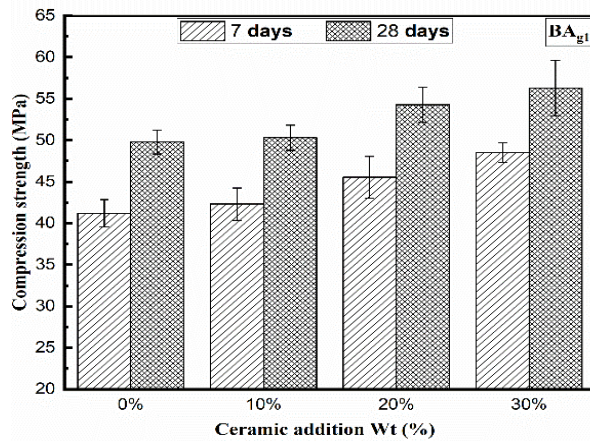


Fig. 3. Compressive strength with Is substitution 3/8.

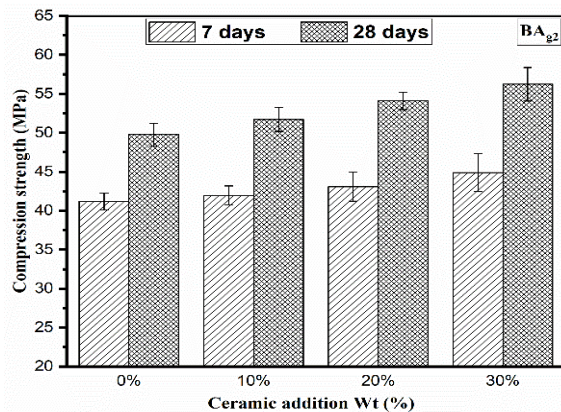


Fig. 6. Compressive strength with Is substitution 8/15

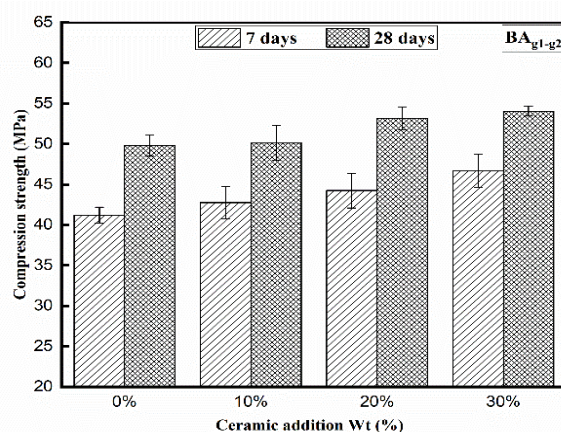


Fig. 7. Compressive strength with Is substitution 3/8 and 8/15

Table 3 grouping together the different values of the water absorption test by capillarity for the different formulations of the self-compacting concretes studied.

Table 3. Water absorption as function of gravel addition

Type of Concrète	Absorption (%) at 7 days	Absorption (%) at 28 days
BA <sub>T</sub>	6.29	4.94
BA <sub>g1</sub>	5.89	3.7
	5.22	2.06
	4.13	1.7
BA <sub>g2</sub>	6.13	3.26
	5.78	2.14
	4.22	1.68
BA <sub>g1-g2</sub>	6.03	3.66
	5.02	2.33
	4.66	1.97

#### IV. CONCLUSION

In this work, we exposed the results of the experimental works which were carried out within the framework of valuation of the waste. We investigated the effect of adding ceramic waste at various percentages (0%, 10%, 20%, 30%) and mixture (5%, 5% and 10%, 10% and 15%, 15%) on the various physic-mechanical properties including compression, water absorption,  $m$ , and also the tests carried out on fresh concrete

According to the results obtained previously, it is concluded that the concretes prepared in fresh states give a good resistance to segregation and for hardened state the concrete gives an increase in resistance with a reduction in porosity due to the pozzolanic reaction of artificial gravels (3/8 and 8/15).

The formulation of artificial aggregate can be used for ordinary concrete but it is necessary to satisfy a certain number of necessary but insufficient criteria to define a correct composition, because this depends on several parameters such as (nature, shape, particle size, etc.). ... aggregates, parameters that are difficult to take into consideration during a theoretical approach.

#### REFERENCES

- [1] Joshi, P. H., & Parekh, D. N. (2023). Valorization of ceramic waste powder as cementitious blend in self-compacting concrete—A review. *Materials Today: Proceedings*.
- [2] Gautam, L., Jain, J. K., Jain, A., & Kalla, P. (2022). Valorization of bone-china ceramic powder waste along with granite waste in self-compacting concrete. *Construction and Building Materials*, 315, 125730.

- [3] EN, N. 933-1.(2012). Tests for geometrical properties of aggregates-Part 1: Determination of particle size distribution-particle size analysis by sieving.
- [4] Norme Française, N. F. P. 18-554 (1979) Mesures des masses volumiques, porosité, coefficient d'absorption d'eau et en teneur en eau des gravillons et cailloux.
- [5] NF, P. P 18-555-Décembre 1990 Granulats-Mesure des Masses Volumiques, coefficient d'absorption et de la teneur en eau de sables.
- [6] EN, N. (2010). 12350-11. Testing Fresh Concrete—Part 11: Self-Compacting Concrete—Sieve Segregation Test.
- [7] EN, B. (2010). 206-9, 2010, Concrete, Part 9: Additional rules for self-compacting concrete (SCC). Lisbon, Portugal. IPQ.
- [8] French standard NF P18-406, Essai de compression, AFNOR, Paris; 1981
- [9] ASTM C373-88Standard test method for water absorption, bulk density, apparent porosity, and apparent specific gravity of fired whiteware products
- [10] EN, N. 206-9, Juin 2010. Béton: partie complémentaires pour le béton autoplaçant.
- [11] Vashistha, P., Kumar, V., Singh, S. K., Dutt, D., Tomar, G., &Yadav, P. (2019). Valorization of paper mill lime sludge via application in building construction materials: A review. *Construction and Building Materials*, 211, 371-382.
- [12] Guendouz, M., Boukhelkhal, D., Bourdot, A., Babachikh, O., &Hamadouche, A. (2020). The effect of ceramic wastes on physical and mechanical properties of eco-friendly flowable sand concrete. *Advanced Ceramic Materials*.



# Title: Elaboration and characterization of perovskite oxide for photocatalyse application

SAMIRA FOUADI<sup>1,\*</sup>, KHADOUDJ GUESSOUM<sup>2</sup>, MELIA HAMICI<sup>1</sup>

1. Ferhat Abbas University, Setif, Algeria

2. A. Mira University, Bejaia, Algeria

Samirafoudi01@gmail.com

## ABSTRACT

*In this work, lanthanum ferrite oxide (LaFeO<sub>3</sub>) was prepared via the sol-gel method. The crystalline structural properties of powders obtained by XRD. Morphological analysis of LaFeO<sub>3</sub> powder surfaces through SEM showed a porous surface. Finally, UV-visible analysis for the study of methyl blue (MB) discoloration under irradiation screws in the presence of nanopowder revealed their strong photocatalytic activity.*

**KEY WORDS** photocatalytic degradation; MB; perovskite; Sol-Gel; SEM.

## I. INTRODUCTION

In recent years, researchers have been working on the development and research of new materials capable of improving performance in the field of water pollution control. Many chemical or physical treatment processes are developed [1-3] and several water treatment methods have been led in recent years to the emergence of new technologies such as advanced POAS oxidation treatment processes [4]-[5]. Heterogeneous photo catalysis is an easy-to-use, clean and promising technology for water pollution control. It is essentially based on the production of active species by a catalyst, ... In addition, materials such as perovskites and became black gold which appreciated as materials that attracted the attention of researchers because of their low cost and remarkable properties guaranteeing their uses in various fields of application . Perovskite oxides are a very special class of materials. Their use in technological applications mainly related to their crystalline structures, electrical [6], catalytic [7], optical and other properties. These properties promote chemical, thermal stability and high catalytic

activity. The crystalline structure of these oxides is generally distinct from the synthesis method. It is well accepted that perovskites can be used in various areas especially for degradation and/or removal of organic pollutants such as dyes.

Perovskite oxides which have the formulation ABX<sub>3</sub>, A is a large cation, B of 6 coordination is a small cation of a transition metal, X anion is usually either oxygen, sulphur, hydrogen, nitrogen or halogen. Thus, perovskites revealed very promising as effective photo-catalysts or irradiation by visible light, because of their crystalline structures and electronic properties.

LaFeO<sub>3</sub> gains significance as a possible "environmentally friendly photocatalyst" because of its abundance, chemical stability, and lack of toxicity.

## II. Materials and Methods

### a. Synthesis of LFO perovskites

The lanthanum ferrite perovskite was synthesized via sol-gel method. According to the stoichiometric composition reactants. Specified amounts of Fe (NO<sub>3</sub>)<sub>3</sub>.9H<sub>2</sub>O and La (NO<sub>3</sub>)<sub>3</sub>.6H<sub>2</sub>O were first dissolved in distilled water (H<sub>2</sub>O). Citric acid (C<sub>6</sub>H<sub>8</sub>O<sub>7</sub> H<sub>2</sub>O) was chosen as a chelating agent (ligands). The molar amount of citric acid was equal to total molar amount of metal nitrates



in solution. The brown gel is placed in an oven for 12 hours at 70°C then the precursor obtained is then crushed, calcined at 650°C.

### b. Photocatalytic Application

3mg of catalyst was poured into beaker 10 ml container of  $10^{-5}$  M MB dey solution with pH=7.6. For two hours, the mixes were held in the dark with continuous magnetic agitation. In order to achieve the adsorption-desorption equilibrium, the latter preparations were exposed to a visible light lamp (150wat) positioned 14 cm above an open-air, double-walled beaker with a cooling system that keeps the reaction temperature at 22°C for two hours while being magnetically stirred.

## III. Results and discussion

### 1.1 Phase analysis

The  $\text{LaFeO}_3$  mixed oxide XR diffractogram prepared with the sol gel method and annealed at 650°C for 6 hours is illustrated in Figure 1. The HIGHSCORE program demonstrated that it was compatible with  $\text{LaFeO}_3$  PDF cards n°01-075-0541. The JANA program refined the peaks such as this method consists of simulating a theoretical spectrum as close as possible to the measured spectrum at from the chemical and crystallographic properties of the present phases and then attempt to minimize the difference between these two by using the least square method. Figure 1 shows the typical XRD patterns of all prepared samples in the  $2\theta$  range of 15–80°. The data show the presence of single phase characteristic of the perovskite structure; therefore, all major diffraction peaks are indexed in the cubic system with preferential growth orientations perpendicular to the crystallographic planes corresponding to the peak (111) (at  $2\theta^\circ = 21.5^\circ$ ), and the  $\text{LaFeO}_3$  lattice parameters are:  $a=3.92\text{\AA}$  of pm3m space group.

The size of the crystallites was calculated using the Scherrer formula [8]:

$$D =$$

$$\frac{\lambda \cdot k}{\beta \cdot \cos \theta}$$

- $\lambda$  (nm): Wavelength of X-ray radiation (1.54178 Å).
- $\beta$  (rad): FWHM, mid-height peak width at any  $2\theta$  in the spectrum.
- K: Scherrer constant usually taken as about 0.89.
- $\theta$ : Angle of diffraction

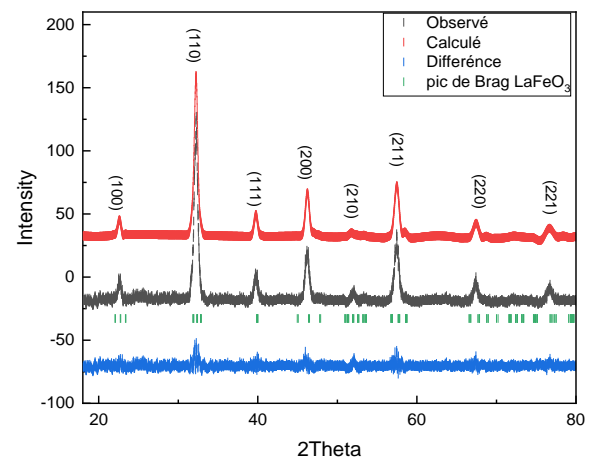


Fig. 1 –  $\text{LaFeO}_3$  x-ray diffraction diffractogram.

**Table 1 - An example of a table g Peak positions, FWHMs and crystallites sizes of the samples.**

Pea k	Position s ( $^\circ 2\text{Th}$ )	FWH M ( $^\circ 2\text{Th}$ . )	d- spacing (Å)	Crystallit es size D(nm)
(100 )	22,624 9	0,472 3	3,9301 5	16.81
(110 )	32,272 9	0,236 2	2,7739 0	33.62
(111 )	39,768 2	0,551 0	2,2666 7	14.41 12.6093
(200 )	46,233 2	0,629 8	1.9636 5	12.6094 11.20
(210 )	52,077 1	0,629 8	1.7562 2	16.81 14.41
(211 )	57,390 3	0,708 5	1.6056 2	
(220 )	67.332 7	0,472 3	1.3906 9	
(221 )	76.743 0	0,551 0	1.2419 3	

## 1.2 Scanning Electron Microscopy (SEM)

The morphological analysis of the powders prepared in this study was made using a scanning electron microscopy (SEM). The morphological aspect obtained is very clear in Figure 2.

Images that the catalysis prepared via the sol gel and annealing method at 650°C are well agglomerated and form clusters of different sizes and shapes. The morphology and distribution of particle size depend on the growth conditions during the synthesis process. The figure shows that the surface has large cavities also MB adsorption can be attributed to the presence of a large number of available empty adsorption sites, This confirms that LFO powder works as well as a catalyst.

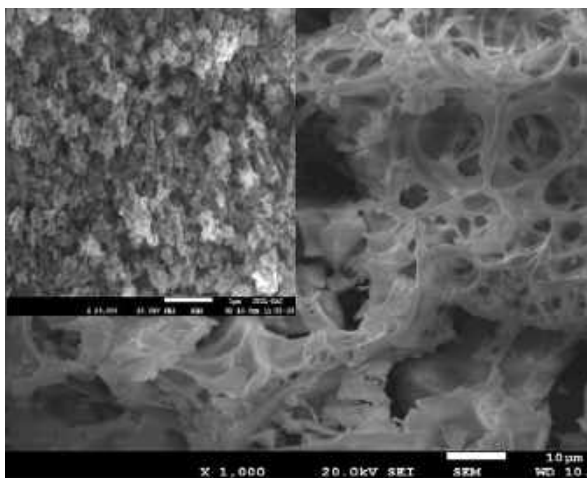


Fig. 2 – SEM image of the as-prepared  $\text{LaFeO}_3$  nanoparticles.

## 1.3 photocatalytic degradation Study

Figure 3 demonstrates that as the initial concentration of organic pollution decreases, the clearance rate of MB rises with time. This is because the dye molecules started to become adsorbed to the solid catalyst particles' surface. Light enhanced the photo-degradation of the MB dye reaction through oxidation and reduction reactions that release potent oxidants ( $\text{OH}\cdot$  hydroxyl radicals) capable of attacking the MB dye molecule to yield ( $\text{H}_2\text{O}$ ,  $\text{CO}_2$ ). With a very high photocatalytic elimination efficiency of 90.02

percent, the photocatalytic activity reaches its peak in roughly 90 minutes.

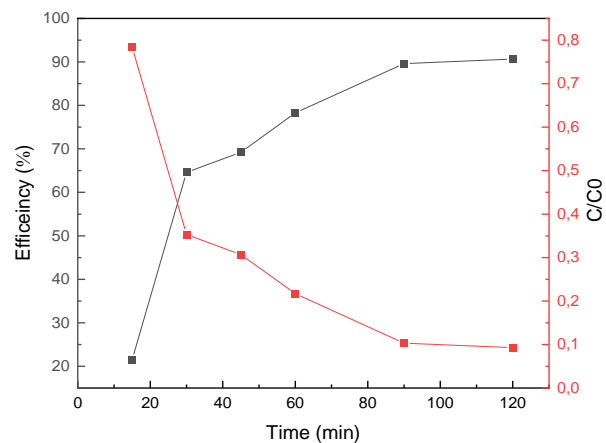


Fig. 3 – Evolution of photo-degradation of MB with LFO catalysts under visible light illumination.

## Conclusion

In this work, we have successfully prepared the photocatalytic nanopowder –lanthanum ferrite  $\text{LaFeO}_3$  with structure perovskite ideal without secondary phase using the sol gel method. The SEM images revealed granular morphologies; apparent cavities are observed, which are favorable for good diffusion of dye molecules. MB degradation experiments confirmed that the catalysts obtained can perform dye removal activity under irradiation by visible light. With a very high photocatalytic elimination efficiency of 90.02 percent.

## REFERENCES

- [1] T. S. Nam, H. V. Thao, N. T. Luan, N. P. Duy, and N. V. Cong, "Optimizing Hydraulic Retention Time and Area of Biological Settling Ponds for Super-Intensive Shrimp Wastewater Treatment Systems," *Water*, vol. 14, no. 6, Art. no. 6, Jan. 2022, doi: 10.3390/w14060932.
- [2] H. Sheetikoff, L. K. Wang, and M.-H. S. Wang, "institutional wastewater treatment by a septic tank, flotation, Filtration and drain

- field system,” \“evolutionary progress in science, Technology, engineering, Arts and mathematics\”, pp. 1–44, Oct. 2022, doi: 10.17613/vdbk-3r92.
- [3] K. Q. Jabbar, A. A. Barzinjy, and S. M. Hamad, “Iron oxide nanoparticles: Preparation methods, functions, adsorption and coagulation/flocculation in wastewater treatment,” *Environmental Nanotechnology, Monitoring & Management*, vol. 17, p. 100661, May 2022, doi: 10.1016/j.enmm.2022.100661.
- [4] P. V. Nidheesh, C. Couras, A. V. Karim, and H. Nadais, “A review of integrated advanced oxidation processes and biological processes for organic pollutant removal,” *Chemical Engineering Communications*, Jan. 2021, Accessed: Oct. 31, 2022. <https://www.tandfonline.com/doi/abs/10.1080/00986445.2020.1864626>
- [5] J. B. Walter, F. Tonholi, and M. B. Rodrigues, “O<sub>3</sub>/UV-type POAs integrated with catalytic material based on scrap iron and mineral clay to degrade 2,4 and 2,6-dinitrotoluene in Red Water,” *Rev. Ambient. Água*, vol. 17, Jun. 2022, doi: 10.4136/ambi-agua.2813.
- [6] F. Zu, D. Shin, and N. Koch, “Electronic properties of metal halide perovskites and their interfaces: the basics,” *Materials Horizons*, vol. 9, no. 1, pp. 17–24, 2022, doi: 10.1039/D1MH01106E.
- [7] C. Feng et al., “Defect engineering technique for the fabrication of LaCoO<sub>3</sub> perovskite catalyst via urea treatment for total oxidation of propane,” *Applied Catalysis B: Environmental*, vol. 304, p. 121005, May 2022, doi: 10.1016/j.apcatb.2021.121005.1016/j.apcatb.2021.121005.
- [8] A. Monshi, M. R. Foroughi, and M. R. Monshi, “Modified Scherrer Equation to Estimate More Accurately Nano-Crystallite Size Using XRD,” *World J. Nano Sci. Eng.*, vol. 02, no. 03, pp. 154–160, 2012, doi: 10.4236/wjnse.2012.23020.

# Elaboration and characterization of ZnO and AZO thin films by Sol-Gel method, the effect of incorporating Ag nanoparticles.

C. DJIDJELI<sup>1\*</sup>, A. CHELOUCHE<sup>1</sup>, T. TOUAM<sup>2</sup>, A. MANSERI<sup>3</sup>, S. OUHENIA<sup>4</sup>, A. H. SOUCI<sup>4</sup> AND D. DJOUADI<sup>1</sup>

1. Laboratoire de Génie de l'Environnement, Université de Bejaia, 06000 Bejaia, Algeria, chahinez.djidjeli@univ-bejaia.dz\*, azeddine.chelouche@univ-bejaia.dz, djamel.djouadi@univ-bejaia.dz
2. Laboratoire des Semi-conducteurs, Université Badji Mokhtar-Annaba, 23000 Annaba, Algeria, touamt@gmail.com
3. Centre de Recherche en Technologie des Semi-conducteurs et Energétique, CRTSE-TESE-02, Bd. Dr. Frantz Fanon, 7 Merveilles, Box 140, 16038 Alger, Algeria, amarmanseri@hotmail.com
4. Laboratoire de Physico-chimie des Matériaux et Catalyse, Université de Bejaia, 06000 Bejaia, Algeria, salim.ouhenia@univ-bejaia.dz, abdelhafid.souici@univ-bejaia.dz

## ABSTRACT

*In this work, we discuss the effects of Ag nanoparticles (AgNPs) on the structural, morphological, electrical, and optical properties of ZnO and Al-doped ZnO (AZO) sol-gel thin films deposited by the dip coating method. X-ray diffraction (XRD) shows that all the samples possess a wurtzite hexagonal structure with a c-axis preferential orientation. AgNPs improve the crystal quality of ZnO and AZO. Scanning electron microscopy (SEM) and atomic force microscopy (AFM) demonstrated a homogenous grain distribution and smooth surface of all films. UV-visible spectroscopy revealed a high transparency in the visible range of the samples. The incorporation of AgNPs increases the average transmittance of AZO films by over 90% and the energy gap up to 3.288 eV. Photoluminescence (PL) and Hall effect measurements showed that AgNPs enhance the defect density of both ZnO and AZO films and improve their electrical properties. The AZO/AgNPs film exhibits, in particular, high charge carriers, lower resistivity, and maximum figure of merit. The presence of Ag NPs enhances the figure of merit from  $2 \times 10^{-9}$  to  $4 \times 10^{-7}$  in ZnO films and from  $3 \times 10^{-5} \Omega^{-1}$  in AZO films.*

## KEY WORDS

ZnO, AZO, AgNPs, sol-gel thin films, physical properties.

# Study of technological parameters of polishing animated by a vibratory movement

MOUNIR HASSENA<sup>1,\*</sup>, ALIOUANE TOUFIK<sup>1</sup>

1. Laboratory of Applied Optics, Institute of Optics and Precision Mechanics, Ferhat Abbas University Setif 1, 19000 Setif, Algeria, hassena.mounir@univ-setif.dz

## ABSTRACT

*In this study, a new polishing technique is presented. It is based on the magnetostrictive principle, where the polishing tool is driven by a vibratory movement that generates a frequency. We present an experimental study between the parameters influencing the vibratory polishing process, namely: polishing time, type of polisher and final state of the optical surface. The results showed that using a frequency of 4.62 KHz with a polisher type Lp66, the surface finish (roughness) and transmission are better ( $R_q = 5.47$  nm and  $T = 98\%$ ) during a one-hour polishing operation with a low material removal rate MRR and a surface profile that tends to be more regular.*

**KEY WORDS** Precision polishing vibration Magnetostriction, Surface finish, Roughness.

## I. INTRODUCTION

Improving the performance of optical instruments is closely related to the quality of the optical components. This goal is still a challenge for technologists; indeed, industrial demands for finer surface finish have led to the application of various surface treatment techniques. Polishing remains an essential technology for the realization of very high precision optical components; in addition, the functional surfaces of optical components are characterized, where a very large number of techniques are used. The polishing of optical components, whatever the spectral range remains an essential technology for the realization of optical instruments. It should be noted that the precision required for these components, as well as the nature of the substrates used, have evolved rapidly in recent years, leading to significant changes in the associated manufacturing processes [1]. Recently, for polishing small optical components, a vibratory motion polishing method has been suggested and successfully used to finish micro-lenses with high shape accuracy and low surface roughness [2].

## II. EXPERIMENTAL PROCEDURE

### A. POLISHING PRINCIPLE

Many methods are used for polishing optical lenses in order to improve their surface roughness and shape accuracy. The method used in this study is the one animated by a vibratory movement [2]. This polishing method has the same principle as conventional polishing except that the rotary motion of the tool is replaced by a vibratory movement see Fig. 1. The development of a vibratory movement polishing tool was designed and manufactured to be able to be integrated into a polishing machine.

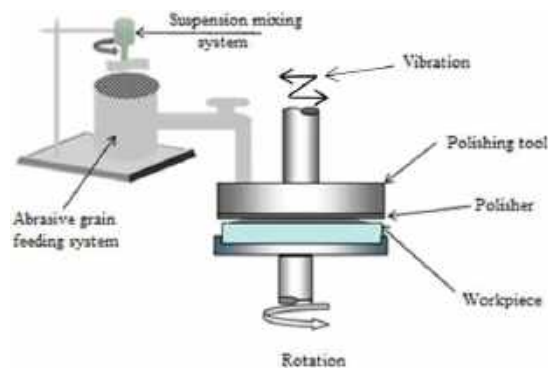


Fig. 1. Principle of polishing animated by a vibratory movement.

### B. RESULTS AND DISCUSSIONS

The obtained results are shown in the following Fig.2, Fig.3 and Fig.4.

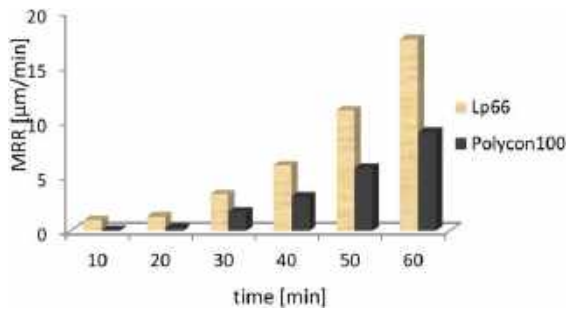


Fig. 2. Material removal rate of BK7.

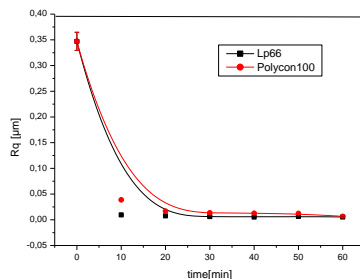


Fig. 3. Roughness quadratic of glass BK7.

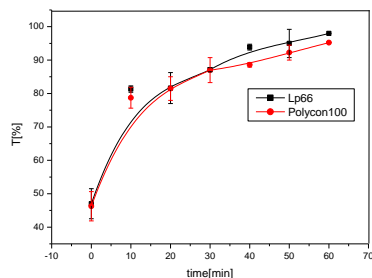


Fig. 4. The transmission of the BK7.

From the results obtained, it can be seen that the material removal rate values increase as the polishing time increases. This is due to the continuous presence of abrasive grains that feed the polishing process. The application of vibration increases the material removal rate which is coherent with the experiments. The material removal modes present in this type of process are principally due to the pressure between the polisher and the surface of the sample produced by the vibrations. Indeed, the surface is worked by the direct impact of the abrasive particles propelled by the tool, and when pressure is applied between the tool (polisher) and the workpiece, the direct hammering of the abrasive particles shapes the surface. Finally, the vibrations transmitted by the suspension liquid to the abrasive grains cause the latter to vibrate on the surface. On the other hand, it can be seen that the material removal rate is higher for the Lp66 polisher than for the Polycon 100

polisher. This can be explained by the porosity of the polishers which plays a very important role in the material removal rate; indeed, the porosity of the Lp66 polisher is higher than that of the Polycon 100 polisher which allows the abrasive grains to stay inside its pores to form a sharp tool and consequently a higher material removal rate [2]. We can see that as the polishing time increases, the roughness decreases. This means that there is an inversely proportional relationship between the material removal rate and the roughness. Roughness of  $R_q (5,47 \pm 1,99)$  nm in the case of polisher Lp66 and  $R_q (6,6 \text{ nm} \pm 1,55)$  for polycon100 were obtained. The evolution of the surface roughness of the BK7 samples as shown in Fig.2 indicate that the roughness decreases up to a certain time and then tends to stabilize. This variation in surface roughness is mostly observed in polishing operations, and it is justified by the fact that the fine polishing grains remove microgeometric defects to leave a smooth surface whose roughness decreases as the polishing time increases. After the polishing process, the transmission is maximum after one hour of polishing (60 min), it differs slightly from one polisher to another. It is  $(98,845 \pm 0.007)$  % for the Lp66 polisher and  $(95,237 \pm 0.019)$  % for the polycon 100 polisher. This may be due to the influence of the time factor, which allows the abrasive grains during the operation to remove the micro-geometric defects, and make the surface smooth, which decreases the light scattering. However, the difference between the polishers may be due to the existence of pores in Lp66.

### III. CONCLUSION

In this study, we showed a new polishing technique used to polish optical glass surfaces. The polishing technique whose tool was developed in our laboratory. According to this study, vibratory polishing is an efficient and economical finishing process. Thus, it offers an excellent surface quality of optical glass BK7. This type of polishing is a promising finishing process and there are ways to improve and increase its efficiency.

### REFERENCES

- [1] A.R. Hooper and al. "Deterministic polishing from theory to practice" ,International Society for Optics and Photonics, p. 96330C (2015).
- [2] H.MOUNIR and al." Technological study of polishing animated by a vibratory movement for BK7 glass",Optik, 247 (2021) 167923.



# Study of friction and wear of polystyrene crystal using Taguchi technique

SOUFYANE AOUNALLAH<sup>1,3</sup>, ABDELHAFID RAHMANE<sup>2</sup>, KAMEL LOUCIF<sup>3</sup>

<sup>1</sup>Dept. physic University of Science and Technology Houari Boumediene, USTHB  
Alger, Algeria, [Aounallahs@univ-setif.dz](mailto:Aounallahs@univ-setif.dz)

<sup>2</sup> Dept Mechanical engineering, University Center Morsli Abdallah Tipaza,  
Tipaza, Algeria [abdelhafid.rahmane@cu-tipaza.dz](mailto:abdelhafid.rahmane@cu-tipaza.dz)

<sup>3</sup>Institute of Optics and Precision Mechanics, Laboratory of non-metallic materials, University Ferhat Abbas  
Sétif1, Algeria

## ABSTRACT

*The present study investigates the tribological behavior of polystyrene crystal obtained through injection molding when sliding against a 100C6 steel counterface. The experiments were conducted using a ball-on-disk tribometer (Nanovia) under dry conditions, employing Taguchi's Lij orthogonal array (OA). The design parameters considered were normal load, rotating speed, and temperature, while the measured responses were friction coefficient and mass loss. The optimal parameter combination for minimizing the friction coefficient was identified as A3B1C1, and the lowest mass loss was achieved at A3B1C1 as well. Analysis of variance (ANOVA) was performed to examine the influence of the design parameters on the friction coefficient and mass loss of polystyrene.*

## KEY WORDS

friction; polystyrene; wear; Taguchi analysis

## I. INTRODUCTION

Tribology, is the science of friction, wear and lubrication, it has an important role in various sectors [1-2], the optimization and understanding of tribological behavior of material are essential setup for improving their used in different mechanical systems

Today polymers are become an important tribological material are widely used in different applications because their good mechanical properties and characteristics, it's low cost, low weight non corrosive, and easy manufacturing

the friction and wear of polymer/metal interface is very complex because there are many parameters influencetheir behavior like environment, condition of used and material characteristics. Many researchers were studies effect of different parameters including load, sliding speed, temperature, lubrication and material properties on tribological behavior and the performance of the tribological system.

Because these, we are search for optimized of this factors and give good information about the material and tribological system.

The main objective of this study is to optimize and analyze the tribological performance of the Crystal polystyrene/100C6 steel system under different operating conditions, including load, temperature and rotational speed. Using three analysis and optimization techniques: Taguchi technique, variance analysis and regression analysis and an experimental analysis of worn surfaces. these are robust optimization methods, we aim to identify the optimal combination of control factors that minimizes the friction coefficient and mass loss

## II. EXPERIMENTAL DETAILS

### A. MATERIAL AND TEST TRIBOLOGY

The material used in this study is an amorphous thermoplastic polystyrene obtained in the injection-molding state, delivered by Condor Company in Algeria. This polymer is considered amorphous due to the presence of benzene in its molecular structure.

The specimens used in this study are a rectangular parallelepiped shape with dimensions of 30.30.4 mm<sup>3</sup> and a remarkably smooth surface. The counter-face material employed in this research is a ball 100C6 steel, with a hardness of 62HRC and 5 mm of diameter.

### B. FRICTION AND WEAR TESTS

The tribological tests are performed using a Ball-On-Disc configuration on a Nanovia American Tribometer. A 5 mm diameter steel ball made of 100C6 steel with a hardness of 62 HRC is utilized as the counterface material against a crystal polystyrene disc under dry sliding conditions.

In this study, we varied the load, speed, and temperature parameters. The normal load was set at 1 N, 2 N, and 5 N. The rotational speeds used were 20 rpm, 60 rpm, and 100 rpm. The temperatures during the tests were maintained at 15°C, 20°C, and 25°C. Each test had a duration of 15 minutes.

### C. TAGUCHI METHOD

Experimental design procedures are very complex and not easy to use. Especially if these procedures are accompanied by a large number of factors and experimental conditions to be taken into account. Therefore, we need a large number of experimental tests to achieve the objective of the studies. The Taguchi method uses a small number of tests for research, by the use of a special design of orthogonal arrays. And the most excellent advantage of the method of Taguchi is to save experimental time and find important factors fast, and save effort during experimentation.

### D. ANALYSIS AND EVALUATION OF EXPERIMENTAL RESULTS USING TAGUCHI DESIGN

The (lower-the better) equation was used for the calculation of the S/N ratio. Table 1 shows the values of the S/N ratios for observations of variation of the Friction ratio and a Mass loss. Analysis of the effect

of each control factor on the (T°C), F (N) and N(rpm) was performed with S/N response table. The tables of responses are shown in Table 2.

The table 2 shows the optimal levels of control factors for the optimal variation Friction ratio and a Mass loss.

Table 1 The results of experiments and S/N ratios values

Test	Friction coefficient ( $\mu$ )	Mass loss
1	4,68521	1,93820
2	-1,85599	-4,60898
3	-4,67045	-7,60422
4	3,69521	0,91515
5	-3,46167	-5,57507
6	-1,07820	-3,52183
7	0,96910	-1,58362
8	5,67351	6,02060
9	0,23994	-2,27887

Table 2 S/N response table for the relative variations of Mass loss and f the first three modes

Levels	Control factors					
	Friction coefficient ( $\mu$ )			Mass loss in g		
	(T°C)	F (N)	N( rpm)	(T°C)	F (N)	N( rpm)
1	-0,6137	<b>3,1165</b>	<b>3,0935</b>	-3,4250	<b>0,4232</b>	<b>1,4790</b>
2	-0,2816	0,1186	0,6931	-2,7272	-1,3878	-1,9909
3	<b>2,2942</b>	-1,8362	-2,3877	<b>0,7194</b>	-4,4683	-4,9210
Delta	2,9079	4,9527	5,4812	4,1444	4,8915	6,4000
Rank	3	2	1	3	2	1

## III. CONCLUSION

We concluded that polystyrene is not considered a suitable material for tribological applications, especially in contact with metallic surfaces. The study provides valuable insights into the wear behavior and tribological characteristics of the polystyrene crystal/100C6 steel pair, which can contribute to the development of strategies for improving wear resistance and optimizing tribological performance in similar material combinations.

Overall, the research sheds light on the limitations and challenges associated with the tribological properties of polystyrene and emphasizes the importance of considering factors such as temperature, wear mechanisms, and material selection in the design and optimization of tribological systems.

## REFERENCES

- [1] Prabhat Kumar Prajapati, Santosh Kumar, K.K. Singh. Taguchi approach for comparative optimization of tribological behavior of glass fabric reinforced epoxy composite with and without graphene nano platelets filler. *Materials Today: Proceedings* 72 (2023) 1605–1612. <https://doi.org/10.1016/j.matpr.2022.09.412>
- [2] VenuYarasu, Peter Jurci, Jakub Hornik, Stanislav Krum. Optimization of cryogenic treatment to improve the tribological behavior of Vanadis 6 steel using the Taguchi and grey relation approach. *Journal of Materials Research and Technology* 2022; 18: 2945-2962. <https://doi.org/10.1016/j.jmrt.2022.03.145>.
- [3] Sangeeta Das, Shubhajit Das, S.S. Gautam, C.R. Gautam. Optimization of wear coefficient and coefficient of friction of borosilicate glass ceramics using Taguchi coupled grey fuzzy logic technique. *Materials Today: Proceedings* 27 (2020) 1579–1589. <https://doi.org/10.1016/j.matpr.2020.03.262>.
- [4] Shanhong Wan, A. KietTieu, Yana Xia, Hongtao Zhu, Bach H. Tran, Shaogang Cui. An overview of inorganic polymer as potential lubricant additive for high temperature tribology. *Tribology International* 102 (2016) 620–635. <http://dx.doi.org/10.1016/j.triboint.2016.06.010>

# Effet des contaminants du sable sur l'usure des contacts élastohydrodynamiques

Abdelhakim DJALAB<sup>1</sup>, Mohamed Rafik SARI<sup>2</sup>

Département de Génie Mécanique, Université Mohamed boudiaf de M'sila BP 166 Ichebilia, 28000 M'sila Algérie

Laboratoire de Mécanique Industrielle, Université Badji Mokhtar d'Annaba BP 12, 23000 Sidi Amar Annaba, Algeria

abdelhakim.djalab@univ-msila.dz

## Résumé :

*Dans cette étude expérimentale, nous avons tenté de répondre à des questions concernant l'influence des particules solides présentes dans les lubrifiants sur le contact mécanique. En effet, nous nous intéressons particulièrement à l'évolution de la température de fonctionnement et à l'usure des contacts roulants EHD. L'objectif principal de cette étude est d'élucider les causes de la durée de vie mécanique réduite dans des milieux pollués.*

**Mots-clés:** Contact. Pollution solide. Lubrification. Frottement. Usure.

## Abstract

In this experimental investigation, we tried to answer questions about the effect of the presence of solid particles in the lubricant on mechanical contacts. Indeed, we are particularly interested on the evolution of temperature and wear of an EHD rolling contact. The main objective of this study is to express the reasons for reducing the life of mechanisms in a contaminated environment.

## 1 Introduction

La durée de vie et la fiabilité des mécanismes augmentent constamment. Ces progrès résultent du développement acquis dans les domaines de l'élaboration et du traitement des aciers, ainsi que dans le domaine de l'usinage, de la lubrification et de la protection contre les pollutions des lubrifiants. L'amélioration de la propreté inclusionnaire des aciers permet notamment une meilleure tenue mécanique en volume. La pollution solide de la lubrification est

donc un sujet d'actualité, notamment pour l'évaluation du cycle de vie LCA [1].

Dans ces dernières années, les effets de la pollution solide sur les contacts lubrifiés ont été abordés avec acuité. Parmi les travaux relatifs à ce sujet, il convient de citer les travaux de Hunt [2] qui a procédé à une classification des particules selon leur morphologie en sept familles. Wedeven et Cusano [3, 4] ont mené des travaux dont l'objectif est de montrer l'influence des indents et des défauts de surface sur la traction par glissement des points de contacts EHD. Dwyer-Joyce et al. [5, 6] ont effectué une étude quantitative sur l'entraînement des particules solides dans un contact EHD roulant. Ils ont ainsi montré que la concentration des particules en volume peut être utilisée comme indicateur qui renseigne sur le taux des particules entrant dans le contact. Le phénomène d'indentation et ses effets sur la durée de vie des mécanismes a été bien menée par Ville et al. [7, 8]. Sari et al [9, 10], ont pu également montrer que la présence des corps abrasifs dans le lubrifiant conduit à des usures et des coefficients de frottement notables dans les endroits à fort taux de glissement.

Dans la présente étude, on s'intéresse plus particulièrement aux effets des paramètres de fonctionnement tels que : charge, vitesse et concentration en polluant, sur l'évolution de la température de fonctionnement et de l'usure des contacts roulants.

## 2 Partie expérimentale

Afin d'étudier le phénomène de la pollution solide de la lubrification et de voir ses

conséquences sur les systèmes tribologiques, on a réalisé une expérience qui simule le fonctionnement d'un mécanisme au Sahara (cas du sud Algérien).

Dans le présent travail, on s'intéresse d'une part, à la compréhension de l'effet de la pollution solide de la lubrification sur les surfaces en contact roulant (contact entre galets cylindriques) et d'autre part, à l'influence des paramètres de fonctionnement tels que : charge, vitesse, concentration en polluant,.....etc. sur l'évolution de la température et de l'usure.

## 2.1 Dispositif expérimental

Les essais sont réalisés sur un dispositif original (Fig. 1) ou sont montés en contact deux roues cylindriques. Ce dispositif reproduit les conditions de fonctionnement d'un contact de roulement de type linéaire. Le principe consiste à faire entrer en contact une éprouvette cylindrique en acier C45 avec une roue cylindrique dure en acier 100C6 (roulement). L'éprouvette est actionnée à des vitesses de rotation différentes à l'aide d'un moteur électrique. La roue guidée en rotation est ensuite mise en mouvement sous l'action de l'éprouvette cylindrique.

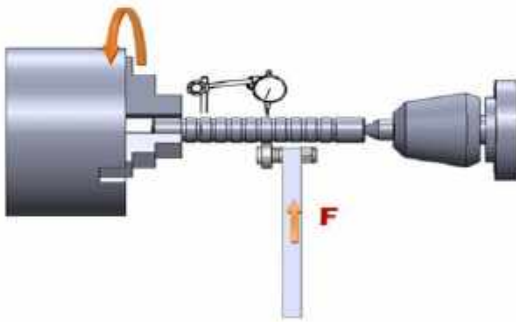


Fig 1: Diagramme schématique du montage expérimental

## 2.2 Le lubrifiant

Les huiles utilisées dans les systèmes mécaniques assurent diverses fonctions. Elles permettent de réduire le frottement, évacuer les calories, refroidir et nettoyer les surfaces. Le lubrifiant utilisé dans notre étude est une huile extrême pression de type ISO VG 220. Il a une viscosité dynamique  $\mu_0 = 0.033 \text{ Pa.s}$  à  $T_0 = 40^\circ\text{C}$  et un coefficient de piezo-viscosité  $\alpha_{p-v} = 18.2 \times 10^{-9} \text{ Pa}^{-1}$ . Il est représentative d'une huile de transmission et couramment utilisé dans la lubrification des engrenages et roulements.

## 2.3 Le Polluant

Le polluant utilisé est une poussière de sable du Sahara, il simule le polluant issu du milieu extérieur. En effet, les particules de sable sont essentiellement constituées de quartz avec 90%, connu pour sa dureté, sa fragilité et qui peut être véhiculée par le vent jusqu'en Europe voire même en Amérique.

## 4 Résultats et discussions

### 4.1 Evolution de la température

Dans cette partie, on s'intéresse à l'évolution de la température au point de contact. Les températures pour différents essais à une vitesse de rotation 1000 tr/min et des charges 100 N et 180 N respectivement. Les températures sont relevées à l'aide d'un thermocouple infrarouge.

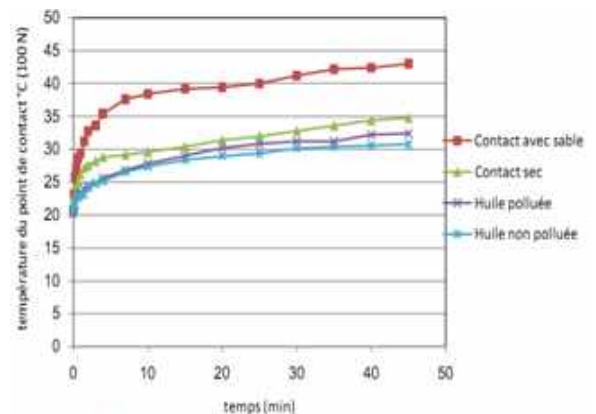


Fig. 2 Evolution de la température en fonction du temps.  
N = 1000 tr/min et FN=100 N.

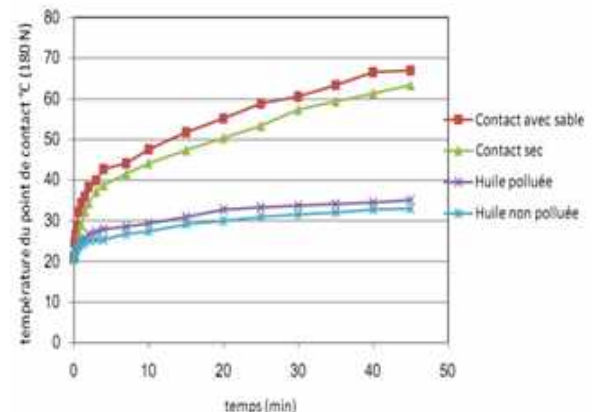


Fig. 3 Evolution de la température en fonction du temps.  
N = 1000 tr/min et FN=180 N.

L'énergie mécanique perdue par frottement, transformée en chaleur, est généralement irrécupérable et parfois très difficile à évacuer. Nous constatons d'après les résultats obtenus (Figures 2 et 3) exprimant l'évolution de la

température au cours du temps, que cette dernière augmente très rapidement de la température ambiante jusqu'à une certaine valeur, puis se stabilise autour d'elle.

D'après les résultats obtenus, on voit clairement que la température est élevée pour un contact sec comparée à un contact lubrifié. En effet, dans un contact lubrifié, le lubrifiant joue un rôle important dans l'évacuation des calories et par conséquent la minimisation de l'échauffement. On constate également que la présence des grains abrasifs dans le lubrifiant (fonctionnement avec une huile polluée par des particules  $\leq 125 \mu\text{m}$ ) qui favorisent le frottement et l'usure, conduit à l'élévation de la température. D'autre part, l'échauffement est d'autant plus élevé avec la présence des particules de forte granulométrie dans un contact sec.

L'échauffement dans un contact roulant est affecté aussi par la charge normale. En effet, il est bien clair que la température à une charge 180 N est supérieure à celle obtenue à une charge 100 N. Dans ces conditions la pression de contact augmente avec l'augmentation de la charge transmise par le contact, ce qui conduit à

l'accroissement de la vitesse des déformations élastiques et plastiques accompagnée de contraintes de frottement, et par conséquent l'échauffement devient important.

## 4.2 Evolution de l'usure

L'usure est évaluée par la mesure de la perte de côte (diminution du diamètre). En effet, on a effectué trois mesures sur le diamètre. C'est la valeur moyenne qui a été considérée.

On constate d'après les résultats présentés dans les (Figures 4 à 7), que l'allure des courbes décrivant la tenue à l'usure (perte de côte) pour l'acier C45 est pratiquement la même pour les différents essais menés. A première vue, on constate qu'elle obéit à la loi universelle de l'usure (rodage, usure normale et usure sévère). Elle augmente avec le temps de fonctionnement et diffère selon les conditions de fonctionnement des mécanismes.

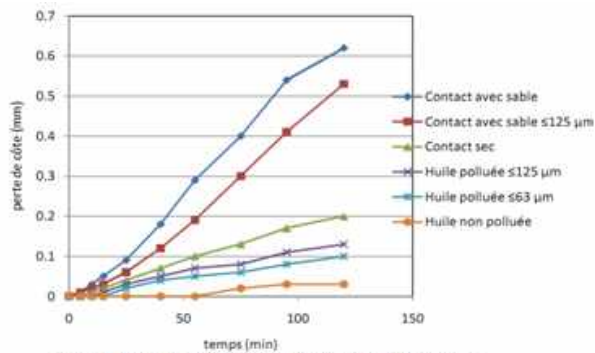


Fig. 4 Evolution de l'usure en fonction du temps.  
 $V = 500 \text{ tr/min}$  et  $F_N=100 \text{ N}$ .

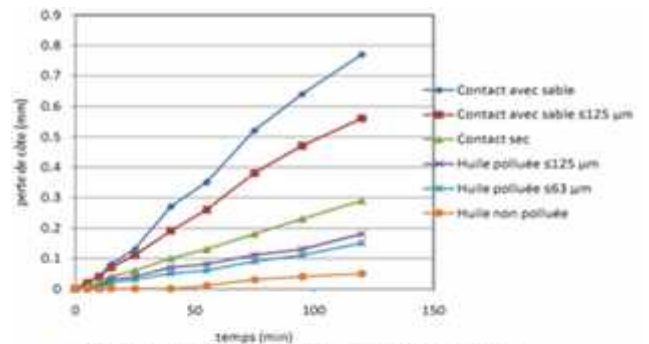


Fig. 5 Evolution de l'usure en fonction du temps.  
 $V = 1000 \text{ tr/min}$  et  $F_N=100 \text{ N}$ .

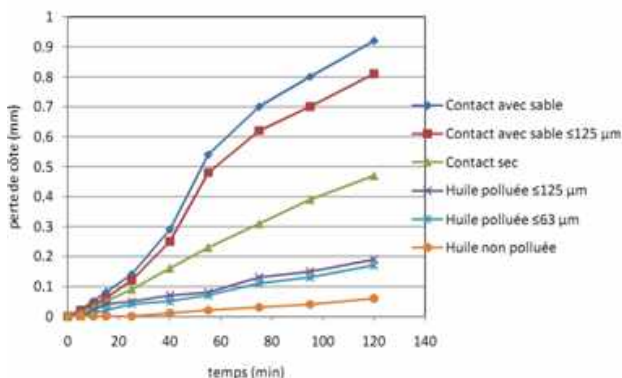


Fig. 6 Evolution de l'usure en fonction du temps.  
 $V = 500 \text{ tr/min}$  et  $F_N=180 \text{ N}$ .

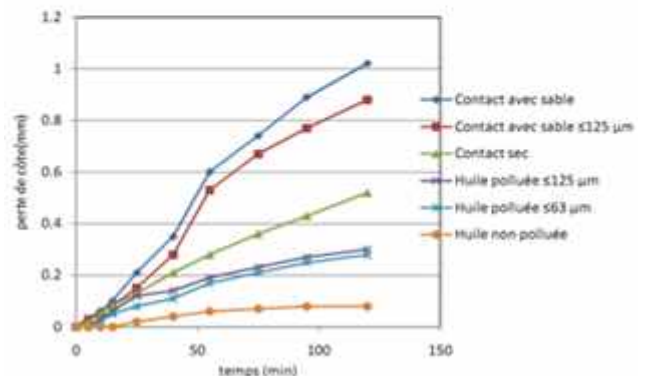


Fig. 7 Evolution de l'usure en fonction du temps.  
 $V = 1000 \text{ tr/min}$  et  $F_N=180 \text{ N}$ .



L'usure la plus faible est observée pour le fonctionnement d'un contact lubrifié où l'huile joue un rôle clé dans la minimisation du frottement et par conséquent la diminution de l'usure. On constate également que la présence de fines particules dans le lubrifiant (63 et 125  $\mu\text{m}$ ), a tendance à augmenter l'usure en comparant à celle obtenue pour un contact lubrifié. Il est bien connu qu'il existe dans un contact EHD, un certain nombre de particules dont la taille est supérieure à celle du film d'huile. Ces particules perturbent la séparation, s'explorent et donnent naissance à des particules de petites tailles. Par absence du lubrifiant (contact sec), l'usure est élevée et elle est notable pour un contact sec avec la présence des grains abrasifs de forte granulométrie. On note également que l'usure est légèrement élevée avec une vitesse de rotation (1000 tr/min). Avec une vitesse élevée, l'éprouvette et le roulement entre plus en contact qu'au fonctionnement à une vitesse moins élevée (500 tr/min par exemple).

#### 4.3 Photographies des éprouvettes après fonctionnement






Type de contact	Avant Utilisation	Contact lubrifié	Contact avec huile polluée	Contact sec	Contact sec avec sable
Photos des éprouvettes					
	Fig. 1	Fig. 2	Fig. 3	Fig. 4	Fig. 5

Tableau.1 Photographies des éprouvettes après fonctionnement.

D'après le tableau (1), les (Figures 2, 3, 4 et 5) qui donnent des images détaillée des éprouvettes après fonctionnement, montre une usure douce pour un contact lubrifié (Fig. 2). Dans ce type de contact, le lubrifiant a pour rôle de minimiser le frottement, ce qui conduit par conséquent à une usure faible. L'usure devient sévère, avec la présence de fines particules du sable dans le lubrifiant. Pour ce type de fonctionnement (Fig. 3), la présence des indents au niveau de la surface est notable. Pour un contact sec (Fig. 4), le frottement entre les

surfaces est important, ce qui justifie une usure très sévère. L'usure est catastrophique (Fig. 5) pour un contact sec avec la présence des particules de forte granulométrie. Au niveau de la surface, l'arrachement de la matière est intense (rayures, sillons, écoulement,.....) et les indents sont très notables au niveau de la surface.

#### 5 Conclusion

L'objectif principal du travail présenté dans ce travail est d'une part de mieux comprendre le phénomène de la pollution solide des lubrifiants et d'autre part de voir ses conséquences sur les systèmes tribologiques (les deux corps en contact en particulier).

D'après les résultats obtenus, on peut tirer les conclusions suivantes :

- Au cours de fonctionnement, les composants machines se dégradent. Cette dégradation est évaluée par l'évolution de la température et de l'usure.
- La présence des particules de sable dans un contact mécanique, favorise et accélère l'avarie.
- La dégradation est plus prononcée pour un contact sec avec présence du sable comparée aux résultats obtenus pour les autres types de fonctionnement.
- La présence des grains abrasifs laboure les surfaces et fait augmenter considérablement l'usure (surtout en présence des particules de forte granulométrie dans un contact sec).
- La vitesse d'usure et la détérioration de la surface croît proportionnellement à la charge normale.

Enfin, les résultats obtenus expriment les raisons de réduction de la durée de vie des systèmes mécaniques.

#### 6 Références bibliographiques

- [1] Taylor R. I., Dixon R. T., Wayne F. D., Gunse S., Lubricants and energy efficiency: Life-cycle analysis, 31<sup>st</sup> Leeds-Lyon symposium on tribology, Leeds, 2004.
- [2] Hunt T. M., Handbook of wear debris analysis & particle detection in liquids. Elsevier Applied Science, 1993.
- [3] L. D. WEDEVEN & C.CUSANO, Elastohydrodynamic film thickness measurements of artificially produced surface dents and grooves, 1978, ASLE Transactions, pp. 369-381.

- [4] C. CUSANO & L. D. WEDEVEN, The Influence of Surface Dents and Grooves on Traction in Sliding EHD Point Contacts, 1982, ASLE Transactions, Vol. 26, pp. 306-310.
- [5] R.S. DWYER-JOYCE, R.S. SAYLES & E. IOANNIDES, Investigations into the mechanisms of closed three-body abrasive wear, Tribology Section, 1993, Vol. 175, Wear, pp. 133-142.
- [6] R.S. DWYER-JOYCE & J. HEYMER, The entrainment of solid particles into rolling elastohydrodynamics contacts, 1996, Proceedings of 22nd Leeds-Lyon Symposium on Tribology Amsterdam: Elsevier, pp. 135-140.
- [7] F. VILLE & D. NELIAS, Influence of the nature and size of solid particles on the indentation features in EHL contacts, 1998, Tribology series "Tribology for Energy Conservation", D. Dowson et al. Editeurs, Elsevier, Amsterdam, Vol. 34, pp. 399-409.
- [8] F. VILLE, S. COULON & A. A. LUBRECHT, Influence de la pollution solide des lubrifiants sur la durée de vie des mécanismes, 2005, Laboratoire de Mécanique des Contacts et des Solides (LaMCoS), UMR CNRS- INSA n°5514, pp. 1-6.
- [9] Sari M. R., Haiahem A., Flamand L., Effect of lubricant contamination on gear wear, Tribology Letters, Volume 27, pp. 119-126, 2007.
- [10] M. R. SARI, A. HAIHAHEM & L. FLAMAND, Effect of lubricant contamination on friction and wear in an EHL sliding contact, 2010, MECHANIKA, Vol. 82, pp. 43-49.

# Navigating Roller Bearing Lubrication Regimes with Emphasis on Elastohydrodynamic Lubrication

ALRIFAI HAZEM<sup>\*1</sup>, HAIAHEM AMMAR<sup>2</sup>

1. Department of mechanic/ Faculty of Technology, University Badji Mokhtar-Annaba, Algeria, alrifai.hazem@univ-annaba.org
2. Department of mechanic/ Faculty of Technology, University Badji Mokhtar-Annaba, Algeria, Ammar.haiahem@univ-annaba.org

## ABSTRACT

*Roller bearings are essential components in most mechanical machines, and It is quite clear that their performance is closely related to the effective lubrication system. Elastohydrodynamic Lubrication (EHL) is the substantial lubrication regime that involves a pressurized lubricant film that prevents wear, reduces friction, and extends bearing life. This work explores the lubrication regimes in roller bearings, with a focus on EHL. It discusses the mechanisms and significance of EHL, as well as the crucial role of film thickness within this regime.*

**KEY WORDS:** Roller bearings; Grease lubrication; elastohydrodynamic.

## I. INTRODUCTION

Lubricants for rolling bearings have the task to reduce friction and wear, to protect the bearings against corrosion (in combination with the sealing), and to avoid the intrusion of external substances, particularly when grease lubrication is used. A separation of the contacting surfaces can be reached by a lubricating film or the formation of surface boundary layers. Both effects prevent the bearing surface from a direct metal-to-metal contact. The separation of the surfaces of the rolling bearings reduces friction and wear. Furthermore, rolling contact fatigue of rolling bearings is correlated with the separation of the surfaces by a lubricating film.[1]

## II. LUBRICATION REGIMES:

### A. BOUNDARY LUBRICATION

Boundary lubrication is associated with metal-to-metal contact between two sliding surfaces of the machine. During initial start-up or shutdown of some equipment (e.g., journal bearings) or under heavily loaded conditions (pins and bushings of construction

equipment), the metal surfaces in a lubricated system may actually come into severe contact with each other. If the lubricating film is not thick enough to overcome the surface roughness of the metal, a lambda value of less than one results.[2]

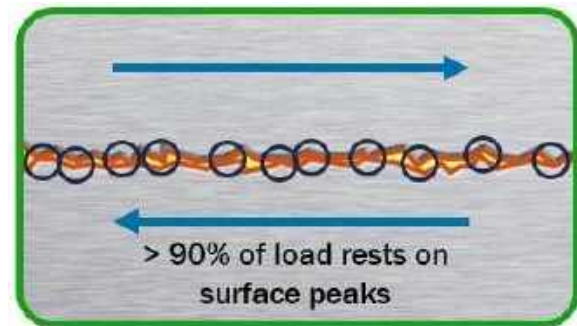


Fig. 1. BOUNDARY LUBRICATION

### B. MIXED LUBRICATION

Mixed lubrication is an intermediate regime that combines aspects of both hydrodynamic and boundary lubrication. In this regime, the lubricant film is neither too thick nor too thin, resulting in a combination of fluid and boundary lubrication effects.[2]

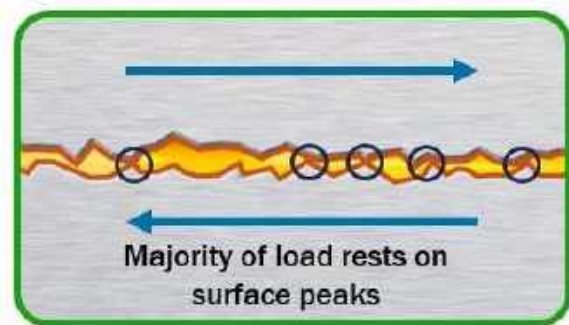


Fig. 2. MIXED LUBRICATION

### C. ELASTOHYDRODYNAMIC (EHL) LUBRICATION

Elastohydrodynamic (EHL) lubrication is a type of fluid film lubrication that occurs in roller bearings when the pressure of the lubricant is high enough to cause elastic deformation of the bearing surfaces. This deformation creates a thin film of lubricant that separates the bearing surfaces and prevents them from coming into contact. EHL lubrication is essential for the proper operation and longevity of roller bearings. It reduces friction and wear, extends bearing life, and prevents overheating. EHL lubrication is typically achieved in roller bearings by using a high-viscosity lubricant and operating at high speeds. The following is a list of some of the benefits of EHL lubrication in roller bearings:

- Reduced friction and wear
- Extended bearing life
- Reduced heat generation
- Improved efficiency
- Increased load-carrying capacity

EHL lubrication is a complex phenomenon, but it is essential for understanding the performance and reliability of roller bearings. By understanding the factors that affect EHL lubrication, engineers can design and operate roller bearings to maximize their performance and lifespan.[3]

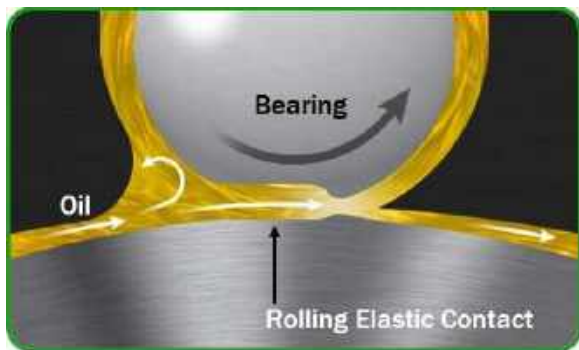


**Fig. 3.** Elastohydrodynamic (EHL) lubrication

### III. FILM THICKNESS

A lubricating grease will only provide a long bearing service life if a sufficiently thick film is developed separating the rolling elements from the raceways [4]. Lubricating film thickness is a crucial parameter in roller bearing lubrication. It is the distance between the rolling elements and the raceways, and it is essential for preventing metal-to-metal contact and reducing friction and wear. The ideal film thickness for a roller

bearing depends on a number of factors, including the bearing load, speed, and lubricant viscosity. However, a general rule of thumb is that the film thickness should be at least twice the sum of the surface roughnesses of the rolling elements and the raceways. There are a number of ways to measure and calculate film thickness in roller bearings. One common method is the Hamrock-Dowson equation, which takes into account the bearing load, speed, lubricant viscosity, and geometry. Another common method is the capacitance method, which uses a capacitor to measure the distance between the rolling elements and the raceways [5].

### IV. CONCLUSION

Elastohydrodynamic lubrication (EHL) is the key lubrication regime in roller bearings. It reduces friction and wear, extends bearing life, and prevents overheating. Film thickness is a crucial parameter affecting bearing efficiency and reliability. Understanding and managing film thickness is essential to optimize roller bearing performance.

### REFERENCES

- [1] Georg Jacobs, Michael Plogmann. "Rolling Bearing Lubrication and Materials".
- [2] Machinery lubrication website, "Lubrication regimes," accessed on 2023-09-30.
- [3] SKF Engineering Handbook, 8th Edition, Section 3.4.1 Lubrication regimes.
- [4] Lugt, Piet M. Grease Lubrication in Rolling Bearings. Springer, 2016.
- [5] Hamrock, Bernard J., and Donald Dowson. "Elastohydrodynamic lubrication of point contacts." Part I - Theoretical formulation. Proceedings of the Institution of Mechanical Engineers.

# Investigating the influence of deposition time on the structural, mechanical, and tribological properties of Titanium-tungsten thin films

BELGUEBLI HAYAT<sup>1\*</sup>, BERBER MESSAOUD<sup>2</sup>

1. Affiliation (Author): departement of Mechanical Engeneniring; Laboratory of Mechanical, Materiels, Energy L2ME, University Abderahman Mira Bejaia, [belgueblihayat@gmail.com](mailto:belgueblihayat@gmail.com)
2. Affiliation (Author): departement of Mechanical Engeneniring, Laboratory of studies and research in industrial technology University Blida1 Blida, [berbergm08@gmail.com](mailto:berbergm08@gmail.com)

## ABSTRACT

*In this research, we have studied the effect of deposition time on the properties of titanium-tungsten (TiW) thin films onto an aluminum 5081 substrate, DC sputtering magnetron technique. The structural, mechanical and tribological properties of the deposited thin films were then characterized and evaluated. Our findings reveal that the deposited thin films are primarily composed of TiW, as confirmed by X-ray diffraction (XRD) analysis and Raman spectroscopy. Furthermore, nanoindentation measurements indicate a significant improvement in the surface hardness of the TiW thin films, with an average value of 14 GPa compared to an initial value of 0.9 GPa for the uncoated sample. Tribological tests were conducted under dry sliding conditions to evaluate the frictional behavior of the TiW films, and a friction coefficient of approximately of 0.40 was observed for the deposition times studie.*

## KEY WORDS

DC magnetron sputtering; friction; Hardness; Thin films; Titanium-Tugsten.

# Tribology of polystyrene sliding against steel

SOUFYANE AOUNALLAH<sup>1,2</sup>, KAMEL LOUCIF<sup>2</sup>

<sup>1</sup>Dept. physic University of Science and Technology Houari Boumediene, USTHB  
Alger, Alegria, [Aounallahs@univ-setif.dz](mailto:Aounallahs@univ-setif.dz)

<sup>2</sup>Institute of Optics and Precision Mechanics, Laboratory of non-metallic materials, University Ferhat Abbas  
Sétif1, Algeria

## ABSTRACT

*In this study, we studied the tribological behaviour of Polystyrene Crystal sliding against ball of Steel 100Cr6 with a 5mm radius. The investigation covered a range of applied loads (1-5N) and sliding speeds (12.5 - 63 mm/s) using a ball-on-disc tribometer in an unlubricated environment.*

*The objective of this study focus on tracking the evolution of the friction coefficient and wear rate in response to variations in sliding speed and the applied normal load. The worn surfaces examined using the Scanning Electron Microscopy (SEM), revealing the presence of several distinct wear mechanisms. These included plastic deformation, abrasion in the track, and adhesion at the edge of track.*

## KEY WORDS

tribology; polystyrene; wear; friction

## I. INTRODUCTION

Polymers material extensive use in a variety of technological applications, including machinery components, electrical devices, cosmetic products, and artificial joints. This application is attributed to their lightweight, low cost, ease of molding, excellent dimensional stability, and resistance to corrosion [1]. Nevertheless, their practical life is frequently compromised by their relatively limited mechanical properties.

many polymers find extensive application in sliding coupling with metals.

Polystyrene is a thermoplastic polymer, exhibits remarkable environmental stability, making it highly resistant to degradation after disposal [2]. It is

recognized for its heightened brittleness when compared to other polymers [3]. As a result, polystyrene is regarded as a promising material for a wide array of applications, ranging from domestic applications to the automotive industry.

Our work is based on understanding the effects of sliding speeds and loads on the friction coefficient and wear rates and to determine the wear mechanisms of a polystyrene crystal sliding against 100Cr6 steel. The friction tests were conducted without lubricant (dry friction) at ambient temperature. The results were compared with the results of other researchers [4] who used different test configurations.

## II. EXPERIMENTAL DETAILS

### A. MATERIAL AND TEST TRIBOLOGY

The material used in this study is an amorphous thermoplastic polystyrene obtained in the injection-molding state, delivered by Condor Company in Algeria. This polymer is considered amorphous due to the presence of benzene in its molecular structure.

The tribological tests were carried out on a Nanovia American tribometer in a ball-on-disc configuration. The test conditions were as follows: contact point steel 100Cr6/Polystyrene crystal; normal loads: 0.5, 1, 2 and 5N; track radius: 6 mm, sliding speeds: 12.5, 38, 56.5 and 63mm/s. The friction and wear tests were performed under ambient conditions and dry environments, and each test lasted 15min. The evolution of the friction coefficient was recorded with a frequency of 20 points/Sec. The wear was monitored by weighing the samples with a Sartorius balance before and after each test. The metallographic observations of the contact area were made at the end of the friction test using an optical microscope of the type Motic B410 Trinocular in addition to a Quanta 650 scanning electron microscope.



### B. RESULTS AND DISCUSSION

The following curves (Fig. 1-2) summarizes the results obtained by the polystyrene friction study for different sliding speeds and different normal loads.

The plots in Fig. 3 show that variation of the friction coefficient as a function of sliding speed is minimal or even almost non-existent; this finding is in agreement with results obtained by Shooter and Thomas. Unlike the variation of friction coefficient as a function of the normal load, the coefficient of friction is increased until reaching a critical load (1N), and then the increase in the normal load leads to a slight decrease in the friction coefficient. The yield strength of polystyrene is low leaves the friction coefficient decreases with the load increasing.

These parameters are collectively interfering in the determination of the behavior in wear and friction of the contact.

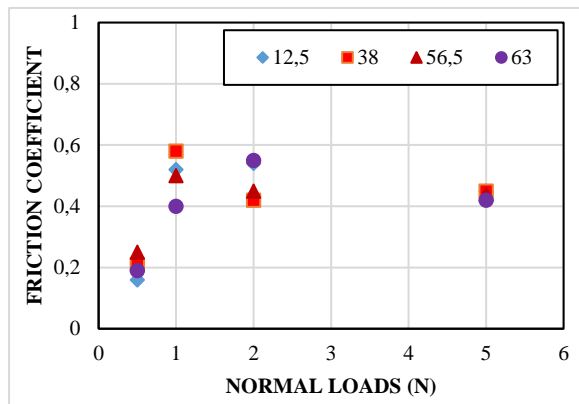


Fig. 1. Variation of friction coefficient as a function of loads for different sliding speed

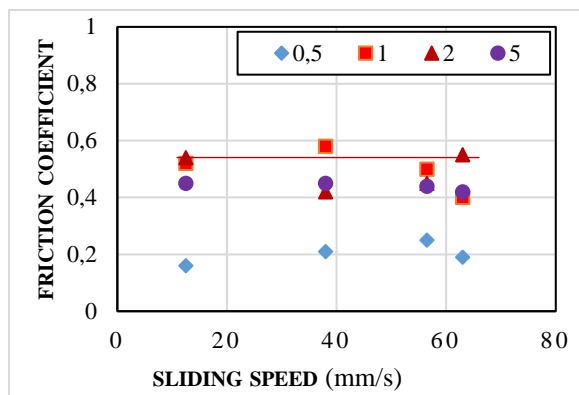


Fig. 2. Variation of friction coefficient as a function of sliding speed for different loads

### III. CONCLUSION

The combination of wear and friction test results, along with microscopic examination, leads to the following conclusions: The friction coefficient has minimal sensitivity to sliding speed but strongly depends on the applied normal load. Polystyrene's wear behavior correlates with its ultimate tensile strength, exhibiting plastic deformation at lower pressures and shifting to abrasion and adhesion at higher pressures. This makes polystyrene unsuitable for tribological applications, as it offers poor wear resistance against steel and has a high friction coefficient when in contact with metallic surfaces, resulting in notable abrasion.

### REFERENCES

- [1] D.W. Gebretsadik, J. Hardell, B. Prakash, Friction and wear characteristics of PA 66 polymer composite/316L stainless steel tribopair in aqueous solution with different salt levels, *Tribology International* 141, 1 (2020);
- [2] Y. Yamaguchi, *Tribology of plastic materials: their characteristics and applications to sliding components* (Amsterdam, Elsevier, 1990).
- [3] K. Shooter and RH. Thomas, *Frictional properties of some plastics*, *Research* 2, 533 (1952).
- [4] H. Unal, U. Sen, A. Mimaroglu, Dry sliding wear characteristics of some industrial polymers against steel counterface, *Tribology International* 37(9), 727 (2004); <https://doi.org/10.1016/j.triboint.2004.03.002>.

# Comparison of the two Fluid Ostwald With Newtonian Fluid Effect in Hydrodynamic Lubrication Slid Bearing Film

DJENDARA ABDELHAKIM AMINE<sup>1,\*</sup>, NEBBACHE MOHAMMED<sup>2</sup>

1. Affiliation (Author): department of mechanical engineering. University of sciences and technologies  
Mohammed Boudiaf Oran, Algeria  
Djendara3188@gmail.com
2. Affiliation (Author): department of mechanical engineering. University of sciences and technologies  
Mohammed Boudiaf Oran, Algeria  
nebbachemohammed31@gmail.com

## ABSTRACT

*The Numerical simulation of flows in the field of tribology is developing day by day. Our study consists in writing a program in FORTRAN language to simulate a new method that compute the non-Newtonian pressure and temperature fields of an oil film contained in a sliding hydrodynamic bearing. The visualization of the results was done by the Tecplot software. The obtained results were compared with the Newtonian fluid which is tested experimentally for many previous works, a good agreement was noticed. The variations within the film were studied for three lubricating oils, one Newtonian that have viscosity indice of  $n = 1$  and two non-Newtonian of fluid of Ostwald with  $n=1, 05$  and  $n=0, 95$ . The results showed that shear-splicing oil gives higher pressures and temperatures than other oils, followed by Newtonian oil and finally, shear-thinning oil. The variation of the friction torque as a function of the rotational speed has also been studied. Proportionality between the friction torque on the one hand, and the speed of rotation as well as the viscosity indices on the other hand, was noticed.*

## KEY WORDS

Hydrodynamic bearing; lubrication; numerical simulation; Newtonian and Non Newtonian fluid.

## I. INTRODUCTION

The Bearings and sealing systems are present in most man-made machines. In order to study and model them, it is often necessary to call on several disciplines such as solid mechanics, mechanics fluids, thermodynamics, materials science, applied mathematics, etc. [1]. The bearings hydrodynamics have been the subject of several works, whether numerically or experimentally. In This introduction, we will cite a few. Maoui and Benabès [2] carried out a numerical modeling of the hydrodynamic and thermal behavior of a cylindrical plain bearing of finite length. Deformations thermo elastic solid parts have been taken into account.

A thermal approach has been proposed in order to consider the elliptical form of the energy equation in the fluid film. Determining the temperature in the three parts of the contact (shaft, fluid film, pad) was carried out by the finite volume method.

The results obtained were commented on and compared to experimental records obtained for the same type of mechanism. Good agreement was observed. The work of REBIAI Moussa [3] aimed to analyze the influence of geometric parameters on the behavior of a plain bearing operating at high speed turbulent by studying the variation of the rotation speed of the shaft and the impact of the load applied on a axially grooved finished plain bearing for various simulated operating conditions. The problem is solved numerically using the computational fluid dynamics (CFD) approach with conditions to the appropriate limits. This study also aimed to better predict the variation in circumferential pressure of the fluid-film. The results showed that the variation of the different geometric parameters and power conditions clearly influence the thermo-hydrodynamic (THD) behavior of a bearing smooth grooved operating in

turbulent regime. Nacer TALA IGHIL in his study [4] modeled and studied the evolution of the static characteristics of a plain bearing with the presence of textures on the surfaces of contact with it. MALKI Maamar et al. [5] studied the influence of machining defects on performance plain bearings of finite dimensions. Their work consisted of analyzing the influence of the surface condition on the hydrodynamic behavior of these mechanisms. For this purpose, a model of variation of the shape of the surface state has been proposed where a periodic and sinusoidal profile is adopted. The fundamental equations of lubrication have been modified taking into account the change in film thickness due to waviness of the rough surface and several tests have been developed. The problem was solved numerically using a finite difference scheme. The results obtained showed that the surface condition has an influence not negligible on the static performances of the bearings and that the increase in the amplitude of roughness of the surfaces induces pressure degradation. This work is the extract of studies and research and creations of equations which combine all the behavior of non-Newtonian lubricants which modify the Reynolds equation especially for Ostwald de Wael power fluids because it describes well the effects non-Newtonian in the rheology of fluids.

## II. FLUID DYNAMICS

Fluid dynamics (hydrodynamics or aerodynamics), is the study of the movements of fluids, whether liquid or gaseous. It is part of fluid mechanics with hydrostatics (statics of fluids). Solving a fluid dynamics problem requires calculating various properties of fluids like velocity, viscosity, density, pressure and temperature as functions of space and time [6]. The study of the behavior of the oil film contained in a plain bearing falls within the field of hydrodynamics. The operating characteristics of our bearing are shown in Figure 1.

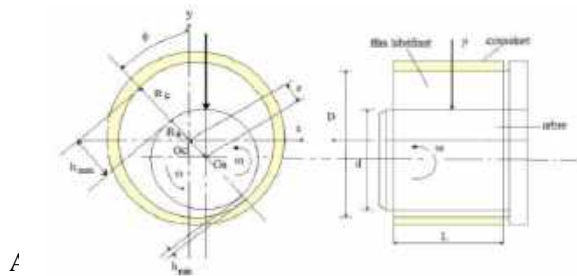


Fig.1: Illustration of the geometrical Characteristics of a

- The relative clearance (C/R).

- The ratio (L/D) of the length to the diameter of the bearing.

The used geometrical characteristics like follows:

	Data	Dimension
Bearing	80	mm
Rod	79.75	mm
Stroke length	60	mm
Radial clearance	0.25	mm
Ratio	0.375	-
Relative Eccentricity	0.5	-

Table 1: the geometrical Characteristics data.

The oil used is an "ISO VG 32" type mineral oil which has a density of 800 kg/m<sup>3</sup>, the consistency indice of 0.112 Pa.s, thermal conductivity of 0.13 J/m. K and a viscosity indice n=1 .

## III. CREATION OF GEOMETRY

The geometry of our bearing is obtained using a FORTRAN program. For the bearing, we have used the equation of a circle, and for the shaft we considered radial play, eccentricity and the pitch angle.

$$x^2 + y^2 = R_c^2 \quad (1)$$

$$(x - x_0)^2 + (y - y_0)^2 = R_a^2 \quad (2)$$

$$x_0 = e * \sin\left(\frac{\pi}{2} - \phi\right) \quad (3)$$

$$y_0 = -e * \cos\left(\frac{\pi}{2} - \phi\right) \quad (4)$$

$$R_a = R_c - C \quad (5)$$

All these equations were written using the Fortran language. The visualization of the geometry of the bearing is made by the Tecplot software (Figure 2) according to a file of data containing the Cartesian coordinates of the necessary points obtained from the program FORTRAN. These points are used to create cloths from which we can generate the different surfaces.

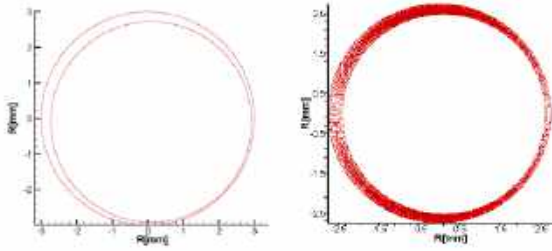


Fig. 2: The used geometry and meshing field.

#### IV. THE GOUVERNING EQUATIONS

$$P(\theta) = \frac{6\mu\omega\left(\frac{R}{C}\right)^2}{(1-\varepsilon^2)^{3/2}} \left[ \psi - \varepsilon \sin \psi - \frac{2\psi - 4\varepsilon \sin \psi + \varepsilon^2 \psi + \varepsilon^2 \sin \psi \cos \psi}{2 + \varepsilon^2} \right] + P_a \quad (6)$$

Pressure equation for a Non-Newtonian fluid:

$$P(\theta) = \frac{6K\omega(R/C)^2((D_0/D_c)N)^{(n-1)}}{(1-\varepsilon^2)^{3/2}} \left[ \psi - \varepsilon \sin \psi - \frac{2\psi - 4\varepsilon \sin \psi + \varepsilon^2 \psi + \varepsilon^2 \sin \psi \cos \psi}{2 + \varepsilon^2} \right] + P_a \quad (7)$$

For the temperature:

$$\begin{aligned} T(\theta) = & \left[ \lambda \left[ \frac{2R^2 L \omega^2 m}{\sqrt{1-\varepsilon^2}} \tan^{-1} \left( \frac{1-\varepsilon}{1+\varepsilon} \tan \frac{\theta}{2} \right) + \frac{RL\omega C P(\theta)}{2} + \frac{\omega e}{2} W \sin \phi \right] \right. \\ & / \left[ \frac{\rho C p_f}{(n+1)(n+2)} \left( \frac{1}{m} \frac{\partial P}{\partial x} \right)^2 \left( \frac{1}{m} \frac{\partial P}{\partial x} y + \frac{U_2 - U_1}{h} - \frac{1}{2m} \frac{\partial P}{\partial x} h \right)^{(n+2)} \right. \\ & - \left( \frac{U_2 - U_1}{h} - \frac{1}{2m} \frac{\partial P}{\partial x} h \right)^{(n+2)} - y(n+2) \left( \frac{1}{m} \frac{\partial P}{\partial x} \right) \left( \frac{U_2 - U_1}{h} - \frac{1}{2m} \frac{\partial P}{\partial x} h \right)^{(n+1)} \\ & \left. \left. + y U_1 \right] \right] \quad (8) \end{aligned}$$

And for the angle  $\theta$ :

$$\cos \theta = \frac{\cos \psi - \varepsilon}{1 - \varepsilon \cos \psi} \quad (9)$$

$$\sin \theta = \frac{(1 - \varepsilon^2)^{1/2} \sin \psi}{1 - \varepsilon \cos \psi} \quad (10)$$

$$d\theta = \frac{(1 - \varepsilon^2)^{1/2} d\psi}{1 - \varepsilon \cos \psi} \quad (11)$$

The table 2 can illustrate the entering the used case data:

	Data	Dimension
The alimentation pressure Pa	0.006127	Mpa

The temperature of alimentation Ta	46	C°
The imposed charge	0.65	Kg

Table 2: The entering boundary condition of data

#### V. RESULTS AND DESCUTION

##### A. PROGRAM VALIDATION

Before presenting the pressure and temperature fields within our bearing, we tried to validate our numerical results by comparing them to experimental results. Figure 5 shows a comparison between the results obtained by our program written in Fortran language. The rotation speed is 2000 rpm. The two curves, experimental and numerical, have the same appearance, with a slight difference for a few angles  $\theta$ . We notice that the pressure increases with the increase in the angle  $\theta$  up to approximately  $100^\circ$  then it descends until reaching its minimum at around  $200^\circ$  then it rises again and the experimental study by DJENDARA [8].

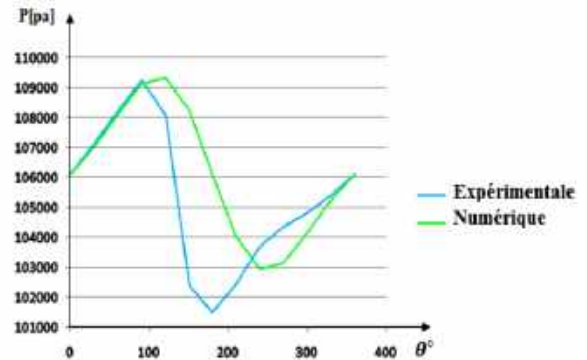


Fig. 3. Comparison between numerical and experimental results for pressure variation as a function of the angle  $\theta$ .

##### B. PRESSURE FIELD WITHIN FLUID FILM

it was able to simulate the hydrodynamic behavior of the film of oil within the bearing for the Newtonian oil, we added two other non-Newtonian oils to compare them with the first Newtonian oil and see which of them will give better behavior for the fluids of viscosity indice  $n = 0.95$  and  $n = 1.05$ . Figures 4-a, 4-b and 4-c show the contours of the pressure field within the oil film, for three oils which have the same consistency indice but different viscosity indicees and speed of rotation of 2000 rpm. We notice that in the three figures there are areas of high pressure as well as low pressure areas. The maximum pressures are at the bottom of the bearing, while the minimum pressures are located on the upper part of the bearing. We also notice that the rheo-

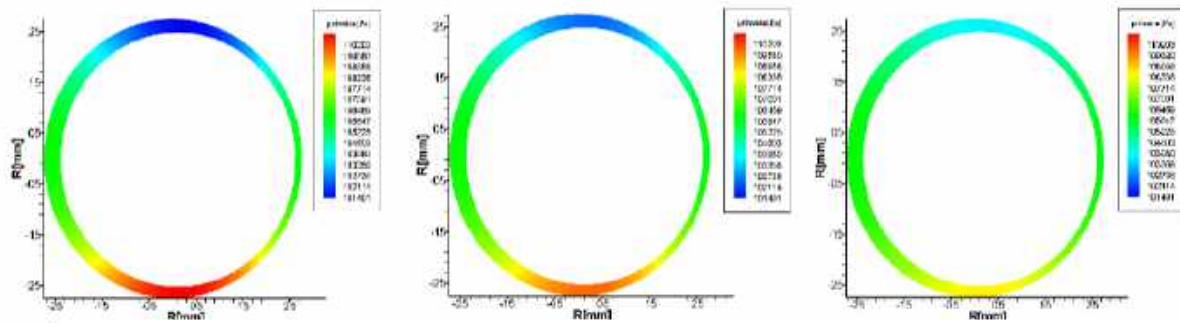


Fig.4. The hydrodynamic pressure distribution for (a) " $n=0,95$ " & (b) " $n=1$ " & (c) " $n=1,05$ ".

### C. TEMPERATURE DISTRIBUTION WITHIN FLUID FILM

Figures a-5, b-5 & c-5 show the contours of the temperature distributions within the oil film for different viscosity indices and a rotational speed of 2000 rpm.

The shape of the temperature distribution is almost the same for the three oils, except that we noticed that the temperature rises each time the viscosity indice increases.

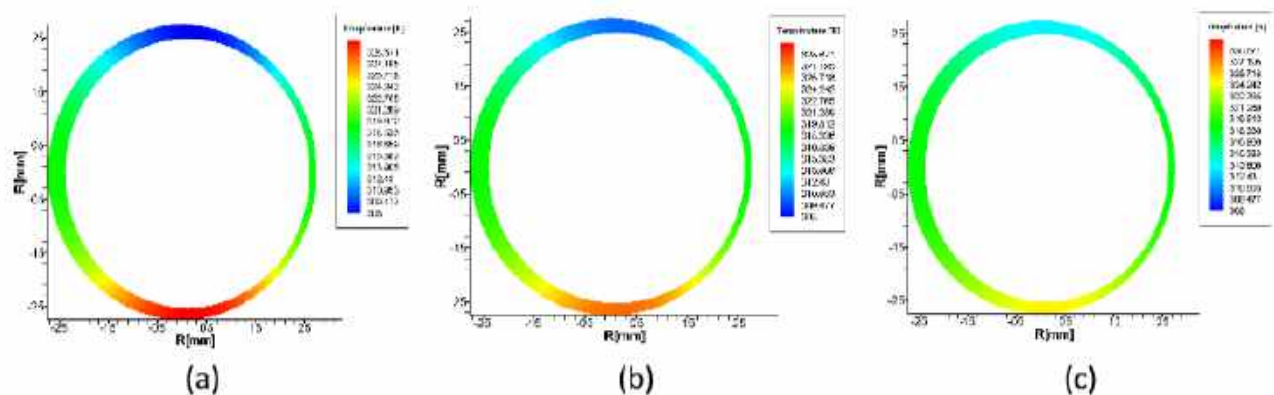


Fig.5. The temperature distribution for (a) " $n=0,95$ " & (b) " $n=1$ " & (c) " $n=1,05$ ".

### D. PRESSURE FIELD WITHIN FLUID FILM

- The variation of the friction torque as a function of the angular speed has an almost linear appearance.
- The friction torque is proportional to the rotation speed.
- The friction torque is proportional to the viscosity indice.
- The friction torque increases more quickly for an oil with a high viscosity indice than for an oil that has a lower viscosity indice.

splicing oil gives the maximum pressure, followed by Newtonian oil and finally shear thinning oil. So there is proportionality between pressure and viscosity indice.

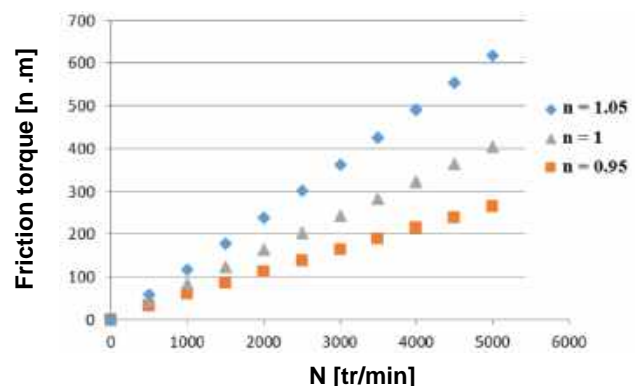


Fig.6. Friction torque as a function of rotation velocity.

In this study, we wrote a method to compute the Non-Newtonian fluid of Ostwald that by mean of a Fortran program language which allowed us to create the geometry of a hydrodynamic bearing, and to simulate the behavior of the lubricating oil that is between its

shaft and its bearing. The visualization of the results was done by Tecplot software. First, we used Newtonian oil with a viscosity indice  $n=1$ , the numerical results were in good agreement with the experimental results, and then we added two other oils, a shear-thinning oil with an indice viscosity of  $n=0.95$ , and a shear thickening oil with  $n=1.05$ . The comparison between the distributions of pressure and temperature showed that the three oils have the same distribution of pressure and temperature, but the maximum pressures and temperatures were achieved by shear thickening oil, then Newtonian oil, and finally shear thinning oil. In addition, the variation of the friction torque in function of the rotational speed showed that there is proportionality between these two parameters. He was also noticed that there is proportionality between the friction torque and the viscosity indice.

## REFERENCES

- [1] Aurelian Fatu, Etude numérique et expérimentale des paliers de moteur thermique et des joints d'étanchéité dynamique, Habilitation à diriger les recherches, Université de Poitiers, 2013
- [2] A. Maoui et B. Benabès, "Modélisation numérique du comportement TEHD des paliers lisses cylindriques", Revue des Energies Renouvelables, CISM'08 Oum El Bouaghi, 239 – 255, 2008.
- [3] REBIAI Moussa, Influence des paramètres géométriques et des conditions d'alimentation sur le comportement THD d'un palier lisse fonctionnant en régime turbulent, Thèse pour l'obtention du Grade de Docteur En Sciences, département de génie mécanique, faculté de génie mécanique, université des sciences et de la technologie d'Oran, Mohamed Boudiaf, 2021.
- [4] TALA IGHIL Nacer, Contribution à l'étude des paliers en régime hydrodynamique instationnaire : influence des états de surface, Thèse de doctorat, Université des sciences et de la technologie Mohamed Boudiaf d'Oran, 2007.
- [5] MALKI Maamar, BOUBENDIR Sid Ali, LARBI Salah, BENNACER Rachid, BENDJAMA Oussama, "Comportement des paliers hydrodynamiques en présence de défauts de forme et de rugosité", Conference Paper, November 2018.
- [6] Dynamique des fluides, Wikipedia, [https://fr.wikipedia.org/wiki/Dynamique\\_des\\_fluides](https://fr.wikipedia.org/wiki/Dynamique_des_fluides) .
- [7] Mihoubi Khalid and Sadini Rachid, Contribution to the study of a smooth hydrodynamic bearing, Thesis presented for obtaining the academic Master's degree, Mohamed Boudiaf Msila University, (2017).
- [8] DJENDARA Abdelhakim Amine, Study of the flow of Newtonian and non-Newtonian fluids in the lubrication of plain hydrodynamic bearings, Master's thesis, University of Sciences and Technology Mohamed Boudiaf of Oran, (2012).



# Recycled polystyrene used as a binder for optical glass finishing pellets

KHELLAF IKRAM<sup>1,3\*</sup>, BELKHIR NABIL<sup>1,3</sup>, AND ZEGADI AKRAM<sup>2,3</sup>

1. Laboratory of Applied Optics, Institute of Optics and Precision Mechanics, University Ferhat Abbas Setif1, 19000 Setif, Algeria
2. Emerging Materials Research Unit, Ferhat Abbas University Setif 1, Algeria,
3. Optics and Precision Mechanics Institute, Ferhat Abbas University Setif 1, Algeria

## ABSTRACT

*The aim of this work is to produce pellets based on alumina and cerium abrasive grains bonded with a recycled organic binder (polystyrene), with high wear resistance and optimum durability, to improve the quality of optical surfaces. The combination of raw materials used and the experimental protocol followed enabled us to produce pellets in large repeat quantities, at lower cost, and with reduced environmental impact compared with the conventional process. The results indicate that these pellets have a homogeneous internal structure, which contributes to their longer service life. The softening and polishing process with the manufactured pellets is carried out on crown optical glass samples. A final root-meansquare (RMS) roughness of  $0.01\mu\text{m}$  was achieved; in addition, a material removal rate of  $0.01\text{g}$  for the glass samples was obtained, leading to a final result that is relatively satisfactory.*

## KEY WORDS (3 to 6 key words)

Recycled polystyrene; surface finish; alumina; cerium oxide; pellets; optical glass.

## I. INTRODUCTION

Due to the effectiveness of bonded abrasive pellets in eliminating surface defects, and their relatively easy control of surface condition compared to free abrasive processes, pellets are finding increasing application in the finishing of optical lenses, ceramics, etc. [1, 3]. The removal rate has been shown to be higher than with conventional processes, and surface quality has been shown to be very fine [4]. The quality of surfaces treated with bonded abrasive pellets is particularly high. influenced by the following manufacturing parameters: compaction pressure, pellet geometry, firing temperature and time, and finally the nature of the material. In this study, new finishing tools for

lapping and polishing optical surfaces based on alumina, cerium and a recycled organic binder (polystyrene) will be produced. This combination not only solves the problems encountered in conventional free abrasive processes, but also reduces the ecological impact by using a binder from a recyclable source. Next, we aim to characterize and experimentally study the wear resistance of these pellets by measuring mass loss during their operation. Finally, to determine their ability to produce high-quality optical surfaces with minimal roughness (RMS) and a relatively low rate of material removal from samples.

## RESULTS AND DISCUSSION

### A. EFFECT OF BINDER TYPE ON WEAR OF LAPPING AND POLISHING PELLETS

The wear of alumina pellets bonded with recycled polystyrene was characterized by loss of mass, and the results obtained are shown in **figure 1**. Indeed, after 30 minutes of doubling, i.e. a complete process in our case, the pellets bonded with recycled polystyrene showed a wear value of  $0.22\text{g}$ , which is quite low compared with the initial mass of the pellets, which is  $3\text{g}$ , reflecting the tool's good resistance, enabling it to perform several lapping cycles and extend its service life.

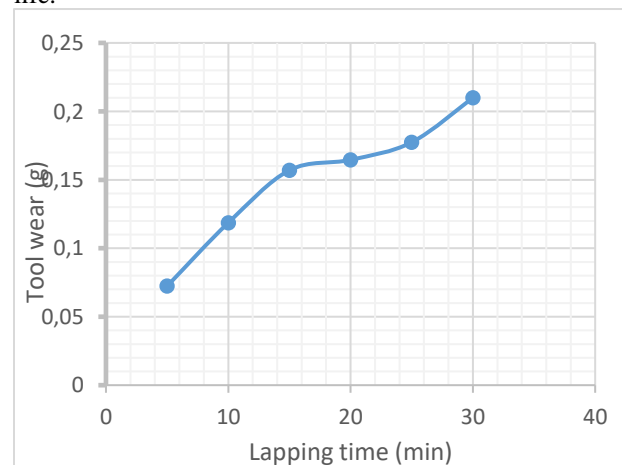


**Figure 1:** Wear variation of alumina liner pellets bonded with recycled polystyrene

*EFFECT OF BINDER TYPE ON THE SURFACE QUALITY OF OPTICAL GLASS GROUND AND POLISHED BY PELLETS*

One of the most relevant parameters for defining the efficiency of lapping and polishing tools is the roughness of the treated glass. In fact, the variation in roughness value during stoving of crown glass with alumina pellets bonded with recycled polystyrene shown in **figure 3** shows a significant decrease, reaching a value of  $0.25 \mu\text{m}$  after a lapping time of 25 minutes. This reduction in surface roughness is due to the material removal phenomenon caused by the abrasive grains present in the stoving pellets, reflecting the operation of a large majority of the abrasive grains in contact with the optical glass surface and an efficient and optimal material removal, resulting in an optimal surface finish for the treated optical glass.

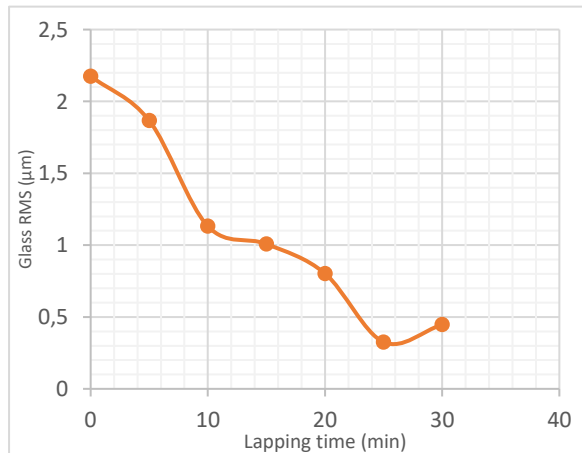


**Figure 3 :** Variation in squared roughness of crown optical glass treated with recycled polystyrenebonded pellets as a function of softening time.

## II. CONCLUSION:

Based on the results obtained, the following conclusions have been drawn: Alumina and cerium oxide pellets bonded to recycled polystyrene play a key role in the lapping and polishing processes, as finishing surfaces by the pellets enable nanoscale quadratic roughness values to be achieved. Wear and tear on the agglomerate tools used for lapping and polishing is relatively low, due to the processing parameters, resulting in appreciable tool life. The nature of the binder has a major influence on surface quality and tablet wear. The choice of polystyrene as a binder strongly encourages not only the recycling of non degradable materials, but also the use of their

relevant properties for a second function.

## REFERENCE:

- [1] Li Y, Wu Y, Wang J, Yang W, Guo Y, Xu Q (2012) Tentative investigation towards precision polishing of optical components with ultrasonically vibrating bound-abrasive pellets. *Opt Express* 20:568–575. <https://doi.org/10.1364/oe.20>.
- [2] Bouzid D, Belkhir N (2014) Investigation of alumina pellets for optical glass grinding. *Arch Mater Sci Eng* 67:14–17
- [3] Hitchiner M, Uhlmann E, Rowe WB, Inasaki I (2006) *Handbook of machining with grinding wheels*, First Edition, CRC Press
- [4] Gillman BE, Jacobs SD (1998) Bound-abrasive polishers for optical glass. *J Appl Opt* 37:3498–3505. <https://doi.org/10.1364/ao.37.003498>.

***Session T8: Materials  
elaboration and  
characterization  
methods***

# Elaboration, Design, characterization and Mechanisms of PANI-MnO<sub>2</sub>

Assia Tounsi<sup>1,2\*</sup>, Ahmed Bahloul<sup>1</sup>, Atef chibani<sup>1</sup>, Lasmi sofiane<sup>1</sup>, Leila Lamiri<sup>1,3</sup>, Ouafia belgherbi<sup>1</sup>, Farid Habelhames<sup>1, 2</sup>

<sup>1</sup>Research Center in Industrial Technologies CRTI, P.O. Box 64, 16014 Cheraga, Algiers, Algeria

<sup>2</sup>Laboratoire d'Electrochimie Et Matériaux (LEM), Faculté de Technologie. Département de Génie Des Procédés, Université Ferhat Abbas, 19000 Sétif 1, Algeria

<sup>3</sup>Département de Génie de L'Environnement, Faculté Des Sciences Et de La Technologie, Université Mohamed El Bachir El Ibrahimi, 34000 El Anceur, Algeria  
e-mail address tounsiassia56@gmail.com

## ABSTRACT

*Intrinsically conducting polymers ICPs can be combined with further electrochemically active materials into composites for use as active masses in supercapacitor electrodes. Typical examples are inspected with particular attention to the various roles played by the constituents of the composites and to conceivable synergistic effects. Stability of composite electrode materials, as an essential property for practical application, is addressed, taking into account the observed causes and effects of materials degradation.*

**KEY WORDS** MnO<sub>2</sub>/PANI, supercapacitors, electrochemical deposition intrinsically conducting polymer

## I. INTRODUCTION

As a sort of classic conducting materials, polyaniline (PANI) possesses good conductivity with specific organic characters that metal cannot match, which has attracted a lot of attentions for its wide applications in capacitance, sensors, ultrafast nonvolatile memory devices, and chemical catalysis [1-3]. Nanostructured materials provide new and exciting approaches to the development of supercapacitor electrodes for high-performance electrochemical energy storage. Electrode materials are the key factor of supercapacitor's capacitance performance. Metal oxides [1], conducting polymers [3], and carbon porous nanoparticles [2] have been identified as the most promising materials for super-capacitors, whose modification and compounds are being used to

enhance the material performance [4]. Large numbers of researchers have applied the nanocomposites of conducting polymers and metal oxides to energy storage. Among the metal oxides, hydrous RuO<sub>2</sub>, NiO, CoOx, and V<sub>2</sub>O<sub>5</sub> have been researched and implemented as electrode material [6-8]. However, the low capacitance and high cost limits their range of applications and have motivated the research into other transition metal oxides. MnO<sub>2</sub> has been regarded as an ideal candidate due to its affordable and easily prepared advantages [9].

## II. Experimental

The electrodeposition of MnO<sub>2</sub>-doped PANI thin films was performed in an electrochemical cell with three-electrode containing saturated calomel electrode (SCE, +0.241 V vs. standard hydrogen electrode, NHE) as reference electrode, A graphite rod bar was used as a counter electrode, and fluorine-doped tin oxide glass substrate (FTO) as a working electrode with an exposed area of 1cm<sup>2</sup>. Prior to any deposition step, the FTO glass substrates were rinsed with distilled water and then degreased in ultrasonic baths with acetone (CH<sub>3</sub>-COCH<sub>3</sub>) and methanol (CH<sub>3</sub>OH) for 15 min to remove the surfaces contamination and finally rinsed with distilled water. The deposition of MnO<sub>2</sub>-doped PANI thin films was carried out potentiostatically at 1.20 V vs. SCE for 180 s as time period. The MnO<sub>2</sub> and the PANI simultaneously deposited. Directly on pre-cleaned FTO glass substrate, by using a computer-controlled potentiostat/galvanostatic (VoltaLab-PGZ-301) as a potential source. The growth electrolytes used for preparing PANI-MnO<sub>2</sub> thin films contained 10 mM aniline (SIGMA-ALDRICH), 1 M H<sub>2</sub>SO<sub>4</sub> (SIGMA-ALDRICH) as supporting electrolyte and different amounts of manganese sulphate MnSO<sub>4</sub>·H<sub>2</sub>O (BICHEM Chemopharma) (100, 200 and 300 mM) as

dopants source. The deposited films have been named as follows, FTO/PANI-MnO<sub>2</sub>100, FTO/PANI-MnO<sub>2</sub>200 and FTO/PANI-MnO<sub>2</sub>300 respectively.

The prepared films were characterized by several technics, such as FTIR (ATR) spectroscopy using a spectrometer (Shimadzu, IR prestige-21, Japan). The morphological investigations of the composite films were performed by scanning electron microscope (Jeol JSM-7001). The electrochemical properties were evaluated at room temperature by mean of PGZ-301 Voltalab coupled with software equipped computer (Voltamaster 4) that gives opportunity to select the electrochemical technique and fix the wanted parameters.

### III. Resultants and discussion

Conducting polymers and transition metal oxides are good electrodes for supercapacitors owing to their high charge storage characteristics. Different techniques have been utilized in fabricating novel nanocomposites of polyaniline (PANI) and manganese dioxide (MnO<sub>2</sub>) for capacitance enhancement. The electrodeposition of all composite films was successfully carried out by mean of technic chronoamperometry; the tests were realized in the same conditions afore mentioned.

A chronoamperometric (current – time transient) study was carried out in order to investigate the electropolymerization of aniline during 180 s deposition times.

Figure 1 illustrates the variation of the current density at 1.2 V versus SCE throughout the imposed period. The illustration is related to the different composite films, FTO/PANI (A) and FTO/PANI-MnO<sub>2</sub>100 (B). What can be clearly noticed is the chronoamperograms' similarity except from limit currents, which is that the 100 mM concentration used during the electrodeposition of PANI film increases the growth of the PANI film on the FTO substrate. These findings confirmed that the deposition process of the PANI is faster and easier with the contribution of MnO<sub>2</sub>doping.

The chronoamperograms depict three plain zones. The first one is related to the very first instant of the starting process. The occurring current decrease illustrates the electrochemical negative double layer stack. The second zone is associated with the increase of the current density intensity, which indicates that the electroactive surface area grows as a function of the amount of material deposition. Finally, the stability current density, according to our own postulation, is consequent to the formation of the homogeneous uniform layer. [1].It is important to indicate that the FTO/PANI-MnO<sub>2</sub>100 film has more conductors and this will be confirmed by

electrochemical impedance spectroscopy analysis

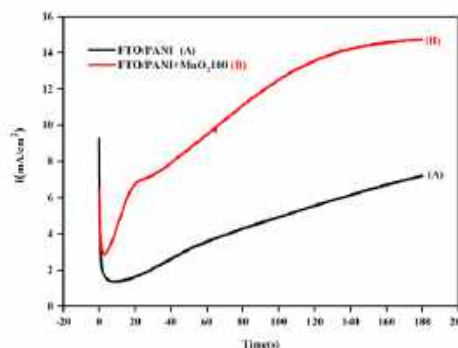


Fig. 1 Chronoamperograms of FTO/PANI (A) and FTO/PANI-MnO<sub>2</sub>100 (B)

Electrodes produced from the proposed materials were examined by CV and EIS measurements and their electrochemical properties were evaluated to investigate their potential use for supercapacitors.

In order to inspect the effect of MnO<sub>2</sub> doping in the electrochemical behavior of the behavior of PANI, the voltammetric measurements were carried out. The electrochemical behavior of thin films of FTO/PANI (A), FTO/PANI-MnO<sub>2</sub>100 (B), FTO/PANI-MnO<sub>2</sub>200 (C) and FTO/PANI-MnO<sub>2</sub>300 (D) were studied through cyclic voltammetry performed under -0.2 to 0.9 V potential range, relative to SCE, in aqueous electrolyte 0.5 M H<sub>2</sub>SO<sub>4</sub> at scan rate 5 mV s<sup>-1</sup>) as shown in Fig. 4.

Each curve shows well-shaped redox peaks instead of rectangular form. The curves got stand for pseudo-capacitive behavior of the synthesized materials. Besides, FTO/PANI-MnO<sub>2</sub>100 composites redox peak densities are clearly higher than those of FTO/PANI, FTO/PANI-MnO<sub>2</sub>200 and FTO/PANI-MnO<sub>2</sub>300 composites owing to the binary composites stronger synergistic effect PANI and MnO<sub>2</sub>100.

As for FTO/PANI, and binary composite films, there are three couples of redox peaks in CV curves. The first redox couple located between 0.1 and 0.2 V vs. SCE refers to the oxidation–reduction of the PANI molecules that shifts from semiconducting state Leucoemeraldine to conductive condition Emeraldine. Similarly, the second redox 0.4 to 0.5 vs. SCE couple, under the same occurrence, i.e., oxidation–reduction phenomenon, refers to the direct consequence of the head-to-tail dimer.

The 0.75 V to 0.9 V vs. SCE third redox couple refers, for its part, to the transformation of Emeraldine to entire oxidation form Pernigraniline [1, 3]

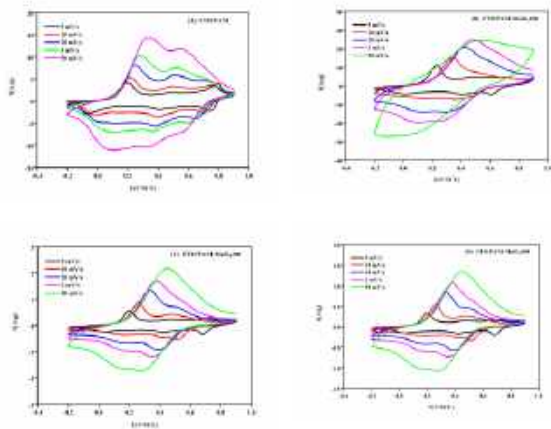


**Fig. 2.** Cyclic voltamogrammes of FTO/PANI (A), FTO/PANI-MnO<sub>2</sub>100 (B), FTO/PANI-MnO<sub>2</sub>200 (C) and FTO/PANI-MnO<sub>2</sub>300 (D), at different scan rates in 0.5 M H<sub>2</sub>SO<sub>4</sub> electrolyte

Electrochemical impedance spectroscopy (EIS) was carried out at different applied potentials in the 100 KHz to 10 mHz frequency range with an alternative current voltage of 10 mV. Figure 4 presents the impedance spectra of the FTO/PANI and FTO/PANI-MnO<sub>2</sub> samples in 0.5 M H<sub>2</sub>SO<sub>4</sub> electrolyte. The EIS spectra have a single semicircle in the high frequency region and a most vertical line in a low-frequency region, characteristic of a charge transfer process and a diffusion process, respectively. The line at the low frequency region is vertical which confirm that these films behave as the nearly ideal capacitors [11]

Electrochemical impedance spectra demonstrate that FTO/PANI-MnO<sub>2</sub>100 film present a much-enhanced conductivity than film FTO/PANI one.

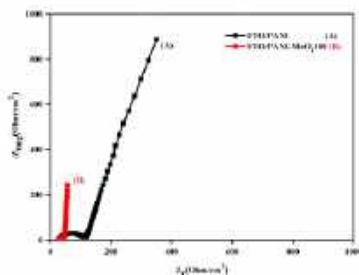


**Fig.3** Nyquist plots of FTO/PANI (A) and FTO/PANI-MnO<sub>2</sub>100 (B) in 0.5 M H<sub>2</sub>SO<sub>4</sub> electrolyte

To obtain more chemical composition of the composites FTO/PANI-MnO<sub>2</sub> were tested with the FTIR spectrum. Figure 2 show a spectrum of MnO<sub>2</sub> (A), PANI (B) and PANI-MnO<sub>2</sub> (C). Figure 4(A) shows a broad intense peak at 3330 cm<sup>-1</sup> which corresponds to the OH band. Typically, the Mn-O stretching mode gains its characteristic peak within 500 cm<sup>-1</sup> to 900 cm<sup>-1</sup>. In this case, the 484 cm<sup>-1</sup> peak MnO<sub>2</sub> spectra owes to the stretching vibration of

MnO<sub>6</sub> octahedral units. The 1049 cm<sup>-1</sup> narrow bands and 1093 cm<sup>-1</sup> low, for their part, to the OH bending vibration combined to the Mn atom. The occurrence of both characteristic peaks at 2883 cm<sup>-1</sup> and 2979 cm<sup>-1</sup> is linked to the effect of organic residues of the MnO<sub>2</sub> surface [1]. Figure 2(B) FTO/PANI spectrum displays different characteristic peaks involving the peaks at 882, 1049, 1192, 1512, 1713, 3232 cm<sup>-1</sup>. The set peaks refers to the vibration modes as follows: bending of C-H out-of-plane on benzene ring (B), bending of C-H in-plane, mode of N = quinoid ring (Q) = N, stretching of aromatic-N, stretching of N-B-N, stretching of N = Q = N, and the peak at 3232 cm<sup>-1</sup> was due to O-H stretching band of water, respectively [1]. Figure 2(C) four peaks 448, 879, 1050, and 1095 cm<sup>-1</sup> PANI-MnO<sub>2</sub> refers to the MnO<sub>2</sub> bending vibration. The same phenomenon takes place for the PANI-MnO<sub>2</sub> sample. Both occurrences certify the successful formation of the composite [1,3].

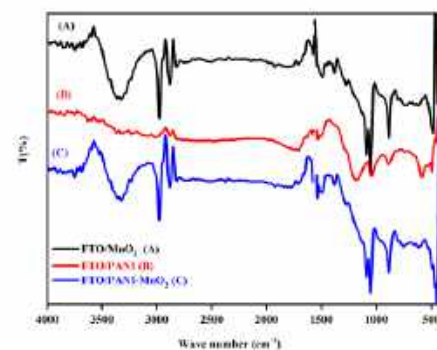


**Fig. 4** FTIR spectrums of MnO<sub>2</sub> (A), PANI (B), PANI-MnO<sub>2</sub> (C)

The influence of the MnO<sub>2</sub> doping on the morphological features of the electrodeposited PANI-MnO<sub>2</sub> thin films was further examined by scanning electron microscopy (SEM). As shown in Fig. 5(A) which indicates that the FTO/PANI has a porous surface with a nanofibrous structure. The observed porous structure nano-fiber is of high interest for supercapacitors appliance conception. Indeed, it is well-established that the porous structure nano-fiber reduces the electrolyte resistance of the electrode matrix [1]. Figure 5(B) shows a micrograph of FTO/PANIMnO<sub>2</sub> with a different morphologies and less porous structure compared to the FTO/PANI morphology. According to these results, we can infer that the good contact between PANI and MnO<sub>2</sub> is conducive to the transfer of electrons, enhancing the specific capacitance. This reveals the high quality of our electrodeposited samples. In particular, by the inclusion of MnO<sub>2</sub> doping, more compact and smoother films were obtained



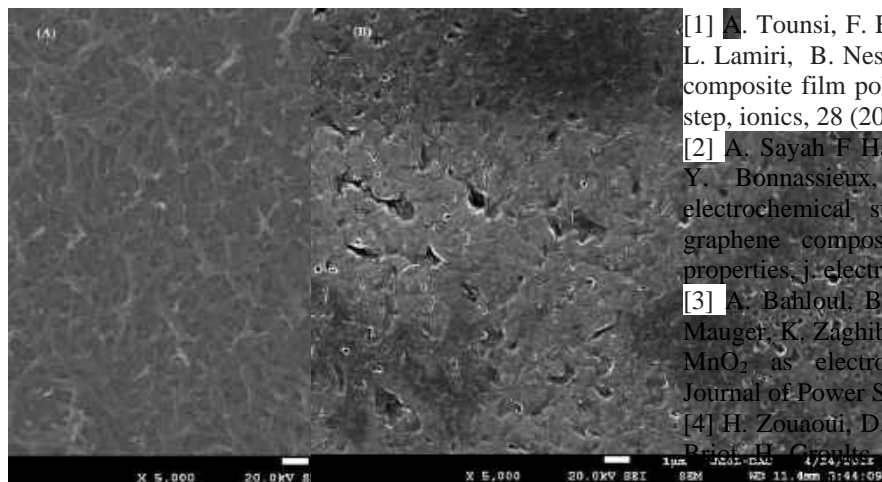


Fig. 5 SEM images of FTO/PANI (A) and FTO/PANI-MnO<sub>2</sub> (B)

#### IV. CONCLUSION

In summary, the study of an electrosynthesis of binary composite material (FTO/PANI-MnO<sub>2</sub>) in a one step with success via chronoamperometry electrochemical technique. Excellent electrochemical performance of the FTO/PANI-MnO<sub>2</sub>100 based electrode is attributed to the synergistic effect of the combination of all constituents. The FTO/PANI-MnO<sub>2</sub>100 composite films were taken as an example for the application to the supercapacitor electrode materials. The obtained specific capacity for the PANI material alone is about 209.90 F g<sup>-1</sup> this value was increased up to 349.60 F g<sup>-1</sup> for the composite film FTO/PANI-MnO<sub>2</sub>100 at 5 mV s<sup>-1</sup>. While the films with polyaniline and MnO<sub>2</sub> give a good capacitance, this is due to the beneficial effect of MnO<sub>2</sub> electronic conductivity. Among the advantages of this electrode are its easy elaboration and its low-cost, which allows us to use it as an electrode for supercapacitors.

#### REFERENCES

- [1] A. Tounsi, F. Habelhames, A. Sayah, A. Bahloul, L. Lamiri, B. Nessark, Electrosynthesis of a ternary composite film polyaniline-MnO<sub>2</sub>-graphene in a one-step, ionics, 28 (2022) 317–328
- [2] A. Sayah F Habelhames, A. Bahloul, B. Nessark, Y. Bonnassieux, D. Tendelier, M. el Jouad, electrochemical synthesis of polyaniline-exfoliated graphene composite films and their capacitance properties, j. electroanal. chem. 818 (2018) 26-34,
- [3] A. Bahloul, B. Nessark, E. Briot, H. Groult, A. Mauger, K. Zaghib, C.M. Julien, Polypyrrole-covered MnO<sub>2</sub> as electrode material for supercapacitor, Journal of Power Sources, 240(2013)267-272,
- [4] H. Zouaoui, D. Abdi, A. Bahloul, B. Nessark, E. Briot, H. Groult, A. Maugerc, C.M. Julien, Electro-Synthesis, characterization and photoconducting performance of ITO/polybithiophene -MnO<sub>2</sub> composite, MSEB, 208 (2016) 29-38
- [5] Y. Ghalimi, F. Habelhames, A. Sayah, A. Bahloul, B. Nessark, H Derbal-Habak, Y. Bonnassieux, J-M. Nunzi, Enhancement of the capacitance properties and the photoelectrochemical performances of P3HT film by incorporation of nickel oxide
- [6] F. Moulai, O. Fellahi, B. Messaoudi, T.Hadjersi, L. Zerroual, Electrodeposition of nanostructured MnO<sub>2</sub> film for photodegradation of Rhodamine B, Ionics, 24(2018)2099-2109
- [7] L. Lamiri, A. Tounsi, D.E. Hamza, R. Yekhle, M.R. Khelladi, M. S. Akhtar, O. Belgherbi, S. Boudour, F. Habelhames, N. Boumaza, N. Maouche, B. Nessark, Ag-MnO<sub>2</sub> composite materials (ferns-like structures) for hydrogen peroxide reduction in alkaline medium, Inorganic Chemistry Communications, 144 (2022) 109853
- [8] Y. Ghalimi, F. Habelhames, A. Sayah, A. Bahloul, B. Nessark, M. Shalabi, J. M. Nunzi, Capacitance performance of NiO thin films synthesized by direct and pulse potentiostatic methods, Ionics, 25(2019)6025–6033
- [9] B.B. Carvalho, V.C.B. Pegoretti, V.G. Celante, P.V.M. Dixini, P.L. Gastelois, W.A.A. Macedo, M.B.J.G. Freitas, Effect of temperature on the electrochemical synthesis of MnO<sub>2</sub> recycled from spent Zn–MnO<sub>2</sub> alkaline batteries and application of recycled MnO<sub>2</sub> as electrochemical pseudocapacitors, 196(2017)126-136
- [10] Misnon II, Jose R (2017) Synthesis and electrochemical evaluation of PANI/δ-MnO<sub>2</sub> electrode for high performing asymmetric supercapacitors. New J Chem 41:6574–6584.
- [11] Sayah A, Habelhames F, Bahloul A, Boudjadi A (2021) The effect of electrodeposition applied potential on the electrochemical performance of polyaniline films. J Mater Sci Mater Electron 32:10692–10701

# Effet de la trempe libre du polypropylène isotactique sur les propriétés thermiques

MERABET SAFIA<sup>1\*</sup>, BENCID ABDESALEM<sup>1</sup>, FARID ROUABAH<sup>2</sup>, MAGALIS FOIS

1. Research Center in Industrial Technologies CRTI, P.O. Box 64 Cheraga 16014, Algiers, Algeria

[safiamerabet@yahoo.fr](mailto:safiamerabet@yahoo.fr)

[abdeslambencid@yahoo.com](mailto:abdeslambencid@yahoo.com)

2. Laboratoire de Physico-chimie des Hauts Polymères, Université Ferhat Abbas Sétif -1, Sétif 19000, Alegria.

[f\\_rouabah2002@yahoo.fr](mailto:f_rouabah2002@yahoo.fr)

## ABSTRACT

*Ce travail porte sur l'étude des propriétés thermiques du polypropylène isotactique (IPP) en présence de contraintes résiduelles (CR). Une échelle de laboratoire, deux méthodes valides pour introduire des contraintes résiduelles dans le polymère, qui sont le refroidissement non uniforme (trempe thermique), et la déformation plastique non uniforme (laminage à froid) est connue. Le quench libre des échantillons a été effectué dans un bain d'eau à différentes températures et leur effet sur la résistance thermique du iPP a été étudié. Lors de l'augmentation de la température de trempe, le taux de cristallinité est resté constant selon l'analyse DSC. A partir des courbes DMA, a été montré la présentation de deux relaxations  $\alpha$ ,  $\alpha'$  pour tous les échantillons étudiés.*

**KEY WORDS** Isotactic polypropylene, trempe, DMA, DSC

## I. INTRODUCTION

La trempe du polypropylène isotactique (iPP) donne lieu à une organisation structurale dans laquelle les phases –amorphe, mésomorphe et  $\alpha$  –monoclinique coexistent [1] Une relation avec les variables de fonctionnement, comme décrit dans les références 2 et 3 pour le sous-refroidissement faible, ne peut toutefois pas être trouvée dans la littérature, car le contrôle de la température à des vitesses de refroidissement très élevées est difficile. *to assist the Local Organizing Committee with the preparation of the conference program and proceedings and to allow efficient reviewing of submissions by the Scientific Organizing Committee.* Les études des iPP trempées visent en effet principalement à identifier la structure de la phase mésomorphe [4], sa relation avec l'organisation morphologique [5-7], et ses propriétés macroscopiques [1,8], ou au vieillissement de la phase mésomorphe avec le temps et la température [9-10] qui culmine finalement avec sa transformation en phase  $\alpha$  – monoclinique à une température avoisinant les 80°C [10]. Dans le présent travail, nous étudions

l'effet de l'histoire thermique sur le comportement de transformation de phase dans iPP. Les expériences ont considéré les échantillons cristallisés sous refroidissement contrôlé et / ou par trempe. Calorimétrie différentielle à balayage, DMA ont été utilisés pour sonder l'effet des échantillons de trempe, permet également la comparaison des valeurs obtenues dans différentes expériences.

## II – EXPERIMENTAL

### A. Matériaux

Le polypropylène isotactique utilisé dans ces études est un homopolymère sous forme de pastilles cylindriques opaques, obtenu par la société SI-Plast (La zone industrielle –Sétif). Le polypropylène isotactique a été utilisé dans un grade 100 -GB25 avec une densité de 0,2086 gr/cm<sup>3</sup> et un indice de fusion (230°C, 2,16 kg) de 12,60 gr/10min.

### b. Moulage par compression du polypropylène

Les éprouvettes en polypropylène isotactique ont été préparées par moulage par compression dans une presse à platine hydraulique de marque CARVER et charge maximale de 25 tonnes. La mise en œuvre des différents échantillons a été réalisée dans les mêmes conditions de fonctionnement. La pression et le temps de maintien sous pression ont été maintenus constants pendant tous les essais et sont respectivement égaux à 250 kg / cm et 8 minutes. La température de la tablette est réglée à 200 °C. *MAPS,*

### c. TRAITEMENT THERMIQUES

#### Trempe

Nous avons trempé les échantillons d'iPP à partir de l'état fondue dans un bain pendant 15 minutes et à des températures de trempe : 0, 5, 10, 15, 20, 30, 40, 50, 60, 70 et 80 °C, suivie d'un refroidissement à l'air libre à la température ambiante. Le volume d'eau

utilisé dans le bain est constant pour différentes températures de trempe.

#### FIGURES

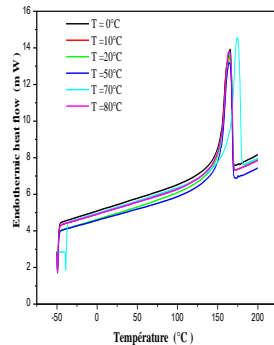


**Fig. 1 :** Thermogrammes d'un échantillon de PPi trempé (au cœur) à 0°C,10°C,20°C,50°C,70°C et 80°C.

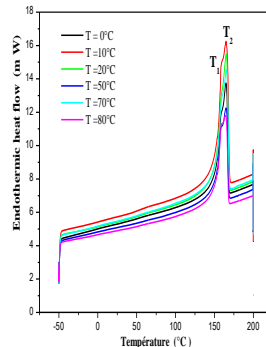


**Fig. 2 :** Thermogrammes d'un échantillon de PPi trempé (à la surface) à 0°C,10°C,20°C,50°C,70°C et 80°C.

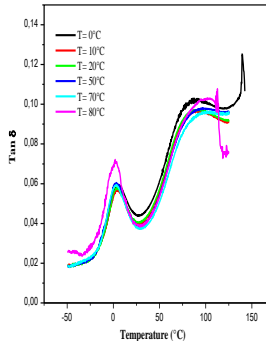
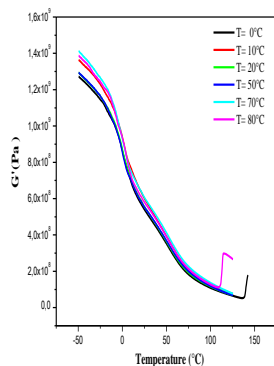


**Fig. 3** montre l'évolution du module  $G'$  (a) Et le facteur de perte  $\tan \delta$ (b) de polypropylène trempé à  $T=0,10,20,50,70$  et 80 °C.

## II. CONCLUSION

L'étude de l'effet de la température de trempe d'un polymère semi-cristallin moulé par compression (iPP)

nous a permis d'obtenir la procédure de trempe est simple, mais très important et efficace pour améliorer les propriétés de l'iPP. Les examens de calorimétrie différentielle à balayage (DSC) ont révélé une augmentation de la cristallinité à une température de trempe de 20 °C. Selon les résultats obtenus de l'analyse DMA, la température de transition vitreuse ( $T_g$ ) n'était pas affectée par des températures de trempe de 0 °C à 50 °C et présentait une valeur inférieure pour l'échantillon trempé à  $T = 80$  °C.

## REFERENCES

- [1] F. Candia, G. De, R. Romano, R. Russo and V. Vittoria.. "Monoaxial drawing behaviour of isotactic polypropylene quenched at different temperatures". *Polymer*. 26, 297(1987).
- [2] F.J. Pedden , H. D. Keith . "Spherulitic Crystallization in Polypropylene". *J. Appl. Phys.* 30, 1479(1959).
- [3] D.R. Northon , A .Keller . "The spherulitic and lamellar morphology of melt-crystallized isotactic polypropylene". *Polymer*. 26 , 7045(1985) .
- [4] P.V. Corradini , C. Petraccone , De Rosa , and G. Guerra . "On the structure of the quenched mesomorphic phase of isotactic polypropylene". *Macromolecules* . 19, 26995(1986).
- [5] D.M. Gezovich , P.H. Geil . "Morphology of quenched polypropylene". *Polym. Eng. Sci.* 8, 202(1968).
- [6] C. C . Hsu , P. H. Geil , H. Miyaji , and K. Asai . "Structure and properties of polypropylene crystallized from the glassy state", *J. Polym. Sci., Part B*. 24 , 2379(1986)
- [7] D. T. Grubb, D.Y. Yoon . Deformation and aging of quenched polypropylene. 8, 210 (1986)
- [8] De, Candia, F, R. Russo, V. Vittori. Mechanical behavior of quenched isotactic polypropylene crystallized by thermal and solvent treatments . *Polym. Eng. Sci.* 34, 689(1987).
- [9] P. J Hendia , J . Vile, H. A. Willis , Zichy V, and M.E.A. Cudby. *Polymer*. 25, 785(1987).
- [10] R. Zannetti , G. Celotti , A. Fichera , and R. Francesconi.. *Makromol. Chem.* 12, 137(1969).

# Influence of quenching temperature on the characteristics of a high strength material: 42CrMo4

D. EMBAREK<sup>1</sup>, D. CHAOUCH<sup>2</sup>

<sup>1</sup>University of Ahmed ZABANA, citéBarmadia rilizan, Algeria, dr.embarek@gmail.com

<sup>2</sup>Laboratory of Elaboration and Physical Mechanical and Metallurgical Characterization of Materials, Algeria, djamel25\_septembre@yahoo.fr

**Abstract** –The use of 42CrMo4 steel in the

automotive and aerospace industry is constantly decreasing due to its low hardness for high load applications. In order to overcome these problems, considerable efforts have been made by various authors to improve the mechanical characteristics.

The search for a better optimization of the relationship microstructure - mechanical properties, leads to an analysis of all the characteristic properties, obtained from experimental methods.

The mechanical characteristics sought concern the yield strength, elongation and tensile strength as well as the fracture energy obtained by resilience measurement. We present the variation of the characteristic parameters according to the tempering treatments applied between 200 and 600°C. These treatments highlight the influence of the tempering phenomenon. They allow the search for a better compromise between the structure of this steel and the mechanical properties in general.

**Keywords** –42CrMo4, mechanical properties, tempering temperature, microstructure, fracture

## I. Introduction

Ferrous alloys form the basis for technological development in various industrial fields. Steels, in particular 42CrMo4, are still preferred in almost all technical and technological fields of application. These include the mechanical, chemical, petrochemical, pharmaceutical and nuclear industries [1]. This steel is used by the BCR OuedRhio unit for the manufacture of bolts and threaded rods due to its high strength, good machinability and high competitiveness. By modifying its chemical composition and the conditions of its obtaining, it is possible to vary its properties.

Several studies [1, 2], have been carried out on 42CrMo4 steel, considering the examination of the effect of ductile and brittle phases of the microstructure on the mechanical properties. The tensile strength of the ferrite-martensite-bainite

(FMB) microstructure increases significantly compared to that of the microstructure before heat treatment.

The objective of this work is to establish a possible correlation between the different parameters, likely to meet the needs of users.

## II. Material and experimental methods

The material used in this study is a 42CrMo4 low-alloy steel, intended for the manufacture of mechanical parts (clamping bolts and threaded rods) by the petroleum and automotive industries. In order to verify the contents of the chemical composition of this steel, an analysis of a sample by means of a spectrometer was carried out.

The problem posed here concerns the serviceability of bolts made from this steel. These tests make it possible to seek the optimal conditions for a better relationship between the heat treatments applied and the mechanical properties of this material

The tensile specimens underwent a 30 min austenitization treatment at 850°C, followed by oil quenching. The evolution of the microstructural states obtained during the tempering treatments of the studied steel was analyzed in this work. The temperature ranges vary from 200°C to 600°C

## III. Result and discussion

In the quenched state, 42CrMo4 steel is two-phase [3]. It consists largely of bainite containing a quantity of martensite in lath. The carbon rejection of these two phases is the main factor controlling all microstructural transformations of the studied steel. A small variation of the low temperature hardness between the quenched condition (56HRC) and the tempered condition at 200°C (49.5HRC) is found. The influence of the tempering heat treatments on the studied steel seems to bring modifications on the mechanical properties. The values of the mechanical characteristics (yield strength, elongation, tensile strength and hardness), vary significantly during these applied tempering heat treatments.

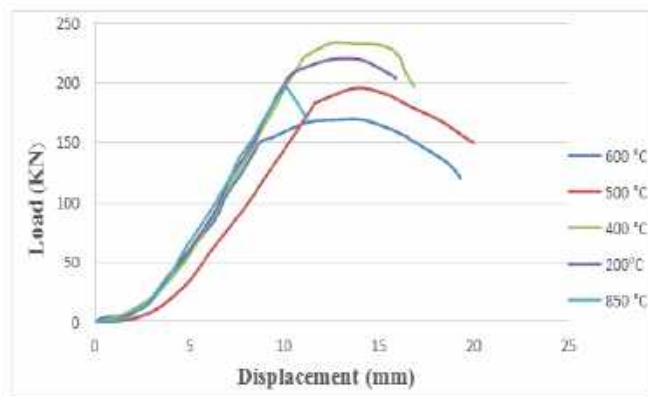


Fig.1 Effect of tempering on mechanical behavior.

#### IV. Conclusions

The influence of the heat treatments of tempering on the studied steel seems to bring modifications on the mechanical properties in general. The values of the mechanical characteristics, evolve significantly during the applied heat treatments of tempering. The values of mechanical characteristics obtained are in the same order of magnitude as those obtained by other authors on comparable steels.

#### References

- [1] Vukelic, G., Brnic, J.: Marine Shaft Steels (AISI 4140 and AISI 5120) Predicted Fracture Toughness by FE Simulation, Materials Science, Vol. 23, No. 1, 2017.
- [2] Stipkovic, M. A., Bordinassi, C., Fariasa, A. and Delijaicova, S.: Surface Integrity Analysis in Machining of Hardened AISI 4140 Steel, Materials Research, December 27, 2016.
- [3] Djamel Chaouch, Seif-Eddine BENDAOUDI and Ahmed Sadok, Effect of charpy impact test on microstructure properties of AISI 4140 steel, LODZ UNIVERSITY OF TECHNOLOGY, Volume 22 Number 4, 2018.

# Mechanical behavior under static, dynamic and cyclic loading test of jute reinforced polyester composite material

DJAMEL DJEGHADER<sup>1\*</sup>, TAHAR TIOUA<sup>1</sup>, BACHIR REDJEL<sup>2</sup>, ADEL BOULEBNANE<sup>2</sup>

Civil and Hydraulic Engineering Department, AbdelHafid Boussouf University Center, Mila, 43000, Algeria.  
Civil Engineering Department, Badji Mokhtar University, Annaba, 23000, Algeria.

## ABSTRACT (1,000 characters)

*The tests under static tensile and bending loads, as well as cyclic 3-point bending fatigue loads, were conducted on prismatic specimens of bidirectional jute polyester composites until complete fracture. These tests made it possible to describe the behavior of these materials and to identify the mechanical characteristics. Under quasi-static stress, the fracture is of the fragile type in direct tension, whereas in bending it is the consequence of the instability of the structure due to damage. In cyclic fatigue loading, the experimental results are described by a Wöhler curve which is characterized by a dispersion in the service lives and which is modeled by a straight line. The concepts of linear elastic fracture mechanics made it possible to interpret the results of dynamic impact tests carried out on notched specimens using the Williams method. The GIC critical rupture energy measurement is characterized by high dispersion. This is essentially due to the heterogeneity of the material, the manufacturing process which induces defects such as voids and air bubbles that are difficult to eliminate, as well as the difficulty of machining a perfect notch base. . The dynamic impact toughness shows a tendency to decrease with the increase in the distance between supports in three-point bending. This is essentially due to the heterogeneity of the material, the manufacturing process which induces defects such as voids and air bubbles that are difficult to eliminate, as well as the difficulty of machining a perfect notch base. . The dynamic impact toughness shows a tendency to decrease with the increase in the distance between supports in three-point bending. This is essentially due to the heterogeneity of the material, the manufacturing process which induces defects such as voids and air bubbles that are difficult to eliminate, as well as the difficulty of machining a perfect notch base. . The dynamic impact toughness shows a tendency to decrease with the increase in the distance between supports in three-point bending.*

## KEY WORDS

Jute/polyester composite ; Fatigue ; Impact ; fracture toughness ; Curve of Wöhler.

## I. INTRODUCTION

Natural fiber reinforced polymer matrix composite materials are receiving increasing attention from various industries. They combine good mechanical properties with a low specific mass and can represent an alternative to those based on ceramic fibers used in certain technical applications or to those reinforced with glass fiber in many applications not requiring heavy loads [1]. Jute fibers are among the best natural fibers currently used in composite materials industry due to their excellent properties and availability. The use of these fibers which have the advantage of being easy to weave as reinforcement in thermoplastics such as polyethylene (PE) and polypropylene (PP) and thermosetting materials such as unsaturated polyester and epoxy resin has been the subject of many interesting studies [2]. These fibers have high specific properties, less abrasive behavior for the treatment material and good dimensional stability. In recent years, many studies have been published on the development and characterization of static loading and fatigue of vegetable fiber or bio-fiber composite materials. However, this type of reinforcement offers poor compatibility with a few plastics as well as insufficient adhesion between the untreated fibers and the polymer matrix which can lead to separation over time [3, 4]. In addition, The fatigue properties of natural fiber reinforced composites are less clear than those of glass fiber reinforced composites because of the lack of systematic and detailed available information [5].

In general, fatigue of composite materials is a fairly complex phenomenon. The properties of these materials show a progressive reduction in strength and stiffness associated with a significant increase in material damping. The damage that initiates is diffuse and its mechanisms, which are numerous, develop by the separation of fibers or bridging of cracks, by microcracking of the matrix and rupture of fibers, by fiber/matrix decohesion, by delamination. This complexity of damage and failure mechanisms makes



behavior modeling and fatigue life prediction complex [6]. Their impact behavior is still rarely studied [7, 8, 9]. Amanda and Torrones [10] show that the incorporation of the jute fabric into the polyethylene resin completely changes the breaking characteristics of these materials and increases their impact strength. Rana et al [11] claim that there is an increase in the impact energy of a composite material with a polypropylene matrix reinforced with short jute fibers with the increase in the percentage of jute fibers. This increase in impact resistance is no longer significant beyond a rate of 50%. Wambua et al [12] examining and comparing the mechanical properties of various composite materials with a polypropylene matrix reinforced by natural fibers such as sisal, kenaf, hemp, jute and coconut fibers, show that the latter have a low impact strength. Another comparison was made with the corresponding properties of composite materials with a polypropylene matrix reinforced by glass fibers. The natural fiber composites examined show low impact strength, unlike hemp and sisal fiber composites, which have comparable strength to glass fiber reinforced composite materials. The specific properties of natural fiber composite materials are sometimes better than those of glass fiber composite materials. The fracture mechanics concepts used to characterize glass-pearl-polyester composite materials for orthopedic use and glass-carbon-polyester composite materials in impact show that the impact test is highly dispersive in its results but remains a rapid means of evaluating the toughness parameters of the widely diffused composite materials for their classification. Thus, the carbon-perlon-polyester composite has a better resistance to cracking under dynamic stress than the glass-perlon-polyester composite.

Composite material fatigue is a very important and significant phenomenon that limits the use of different types of materials even when the loads are not significant. Much work has been published in this field with the aim of deducing the long-time behavior of composite materials under a cyclic load and of developing improved analytical and experimental methods for establishing reliable models for predicting mechanical behavior over lifetime [13, 14, 15, 16]. Ray et al [17] estimated lifetime by applying the cyclic impact test to a jute fiber reinforced composite material by plotting the fatigue curve. Katogi et al [18] carried out static and cyclic tests on

a composite reinforced with jute fibers, and show that fatigue strength decreases with increasing number of loading cycles up to a level of 55% of the breaking load. Gassan [5] presented the influences of natural fiber type (flax, jute), fiber architecture, fiber-matrix bonding, and fiber mechanical properties on monotonic tensile cyclic fatigue. Considerable interfacial damage was noted by Towo and Ansell [19] during the fatigue test on a flax fiber composite material based on thermal, mechanical and dynamic analysis as a function of the number of fatigue cycles and temperature.

In this work, the general characteristics of a polyester matrix composite material reinforced with short bidirectional jute fibers were examined initially in terms of mechanical properties in direct tensile and bending static stress and in the judgment behavior of the three-point bending cyclic fatigue phenomenon. The effect of seawater absorption on the cyclic fatigue strength of the Jute/polyester composite at different periods of immersion in water was highlighted in a second step. Moreover, one of the objectives of this work is to interpret the results of the impact tests carried out on notched specimens using the Williams method [20, 21, 22, 23, 24, 25] based on the principles of the elastic linear mechanism of rupture.

## II. EXPERIMENTAL MATERIALS AND PROTOCOLS

### A. MATERIAL

The material used in this study is a composite with a polyester matrix reinforced by three layers of bidirectional jute fiber and manufactured by the pressure molding method with a percentage of gel coat as hardener of between 0.1% and 0.2%. This process, which represents the oldest method of implementing composites, makes it possible above all to produce parts of small series. The mold coated with the mold release agent receives the surface layer and then reinforces it in the form of jute fabric impregnated manually with polyester resin until the desired thickness is obtained, which in our case is  $4 \pm 0.5$  mm on average. The polymerization is carried out at room temperature. Plates of  $350 \times 210$  mm<sup>2</sup> are thus manufactured with a volume fraction of 40% of jute fibers.

After hardening of the resin, the plate is then removed from the mold. A bubble roller is used to remove air bubbles. Next, the operation of cutting the test pieces into rectangular bars of standardized dimensions is carried out using a diamond saw.

### B. COMPONENTS

The bidirectional jute fiber having an average density of 1300 kg/m<sup>3</sup>, and an elongation at break of about 1.6% constitutes the surface reinforcement used. The implementation is carried out in a flat mold, coated with a demolding agent which first receives the surface layer consisting of gel-coat. Contact molding lamination begins when the polymerization of the gel coat is deemed sufficient. The operation consists in successively depositing plies of jute reinforcement impregnated manually with polyester resin until the desired thickness is obtained, which is 4 mm on average. A bubble roller removes air bubbles. After hardening of the resin, the part is removed from the mold. The test pieces are then machined using a diamond saw.

The unsaturated polyester resin used consists of a monomer (styrene) and is cross linked at room temperature by the addition of an organic peroxide catalyst. It passes successively from the initial viscous liquid state to the gel state and then to the state of infusible solid. The bending modulus  $E$  measured is approximately 2350 MPa, with a tensile strength under this same load equal to 72 MPa. It shows a tensile strength of 45 MPa, a density of 1.11 g/cm<sup>3</sup> at ambient temperature and a viscosity of 20 dPa•s. The measured value of the impact toughness GIC is of the order of 1.63 KJ/m<sup>2</sup>. Thus, unreinforced polyester resins appear as relatively fragile polymers..

### C. TEST SPECIMENS

The maps, figures and tables are placed after the The test pieces used in static stress are of prismatic, rectangular shape cut from jute-polyester plates. For direct tensile test, they are of length  $L = 150 \pm 0,2$  mm, width  $b = 10 \pm 0,2$  mm and thickness  $h = 5 \pm 0,2$  mm as recommended by ASTM D 5083 (ASTM 08-02, 2013) [26]. For the case of three-point bending, the ASTM D 790 [27] standards recommend the following dimensions (ASTM 08-01, 2013): length of the test piece is  $100 \pm 0,2$  mm, width  $b$  about  $15 \pm 0,2$  mm, thickness  $h=5 \pm 0,2$  mm, distance between bearing  $L=80 \pm 0,2$  mm.

The test pieces used in cyclic fatigue were cut to dimensions of 80×15 mm on plates of 350×210 mm<sup>2</sup>. The distance between the supports is taken to be equal to 64 mm. Fig. 1 shows the geometry of the test pieces used



Fig. 1. Fatigue Test Pieces

The samples were immersed in a freshwater tank for 90, 180 and 270 days, respectively.

The test specimens used in dynamic impact stress are prismatic in shape, 10 mm wide and  $4 \pm 0.5$  mm thick, with a lateral notch of the SEN (single edge notch) type. The dimensions of the test pieces shall be accurately measured by means of a caliper. The length of the groove is within the range of  $0.2 < a/d < 0.6$ .  $A$  and  $D$  are the cut length and specimen width, respectively in Fig. 2.

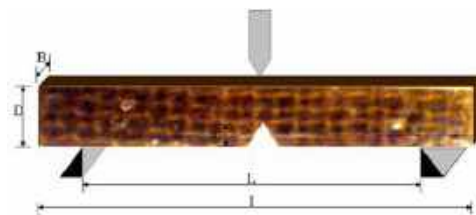


Fig. 2. Test specimen used in shock

### D. EXPERIMENTAL DEVICES

The quasi-static and cyclic tests were carried out on a machine of the Zwick/Roell Z020 type with a maximum capacity of 20 KN, as illustrated in Fig. 3. For the quasi-static tests carried out until the total rupture of the sample, the speed of displacement of the cross-member was set at 2 mm/min.

The cyclic fatigue tests are controlled at a load imposed at a frequency of 1.3 Hz, i.e. a load fixed at the minimum possible of 78 cycles/second. The

choice of the low frequency makes it possible to avoid any side effect due essentially to the heating of the material.

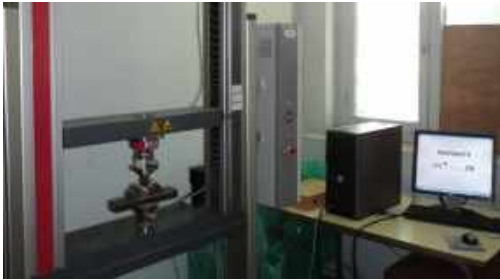


**Fig. 3.** Zwick/Roell Machine

The test specimens undergo different loading levels with respect to the maximum static bending load three points: 80%, 70%, 60%, 55%, 45%, 35% and 25%. For each load level, a minimum of three test pieces was tested. The load measured at static bending of the samples averaged about 208 N.

For the impact device, three fixed bearing distances of 40 mm, 60 mm and 70 mm are imposed by the impact device. Three corresponding lengths of test pieces of 50 mm, 70 mm and 80 mm respectively were tested. The NF EN ISO 179-1 standard recommends for this type of plate test pieces of 80 mm length with between supports of 62 mm [29]. However, the limitation of the between supports fixed by the assembly used imposed on us the 3 geometries tested. All these approaches were adopted in order to respect the L/D ratios used by Williams to tabulate the form factor  $\phi$  [20, 21, 22]. The tests were carried out on a shock machine, a Charpy pendulum sheep of the Zwick 5113 type in 3-point bending. The tripping angle of the aircraft is  $160^\circ$  and the impact speed is 3.85 m.s<sup>-1</sup>. The pendulum used for the study materials has an energy of 7.5 joules. FIG. 6 shows the experimental device used and the device for data acquisition and processing by a microcomputer equipped with “expert test” software.



**Fig. 4.** Charpy impact machine

The Williams method based on the principles of linear elastic fracture mechanics was used to interpret the results of the impact tests obtained on the notched test pieces [20, 21, 22]. This method provides an estimate of the fracture energy or toughness GIC intrinsic material parameter from the total dissipated energy U during the impact according to the equation:  $U = GIC \cdot B \cdot D \cdot \phi$ .

B and D are respectively the thickness and width of the test piece and  $\phi$  is a calibration factor which depends on the geometry of the test piece and which has been tabulated by J. G. Williams for different lengths of notches and for different L/D ratios [23]. Thus, the recording of the energy lost by the hammer at the moment of impact for each notch carried on a  $U=f(BD\phi)$  diagram is a straight line whose slope gives an estimated value of GIC measurement [20-23]. It should be noted that, despite the advantage of this very rapid method, which is always used for the purpose of comparing or classifying materials according to their breaking energy, it is possible to go even further in interpreting the dynamic behavior mechanisms of composite materials by using instrumentation and access to the load-time curve during impact. Indeed, the method of J.G. Williams should be noted with the instrumented impact has greatly advanced and evolved in terms of methods of analysis since 1975 [28].

### III. RESULTS AND DISCUSSION

#### A. BEHAVIOR AND PROPERTIES UNDER TENSILE AND BENDING TEST

Fig. 5 shows an example of a stress-strain curve

reading for direct tensile stress. These curves obtained on different identical test pieces exhibit a linear behavior up to total rupture, reflecting the elastic behavior and the fragile nature of these materials in this type of stress.

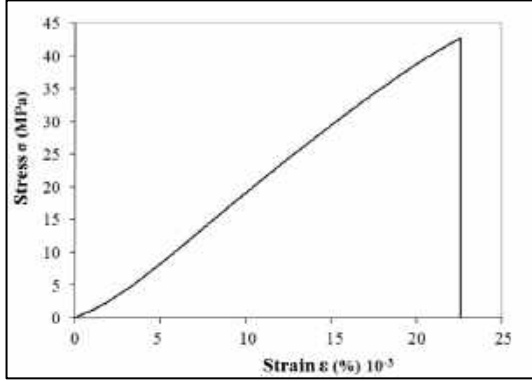


Fig. 5. Stress-strain curves ( $\sigma - \epsilon$ ) of the jute - polyester composite under static tensile stress.

In 3-point bending, the behavior is different as illustrated by Fig. 6, which shows an example of a stress-strain curve reading obtained in this type of stress. Unlike those obtained in traction, these behavior curves show three phases: a first linear phase reflecting the elastic behavior of the material followed by a second phase which is equally linear but of lower slope corresponding to the take-up of the forces by the fibers following the multi-cracking of the matrix and to the development of the damage which occur progressively within the material during loading and finally a drop in the stress beyond the maximum load announcing the unstable failure of the test piece.

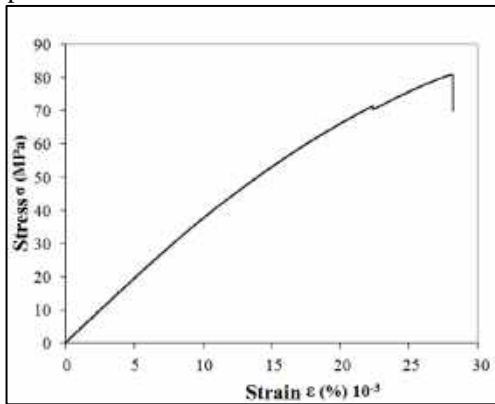


Fig. 6. Stress-strain curve of the jute-polyester composite in bending test

It should be noted that the damage occurring within the test piece is manifested at a stress intensity lower than that of the breaking stress. The two linear phases of the behavior law are connected by an “elbow”

point or “knee point” known as a “nee point” and observed on many SMC composite materials loaded in static bending [29]. Table 1 summarizes the mean values of the measured elastic and rupture properties of this material as well as the standard deviations measuring the dispersion.

Table 1: Mechanical characteristics of the composite

Test	Tensile	Bending
Elastic modulus (MPa)	$1937 \pm 37$	$2832 \pm (388)$
Fracture stress (MPa)	$38 \pm (2.2)$	$71 \pm (7.1)$

The mean modulus of elasticity for the jute-polyester composite measured in direct tension is of the order of  $1937 \pm 37$  MPa. This value is close to the results obtained on a similar jute-polyester unidirectional composite [30].

These measurement results show a dispersion in the measured values of the mechanical properties which is now accepted as a characteristic of these materials studied and can be attributed both to the heterogeneity of the microstructure and to the presence of defects such as the microporosities of different shapes and dimensions randomly distributed in the volume or the weaknesses of the interfaces.

The order of magnitude of these dispersions is acceptable and falls within the ranges usually reported in the technical and scientific literature for this type of composite material. It should be noted that the dispersion in the values of the elastic modulus which can be attributed to differences in state in the material (fiber content and orientation) is less than that recorded on the breaking stresses which is influenced by the presence of defects as already mentioned.

There is a significant difference between the resistances measured in these two types of stress. The resistance measured in bending is much greater than that measured in a direct tensile test. The ratio is 1.86 in favor of the former. This difference is the consequence of a different state of deformation between these two types of stresses.

In a direct tensile test where the entire volume is subjected to a tensile state, the results represent an average value of the stresses across the section of the test piece, whereas in flexure the maximum tensile stress is reached only on the end face of the test piece. The deviation is then explained by the uninformed distribution of defects in the thickness of the material. Since the skins are poorer in deformations, the bending limit stress is higher.

On the other hand, this difference can be explained by the non-uniform distribution of stresses in a bending test as well as by the statistical aspect of the break which is significantly influenced by the effect of size and volume. It has been established by Weibull [31]

that the strength of brittle materials is highly dependent on the volume and distribution of stresses. Because of these effects, the average tensile strength of a rectangular bar subjected to bending is greater than that of an identical test piece subjected to direct traction

#### B. BEHAVIOR AND PROPERTIES UNDER CYCLIC FATIGUE STRESS

The fatigue life at a given loading level is measured by the number of cycles reached at the time of test piece failure. Fig. 7 shows the Wöhler curve plotted in the form of the maximum cycling bending load applied as a function of the logarithm of the number of cycles at break representing the lifetime of the samples. The criterion adopted in this study is the complete rupture of the test piece. However, after 105 cycles and for practical reasons at laboratory level, the test is stopped even if the test piece is not broken. Then it is assumed that there is no longer a rupture.

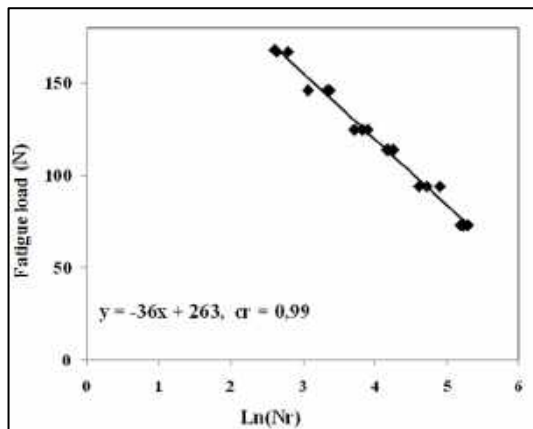


Fig. 7. Wöhler curve of the jute-polyester composite

It is generally possible to distinguish on this curve three phases. For a higher loading level above 70% of the breaking load representing polygocyclic fatigue, the damage is very rapid to occur and the service life is relatively very short. For the intermediate loading levels (35%, 45%, 55% and 60% of the bending breaking load), the test specimens have a limited cycle time before breaking. The number of cycles increases as the maximum stress of repeated cyclic stress decreases. It is a limited area of endurance. Below the maximum loading level equal to 25% of the static breaking load, the test pieces do not break and the damage is very gradual. It is an area of unlimited endurance to define a probable endurance limit.

Lieurade quoted by Bathias & Baillon [32] reviewed the various models proposed in the literature to describe and represent the results of fatigue endurance tests as the Basquin equation which

accounts for an asymptotic branch for high cycle numbers and whose coefficients are easy to identify from the experimental results.

For our case, and despite the dispersion observed over lifetime for the same loading level, the experimental points can be modeled by a linear regression line given by the equation:  $F = 263 - 36 \ln.Nr$

F and Nr represent respectively the applied load level and the number of cycles at break. The correlation coefficient ( $cr=0.99$ ) close to 1 is satisfactory and therefore indicates an acceptable arrangement of the experimental points around the linear regression line.

The parameters representing the slope of the line and the ordinate at the origin are considered as intrinsic constants of the material. For some authors, the latter parameter represents the stress at break under static loading, which is in fact only an extrapolation to a cycle.

A comparison between this value of the ordinate at the origin of 263 N and the mean value of the breaking force under static bending loading of 3 points measured in our case and which is 208 N shows that the difference is slightly large. This is estimated at 20% and is generally the consequence of the dispersion due to the heterogeneity of the material, to the dispersions due to the fatigue and static tests and to the large difference between the stress rates in these two tests.

It should be noted that the absence of a clear definition of a fatigue failure criterion as reported in the scientific and technical literature remains one of the sources of the observed dispersions in the lifetime results of composite materials. In contrast to metals for which cracking initiation occupies a significant part of the number of cycles at failure, composite materials begin to show variations in their mechanical properties, typically in the early stages of life [33, 34].

Despite the dispersion observed over the lifetime for the same level of repeated cyclic loading, it is clear that the Wöhler linear equation due to its simplicity gives an often good representation of the mean part of the curve. However, within the limits of these experiments, it does not account for a horizontal branch that can define an endurance limit.

In general, damage in composite materials is the result of matrix microcracking, interfacial discohension, fiber loosening and rupture, delamination, and transverse cracking. Thus, accumulation and progressive degradation evolution give the material a damage kinetics conditioned by its microstructure and by the type of loading and which can be identified from the experimental results. Numerous studies report that the stages of damage evolution in the case of cyclic loading are of the same nature as those encountered in static loading but of



different chronology and magnitude. The deterioration of the composites takes place during the first fatigue loading cycles and increases progressively in density until the final rupture.

The state of fatigue damage reported in the scientific literature on composite materials reinforced with long unidirectional or short randomly distributed fibers is very complex to identify and quantify [35, 36]. This makes it difficult to model these states both in monotonic static loading and in cyclic loading [37, 38, 39]. These numerous mechanisms of damage and rupture, which include matrix microcracking, fiber/matrix decay, fiber rupture, transverse rupture and delamination, can be described in the case of unidirectional or bidirectional laminates at the laminate scale, at the fold scale, at the fiber scale from different types of models [40]. It is clear that a particular structure can thus show one or more of these modes of damage, which complicates the a priori prediction of the dominant one which causes the rupture.

In general, fatigue damage to composite materials is characterized by a combination of density and orientation of microcracks, the formation and evolution of which is affected by the level and amplitude of loading. This damage in the case of the jute-polyester composite materials of this study is mainly due to mechanisms of microcracking of the matrix, of interfacial discohension, of loosening and rupture of the fibers, and of delamination.

Taking the ordinate at the origin of the Wöhler straight line as the static breaking force in three-point bending as already mentioned, the Wöhler equation can also be written:  $F_{max}/263 = 1 - (36/263) \cdot \ln(N_r)$

That is:  $F_{max}/263 = 1 - (0,137) \cdot \ln(N_r)$

This form of equation makes it possible to plot a monotonous normalized line of decreasing slope -  $(36/263)$ , that is to say the ratio of the two constant parameters of the Wöhler line, from ordinate 1, that is to say from 1 cycle corresponding to the fact of the static bending force (extrapolation of  $1/4$  of a cycle). This form of presentation makes it possible to demonstrate a constant degradation rate per cycle decade quantified by the absolute value of the slope of the normalized line and which is 13.7% of the static breaking force as illustrated by Fig. 8.

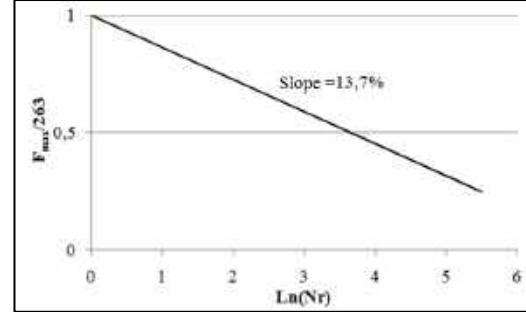


Fig. 8. Normalized Static Tensile Stress Curve

This constant rate of degradation per cycle decade in composite materials has been reported by numerous authors and in particular by Mandell et al [41], by Redjel [33] and by Redjel and De Charentenay [42] on a series of short-fiber SMC composite materials oriented at random under cyclic fatigue stress. These authors quantify it, estimate it at 10% and offer no explanation for this phenomenon.

### C. DYNAMIC IMPACT BEHAVIOR

The graphical representations of the measurement points of the total breaking energy lost by the hammer U as a function of the broken crack surfaces for the three bearing distances used are shown in Fig. The results obtained show that the increase in the total energy of rupture with the increase in the broken surfaces results in the fact that rupture is an energy-consuming phenomenon. Thus, increasing the number of broken surfaces requires greater breaking energy. The dispersion of the experimental points around the linear regression lines is important for all cases tested as indicated by the low calculated correlation coefficients.

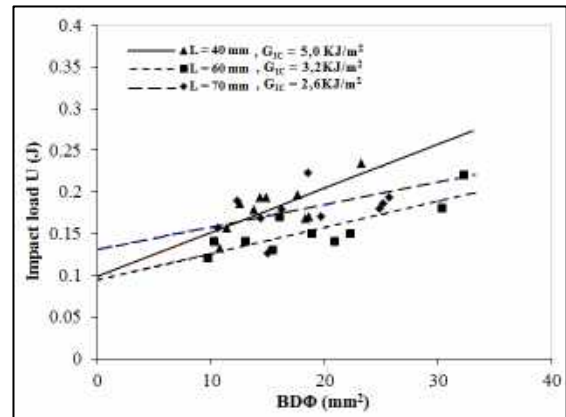


Fig. 9. Total Breaking Energy U Based on BDφ Broken Surfaces

Indeed, the linear regressions established on the experimental points for the distances between supports of 40 mm, 60 mm and 70 mm are given with correlation coefficients much less than 1, reflecting



the fairly large differences of these experimental points around the regression lines. This high dispersion is a characteristic of heterogeneous materials and is mainly the result of the heterogeneity of the material on the cracking path, the method of manufacture of the test pieces and notches and the dispersion of the mechanical test itself. The presence of defects of different types and geometries during the manufacture of the test pieces is also a parameter favoring the variability of the measurement. Indeed, the distribution of the content of jute fibers in the polyester matrix and their orientation is not uniform within the volume of the material, which causes breaking paths which are often tortuous and which do not necessarily follow the direction and the plane of the initial notch and which are different from one test piece to another. Figure 10 shows an example of a test piece broken in impact.



Fig. 10. Example of a test piece damaged in impact

#### D. MECHANISMS OF DAMAGE

Fatigue damage states are very complex to identify and quantify [39-40]. It then becomes difficult to model these states both in monotonic static loading and in cyclic fatigue loading or dynamic impact loading [28, 41, 42, 43].

It is interesting to note that fatigue damage to jute-polyester composite materials is characterized by a combination of density and orientation of microcracks whose formation and evolution are affected by the loading level and amplitude as illustrated in Fig. 11(a) which shows an example of fiber concentration and density in a section as well as voids and porosity density. In addition, the long cracked jute fibers of the composite have significant strength and are effective in the reinforcement operation (Fig. 11(b)). The damage and rupture mechanisms are thus numerous, the main ones being matrix microcracking, fiber/matrix interface decay, fiber rupture, transverse rupture and delamination. (Fig. 11(c))

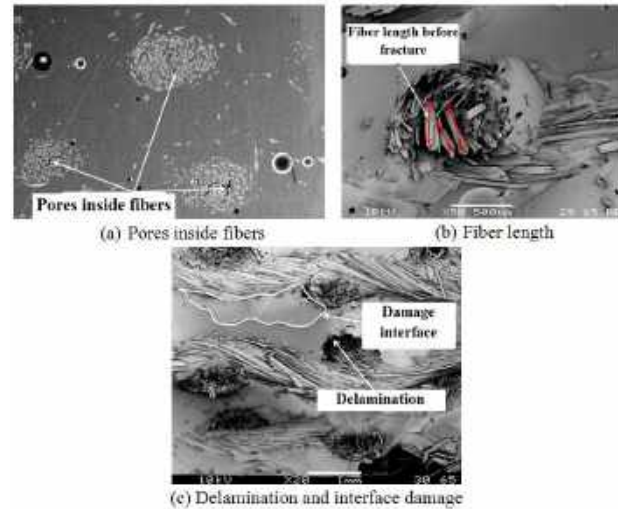


Fig. 11. SEM photographs of jute polyester composites

Thus, the stages of damage evolution in the case of cyclic loading are of the same nature as those encountered in static loading but of different chronology and magnitude. The deterioration of the composites occurs from the first fatigue loading cycles and gradually increases in density until the final rupture and consequently an increase in the volumes of the pre-existing pores and voids inside the fibers.

#### IV. CONCLUSION

The following conclusions can be drawn:

- The static behavior of the jute/polyester composite materials shows a brittle breaking character.
- The results of the mechanical characteristics tests show that the measured values of the bending breaking stress are considerably greater than those obtained values in tensile test. This divergence is justified by the difference in the distribution of the stress field in these two types of load.
- The three-point static bending stress-strain curves show two straight lines of different slopes connected by an elbow. This behavior reflects a linear elastic phase followed by progressive and extensive damage to the material before fracture. This damage may be the consequence of micro-cracks in the matrix and fibers and of interfacial delamination.
- Fatigue results show dispersion in life span for the same loading level due to the material manufacturing method.
- The experimental points are modeled by a Wöhler straight line which gives a good representation of the mean part of the curve. However, it is difficult to clearly identify an endurance limit.

- A constant degradation rate per cycle decade of 15% of the static breaking force characterizes the evolution of the damage in these materials.

- The preponderant phenomena of damage processes in these materials are fiber-matrix delamination and matrix cracking.

- The tested specimens of jute/polyester composite material failed brittle in impact.

- The measurement of the critical breaking energy GIC obtained in impact on the jute-polyester bidirectional composite materials using the pendulum sheep and determined by the conventional method of Williams is characterized by a high degree of dispersion. This is mainly due to the heterogeneity of the material, to the process of manufacture by the contact process which induces defects such as voids and air bubbles which are difficult to remove, and to the difficulty of machining a very acute perfect notch bottom.

- Dynamic impact strength of jute-polyester composite materials shows a decreasing trend with increasing distance between three-point bending supports. This toughness remains very low compared with that usually measured on glass-polyester composites.

## REFERENCES

- [1] C. Santulli., "Biomimetic interest and possibilities for replacement of glass fibres with plant fibres in composite materials: the case of impact damage," Proceedings of the International School on Advanced Material Science and Technology, 26th- 29th August, – Jesi – Ancona –Italy (2003).
- [2] A.K. Mohanty and M. Misra., "Studies on jute composites, a literature review," Polym-Plast Technol Eng, 34 (1995),
- [3] K.H. Wang e al., "A review on the tensile properties of natural fiber reinforced polymer composites", Compos : B, 42, 856–873 (2011).
- [4] R. Malkapuram, et al., "Recent development in natural fiber reinforced polypropylene composites," J Reinf Plastic Compo, , 28,1169–1189 (2009).
- [5] J. Gassan., "A study of fibre and interface parameters affecting the fatigue behaviour of natural fibre composites," Compos : A , 33, 369-374 (2002)
- [6] K.L. Reifsnider, et al., "Long-term fatigue behaviour of composite materials," ASTM STP 813, , Philadelphia: ASTM (1983).
- [7] S. Sangthong, et al., "Mechanical property improvement of unsaturated polyester composite reinforced with admicellar-treated sisal fibers," Comp: t A, 40, 687-694 (2009).
- [8] F.A. Silva, et al., "Physical and mechanical properties of durable sisal fiber cement composites," J. Mat. Sci. and Eng. A 527, 5507-13 (2010).
- [9] A. Athijayamania, et al., "Effect of Moisture Absorption on the Mechanical Properties of Randomly Oriented Natural Fibers/Polyester Hybrid Composite," J. of Mat. Sci. and Eng. A, 517, 344-353 (2009).
- [10] C. Amanda and L.A.H. Torrones., "Impact rupture characteristics of polyethylene composites reinforced with jute fabric," Acta Microscopica, 16, 1-2 (2007).
- [11] A. K. Rana, et al., "Short jute fiber-reinforced polypropylene composites: effect of compatibilizer," J. Appl. Polym. Sci, 69, 329-338, (1998).
- [12] P. Wambua, et al., "Natural fibres: can they replace glass in fibre reinforced plastics," Compos. Sci. Technol, 63, 1259-1264, (2003).
- [13] S. Pavlidou and C.D. Papaspyrides., "The effect of hygrothermal history on water absorption and interlaminar shear strength of glass/polyester composites with different interfacial strength," Compos: Part A, 34, 1117–1124 (2003).
- [14] E. Wu and K. Shyu, "Response of composite laminates to contact loads and relationship to low-velocity impact," J. Compos. Mater 27 (15), 1443–1464 (1993).
- [15] M.S. Found and I.C. Howard "Single and multiple impact behavior of a CFRP laminate," Compos Struct 32, 159–163, (1995).
- [16] D. Ray, et al., "Impact fatigue of glass fibre-vinylester resin composites," Compos Part A: Appl. Sci. Manuf, 32, 871–876 (2001).
- [17] D. Ray, et al., "Impact fatigue behaviour of vinylester resin matrix composites reinforced with alkali treated jute fibres", Compos Part A: Appl. Sci. Manuf, 33, 233–241 (2002).
- [18] H. Katogi, et al., "Fatigue behavior of unidirectional jute spun yarn reinforced biodegradable resin" 18th International Conference on Composite Materials, Korea (2011).
- [19] A. N. Towo and M. P. Ansell, "Fatigue evaluation and dynamic mechanical thermal analysis of sisal fibre–thermosetting resin composites," Compos. Sci. Technol, 68, 925–932 (2008).
- [20] C.E. Turner, Fracture toughness and specific fracture energy: A re-analysis of results," Mater. Sci. Eng. 5, 275-282, (1973), Mat. Sci. and Eng. 11, 275-282.
- [21] J.G. Williams, "Fracture Mechanics of Polymers," Polym. Eng. and Sci., 17, 144-149 (1977).
- [22] B. Redjel and F.X. De Charentenay, "Résistance au choc des matériaux composites SMC à base de résinephénolique, " Journal de physique IV, Colloque C3, Suppl. au Journal de Physique III, V. 1, Octobre 1991, pp. 297-304 (1991).
- [23] E. Plati, J.G. Williams, "The determination of fracture parameters in impact," Polym. Eng. and Sci., 15, N° 6, 1975, 470-477 (1975).
- [24] C. Schmitt, "Influence d'un défaut de fabrication sur le comportement mécanique d'un matériau composite verre-époxyde, " J. Mat. Proc. Technol. 101, 298-305 (2000).
- [25] P.S. Leever., et al., "High rate fracture toughness testing of thermoplastics," Polymer Testing, 33, 79-87 (2014).
- [26] Standard Test Method for Tensile Properties of Reinforced Thermosetting Plastics Using Straight-Sided Specimens. ASTM Volume 08.02, June (2013).

- [27] Standard Test Methods for Flexural Properties of Unreinforced and Reinforced Plastics and Electrical Insulating Materials. ASTM Volume 08.01, June (2013).
- [28] D. Djeghader and B. Redjel, "Ténacité dynamique en flexion 3 points de matériaux composites bidirectionnels jute-polyester", Sciences & Technologie B , 42, 43 - 47(2015).
- [29] B. Redjel and F.X. De Charentenay. "Comportement mécanique des matériaux composites SMC," Matériaux et Techniques, 5-6, 221-228 (1987).
- [30] S. Far., "Etude du comportement mécanique d'un matériau composite époxyde jute," mémoire de Magister, option construction mécanique, Département de Génie mécanique, Université de Annaba (2008).
- [31] W. Weibull, "A statistucal distribution function of wide applicability," J. Applied Mechanics, 18 (1951).
- [32] C. Bathias and J.P. Baillon, "La fatigue des matériaux et des structures," collection UTC, Ed. SA Maloine, Paris (1980).
- [33] B. Redjel, "Fatigue damage in short fiber reinforced composite materials," 8th International Conference on Fatigue of Composites, SF2M, Eighth International Spring Meeting, Paris, France, 3-4-5 165-172 (1997).
- [34] D. Djeghader and B. Redjel "Etude du comportement mécanique d'un matériau composite bidirectionnel jute-polyester sous chargements statique et de fatigue," Journal of Materials, Processes and Environment, JMPE, 1,2 (2013).
- [35] Y. Thollon and C. Hochard, "Endommagement de composites stratifiés verre/epoxy sous sollicitation statique et de fatigue," 18 ème Congrès Francais de Mécanique, Grenoble (2007).
- [36] A.K. Roy, "Comparison of in situ damage assessment in unbalanced fabric composite and model laminate of planar crimbing," Compos. Sci. Technol, 58 (1998).
- [37] K. Reifsnider, "Durabilityand damage tolerance of fibrous composite systems, Handbook of composites," edited by S.T. Peters, 35, 794-809 (1998).
- [38] J. Payan and C. Hochard, "Damage modelling of carbon/epoxy laminated composites under static and fatigue loads," Int. J. of fatigue, 24,299-306 (2002).
- [39] H. Mao and S. Mahadevan, "Fatigue damage modelling of composite materials," Compos. Struct, 58, 405-410 (2002).
- [40] A. S. D. Wang, "Strength, failure and fatigue analysis of laminates," Engineered Materials Handbook, ASM, 1, 236-251 (1987).
- [41] J. F. Mandell, et al., "Tensile fatigue performance of glass fiber dominated composites," Compos. Technol. Rev, 396-102 (1981).
- [42] B. Redjel, and F.X. De Charentenay, "Etude du comportement en fatigue des matériaux composites SMC", Comptes Rendus des 7 èmes Journées Nationales sur les Composites (JNC 7), Editions Pluralis, Lyon, France (1990).
- [43] D. Djeghader and B. Redjel, "Fatigue resistance of randomly oriented short glass fiber reinforced polyester composite materials immersed in natural seawater environment," Mech. Ind, 18, 604 (2017).

# Mechanical and thermal properties of poly (ethylene-co-vinyl acetate)/mesoporous silica nanocomposites

LASMI SOFIANE<sup>1, a\*</sup>, ZOUKRAMI FOUZIA<sup>2, b</sup>, TOUNSI ASSIA<sup>1, c</sup>, BOUCHOUL BOUSSAHA<sup>1, d</sup>, LAMIRI LEILA<sup>1, e</sup>

1. Research Center in Industrial Technologies CRTI, P.O. Box 64, Cheraga 16014, Algiers, Algeria

<sup>a</sup> lasmi\_sofiane@yahoo.com, <sup>b</sup> zoukramifouzia@yahoo.fr, <sup>c</sup> tounsiassia56@gmail.com, <sup>d</sup> b\_bouchoul@yahoo.com, <sup>e</sup> lamiri.lila@yahoo.fr

2. Unité de Recherche Matériaux Emergents (URMES), Université Ferhat Abbas Sétif-1, Sétif, Algeria

## ABSTRACT

*Poly (ethylene-co-vinyl acetate)/ mesoporous silica (EVA/SBA-15) nanocomposites were prepared by melt blending in internal mixer. The mesoporous silica SBA-15 was synthesized by the sol-gel method. A terpolymer of ethylene-butyl acrylate - maleic anhydride (E-BA-MA) was added as a compatibilizer at 2wt % to nanocomposites including unmodified SBA-15. The EVA/SBA-15 nanocomposites were characterized by several technics, such as Fourier transform infrared spectroscopy (FTIR), differential scanning calorimetry (DSC), thermogravimetric analysis (TGA); morphological and mechanical studies were carried out. The results from FTIR and SEM confirm the successful synthesis of SBA-15. The DSC results showed a reduction of the crystallinity of the nanocomposites and increases of Young's modulus increased with the incorporation of the filler and in the presence of terpolymer as compatibilizer, whereas elongation at break and tensile strength kept almost the values of the matrix. The thermal stability of EVA/SBA-15 nanocomposites was enhanced as compared with the pure EVA matrix.*

## KEY WORDS

Nanocomposites; SBA-15; mechanical properties; thermal stability; compatibilization; interfaces compatibility.

## I. INTRODUCTION

In the last decades, polymer-based nanocomposites have received increasing interest of both academia and industry due to the significant change of the properties, combining the advantages of inorganic nanoparticles (e.g. rigidity and thermal stability), and organic polymers (e.g. flexibility, dielectric, ductility,

and processability). On the one hand, poly (ethylene-co-vinyl acetate) (EVA) is an important thermoplastic widely used in electrical insulation, cable jacketing, and encapsulation...ect. However, the relatively low tensile strength and rather poor thermal stability of EVA limit its application in some fields, like electronic appliances where high thermal stability is required and in electric high voltage cable [1]. In order to overcome the above mentioned drawbacks and achieve the required strength and thermal stability; many studies reported that the insertion of mesoporous silica can improve the properties of EVA [2, 3]

## II. MATERIALS AND TECHNIQS

### A. MATERIALS

Triblock copolymer EO<sub>20</sub>PO<sub>70</sub>EO<sub>20</sub>, (Pluronic P123) used in this study as template and tetraethylorthosilicate (TEOS, (99%) used as silica source were supplied by Sigma-Aldrich Co., Ltd. (USA). Poly (ethylene-co-butyl acrylate-co-maleic anhydride, E-BA-MAH) compatibilizer, with 6% butyl acrylate, 3% maleic anhydride (Lotader 3210) was purchased from Arkema, France. Ethylene vinyl acetate copolymer (EVA) containing 18% vinyl acetate used as the polymer matrix, with density of 0.93 g/cm<sup>3</sup> and melt flow index of 2.5 g/10 min (at 190°C/2.16 kg) TAISOX 7350M was purchased from Formosa Plastics corporation (Taiwan).

### B. Synthesis of mesoporous silica materials

Mesoporous silica SBA-15 was synthesized by using EO<sub>20</sub>PO<sub>70</sub>EO<sub>20</sub> Triblock copolymer as a template via a sol-gel process according to literature [4]. Typically, 16 g of P123 were dissolved in 480 mL of distilled

water and 80 mL of 37% HCl solution under magnetic stirring at 35°C for 2 h. Then, 32.7g of TEOS were added into the homogenous solution with stirring at 35°C for 24h. After that, the mixture was aged in a Teflon bottle at 100°C for 24 h without stirring. The obtained particles were collected by filtration, washed several times with ethanol, and dried at 80°C. The organic template was completely removed by calcinations at 500°C for 5 h (heating rate of 2°C/min to 500°C followed by isothermal treatment at 500°C for 5 h and cooling in air at ambient temperature) after which the mesoporous SBA-15 material was obtained.

### C. PREPARATION OF EVA/SBA-15 NANOCOMPOSITES

EVA/SBA-15 nanocomposites containing unmodified SBA-15, with or without 2wt % E-BA-MAH compatibilizer were prepared by melt blending in an internal mixer (Brabender). Mixing of EVA with SBA-15 was accomplished at 160°C and 60 rpm for 8 min. After mixing, the samples were hot-pressed at 10 MPa for 5 min at 160°C to form sheets with suitable thickness.

## III. TECHNICS

**Fourier transform infrared spectra (FTIR)** of SBA-15 and EVA/SBA-15 nanocomposites films were obtained by using a Perkin–Elmer spectrum one spectrometer (Universal ART sampling accessory) in the range of 4000–600cm<sup>-1</sup> at a resolution of 4cm<sup>-1</sup>

**Thermal analysis** was performed using on a METTLER TOLEDO DSC 822° differential scanning calorimeter under nitrogen atmosphere. The crystallinity percentage ( $\chi_c$  %) of the samples was calculated using the following equation.

$$\chi_c(\%) = \frac{\Delta H_f}{\Delta H_f^0 \Phi_m} * 100\%$$

**The mechanical properties**, such as tensile strength, elongation at break and modulus of EVA/SBA-15 nanocomposites were measured using a MTS apparatus, CRITERION model 45 tensile tester at room temperature with a crosshead speed of 50 mm/min. The shaped specimens and the measurement were carried out according to ISO 527-2. Seven specimens were tested for each sample.

**The morphology** of pure EVA and EVA/SBA-15 nanocomposites were photographed using scanning electron microscope (SEM, Philips, XL30).

**The thermal stability** of EVA and EVA/SBA-15 nanocomposites was conducted in a nitrogen atmosphere (100 mL/min) using a TA instrument (model Q600) in Hi-Resolution mode with an initial heating rate of 10°C/min, recording the mass loss as a

function of temperature

## IV. CONCLUSION

Mesoporous silica type SBA-15 was successfully synthesized, and EVA nanocomposites containing unmodified SBA-15, and unmodified SBA-15 compatibilized with E-BA-MA were prepared in molten state to study their effect on the properties. From FTIR analysis, the existence of dipole–dipole interactions between the -OH surface groups of mesoporous silica and -C=O groups in EVA matrix detected. The crystallinity of the EVA matrix was decreased by the presence of the nanofiller, more for the compatibilized filler than for the unmodified filler, to a maximum of 29% decrease, due to the restriction to the movement of the polymer chains interaction with the surface of the filler. This decrease in the crystallinity did not affect negatively the mechanical properties of the nanocomposites.

SEM images showed that the increase in mechanical properties were due to the improvement on the interfacial adhesion of the filler surface with the matrix and the good dispersion of the compatibilized fillers with a significant agglomeration of the particles at 4% weight concentration leading to a decrease in the mechanical properties.

The nanocomposites show an improvement in thermal stability respect to the EVA matrix

## REFERENCES

- [1] B. Wang et al., “Effect of Vinyl Acetate Content and Electron Beam Irradiation on the Flame Retardancy, Mechanical and Thermal Properties of Intumescent Flame Retardant Ethylene-Vinyl Acetate Copolymer,” *Radia. Phys. Chem.* 81, 308–315, 2012.
- [2] Y. Lu et al., “Investigation on the Preparation and Properties of Low-Dielectric Ethylene-Vinyl Acetate Rubber / Mesoporous Silica Composites,” *J. Polym. Res.* 22, 56, 2015.
- [3] S. Lasmi et al., “Influence of modified mesoporous silica SBA-15 and compatibilizer on the properties and structure of ethylene-vinyl acetate copolymer-based nanocomposites,” *Polym.-Plast. Technol. Mater.* 59, 2003–2017, 2020.
- [4] D. Zhao et al., “Triblock Copolymer Syntheses of Mesoporous Silica with Periodic 50 to 300 Angstrom Pores,” *Science*. 279 548–552, 1998.

# Nano-indentation of bcc Vanadium: Atomistic simulation of plastic deformation

SOUMIA HAMDANI<sup>1,\*</sup>

1. Laboratory of physics and mechanics of metallic materials, Optics and Precision mechanic Institute, University of Ferhat Abbas, 19000, Setif, Algeria, [soumia.hamdani02@gmail.com](mailto:soumia.hamdani02@gmail.com)

## ABSTRACT

*In this work, MD simulations were performed on a bcc Vanadium single crystal to investigate its plastic deformation mechanism during (010) Nano-indentation. The EAM potential has been used to run simulations on LAMMPS code (Large Scale Atomic Molecular Massively Parallel Simulator), and OVITO software was used to track the development of the deformed atomic structure and dislocations during the Nano-indentation process. The results show that Twinning deformation is the dominant plastic deformation, besides the evolution of 1/2 <111> shear loops and a pinching of prismatic loop.*

## KEY WORDS

Indentation; plastic deformation; dislocation; twinning; bcc Vanadium; MD simulation.

## I. INTRODUCTION

It is widely believed that, MD simulation is a powerful method for materials characterization at atomic scale. In despite the fact that, focus of many research has been on this aspect for a variety of materials, studies on the mechanical behavior of bcc vanadium single crystal are still lacking. In this work, we study Plastic deformation and mechanical behavior of Single Crystal bcc Vanadium by molecular dynamic simulation of Nano-indentation on (010) plane Using LAMMPS code (Large Scale Atomic Molecular Massively Parallel Simulator)[1] and OVITO Visualization software [2].

## II. SIMULATION METHOD

Simulation in this study has been conducted using the

embedded-atom potential EAM developed by Mendelev et al [3]. Measurements of simulation block is set to be 20.272\* 8.177\* 20.272 nm<sup>3</sup> on x, y and z directions respectively using lattice units. The basal layers colored in yellow of V atoms are fixed and nearly 2nm thick on either sides; they remain rigid during simulations to avoid any solid body motion of the domain during the indentation process in the y-direction. Fig.1 depicts the bcc Vanadium Single crystal simulation model of our simulation. Periodic boundary conditions have been employed in the lateral x and z directions, while non-periodic is applied in y, where the indentation strain proceeds. In this work, Strong repulsive potential represents purely rigid spherical indenter tip. This particular indenter has no force in the tangent direction to the tip sphere, of magnitude

$$F(r) = \begin{cases} -K(r-R)^2 & r < R \\ 0 & r \geq R \end{cases} \quad (1)$$

Where  $K=100\text{ev}/\text{\AA}^3$ ,  $K=16\text{TPa}$  it is the specified force constant,  $r$  is the distance from the atom to the center of the indenter, and  $R$  is the radius of the indenter. The indenter is initially placed 0.3 nm above the center of the simulation cell. In addition, we have selected  $R=5\text{nm}$  as indenter radius, lower indenter speed  $v=10\text{m/s}$  (0.1/ps), and an indentation depth of 1.5 nm. Equilibrium configuration have found by energy minimization using the Conjugate Gradient (cg) algorithm; energy and force convergence were set to  $10^{-15}$ , to acquire partially relaxed interface. In addition, NVT (Nose-Hoover) ensemble, thermostats



the system at temperatures  $T=10\text{K}$ .

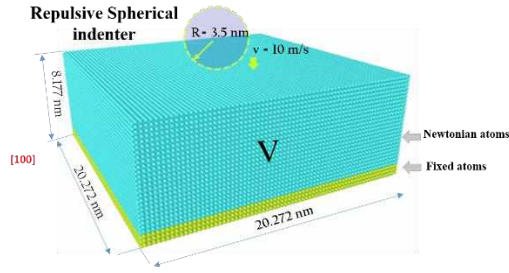


Fig. 1. Schematic descriptive of the simulated V model.

### III. RESULTS AND DISCUSSION

#### A. LOAD AND HARDNESS VS. INDENTATION DEPTH CURVES

Papers Fig.2 shows the load curve (a) and hardness curve (b) vs. indentation depth of V single crystal. It can be seen that load curve follows the Hertzian analytical law. Thus, the V crystal undergoes elastic deformation, which follows the Hertzian curve up to the first yield point at an indentation depth of  $4.9\text{\AA}$ . Then the load drops, indicating the onset of plastic deformation.

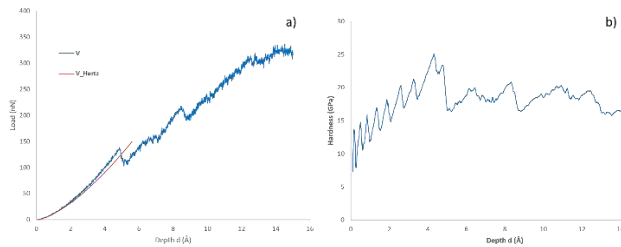


Fig. 2. (a) Load and (b) Hardness vs. indentation depth curves of V single crystal.

#### B. PLASTIC DEFORMATION AND DISLOCATION DEVELOPMENT

To highlight the major steps of plastic deformation during the indentation process, Fig.3 displays snapshots of defected atoms and dislocations for different indentation depths, ranging from  $4.9\text{\AA}$  to  $11\text{\AA}$ . At  $d=4.9\text{\AA}$ , planar defects nucleate beneath the indenter without dislocation emission. Subsequently, when the indenter reaches a depth of  $5\text{\AA}$ , we can observe the first dislocation emission with Burgers vector  $a/2\langle 111 \rangle$  of a value equal to  $2.15\text{\AA}$ . With further indentation at  $d=7.9\text{\AA}$ , more generated dislocations and planer defects lead to the formation of a flower-shaped dislocation structure with four symmetric shapes due to dislocation multiplication, which mainly glide in four different directions. When

the indentation depth increases further; at a depth of  $8.2\text{\AA}$ ; the  $a/2\langle 111 \rangle$  formed dislocations evolve to shear loops multiplication. At  $d=9.1\text{\AA}$ , the nucleation of a prismatic loop from a shear loop starts. After that at  $d=11\text{\AA}$ , the prismatic loop is completely formed and moves towards the bottom of the cell.

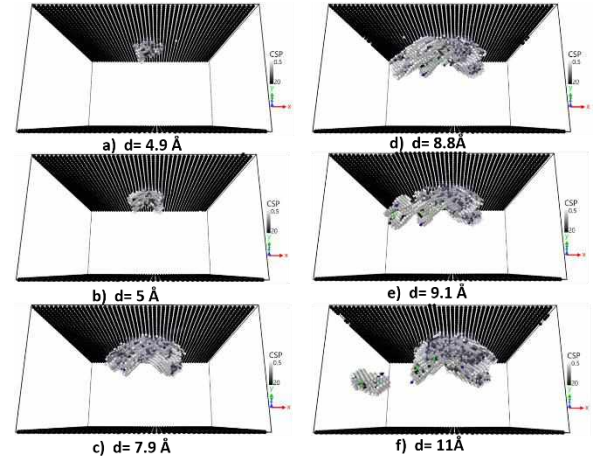


Fig. 3. Snapshots of atomic defects in pure V during indentation at different depths.

### IV. CONCLUSION

The results demonstrate that the dominant mode of plastic deformation of pure V is twinning. Moreover, it should be noted that the most activated dislocations are dislocations with  $a/2\langle 111 \rangle$  type. Whereby,  $a/2\langle 111 \rangle$  shear loops multiply and evolve, and then a pinching of prismatic loop stands remarkable during this plastic deformation. Regarding the hardness results, it is obvious that the average of indentation hardness values at the end of plastic deformation of pure V is approximately  $17\text{GPa}$ . This result is overestimated in comparison with the experimental results, as the structure of our crystal is perfect. Our findings agreed with previous experimental and simulation studies.

### REFERENCES

- [1] LAMMPS Molecular Dynamics Simulator, <http://lammps.sandia.gov>
- [2] Young M, Stukowski A. (2010). Visualization and analysis of atomistic simulation data with OVITO—the open visualization tool. Modelling Simul. Mater. Sci. Eng. 18, 015012. Retrieved from <https://doi.org/10.1088/0965-0393/18/1/015012>.
- [3] Mendelev MI S, Han W, Ackland Son GJ, Srolovitz DJ. (2007). Simulation of the interaction between Fe impurities and point defects in V. Physical review B. 76 (21), 214105. DOI:10.1103/PHYSREVB.76.214105.

# Structural, magnetic and electrical properties of thermally evaporated $\text{Ni}_x\text{Fe}_{1-x}$ thin films

Lamine TABERKANI<sup>1\*</sup>, Ahmed KHARMOUCHE<sup>1\*\*</sup>

<sup>1</sup> Laboratory of surfaces and Interfaces Studies of Solid Materials (LESIMS), Ferhat ABBAS Setif1 University

\*Email [tabrkanilamine@gmail.com](mailto:tabrkanilamine@gmail.com)

\*\* Email [kharmouche\\_ahmed@univ-setif.dz](mailto:kharmouche_ahmed@univ-setif.dz)

**ABSTRACT** Using thermal evaporation under vacuum, we elaborated polycrystalline  $\text{Fe}_x\text{Ni}_{1-x}$  thin films,  $x$  ranging from 0.2 to 0.45. We used Rutherford Backscattering Spectrometry, X-ray diffraction, atomic force microscopy, Hall Effect measurement system (HMS-5300) and Vibrating Sample Magnetometer tools, to study their structure, microstructure, surface morphology, chemical compositions, electrical and magnetic properties. It was found that X-ray diffraction spectra exhibited face centered cubic structure with  $\langle 111 \rangle$  preferred orientation, the crystallite size and lattice parameter increasing with increasing iron content. Electrical resistivity and magnetoresistance decrease with increasing film thickness, but mobility increases. curves infer an in-plane easy axis without any preferential direction. It is also found that the saturation magnetization  $M_s$  increases and the coercive field  $H_c$  decreases with iron content.

## KEYWORDS

NiFe alloys; RBS; XRD; VSM; Electrical resistivity

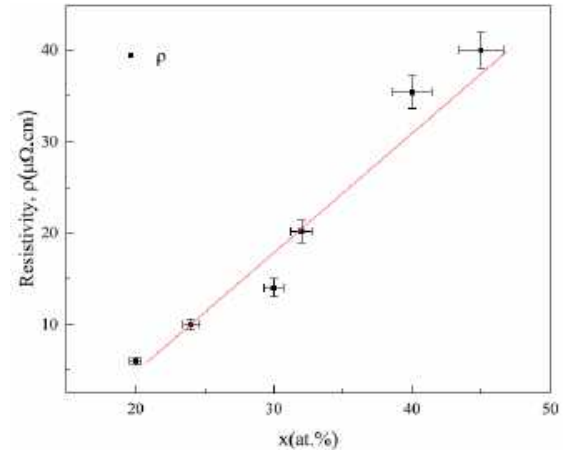


Fig. 2. Electrical resistivity  $\rho$  as a function of iron content  $x$ .

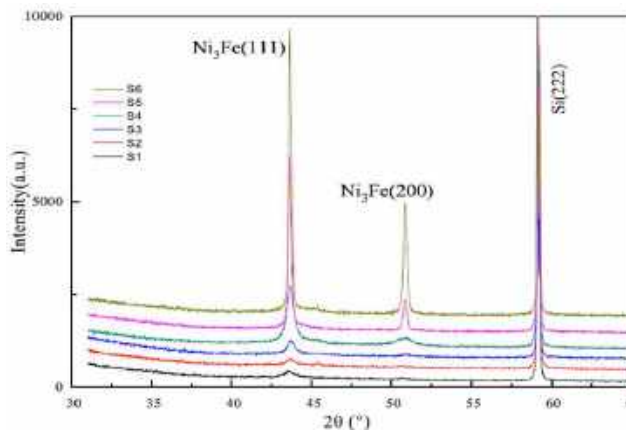


Fig. 1. XRD patterns of  $\text{Fe}_x\text{Ni}_{1-x}$  thin films.

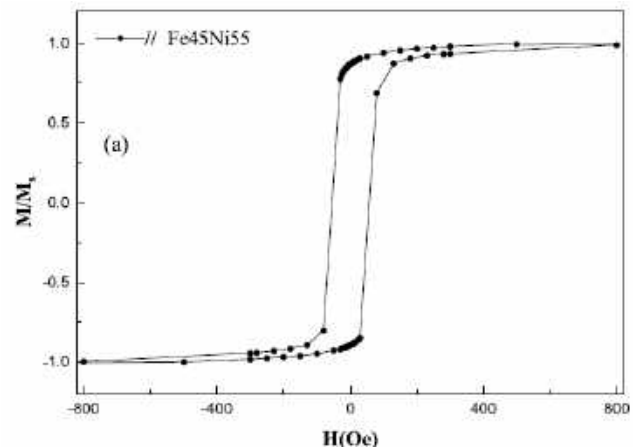


Fig. 3. Specimen of magnetization curves in the longitudinal configuration

# ***Efficacité des stéarates de Cobalt dans l'amélioration de l'oxo-biodégradation des films de polyéthylène***

Samira kerouani<sup>1</sup>

<sup>1</sup>Laboratoire Préparation, Modification et Application des Matériaux Polymériques et Multiphasiques,  
université Ferhat Abbas Sétif1, Algérie

[samirakerouani89@gmail.com](mailto:samirakerouani89@gmail.com)

## **RESUME**

Une préoccupation majeure, liée aux produits plastiques utilisés principalement dans les secteurs de l'emballage et de l'agriculture est représentée par la question liée à leur élimination en fin d'utilisation. Par conséquent, l'introduction sur le marché de PE caractérisé par une durée de vie contrôlée serait très utile pour réduire la charge liée à la réduction des déchets plastiques. À cet égard, l'introduction d'additifs pro-oxydants, capables de favoriser l'initiation de la dégradation, conduisant à des fragments oxydés, devrait être la clé pour la biodégradation ultime du PE. Les pro-oxydants les plus actifs sont en particulier Fe, Co et Mn.

L'objectif du travail a été de présenter et d'étudier l'analyse structurale des films de PE (PEBD) formulés avec un additif pro-oxydant St Co préalablement exposés à un vieillissement naturel durant 6 mois. Les films oxydés ont été par la suite soumis à une biodégradation en milieu solide. Les résultats ont montrés que les stéarates de Cobalt améliorent la vitesse d'oxydation du PE rendant ainsi les fragments oxydés plus accessibles par les microorganismes.

## **MOTS CLES**

PEBD; Pro-oxydant; Vieillissement; Biodégradation ;

## **I. INTRODUCTION**

Parmi tous les déchets plastiques, le polyéthylène (PE) représente près de 40% en raison de son utilisation à court terme et de sa fonctionnalité à long terme. L'hydrophobicité, le haut poids moléculaire du PE limitent sa dégradation. L'une des actions prises pour l'élimination de ces déchets consiste en la préparation d'un PE dégradable, favorable à l'environnement.

De nombreux chercheurs ont conclu que l'attaque par les micro-organismes est un processus secondaire dans la dégradation des polymères. Le processus primaire est l'oxydation, qui est la première et principale étape de la biodégradation.

Des tentatives ont donc été faites pour diminuer la fonctionnalité à long terme du PE en le mélangeant avec des pro-oxydants. Le PE oxydé avec un bas poids moléculaire et une hydrophilicité plus élevée est plus susceptible d'être attaqué par les micro-organismes.

Les principaux objectifs de ce travail visent à confirmer l'effet catalytique des pro-oxydants dans l'améliorer du degré d'oxydation abiotique du PE et d'étudier l'effet de cette oxydation sur l'assimilation microbienne des

fragments de PE oxydés. Deux types de films de PE ont été étudiés ; un film pris comme référence PEBD/Antioxydant sans additifs pro-oxydants (**F1**), et un film préparé au niveau du laboratoire PEBD/Antioxydant/2%Co (**F5**).

## **II. Résultats**

### **A. Vieillissement naturel**

#### **A.1 Caractérisation par spectroscopie infra rouge à transformé de Fourier (IR-TF)**

Les plus significatifs changements des spectres IR-TF en fonction du temps de vieillissement naturel sont enregistrés dans la région carbonyle, comme illustrés par la figure 1. En examinant cette région entre 1800 et 1680  $\text{cm}^{-1}$ , on constate que tous les pics de cette région possèdent la même forme avec des épaulements et qu'ils évoluent tous d'une façon similaire avec le temps d'oxydation; confirmant ainsi la formation de nombreux et différents produits oxygénés.

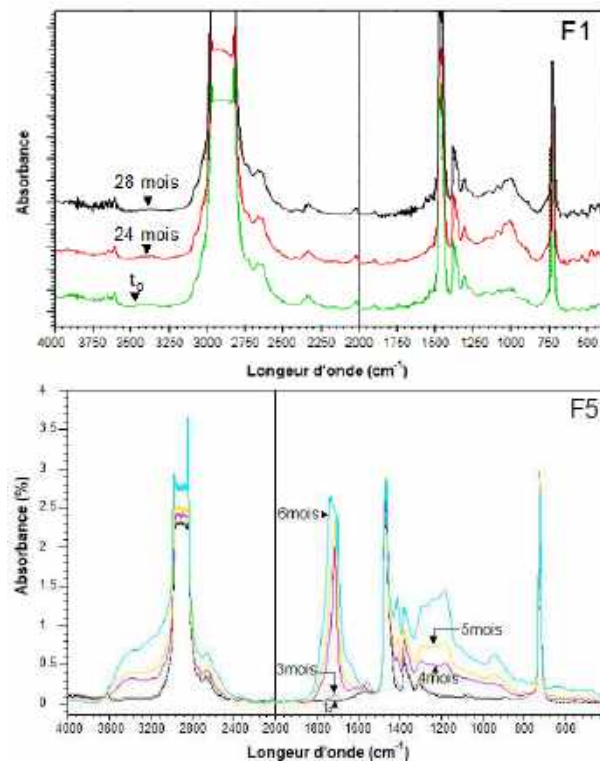


**Fig. 1. Spectres IR-TF des films PEBD/antioxydant et PEBD/pro-oxydant en fonction du temps de vieillissement naturel**

Le maximum d'absorption peut être assigné aux acides carboxyliques ( $1700\text{ cm}^{-1}$ -  $1710\text{ cm}^{-1}$ ) et cétones ( $1715\text{ cm}^{-1}$ -  $1720\text{ cm}^{-1}$ ) comme étant les majeurs produits de dégradation suivis par les esters ( $1720\text{ cm}^{-1}$  -  $1740\text{ cm}^{-1}$ ) Le film **F5** (2% Co) est le plus sensible à l'oxydation naturelle par rapport au film **F1** ne contenant aucun pro-oxydant.

#### A.2. Caractérisation par microscopie à force atomique

La figure.2 présente des images AFM qui montrent la différence entre les états de surface des films de PEBD et PEBD/pro-oxydants avant et après 6 mois d'exposition aux conditions environnementales. Ces images révèlent un effet significatif des conditions environnementales sur l'état de surface des films de PEBD/St Co en comparaison avec celle des films de PEBD sans pro-oxydants, montrant ainsi l'effet positif de la présence de pro-oxydant dans les films de PE sur l'évolution de l'oxydation.

Les échantillons de PE contenant le pro-oxydant (**F5**) a montré dans ces conditions de vieillissement, l'apparition de rugosités de petites dimensions, avec apparition de quelques nodules de très faible taille. Nous pouvons supposer que ces nodules sont composés de fragments de chaînes polymères oxydées.

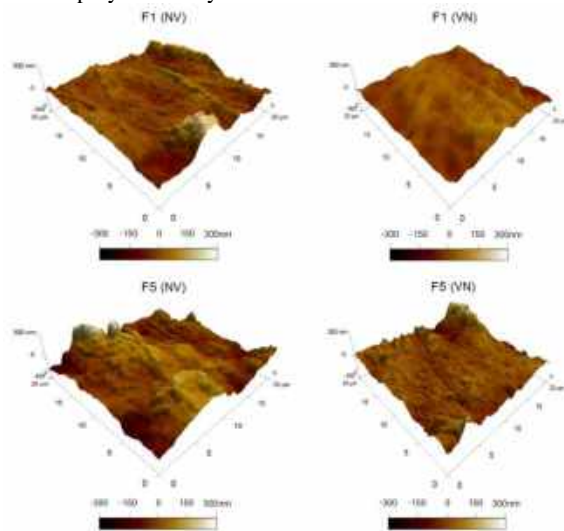


Fig.2. Micrographies en AFM de la topographie de la surface du PEBD et PEBD/St Co avant vieillissement naturel (NV) et après (VN)

#### B. Biodégradation en milieu solide

##### B.1. Test de respirométrie

Du début de l'essai jusqu'à 28 jours d'incubation dans le sol à température ambiante, aucune libération de  $\text{CO}_2$  n'est observée, pour le matériau **F1** cette période correspond à une phase de latence pour les deux échantillons.

La phase de conversion en  $\text{CO}_2$  dure 90 jours (plateau) pour le film sans pro-oxydant **F1** avec une minéralisation finale à 120 jours de 15,60 %.

Pour le matériau **F5** la minéralisation démarre pratiquement après une courte phase de latence de 10 jours, une phase de dégradation rapide, atteignant environ 20 % en 70 jours ; le

taux final de libération de  $\text{CO}_2$  atteint au cours des 120 jours d'incubation dans le sol est de 29 %.

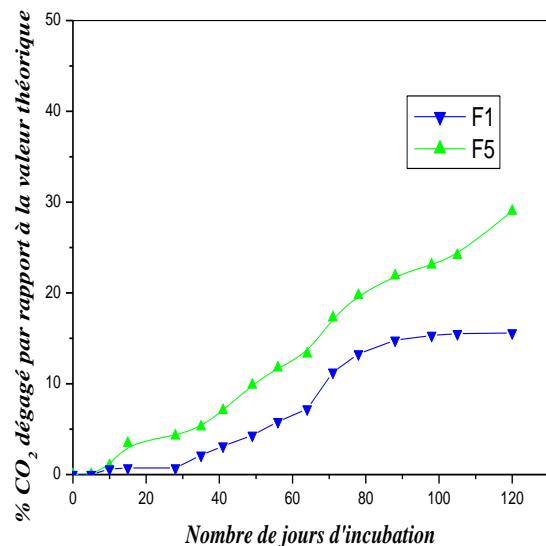


Fig.3. Graphe montrant le %  $\text{CO}_2$  dégagé par rapport à la valeur théorique des matériaux PEBD (F1) et PEBD/St Co (F5): incubation en milieu solide (test respirométrique)

#### C. CONCLUSION

En conclusion, le vieillissement dans les conditions réelles (vieillissement naturel et biodégradation), n'a induit qu'un très faible changement de la surface du PEBD pur donc il est resté très résistant à l'effet des paramètres environnementaux, contrairement au matériau contenant le pro-oxydant (Co) ; ce matériau a subi une rapide oxydation après une courte période d'induction

Donc l'effet des stéarates de cobalt est très significatif sur la dégradation abiotique ainsi que sur le potentiel de biodégradabilité ultime du PEBD.

#### REFERENCES

- [1]: Sudhakar, M., Doble, M., Murthy, P.S., Venkatesan, R., Marine Microbemediated Biodegradation of Low and High-Density Polyethylenes, International Biodeterioration and Biodegradation, 2008, 61(3): 203-213.
- [2]: Abrusci, C., Pablos, J.L., Marin, I., Espi, E., Corrales, J., Comparative Effect of Metal Stearates as Pro-oxidant Additives on Bacterial Biodegradation of Thermal- and Photodegraded Low Density Polyethylene Mulching Films, International Biodeterioration and Biodegradation, 2013, 83, 25-32.
- [3]: Shalini, R., Sasikumar, C., Biodegradation of Low Density Polythene Materials Using Microbial Consortium- An Overview, International Journal of Pharmaceutical and Chemical Sciences, 2015, 4(4): 507-514.
- [4]: Corti, A., Muniyasam, S., Vitali, M., Imam, S.H., Chiellini, E., Oxidation and Biodegradation of Polyethylene Films Containing Pro-oxidant Additives: Synergistic Effects of Sunlight Exposure, Thermal Aging and Fungal Biodegradation, Polymer Degradation and Stability, 2010, 95 (6): 1106-1114.

## **Determination of the relation between the pressures, young's modulus and poison's ratio from continuous conical indentation testing**

AISSA Boudilmi<sup>a,b</sup>

- a) Department of Mechanical Engineering, Faculty of Technology, Mohamed Boudiaf University ,M'sila,ALGERIA
- b) Non-metallic Materials Laboratory, Institute of Optics and Precision Mechanics, Ferhat Abbas University of Sétif 1, Sétif, Algeria.

### **Abstract**

Applying the relationships developed newly for conical indentation in elastic–plastic solids, we establish a relationship expression between the hardness and the Young's modulus and the Poisson's ratio of solids.

As, the hardness formula is defined as the maximum load divided by the contact area of the penetrator and where the load expression is expressed by the Love (1939) and by Sneddon (1965) expression, We have concluded a mathematical expression of the hardness of a solid material in function of the Young's modulus (E) and the Poisson's ratio( $\gamma$ ) of the tested material and the semi-included angle of the conical indenter.

In this work mathematical concepts of the right circular cone have been established then the hardness formula of the bulk material was derived from the general function of the hardness and the Love and Sneddon workers.

Finally, a comparison study was done between bulk hardness formulas (H) of different conical indenter having different semi-included angle ( $\theta$ ).

**Key words:** Hardness, cone contact, geometric modeling, indentation;

### **References:**

- [1] Li, X., An, B., & Zhang, D. (2015). Determination of elastic and plastic mechanical properties of dentin based on experimental and numerical studies. *Applied Mathematics and Mechanics*, 36(10), 1347-1358.
- [2] Yong Yee Lim & M. Munawar Chaudhri (2004) Indentation of elastic solids with rigid cones, *Philosophical Magazine*, 84:27, 2877-2903, DOI: 10.1080/14786430410001716782

- [3] M. Munawar Chaudhri, the Love Equation for the Normal Loading of a Rigid Cone on an Elastic HalfSpace and a Recent Modification: A Review Materials Transactions, Vol. 60, No. 8 (2019) pp. 1404 to 1410
- [4] BOUDILMI, Aissa et LOUCIF, K. Hardness Measurements via an Ellipsoid-Shaped Indenter. *Strength of Materials*, 2016, vol. 48, p. 419-425.
- [5] BOUDILMI, Aissa et LOUCIF, K. A theoretical study of indentation with an oblate spheroid shape. *Transactions of the Indian Institute of Metals*, 2017, vol. 70, p. 1527-1531.
- [6] BOUDILMI, A. et LOUCIF, K. Modelling of thin films hardness measured by a spherical indenter. *Металлофизика и новейшие технологии*, 2018.
- [7] AISSA, BOUDILMI. The form of the balancing coefficients of the surfaces mixture model for an ellipsoidal indenter. In : *International Conference on Materials Science ICMS2018*. 2018.
- [8] BOUDILMI, A. et LOUCIF, K. The Indentation Performance of a Novel Indenter with a Prolate Spheroid Tip. *Strength of Materials*, 2022, vol. 54, no 1, p. 154-164.
- [9] BOUDILMI, A., LOUCIF, K., SLAMANI, M., *et al.* New Method for the Micro-and Nanohardness Measurement of Thin Film of Monolayer Solid by the Indentation of a Sharp Needle of a Cone Tip. *Strength of Materials*, 2023, p. 1-14.
- [10] BOUDILMI, A. Estimation of Micro-and Nanohardness of the Thin Film of a Coated Material Measured Using Spherical-Tip Indentation. *Russian Physics Journal*, 2023, vol. 66, no 3, p. 290-297.
- [11] BOUDILMI, A. et LOUCIF, K. Film Hardness Evaluation in Hard Film/Substrate Composites by Conical Indentation. *Металлофизика и Невейсје Тевнологии*, 2023, vol. 45, no 4.
- [12] BOUDILMI, Aissa, *et al.* *ETUDE THEORIQUE ET EXPERIMENTALE DES ESSAIS DE DURETE POUR MATERIAUX MASSIFS ET REVETUS*. Mémoire de Magister. University of M'sila.



# Effect of Temperature and Humidity on the Mechanical Behavior of a Cotton Yarn

A.MANGOUCI<sup>1</sup>, MZ. BESSENOUCI<sup>2</sup>, F. BENKHENAFOU<sup>1</sup>

1. : Department of Mechanical Engineering, University of Abou Bekr Belkaid Tlemcen, Algeria, [fethi.benkhenafou13@gmail.com](mailto:fethi.benkhenafou13@gmail.com)

2. Department of Mechanical Engineering, University Center of Salhi Ahmed, Naama, Algeria, [mzbessenouci@cuni-naama.dz](mailto:mzbessenouci@cuni-naama.dz)

## I. INTRODUCTION

In terms of the global environment, we use textile materials on a large scale in many areas. Therefore, almost every time we look for durable textile yarns, we have to specify some particular characteristics for each use.

This work constitutes a contribution to the study of the influence of humidity and temperature on the breaking strength and deformation of cotton textile yarns. We have carried out mechanical tests on cotton textile yarn with the aim of improving their mechanical characteristics. The results show the importance of humidity levels during the weaving production chain and after

In order to obtain better cotton yarn with the best environmental resistance, there must be a certain ratio of humidity and temperature during industrial processing. We have developed a sizing solution based on local and economical natural products with the aim of increasing the mechanical resistance and reducing breakage of the sized cotton thread, used during the weaving process.

It can also be concluded from the test that twisting the yarn generally improves the mechanical properties at breakage of the yarn at a certain humidity level. On the other hand, the increase in temperature affects the latter.

**KEY WORDS** : Fibrous materials; mechanical behavior; characterization ; humidity ; temperature ; gluing

## II. EXPERIMENTATION

### A Material and methods

The material used during our study is a cotton thread

with a metric number 1/24cc, having a diameter of 0.26μm, useful length of 500 mm and the number of tests is 20 on a Textechna traction machine with a speed of 400 mm/min, at an ambient temperature of 23°C and a humidity level of 62%.

### B. Results – Discussion

Figures 1 illustrates the variation in fracture behavior as a function of temperature. We note that the increase in temperature favors the reduction in the breaking strength of the two types of yarns (virgin and sized), hence a necessary humidification of the yarn to maintain a certain resistance during weaving (fig 2; 3 ).

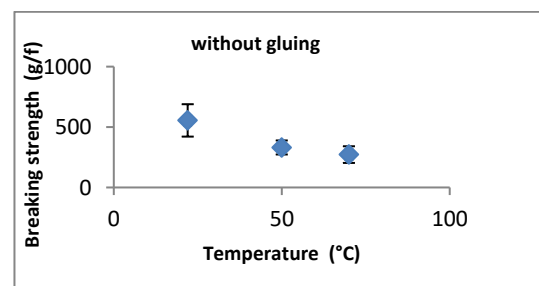


Figure 1: Effect of temperature on the breaking strength of virgin 1/24 cc wire.

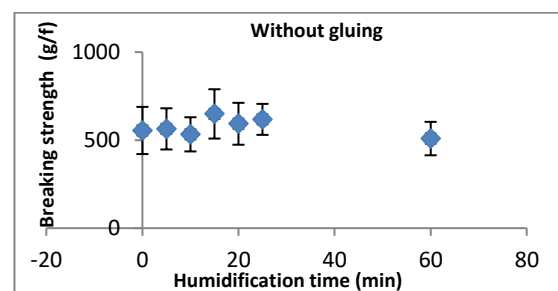


Figure 2.: Effect of humidification time on the breaking strength of a virgin 1/24 cc wire.

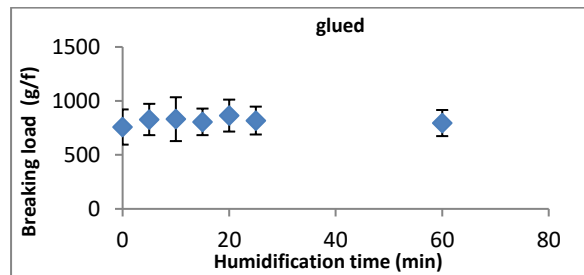


Figure 3: Effect of humidification time on the breaking load of a glued 1/24 cc wire

### Twisting effect

We carried out mechanical tests for two assembled cotton threads and two others twisted and the results are very interesting as shown in Table 1. Twisting clearly improves the mechanical characteristics of the cotton thread (in our case, it is with a twisting rate of 540 rpm).

Table 1 Effect of twisting on the mechanical behavior at breakage of a virgin 1/24 cc wire.

Wire structure	Breaking strength (g/f)	$\Delta R$ (g/f)	Elongation at break (%)	$\Delta A$ (%)
2 wires assembled	1029	$\pm 72$	5,4	$\pm 0,72$
2 twisted threads	1645	$\pm 85$	8,8	$\pm 0,84$

### III. CONCLUSION

We note that sizing and twisting considerably increase the mechanical breaking characteristics of cotton threads. We then deduce that the surface treatment of the yarn by sizing greatly reduces yarn breakage during weaving. We note that the increase in temperature favors the reduction in the breaking strength of the two types of yarns, hence a necessary humidification of the yarn to maintain a certain resistance during weaving.

### REFERENCES

[1] Gilbert, N.L., Guay, M., Miller, J.D., Judek, S., Chan, C.C., and Dales, R.E. Levels and Determinants of Formaldehyde, Acetaldehyde and Acrolein in Residential Indoor air in Prince Edward Island, Canada. Environ. Res. Vol. 99, p. 11-17. (2005).

[2] Rollins, ML: The Cotton Fiber, American Cotton Handbook. 3rd ed. D.S. Hamby, Ed, Interscience Publishers, New York .U.S.A. (1995). 6. USA. (1993).

[3] <https://www.futura-sciences.com/tech/dossiers/technologie-vegetal-textiles-585/page/2/>

[4] Michèle Mosiniak, Roger Prat. Du végétal au textile. Biologie et Multimédia - Université Pierre et Marie Curie - UFR de Biologie <http://www.snv.jussieu.fr/bmedia/textiles/04-coton-traitement.html>. Dernières modifications : 23 mai 2005.

[5] Bojana Voncina, Dominika Bezek, Alenka Majcen le Marechal Eco-Friendly Durable Press Finishing of Textile Interlinings. Fibres and Textiles In Eastern Europe July/September p.68-71 (2002).

[6] Prévention de la pollution dans l'Industrie textile dans la région méditerranéenne. Centre d'activités régionales pour la production propre (CAR/PP). Barcelone. Espagne. (2002).

# Effect of thickness on the physical properties of evaporated Permalloy/GaAs(100) thin films

Ounissa CHERRAD<sup>1\*</sup>, Ahmed KHARMOUCHE<sup>1\*\*</sup>

<sup>1</sup> Laboratory of Surfaces and Interfaces Studies of Solid Materials (LESIMS), Ferhat ABBAS Setif1 University

\*Email [cherradphysiquem2@gmail.com](mailto:cherradphysiquem2@gmail.com)

\*\*Email [kharmouche\\_ahmed@univ-setif.dz](mailto:kharmouche_ahmed@univ-setif.dz)

## ABSTRACT

Thermally evaporated Permalloy  $\text{Ni}_{80}\text{Fe}_{20}$  (Py) thin films on GaAs (100) substrates, for thickness ranging from 132 to 277 nm, are examined. In this work we focus on how Py thickness affects their physical properties. The deposited Py films were examined using X-ray diffraction (XRD), scanning electron microscopy equipped with an energy dispersive X-ray analyzer (SEM-EDS), atomic force microscopy (AFM), and the Hall Effect measurement system (HMS-5300) tools in order to determine their structure, surface morphology, chemical compositions, and electrical properties. All samples crystallize in the FCC structure with the preferred orientation  $\langle 111 \rangle$ , according to the acquired X-ray diffraction spectra. With increasing thickness, both the lattice parameter and grain size increase. Very dense structure without microcracks and very fine spherical grain distribution were seen in SEM micrographs. For all deposited Py films, AFM images revealed a very smooth surface. Electrical measurements revealed that the electrical resistivity decrease with increasing film thickness.

## KEY WORDS

$\text{Ni}_{80}\text{Fe}_{20}$  thin films; XRD; SEM-EDS; AFM; Electrical resistivity

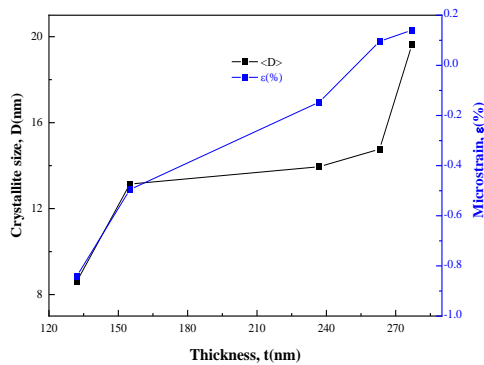


**Fig.1.** Variations of crystallite size  $\langle D \rangle$  (nm) and microstrain  $\epsilon$  (%) as functions of film thickness.

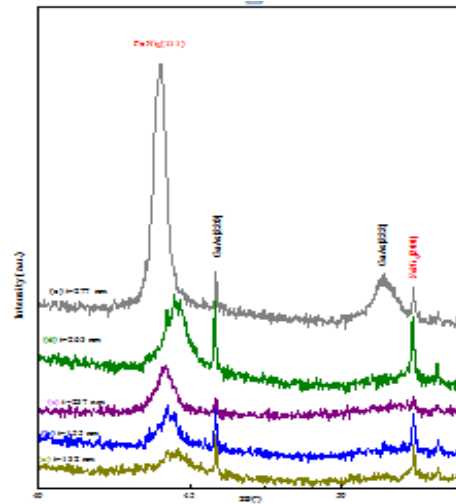


**Fig.**

2. X-rays patterns of Py thin films with different thicknesses: (a) 132 nm, (b) 155 nm, (c) 237 nm, (d) 263 nm and (e) 277 nm.

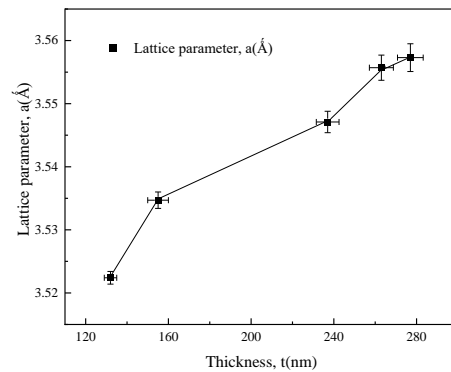


**Fig.3.** Lattice parameter  $a$  as a function of  $\text{Ni}_{80}\text{Fe}_{20}$  film thickness.

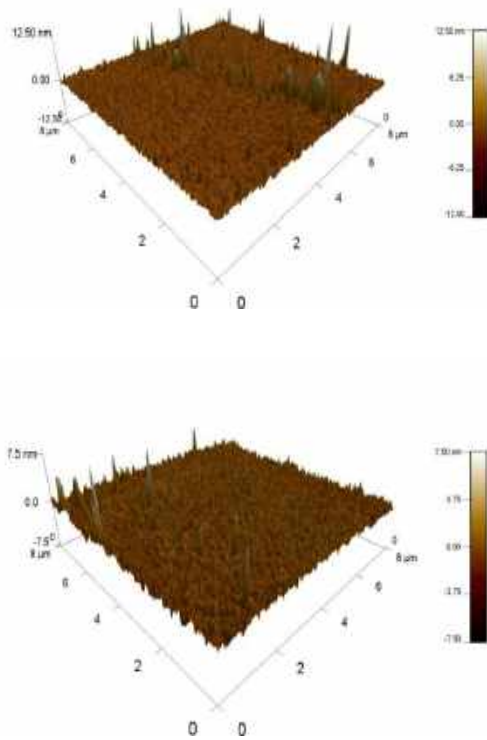


**Fig. 4.** Example of AFM images for Py/GaAs(100) sample with a thickness of 237nm and 263nm.

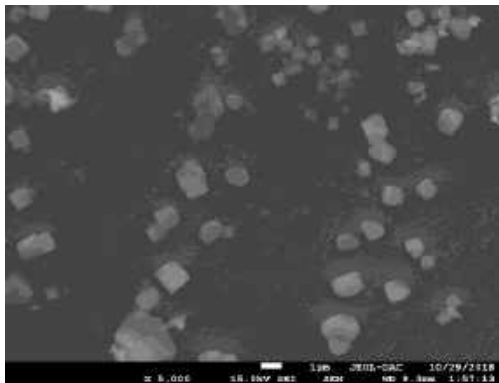


**Fig.5.** Example of SEM micrographs: Py/GaAs (100) sample, 263 nm thick.

## CONCLUSION

In this work, we have investigated the effect of an increasing thickness on the properties of Permalloy thin films prepared by thermal evaporation under vacuum onto GaAs(100) substrates at room temperature. The XRD results indicate that the obtained Py samples are polycrystalline and exhibit the face-centered cubic  $\text{Ni}_3\text{Fe}$  structure, with a preferential orientation  $\langle 111 \rangle$ . The crystallite size and the lattice parameter increase with the increase in the thickness. The SEM observations show a very dense surface with coalescing and agglomerating nanoparticles with a diameter of about [22-30] nm and without any presence of micro cracks on the surface. From AFM observations, most of the layers are smooth with roughness not exceeding  $\sim 14\text{nm}$ , and the best surface quality, reflecting good crystallinity, was observed for the 263 nm thick film with an average rms of 0.641nm. Both the electrical resistivity and decrease with increasing thickness, this evolution being due to the surface morphology of the films.

## REFERENCES

- [1] P. Prieto, J. Camarero, J. F. Marco, E. Jiménez, J. M. Benayas, and J. M. Sanz, *IEEE Trans. Magn.* **44** (2008) 3913-3916.
- [2] F. Czerwinski, J. A. Szpunar, U. Erb, *J Mater Sci: Mater Electron* **11** (2000) 243-251.
- [3] Baicheng Zhang, Nour-Eddine Fenineche, Hanlin Liao and Christian Coddet, *J. Magn. Magn. Mater.* **336** (2013) 49–54.
- [4] R. Balachandran, H.K. Yow, B.H. Ong, K.B. Tan, K. Anuar, H.Y. Wong, *Int. J. Electrochem. Sci.*, Vol. **6** (2011) 3564 – 3579.
- [5] Movaffaq Kateb, Egill Jacobsen and Snorri Ingvarsson, *J. Phys. D: Appl. Phys.* **52** (2019) 075002 (12pp).

# Title: Strength and Mechanical Behavior of Fiber Reinforced Clayey Soil: Experimental Study

LACHACHE RAFIKA<sup>1</sup>, KOULOUGHLI SALIM<sup>2</sup>

1. University brothers Mentouri-Constantine, Faculty of science and technology, department of civil engineering, lachacherafika25@gmail.com
2. University brothers Mentouri-Constantine, Faculty of science and technology, department of civil engineering, salimkouloughli@umc.edu.dz

## ABSTRACT

*Soils used as barrier materials in the final cover system at the top of the municipal solid waste landfills generally are clays that are compacted to allow hydraulic conductivity. However, this barrier encounters problems, in particular, related to mechanical loading which can cause the clay layer to crack.*

*Randomly distributed fibers have been successfully used for the reinforcement of soils to enhance their engineering properties. Soil reinforcement by fiber material is considered an effective ground improvement method because of its cost effectiveness, easy adaptability and reproducibility. Hence, in present study, straw fiber has been chosen as the reinforcement material with diverse content (0-0.3-0.6 and 0.9% by dry weight of the soil. The composite soils were laboratory tested for compaction, unconfined compression strength and indirect tensile tests. The test results indicated that: the optimum fiber content for clay samples reinforced with straw fibers is approximately 0.6 % of the dry weight of the soil and the addition of 0.6% of straw fiber improves the strength of the soil by increasing the elasticity and reducing the displacement.*

**KEY WORDS:** Landfill; clay; straw fiber; fiber-reinforced soil.

## I. INTRODUCTION

The final cover system at the top of the municipal solid waste landfills is usually composed of several layers including allow permeability barrier layer. Soils used as barrier materials generally are clays that are compacted to a hydraulic conductivity no greater than  $10^{-6}$  cm/sec. However, this barrier encounters problems in particular related to mechanical loading which can cause the clay layer to crack. The resulting cracks mean that the integrity of the barrier can not be guaranteed in terms of its hydraulic characteristics. It was proposed to improve the mechanical properties of the clay by fiber-reinforcement addition ([1]–[2]–[3]–[4]–[5]–[6]–[7]). However an increasing number of experimental and numerical studies have been conducted by several researchers to evaluate the effect

of the inclusion of randomly distributed discrete fibers in a soil mass [8]–[9]–[10]–[11]–[12]–[13], but the applications to landfills cover barrier are not so numerous.

The main objective of this study is to investigate the effect of fiber reinforcement on the mechanical properties of a sediment soil. A series of Brazilian tests and unconfined compression tests were carried out on the sediment alone and the fiber-reinforced sediment samples that were prepared at different percentages (0.3–0.6 and 0.9%) of fiber straw content.

## II. METHODOLOGY

The experimental program was carried out in three parts: First, the geotechnical properties of the soil and fibers were characterized. Then the effects of adding straw fiber on the behavior of clayey soil (sediment). Finally the application of the results to the clay barrier.

## III. RESULTS

### A. Effect Of Fiber Content On Unconfined Compressive Strength

The inclusion of fibers has a positive effect. However, the increase in strength is 6–30 % with the inclusion of 0.1 – 0.9 % of 15mm fiber length. The optimum fiber length and fiber content were found as 15 mm and 0.6%, respectively. (Fig. [1]).

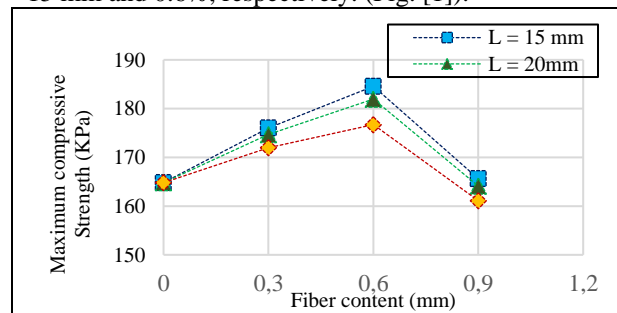


Fig. 1. Evaluation of the maximum stress capacity of the sediment in compression.

### B. Effect of fiber content on tensile strength

The results indicated that the short fibers were found

more effective than longer fibers to improve tensile strain characteristics of the reinforced soil by delaying crack initiation and reducing its propagation (fig [2]).

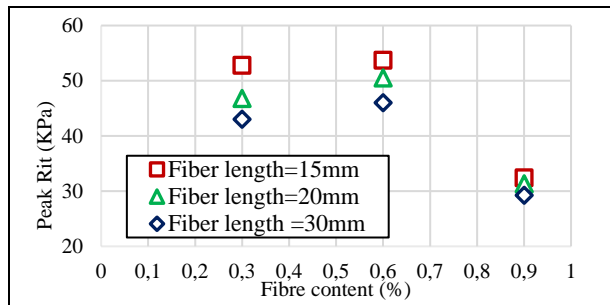


Fig. 2. . Evaluation of the maximum stress capacity of the sediment in tension.

### C. Application to the clay barrier

#### ➤ Strength limiting values

The failure envelope can be draw according to Caquot and Kérisel (1966). The criterion presents a parabolic shape, in the plan of stress, under the form:

$$\sigma = a \times \tau^2 + b$$

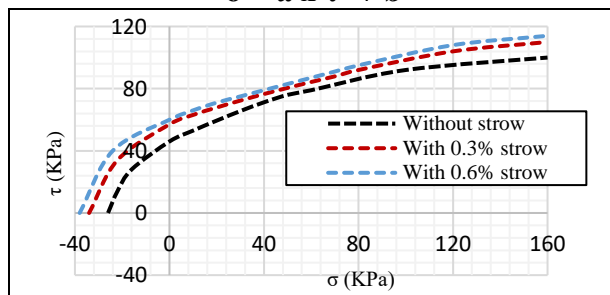


Fig. 3. Failure envelope for reinforced and unreinforced sediment.

#### ➤ Post peak behavior

The ductility or the rigidity of a soil can be quantified by comparing the peak and residual strength using a brittleness index, which can be defined by:

$$IB = 1 - (\sigma_r / \sigma_{max})$$

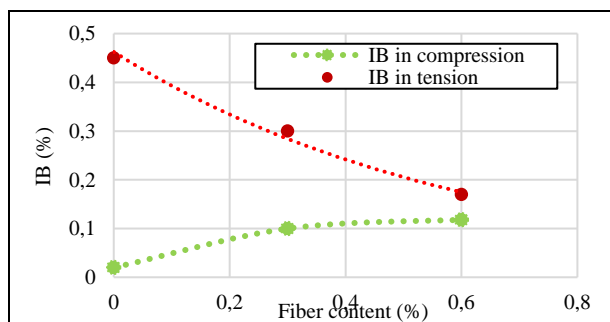


Fig. 4. Effect of the fiber content on the brittleness index.

## IV. CONCLUSION

- The addition of straw fiber reduces the maximum dry density dramatically to 14.86 kN/m<sup>3</sup> and increases the optimum water content to 16.49 %.

- The increase in UCS is 6-30 % with the inclusion of 0.1 – 0.9 % of 15mm fiber length respectively and the optimum fiber length and fiber content were found as 15 mm and 0.6%, respectively.

- As the fiber content increases from 0% to 0.6% the tensile strength increases by 75%

- In compression, an increment in the fiber content produces an increment in the brittleness index.

- In tension, an increment in the fiber content produces a decrement in the brittleness index.

- The benefit of ductility can reach 62% and the composite material becomes more and more ductile.

## REFERENCES

- [1] Gray, DH. and Ohashi, H. (1983) "Mechanics of fiber reinforcement in sand," *Geotech Engineering*, ASCE 109 (3), PP. 335-353.
- [2] Maher, MH. and Cray, DH. (1990) "Static response of sands reinforced with randomly distributed fibers," *Geotec Engineering*, ASCE 116(11), PP. 1661-1677.
- [3] Dall'Acqua, G.P. (1999) "Fiber reinforced stabilized soil. Ph.D thesis," University of Birmingham.
- [4] Yetimoglu, T. and Sallbas, O. (2003). "A study on shear strength of sands reinforced with randomly distributed discrete fibers," *Geotextiles and Geomembranes*, vol. 21, pp.103-110.
- [5] Krishna, S.V., Rao and Ahmed, M.A. Nasr. (2011), "Laboratory study on the relative performance of silty-sand soils reinforced with linen fiber," *Geotech Geol Eng*, vol.30, pp. 63-74.
- [6] Aqeel, AD., Giovanni, S. and Rafiq, A. (2012) "Strength of soil reinforced with fiber materials (Papyrus)," *Soil Mechanics and Foundation Engineering*, vol. 48, PP. 241-247.
- [7] Anggraini, V., et al. (2015). Effects of coir fibers on tensile and compressive strength of lime treated soft soil. *Measurement* 59,372-381.
- [8] Dutta, R. K., et al. (2015). Effect of addition of treated coir fibres on the compression behaviour of clay. *Jordan Journal of Civil Engineering* 6(4).
- [9] Yixian, W., et al. (2016). Study on strength influence mechanism of fiber-reinforced expansive soil using jute. *Geotechnical and Geological Engineering* 34(4), 1079-1088.
- [10] Anggraini, V., et al. (2016). Effects of coir fibres modified with Ca (OH) 2 and Mg (OH) 2 nanoparticles on mechanical properties of lime-treated marine clay. *Geosynthetics International* 23(3), 206-218.
- [11] Gutiérrez-Orrego, et al. (2017). Mechanical and physical properties of soil-cement blocks reinforced with mineral wool and sisal fiber. *Journal of Materials in Civil Engineering* 29(3), 04016225.
- [12] Menezes, L. C. P. (2018). Analysis of the mechanical behavior of arenoargillous soil reinforced with green coconut fibers. Master's Dissertation. Polytechnic School of the University of Pernambuco.
- [13] Kafodya, I., Okonta, F. (2018). Effects of natural fiber inclusions and pre-compression on the strength properties of lime-fly ash stabilised soil.



# Tribological and Morphological properties of films deposit on metallic prostheses

DERGHOUM ROMAYSSA<sup>1</sup>, KAHLOUL LATIFA<sup>1</sup>, MEDDAH SOUMAYA<sup>2</sup>

1. Department of Materials Science and Engineering National Higher School of Technology and Engineering, Annaba, Algeria, [r.derghoum@ensti-annaba.dz](mailto:r.derghoum@ensti-annaba.dz)
2. Research center in industrial technology CRTI-Annaba, Algeria, [meddahsoumaya@gmail.com](mailto:meddahsoumaya@gmail.com)

## ABSTRACT

*Stainless steel, titanium and CoCrMo alloys are the most widely used biomaterials for orthopedic applications. The most common causes of failure of orthopedic implants after implantation are infection, poor corrosion resistance, low mechanical strength, dissolution of toxic elements and excessive wear. To solve the problems associated with implant materials, various design, material and surface modifications have been developed. Among the different methods, the coating is an effective method to improve the performance of implant materials. This work aims to synthesize hydroxyapatite coatings on metal prostheses to improve biocompatibility and increase the corrosion resistance, wear and find better osseointegration. The hydroxyapatite coating will be prepared by the sol-gel technique that has an excellent potential for deposition the biocompatible HAp and has many advantages over other methods and we will study the effect of the temperature, PH and Ca/P molar ratio on the tribological and morphological properties of hydroxyapatite. The results obtained indicate that hydroxyapatite synthesized by sol-gel technique is more advantageous and that this coating improves the resistance to corrosion and wear, also, indicate that had a low friction coefficient and the surface morphology of HAp observed by SEM shows that the deposit has a uniform and homogenous appearance. The results also showed that the realized coating has good properties and could be a potential and promising implant for orthopaedic surgery.*

## KEY WORDS

Hydroxyapatite ; tribological ; sol-gel ; morphological

## I. INTRODUCTION

With the growing demands for bone implant therapy, titanium (Ti) and its alloys are considered as suitable choices for load-bearing bone implant substitutes due to their high hardness, excellent corrosion resistance in the corporal environment, high wear resistance and higher biocompatibility. However, the interaction of

based implants with tissues is critical to the success of the implants for the long-term stability. Therefore, surface modification of Ti implants with biocompatible hydroxyapatite coatings before implantation is important and of growing interest. Hydroxyapatite is a material from the ceramic category, which is an excellent candidate for coating these metals for biomedical application because it is the basic component of bone (about 70%).

## II. MATERIALS AND METHODS

### Before deposition :

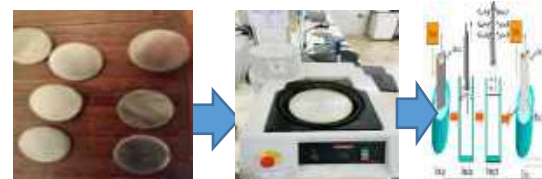
The TA6V4 samples were removed with sillicium carbide (SiC) papers and then cleaned with water, alcohol and acetone as well as distilled water.

### Coating deposition:

the layers were deposited by sol-gel technique using calcium nitrate tetrahydrate and phosphorus pentoxide as precursors and according to well determined parameters (temperature, fritting time, PH, aging time, calcination temperature).

SEM and tribometer characterized the samples obtained.

### Synthesis of deposits



the wear rate of coated samples is lower than uncoated samples .

### MORPHOLOGICAL BEHAVIOR

### Deposit characterisation

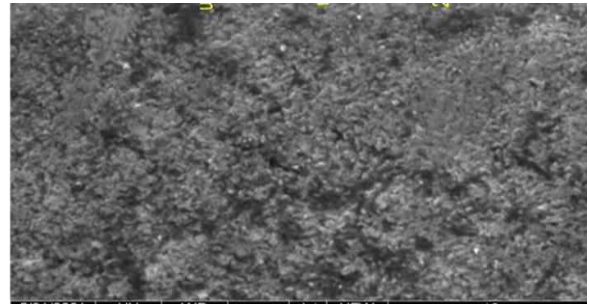


Fig 3 : SEM micrograph of coated sample

The morphology of the coated sample is uniform and homogeneous than the uncoated sample

### RESULTS

### TRIBOLOGICAL BEHAVIOR

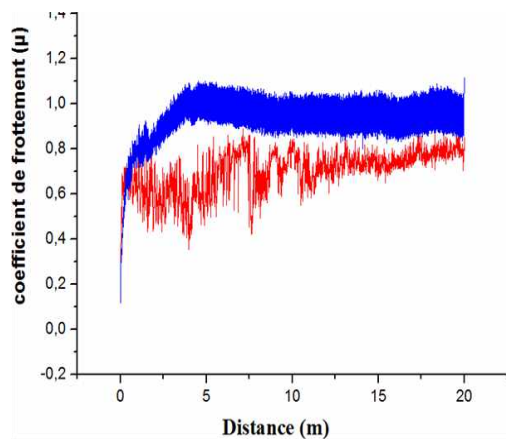


Fig 1 : Evolution of the coefficient of friction as a function of the sliding distance.

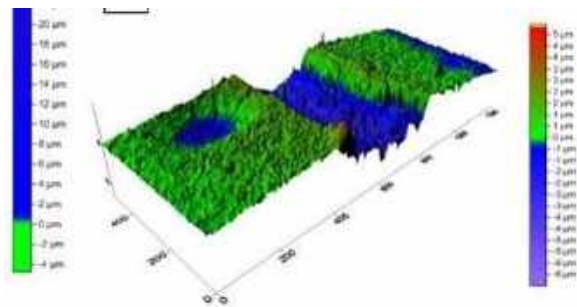


Fig 2 : 3D photos of the wear groove of coated sample

The coefficient of friction decreases to 0.2  $\mu\text{m}$  for coated samples.

### III. CONCLUSION

The main results obtained can be summarized as follows :

The coefficient of friction decreases to 0.2  $\mu\text{m}$  for coated samples.

The wear rate of coated samples is lower than uncoated samples.

The results also showed that the realized coating has good properties and could be a potential and promising implant for orthopaedic surgery.

# Tribological and Morphological properties of films deposit on metallic prostheses

DERGHOUM ROMAYSSA<sup>1</sup>, KAHLOUL LATIFA<sup>1</sup>, MEDDAH SOUMAYA<sup>2</sup>

1. Department of Materials Science and Engineering National Higher School of Technology and Engineering, Annaba, Algeria, [r.derghoum@ensti-annaba.dz](mailto:r.derghoum@ensti-annaba.dz)
2. Research center in industrial technology CRTI-Annaba, Algeria, [meddahsoumaya@gmail.com](mailto:meddahsoumaya@gmail.com)

## ABSTRACT

*Stainless steel, titanium and CoCrMo alloys are the most widely used biomaterials for orthopedic applications. The most common causes of failure of orthopedic implants after implantation are infection, poor corrosion resistance, low mechanical strength, dissolution of toxic elements and excessive wear. To solve the problems associated with implant materials, various design, material and surface modifications have been developed. Among the different methods, the coating is an effective method to improve the performance of implant materials. This work aims to synthesize hydroxyapatite coatings on metal prostheses to improve biocompatibility and increase the corrosion resistance, wear and find better osseointegration. The hydroxyapatite coating will be prepared by the sol-gel technique that has an excellent potential for deposition the biocompatible HAp and has many advantages over other methods and we will study the effect of the temperature, PH and Ca/P molar ratio on the tribological and morphological properties of hydroxyapatite. The results obtained indicate that hydroxyapatite synthesized by sol-gel technique is more advantageous and that this coating improves the resistance to corrosion and wear, also, indicate that had a low friction coefficient and the surface morphology of HAp observed by SEM shows that the deposit has a uniform and homogenous appearance. The results also showed that the realized coating has good properties and could be a potential and promising implant for orthopaedic surgery.*

## KEY WORDS

Hydroxyapatite ; tribological ; sol-gel ; morphological

## I. INTRODUCTION

With the growing demands for bone implant therapy, titanium (Ti) and its alloys are considered as suitable choices for load-bearing bone implant substitutes due to their high hardness, excellent corrosion resistance in the corporal environment, high wear resistance and higher biocompatibility. However, the interaction of

based implants with tissues is critical to the success of the implants for the long-term stability. Therefore, surface modification of Ti implants with biocompatible hydroxyapatite coatings before implantation is important and of growing interest. Hydroxyapatite is a material from the ceramic category, which is an excellent candidate for coating these metals for biomedical application because it is the basic component of bone (about 70%).

## II. MATERIALS AND METHODS

### Before deposition :

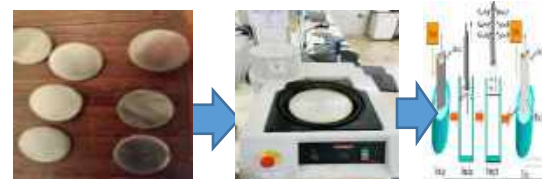
The TA6V4 samples were removed with silicium carbide (SiC) papers and then cleaned with water, alcohol and acetone as well as distilled water.

### Coating deposition:

the layers were deposited by sol-gel technique using calcium nitrate tetrahydrate and phosphorus pentoxide as precursors and according to well determined parameters (temperature, fritting time, PH, aging time, calcination temperature).

SEM and tribometer characterized the samples obtained.

### Synthesis of deposits



the wear rate of coated samples is lower than uncoated samples .

### MORPHOLOGICAL BEHAVIOR

### Deposit characterisation

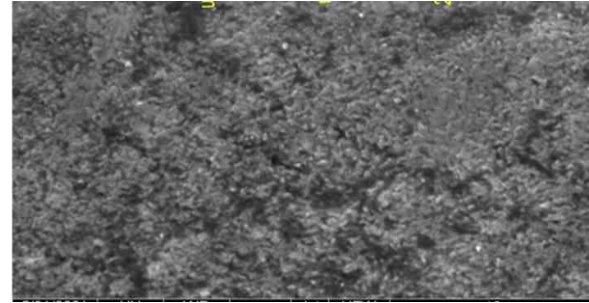


Fig 3 : SEM micrograph of coated sample

The morphology of the coated sample is uniform and homogeneous than the uncoated sample

### RESULTS

### TRIBOLOGICAL BEHAVIOR

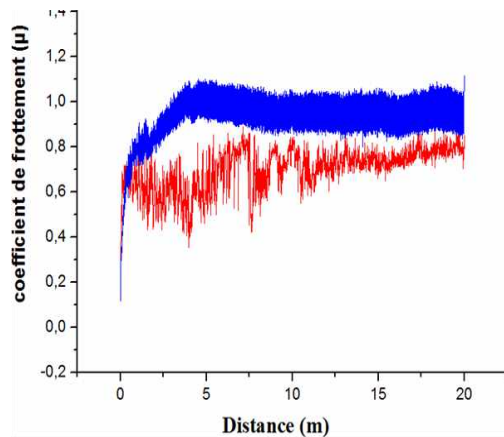


Fig 1 : Evolution of the coefficient of friction as a function of the sliding distance.

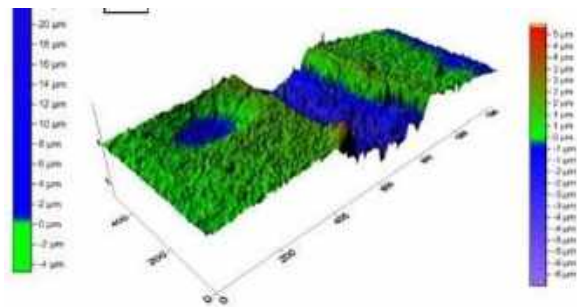


Fig 2 : 3D photos of the wear groove of coated sample

The coefficient of friction decreases to 0.2  $\mu\text{m}$  for coated samples.

### III. CONCLUSION

The main results obtained can be summarized as follows :

The coefficient of friction decreases to 0.2  $\mu\text{m}$  for coated samples.

The wear rate of coated samples is lower than uncoated samples.

The results also showed that the realized coating has good properties and could be a potential and promising implant for orthopaedic surgery.



# Title: Elaboration Processes of $\text{Fe}_2\text{O}_3$ -Aluminosilicate Glass for Energy-Efficient Coatings.

ABDELAZIZ GAHMOUSSE<sup>1,\*</sup>, KOUIDER FERRIA<sup>1</sup>, JUAN RUBIO ALONSO<sup>2</sup>

1. Institute of Optics and Precision Mechanics, University Ferhat Abbas Setif 1  
Setif, Algeria, [abdelaziz.gahmousse@univ-setif.dz](mailto:abdelaziz.gahmousse@univ-setif.dz)
2. Ceramics and Glass Institute, CSIC  
Madrid, Spain, [jrubio@icv.csic.es](mailto:jrubio@icv.csic.es)

## ABSTRACT

*The production of Aluminosilicate glasses with varying  $\text{Fe}_2\text{O}_3$  concentrations was accomplished using specific techniques. The starting point involved creating the parent glass, known as HLEG0, which did not contain  $\text{Fe}_2\text{O}_3$ . To prepare HLEG0, raw materials were mixed using a powder mixer for 30 minutes, repeated four times, before being weighed using a 4-digit scale. The resulting mixture was pressed into pellets via a hydraulic press, then placed in an alumina crucible to be calcinated at  $900^\circ\text{C}$ . The compressed pellets were melted in a propane-air gas furnace at  $1450^\circ\text{C}$  for two hours. The melted composition was then rapidly poured onto a pre-heated metal plate and allowed to cool to room temperature at its own pace. Subsequently, this parent glass was pulverized, mixed with varying amounts of  $\text{Fe}_2\text{O}_3$ , and subjected to the same preparation steps outlined earlier. The resulting mixtures were remelted using an electric furnace at  $1450^\circ\text{C}$  for two hours and poured over a pre-heated metal plate. The materials collected were labelled as HLEG1, HLEG2, HLEG3, HLEG35, and HLEG5, respectively, signifying the incorporation of  $\text{Fe}_2\text{O}_3$  in 10, 20, 30, 35, and 50 weight %, in that order.*

## KEY WORDS

Elaboration;  $\text{Fe}_2\text{O}_3$ ; Glass; Pressing; Calcination; Melting.

## I. INTRODUCTION

Numerous inorganic materials have been used in bulk or as coatings for thermal insulation, solar energy absorption, energy saving structures and heat transfer enhancement [1]. Research has yielded that among various materials tested in high-temperature applications ( $800$ - $1400^\circ\text{C}$ ), iron oxide ( $\text{Fe}_2\text{O}_3$ ), which was used in this experiment, has a high total emissivity and is widely available. Conversely, for medium temperatures ( $300$ - $700^\circ\text{C}$ ), aluminosilicate glasses have the highest normal total emissivity values. The

objective of this experiment is to demonstrate the various methods and techniques used to produce aluminosilicate glasses with varying concentrations of  $\text{Fe}_2\text{O}_3$ . These glasses will be applied as coatings to ceramic tiles to enhance their energy efficiency [2].

## II. EXPERIMENTAL PROCEDURES

### A. WEIGHING, MIXING AND PRESSING POWDERS

To prepare the primary glass, a mixture of raw material powders weighing  $100.28\text{ g}$  is required. The mixture comprises  $56.68\text{ g}$  of silica flour, containing 90% pure silica and 10% potassium feldspar (also known as Orthoclase or orthoclase feldspar, with the end formula  $\text{KAlSi}_3\text{O}_8$ ). Additionally,  $28.9\text{ g}$  of sodium carbonate  $\text{Na}_2\text{CO}_3$  (with a purity of  $>99.5\%$ ),  $11.7\text{ g}$  of potassium carbonate  $\text{K}_2\text{CO}_3$  (with a purity of  $>99.5\%$ ), and  $3\text{ g}$  of alumina  $\text{Al}_2\text{O}_3$  (with a purity of  $>99.9\%$ ) are mixed. All of the components are weighed systematically on a four-digit scale, and then mixed for four cycles of thirty minutes each time using a Turbula powder mixer. The aim is to homogenize the mixture of powder, as demonstrated in figure 1. The technique of the three-dimensional mixer is formulated on the basis of Schatz's theory of geometric inversion, which comprises multiple motions such as rotation, translation, and inversion.



**Fig. 1.** Weighing the different powders of the mixture and mixing in the Turbula mixer.

Once the powders have been mixed and homogenized,

they are pressed into pellets of around 1-2cm in height using a vertical hydraulic press, as depicted in figure 2. The powder mixture is divided into several quantities of approximately 20g to enable pressing and eliminate any air particles that may be present. Each pellet is held under a pressure of 1000 kg/cm<sup>2</sup> for 5 minutes.



**Fig. 2.** Vertical hydraulic press and tools used to compress the powder mixture.

### **B. THERMAL CALCINATION AND FUSION PROCEDURES DE CALCINATION ET DE FUSION DU MELANGE VITREUX**

The prepared pellets are placed in an alumina crucible and heated to 900°C for four hours with a heating rate of 10°C per minute, starting at 25°C, in a mini electric calcination furnace (Carbolite) as shown in Figure 3. This stage is called calcination and it allows for the removal of CO<sub>2</sub> from the chemical composition of the mixture by decarbonating the raw material powders [3].

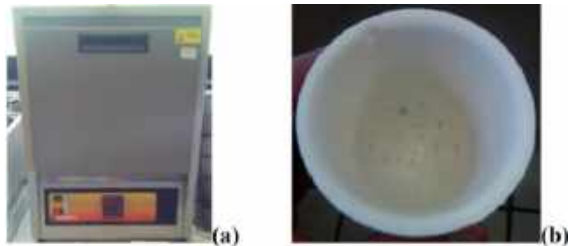


**Fig. 3.** (a): Mini electric furnace in operation, used for calcination  
(b): Alumina crucible containing pellets after calcination.

The melting stage involves putting the calcined pellets in an alumina crucible and then placing it in a propane-air furnace. The temperature gradually increases from around 400°C to 1450°C, while adjusting the "propane-oxygen" flow rate. The maximum temperature is maintained for 2 hours until the pellets completely liquefy. The molten mixture is swiftly poured onto a preheated metal plate at 350°C (± 2°C) to avoid thermal shock, and then cooled down to room temperature at its own rate to obtain the preliminary glass sample called HLEG0, which does not yet contain Fe<sub>2</sub>O<sub>3</sub>, as shown in Figure 4.

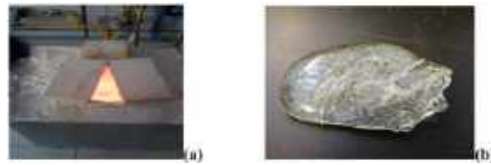


**Fig. 4.** (a): Propane-air furnace operating at 1450°C. (b): parent glass HLEG0 after pouring and cooling.

### **C. INTRODUCTION OF FERRIC OXIDE**

The preliminary HLEG0 has a few imperfections such as air bubbles and unfused powders. These defects in the initial glass do not cause any difficulties since the glasses need to be ground to powder once again. After which, they're mixed with determined percentages of Fe<sub>2</sub>O<sub>3</sub> (purity ~ 99.95%) indicated in figure 5 to begin the second melting of the mixture.



**Fig. 5.** (a): Images of the used ferric oxide (hematite) (b): A pressed pellet before melting.

The aluminosilicate glass powder (SiO<sub>2</sub>, Na<sub>2</sub>O, Al<sub>2</sub>O<sub>3</sub>, K<sub>2</sub>O) was created using an automated mortar mill and a 100 µm sieve, as shown in Figure 6. Ferric oxide Fe<sub>2</sub>O<sub>3</sub> will be added to the glass powder in weight percentages (wt%).

These mixtures were then mixed in the Turbula mixer for 30 minutes and pressed (Fig. 5). The pressed pellets were remelted in alumina crucibles in an electric furnace at 1450 °C for 2 h (Fig. 6), starting from 25 °C, for a total melting time of 4 h 20 min at a heating rate of 10 °C/min. Finally, they are poured onto preheated metal plates. The materials obtained were designated HLEG1, HLEG2, HLEG3, HLEG35 and HLEG5, corresponding to the addition of Fe<sub>2</sub>O<sub>3</sub> of 10%, 20%, 30%, 35% and 50% by weight, respectively, such as :

- HLEG1 = 90 % HLEG0 + 10 % Fe<sub>2</sub>O<sub>3</sub>
- HLEG2 = 80 % HLEG0 + 20 % Fe<sub>2</sub>O<sub>3</sub>
- HLEG3 = 70 % HLEG0 + 30 % Fe<sub>2</sub>O<sub>3</sub>
- HLEG35 = 65 % HLEG0 + 35 % Fe<sub>2</sub>O<sub>3</sub>
- HLEG5 = 50 % HLEG0 + 50 % Fe<sub>2</sub>O<sub>3</sub>.





**Fig. 6.** Secondary melting electric furnace and mortar grinder utilized.

The three glass samples (HLEG1, HLEG2, and HLEG3) underwent melting at a temperature of 1450°C. However, due to a high ferric oxide percentage of 50%, both the HLEG35 and HLEG5 glass samples experienced interaction with the alumina crucible, as depicted in Figure 7.



**Fig. 7.** HLEG2, HLEG3 and HLEG5 after fusion.

### III. CONCLUSION

Elaboration of the  $\text{Fe}_2\text{O}_3$  aluminosilicate glass was accomplished successfully by precisely following a series of steps and processes. The production process commences with mixing of raw materials and culminates in controlled melting through a specific heating cycle. There are numerous significant steps to observe in between these two procedures. Adherence to these steps in the correct sequence is crucial.

### REFERENCES

- [1] S. Takeuchi, "Spectral Emissivity Measurement Using FTIR Spectrophotometry," FTIR talk letter, 13, (2010).
- [2] J.M. Jones et al., "A compilation of data on the radiant emissivity of some materials at high temperatures." *Journal of the Energy Institute* 92:523–534 (2019).
- [3] A.D. Mcnaught et al. "*Compendium of chemical terminology*." (vol. 1669). Oxford: blackwell science (1997).

# NiP Thin Films Synthesis With Desired Properties Via Electrodeposition

NADA BOUMAZZA<sup>1,\*</sup>, WISSEM BOUGHOUICHE<sup>1</sup>, IMENE ABID<sup>1</sup>, BENATHMANE HALIMA<sup>1</sup>, YAZID MESSAOUDI<sup>1</sup> AND AMOR AZIZI<sup>1</sup>

1. Laboratoire de Chimie, Ingénierie Moléculaire et Nanostructures, département de chimie,  
Faculté de science, Université Ferhat Abbas Sétif 1, Sétif 19000, Algeria.

## ABSTRACT

*Nickel-phosphor films were synthesized by the electrodeposition method from a sulfate bath. The effect of electrodeposition parameters such as current density and species concentration on the composition, morphological, and electrochemical properties of the electrodeposited thin films were investigated via scanning electron microscopy (SEM), X-ray fluorescence (XRF), and electrochemical impedance spectroscopy (EIS). As a result, the SEM image reveals that the morphology changed as the concentration of precursor changed from a surface compact to a lamellar shape with a granular shape, which gave it a clove appearance. In contrast, these cloves become disappeared as the current density increases. These modifications in the morphology of these alloys can be inferred from the composition of phosphor in the electrode, where the amount of phosphor increases to 7.01% atoms as the concentration of phosphor in the bath increases. This increase in phosphor amount in the coatings leads to an increase in the real surface area with a high roughness factor (Rf) value and a high capacity of the double layer (Cdl).*

**KEY WORDS** alloys, electrodeposition, Ni-P, thin films.

## I. INTRODUCTION

NiP alloys have attracted great attention owing to their interesting properties, particularly their exceptional corrosion resistance, high hardness, and excellent wear resistance [1]. These characteristics make NiP alloys promising candidates for use in a wide array of applications across various fields. While several methods are available for synthesizing NiP, such as hydrothermal and chemical vapor deposition, these techniques often demand high temperatures and pressures. Electrodeposition emerges as a superior alternative for alloy fabrication, offering numerous advantages, such as lower synthesis temperature and cost-effectiveness compared to other deposition methods. Moreover, the electrochemical technique provides a high level of

control and versatility, enabling the production of dense, high-quality thin films by adjusting various parameters, including bath composition, current density, additive type, bath temperature, pH, and more [2]. In this work, NiP is synthesized via the electrodeposition method, with an emphasis on varying precursor concentration and current density. The resulting NiP alloys were characterized through scanning electron microscopy (SEM) and X-ray fluorescence (XRF) analysis. This analysis allowed for a quantitative assessment of the alloy's elemental content and the influence of the synthesis parameters on its composition.

## II. EXPERIMENTAL

The Ni-P alloys are fabricated by electrodeposition from an electrolyte consisting of analytical-grade reagents of NiSO<sub>4</sub> and NaH<sub>2</sub>PO<sub>2</sub> as sources of nickel and phosphor ions. CitNa<sub>3</sub> and Na<sub>2</sub>SO<sub>4</sub> were added as crystal modifiers and conductivity agents, respectively. The electrodeposition was carried out at two current densities: -100 mA/cm<sup>2</sup> and -150 mA/cm<sup>2</sup>. The control of the atomic ratio is performed a priori by using the corresponding molar ratios of metal salts in the synthesis and the as-prepared coatings were labeled NiP<sub>1/2</sub>, NiP<sub>1/1</sub>, and NiP<sub>2/1</sub>. The elemental composition and morphology of the alloys were determined by X-ray fluorescence spectroscopy (XRF) and scanning electron microscopy (SEM), respectively.

## III. RESULTS AND DISCUSSIONS

As shown in the SEM image (figure1), the morphology of NiP changed, as did the current density and concentration. When the concentration of P increased in the bath (NiP<sub>1/2</sub>), the morphology changed from a surface compact (NiP<sub>2/1</sub>) to a lamellar shape with a granular shape, which gave it a clove-like appearance. However, this appearance disappeared when the current density increased to -

150 mA/cm<sup>2</sup>. These modifications in the morphology are due to the amount of phosphorous in the electrode. As the concentration of phosphorous in the bath is high, its amount reaches 7.01% atom (table.1). But this amount decreases as the current increases. In addition, the amount of P deposited is low, which indicates that the co-deposition of NiP is co-deposition induit.

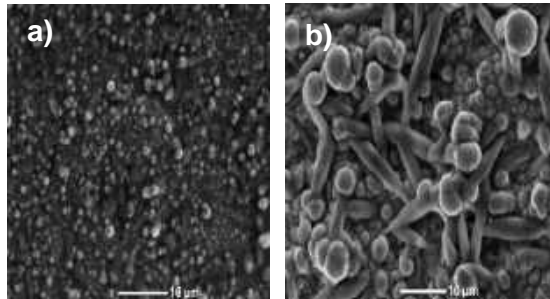


**Figure.1:** SEM images of NiP rich on P ratio 1/2 at two current densities: a) -100mA/cm<sup>2</sup> and b)-150mA/cm<sup>2</sup>.

**Table1:** XRF analysis of different NiP alloys at Different current densities.

Current densities	Ratio	Ni % atom	P % atom
-100mA/cm <sup>2</sup>	2/1	97.16	2.84
	1/1	95.21	4.79
	1/2	92.99	7.01
-150mA/cm <sup>2</sup>	2/1	96.45	3.55
	1/1	95.49	4.51
	1/2	93.35	7.12

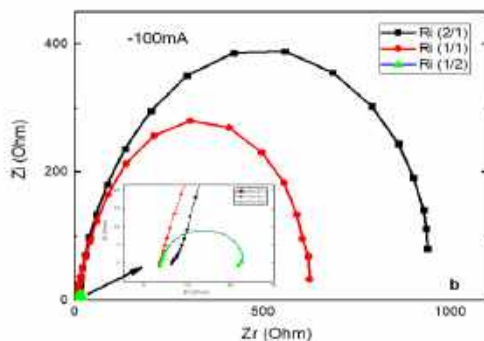


**Figure.2:** Nyquist plot for different NiP alloys at current densities -100mA/cm<sup>2</sup>.

#### IV. CONCLUSION

Electroplating is one of the most widely used techniques for developing alloys with desired properties via simple control of the parameters, particularly current densities and concentration.

The morphology and properties of NiP depend on the amount of phosphorus in the alloys, and the poor amount of P deposited indicates the induced co-depositon induit of NiP.

In the next stage of our research, we will mainly focus on exploring these alloys as electrocatalytics for hydrogen production.

#### REFERENCES

- [1] Vlaic, C. A., Kurniawan, M., Peipmann, R., Lalău, C. C., Stich, M., Schmidt, U., & Bund, A. Improved wear resistance of alternating amorphous and crystalline layers in electrodeposited NiP multilayers. *Surface and Coatings Technology*, 386, 125470. (2020).
- [2] Tebbakh, S., Mentar, L., Messaoudi, Y., Khelladi, M. R., Belhadj, H., & Azizi, A. Effect of cobalt content on electrodeposition and properties of Co-Ni alloy thin films. *Inorganic and Nano-Metal Chemistry*, 51(12), 1796-1802. (2021).

# Investigation of magnetic and structural properties of $\text{Co}_x\text{Fe}_{100-x}$ thin films thermally evaporated onto amorphous silicon and Si(111) substrates

Ahlem MELLOUL and Ahmed KHARMOUCHE

e-mail: [melloul.ahlem@physicist.net](mailto:melloul.ahlem@physicist.net)

*Laboratory of Surfaces and Interfaces Studies of Solid Materials (LESIMS)*

*Ferhat ABBAS Setif1 University, Algeria*

## Abstract:

In this work, the magnetic and structural properties of  $\text{Co}_x\text{Fe}_{100-x}$  thin films thermally evaporated onto **amorphous silicon and Si (111) substrates** have been studied. The atomic compositions evaluated from X-Ray Fluorescence (XRF) analysis, are found to range from 38 to 75 at.%. X-Ray diffraction spectra present (110) and (211) Bragg peaks for all the samples deposited onto Si (111). For samples deposited onto amorphous silicon substrate, the X-ray patterns present one Bragg peak situated at  $2\theta$  equal to  $45^\circ$ , corresponding to (110) Miller indices. The preferential orientation for all samples is  $\langle 110 \rangle$  with a bcc-phase. The lattice parameter  $a$  varies with the atomic composition. The magnetic properties have been analysed by means of a Vibrating Sample Magnetometer (VSM) apparatus. The saturation magnetization ( $M_s$ ), the coercive field ( $H_c$ ) and the squareness ( $S$ ) evolutions versus cobalt content are studied, for the two series and they have been found to present the same behaviour. The saturation magnetization ( $M_s$ ) decreases with increasing  $x$ . The  $\text{Co}_x\text{Fe}_{100-x}$  thin films are magnetically soft and there is no clear substrate effect noticeable.

## References

- [2] Yahui Zhang and Douglas G. Ivey. Materials Chemistry and Physics, **204**, 171-178, (15 January 2018)
- [3] Premkumar Murugaiyan , Anand Abhinav , Rahul Verma , Ashis K. Panda , Amitava Mitra , Sandip Baysakh , Rajat K. Roy. Journal of Magnetism and Magnetic Materials, **448**, 66 -74, (2018)
- [4] Jing Zhou, Shaohai Chen, Weinan Lin, Qing Qin, Liang Liu, Shikun He, Jingsheng Chen. Journal of Magnetism and Magnetic Materials, **441**, 264-270, (2017)

# Évaluation de l'effet pouzzolanique à l'aide d'une méthode basé sur la conductivité électrique.

RIZI HADJER<sup>1\*</sup>, Pr BENALI FAROUK<sup>2</sup>

1. Laboratoire de matériaux non métallique  
Sétif, Algérie, hadjar.rizi@yahoo.com
2. Laboratoire de matériaux non métallique  
Sétif, Algérie, benalifarouk@univ-setif.dz

## RESUMÉ

Les matériaux à valeur cimentaires sont caractérisés par leur habilité à interagir, en présence d'humidité, avec des hydroxydes alcalins et alcalino-terreux. Afin d'étudier ces réactions, plusieurs méthodes sont développées, une en particulier est traitée dans cet article. Le but de cette étude est l'évaluation du caractère pouzzolanique de trois matières (verre mixte, verre optique et une roche locale) par la mesure de la conductivité électrique de la suspension ciment-pouzzolane.

## MOTS CLES:

Réaction pouzzolanique, activation chimique, matériau cimentaire

## I. INTRODUCTION

Les matériaux pouzzolaniques font l'objet de plusieurs recherches ces dernières années. Leur introduction dans le secteur du bâtiment est amplement sollicitée par les industries du ciment. En effet, l'introduction de tels matériaux dans la composition du ciment permet à la fois la préservation des ressources naturelles mais aussi à la réduction de l'impact environnemental due aux émissions carboniques. Un matériau pouzzolanique est caractérisé par un taux élevé en silice, une grande surface spécifique et doit être amorphe[1]. Parmi les adjuvants utilisés on distingue ; les cendres volantes, fumée de silice, pouzzolane naturelle, déchets de verre...etc. L'utilisation du verre dans la composition du ciment a été approuvée et démontrée par plusieurs chercheurs [3][5][6]. L'objectif de cette étude est la caractérisation et l'évaluation de l'aspect pouzzolanique en utilisant une méthode basée sur la conductivité électrique développée par Sinthaworn [4].

## PARTIE EXPERIMENTALE:

### A. MATERIELS ET METHODES:

Trois différents adjuvants minéraux ont été utilisés dans cette étude : verre de récupération (verre mixte), poudre éjectée lors du taillage de lunetterie (verre optique) et une roche locale (Tafza). Le ciment (type I) est issu de la cimenterie d'Ain ElKebira de Sétif. La composition chimique des matériaux testés est représentée dans le tableau 1. La roche utilisée présente un taux très élevée en silice avec un pourcentage de 93,7% par comparaison avec les deux types de verre ; mixte et optique, qui contiennent 70,4% et 57,66% de silice, respectivement.

Composition (p%)	SiO <sub>2</sub>	Fe <sub>2</sub> O <sub>3</sub>	Al <sub>2</sub> O <sub>3</sub>	CaO	MgO	Na <sub>2</sub> O	K <sub>2</sub> O	SO <sub>3</sub>
Verre optique	57,6	0,292	1,26	21,3	2,49	6,46	4,55	1,01
Verre mixte	70,4	0,450	1,44	11,9	1,10	13,8	0,559	0,0843
Tafza	93,7	0,939	4,31	0,092	0,113	-	0,285	0,0363

Tableau 1: composition chimique des matériaux étudiés

	d(0,1)	d(0,5)	d(0,9)	Diamètre moyen
Verre optique	5.43	16.09	176.15	59.65
Verre mixte	7.07	24.21	123.07	47.97
Tafza	3.41	8.70	24.25	11.90

Tableau 2: distribution granulaires des poudres

La matière première a été réduite à une échelle de quelques micromètres, ce qui permet l'activation mécanique afin de favoriser le déclenchement de la réaction pouzzolanique, les résultats de la distribution granulair sont représentés dans le tableau 2. 90% de particules de la roche Tafza sont inférieures à 24,25 µm, qui est lié à son aspect friable, la granulométrie est approximativement la même pour les poudres de verre (mixte et optique), avec un diamètre moyen inférieur à 60 microns. La cristallinité des matériaux bruts a été évaluée par la diffraction des rayons X, les diffractogrammes obtenus sont illustrés dans la figure 1. Pour le verre optique, l'allure de la courbe est caractéristique d'une structure 100% amorphe, à la différence de la roche Tafza dont la présence du quartz est caractérisée par les trois pics les plus intenses, qui est une forme cristalline de la silice.

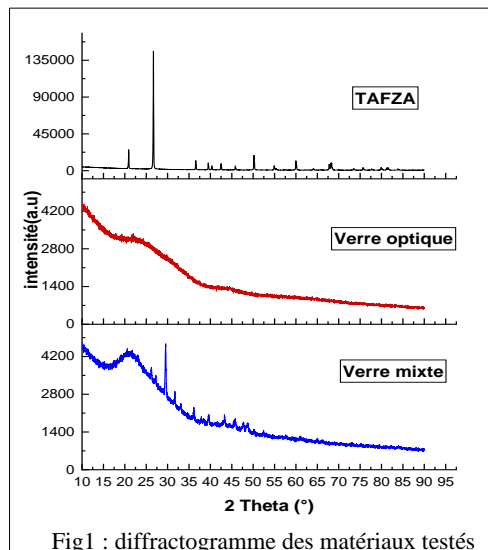
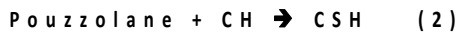
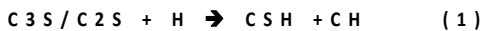


Fig1 : diffractogramme des matériaux testés

La méthode de caractérisation adoptée est comme suit ; un mélange d'eau et de ciment portland est préparée selon sinth, et laisser pendant 30 min pour permettre la précipitation. La solution limpide formée est récupérée ; la conductivité électrique de cette dernière doit être comprise entre 10 et 11 mS/cm à une température de 25°C. 1g d'adjuvant (pouzzolane testé) est introduit dans 180ml de solution sous agitation continue. La variation de conductivité électrique est enregistrée.

Lors de l'hydratation du ciment, il en résulte deux composantes ; calcium silicate hydraté (gel C-S-H) et l'hydroxyde de calcium (la portlandite C-H) suivant l'équation 1. On dit qu'il est une réaction pouzzolanique lorsque la silice réagit avec la portlandite CH pour former plus de composés CSH, tel énoncé dans la deuxième équation :



### RÉSULTATS ET DISCUSSIONS :

La figure 2 représente la variation de la conductivité en fonction du temps. On constate que les matériaux testés enregistrent une diminution continue de la conductivité électrique due la consommation des ions Ca dans la réaction pouzzolanique afin de former des composés stable [2].

D'après Sinthaworn and al. , plus l'écart entre la valeur de la conductivité initiale et la conductivité stable (finale) n'est important, plus le matériau n'est réactif. Dans cette étude, on note que le verre optique présente une réactivité considérable par rapport aux autres matériaux testés. De même, une courte durée pour la stabilisation de la conductivité électrique indique une forte réactivité ; affirme l'auteur. Il est à noter que la phase amorphe favorise la dissolution de la silice dans le milieu alcalin, par conséquent, la réaction entre la silice contenu dans la poudre de la roche (Tafza) et les produit d'hydratation du ciment n'as pas eu lieu, vu l'état cristallin du matériau, bien

que le temps entrepris pour la stabilisation était bref. Par comparaison, le verre optique enregistre un temps plus au moins court comparé au verre mixte, qui peut être expliqué par le degré de réactivité.

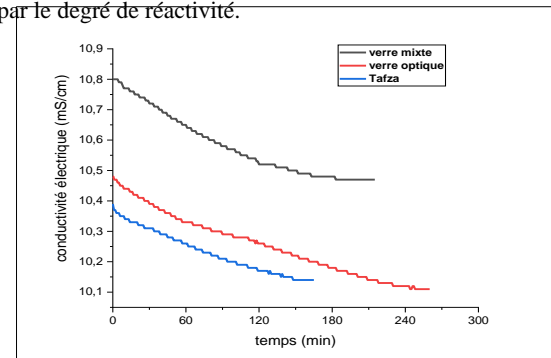


Fig2: la variation de la conductivité électrique en fonction du temps

### CONCLUSION

D'après cette brève étude portée sur la détermination de la pouzzolanicité :

- La réaction pouzzolanique est fortement lié à la cristallographie des matériaux étudiés,
- La mesure de la conductivité électrique permet une étude précise sur le taux de consommation des cations  $Ca^{2+}$ , et interprète la contribution du la silice dans le milieu alcalin,
- La poudre du verre optique présente réactivité notable comparé au verre de récupération.

### REFERENCESCONCLUSION

- [1] shao, y., lefort, t., moras, s., & rodriguez, d. (2000). studies on concrete containing ground waste glass. cement and concrete research, 30(1), 91-100.
- [2] tashima, m. m., soriano, l., monzó, j., borrachero, m. v., akasaki, j. l., & payá, j. (2014). new method to assess the pozzolanic reactivity of mineral admixtures by means of ph and electrical conductivity measurements in lime: pozzolan suspensions. materiales de construcción, 12.
- [3] jiang, y., ling, t. c., mo, k. h., & shi, c. (2019). a critical review of waste glass powder—multiple roles of utilization in cement-based materials and construction products. *journal of environmental management*, 242, 440-449.
- [4] sinthaworn, s., & nimityongskul, p. (2009). quick monitoring of pozzolanic reactivity of waste ashes. *waste management*, 29(5), 1526-1531.
- [5] sobolev, k., türker, p., soboleva, s., & iscioglu, g. (2007). utilization of waste glass in eco-cement: strength properties and microstructural observations. *waste management*, 27(7), 971-976.
- [6] monawar, t. (2003). *u.s. patent application no. 10/272,132*.



# Title: Synthesis of $\text{CaCO}_3$ particles using oleic acid: effect on particle size and morphology

**KHALIDA CHABANE<sup>1,\*</sup>, SALIM OUHENIA<sup>1</sup>, BOGDAN PARAKHONSKIY<sup>2</sup>, ANDRE SKIRTACH<sup>2</sup>**

1. Affiliation (Author): Laboratoire de Physico-Chimie des Matériaux et Catalyse (LPCMC), Abderrahmane MIRA, University of Bejaia, Algeria
  2. Affiliation (Author): NanoBioTechnology Laboratory. Faculty of Bioscience Engineering, Ghent University, 9000 Ghent, Belgium
- \* khalida.chabane@se.univ-bejaia.dz

## ABSTRACT

This abstract presents a detailed exploration of the synthesis of Calcium carbonate ( $\text{CaCO}_3$ ), which is a versatile compound with numerous applications in various industries, including pharmaceuticals [1, 2], construction [3], and environmental remediation [4]. This study explores the synthesis of  $\text{CaCO}_3$  particles utilizing oleic acid as a capping agent under different concentration conditions. The objective of this research is to understand the influence of both oleic acid and reactants concentration on the size, morphology, and crystalline properties of the synthesized  $\text{CaCO}_3$  particles.

The primary aim of the research is to establish a clear relationship between the concentration of oleic acid and the resultant morphology of the synthesized  $\text{CaCO}_3$  particles. Scanning electron microscopy (SEM) and X-ray diffraction (XRD) (fig 1) analyses reveal a direct correlation, indicating that varying oleic acid concentrations lead to distinct variations in particle size. Lower concentrations of oleic acid foster the development of smaller, well-defined particles with uniform crystal structures, while higher concentrations promote the formation of larger, irregularly shaped particles with altered crystal habits.

Furthermore, the study delves into the underlying mechanisms governing the complex interplay between oleic acid and the  $\text{CaCO}_3$  surface, shedding light on the adsorption and surface modification processes dictating the ultimate particle morphology.

Spectroscopic analysis confirms the formation of a stable calcium oleate complex on the particle surface, highlighting the intricate dynamics between the organic and inorganic constituents during the synthesis process.

This comprehensive investigation not only advances our understanding of the nuanced dynamics involved in the synthesis of  $\text{CaCO}_3$  using oleic acid but also underscores its potential applications in tailoring materials for various industrial applications. The findings provide crucial insights for the development of  $\text{CaCO}_3$ -based materials with tailored properties, thereby contributing significantly to sectors such as pharmaceuticals, materials engineering, and environmental sciences.

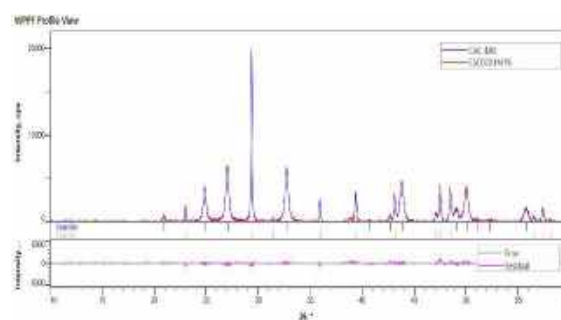


Fig 1 : XRD pattern of  $\text{CaCO}_3$  sample using 1% oleic acid

[1] G. Choukrani, B. Maharjan, C.H. Park, C.S. Kim, A.R.K. Sasikala, Biocompatible superparamagnetic sub-micron vaterite particles for thermo-chemotherapy: From controlled design to in vitro anticancer synergism, Materials Science and Engineering: C 106 (2020) 110226.

- [2] J. Dou, F. Zhao, W. Fan, Z. Chen, X. Guo, Preparation of non-spherical vaterite  $\text{CaCO}_3$  particles by flash nano precipitation technique for targeted and extended drug delivery, *Journal of Drug Delivery Science and Technology* 57 (2020) 101768.
- [3] B.H. Nam, J. An, H. Youn, Accelerated calcite precipitation (ACP) method for recycled concrete aggregate (RCA), *Construction and Building Materials* 125 (2016) 749-756.
- [4] X. Guo, L. Liu, W. Wang, J. Zhang, Y. Wang, S.-H. Yu, Controlled crystallization of hierarchical and porous calcium carbonate crystals using polypeptide type block copolymer as crystal growth modifier in a mixed solution, *CrystEngComm* 13 (2011) 2054-2061.

# Determination of the Mechanical Properties of Thermal Sprayed NiCrAlY Coatings using Experimental and Numerical Simulations

BARBERIS MARWA<sup>1\*</sup>, FIZI YAZID<sup>1</sup>, AND BOUSSOUAR LAYACHI<sup>1</sup>

1. Department of Precision Mechanics, Ferhat Abbas Sétif-1 University, Sétif, Algeria,  
yazid.fizi@univ-setif.dz.

## ABSTRACT

*The objective of our study is to characterize the coatings obtained through the plasma thermal spray process. Metallographic characterization allows for a more in-depth analysis of the deposit's microstructure, particularly focusing on microhardness. In this study, an examination of the coating behavior is conducted using the ABAQUS® computational code. To assess the properties of the deposit produced by the plasma process, a hardness study is proposed, which enables the acquisition of a microhardness profile across the entire sample surface.*

## KEY WORDS

Thermal spray; Characterization; Coating; Element finis; Indentation test

## I. INTRODUCTION

Thermal spraying, as a coating process, entails the deposition of particles composed of the coating material in semi-molten, molten, or solid states. These particles are accelerated towards the substrate by a carrier gas. The accumulation of millions of flattened and solidified particles on the substrate creates the coating. Common thermal spraying techniques include Air Plasma Spraying (APS), Vacuum Plasma Spraying (VPS), High Velocity Oxygen Fuel (HVOF), cold spraying, and wire arc spraying (WAS). Thermal spraying is a widely used technique for applying coatings to large surfaces, primarily chosen for their desired tribological and chemical resistance properties. These coatings find applications in various industries, including the process industry where they are used in center press rolls, dewatering elements for paper machines, mechanical seals, and process valves. Ceramic coatings, deposited from ceramic feedstock, are often preferred for their exceptional wear

resistance and chemical inertness in such demanding environments [1,2]. However, their brittleness poses a significant drawback, limiting their suitability in applications that require impact resistance and ductility. As a result, brittle fracture with minimal plastic deformation is the typical failure mechanism observed in ceramic coatings. Extensive efforts have been made to enhance the toughness of ceramic coatings through material processing techniques such as incorporating additional ceramic or metallic phases or utilizing novel spray processing methods [3–6]. Despite advancements in fracture toughness, the understanding of damage development during fatigue in these coatings remains incomplete and influenced by various factors.

The objective of this study is to examine the mechanical properties of plasma sprayed NiCrAlY. microindentation tests provided experimental method for determining the modulus of alloy 625 coating. The mechanical properties and load-displacement curve of the coating are tested by nanoindentation. Through finite element method (FEM) and Hollomon hardening models are utilized to characterize the stress of the coating.

## II. PLASMA SPRAYED COATING

### A. MICROSTRUCTURE

In this work, a MP200 of Swiss company (Fig 1). was used to spray NiCrAlY coating on low carbon steel, the powder 5546NS with a diameter of  $45 \pm 5.5 \mu\text{m}$  being used as feedstock material. Metco 5546NS is a blend of a wear-resistant chromium carbide and a hot corrosion resistant NiCrAlY (nickel-chromium-aluminum-yttrium) alloy. The coating structure produced by Metco 5546NS consists of chromium carbide particles that are finely dispersed in the

NiCrAlY matrix. The chromium carbide constituent provides excellent high temperature erosion resistance. The coatings were sprayed on the top of steel substrates, after cleaning and grit blasting using corundum abrasive particles (400, 600, 800, 1000, 1200, 1400, 1800, and 2000). The mean roughness,  $R_a$ , of the substrate surface after blasting was 5  $\mu\text{m}$ .



Fig. 1. MP200 AMT-AG Plasma torch system [7]

The microstructure of the NiCrAlY coating can be observed through microscopic examination (Fig 2). It shows a lamellar structure with the presence of pores. At the interface between substrate and NiCrAlY coating, there are no visible macroscopic defects such as delamination or decohesion.

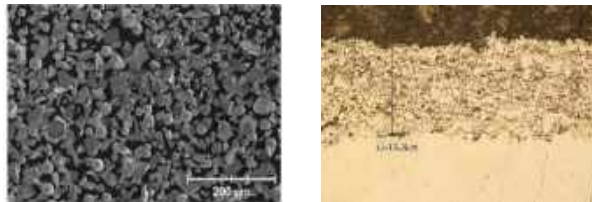


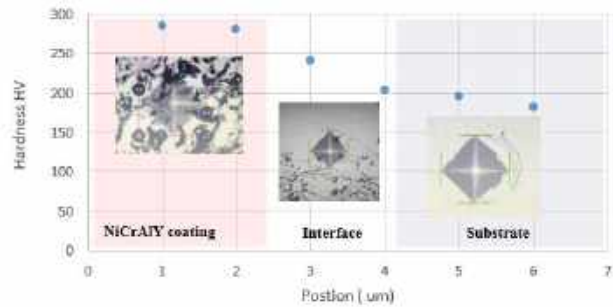
Fig. 2. a) Morphology of Metco 5546NS [8], b) SEM micrographs of arc sprayed NiCrAlY coating cross section

Microhardness tests using a Vickers indenter were conducted on the sample following conventional methods. The hardness profile was determined by applying a load of 1N on a cross section. The results obtained are shown in fig 3. It is observed that the microhardness values differ between the coating and the substrate. The microhardness of the NiCrAlY coating reaches 285 HV, which is significantly higher compared to the substrate hardness.

### B. INDENTATION TEST

Experimental load-displacement curves of the composite coating were obtained by conducting instrumented indentation measurements on the cross-

sections of the three examined samples. A micro-indenter Z2.5 with a Vickers tip was employed for these measurements using Zwick/Roell equipment, which had resolutions of  $\pm 0.01\%$  in force and 0.02  $\mu\text{m}$



in displacement. Fig 4 presents the experimental curve obtained by instrumented indentation.

Fig. 3. Evolution of micro-hardness profile  $HV_{0.1}$

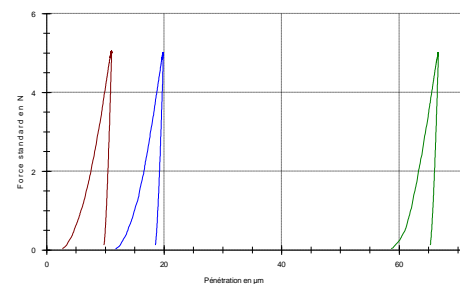


Fig. 4. Experimental data of indentation curve with the indentation load of 5N

### III. FINITE ELEMENT MODEL

The finite element software ABAQUS® was utilized to conduct modeling of instrumented indentation. The interaction between the indenter and the coating was simulated, with the Vickers indenter using a semi-vertical angle of  $68^\circ$ . To accurately represent the indenter, a spherical rounding with a radius of 5  $\mu\text{m}$  was incorporated at the tip. Fig. 5 shows an example of stress variation at the coating for the maximum penetration depth.

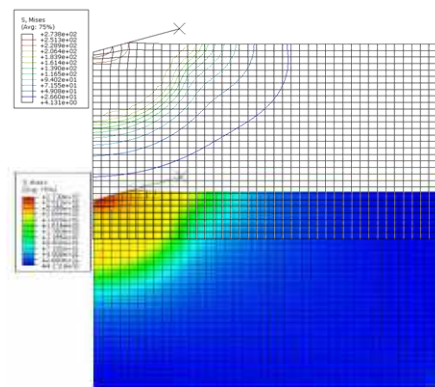


Fig. 5. Contours of Von-mises stress

#### IV. CONCLUSION

The characteristics of the mechanical properties of thermal sprayed NiCrAlY coatings were outlined in this study. The micrographs obtained by optical microscope confirm the lamellar structure of the thermally projected deposits. Thus this step focused on measuring micro-hardness, two types of stresses were used for this test: micro-hardness from which the value of the NiCrAlY coating hardness was obtained. As well as adhesion, in this case very localized measurements of coatings were carried out through the interfacial indentation test. Concerning the underlayer/substrate interface, the tests show that the cracks generated by the indenter did not propagate for a load of 10 N. Finite element analysis can measure and predict the stress variation at the coating.

#### REFERENCES

- [1] P. Vuoristo, Thermal spray coating processes, in: S. Hashmi (Ed.), Compr. Mater. Process. Film. Coatings Technol. Recent Dev. Vol. 4 Elsevier, 2014
- [2] L. Pawlowski, The Science and Engineering of Thermal Spray Coatings, Second Ed, John Wiley & Sons, West Sussex, England, 2008
- [3] D. Chen, E.H. Jordan, M. Gell, X. Ma, Dense TiO<sub>2</sub> coating using the solution precursor plasma spray process, J. Am. Ceram. Soc. 91. 2008
- [4] J.W. Murray, A. Leva, S. Joshi, T. Hussain, Microstructure and wear behaviour of powder and suspension hybrid Al<sub>2</sub>O<sub>3</sub>–YSZ coatings, Ceram. Int. 2018
- [5] F.L. Toma, L.-M. Berger, T. Naumann, S. Langner, Microstructures of nanostructured ceramic coatings obtained by suspension thermal spraying, Surf. Coat. Technol. 2008
- [6] G. Bolelli, V. Cannillo, R. Gadow, A. Killinger, L. Lusvarghi, J. Rauch, Properties of high velocity suspension flame sprayed (HVSFS) TiO<sub>2</sub> coatings, Surf. Coat. Technol. 2009
- [7] Y. Fizi, Analyse par simulation numérique du comportement des structures élastiques et élasto- plastiques sous différentes sollicitations mécaniques. Thèse de Doctorat, IOMP. Université Sétif, 2016
- [8] Oerlikon Metco, DSM-0376.0 – Cr<sub>3</sub>C<sub>2</sub> – NiCrAlY Powder Blend Material Product Data Sheet Chromium Carbide – NiCrAlY Powder Blend. 2022

# Effect of the addition of aluminum hydroxide $\text{Al}(\text{OH})_3$ on the sintering of djebel Debagh kaolin

M.L. BELLA<sup>(1, 2, 3)</sup>, M. HAMIDOUCHE<sup>(1, 2)</sup>, L. GREMILLARD<sup>(3)</sup>

1 EMERGING MATERIALS RESEARCH UNIT, UNIVERSITY FERHAT ABBAS SETIF 1, 19000, SETIF, ALGERIA

2 OPTICAL AND PRECISION MECHANICS INSTITUTE, UNIVERSITY FERHAT ABBAS SETIF 1, 19000, SETIF, ALGERIA.

3 MATEIS UMR CNRS 5510, INSA-LYON, BAT BLAISE PASCAL, 7 AV. JEAN CAPELLE, VILLEURBANNE, 69621, LYON, FRANCE.

## ABSTRACT

*The objective of this work is to reduce amorphous phase by adding aluminium hydroxide to obtain a secondary mullite. A mullite and mullite-alumina composite were prepared by using Algerian kaolin and amorphous aluminium hydroxide as starting materials. Three mixtures were used by varying the amorphous aluminium hydroxide content 61.5%, 50 wt % and 45.5%. an abundant kaolin has been chosen with a high alumina content and an amorphous alumina trihydrate to lower the temperature of the reaction with the excess of silica in the kaolin. The advantage of adding an amount of amorphous aluminium hydroxide is that it reacts at high temperature with the amorphous phase of silica issue from kaolin. The objective is to increase the amount of the mullite phase formed. When alumina is added in excess, a part will be dispersed in the mullite matrix to form a mullite-alumina composite.*

*The results revealed that mullite is the major phase and alumina the minor phase in the samples sintered at 1600 °C in composition M1. At this firing temperature, no silica phases ( $\text{SiO}_2$ ) are detected. The microstructure shows a higher aspect ratio of mullite crystals. The addition of alumina reduces the size of mullite grains and their aspect ratio. The density of the resulting mullite and mullite-alumina composites increase with sintering temperature and alumina content.*

**KEY WORDS :** Kaolin, mullite, aluminum hydroxide, secondary mullite.

## I. INTRODUCTION

Kaolins are an extraordinary clay with an excellent properties, due to its traditionally used in the manufacture of triaxial porcelain since the time of the Ming dynasty [1,2] (XIV century), kaolins are rocks that are mostly composed by different minerals, along

with impurities like quartz, mica, anatase, rutile, and ilmenite. These minerals are part of the kandite group, which also includes kaolinite, dickite, nacrite, and halloysite. In particular, kaolinite ( $\text{Al}_2\text{Si}_2\text{O}_5(\text{OH})_4$ ) is a phyllosilicate 1:1 or a T-O that is created when an individual layer of octahedral alumina is linked to a sheet of tetrahedral silica. Three hydroxyl groups in kaolinite hold consecutive layers together, with the fourth hydroxyl group remaining inside the kaolinite layers (**Fig. 1**) [3]

When kaolin is sintered at a temperature above 1000 °C, it transforms into mullite ( $3\text{Al}_2\text{O}_3 \cdot 2\text{SiO}_2$ ) and cristobalite ( $\text{SiO}_2$ ) [4]. Then, cristobalite transforms into amorphous phase at temperatures above 1400 °C [5]. Mullite is only the stable crystalline compound in the  $\text{Al}_2\text{O}_3/\text{SiO}_2$  phase diagram under normal atmospheric pressure from room temperature to its melting temperature at 1810 °C [6]. It has interesting properties such as good resistance to thermal shock, high refractory property, low thermal expansion, good creep resistance and good mechanical resistance at high temperatures [[7], [8], [9]].

However, mullite formed from natural clays most often contains a high amount of glass phase. A combination between kaolin clay and alumina may be the right solution in this case. Indeed excess alumina can react with the amorphous phase to form additional mullite. The addition of adequate amount of alumina ( $\text{Al}_2\text{O}_3$ ) can therefore suppress the amorphous phase and thus increase the amount of mullite in the final material. The decrease of the amount of glassy phase has a positive effect on the mechanical properties of mullite, especially at high temperature.

In this work, Algerian kaolin is used as source



materials to process mullite, referenced DD1. He is extracted from Djebbel Debbagh, located in the northeast of Algeria. He is considered as a kaolinite clay rich in alumina (41 wt %). This makes it very suitable for the manufacture of structural ceramics based on aluminosilicate compounds.

The formation of mullite prepared by reactive sintering between kaolin and an aluminum hydroxide are studied. In particular, the kinetics of formation of mullite are assessed, as well as, the microstructure development and the Vickers hardness, with respect to the different compositions and sintering conditions.

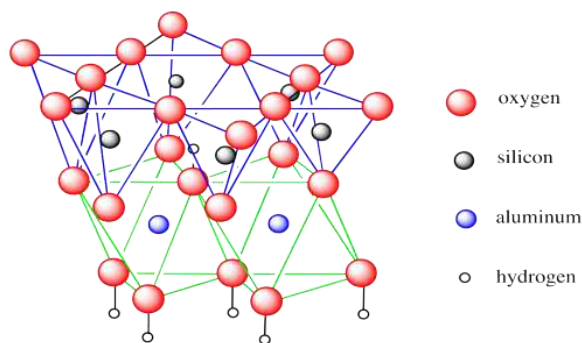


**Fig. 1.** Kaolinite structure where Si, Al and OH groups are indicated.

## II. EXPERIMENTAL PROCEDURES

### A. EXPERIMENTAL TECHNIQUES

The particle size distribution of the starting powders were measured by a laser granulometer (Malvern Mastersizer 2000). The chemical compositions of the raw materials (kaolin and aluminum hydroxide) were assessed by X-ray fluorescence spectroscopy (Rigaku ZSX Primus IV, Japan). X-ray diffraction (BRUKER D8 Advance with Cu K $\alpha$  radiation) was used to detect and identify the different phases:  $2\theta$  between  $5^\circ$  and  $80^\circ$ ,  $0.05^\circ$  step size, exposure 0.08 s per step. Differential thermal and thermogravimetric analyzes (DTA and TGA) were carried out in air between ambient and  $1400^\circ\text{C}$  with a heating rate of  $5^\circ\text{C}/\text{min}$  using a TA instrument SDT Q 600 V20.9 Build 20 apparatus. the microstructures were examined by scanning electron microscopy (SEM, SUPRA 55VP, Zeiss, Germany).

### B. MATERIALS

aluminum hydroxide  $\text{Al}(\text{OH})_3$ , commercialized by

sigma-Aldrich company, was used as a starting powder. **Table 1** gives its chemical composition. It has a density of  $2.23\text{ g/cm}^3$  and it has a narrow, monomodal particle size distribution by volume centered on an average grain size of  $6\text{ }\mu\text{m}$  (**Fig. 2**).

$\text{Al}_2\text{O}_3$	$\text{SiO}_2$	$\text{Na}_2\text{O}$	$\text{MgO}$	$\text{P}_2\text{O}_5$
$\text{SO}_3$	Cl	$\text{K}_2\text{O}$	$\text{CaO}$	$\text{Fe}_2\text{O}_3$
$\text{Al}(\text{OH})_3$	72,90	1,15	1,20	1,32
0,01	0,50	0,03	0,04	0,45
0,04				

**Table 1.** Chemical composition of starting alumina tri-hydroxide (wt %).

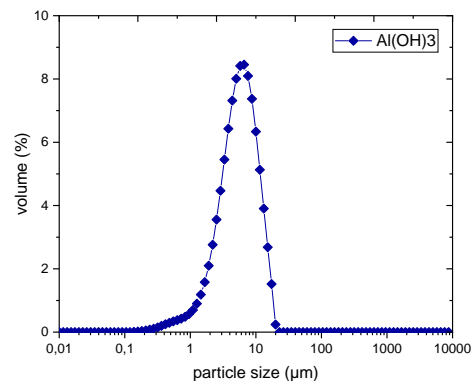


**Fig. 2.** Particle size distribution by volume of aluminum hydroxide powder used.

The kaolin used in this study are extracted from the mountains of Djebel Debbagh (northeast of Algeria). he is referenced DD1 with whitish color, the Kaolin contain in mass, approximately 42% of alumina and 48% of silica. **Table 2** gives the average chemical composition of this Kaolin.

	Al2O3	SiO2	Na2O	MgO	P2O5
	SO3	Cl	K2O	CaO	MnO
	Fe2O3	NiO	ZnO	As2O3	SrO
DD1	41,90	48,80	0,05	0,01	0,01
	0,13	/	0,01	0,21	/
	0,04	0,02	0,01	0,05	/

**Table 2.** Chemical composition of kaolin DD1 (wt %).

For preparation of the mullite samples by reactive sintering, kaolin was ground to a particle size less than 63  $\mu\text{m}$ . Then three mixtures with alumina trihydrate were prepared, denoted M1, M2 and M3 according to the compositions mentioned in **Table 3**.

Composition	M1	M2	M3
Kaolin (%)	38.46	50	54.5
Al(OH) <sub>3</sub> (%)	61.54	50	45.5

**Table 3.** Compositions for both studied subsystems (Kaolin + aluminum hydroxide) in (% wt).

### C. PREPARATION OF MIXTURE

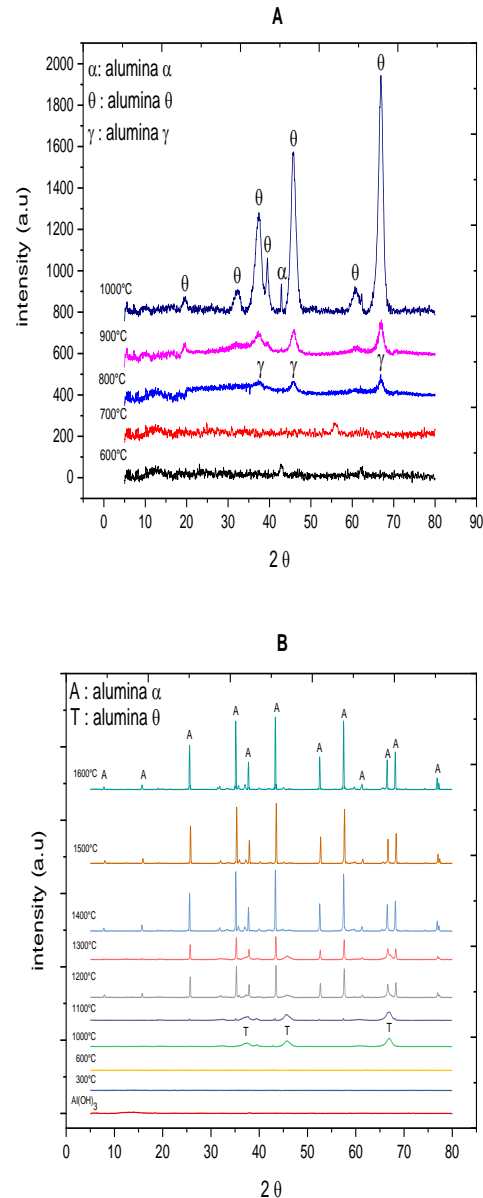
The mixtures were dispersed in ionized water according to the following ratio: 50% of powder mixture/50% of water (in mass). The suspension was ground for 48 h using an attrition grinding mill with alumina balls ( $\varnothing \approx 1.5\text{--}2.5\text{ mm}$ ). The quantity of balls used was 3 times the mass of the ground powder. The particle size was controlled during grinding until obtaining an average size of 2.5  $\mu\text{m}$ . Then the suspensions were dried at 110 °C to guarantee their complete drying. Then, the powders were de-agglomerated in a mortar and then sieved to obtain agglomerates of less than 63  $\mu\text{m}$ .

The interest of this act is to bring the two particle size distributions (kaolin-aluminum hydroxide) closer to each other to have a very narrow and rapid reactivity to sintering between the particles.

### III. Results and discussions

Fig. 3a and b shows the X-ray diffraction diagrams of aluminum hydroxide fired at different temperatures from ambient to 1600 °C. Aluminum tri-hydroxide is completely amorphous between room temperature and 800 °C. This type of aluminum hydroxide has been produced by grinding during for long periods [10]. Characteristic peaks of  $\gamma$ -alumina transition phase are observed between 800 °C and 900 °C. Between 1000 °C and 1100 °C,  $\gamma$ -alumina transforms into another transition alumina ( $\theta$  phase) and  $\alpha$ -Al<sub>2</sub>O<sub>3</sub> phase starts to form [11]. Above 1200 °C, only the stable  $\alpha$ -Al<sub>2</sub>O<sub>3</sub> phase is observed. This sequence of transformations is coherent with the work of Sato et al. [12], who have

shown that amorphous aluminum hydroxide transforms with temperatures increasing from ambient to above 1200 °C, as follows: Amorphous Al(OH)<sub>3</sub>  $\rightarrow$  amorphous AlOOH  $\rightarrow$   $\gamma$ -Al<sub>2</sub>O<sub>3</sub>  $\rightarrow$   $\theta$ -Al<sub>2</sub>O<sub>3</sub>  $\rightarrow$   $\alpha$ -Al<sub>2</sub>O<sub>3</sub>.

**Fig. 3.** X-ray diffraction pattern of aluminum hydroxide: (A): fired between 600 °C and 1000 °C; (B): fired at different temperatures.

X-ray diffraction analyses (**Fig. 4**) show that the different phases present in the kaolin at room temperature are essentially kaolinite (Al<sub>2</sub>Si<sub>2</sub>O<sub>5</sub>(OH)<sub>4</sub>) and halloysite (Al<sub>2</sub>Si<sub>2</sub>O<sub>5</sub>(OH)<sub>4</sub>·2H<sub>2</sub>O). The two major phases, namely kaolinite and

halloysite, transform between 600 °C and 950 °C into amorphous phases, then above 1200 °C into mullite and cristobalite. According to literature [13,14], cristobalite transforms into an amorphous phase at very high temperature (**Fig. 4** shows it to happen above 1500 °C), and mullite remains as the only crystalline phase.

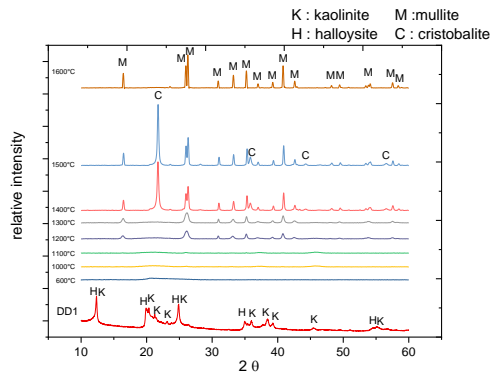


**Fig. 4.** XRD pattern of kaolin DD1 treated at different temperatures.

#### A. Phase evolutions of the mixtures with temperature

**Table 4** groups the results of the apparent density measured for the different compositions sintered at different temperatures. The values of composition M1 are higher than those of compositions M2 and M3, the first composition contains more alumina. The densification of the samples takes place at temperatures below 1600 °C due to the small particle size of the starting powders. The large specific surface area reduces the diffusion distances, which increases the driving force of sintering as also noted by other authors [15].

The low density observed for the mixtures sintered at  $T = 1400$  °C in composition M3 is due to the presence of the compounds before the reaction (silica, alumina). This proves the non-completion of the silica-alumina reaction but also prevents diffusion from accelerating the sintering. These results confirm those obtained by Chantale Njiomou Djangang et al. [16].

The density increases with increasing sintering temperature for the different compositions studied, due to pore closure. In all cases, the density is lower than the absolute density of mullite (3.16 g/cm<sup>3</sup>),

suggesting residual porosity, especially since the presence of alumina dispersoids which should increase the density.

Sintering during

5 hours Composition M1

Apparent density (g/cm<sup>3</sup>) Composition M2

Apparent density (g/cm<sup>3</sup>) Composition M3

Apparent density (g/cm<sup>3</sup>)

Sintering temperature      1400 °C 1500 °C 1600 °C  
 1400 °C 1500 °C 1600 °C 1400 °C 1500 °C  
 1600 °C

DD1 + Al(OH) 3 2.97

±0.02    3.06

±0.05    3.07

±0.01    2.95

±0.04    3.03

±0.04    2.98

±0.02    2.83

±0.06    2,85

±0.02

2,84 ±0.04

**Table 4.** Apparent density of composition M1, M2 and M3 of the samples sintered for 5 hours between 1400°C and 1600°C.

#### B. Mineralogical analyses of compositions by XRD

The XRD diagrams of the mixtures M1, M2 and M3, sintered for 5 h at 1400 °C, 1500 °C and 1600 °C, are gathered in Fig. 5. Mullite is the predominant main phase, and no cristobalite is detected (at these temperatures, cristobalite became amorphous and then reacted with alumina to form secondary mullite).

Primary mullite results from the transformation of kaolinite while secondary mullite results from the reaction between alumina and the excess of silica in kaolin. The later one is formed by a mechanism of dissolution precipitation through the vitreous phase as mentioned also by other authors [17]. In the case of the compositions referenced M2 and M3, no trace of  $\text{Al}_2\text{O}_3$  nor any another phase is detected apart from the mullite. However, the mixtures M1 contain  $\alpha\text{-Al}_2\text{O}_3$  up to 1600 °C, due to the excess of  $\text{Al}_2\text{O}_3$  added and which could not react once the amorphous phase was entirely consumed in the reaction.

For the different compositions, increasing the sintering temperature accelerates the formation of secondary mullite. Indeed, from 1500 °C, the reaction between alumina-vitreous silica of kaolin seems to be complete. The fine size of the alumina grains combined with the presence of impurities in the starting kaolin, promotes the reduction of the viscosity of the glassy phase at these temperatures. This promotes the reaction of alumina with the glassy phase to form more secondary mullite, resulting in total crystallization of the compound.

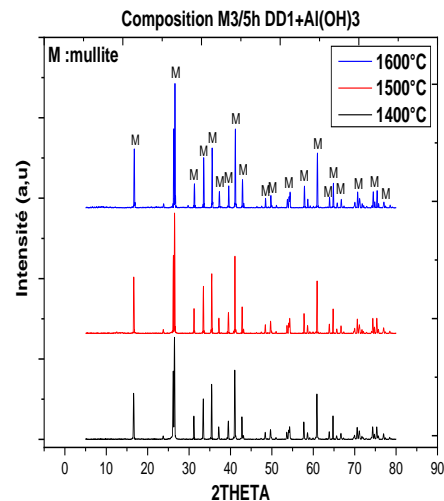
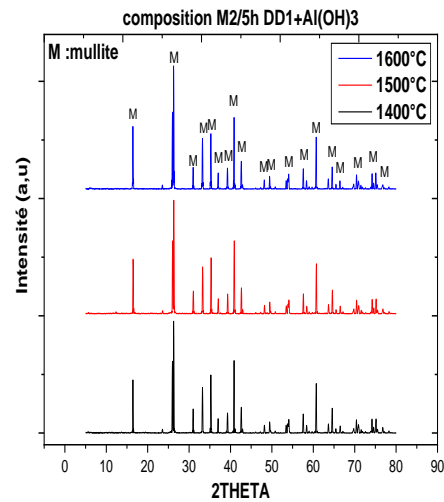
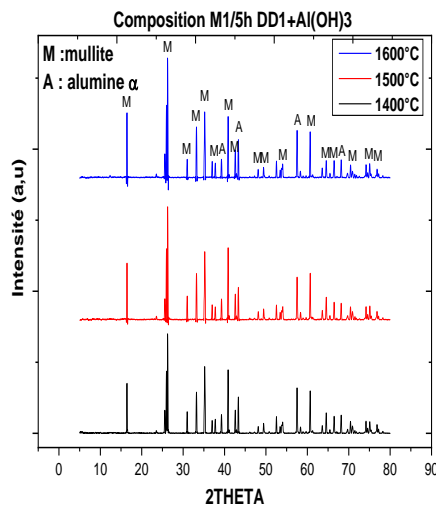


**Fig. 5.** XRD pattern of composition M1,M2 and M3 sintered at different temperature.

### C. Microstructure of compositions

**Fig. 6** show the microstructures, obtained by SEM, of mixtures (kaolins - alumina) sintered respectively at 1500 °C and 1600 °C for 5 h. The morphology of the microstructures does not present significant differences between the two mixtures M1 and M2. A high porosity is observed for all sintered mixtures at different temperatures. However the structure of composition M3 present more porosity.

in the structures, three distinct phases are observed,

namely:

- A matrix of secondary mullite grains with acicular form and small grain size ( $<1\ \mu\text{m}$ ), resulting from the reaction of kaolin silica and alumina. They are around 100 nm–200 nm in all cases. The reaction between alumina and the vitreous phase generally takes place by a dissolution-diffusion-precipitation mechanism. Aluminium hydroxyde react early with liquid phase formed by dissolution of cristobalite and reduce its viscosity. It will lower the temperature of the dissolution and diffusion mechanism and allow the secondary mullite to precipitate at temperatures below. it is observed in the XRD diagrams (**Fig. 5**) that the cristobalite has not even had time to form since. Malou et al. [18] have shown that the dissolution of alumina in the vitreous phase increases until the nucleation of the mullite then its crystallization. The rapid formation of mullite traps alumina particles and pores which inhibits densification of the composite. The equiaxial form of secondary mullite is caused by the presence of a large amount of alumina.

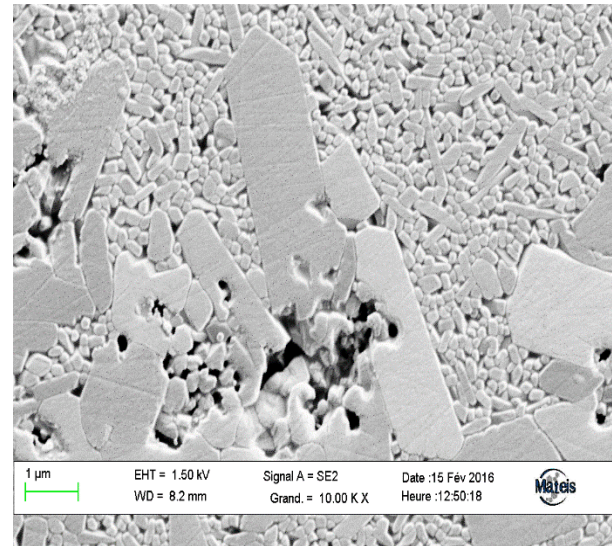
- Large primary mullite crystals of very elongated shape formed from the final crystallization of kaolinite. They are randomly oriented and uniformly dispersed in the matrix of secondary mullite grains.

- M.A. Sainz et al. [19] found that the compositions of the primary and secondary mullites vary significantly according to the  $\text{Al}_2\text{O}_3$ - $\text{SiO}_2$  diagram. Secondary mullite is richer in alumina (74.1%) than primary mullite (71.7%).

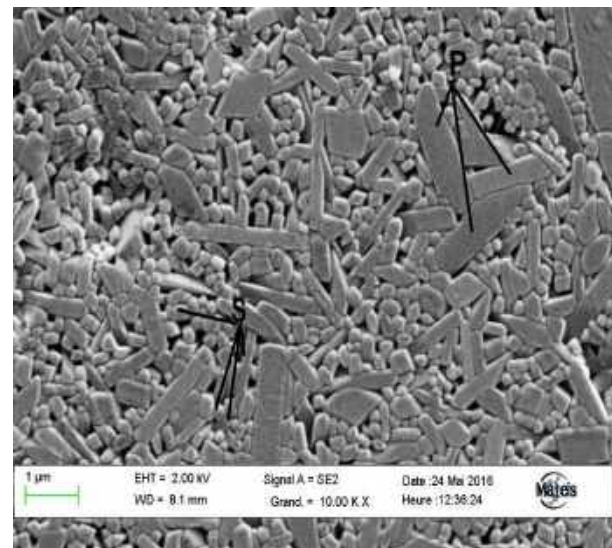
- Isotropic Alumina grains of a few micrometers dispersed in the mullitic matrix. This alumina phase comes from the excess of the alumina addition, which did not react with the kaolin silica. For mixture M1, the composition are not stoichiometric. This finding is confirmed by the spectra of analysis by X-ray diffraction.

- Mullitization occurs from the alumina - silica phase by nucleation and growth due to a reaction between alumina from aluminum hydroxide and amorphous silica from kaolin. The growth rate is controlled by the dissolution of  $\text{Al}_2\text{O}_3$  in  $\text{SiO}_2$ . At high temperatures, nucleated mullite will grow at the interface between  $\text{Al}_2\text{O}_3$  and  $\text{SiO}_2$  particles by diffusion of  $\text{Al}^{3+}$  and  $\text{Si}^{4+}$  via a crystal lattice. Rapid

dissolution of alumina in the amorphous siliceous phase promotes homogeneous nucleation and growth of mullite within the residual vitreous phase [20]. Indeed, some intragranular alumina grains remained trapped in clusters of formed secondary mullite. Mullite

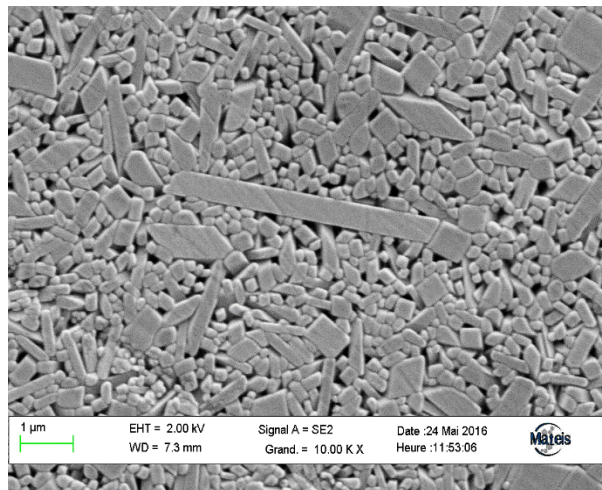


**DD1+Al(OH)3 M1 1400 °C During 5h**

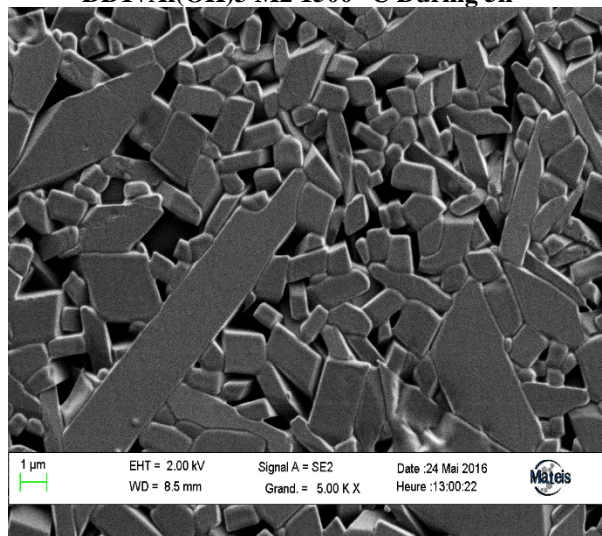


**DD1+Al(OH)3 M1 1500 °C During 5h**

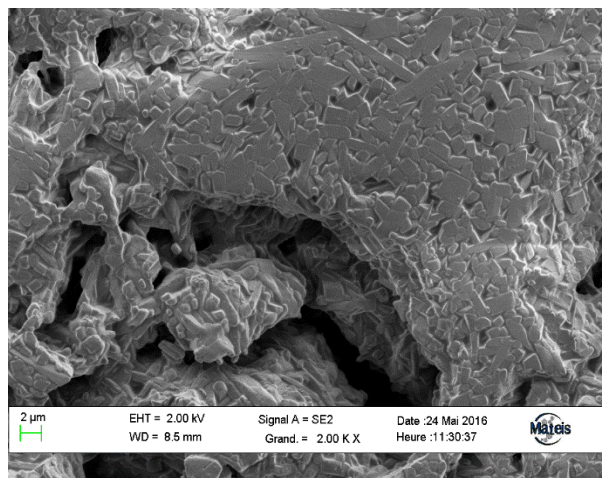




**DD1+Al(OH)3 M2 1500 °C During 5h**



**DD1+Al(OH)3 M2 1600 °C During 5h**



**DD1+Al(OH)3 M3 1600 °C During 5h**

**Fig. 6.** SEM micrographs samples of the M1,M2 and M3 compositions sintered at different temperature during 5 h..

#### IV. CONCLUSION

In the present investigation, a composite consisting of mullite and corundum crystals has been prepared by reaction sintering of different mixtures referenced M1,M2 and M3 of kaolin and amorphous aluminum hydroxide powder at three different temperatures 1400 °C, 1500 °C and 1600 °C. At 1400 °C, very little densification occurs. At 1500 °C, the densification improves much better, but needle shaped mullite nucleated at this temperature, and it grew and crystallized very well at 1600 °C. After formation of mullite by the reactions of alumina and amorphous silica, the excess alumina recrystallized as corundum crystals in composition M1..

#### REFERENCES

- [1] J. Wu et al., EDXRF studies on blue and white Chinese Jingdezhen porcelain samples from the Yuan Ming and Qing dynasties. *X-Ray Spectrom*, 29 (2000), pp. 239-244.
- [2] P.A. Schroeder, G. Kaolin Erickson., From ancient porcelains to nanocomposites *Elements*, 10 (3) (2014), pp. 177-182.
- [3] Suzanne Christine Aboudi Mana, Marlia Mohd Hanafiah & Ahmed Jalal Khan Chowdhury., Environmental characteristics of clay and clay-based minerals *Geology, Ecology, and Landscapes*, 1 (3) (2017), pp. 155-161.
- [4] J.A. Pask, A.P. Tomsia., Formation of mullite from sol-gel mixtures and kaolinite., *J. Am. Ceram. Soc.*, 74 (1991), pp. 2367-2373.
- [5] C.Y. Chen, G.S. Lan, W.H. Tuan., Microstructural evolution of mullite during the sintering of kaolin powder compacts., *Ceram. Int.*, 26 (2000), pp. 715-720.
- [6] Y. Li, K.A. Khor., A study of processing parameters in thermal-sprayed alumina and zircon mixtures., *J. Therm. Spray Technol.*, 11 (2) (2002), pp. 156-194.
- [7] R. Torrecillas, G. Fantozzi, S. De Aza, J.S. Moya., Thermomechanical behavior of mullite., *Acta Mater.*, 45 (3) (1997), pp. 897-906.
- [8] T.I. Mah, K.S. Mazdiasni., Mechanical properties of mullite., *J. Am. Ceram. Soc.*, 66 (1983), pp. 699-703.
- [9] H. Schneider, J. Schreuer, B. Hildmann., Structure and properties of mullite - a review., *J. Eur. Ceram. Soc.*, 28 (2008), pp. 329-344.
- [10] T. Tsuchida, N. Ichikawa., Mechanochemical phenomena of gibbsite, bayerite and boehmite by grinding., *React. Solid*, 7 (1989), pp. 207-217.
- [11] T. Sato., Thermal decomposition of aluminum hydroxides to alumina., *Thermochim. Acta*, 88 (1) (1985), pp. 69-84.
- [12] T. Sato., The thermal transformation of gelatinous aluminium hydroxide., *Z Anorg. Allg. Chem.*, 391 (1972), pp. 167-173.
- [13] M. Gonon et al., Etude de la transformation de trois nuances de kaolin en fonction de la température, *Silicates*



Industriels Ceramic Science and Technology, 65 (N°11–12) (2000), pp. 119-124.

[14] M. Chargui et al., Mullite fabrication from natural kaolin and aluminum slag., *Boletín Soc. Española Cerámica Vidr.*, 57 (2018), pp. 169-177.

[15] F. Sahnoune, M. Chegaar, N. Saheb, P. Goeuriot, F. Valdivieso., Algerian kaolinite used for mullite formation, *Applied clay science*, 38, 2008, 304–310.

[16] C. N Djangang et al., Reaction sintering and microstructural evolution in metakaolin-metastable alumina composites, *J. Therm. Anal. Calorim.*, 117, 2014, 1035–1045.

[17] K.C. Liu, G. Thomas, A. Caballero, J.S. Moya, S. Aza., Mullite formation in kaolinite -  $\alpha$ -alumina., *Acta Metall.*, 42 (1994), pp. 489-495.

[18] Z. Malou, M. Hamidouche, H. Belhouchet., Thermal shock resistance of Mullite obtained from Kaolin and tri-hydrated alumina., *High. Temp. - High. Press.*, 47 (N°2) (2017), pp. 179-190.

[19] M. Sainz, F. Serrano, J. Amigo, J. Bastida, A. Caballero., XRD microstructural analysis of mullites obtained from kaolinite–alumina mixtures., *J. Eur. Ceram. Soc.*, 20 (2000), pp. 403-412.

[20] H.-J. Kleebe, F. Siegelin, T. Straubinger, G. Ziegler., Conversion of  $\text{Al}_2\text{O}_3$ - $\text{SiO}_2$  powder mixtures to 3:2 mullite following the stable or metastable phase diagram., *J. Eur. Ceram. Soc.*, 21 (2001), pp. 2521-2533.

# Title: Development of ZnO nanoparticles for polymer reinforcement

FAYSSAL BOUFELGHA<sup>1,2,\*</sup>, RAHIMA ZELLAGUI<sup>1</sup>, MOHAMED CHERIF BENACHOUR<sup>1</sup>, HEIDER DEHDOUH<sup>1</sup>, NOUREDDINE BRIHI<sup>2</sup>, SLIMENE HADJEB<sup>2</sup>, F. LABRECHE<sup>2</sup>, M. KHIAT<sup>1</sup>.

1. Research Center in Industrial Technologies CRTI, P.O.Box 64, Cheraga 16014, Algiers, Algeria
2. Laboratoire Physique de la Matière Condensée et Nanomatériaux (LPMCN), Département de Physique, Faculté des Sciences Exactes et Informatique, Université de Jijel, 18000 Algeria

## ABSTRACT

*In modern technology and in the new industry, composite materials find several applications in various fields such as aeronautics, energy and naval, this importance is due to the excellent characteristics of these materials. In the present work we prepared the ZnO powder to improve the properties (based on the mechanical properties) of polymer materials (PLA), (to use it as a reinforcement in the future), ZnO semiconductor nanoparticles were synthesized by using the co-precipitation method. The obtained nanoparticles were characterized by several techniques, such as FT-IR, UV-vis, and SEM. The FTIR results showed the characteristic vibrations of the Zn-O bond abdicated at  $446.66\text{ cm}^{-1}$ , the band gap value is obtained  $3.19\text{ eV}$ .*

## KEY WORDS

aeronautics, energy, naval, PLA, FTIR, ZnO NPs.

## I. INTRODUCTION

ZnO is one of the common inorganic oxide materials which have been explored for the variety of uses and applications. The basic nature of ZnO is consist of insolubility in water but dissolving tendency in acids and bases. Wurtzite and zinc blende are two most common forms of the ZnO which can be differentiated on stability in ambient conditions. Among the nano-sized materials, zinc oxide (ZnO) nanoparticles is an important metal oxide with specific physical and chemical properties utilized in different fields [1]. Such as the rubber composite's wear proof, polymer antiaging, polymer toughening [2], strong UV absorber in cosmetics and sunscreen [3], fiber additive in the textile industry for UV and visible light resistance [4], photo-catalyst [5], concrete productive [6], etc. In addition, zinc is an essential trace element in bone, skin, muscle, brain, and various enzyme systems [7]. PLA is one of the aliphatic thermoplastic

biopolymers extracted from agricultural sugars such as corn and beet, with the increasing demand for biopolymers, PLA is receiving great attention in several applications such as packaging, biological and textile applications. Although PLA has excellent properties such as good biodegradability and biocompatibility, its limitations in functional properties limit its use in better downstream applications [8]. To improve mechanical, chemical and physical properties, researchers use one of the main approaches to developing nanocomposites constituted by a polymeric matrix reinforced with nanoparticles (NPs), which can be either organic or inorganic [9]. The need for multifunctional active films is therefore essential at this stage to simultaneously improve thermal and antimicrobial (or photocatalytic) activities. Researchers have used different types of nanoparticles to improve the thermomechanical properties of PLA, such as silver [10], copper [11], and zinc oxide [12, 13]. Among these metal nanoparticles, zinc oxide occupies a prominent place due to its non-toxicity (GRAS certification (generally recognized as safe), its great stability at high temperatures and pressures, its inorganic nature and its respect for environmental protection [8].

The main objective of this work is to explore the structures, optical, defects and phases aspects of, synthesis of ZnO nanoparticles by Co-precipitation method for used in reinforcement of polymer (PLA).

## II. EXPERIMENTALE

Co-precipitation synthesis of ZnO nanoparticles is carried out using analytical grade chemicals without any further purification. The reagents used are zinc acetate di-hydrate  $[\text{Zn}(\text{CH}_3\text{COO})_2 \cdot 2\text{H}_2\text{O}]$ , sodium hydroxide  $[\text{NaOH}]$ , methanol and ethanol. Initially, a solution of 0.1 M zinc acetate is prepared in 50 ml of methanol. The obtained solutions are vigorously stirred on a magnetic stirrer for 2 h at a temperature of  $80\text{ }^\circ\text{C}$  to form a homogeneous mixture. Consequently,

0.5 M sodium hydroxide solution is added drop-wise to gradually increase the pH of the solution to 11. After the addition of NaOH, the metal ions start to co-precipitate in the form of metal hydroxide thereby initiating nuclei formation. The precipitated nanoparticles are filtered with paper filtered and washed with distilled water and ethanol. The washed precipitates are dried at 150 °C for 2 h in the oven during which metal hydroxide forms metal oxide. Finally, the obtained product is grounded in mortar and pestle and after that annealed at 500 °C for 1 h. The absorbance of NPs of ZnO over the visible range was recorded by UV-vis Shimadzu UV 2600i Spectrophotometer and FTIR spectrum analysis for functional group identification was done by making pellets of the samples using a jasco FT/IR 6800 spectrometer. JEOL JCM-5000 neoscope Scanning Electron Microscope (SEM) was employed to investigate the morphology of nanoparticles.

### III. RESULTATS AND DISCUSSION

#### A. FOURIER TRANSFORM INFRARED SPECTROSCOPY FTIR

To identify the various functional groups present in the synthesized NPs, characteristic bands are analyzed through FTIR spectra. The FT-IR works by plotting sample absorption of IR radiations are against the wavelength. Figure 1. Displays the FTIR spectra of the synthesized ZnO in the range of 4000–400 cm<sup>-1</sup>. FTIR spectrum of pure ZnO nanoparticles, the peak at 446.56 cm<sup>-1</sup> was the characteristic absorption of Zn-O bond and the broad band peak at 3506.9 cm<sup>-1</sup> can be attributed to the characteristic absorption of O-H group. These data are similar to the results observed by others [14].

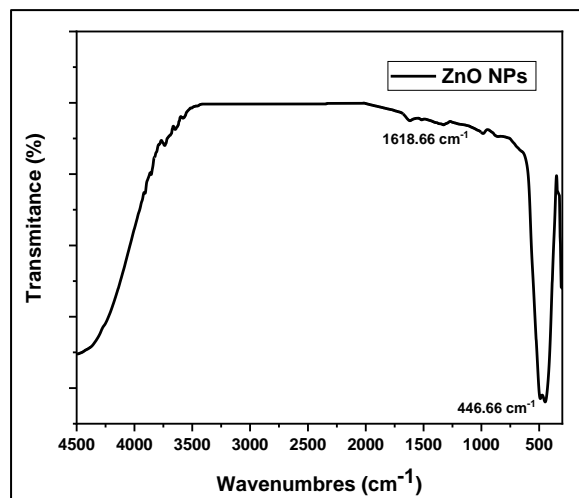


Fig. 1. FTIR specter of ZnO NPs.

#### B. UV-VISIBLE ABSORPTION

Figure 2 depicts the absorption spectrum of ZnO NPs, and we note that the maximum absorption point is 371 nm, and this value is typical for ZnO in previously reported works in the literature, which is attributed to the intrinsic absorption bandgap of ZnO [14].

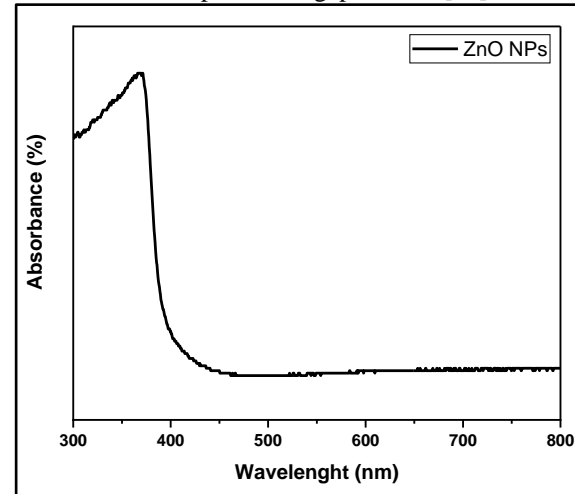


Fig. 2. Spectre d'absorption des NPs ZnO pure

We use the TAUC method to calculate the bandgap of semiconductor nanoparticles from UV-visible spectra. Using the equation  $\alpha(h\nu) = A(h\nu - E_g)^n$  where  $h\nu$  is the energy of the incident photon. [15].  $E_g$  is the authorized energy difference,  $A$  is a constant,  $\alpha(h\nu)$  is the absorption coefficient of the Lambert-Beer law and  $n = 1/2$  for the authorized direct transition [16]. The following procedure was performed. First, by comparing the TAUC equation and the straight-line equation (Eq. (1) and (2)) setting the y-axis equal to zero will give us the equation of the x-axis. (3), then plot the extrapolation of the first linear region on the x-axis, will be the bandgap energy Eq. (4).

$$\alpha(h\nu) = A(h\nu - E_g)^n \quad (1)$$

$$y = m(x) \quad (2)$$

$$0 = A(h\nu - E_g) \quad (3)$$

$$h\nu = E_g \quad (4)$$

Figure 3 shows the extrapolating the linear part of the curve between  $(\alpha h\nu)^2$  and photon energy ( $h\nu$ ), the value of the optical bandgap of ZnO NPs is 3.19 eV.

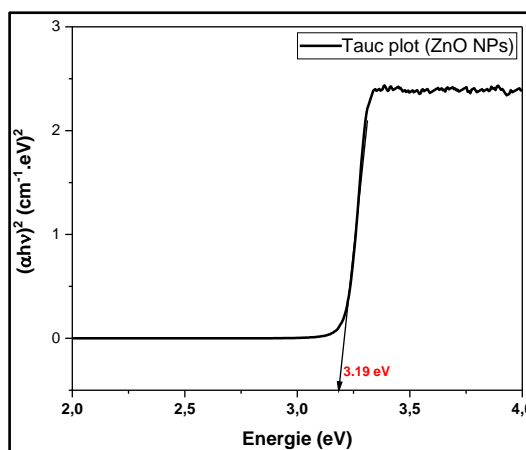


Fig .3. Eg of ZnO NPs

### C. SURFACE MORPHOLOGICAL

Figure 5 shows the SEM image of the ZnO surface, it is observed that the surface morphology is quasi-spherical with some agglomeration.

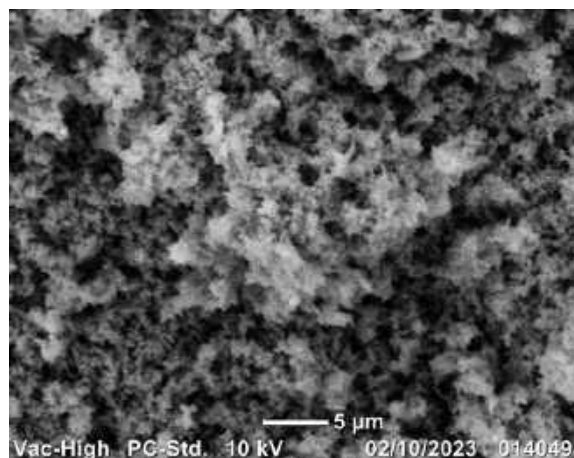


Fig. 4. SEM image of ZnO NPs

## IV. CONCLUSION

In summary, synthesize semiconductor ZnO nanoparticles in an environmentally friendly manner, replacing toxic chemicals with molecules acting as stabilizing agents. FT-IR spectroscopy confirmed the presence of characteristic bands of Zn-O bond molecules at 480 cm<sup>-1</sup>. The bandgap value was 3.19 eV.

## REFERENCES

[1] Narges Johari, Faezeh Zohari, Fatemeh Rafati et al. ZnO and CuO nanoparticles prepared via the co-precipitation

method: the evaluation of morphology and formation mechanism, 22 June 2021, PREPRINT (Version 1) available at Research Square [https://doi.org/10.21203/rs.3.rs-640074/v1]

[2]. A. Kołodziejczak-Radzimska, T. Jesionowski, Zinc oxide—from synthesis to application: a review, *Materials* 7(4) (2014) 2833–2881.

[3]. S. Nayak, A. Chaudhari, B. Vaidhun, Synthesis, characterization and ameliorative properties of food, formulation and cosmetic additives: Case study of Zinc oxide nanoparticles, *Journal of Excipients Food Chemicals* 11(4) (2020) 79–92.

[4] A.K. Anbalagan, S. Gupta, A. Kumar, S.-C. Haw, S.S. Kulkarni, N.-H. Tai, F.-G. Tseng, K.C. Hwang, C.-H. Lee, Gamma Ray Irradiation Enhances the Linkage of Cotton Fabrics Coated with ZnO Nanoparticles, *ACS omega* 5(25) (2020) 15129–15135.

[5] M. Golmohammadi, M. Honarmand, S. Ghanbari, A green approach to synthesis of ZnO nanoparticles using jujube fruit extract and their application in photocatalytic degradation of organic dyes, *Spectrochimica Acta Part A: Molecular Biomolecular Spectroscopy* 229 (2020) 117961.

[6] M. Kumar, M. Bansal, R. Garg, An overview of beneficiary aspects of zinc oxide nanoparticles on performance of cement composites, *Materials Today: Proceedings* 43 (2021) 892–898.

[7] R. Alimohamady, H. Aliarabi, R.M. Bruckmaier, R.G. Christensen, Effect of different sources of supplemental zinc on performance, nutrient digestibility, and antioxidant enzyme activities in lambs, *Biological trace element research* 189(1) (2019) 75–84.

[8] Rangika T. De Silva, Pooria Pasbakhsh, Lee SuiMae, Aw Yoong Kit, ZnO deposited /encapsulated halloysite–poly (lactic acid) (PLA) nanocomposites for high performance packaging films with improved mechanical and antimicrobial properties, *Applied Clay Science* 111 (2015) 10–20

[9] Suresh Chand Mali, Anita Dhaka, Sheetal Sharma, Rohini Trivedi, Review on biogenic synthesis of copper nanoparticles and its potential applications, *Inorganic Chemistry Communications* 149 (2023) 110448

[10] Shameli, K., Ahmad, M.B., Yunus, W.M.Z.W., Ibrahim, N.A., Rahman, R.A., Jokar, M., Darroudi, M., 2010. Silver/poly (lactic acid) nanocomposites: preparation, characterization, and antibacterial activity. *Int. J. Nanomedicine* 5, 573.

[11] Imai, H., Kimura, K., 2013. Antimicrobial Composition, Process for Preparing the Same, and Utilization Thereof. Google Patents.

[12] Pantani, R., Gorrasi, G., Vigliotta, G., Murariu, M., Dubois, P., 2013. PLA-ZnO nanocomposite films: water vapor barrier properties and specific end-use characteristics. *Eur. Polym. J.* 49, 3471–3482.

[13] Therias, S., Larché, J.-F., Bussière, P.-O., Gardette, J.-L., Murariu, M., Dubois, P., 2012. Photochemical behavior of polylactide/ZnO nanocomposite films. *Biomacromolecules* 13, 3283–3291.

[14] A. Villegas-Fuentes, H.E. Garrafa-Gálvez, R.V. Quevedo-Robles, M. Luque-Morales, A.R. Vilchis-Nestor, P.A. Luque, Synthesis of semiconductor ZnO nanoparticles using Citrus microcarpa extract and the influence of

concentration on their optical properties, Journal of Molecular Structure 1281 (2023) 135067

[43] P. Makuła, M. Pacia, W. Macyk, How to correctly determine the band gap energy of modified semiconductor photocatalysts based on UV-Vis spectra, J. Phys. Chem. Lett. 9 (2018) 6 814–6 817, doi: 10.1021/acs.jpcllett.8b02892 .

[44] J. Sahu, S. Kumar, V.S. Vats, P.A. Alvi, B. Dalela, S. Kumar, S. Dalela, Lattice de- fects and oxygen vacancies formulated ferromagnetic, luminescence, structural properties and band-gap tuning in Nd 3 + substituted ZnO nanoparticles, J. Lu- min. 243 (2022) 118673, doi: 10.1016/j.jlumin.2021.118673 .

# Micromechanical behavior study of delta phase of the different morphologies of 316L alloy elaborated by WAAM

SALIMA ABERKANE<sup>1,\*</sup>, ABDELBASSET BERRIAH<sup>1</sup>, MOHAMED ZIANE BOUTEBINA<sup>1</sup>, BRAHIM MEHDI<sup>1</sup> AND RIAD BADJI<sup>2</sup>

1. Materials Physics Laboratory, Faculty of Physics, University of Science and Technology Houari Boumediene USTHB, Bab-Ezzouar, Algiers, Algeria.
2. Research Center in Industrial Technologies CRTI, Cheraga, Algiers, Algeria.

## ABSTRACT

*This research aims to investigate the micromechanical behavior of the different delta ferrite morphologies obtained in the 316L as-built state of wire arc additive manufacturing WAAM. The microhardness, young's modulus, initial yield stress  $\sigma_y$  and strain hardening exponent  $n$  were obtained for the three typical morphologies. The results show that  $H$  and  $E$  values are close,  $\sigma_y$  and  $n$  remain constant with different loads in the three morphologies and  $n$  is inversely correlated with  $\sigma_y$ .*

## KEY WORDS

WAAM ; 316L ; micromechanical behavior.

## I. INTRODUCTION

Additive manufacturing (AM) is a modern method of creating products by continuously adding material based on a computer-aided design model [1]. Wire Arc Additive Manufacturing (WAAM) is one specific technique within AM, which falls under the Directed Energy Deposition (DED) category of metal additive manufacturing. The micromechanical properties resulting from this process are still poorly known, particularly for 316L alloy as the most important austenitic steels investigated with WAAM process [2]. This research aims to fill this knowledge gap of the as-built state of the additive manufacturing process.

## II. EXPERIMENTAL METHODOLOGY

The wall was deposited by Fronius TPS 500i power source which is an advanced version of the GMAW machine based on short-circuit transfer, and the mode CMT was adopted. The feedstock was a 1 mm diameter commercial 316LSi stainless steel wire.

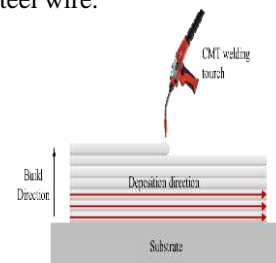


Fig. 1. Schematic diagram of deposition process

## III. EXPERIMENTAL RESULTS

### A. MICROSTRUCTURE

Figure 2 shows the microstructure of 316L steel showing the ferrite  $\delta$  phase obtained after WAAM treatment. We present the three morphologies: vermicular, columnar and lathy forms.



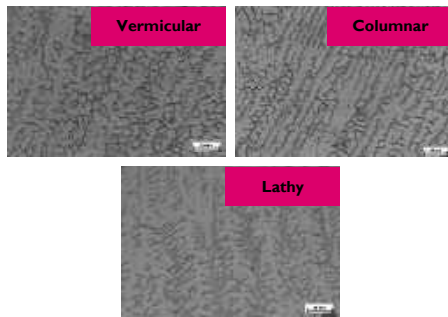


**Fig. 2.** Microstructures of the as build 316L alloy showing the different morphologies of  $\delta$ -ferrite.

### B. MICROMECHANICAL PROPERTIES

Figures 3-5 show the variation of the microhardness, the Young's modulus and the work hardening coefficients respectively of the three morphologies obtained. We show that microhardness and Young's modulus drop sharply with increasing applied load. This proves the variation in the concentration of dislocations from the surface layer having undergone the treatment.

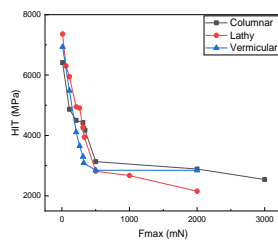


**Fig. 3.** Microhardness H of three typical morphologies

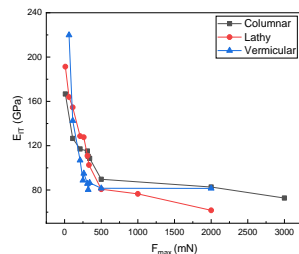


**Fig. 4.** Young modulus E of three typical morphologies

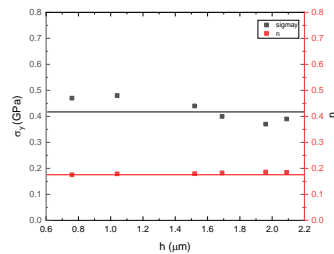


**Fig. 5.** Values of  $\sigma_y$  and  $n$  at different indentation depth of Vermicular  $\delta$ -ferrite

consequently these steels will have the same plastic flow.

### IV. CONCLUSION

- H of three typical morphologies evidently decreases with the increase of  $h$ .
- E of three typical morphologies decrease with the increase of  $h$  as a whole, which can be interpreted by increasing damage caused by accumulated dislocation.
- $\sigma_y$  and  $n$  remain constant with different loads in four morphologies.  $n$  is inversely correlated with  $\sigma_y$ .

### REFERENCES

- [1] "Standard Terminology for Additive Manufacturing—General Principles—Terminology," ISO/ASTM, 2015.
- [2] W. Jin et al., "Wire Arc Additive Manufacturing of Stainless Steels: A Review applied sciences Wire Arc Additive Manufacturing of Stainless Steels" Appl. Sci. 10, 5 (2020)

For the work hardening coefficients, we determine  $n=0,2$  and  $\sigma_y=400\text{MPa}$ . Which proves that the three morphologies have the same coefficients and

# Characterization of fiber of palm for reinforced polymer

ZELLAGUI RAHIMA<sup>1,\*</sup>, BOUFELGHA FAYSSAL<sup>1</sup>, BENACHOUR MOHAMED CHERIF<sup>1</sup>, DEHDOUH HEIDER<sup>1</sup>, ABDELMADJID KHIAT<sup>1</sup>

1. Research Center in Industrial Technologies CRTI, P. O. Box 64, Cheraga 16014, Algiers,  
[rahima32@hotmail.fr](mailto:rahima32@hotmail.fr), [r.zellagui@crti.dz](mailto:r.zellagui@crti.dz)

**ABSTRACT** (1,000 characters)

*Interest in natural fiber-reinforced polymer composite materials is growing rapidly, both in terms of industrial applications in the field of additive manufacturing and fundamental research. For this reason in this work we synthesize the palm fibers and characterize to have their structural properties examined by FTIR, morphological observed by SEM and optical is measured by absorbance.*

**KEY WORDS** additive manufacturing, natural fiber, polymer composite, palm, FTIR, DRX.

## I. INTRODUCTION

Additive manufacturing (AM) is a common name used for a group of techniques applied to the manufacture of different elements. AM is used to print features in a layer-by-layer process, where successive layers of material are formed under computer control to create an entire feature [1–3]. The main advantages of AM are the variety of materials it uses (polymers, metals and ceramics) and the possibility of manufacturing elements of complex shapes in various fields such as mechanics [2], biomedical [3], construction [4], aerospace [5] and food industries. AM has 7 different fundamental processing methods, namely binder jetting, direct energy deposition, material extrusion, material jetting, powder bed fusion, sheet rolling, and photopolymerization tanks [6]. Fused Deposition Modeling (FDM) or Fused Filament Fabrication (FFF) is one of the most popular types of commercial 3D printing technologies today. It is largely a material extrusion technology based on thermoplastics. Thermoplastics such as polylactic acid (PLA), acrylonitrile butadiene styrene (ABS), polystyrene (PS), polyethylene (PE), polyethylene terephthalate (PET), polycarbonate (PC), polycaprolactone (PCL), polyether ether ketone (PEEK), nylon, and

thermoplastic urethane (TPU) are some of the materials that have been used to make 3D printed products for various applications. Due to the lack of superior mechanical properties of polymers. These limitations encouraged researchers to find a solution to establish increased strength in FDM parts. In recent years, fiber composites based on polymers have been developed by FDM. The inclusion of fibers in the thermoplastic matrix provided improved modulus, tensile strength, and flexural strength compared to the pure thermoplastic material. This increases the chances of using FDM printed materials in load-bearing applications. However, uncertainties in the FDM manufacturing process such as the formation of voids, defects, and ineffective layer bonding increase the chances of failure of polymers and their composites. The objective of this work is to synthesize the palm fibers and characterize to have their structural properties examined by FTIR, morphological observed by SEM and optical is measured by absorbance. For this, we thought of composites (reinforced polymers).

## II. EXPERIMENTAL PROCEDURE

In order to prepare the palm leaves, we let's go through the steps represented by: 1st step is The palm leaves are washed with cold water to remove impurities and then placed on a clean surface to dry in the open air. 2nd step is The palm fibers are cut to a length of 1 to 2 cm, then they are ground by a pepper grinder then using an electric mill and finally this involves sieving the fibers obtained through several sieves of different diameters. The absorbance of fiber of palm over the visible range was recorded by UV–vis Shimadzu UV 2600i Spectrophotometer and FTIR spectrum analysis for functional group identification was done by making pellets of the samples using a Jasco FT/IR 6800 spectrometer. JEOL JCM-5000 Neoscope Scanning Electron Microscope (SEM) was employed to investigate the morphology of nanoparticles.

### III. Results and discussion

#### a- Morphological surface

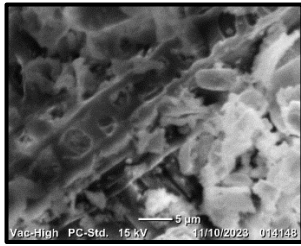


**Fig. 1.** Image SEM of fiber of palm.

We examined the optimized surface by SEM imaging and the resulting photo is presented in Figure 1. On the microscopic scale, the structure is constituted by the needle. It contains fibers of different sizes. This rearrangement of the fibers leads to a structural anisotropy which is observed in Figure 1. Consequently, the structure is not homogeneous and can be compared to a two-phase system consisting of a skeleton of fibers and dense pores. This unique structure often has special properties such as thermal insulation.

#### b- Absorbance

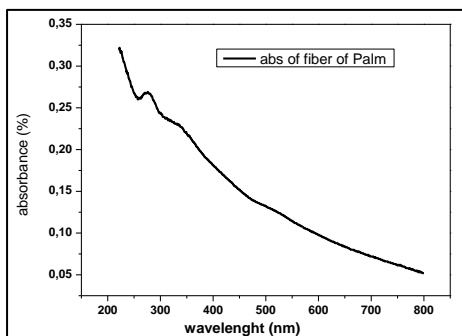


**Fig. 2.** Absorbance specter of fiber of palm.

Figure 2 shows the absorption spectrum of natural palm fibers, and we note that the optical absorption is in the 200-400 nm region with a peak at 276 nm.

### IV. CONCLUSION

The valorization of natural fibers has become a research theme which is of increasing interest to national and international research structures. This is due on the one hand to the soaring prices of petrochemical products and their impact on the environment and on the other hand, to the advantages offered by these fibers, namely their low cost, their

biodegradability and their mechanical performance. either in application in polymer reinforcement. for sustainable improvements.

### REFERENCES

- [1] A. Gebhardt, Understanding additive manufacturing, Carl Hanser Verlag GmbH & Co. KG; 2011.
- [2] Dilberoglu UM, Gharehpapagh B, Yaman U, Dolen M. The role of additive manufacturing in the era of industry 4.0. *Procedia Manuf* 2017;11:545–54.
- [3] Harun WSW, Manam NS, Kamariah MSIN, Sharif S, Zulkifly AH, Ahmad I, et al. A review of powdered additive manufacturing techniques for Ti-6al-4v biomedical applications. *Powder Technol* 2018;331:74–97.
- [4] Delgado Camacho D, Clayton P, O'Brien WJ, Seepersad C, Juenger M, Ferron R, et al. Applications of additive manufacturing in the construction industry– a forward-looking review. *Autom Constr* 2018;89:110–9.
- [5] Jyothish Kumar L, Krishnadas Nair CG. Current trends of additive manufacturing in the aerospace industry. In: *Advances in 3D Printing and Additive Manufacturing Technologies*, Springer Singapore; 2016: pp. 39–54
- [6] Lipton JJ, Cutler M, Nigl F, Cohen D, Lipson H. Additive manufacturing for the food industry. *Trends Food Sci Technol* 2015;43:114–23.

# The Effect Of Welding Current And Speed On The Thermal And Residual Stress Distributions Of A 100% Austenitic Pipes Butt Weld

MOHAMMED AMINE BELYAMNA<sup>1\*</sup>, CHOUAIB ZEGHIDA<sup>1</sup>, ABDELMOUMENE GUEDRI<sup>1</sup>,  
ABDELHALIM ALLAOU<sup>2</sup>

1. Infra-Res Laboratory, Department of Mechanical Engineering, University of Souk Ahras, Algeria; E-Mails: [m.belyamna@univ-soukahras.dz](mailto:m.belyamna@univ-soukahras.dz) ; [c.zeghida@univ-soukahras.dz](mailto:c.zeghida@univ-soukahras.dz) ; [a.guedri@univ-soukahras.dz](mailto:a.guedri@univ-soukahras.dz) ;
2. Department. of mechanical engineering, University of Khenchela, Algeria; E-Mail: [allaoui.abdelhalim@univ-khenchela.dz](mailto:allaoui.abdelhalim@univ-khenchela.dz)

## ABSTRACT

*The research effort presented in this paper, which is based on parametric analyses, mainly examines the influence of important welding process parameters (welding speed and welding current). To achieve the desired optimum residual stress level, the net heat input to the weldments can be optimized by adjusting the welding current and/or welding voltage or by controlling the welding speed. The basic parameters for the numerical simulations are acquired from the welding parameters used during the manufacture of thin-walled cylinders with similar geometry and materials on the shop floor. Five parametric studies on the influence of welding process parameters on residual stress employ three distinct values of welding speed and welding current in total. The applied simulation approach, FE model, heat source model, and material model's specifics have already been covered. Evaluated and the results could be obtained using lower heat input values, heat input regulated by adjusting welding speed, and welding voltage. Finally, on the inner and outer surfaces away from the weld line, compressive and tensile axial residual stresses are created.*

## KEY WORDS

Residual stresses; Distortions; Finite element analysis; Austenitic piping; Arc welding

## I. INTRODUCTION

For many years, the main issue facing the welding industry has been the lower strength of structures in and around the weld zone as a result of residual stresses unique to the arc welding process. To assure the structural integrity of welded structures, it is crucial to anticipate the transient and residual stress fields before, during, and after the welding process, therefore to save time and cost of experiments, numerical techniques can be employed to simulate the welding process and optimize welding parameters.

It is difficult to simulate any welding process using Finite Element (FE) because of the interaction of thermal, mechanical, and metallurgical processes [1-3]. Hibbitt et al. [4] used a highly focused heat source in motion to address a heat transfer issue when conducting a thermal evaluation of a welding operation. One of the most widely used heat source models in welding analysis is the moving double ellipsoidal heat source model, which was created by Goldak et al. [5]. One of its advantages is that it can withstand a variety of fusion welding procedures. Due to the highly concentrated heat source, mesh refinement is required along the entire welding route, which increases the computational cost of welding analysis using FEA.

Current, voltage, welding speed, current density, and preheat temperature are the welding parameters that must be adjusted to generate a satisfactory weld [6]. Controlling the input welding parameters is therefore crucial to achieve a high-quality weld and therefore boosting process productivity.

## II. MATHEMATICAL MODEL

A moving heat source is a type of heat transfer phenomenon that can be applied to a variety of technical tasks, including welding. By figuring out the temperature distribution and cooling rate utilizing theoretical solutions to this problem, engineers may be able to better understand the impacts of heat input and the performance of the finished product. These solutions have applications in welding for determining the microstructure, joint strength, residual stresses, cold cracking, size of the heat-affected zone (HAZ), and deformation. The equations below state the double ellipsoid heat source model, which best describes the heat source

for arc welding:

- For the front heat source:

$$Q(x, y, z, t) = \frac{6\sqrt{3}f_f Q_w}{a_f b c \pi \sqrt{\pi}} e^{-3x'^2/a_f^2} e^{-3y'^2/b^2} e^{-3z'^2/c^2} \quad (1)$$

- For the rear heat source:

$$Q(x, y, z, t) = \frac{6\sqrt{3}f_r Q_w}{a_r b c \pi \sqrt{\pi}} e^{-3x'^2/a_r^2} e^{-3y'^2/b^2} e^{-3z'^2/c^2} \quad (2)$$

Where  $x$ ,  $y$ , and  $z$  are the welded pipe's local coordinates, and  $f_f$  and  $f_r$  are parameters that indicate the proportion of heat deposited in the front and rear portions, respectively. Note that  $f_f + f_r = 2.0$ . The welding heat source's power is  $Q_w$ . Calculations can be made based on the welding current, arc voltage, and arc efficiency. It is assumed that the TIG welding technique has an arc efficiency  $\eta$  of 80%.

Affecting the characteristics of the welding heat source are the parameters  $a_f$ ,  $a_r$ ,  $b$  and  $c$ . Under the welding requirements, the heat source's specifications can be changed to produce the necessary melted zone.

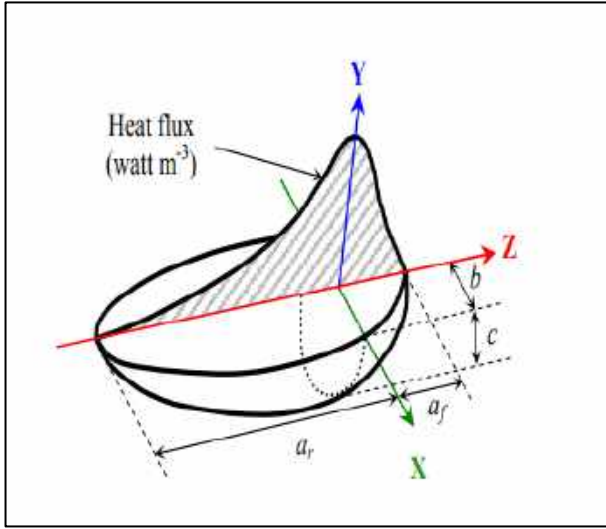


Fig.1. Heat source geometry [5]

$$\text{Heat input} = \frac{V \cdot I}{1000 \cdot WS} \quad (MJ \cdot m^{-1}) \quad (3)$$

Where  $V$  is arc voltage in volts,  $I$  is welding current in ampere and  $WS$  is the speed of welding in mm/s.

The most efficient way to simulate arc operations is to use the approach in Figure 1.

The parameters for the welding process and the heat source are displayed in Tables 1 and 2, respectively.

Table 1. Goldak heat source specifications

Parameters	Value
Length of front ellipsoidal, $a_f$ [mm]	5
Length of rear ellipsoidal, $a_r$ [mm]	15
Width of heat source, $2b$ [mm]	10
Depth of heat source, $c$ [mm]	3
Fraction of heat in front ellipsoidal, $f_f$	1.25
Fraction of heat in rear ellipsoidal, $f_r$	0.75

Table 2. Parameters of the welding process

Parameters	Value		
Welding voltage, (volts)	WC1	WC2	WC3
	12.5	12.5	12.5
Welding current, (amperes)	150	200	250
Welding process efficiency, $\eta$ (%)	75	75	75
Welding speed, $v$ (mm.s <sup>-1</sup> )	WS1	WS2	WS3
	1	3	5

### III. RESULTS

#### A. Effects of welding current

To investigate the effect of welding current on the axial temperature and residual stress distribution, three states of WC1, WC2, and WC3 (with a current of 150, 200, and 250 A, respectively, and with the same welding speed and voltage) are compared together, as shown in figure 2-3.

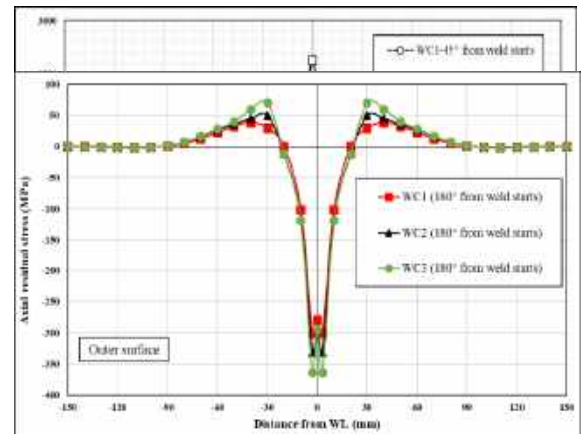
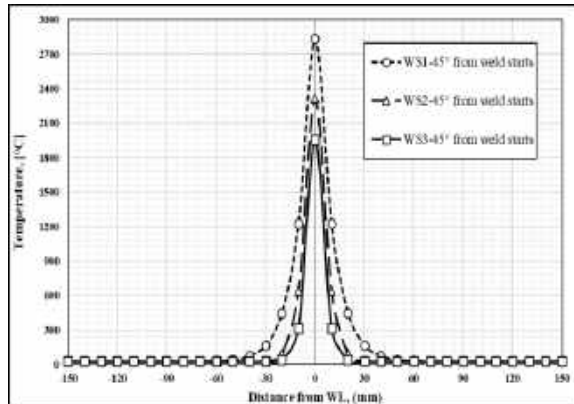


Fig.2. Axial temperature distribution for three states of welding current, [°C]

**Fig. 3.** Axial residual stress distribution at  $180^\circ$  from weld starts for three states of welding current, [MPa]

### B. Effects of welding speed

To examine the impact of welding speed on the axial residual stress and temperature distribution. Three modes of WS1, WS2, and WS3 are compared with welding speeds of 1, 3, and 5 mm/s, respectively, and welding currents and voltages of 200 A and 12.5 V, respectively, as shown in figure 4-5.



**Fig. 4.** Axial temperature distribution for three states of welding speed, [°C]

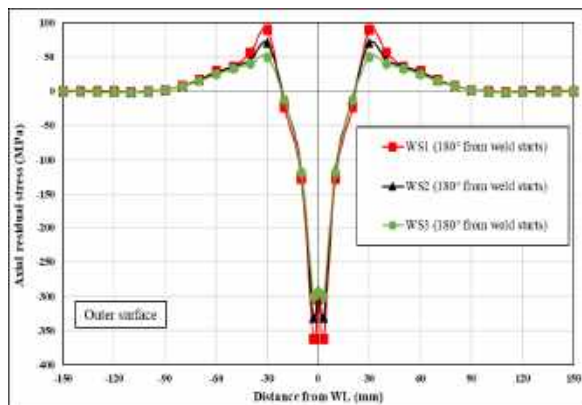


**Fig. 5.** Axial residual stress distribution at  $180^\circ$  from weld starts for three states of welding current, [MPa]

## IV. DISCUSSION

by referring to figure 3, the results show that the maximum compressive stresses in WC1, WC2, and WC3 are 300, 330, and 360 MPa respectively, which shows that compressive stresses increase with increasing current. On the contrary, figure 5 shows that the compressive stresses decrease with increasing velocity.

From the previous figures, it's obvious that more heat input per unit volume in the case of WP3 (1.04 MJm<sup>-1</sup>) and WS1 (2.5 MJm<sup>-1</sup>) produces maximum residual stress. Similarly, in the case of WP1 (0.625 MJm<sup>-1</sup>)

and WS3 (0.5 MJm<sup>-1</sup>) lowest residual stresses are observed.

## V. CONCLUSION

The following conclusions for the FE modeling were drawn:

- ▶ Along and near the weld line, high compressive axial residual stresses occur on the outer surfaces.
- ▶ Controlling the heat input by altering the welding speed and welding current may yield varied effects, it's obvious that increasing arc energy produces maximum residual stress. Similarly, the lowest residual stresses are observed when the arc energy is decreasing.

## REFERENCES

- [1] S.A. Tsirkas, P. Papanikos, T. Kermendis, "Numerical simulation of the laser welding process in butt-joint specimens". Journal of Material Processing Technology 134:59-69. (2003).
- [2] William, Perret, "Welding Simulation of Complex Automotive Welded Assembly - Possibilities and Limits of the Application of Analytical Temperature Field Solutions", ISBN3981594401 BAM, 184 pages. (2013).
- [3] Dipl.-Ing. William Perret, Dr.-Ing. Christopher Schwenk, Prof. Dr.-Ing. Michael R. Ethmeier, Mr. Thate R. Raphael, Mr. Uwe Alber, "Case Study for Welding Simulation in the Automotive Industry", Welding in the World, Volume 55, Issue 11-12, 89-98. (2011).
- [4] H. D. Hibbitt, & P. V. Marcal, "A numerical thermo-mechanical model for welding and subsequent loading of a fabricated structure". Comp. & Struct. 3, 1145-1174. (1973).
- [5] J. Goldak, M. Bibby, A. Chakravarti, "A New Finite Element Model for Welding Heat Sources". Metallurgical Transactions B, Volume 15, 229-305. (1984).
- [6] D. Venkatkumar, D. Ravindran, G. Selvakuma. "Finite element analysis of heat input effect on temperature", residual stresses and distortion in butt welded plates [J]. Materials Today Proceedings, 5: 8328-8337. (2018).



# Numerical Simulation of Fatigue Crack Propagation In 304L Stainless Steel

ABDELHALIM ALLAOUI<sup>1,\*</sup>, ABDELMOUMENE GUEDRI<sup>2</sup>, MOHAMMED AMINE BELYAMNA<sup>2</sup> AND CHOUAIB ZEGHIDA<sup>2</sup>

1. Department. of mechanical engineering, University of Khenchela, Algeria;

E-Mail: [allaoui.abdelhalim@univ-khenchela.dz](mailto:allaoui.abdelhalim@univ-khenchela.dz)

2. Infra-Res Laboratory, Department of Mechanical Engineering, University of Souk Ahras, Algeria;

E-Mails: [a.guedri@univ-soukahras.dz](mailto:a.guedri@univ-soukahras.dz); [m.belyamna@univ-soukahras.dz](mailto:m.belyamna@univ-soukahras.dz); [c.zeghida@univ-soukahras.dz](mailto:c.zeghida@univ-soukahras.dz)

## ABSTRACT

*In this work, the Chaboche and Lemaître model is used to simulate the behavior of the material (AISI 304L) under cyclic loads. To describe the behavior of this type of material, isotropic hardening, and nonlinear kinematic hardening must be taken into account. The crack propagation speed curves were created using the simulation results on a CT-type specimen. These numerical results are compared to measured values.*

## KEY WORDS

Chaboche and Lemaître model; 304L; Fatigue; Crack

## I. INTRODUCTION

The fatigue aspect and more specifically the study of the propagation of cracks in a 100% austenitic steel of the AISI 304L type will be studied. The numerical simulation of fatigue damage is based on low-cycle fatigue data. This approach is based on the implicit hypothesis that the behavior in the damaged zone at the tip of a crack is similar to the behavior of a mini low-cycle fatigue specimen. In the first part, studies of the cyclic behavior of the material revealed a very marked Bauschinger effect, cyclic hardening, and an unstabilized stress-strain hysteresis loop during imposed stress tests, a phenomenon commonly called the Rochet effect. To model the behavior of this type of material, we had to use a model that takes into account the Bauschinger effect as well as the Rochet effect [1]. The relation which gives the elastoplastic behavior law of the material is deduced from the preceding relations and is expressed in the following way in the case of a monotonous uniaxial loading:

$$\sigma = E\varepsilon_e + Q \left( 1 - \exp \left( -b\varepsilon_{eq}^p \right) \right) + \frac{C}{\gamma} \left( 1 - \exp \left( -\gamma\varepsilon_{eq}^p \right) \right) \quad (1)$$

Parameter values  $b$ ,  $Q$ ,  $C$  and  $\gamma$  as well as those of the Young module, of the Poisson's ratio, and the

elastic limit are given in Table.1 . The model above, has been introduced in the Abaqus/Standard finite element code [2].

$E(MPa)$	198000	$b$	4
$\nu$	0.3	$C(MPa)$	24000
$\sigma_e(MPa)$	165	$\gamma$	335
$Q(MPa)$	180	-	-

Table .1. Parameters Behavior law [3]

This work was consecrated to the realization of simulations of cyclic loadings on a CT specimen. These simulations will allow us to plot crack propagation curves, to compare these results with the experimental data provided to us [3]. It should be noted that these comparisons were made in terms of  $\Delta K_{eff}$ , since the numerical simulation does not take into account the effect of the plastic wake which leads to the closure of the crack at stresses greater than  $\sigma_{min}$

## II. SPECIMEN CT DESIGN AND MESH

To realize simulations of cyclic loads, we have modeled a CT specimen (Compact Tension) (Fig. 1).

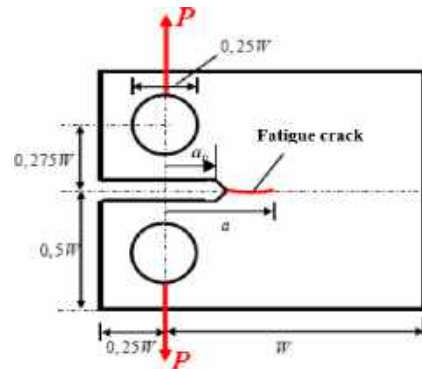


Fig. 1.. CT 50 specimen

For this type of specimen, widely used for fatigue testing, a low load leads to high values of the stress intensity factor in mode I; which is a considerable advantage concerning the capacity of the testing machines. This specimen has a ligament length  $w - a_0$  relatively important: it is used in particular in the study of the propagation of fatigue cracks as well as to determine the toughness of material after pre-cracking of the order of  $a/w \approx 0,5$ . The modeling of the CT specimen (CT 50,  $w=50\text{mm}$ ), used in this work is shown in Fig. 1. Dimensions are in accordance with ASTM E399. The calculations are realized in 2D and only half of the specimen is modeled due to its symmetry. Symmetry and loading conditions were applied to the specimen. A zone extending from the tip of the crack to the bottom of the specimen has been blocked (no vertical movement and no rotation around the axis perpendicular to the specimen).

### III. SIMULATIONS UNDER CYCLIC LOADINGS

We realized various simulations under cyclic loading. The purpose of these calculations is to determine the propagation speeds of the crack. The calculations of the speed of propagation are made on a stabilized cycle. Firstly, it was necessary to determine the number of cycles necessary for this stabilization. Since we will have to make various calculations at different loading rates, we have determined the number of cycles necessary for stabilization for the highest loading.

### IV. SIMULATIONS AND CALCULATION OF PROPAGATION VELOCITY

To account for the physical propagation process mentioned above, McClintock [4] proposed that the advance of the crack is due to the accumulation of damage in an area located around the tip of the crack until the brutal rupture. The size of this activity zone is taken as a fraction of the cyclic plastic zone. Other authors have also used a similar approach by considering the average distance between inclusions [5] or the size of grain [6] as the smallest element of material to which one can apply a failure criterion resulting from a macroscopic law.

It is assumed that the successive deformations undergone by an element of material over time are those encountered at a given moment at the front of the crack. Under these conditions, the damage necessary for the rupture of an element is equivalent to the sum of the accumulated damage, after a fatigue cycle, in each of the elements located in the activity area [7]. The elementary damage is given by :

$$d_i(\varepsilon_i) = \frac{n_i(\varepsilon_i)}{N_f(\varepsilon_i)} \quad (2)$$

$n_i$  is the number of cycles at the level of the plastic deformation  $\varepsilon_i$  and  $N_f$  the number of cycles to failure corresponding to this amplitude of deformation.

Models used to treat fatigue damage, are divided into two main categories: those that quantify the damage using strain or equivalent energy, and those that associate fatigue with a particular failure plane or critical plane.

Models based on both the energy density and the critical plane are the ones that best describe the damage. In the case of our study which is interested in the propagation in mode I, only traction compression is taken into account with  $\alpha=1$  and  $\beta=0$ . The damage parameter, called the fatigue parameter  $FP$ , is defined by:

$$FP = \langle \sigma^{\max} \rangle \left( \frac{\Delta \varepsilon}{2} \right) \quad (3)$$

with  $\langle x \rangle = 0.5(|x| + x)$ ;  $\sigma^{\max}$  is the maximum stress normal to the plane of the crack;  $\Delta \varepsilon$  is the variation of the strain normal to the plane of the crack. The fatigue life  $N_f(\varepsilon_i)$  is calculated in the plane of crack by the following relation:

$$FP = \langle \sigma^{\max} \rangle \left( \frac{\Delta \varepsilon}{2} \right) = \frac{\sigma_f'^2}{E} (2N_f)^{2b} + \sigma_f' \varepsilon_f' (2N_f)^{b+c} \quad (4)$$

$b$  is the fatigue strength exponent  $\sigma_f'$  is the true fatigue failure stress,  $c$  is the fatigue ductility exponent and  $\varepsilon_f'$  the true fatigue failure strain. These low-cycle fatigue parameters are generally dependent on the environment in which the testing is conducted. Low cycle fatigue parameter values are determined experimentally (Table .2):

**Table .2.** Parameters of Low cycle fatigue [3]

$\sigma_f' (MPa)$	3040	$b$	-0.256
$\varepsilon_f'$	0.302	$c$	-0.494

By taking a law of cumulation of the linear damage (Miner's rule), the progress of the crack will take place

$$\text{when : } \sum d_i = 1 \quad \text{soit} \quad \sum \frac{n_i(\varepsilon_i)}{N_f(\varepsilon_i)} = 1 \quad (5)$$

The approach based on Miner's rule can be criticized insofar as it induces a linear accumulation of fatigue damage. In the case of sequential tests at two levels of imposed deformation, this rule overestimates the lifetime when the first cycling sequence is performed at the most damaging level. On the other hand, it is much more satisfactory when cycling at the least damaging level is applied first.

Neglecting the variations of the amplitude of the stress intensity factor  $\Delta K$ , which amounts to considering that the speed of propagation  $da/dN$  is constant. We deduce the final relation which binds the speed of cracking to the width of the elements located at the tip of the crack and to the number of cycles to rupture, [7]:

$$\frac{da}{dN} = \sum_{X=0}^{R_p} \frac{\Delta X}{N_f(\varepsilon)} \quad (6)$$

where  $R_p$  is the dimension of the cyclic plastic zone,  $X$  is the distance to the tip of the crack, and  $\Delta X$  the width of the element on which the calculation by finite elements gives the amplitude of the equivalent deformation  $\varepsilon$  after a charging cycle  $N_f(\varepsilon)$  is calculated by equation (4), [8]. Various calculations for different loads, and therefore for different  $\Delta K$ , were done using the finite element code ABAQUS/STANDARD. Each calculation with a given loading  $P$  allows us to calculate and represent a point on a propagation curve  $da/dN - \Delta K$ . According to the recommendations of the standards ASTM E399 et AFNOR A03 404, the values of the stress intensity factor  $K$  are calculated using the following relationship:

$$K = \frac{P}{B\sqrt{W}} f\left(\frac{a}{W}\right) \quad (7)$$

It remains to determine the number of cycles to failure, which, by substituting it with its value in (6), will allow us to determine the cracking rate corresponding to  $\Delta K$  previously found. This is possible using Jiang Sehitoglu's fatigue parameter. The value of  $\sigma_{\max}$  in (4) is determined on a stabilized cycle.

## V. RESULTS

The calculation procedure used considers a stationary crack without a plastic wake. Fig. 2 represents the

results at  $R=0$  and  $R=0,5$  from calculations, using the Sehitoglu model [8].

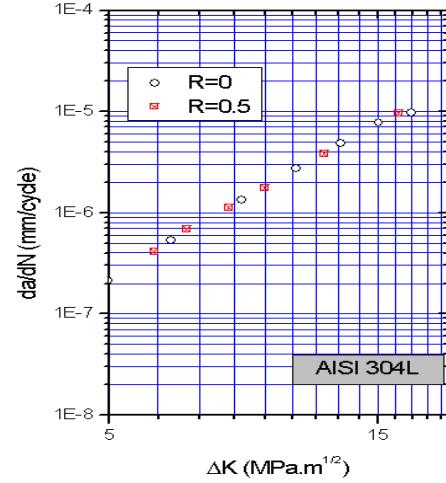


Fig. 2. Comparison of cracking rates for two different load ratios

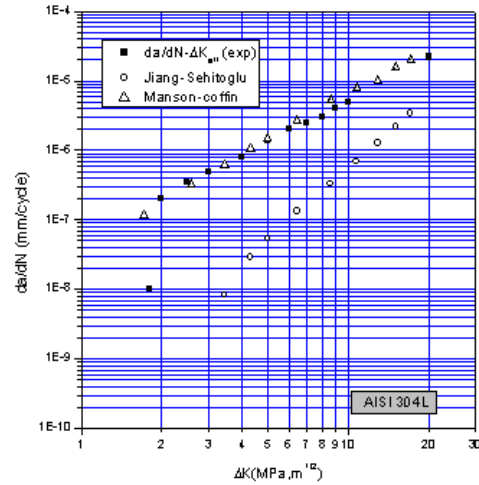


Fig. 3. Comparison of experimental and numerical propagation curves

These results show that the load ratio has no influence. This is explained by the absence of the plastic trail, and therefore closing stresses on the lips of the crack. These results are therefore directly expressed in terms of  $\Delta K_{eff}$ . A comparison of cracking rates  $da/dN$  in terms  $\Delta K_{eff}$  calculated by the two models used with the experimental propagation curve shows that the model based on the maximum energy density gives results close to those obtained experimentally, although slightly higher (Fig. 3).

## VI. CONCLUSION

This paper proposes an interesting method for modeling and calculating cracking speeds in AISI

304L, a 100% austenitic steel. The cyclic model of Lemaître and Chaboche's behavior with isotropic work hardening and nonlinear kinematics was employed.

The method for determining crack propagation speeds was described, and the impact of various parameters was explored. The simulations reveal that the model of Jiang - Sehitoglu based on energy density offers predictions that are extremely close to the experimental results. This is explained by taking into consideration the triaxiality of the stresses that are particularly present around the crack lips. Because there is no plastic wake, the load ratio has no effect.

## REFERENCES

- [1] J. Lemaitre, & J. L. Chaboche, , “Mécanique des matériaux solides”. (1985)
- [2] ABAQUS/STANDARD. version 6.14.5 manuals. Hibbit, Karlsson and Sorensen Inc”. Pawtucket, USA. (2017)
- [3] N. Lesur, “Propagation par fatigue des fissures physiquement courtes dans un acier inoxydable de type 304L”: rôle de la fermeture et de la plasticité. Thèse de doctorat: ENSMA, Poitiers. (2006)
- [4] McClintock, F. A. “Fracture of solids”. New York. (1963)
- [5] W. L. Morris, M. R. James, & O. Buck, Engng. Fract. Mech 13, 213. (1980)
- [6] G. Chalant, & L. Remy, Engng. Fract. Mech 18, 939. (1983)
- [7] A. Zeghloul, “Comparaison de la propagation en fatigue des fissures courtes et des fissures longues”: Thèse de doctorat, ENSMA, Poitiers. (1988)
- [8] H. Sehitoglu, & Y. Jiang, “Fatigue and stress analyses of rolling contact”. Technical Report, Materials Engineering—Mechanical Behavior. College of Engineering, University of Illinois at Urbana-Champaign. (1992)

# Intergranular Stress Corrosion Cracking Mitigation Using Mechanical Stress Improvement Process

CHOUAIB ZEGHIDA <sup>\*1</sup>, ABDELMOUMENE GUEDRI <sup>1</sup>, ABDELHALIM ALLAOUI <sup>2</sup>  
AND MOHAMMED AMINE BELYAMNA <sup>1</sup>

1. Infra-Res Laboratory, Department of Mechanical Engineering, University of Souk Ahras, Algeria; E-Mails: [c.zeghida@univ-soukahras.dz](mailto:c.zeghida@univ-soukahras.dz); [a.guedri@univ-soukahras.dz](mailto:a.guedri@univ-soukahras.dz); [m.belyamna@univ-soukahras.dz](mailto:m.belyamna@univ-soukahras.dz)
2. Department. of Mechanical Engineering, University of Khenchela, Algeria; E-Mail: [allaoui.abdelhalim@univ-khenchela.dz](mailto:allaoui.abdelhalim@univ-khenchela.dz)

## ABSTRACT

*The utilization of the Mechanical Stress Improvement Process (MSIP) is a widely employed technique in nuclear power plants. Its purpose is to effectively prevent stress corrosion cracking (SCC) by eliminating residual tensile stresses present in weldments. To demonstrate the effectiveness of the MSIP in reducing stress concentrations and improving structural integrity, this work provides backgrounds and numerical simulations concerning MSIP and assesses their impact on SCC in butt-welded austenitic piping systems.*

**KEYWORDS :** Mechanical Stress Improvement Process, residual stresses, structural reliability, intergranular stress corrosion cracking, pressured pipes.

## I. INTRODUCTION

Welding introduces a myriad of stresses within materials due to localized heating and subsequent cooling. These thermal stresses arise from differential expansion and contraction caused by temperature gradients. After welding, the remaining locked-in stresses, termed residual stresses, are often highest within the weld bead and its adjacent heat-affected zone (HAZ) [1, 2]. The HAZ, being a transition between the molten weld pool and the unaffected base material undergoes a distinct thermomechanical evolution, making it particularly susceptible to these stresses. Understanding and managing these stresses is crucial, as they can impact the structural integrity, performance, and longevity of the welded component. The MSIP technique exudes a remarkable ability to generate compressive stresses at the weldment

mechanically [3-5]. This is achieved by the deployment of a hydraulic mechanical clamp, which contracts the pipe on one side of the weldment.

In Fig.1, the fundamental principles of the MSIP are meticulously illustrated, offering a step-by-step visualization of this intricate method. The first panel, labeled (a), depicts the application of pressure onto the pipe, causing it to contract (where a: represents clamping placement on the welded pipes and b: represents the width of the clamps). This contraction serves as a precursor to the permanent deformation visualized in panel (b), which provides a schematic representation of the post-MSIP structural changes. Finally, panel (c) delves into the underlying mechanics of the process, showcasing how compression is generated in both axial and hoop directions. Together, these panels provide a cohesive and in-depth overview of the MSIP, elucidating the mechanics and outcomes at each pivotal stage.

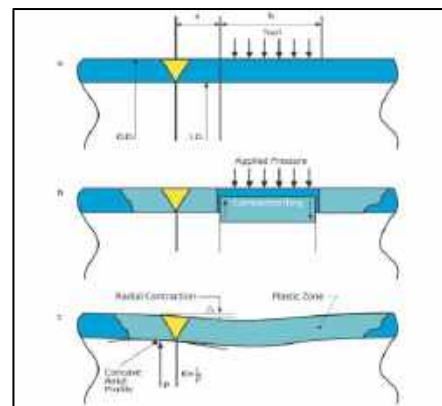


**Fig. 1.** The basic concept of MSIP:(a) Application of pressure to contract pipe; (b) Schematic of permanent deformation after MSIP; (c) Mechanism of compression generation in axial and hoop directions.

It is noteworthy that the pipe is only squeezed locally in the direct proximity of the circumferential weld, but not at the weld itself, as depicted in Fig.1(a). The plastic zone, which spans throughout the weldment region, is facilitated by the contraction of the pipe and the position of the tool. The contracted ring exerts a radially inward force on the pipe and the weld, as shown in Fig.1(b). The deformation compatibility along the pipe, illustrated in Fig.1(c), necessitates a concave axial profile of the pipe in the weld root region. The outcome of this process is the generation of residual compressive stresses at the inner pipe surface in both the axial and hoop directions, respectively. The extent of contraction required for stress redistribution is dependent on the joint geometry and materials. Typically, the required change in pipe circumference before and after the process remains in the range of 0.5 to 0.8%.

The pipe contraction at the weldment is only about 0.2 to 0.3%. It is important to note that the maximum contraction is limited by the tool design, which incorporates spacers and shims. Since the process is displacement-controlled, prior knowledge of actual material strength is not a prerequisite for establishing process parameters. The verification of MSIP for each application is achieved by merely measuring the circumferential pipe contraction (Fig.2).



**Fig. 2.** After undergoing MSIP, the welded joint exhibits a distinctive curved configuration along the upstream region of the weldment [6].

## II. SIMULATION

A FEM with three dimensions was created using Simufact-Welding to replicate the momentary tension during the MSIP process. To gain an understanding of the factors involved in MSIP, the following actions were taken: Firstly, the initial step involved the presentation of results obtained from the mechanical model after the welding simulation. Secondly, clamps were introduced to the welded pipes (as illustrated in Fig.3).

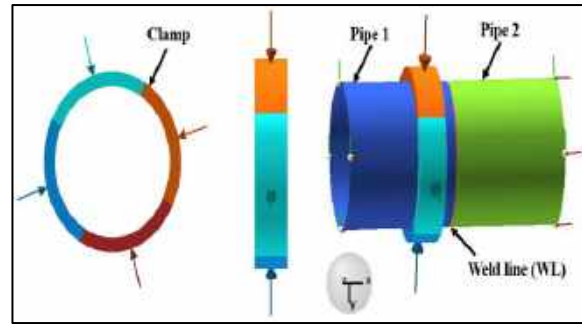


**Fig. 3.** Typical design of MSIP tools for numerical simulation.

Fig.4 showcases an intricate 3D FE mesh model that encapsulates the structural details of welded pipes in conjunction with the MSIP tools.

This high-fidelity representation serves to highlight the complexities involved in the interaction between the welded structures and the MSIP apparatus. The mesh aids in providing a granular view of stress distribution, potential deformation regions, and the probable impact zones of the MSIP tools on the welded pipes. Such a detailed visualization is instrumental in understanding the mechanical behavior of the system, ensuring that the application of the MSIP tools is both precise and effective in optimizing the mechanical properties of the welded joints.

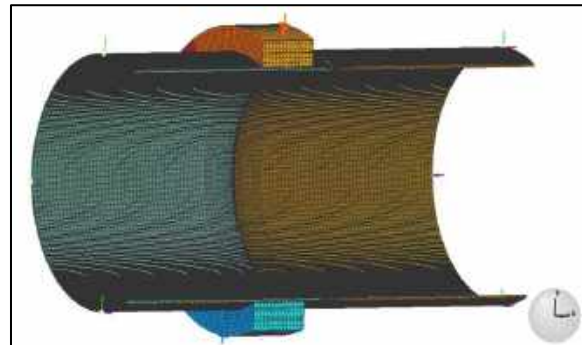


**Fig. 4.** 3D FE mesh of the welded pipes and MSIP tools.

## III. RESULTS AND DISCUSSION

In the field of piping system maintenance and repair, the MSIP presents a potent technique for addressing stress-induced cracks. Our numerical simulations indicate that this method can effectively redistribute stress in uncracked piping systems, consequently diminishing the likelihood of crack onset. We introduced a circumferential crack with a depth of 1mm beneath the WL. Following the simulated welding process, there was a marked opening of the crack as delineated in Fig.5.



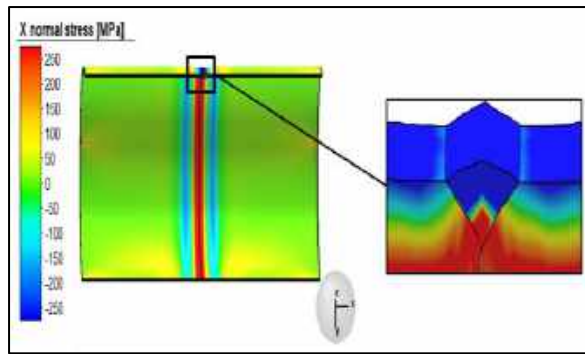


**Fig. 5.** Axial residual stress distribution post-welding with a detailed zoom-in on the WL highlighting crack formation.

Despite this initial widening post-welding in our simulation, we employed the MSIP method as a remedial strategy. The simulation showed that, by inducing compressive stresses via MSIP, it was possible to offset the tensile stresses that caused the crack to open, culminating in its closure, as evident in Fig.6. This numerical investigation underscores both the preventive and corrective potential of MSIP in modeled piping systems.

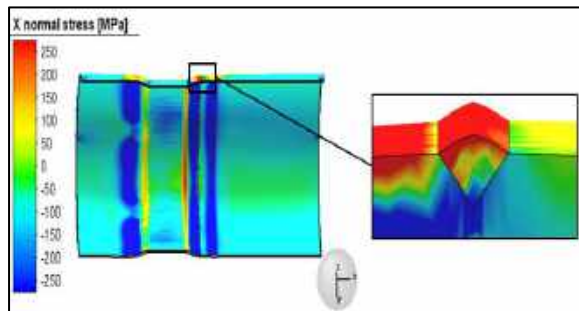


**Fig. 6.** Axial residual stress distribution post-MSIP with a detailed zoom-in on the WL highlighting crack information.

Following the results extracted from Fig.5 and 6 the MSIP stands out as a pivotal innovation in the mitigation of stress-induced cracks within piping systems. Its multi-faceted capabilities encompass the creation of an optimized stress distribution that not only caters to the immediate vicinity of the weld but also radiates beneficial effects to the adjacent material. By systematically reducing residual stresses, MSIP invariably bolsters the overall structural integrity of the piping. Furthermore, the enhancement of the weld's mechanical properties is a testament to the holistic improvement introduced by the process. Beyond just repair, MSIP represents a proactive approach, potentially preempting stress concentrations that could culminate in cracks. This comprehensive suite of benefits renders MSIP not just as a solution but as a forward-thinking strategy for ensuring the longevity and reliability of piping systems.

#### IV. CONCLUSION

The MSIP emerged as a beacon of hope, especially in the realm of butt-welded austenitic piping. By placing the MSIP strategically outside the HAZ, it's possible to achieve desired mechanical stress improvements in specific areas. This results in a helpful stress distribution that reduces tensile residual stresses and introduces compressive stresses. This approach can work for both pipes that haven't cracked yet and those that have. It's a flexible solution for handling stress-induced cracks in piping. The MSIP technique has several advantages over traditional welding methods. Firstly, it enables the creation of compressive stresses in the weld and surrounding material, which can deter crack formation. Secondly, it can minimize the residual stresses that often emerge during welding, a factor linked to SCC. Lastly, the MSIP approach can enhance the mechanical properties of the weld and nearby material, boosting overall durability and resistance to corrosion. By applying MSIP early, the need for pipe replacement can be eliminated, inspection frequency can be reduced, and utility providers can save money.

#### REFERENCES

- [1] R. M. Chrenko, "Weld residual stress measurements on austenitic stainless-steel pipes," *Weldments Phys. Metall. Fail. Phenom.*, pp. 195–205, 1978.
- [2] W. Jiang and K. Yahiaoui, "Effect of welding sequence on residual stress distribution in a multipass welded piping branch junction," *Int. J. Press. Vessels Pip.*, vol. 95, pp. 39–47, Jul. 2012, doi: 10.1016/j.ijpvp.2012.05.006.
- [3] L. F. Fredette, P. M. Scott, and F. W. Brust, "An Analytical Evaluation of the Efficacy of the Mechanical Stress Improvement Process in Pressurized Water Reactor Primary Cooling Piping," in *ASME Pressure Vessels and Piping Conference*, 2008, pp. 467–476.
- [4] E. J. Sullivan and M. T. Anderson, "Assessment of the Mechanical Stress Improvement Process for Mitigating Primary Water Stress Corrosion Cracking in Nickel Alloy Butt Welds in Piping Systems Approved for Leak-Before-Break," *Pacific Northwest National Lab.(PNNL), Richland, WA (United States)*, 2013.
- [5] G. G. Facco, P. A. Raynaud, and M. L. Benson, "Finite Element Analysis of the Effect of Mechanical Stress Improvement Process on Weld Residual Stress and Flaw Growth in a Thick-Walled Pressurizer Safety Nozzle," in *Pressure Vessels and Piping Conference*, American Society of Mechanical Engineers, 2017, p. V06BT06A070.
- [6] M. T. Anderson, S. E. Cumblidge, and S. L. Crawford, "Technical Letter Report-Analysis of Ultrasonic Data on Piping Cracks at Ignalina Nuclear Power Plant Before and After Applying a Mechanical Stress Improvement Process, JCN-N6319, Task 2," *Pacific Northwest National Lab.(PNNL), Richland, WA (United States)*, 2008.

## Fabrication et caractérisation de composites flexibles à matrice silicone renforcées par des nanoparticules céramiques KNN

**Malika Saidi<sup>\*1</sup>, Zahia Chelli<sup>1</sup>, Nadia Serkhane<sup>1</sup>, Saliha Rabehi<sup>1</sup>, AHCÉNE Chaouchi<sup>1</sup>, Yannick Lorgoillioux<sup>2</sup>, Mohamed Rguiti<sup>2</sup>, Christian Courtois<sup>2</sup>**

1. Laboratoire de Chimie Appliquée et Génie Chimique de l'Université Mouloud Mammeri de Tizi-Ouzou, Algérie.
2. Laboratoire de Matériaux Céramiques et Mathématiques de l'université Polytechnique Hauts-de-France
3. [\\*malikasaidi878@gmail.com](mailto:malikasaidi878@gmail.com)

### ABSTRACT

**Notre travail est consacré à la synthèse par voie solide des poudres céramiques sans plomb de la composition de type  $[(\text{Na}_{0.535}\text{K}_{0.480})_{0.966}\text{Li}_{0.058}](\text{Nb}_{0.90}\text{Ta}_{0.10})\text{O}_3$  (KNN) et à l'élaboration des composites à matrice silicone renforcée par la poudre KNN à différentes proportions massiques (5,10,15,20,25,30,40 et 50%).**

**KEY WORDS :** : céramique KNN silicone, diélectrique, composite

### INTRODUCTION

Depuis les années soixante, les céramiques piézoélectriques ont été utilisées dans divers applications suite à leur aptitude de convertir l'énergie mécanique en énergie électrique et vice versa [1-3]. Cependant, ils sont fragiles et très rigides, ce qui limite leur domaine d'utilisation. De nombreux efforts ont été fournis afin d'aboutir à des matériaux piézoélectriques pouvant subir de grandes déformations. L'une des solutions qui a été proposée par les chercheurs et les industriels est l'amincissement des matériaux piézoélectriques céramiques conventionnels [4]. Néanmoins, cette solution proposée semble être limitée car la souplesse atteinte n'est pas satisfaisante vu les propriétés mécaniques intrinsèque du matériau de base.

De nombreux groupes de recherche se sont focalisés ensuite sur l'élaboration des composites par dispersion des nanoparticules piézoélectriques dans une matrice polymère, car les nanocomposites hybrides non seulement héritent des fonctionnalités des nanoparticules piézoélectriques, mais

possèdent également les avantages des polymères tels que la flexibilité.

Le travail effectué a pour objectif d'élaborer des matériaux composites à base de silicone renforcés par des particules piézoélectriques sans plomb de type (KNN) pour une application dans la récupération d'énergie. Les matériaux flexibles élaborés ont été caractérisés par spectroscopie Infrarouge, par microscope électronique à balayage (MEB) et par impédancemétrie (permittivité, impédance (Z), indice de perte et conductivité). Les mesures ont été effectuées à la température ambiante et à différentes fréquences allant de  $10^2$  à  $10^6\text{Hz}$ .

L'analyse par spectroscopie infrarouge a révélé la présence de la bande caractéristique de la poudre KNN ainsi que les bandes des polymères pour les différents composites élaborés, ce qui confirme la formation des composites. L'intensité de cette bande augmente avec la quantité de KNN présente dans le composite.

La caractérisation par spectroscopie d'impédance des films composites métallisés a montré que les propriétés diélectriques et électriques sont influencées par différents paramètres, notamment le taux de charge et la fréquence. La permittivité relative augmente avec la quantité de KNN incorporée.

La permittivité relative, la conductivité et les pertes diélectriques sont inversement proportionnelle à la fréquence.

Les valeurs de l'impédance( $Z$ ) sont très élevées à des basses fréquences donc on a des fortes résistances, puis un relâchement des charges d'espace ce qui provoque l'augmentation de la conductivité à des hautes fréquences.

Les pertes diélectriques ( $\tan\delta$ ) sont faibles à la température ambiante pour tous les échantillons.

## II. CONCLUSION

. Ces résultats montrent que ces composites peuvent constituer un choix prometteur pour l'alimentation des dispositifs électroniques portables et implantables à faible consommation.

## REFERENCES

- [1] Cross, E.; Lead-free at last. *Nature*, 432(7013). 2004, 24-25(2004).
- [2] Saito, Y.; Takao, H.; Tani, T.; Nonoyama, T.; Takatori, K.; Homma, H.; ... & Nakamura, M. Lead-free piezoceramics. *Nature*, 432(7013), 84-87(2004).
- [3] Li, J. F.; Wang, K.; Zhu, F. Y.; Cheng, L. Q.; & Yao, F. Z. (K, Na)  $\text{NbO}_3$ -Based Lead-Free Piezoceramics: Fundamental Aspects, Processing Technologies, and Remaining Challenges. *Journal of the American Ceramic Society*, 96(12), 3677-3696(2013).
- [4] Colin, M. ; Mortie, Q. ; Basrour, S. ; et Bencheikh, N. Compact and low-frequency vibration energy scavenger using the longitudinal excitation of a piezoelectric bar. *Journal of Physics : Conference Series*, 476 -012135, (2013)

# Optimization of the aluminum dross washing for subsequent use in the synthesis of the spinel ( $\text{MgAl}_2\text{O}_4$ )

S. KHELFI <sup>a,b</sup>, I. NOUAR <sup>a,b</sup>, A. BENKHELIF <sup>a,b</sup>,

M. KOLLI <sup>a,b</sup>, M. ALTINER <sup>c</sup>,

<sup>a</sup> Ferhat Abbas Setif 1 University, Emergent Materials Research Unit, Setif, Algeria

<sup>b</sup> Ferhat Abbas Setif 1 University, Optics, and Precision Mechanics Institute, Setif, Algeria

<sup>c</sup> Çukurova University, Mining Engineering Department, Adana, Turkey

\* [celiakhalfi19@gmail.com](mailto:celiakhalfi19@gmail.com)

## ABSTRACT

In this work, we attempted to synthesis spinel from economically starting material (aluminum dross recovered from aluminum local industry) by a relatively fast and uncomplicated process that consists of three main stages: leaching-precipitation-calcination. The preparation was carried out by grinding aluminum dross then washing with distilled water at different temperatures to eliminate the contained salts and release the toxic gases. Before used, these raw materials were submitted to several characterization tests such as XRF, XRD, laser granulometry and FTIR. X-ray fluorescence (XRF) results revealed that alumina is the major component (~ 59.80% in wt.) in the used aluminum dross. The major crystalline phases identified were aluminum oxide ( $\text{Al}_2\text{O}_3$ ), spinel ( $\text{MgAl}_2\text{O}_4$ ), magnesium oxide ( $\text{MgO}$ ) as well as a small amount of aluminum in the metallic state ( $\text{Al}$ ). The mean particle size was found  $d_{50} = 255.8 \mu\text{m}$ . The transmittance curves recorded by Fourier Transform Infrared spectroscopy (FTIR) carried out on aluminum dross showed absorption bands at  $418 \text{ cm}^{-1}$  due to Ca-O stretching, and two bands at  $437$  and  $473 \text{ cm}^{-1}$  corresponding to the Mg-O bending.

## KEY WORDS

spinel, aluminum dross, alumina, washing.

## I. INTRODUCTION

Spinel has received a great deal of attention from academic researchers and the industry sector on account of its best combination of several important properties[1][2], such as high melting point ( $2135^\circ\text{C}$ )[3][4], high hardness value (16 GPa), relatively low density ( $3.58 \text{ g cm}^{-3}$ ), high mechanical strength both at room temperature (135-216 MPa) and elevated temperatures (120–205 MPa at  $1300^\circ\text{C}$ ), high resistance against chemical attack, wide energy band gap, high electrical resistivity, relatively low thermal expansion coefficient ( $9 \times 10^{-6} \text{ }^\circ\text{C}^{-1}$  between 30 and  $1400^\circ\text{C}$ ), high thermal shock resistance...[5]. To prepare  $\text{MgAl}_2\text{O}_4$  spinel, several routes can be considered. Conventionally,  $\text{MgAl}_2\text{O}_4$  spinel can be prepared by

sintering mixtures of  $\text{MgO}$  and  $\text{Al}_2\text{O}_3$  powders. However, this route involves high temperatures that can exceed  $T = 1600^\circ\text{C}$ . The aluminum dross floating on top of molten bath during aluminium melting, is generally regarded as having little commercial value and, indeed, representing a disposal problem. These dross containing significant amounts of alumina can be used as alumina source for spinel preparation[6].

## 2. EXPERIMENTAL PROCEDURE

### 2.1. METHODS

To eliminate salts and release the toxic gases, aluminum dross was washed with distilled water (2 step). The first washing was at  $T = 50^\circ\text{C}$  and the second washing was at deferent temperatures ( $30^\circ\text{C}$ ,  $50^\circ\text{C}$ ,  $70^\circ\text{C}$ ).

### 2.1. RESULTS

**Table 1:** Chemical composition of aluminium dross

	Raw Slag	First washing at $50^\circ\text{C}$	Second washing at $30^\circ\text{C}$	Second washing at $50^\circ\text{C}$	Second washing at $70^\circ\text{C}$
$\text{SiO}_2$	5.46	5.77	11.73	12.05	11.48
$\text{Al}_2\text{O}_3$	59.80	72.34	68.80	71.26	69.45
$\text{Fe}_2\text{O}_3$	1.25	0	0	0	0
$\text{CaO}$	6.26	3.55	2.80	2.17	2.43
$\text{MgO}$	12.75	16.71	16.46	13.51	15.65
$\text{SO}_3$	0.79	0.15	0.14	0.14	0.14
$\text{K}_2\text{O}$	1.24	0.69	0.63	0.55	0.61
$\text{Na}_2\text{O}$	4.15	0.7	0.51	0.47	0.51
$\text{Cl}$	1.15	0.43	0.16	0.12	0.17

**Table 2:** Chemical composition of the washing residue

$\text{Al}_2\text{O}_3$	$\text{MgO}$	$\text{SO}_3$	$\text{K}_2\text{O}$	$\text{Na}_2\text{O}$	$\text{Cl}$	LOI
5.92	0.14	3.03	5.44	42.54	13.97	29.91

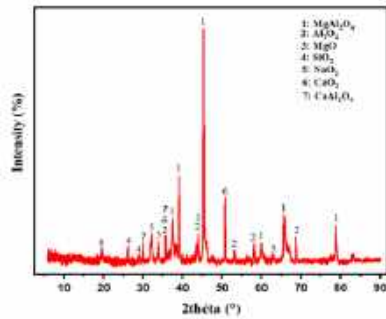


Fig 1: X-ray diffraction pattern of aluminum dross

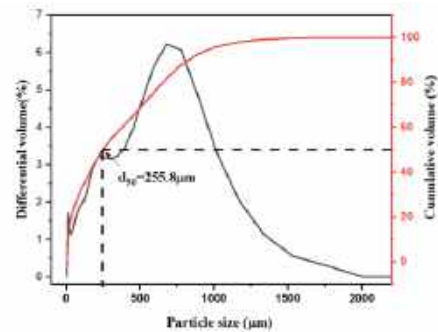


Fig 5: Particle size distribution of aluminium dross

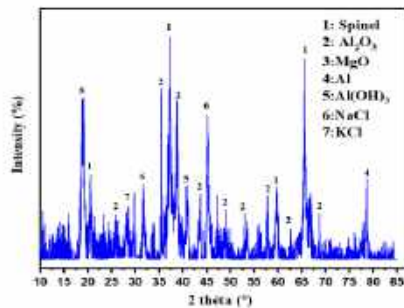


Fig 2: X-ray diffraction pattern of washed aluminum dross

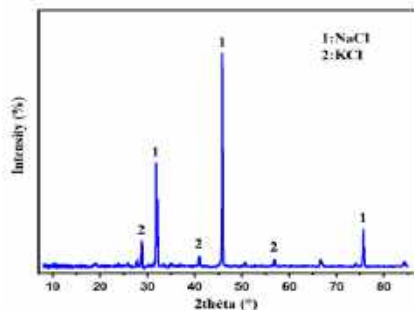


Fig 3: X-ray diffraction pattern of washing residue.

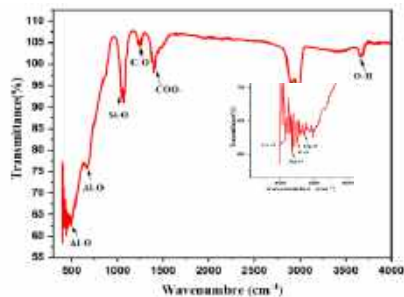


Fig 4: FTIR of Aluminium dross

## II. CONCLUSION

Alumina is the major component (~59.80% in wt.) in used aluminum dross. several other oxides are present at lower quantities, such as mgo (~12.75% wt.), cao (~6.26% wt.), and sio2 (~5.46% wt.). we also note the presence of certain impurities of relatively low content (na2o and fe2o3). after washing by water, xrf showed the improvement of the alumina percentage in the washed dross (~72%) du to the remove of the salts (nacl and kcl) as was suggested by the xrd tests conducted on the washing residue, the second washing at different temperatures improved that optimal washing was at 50 °c (cl ~0.1%, na2o ~0.47 %, k2o ~0.55%). these results demonstrated the importance of washing aluminum dross (2 steps at 50°C each one) to be adopted as previous step in all spinel synthesis experiments.

## REFERENCES

- [1]I.Genesh, int materials review,63-109 (2013).
- [2] Emad M.M. Ewais, Bahgat E.H. El-Anadoul, journal of allos and compounds 691,822-833(2017).
- [3] C. Pacururiu, I.Lazau, Z.Ecsedi, R.Lazau, P.Barvinschi b, G.Margineam, Journal of the Eurorpean Ceramic Society ,707-710 , 27(2007).
- [4] Zhihui Zhang, Nan Li, Ceramics International , 583-589,31 (2005).
- [5] Guotian Ye, George Oprea ,Tom Troczynski ,J.Am.Ceram.Soc, 3241-3244,88 (2005).
- [6] Takeshi Hashishin ,Yasuhiro Kodera, Takeshi Yamamoto, Manshi Ohyanagi, J.Am.Ceram.soc, 496, 87(2004).

# Ni-W Thin Films: Elaboration and Characterization

WISSEM BOUGHOUCHE<sup>1\*</sup>, IMANE ABID<sup>1</sup>, NADA BOUMAZZA<sup>1</sup>, BENATHMANE HALIMA<sup>1</sup>, YAZID MESSAOUDI<sup>1</sup>, HAMZA BELHADJ<sup>2</sup> AND AMOR AZIZI<sup>1</sup>.

1. Laboratoire de Chimie, Ingénierie Moléculaire et Nanostructures, Département de Chimie, Faculté des Sciences, Université Ferhat Abbas Sétif 1, Sétif 19000, Algeria.
2. Unit of Research in Nanosciences and Nanotechnologies (URNN), Center for Development of Advanced Technologies (CDTA), Ferhat Abbas Setif 1 University, Setif 19000, Algeria.

## ABSTRACT

For aim to develop materials for different applications because of the different properties of the Nickel (Ni) that help to up their active surface. We elaborate In this work a serial of electrodes (6 electrodes) of Ni-W thin films at different current density (-100 and -150 mA/cm<sup>2</sup>) and different concentration ratio (1/2, 1/1 and 2/1) by electrodeposition method with three electrodes electrochemical cell (reference electrode: saturated silver chloride (AgAgCl); contre electrode: Platinum (Pt) and work electrodes: copper substrat (Cu)). The obtained samples were characterized by: scanning electron microscopy (SEM), X-ray fluorescence (XRF) and electrochemical impedance spectroscopy (EIS). The morphological, elementary and electrochemical results improve that the sample with a 1/2 molar ratio have the best surface, and the hight active surface area than the 2/1 and 1/1 molar ratio with a values of active surface area (ECSA) is respectively: 164, 127.5 and 126 cm<sup>2</sup> for (-150 mA/cm<sup>2</sup>) and :176.5, 143.5 and 134 cm<sup>2</sup> for (-100 mA/cm<sup>2</sup>).

## KEY WORDS

Alloys Elaboration; Characterization; NiW alloys; Electrodeposition.

## I. INTRODUCTION

As a result of their distinct combination of tribological, magnetic, electrical, and other properties, nickel-tungsten (Ni-W) alloys have attracted more attention in recent years. These alloys have good mechanical qualities, such as high tensile strength and superior exceptional abrasion resistance, high melting point, good oxidation resistance, and high hardness. [1] Applications for Ni-W alloys today and in the future could include barrier layers or capping layers in copper metallization for micro-electromechanical systems (MEMS) or ultra-large-scale integration (ULSI) devices, mold inserts, magnetic heads and relays, bearings, resistors, and electrodes accelerating

environmental hydrogen evolution from alkaline solutions safe alternative to aerospace's harsh chromium plating business, etc. [2]

## II. EXPERIMENTAL

### A. ELABORATION METHOD

In this work, Ni-W electrodes were electrochemically deposited onto the surface of copper using defferent molar ratio of Nickel and tungsten (1/1, 1/1 and 2/1) for different current density (-100 a, and -150 mA/cm<sup>2</sup>); the electrodeposition of Ni-W were performed on a electrochemical work station in three electrodes cel using copper substrat as working electrode a saturated silver chloride as reference electrode and platinum as a counter electrode. The carachtirization are performed in alkaline medium (1M KOH).

### B. RESULTS AND DISCUSSION

Some results of characterization (morphological and composition and electrochemical) related to the best samples are shown in next section.

#### ▪ Scanning electronique microscopy

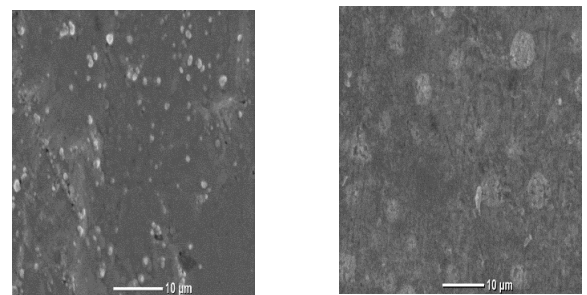


**Fig.1.** SEM images of Ni-W 1/2 ratio elaborated at: 100 mA/cm<sup>2</sup> and -150 mA/cm<sup>2</sup> respectively.



### ▪ Xray fluorescence (XRF)

**Tab.1:** Elementary analysis of Ni-W deposits

Current density	Concentration ratio	Ni % mass	W % mass	Ni at %	W at %
-100 mA/cm <sup>2</sup>	1/2	94.3	5.65	98.12	1.88
-150 mA/cm <sup>2</sup>	1/2	95	4.49	98.51	1.49

### ▪ electrochemical impedance spectroscopy (EIS).

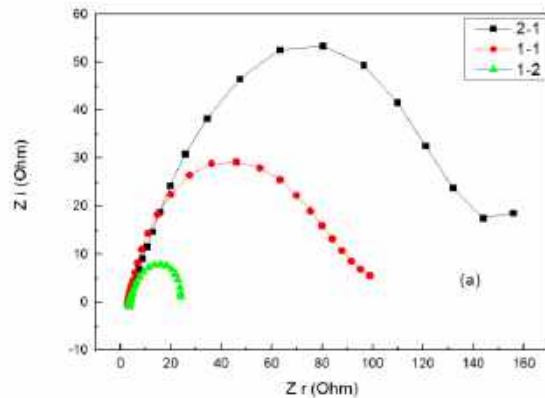


**Fig.2:** Nyquist curve of samples deposited with different concentration ratios at -100mA/cm<sup>2</sup>.

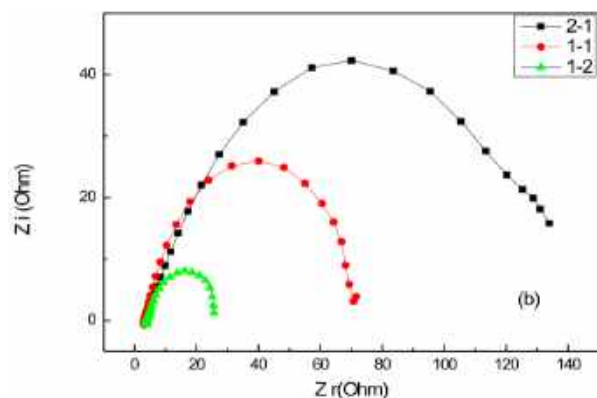


**Fig.3:** Nyquist curve of samples deposited with different concentration ratios at -150mA/cm<sup>2</sup>.

**Tab.2:** active surface area of different Ni-W samples.

Current density	Concentration ratio	Active surface area
-100mA/cm <sup>2</sup>	1/2	176.5
	1/1	134
	2/1	143.5
-150mA/cm <sup>2</sup>	1/2	164
	1/1	126
	2/1	127.5

### III. CONCLUSION

-morphological analysis shows that the increased concentration of tungsten in deposition baths reduces the cracks of deposits.

-the EIS analysis revealed that the HER reaction occurs at a significant speed at a 1/2 ratio

### REFERENCES

- [1] O. Younes, E. Gileadi, Electrochem. Solid-State Lett. 3 (12) (2000)543.
- [2] N.D. Sulit,anu, Mater. Sci. Eng. B 95 (2002) 230.

# ***Session T9: Materials damage and fatigue***

# A new algorithm to optimize the effect of manufacturing errors on the kinematic and dynamic performances of a planar mechanism

Belkadi Noufel<sup>1</sup>, Hosna Abdenour<sup>1</sup>, Djeddou Ferhat<sup>1</sup>, Smata Lakhdar<sup>1</sup>.

<sup>1</sup>Applied Precision Mechanics Laboratory, Institute of Optics and Precision Mechanics, University Setif1, 19000 Setif, Algeria

## ABSTRACT

*Optimization is essential in mechanical engineering problems that mostly are non-linear, depend on mixed decision variables and usually subject to constraints. In real life, the design parameters differ from their theoretical values. This difference is due to the manufacturing errors of mechanism parts. In this paper, a new hybrid approach is proposed to study the effect of manufacturing errors on the kinematic and dynamic performances of a planar mechanism. Furthermore, an analytical method based on the partial derivatives is used to study to determine the mathematical equation representing the kinematic errors of the mechanism. The Lagrangian equation is adopted define the mathematical expression of the mechanism motion. Two objectives are considered regarding the acceleration error and dynamic performance. In the optimization process, a new hybrid algorithm between Particle Swarm Optimization and JAYA is used to achieve better kinematic and dynamic performances of the planar mechanism. Moreover, the obtained results reveal really that the developed algorithm is a promising approach to optimize the effect of manufacturing errors and the used methodology was found to be helpful to achieve optimal kinematic and dynamic behaviour for a planar mechanism.*

## KEY WORDS

Manufacturing errors ; optimization ; PSO algorithm ; JAYA algorithm ; Planar mechanism

## I. INTRODUCTION

The word optimization in mechanical engineering refers to the pursuit of a better solution or better design to certain products or system. On the other hand, there are always difference in values between real and theoretical counterpart's values of mechanism. This difference is mainly due to the manufacturing errors. In many mechanisms, the variation of link dimensions and joint clearance due to manufacturing errors affects the dynamic and kinematic performance of mechanisms. On the other hand, there is a huge need to develop new methods to tackle the synthesis of mechanisms since pit has a significant effect on their performances. In the present work, the kinematic errors (position, velocity and acceleration) due to the error manufacturing of dimension links are

investigated using an analytical method. This technique is based on the partial derivatives of the motion constraint equations. In the first step, the acceleration error is considered as the first objective to minimize the kinematic error and to determine the direction of clearance joints. Secondly, the results obtained from the first step are used to optimize the design parameters of slider-crank mechanism. The second objective is to minimize the effect of manufacturing errors and clearance joints on the dynamic performance of this mechanism. In this step, the Lagrangian function is adopted for modeling the motion of mechanism and optimize the mass distribution of the links in order to reduce the effect of manufacturing errors [1,3]. A new hybrid PSO and JAYA algorithm is used to solve this problem [2].

## II. THE MODEL OF JOINT CLEARANCE

Throughout this study, links of mechanism are assumed to be connected with each other by revolute joints with clearance. This clearance can be defined as the radii difference between the pin and socket (as shown in Fig.1). when considering the assumption of the continuous contact model between pin and socket at the joint, the clearance may be modeled as vectors corresponding to mass-less virtual connection with lengths equal to joint clearance [2]. The virtual joint clearance  $r_c$  (Fig.1) is determined as:  $r_c = r_B - r_j$

## III. CASE STUDY: SLIDER-CRANK MECHANISM WITH JOINT CLEARANCES

In this work, the slider-crank mechanism with two joint clearance ( $\gamma_2, \gamma_3$ ) is taken as a case study (Fig.2).

### A. Optimization of the acceleration error

In this study, the acceleration error of the slider is formulated as an optimization problem and is defined as follows:

$$\text{Minimize } F_1(X_1) = \delta \ddot{x}_{G4} = (C_1 \tan \theta_3 + D_1) \delta l_2 + (C_2 \tan \theta_3 + D_2) \delta l_3$$

### B. Optimization of the dynamic performance of the mechanism

In this section, the dynamic performance of the mechanism is optimized. The mechanism links are assumed to be rigid; as a result, the direction of the clearance vector can be derived using Lagrange's equation [2,3] which is may be given in the following expression:

$$\begin{aligned} \text{Minimize } F_2(X_2) = & \sum_{i=2}^4 \left( I_i \ddot{\theta}_i \frac{\partial \theta_i}{\partial \gamma_j} \right. \\ & + m_i \left( \ddot{x}_{Gi} \frac{\partial x_{Gi}}{\partial \gamma_j} + \ddot{y}_{Gi} \frac{\partial y_{Gi}}{\partial \gamma_j} \right) \\ & \left. + m_i g \frac{\partial y_{Gi}}{\partial \gamma_j} + C_{\theta i} \dot{\theta}_i \frac{\partial \theta_i}{\partial \gamma_j} \right) + C_\gamma \dot{\gamma}_j = 0 \end{aligned}$$

### C. The proposed hybrid method

The hybridization proposed in this method uses both the velocity changing particles of PSO and the best and worst changing population concept of JAYA. One can also say it is an introduction of JAYA rules into PSO in order to help stabilize the optimization algorithm and to avoid falling into local optimum which is a problem we can face using PSO.

## IV. RESULTS AND DISCUSION

Kinematic and dynamic optimization performances of slider mass center are illustrated in Fig.3 and Fig.4.

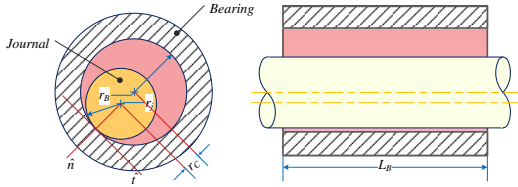


Fig. 1. The model of revolute joint with clearance.

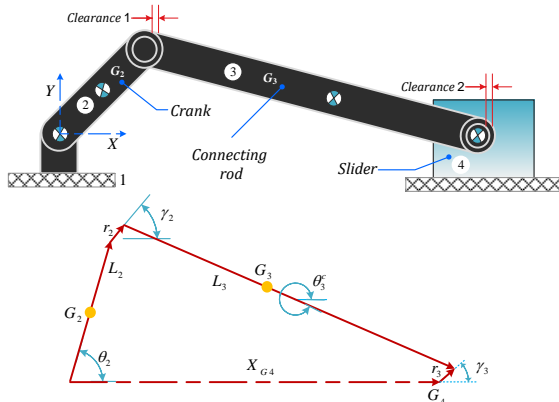


Fig. 2. Slider-crank mechanism with joint clearances.

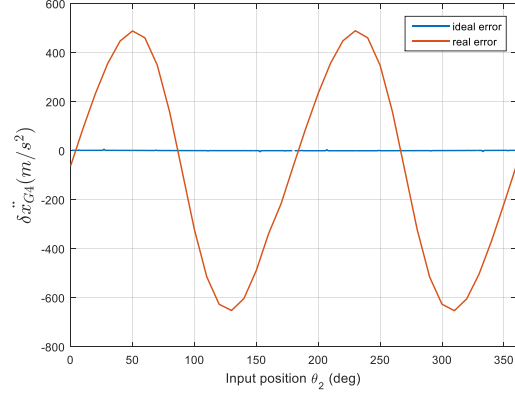


Fig. 3. Ideal and real linear acceleration error of slider.

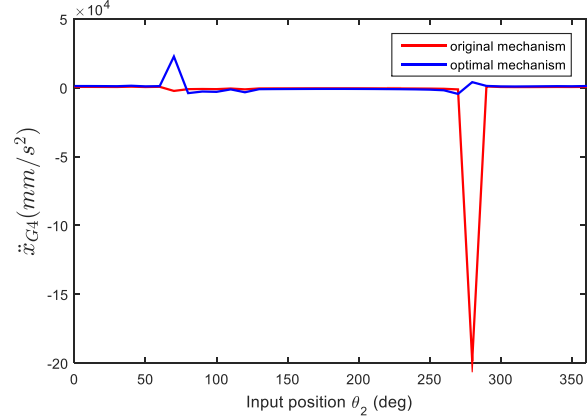


Fig. 4. Angular acceleration of connecting rod.

## V. CONCLUSION

In this study, the effect of manufacturing errors in the kinematic and dynamic performances of a planar mechanism are studied and optimized. furthermore, a new hybrid PSO-JAYA algorithm is developed and used to solve this problem. Finally, the results showed that the optimal parameters of the mechanism offer better kinematical and dynamical performances than the original mechanism.

## REFERENCES

- [1] Belkadi.N et al (2022) Optimization Study of the Effect of Manufacturing Tolerances on the Kinematic and Dynamic Performances of a Planar Mechanism. SAE. Int. J. Mater. Manuf. volume 16, issue1,2023. <https://doi.10.4271/05-16-02-00011>
- [2] Hosna.A et al (2023) A New Hybrid Particle Swarm Optimization and Jaya Algorithm for Optimal Weight Design of a Gear Train. SAE. Int. J. Mater. Manuf. volume 16, issue2,2023. <https://doi.10.4271/05-16-01-0005>
- [3] A.Sardashti, H.M.Daniali, S.M.Varedi(2013) Optimal free-defect synthesis of four-bar linkage with joint clearance using PSO algorithm. Meccanica 48:1681-1693. <https://DOI.10.1007/s11012-013-9699-6>

# Electron-impact ionization of Argon 3p

BECHANE KAWTHER<sup>1</sup>

1. LPQSD, Department of Physics, Faculty of Sciences, University Sétif1, Sétif 19000, Algeria,  
bechanekawther34@gmail.com

## ABSTRACT

*Ionization of atoms by electron impact is part of basic research which enables to study the importance of fundamental interactions. Triple differential cross sections (TDCSs) are presented for the electron impact ionization of a 3p shell of argon, using a new model called (3CWZ). Within this model, the projectile as well as the ejected electrons are represented by variable charges  $Z(r)$  instead of an effective charge, the post collision interaction (PCI) is also included. Our results are compared with recent experiments and other theoretical predictions in a range of several kinematics.*

**KEY WORDS** (Ionization, electron, cross section, post collision interaction, variable charge)

## I. INTRODUCTION

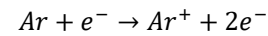
Electron impact ionization of atoms and molecules represent theoretically a few body problems. The triple differential cross section (TDCS) represents a rigorous test for the most efficient models, the (TDCS) measured in (e,2e) experiments provides the probability that the scattered and ejected electrons are selected in energy and direction and detected in coincidence. In the present work we introduce an improved theoretical approach to describe the (e,2e) reaction for atoms, it is in fact an extension of our earlier studies which provided rather good agreement between experiment and theory, The present theoretical description is a fully quantum mechanical approach, it is actually a kind of (BBK). We present a new model to study the dynamics of electron impact ionization of atoms called (3CWZ).

## II. THEORY

In the (BBK) model the ejected and the scattered electrons are both represented by Coulomb waves with an effective charge ( $Z=1$ ), the post collision interaction (PCI) is introduced and treated exactly

to all orders, while the incident electron is described by a plane wave.

In the (3CWZ) model the three electrons ejected, scattered and incident are described by Coulomb wave with a variable charge  $Z(r)$ , in this work we take into account the exchange effects. The electron impact ionization of argon atoms in its ground state is schematized as:



### A. OBJECTIVES

The object of this work concerns the use of this variable charge scheme, which somehow represents a full approximate distorted wave model (a kind of a (3DW) model), and check how this will affect the (TDCS) in the (e,2e) reaction of argon 3p. The model is called (3CWZ), the obtained results within this model are compared with experiments and other theories like the (BBK2CWZ) model [3] (BBK2CWZ) model is improved by representing both outgoing electrons with a Coulomb wave with a variable charge, while the incident electron is described by a plane wave).

### B. RESULT

(TDCS) for the ionization of Ar 3p as a function of the ejection angle at fixed scattering and ejected energies  $E_a = 500$  eV and  $E_b = 205$  eV. The projectile is scattered at a fixed scattering angle  $\theta_1 = 3^\circ$ . Theoretical results are blue solid line (3CWZ), red solid line (BBK2CWZ). The experimental data are black squares taken from [1], as shown in Fig1.

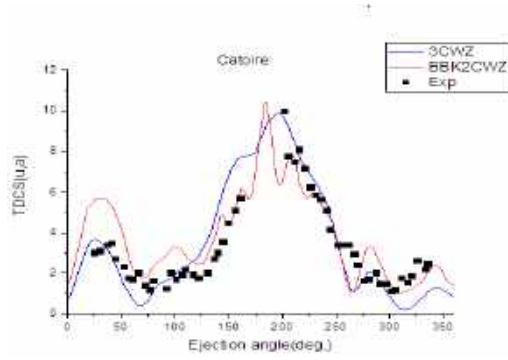


Fig. 1.(TDCS) for the ionization of Ar 3p as a function of the ejection angle.

### C. RESULT2

Absolute (TDCS) for the ionization of Ar 3p as a function of the ejection angle at fixed scattering angle  $\theta_1=15^\circ$ . The incident and ejected electrons have respective energies  $E_0=200\text{ev}$  and  $E_b=10\text{ev}$ . Theoretical results are blue solid line (3CWZ), red dash line (3DW). The experimental data are black squares taken from [3], as shown in Fig2.

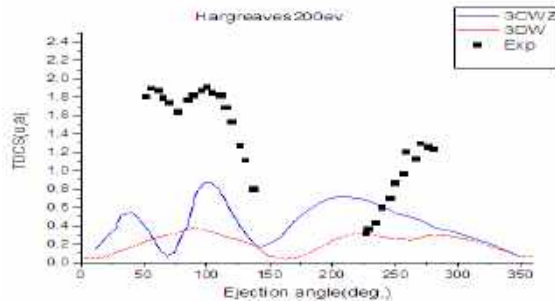


Fig. 2. (TDCS) for the ionization of Ar 3p as a function of the ejection angle.

## III. CONCLUSION

In this work, an (e,2e) theoretical study of Ar 3p has been used to investigate the (e,2e) ionization reaction in several kinematics.

-In a first step (3CWZ) results turned out to be in good agreement with the experimental data better than (BBK2CWZ).

-In a second step we can state that (3CWZ) model doesn't describe correctly the experimental data but reproduces qualitatively the shape of the (TDCS), while (3DW) predict nearly the same shape.

## REFERENCES

- [1] F. Catoire, E. M. Staicu-Casagrande, M. Nekkab, C. Dal Cappello, K. Bartschat and A. Lahmam-Bennani, J. Phys. B 39, 2827 (2006).
- [2] R. L. Hargreaves, M. A. Stevenson and B Lohmann, J. Phys.B 43, 205202 (2010).
- [3] Attia M, Houamer S, Khatir T, Bechane K and Dal Cappello C J.phys.B 56 075201 (2023).



# Acoustic Environment Analysis for Launch Vehicles and Satellite Impacts

MOHAMMED AMINE ZAFRANE<sup>1\*</sup>, ABES BACHIR<sup>2</sup>, AND AHMED TAHIR<sup>3</sup>

1. Signal, Data and System Laboratory, Department of electronic, University of Science and Technologies of Oran- Algeria. email: [amine.eln@hotmail.com](mailto:amine.eln@hotmail.com)
2. Department of mechanic, University of Science and Technologies of Oran- Algeria. email: [bachir-gm@hotmail.com](mailto:bachir-gm@hotmail.com)
3. Signal, Data and System Laboratory, Department of electronic, University of Science and Technologies of Oran- Algeria. email: [tahiroahmed@yahoo.fr](mailto:tahiroahmed@yahoo.fr)

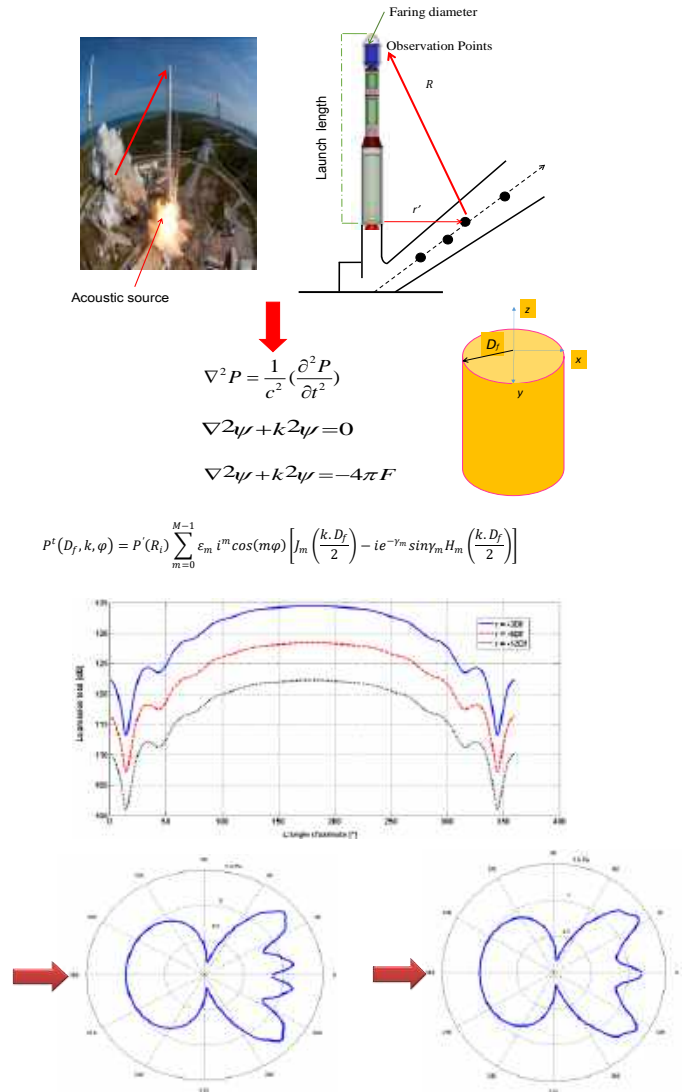
## ABSTRACT

During a spaceflight mission, the spacecraft faces intense external pressure fluctuations as its rocket propulsion system operates within the Earth's atmosphere. These pressure variations, acoustic in nature, originate from the broad-spectrum acoustic field produced by the interaction of the rocket exhaust stream with the surrounding air. This acoustic loading serves as the primary source of structural vibrations and internal noise during the launch phase, impacting both the launcher's components and its valuable payload, such as satellites.

The interplay between acoustic waves and the launcher's structure can induce vibrations that propagate to the satellite integrated within the payload fairing. This phenomenon is characterized by the concept of acoustic coupling between the satellite and the launcher. The objective of this study is to progressively develop a mathematical model for sound propagation based on the wave equation. It involves evaluating the total acoustic spectrum, encompassing incident and reflected waves, and analyzing the distribution concerning the propagation distance. This research aims to enhance our understanding of the complex interaction between acoustics and the structural dynamics of launch vehicles, with implications for optimizing spacecraft design and reliability.

**KEY WORDS:** SATELLITE, LAUNCH VEHICLE, ACOUSTIC, PROPAGATION AND FAIRING.

## GRAPHICAL ABSTRACT



# Investigation on solid particle erosion behavior of jute fiber reinforced polyester composite

LAOUAMRI H.<sup>1</sup>, MOUHOUBI S.<sup>1,2</sup>, FOURA C.<sup>1</sup>

<sup>1</sup>Laboratory of Non-Metallic Materials, Institute of Optics and Precision Mechanics University Ferhat Abbas Setif 1- 19000, Algeria.

<sup>2</sup>Emerging Materials Research Unit (URMES), University Ferhat Abbas Sétif 1, 19000, Algeria

Corresponding author: [hlaouamri@gmail.com](mailto:hlaouamri@gmail.com)

## ABSTRACT

In this study, the solid particle erosion behaviour of jute fiber reinforced polyester composite has been characterized at different impingement angles (30, 60 and 90°). The particles used for the erosion measurements were natural sand with diameter fraction of ( $\phi < 400 \mu\text{m}$ ), and impact velocity of 30 m/s. The studied composite showed fragile erosion behaviour, with maximum erosion rate at 90° impingement angle. The projected sand mass had a significant influence on erosion. The morphology of eroded surfaces was examined by using optical microscopy.

## KEY WORDS

Solid particle erosion, fiber reinforced composites, impingement angle, optical microscopy.....

## I. INTRODUCTION

Solid particle erosion is a common material degradation mechanism encountered in a number of structural and engineering components. Polymers and their composites have generated wide interest in various engineering fields; they acquire a significant place when it comes to operating in a dusty environment where resistance to erosion becomes an important feature [1].

Generally the erosion wear of Fiber Reinforced Polymers (FRP) caused by the surface impact of hard particles is a complex phenomenon, controlled by the type of fiber, the composition, the nature of the erodent and the impingement conditions [2].

Erosion wear behavior can be grouped as ductile and brittle categories although this grouping is not definitive. Thermoplastic matrix composites usually show ductile erosion while the thermosetting ones erode in a brittle manner. However, there is a dispute about this failure classification as the erosive wear behavior depends strongly on the experimental

conditions and the composition of the target material [3]. The aim of this work is to determine the solid particle erosion behaviour of jute fiber reinforced polyester composite.

## II. MATERIALS AND METHODS

### A. COMPOSITE MANUFACTURING

Laminates of jute fiber reinforced polyester composite were prepared by hand lay-up technique. In this case, jute fabric with a surface weight of 430 g/m<sup>2</sup> was used as reinforcement in our composite. The jute fabric plies were soaked in water, then hot-pressed at 110°C, under a pressure of 18KN for 2 minutes. The aim of hot-pressing fabric is to reduce its thickness, thereby increasing the volume fraction of reinforcement in the composite.

The laminate was stacked ply by ply, while each layer was impregnated with 2% accelerated and catalyzed polyester resin. Cross-linking of the laminate took place inside a vacuum chamber. The composite plate was unmolded after approximately 8 hours.

### B. EROSION TEST

The solid particle erosion test experiments were carried out using a horizontal jet impingement system as recommended by the standards for airborne particles erosion testing (ASTM G76-95). It consists in exposing the samples to a projection of erodent particles. In this study, the flux rate and velocity were kept constant to 1.25 g/s and 30 m/s respectively, the distance from the nozzle to the sample  $D = 80 \text{ mm}$ . The projected sand mass  $M = 1400 \text{ g}$ . The variable parameter was the impact angle  $\alpha$  (30, 60 and 90°); these angles were selected to evaluate the composite material at low and high incident angles. The eroding material used in this study was natural sand coming from Algerian desert with diameter fractions of ( $\phi < 400 \mu\text{m}$ ). The erosion test was carried out at room temperature.

The erosion rate  $E_r$ , defined as the ratio of material mass loss against the mass of the projected erodent particles, was determined by weighing the samples before and after sandblasting. A precision electrical balance type (Ohaus) was used with accuracy of  $\pm 0.1$  mg.

To characterize the morphology of the eroded composites and to understand the mechanism of material removal, the eroded samples were observed using an optical microscopy (Oxion-Euromex).

### III. RESULTS AND DISCUSSION

Figure 1 shows the evolution of erosion rate of jute fiber reinforced composite depending on the impact angle for a projected sand mass of 1400 g.

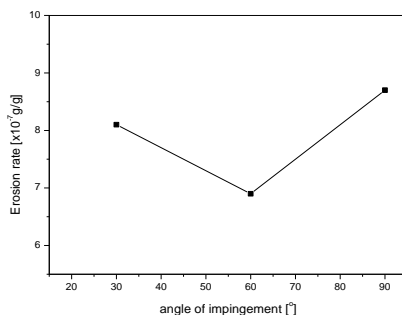


**Figure 1:** Erosion rate evolution with impact angle.

The results indicate that the maximum erosion rate occurs at normal impact ( $\alpha=90^\circ$ ), this reveals the composites brittle nature. It has been shown in the literature that  $30^\circ$ – $45^\circ$  impingement angles had maximum erosion rate in all types of jute/polyester fiber reinforced composites [4]. Another researcher reported that the erosion behavior of multi-fiber reinforced polyester is regarded as semi-ductile, with maximum erosion rate at  $60^\circ$  [5]. The differences in the erosion behavior of the composites can be attributed to the experimental conditions and the composition of target materials. It is well known that in the phenomenon of erosion, the combined reaction of many control components influences the responses.

The morphology of eroded surfaces is presented in figure 3. The micrograph (3. a) shows local removal of polyester material from the impacted surface resulting in exposure of the fibers to the erodent particles. It is clear that erosion damage occurs mainly because of matrix removal, breaking of fiber (3. c) and fiber matrix debonding (3. d).

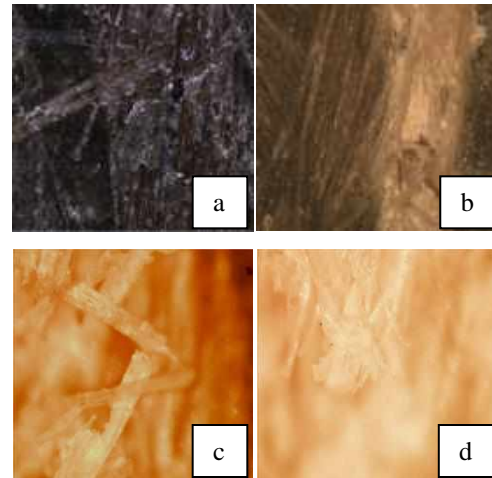


**Figure 3:** Micrographs of eroded surfaces of jute fiber reinforced polyester at  $90^\circ$  impact angle.

### IV. CONCLUSION

Based on this experimental investigation into the erosion behavior of jute fiber reinforced polyester composite, the conclusions can be summarized as follows:

- The studied composite showed fragile erosion behaviour, with maximum erosion rate at  $90^\circ$  impingement angle.
- The morphologies of eroded surfaces clear that erosion damage occurs mainly because of matrix removal, breaking of fiber and removal from the matrix.

### REFERENCES

- [1] Ritesh Kaundal, Role of Process Variables on the Solid Particle Erosion of Polymer Composites: A Critical Review, *Silicon* (2014) 6:5–20.
- [2] Suresh Kumar Shanmugam, et al., Solid Particle Erosion Studies of Varying Tow-Scale Carbon Fibre Reinforced Polymer Composites, *Materials* 2022, 15, 7534.
- [3] Amar Patnaik, et al., Effect of Particulate Fillers on Erosion Wear of Glass Polyester Composites: A Comparative Study using Taguchi Approach, *Malaysian Polymer Journal*, Vol. 5, No. 2, p 49-68, 2010.
- [4] Sangilimuthukumar Jeyaguru, et al., Solid particle erosion, water absorption and thickness swelling behavior of intra ply Kevlar/PALF fiber epoxy hybrid composites, *Polymer Composites*. 2022; 1–15.
- [5] U K Debnath, et al., Erosive wear characteristics of multi-fiber reinforced polyester under different operating conditions, *IOP Conf. Series: Materials Science and Engineering* 114 (2016) 012113.

# Damage behaviour of polyurethane foam-cored sandwich panel subjected to localized indentation

ARIANE KHALISSA<sup>1\*</sup> AND KESKES BOUALEM<sup>1</sup>

1. Applied Precision Mechanics Laboratory, Institute of Optics and Precision Mechanics, Ferhat Abbas University Setif 1, Setif, Algeria

[khalissa.ariane@univ-setif.dz](mailto:khalissa.ariane@univ-setif.dz)

## ABSTRACT

*This paper investigated the indentation behaviour of sandwich panels with polyurethane foam-cored. Samples of size 80 mm × 80 mm were cut from the panels and subjected to low-velocity indentation loading using a standard 50 KN Zwick/Roell servo-hydraulic testing machine. Different head shapes indenters were used (spherical, conical and cylindrical). The different specimens exhibited similar load/displacement curves and the differences observed were due to the behaviour of the different materials and the head shape of different indenters. The results indicate that localized structural damage behaviour varies with indenter head shape and foam-core height.*

## KEY WORDS

Sandwich panel; Quasi-static test; Indentation behaviour; Foam core.

## I. INTRODUCTION

Sandwich panel is a kind of simple artificial hierarchical structure, characterized by a relatively soft but thick core sandwiched between two thin and stiff face-sheets. Face-sheet play a key role in maintaining in-plane and bending loads, while the core resists shear and lateral compression, enhances the bending stiffness and energy absorbed ability of the composite structures [1]. It is challenging to improve the impact resistance while maintaining the required mechanical performance under quasi-static and dynamic loadings. The low-velocity indentation is an interesting research topic, which focuses on localised damage to the skin sheets and core.

Recently, many researchers have investigated the indentation resistance of composite sandwich panels with different core geometries under low-velocity impact. Wang et al. investigated the medium velocity impact response of sandwich panels with low-density balsa wood, cork, polypropylene honeycomb, and

polystyrene foam cores [2]. It was obtained that the polystyrene foam core performed better penetration resistance. Furthermore, Sun et al. investigated the impact mechanisms of sandwich panels with homogenous and sequentially graded foam cores subjected to low-velocity impacts [3]. It was reported that the density gradient of graded foam cores significantly influenced the impact deformation of the core structure.

This work predicted the indentation resistance of the polyurethane foam-cored sandwich panels with different high under low-velocity loading using different head shape indenters.

## II. EXPERIMENTAL PROCEDURE

### A. SANDWICH PANEL SPECIMEN

The sandwich panels are composed of galvanized steel facesheets and Polyurethane form core with an in-plane dimension of 80 mm × 80 mm. The face-sheets were 1 mm thick while the cores were of different thicknesses (30, 40 and 50 mm).

### B. INDENTATION TEST

In order to investigate the mechanical behaviour of sandwich structures exposed to localized point loads, indentation tests were performed. The sandwich panel specimens were supported by a steel substrate, thus the overall bending on the specimen was avoided. The tests were carried out in a standard 50 KN Zwick/Roell servo-hydraulic testing machine under displacement control at a loading rate of 1 mm/min to obtain a quasi-static test (Fig. 1).

The indentation load was applied through several head shape indenters: conical, cylindrical and hemispherical with a radius of 16 mm, but with the same overall diameter; 30 mm.

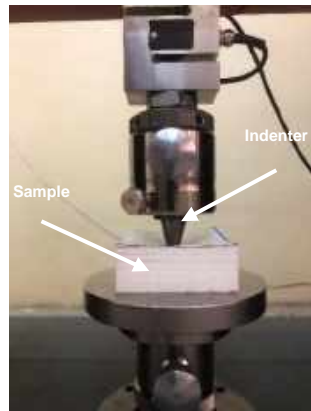


Fig. 1. Indentation test set up

### III. RESULTS AND DISCUSSIONS

Fig. 2 shows load-displacement curves using conical hemispherical and cylindrical indenters for different samples' thickness (30, 40 and 50 mm).

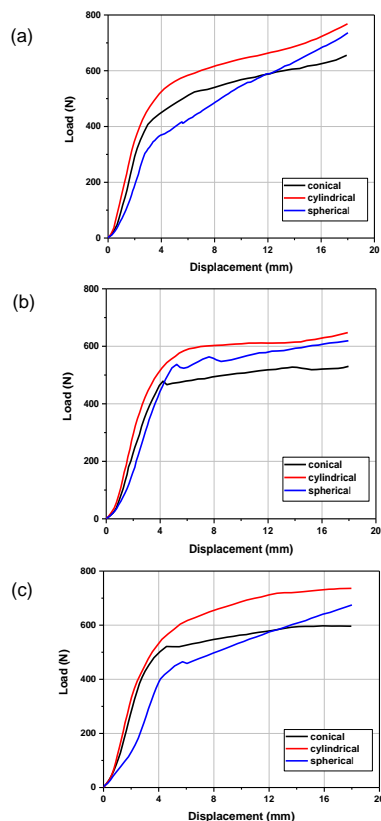


Fig. 2. Load-displacement curves using several indenters for different thicknesses: (a) 30 mm, (b) 40 mm and (c) 50 mm.

The phenomena occurring during the indentation event clearly show the load undergoes an initial linear trend with the displacement attributable to the continuous deformation of the face sheet, until the indenter reaches a penetration of 4-5 mm. We observe that after

the elastic phase, in which the sandwich panel undergoes elastic deformation; the linear growth phase, in which plastic deformation occurs, in which the contact force remained approximately constant. Because the front face-sheet is not broken, the indentation energy is mainly absorbed by the plastic deformation of the front face-sheet and sandwich core, and the deformation is mainly concentrated in the local area of the front face-sheet and foam core in contact with the indenter.

The slope of the loading part of the force-displacement curve, which represents the bending stiffness of the panels, is higher for the cylindrical indenter.

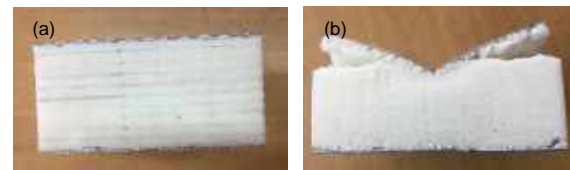


Fig. 3. Sample of 30 mm thickness: (a) before and (b) after the indentation test (conical indenter)

The post indentation visual inspections of several tested sandwich panels are illustrated in Fig. 3. During the tests, the sample took the same shape as the surface of the indenter. Moreover, indentation of the upper facesheet are observed; also, there is no visible damage on the bottom facesheet.

The panel of 30 mm of thickness behaves in a more rigid manner than the other panels, and the damage of the facesheet is lower.

### IV. CONCLUSION

An experimental study on the indentation response of foam core sandwich panels subjected to low velocity impact is performed. The results indicate that localized structural damage behavior varies with indenter head shape and foam-core height.

### REFERENCES

- [1] Q.-W. Li and B.-H. Sun, "Numerical analysis of low-speed impact response of sandwich panels with bio-inspired diagonal-enhanced square honeycomb core", *International Journal of Impact Engineering* 173 (2023) 104430.
- [2] Hongxu Wang, Karthik Ram Ramakrishnan and Krishna Shankar, "Experimental study of the medium velocity impact response of sandwich panels with different cores *Materials and Design*", 99 (2016) 68–82.
- [3] G. Sun, E. Wang, H. Wang, Z. Xiao, Q. Li, "Low-velocity impact behaviour of sandwich panels with homogeneous and stepwise graded foam cores", *Mater. Des.*, 160 (2018), pp. 1117-1136.



# Effect of variation in stiffener shape on panel behavior under dynamic loading

IKRAM KADRI\*, KHAMIS HADJAZI\*, OUDJDANE BAHAR\*, KHAOULA BOURAS\*, MOHAMMED EL ARBI BENNEGADI\*

\*University of Science and Technology 'USTO MB', Oran, Marine Engineering Departement

[kadrikram@gmail.com](mailto:kadrikram@gmail.com)

[khamishadj@yahoo.fr](mailto:khamishadj@yahoo.fr)

[oudjdane.98@gmail.com](mailto:oudjdane.98@gmail.com)

[bouraskhaoula32@gmail.com](mailto:bouraskhaoula32@gmail.com)

[larbi-68@hotmail.com](mailto:larbi-68@hotmail.com)

## ABSTRACT

*Determination and evaluation of all the stresses in a ship's stiffened hull caused by hydrodynamic forces has a major influence on the service life and operation of our structure. In the present work, a numerical simulation using the finite element method and the calculation code workbench was carried out on stiffened panels subjected to a dynamic load. This study enabled us to solve this type of problem and to follow the evolution of stress concentration and deformation along the planking. In the course of our study, we investigated the effect of varying the shape of the stiffness of our stiffened planking.*

## KEY WORDS

Deformation; stiffened plate; equivalent stress ; Dynamic load

## I. INTRODUCTION

However, the use of a large non-stiffened plate is rarely used in practice, as it is too sensitive to instability phenomena. On the other hand, adding stiffeners contributes substantially to the structure's strength and stability. Depending on the relative stiffness of the stiffeners with respect to the plate, a stiffened plate can warp in several ways. Several analytical, numerical and experimental studies have been carried out to study these assemblies, analyze their failure modes and improve their structural efficiency [2-3]. Phillips and al have attempted to quantify the damage between the omega stiffener and the base plate in an FRP naval structure. Another work was done by adrien and al [1] to predict the load and displacement at failure of a self-stiffened

composite panel with integrated structure, during a post-buckling test. A phenomenological and quantitative study is presente.

## II. SAMPLING REINFORCED PANELS

### A. MAIN GEOMETRIC FEATURES.

stiffened plate	Dimensions (mm)
Plate length (L)	800
Plate width (W)	280
Plate thickness (ep)	10
Spacing (E0)	600
Stiffener thickness (er)	11
Stiffener web height (H)	20

**Tabl.1.** Geometric properties of the project stiffened panel.

### B. NUMERICAL MODEL

Numerical modeling using ansys Workbench is carried out on a thin steel plate reinforced with two transverse stiffeners.

In our study, the numerical model is constrained according to a dynamic load that reproduces a load on the stiffeners. A surface load in the longitudinal direction is placed on the upper surface of the sheet.



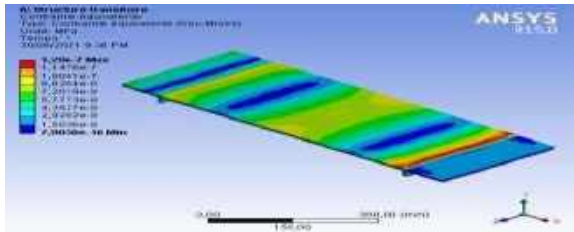


Fig. 1. Variation in equivalent von-mises stress along the panel.

### III. PARAMETRIC STUDY

#### ✓ Load effect

Figure 2 represents the variation of the stress as a function of the variation of the time of passage of the dynamic load (the position of the load), at the level of the neutral line of the stiffened sheet for different intensity of the dynamic load. Firstly, due to the geometric symmetry of the problem we can clearly visualize that the evolution of the three parameters studied admits a plane of symmetry with respect to the longitudinal plane.

From (figure 2), it clearly appears that the variation in the intensity of the load has a considerable effect on the evolution of the deformation and the equivalent stress along the stiffened panel where it admits maximum values between. On the other hand, at the level of stiffening, they take low values due to the increase in the rigidity of the sheet metal in this zone. Going towards the two ends, the deformation and the equivalent stress are zero due to the fixing conditions.

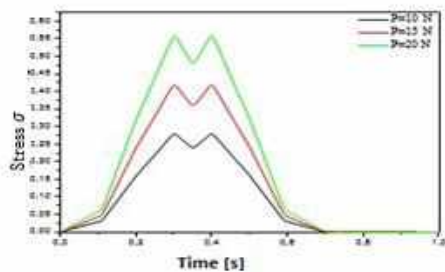


Fig. 2. Variation of von-mises equivalent stress as a function of time.

#### ✓ Effect of variation in stiffener shape

To better quantify transverse displacement, deformation and equivalent stress, three types of stiffening (flat, L-shaped and omega) were compared. This comparison was carried out while maintaining the same volume for all three sections.

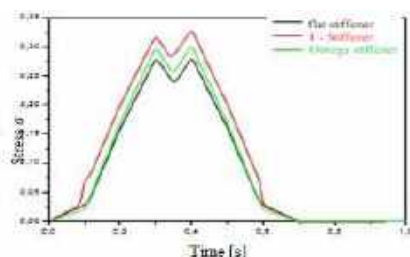


Fig. 3. Variation of von-mises equivalent stress as a function of time.

In Figure 3 we represent the variation of the equivalent stress in the stiffening plate assembly as a function of the variation in the time of movement of the dynamic load. This figure clearly shows that the evolution of the three parameters studied is influenced by the variation in the type of stiffening. Furthermore, varying the type of stiffening dampens the equivalent stress and reduces the displacement and deformation along the stiffened structure. This results in the fact that moment of inertia of the flat profile is greater than that of the other two profiles (because a large part of the load is absorbed by the profile), for this the use of the flat profile increases the rigidity of the reinforced structure.

### IV. CONCLUSION

In this work, a numerical simulation of the behavior of a stiffened steel panel was carried out using the ANSYS Workbench software. The concentration of stresses at the stiffeners and the different parts of the panel can cause breakage or damage to the structure. In fact, this work aims to highlight the parameters which influence the rigidity and resistance of the panels.

To visualize the behavior of the stiffened structure, we gradually varied the intensity of the dynamic load applied to the panel to estimate the evolution of the displacement, the deformation and the equivalent stress along the panel. The increase in load allowed us to quantify the displacement, deformation and equivalent stress. In order to remedy this type of problem, stiffeners (flat, L-shaped, Omega-shaped) can be placed in order to absorb the greatest stress causing the deformation of the panels

### REFERENCES

- [1] H.J. Phillips, R.A. Sheno, C.E. Moss, Damage mechanics of top-hat stiffeners used in FRP ship construction Marine Structures 12 (1999) 1}19.
- [2] J.I.BLACK, R.A. SHENOI et AL, Strength modelling in stiffened FRP structures with viscoelastic inserts for ocean structures, university of Southampton, 2001, SO17 IBJ, UK.
- [3] P Davies, D Choqueuse, B Bigourdan, C Gauthier, Joannic, P Parneix and J L'Hostis, Design, manufacture and testing of stiffened panels for marine structures using adhesively bonded paltruded sections, Infermer Materials and Structures Group, PlouZané, France.

# Validation of a mathematical model for fatigue-induced damage in composite sandwich structures

AHCENE OUBOUZID<sup>1\*</sup>, BOUALEM KESKES<sup>1</sup>, BENOIT VIELLE<sup>2</sup>

1. Laboratory of Applied Precision Mechanics (LMPA), Institute of Optics and Precision Mechanics (IOMP), Ferhat Abbas University Setif-1, Algeria
2. Group of Materials Physics (GPM) – National Institute of Applied Sciences (INSA), France

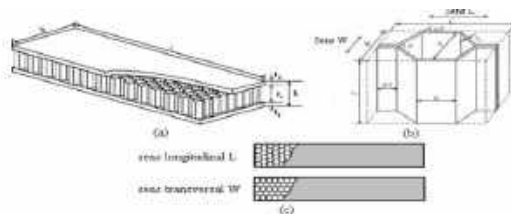
## ABSTRACT:

*An experimental methodology to study the damaging behavior in fatigue under repeated impacts of sandwich panels combining aluminum skins and a Nomex<sup>TM</sup> or aluminum honeycomb core is proposed. First, low-energy impacts were imposed using an original cyclic impact machine developed in the laboratory. In order to assess the severity of the damage induced by the impacts on the structural capacities of the material, 3-point bending tests were carried out to quantify the residual bending stiffness. 3D optical microscope observations of the impacted samples made it possible to evaluate the profile and extent of the impact zone, which is correlated with the reduction in bending stiffness. This methodology was implemented on sandwich composites with different values of core density in order to analyze the influence of density on a damage parameter  $S$ . In a second step, the results of the tests carried out were confronted with the model developed by Oubouzi et al [1]. This model makes it possible to satisfactorily predict the evolution of the damage parameter  $D$  as a function of the number of impact cycles.*

**KEYWORDS:** honeycomb sandwiches, cyclic impact, buckling stress damage parameter, bending tests

## EXPERIMENTAL MATERIALS AND PROCEDURE

**Description of the material** The two types of honeycomb core sandwich materials used in this study are aluminum-aluminum (Alu-alu, ECM Fs270) and aluminum-aramid fibers (alu-Nomex, ECA Fs 274), (Fig. 1)



The structure of the two types of sandwich is made up of two-dimensional cells placed in the sandwich plane whose skins are made of Aluminum (AlMg3). The honeycomb cores are either made of aluminum (82 kg/m<sup>3</sup>) of density or in Nomex aramid fibers (80 kg/m<sup>3</sup>) density. The specimens intended for the test (fig.3a) were cut using a water jet machine from sandwich plates with a surface area of 50x50x1c m<sup>3</sup>. The specimens used for the cyclic impact test have a length of 120 mm, a width of 90 mm and a thickness  $h$  of 10 mm. The thickness of the  $t_c$  core is 8.8 mm (table 1).

Table .1 Geometric parameters of the specimens used in this study

$l$ (mm)	$b$ [mm]	$h$ [mm]	$t_c$ [mm]	$t_f$ [mm]	$d = t_c + t_f$ [mm]
150	125	10	8.80	0.60	9.40

The structural parameters of such a sandwich honeycomb composite for the repeated impact test. The number of samples is 12 for the Nomex<sup>TM</sup> core density of 80 kg/m<sup>3</sup>, and 11 samples for the aluminum core density of 82 kg/m<sup>3</sup>. The mechanical properties of the sandwich composites are given in Tables 2-3.

Table.2 Mechanical properties of skins (AlMg3 (AA5754)).

Young's Modulus (MPa)	Failure strength (MPa)	Tensile strength (MPa)	Maximum elongation (%)
70.000	268	367	13

Table .3 Mechanical properties of aramid fiber core (Nomex<sup>TM</sup>)

Matériau : Aluminium-Aluminium	ECA core in Nomex	ECM cœur en Aluminium
Cœur ECA-ECM	F274	F270
Densité du Cœur [kg/m <sup>3</sup> ]	80	82
Taille de cellule [mm]	9.6	9.6
Épaisseur de la paroi cellulaire [mm]	0.076	0.08
Résistance à la compression [MPa]	2.75	4.5

## REPEATED IMPACT TESTS

The literature review showed that very few authors have studied the repeated impact behavior of honeycomb sandwich structures; the main reason is probably the lack of test standardization for this type of test. There are very few testing machines capable of subjecting samples of composite materials to repeated impacts at low speed. In addition, each study on this subject uses a specific device making it difficult to compare results without running into the problem of reliability of experimental techniques. In order to analyze the influence of low energy impact fatigue on the fracture behavior of honeycomb sandwich structures, a repeated impact testing device (Fig.2) Our fatigue bench is based on a connecting rod-crank system, which transforms a continuous rotational movement into an alternating translational movement, and which makes it possible to provide cyclical impacts. This system is driven by an asynchronous motor. The variation which allows you to modify the frequency of impacts (up to 15Hz) using a frequency variator, the projectile speed and therefore the impact force. The rotational movement transmitted from the driving shaft (1) is transmitted by the driving pulley (2) to a receiving pulley (3) via a belt (4), the movement received at the receiving pulley turns the crank (5). A connecting rod (6) is fixed on the crank with a maximum eccentricity of 45mm (eccentricity distance adjustable depending on the stroke of the impactor). The connecting rod-crank system (5,6) transmits the reciprocating translation movement back and forth to the fork (7). The latter ensures the repeated translation of the projectile cylinder (9) with a hemispherical head (8). For each cycle the impactor (8, 9) strikes or impacts the sandwich composite plate embedded in the sample holder (11). projectile cylinder (9) is guided in

translation by two ball bushings (10).

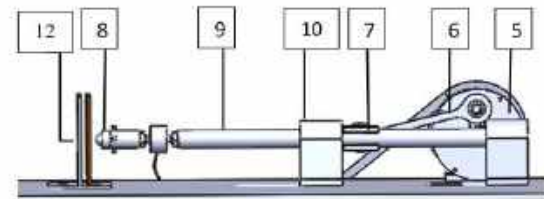
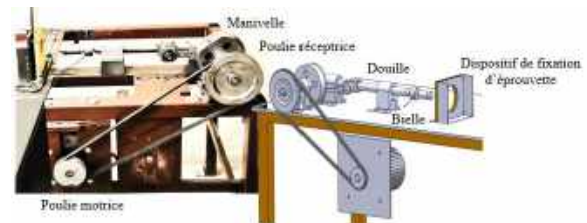


Figure 2: Experimental setup of the repeated impact test

The number of impacts is defined by a cycle counter. The honeycomb sandwich plates are held in position in the impact fatigue machine using a specific clamping system. In order to measure the residual stiffness after impact on different plates, the clamping system is mounted on a universal testing machine. During the test, the impact energy was calculated from the kinetic energy as follows:  $E = \frac{1}{2} M v^2$  where M and v are respectively the mass of the impactor and the translation speed measured before the impact. A frequency meter allows you to regulate the rotation speed of the motor and then determine the desired impact speed. Repeated impact tests are interrupted at regular time intervals to perform three-point bending tests on damaged plates. The loading frequency was maintained at 5.25 Hz corresponding to a rotation speed of the crank rod of approximately 315 rpm. The translation speed is 0.65 m/s. As a result, the impact energy is equal to 0.177J.

## RESIDUAL PROPERTIES AFTER IMPACT

Impact-induced damage results in changes in the slope of the load-displacement curve. Before and after the impact-fatigue period, measurements of the plates were carried out with a Zwick/Roell type Z100 tensile

testing machine (Fig.5)

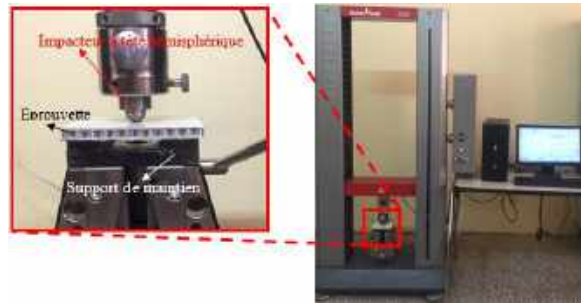


Figure 5: Three-point bending device mounted on a tensile testing machine.

at a crosshead speed of 1 mm/min. The load is applied using a 20 mm steel cylinder equipped with a hemispherical indenter. The plate is fixed on two edges in the same clamping system as that used for the impact fatigue test. The deflection of the specimen was measured using an LVDT (Linear Variable Differential Transformer) transducer connected between the testing machine frame and the hydraulic actuator head. For each test, the load-displacement curve was recorded.

This allows us to determine a damage indicator in impact experiments defined by the ratio between current loads and the corresponding displacement measured from three-point bending tests [36]. The residual stiffness  $R_i$  ( $i=1, \dots, N$ ) of the specimen in bending is determined from the load-displacement curves, using the ratio of the load applied to the corresponding displacement (Eq.2) after impacts. Neither.

$$R_i = \frac{P_i}{d_i} \quad (2)$$

where  $P_i$  and  $d_i$  are the bending load and displacement respectively. By analogy with the definition of damage introduced by Kachanov [37], the damage is characterized by a scalar variable  $D$  based on the loss of rigidity of the material and defined as follows:

$$D = \frac{R_0 - R_i}{R_0} \quad (3)$$

The suffix 0, in the equation above, designates the

initial stiffness of the undamaged sample.

## OBSERVATION OF DAMAGE

Repeated impacts applied to sandwich panels cause significant damage that is clearly visible and easily measurable. A simple visual inspection is used to observe such damage on the impacted and rear surfaces. This damage has the shape of a crater on the impacted surface and the shape of longitudinal and transverse cracks (on the rear side). The hemispherical indenter leaves a well-defined circular indentation. The crater depth is measured with the crosshead displacement of the tensile testing machine during the post-impact bending test. Resetting this depth value to zero before carrying out the static bending test allows the position of the crosspiece to be memorized. After several impacts, the position memorized at the previous end of the test makes it possible to measure the evolution of the depth of the crater (associated with the permanent indentation). Before performing the three-point bending tests, the crosshead moves until the upper cylinder is on the impacted area of the specimen only at the impact area. Thus, the depth of the crater is known at all times because it corresponds to the difference in position of the loading cylinder between two consecutive bending tests. The depths of the impacted areas are measured by the micrometer screw of the depth gauge (Mitutoyo 128\_105 Vernier depth gauge, micrometer type, 0-1' Range: 0.001' graduation: +/- 0.003 mm precision). For more information on the profile of the damaged area, a digital optical microscope (Keyence VHX-5000) was used to determine the crater profile and sample dimensions at failure.

## DAMAGE MODEL PROPOSED FOR HONEYCOMB STRUCTURES

Studies on modeling complex failure modes in composite materials have demonstrated that when all damage is detected, located and quantified, the probability of accurately predicting the ultimate failure of the sample given accurate information on future charges is high. For example, considering the work of Azouaoui et al is based on the "S" shape of the damage curves for different impact energies, they modeled the damage of glass/epoxy and are based on the mathematical model of Mankowsky which defines

by:

$$D = a \cdot \frac{\tilde{t}^b}{(a+1) - \tilde{t}^c} \quad (4)$$

With :

$D$  - damage parameter,

$\tilde{t}$  - normalized time (time at an instant  $t_i$  / rupture time  $t_r$ ),

$a$ ,  $b$  and  $c$  – are experimental constants

It is clear that the damage variable  $D$  tends towards infinity for a normalized time equal  $\tilde{t}$  to unity:

$$\lim_{\tilde{t} \rightarrow 1} D = \infty$$

A modification at the level of the denominator of the non-linear Mankowsky relationship is necessary, in order to find the boundary conditions of the damage variable, namely:

$$\lim_{\tilde{t} \rightarrow 0} D = 0 \quad \text{and} \quad \lim_{\tilde{t} \rightarrow 1} D = 1$$

which gives the following final relation:

$$D = a \cdot \frac{\tilde{t}^b}{(a+1) - \tilde{t}^c}$$

This model makes it possible to deduce the role of each coefficient in the shape of the curve describing this function. And, the parameters  $a$ ,  $b$  and  $c$  respectively control the level of the second zone of the damage curve, the slope of the first zone and the start (initial point) of the third zone

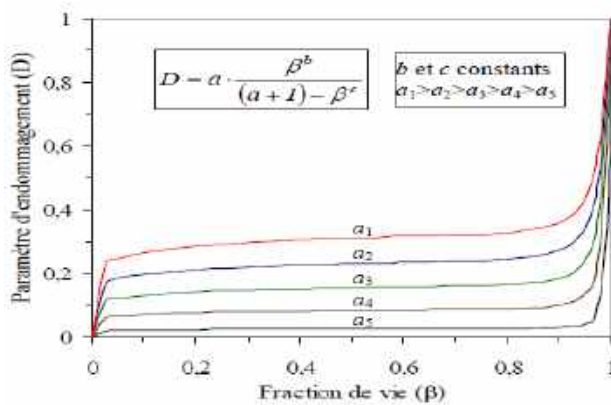


Fig.7. Shape of the damage curve as a function of the

variation of parameter  $a$ .

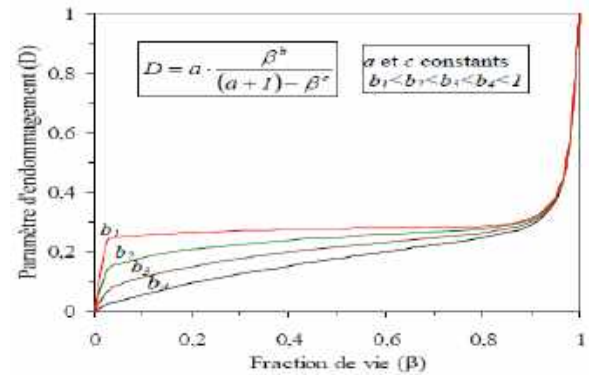


Fig.8. Shape of the damage curve as a function of the variation of parameter  $b$ .

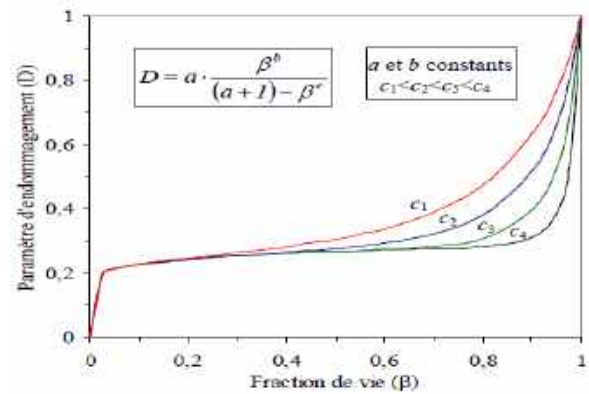


Fig.9. Shape of the damage curve as a function of the variation of parameter  $c$ .

The damage evolution model (Azouaoui et al. Model) follows an "S" curve and takes into account the initial damage at the beginning of the lifespan. This evolution law is described by three parameters, each controlling a crucial aspect of the evolution. The parameter " $a$ " controls the damage level during the period of relative stability, the parameter " $b$ " controls the initial damage rate, and the third parameter " $c$ " represents the fraction of life at which the final phase of damage appears. Applying Equation (4) to the Azouaoui case study allows for modeling the damage of glass/epoxy subjected to cyclic impact. Based on the above, it can be written as:

$$D = a \cdot \frac{\beta^b}{(a+1) - \beta^c}$$



Where:

$D$  is the damage indicator in impact experiments.  
 $\beta$  is the fraction of lifespan defined as the ratio of the number of impacts  $N_i$  to the number of failure impacts  $N_f$ .

$a$ ,  $b$ , and  $c$  are experimental constants.

These parameters respectively control the damage level throughout the non-evolutionary period, the buckling of the cell walls, the initial damage rate, and the fraction of lifespan relative to ultimate failure. To describe the damage parameter of honeycomb sandwiches, an empirical damage evolution law based on modified Mankowsky's law is proposed. The damage evolution with the number of impacts, for different cell densities, is consistently represented by an S-shaped curve (Fig. 9). This shape allows for modeling the damage indicator using the Azouaoui model, with a modification to account for the effect of honeycomb density. In this case, the effect of honeycomb density is incorporated by adding a second term to Equation (4), considering a logarithmic equation based on the cell diameter and cell wall thickness. From the evolution of the curves, the following empirical relationships between damage and the parameter's lifespan fraction can be expressed as follows:

$$D = a \cdot \frac{\beta^b}{(a+1) - \beta^c} + \phi^{-n} t^n \log\left(\frac{d}{d-1}\right)$$

Where:

$a$ ,  $b$ ,  $c$ , and  $n$  are empirical constants dependent on the constituent material.

$d$  and  $t$  represent the diameter, densities, and thickness of the honeycomb core cell wall.

The various constant values were identified using curve fitting via the optimization method. In recent years, significant efforts have been made to discover the best procedures for fitting equations to data or curves, with the least squares method remaining dominant and being used as one of the important methods for identifying and estimating unknown state variables. In this study, a nonlinear optimization technique, including MATLAB, was used, and an iterative procedure technique based on the Nelder-Mead simplex (NMS) algorithm was successfully applied to identify and estimate the best damage fitting parameters. The method aimed to obtain the best estimation of unknown state variables based on the least squares theory. For the NMS approach calculation, the `fminsearch` function of MATLAB software incorporating this algorithm was used to find the optimal values of the damage parameters. The parameter that leads to the best fitting agreement represents the evolution of the damage parameter. This fitting method is illustrated in Fig. 9.

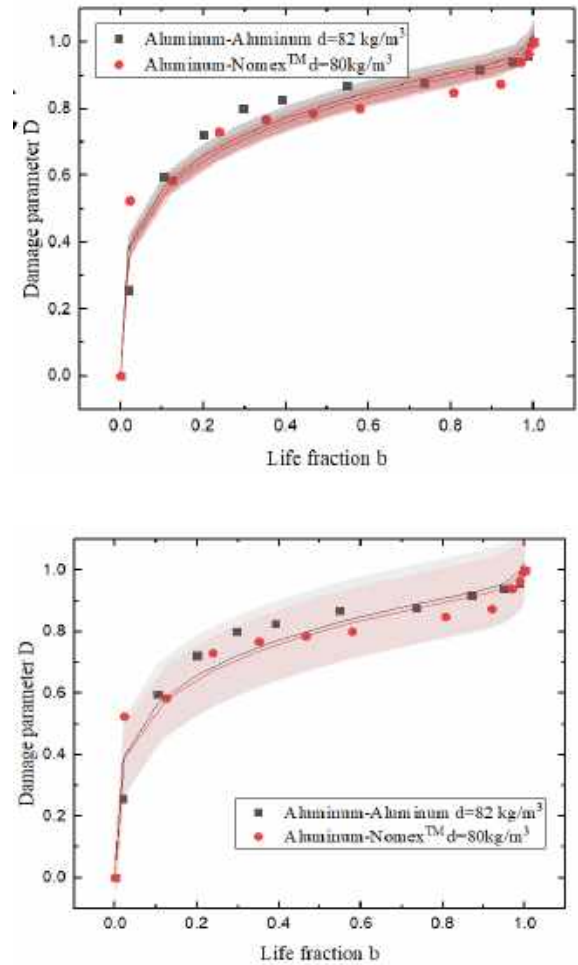


Figure 9. Representation of the evolution of the damage parameter  $D$ : a) fitting of the curves, b) the confidential band of the curves. c) curve prediction band.

The difference between the density 80 for Alu-Nomex and 82 for Alu-Alu are presented, confidence curves and prediction band. The confidence band is used in statistical analysis to represent the uncertainty in an estimate of a curve or function based on limited or noisy data. Similarly, a prediction band is used to represent the uncertainty in the value of a new data point on the curve, but subject to noise. Confidence and prediction bands are often used as part of graphical presentation of the results of a regression analysis. Confidence bands are closely related to confidence intervals, which represent the uncertainty of an



estimate of a single numerical value. "As confidence intervals, by construction, only refer to a single point, they are narrower (at this point) than a confidence band which is supposed to hold at many points simultaneously.

## CONCLUSION:

The results of this study contribute to the understanding of the fatigue behavior by repeated impact of honeycomb core sandwich composite panels (Aluminum-Aluminium) by varying the density of the core. We studied the effect of the number of impacts on the residual rigidity of the sandwich panels and on the evolution of the damage. The results obtained allowed us to draw the following conclusions:

- The rigidity of sandwich panels measured with the slope of the load-displacement curves, obtained from local bending tests, decreases with the number of impacts, thus characterizing the irreversible damage of the materials.

- The sandwich material studied presents a different fatigue behavior under the effect of the number of impacts and the density of the core.

The evolution of the loss of rigidity as a function of impact number shows three distinct zones.

- In the first zone, the rigidity of the sandwich panels decreases rapidly from the first cycles.

- The second zone presents a slightly horizontal plateau and the residual stiffness remains constant, which indicates a slowing down of the damage process.

- In the third zone there is a rapid drop in stiffness values until final failure.

It can be seen that the phase of stiffness degradation (zone 2) increases with the increase in the density of the core of the sandwich panel.

This study made it possible to highlight three stages of damage to the sandwich panel (Alu-Alu) occurring in three distinct stages.

- In the first stage, the damage parameter increases rapidly depending on the number of impacts with the formation of buckling of the core cells, indentation of the skin and micro-delaminations.

- In the second stage shows saturation of the damage, punching the upper skin of the point of impact reveals an imprint left by the projectile in the form of a crater around the point of impact of the skin.

- In the third stage, an acceleration of damage is observed, there is a formation of large cracked craters at the point of impact and a multiplication of the

decohesion of the skin-core cell interface.

It has been found that the density of the core of sandwich panels influences the damage behavior.

Finally, a damage model is proposed for the core sandwich panel which involves three constants. Examining the fracture patterns allowed us to identify and monitor the evolution of the different damages depending on the number of impacts. And we will verify it by the aluminum core sandwich panels.

## REFERENCES

- [1] Wang L, Zhang YW, Ho JCM, et al. Fatigue behavior of composite sandwich beams strengthened with GFRP stiffeners. *Eng Struct* 2020; 214: 110596.
- [2] NomexVR cores, <http://www.eurocomposites.com>, <http://www.euro-composites.com/fr/nomex-wabe/> (accessed 24 August 2021).
- [3] Shin, K.B., J.Y. Lee, and S.H. Cho, An experimental study of low-velocity impact responses of sandwich panels for Korean low floor bus. *Composite structures*, 2008. **84**(3): p. 228-240.
- [4] Rhodes, M. Impact fracture of composite sandwich structures. in *16th Structural Dynamics, and Materials Conference*. 1975.
- [5] Kim, C.-G. and E.-J. Jun, Impact resistance of composite laminated sandwich plates. *Journal of composite materials*, 1992. **26**(15): p. 2247-2261.
- [6] Bernard, M.L. and P.A. Lagace, Impact resistance of composite sandwich plates. *Journal of Reinforced Plastics and Composites*, 1989. **8**(5): p. 432-445.
- [7] Horrigan, D., R. Aitken, and G. Moltschanivskyj, Modelling of crushing due to impact in honeycomb sandwiches. *Journal of Sandwich Structures & Materials*, 2000. **2**(2): p. 131-151.
- [8] Williamson, J. and P. Lagace. Response mechanisms in the impact of graphite/epoxy honeycomb sandwich panels. in *Proceedings-American Society For Composites*. 1993. TECHNOMIC PUBLISHING AG.
- [9] Tsotsis, T.K. and S.M. Lee, Characterization of localized failure modes in honeycomb sandwich panels using indentation. *ASTM special technical publication*, 1996. **1274**: p. 139-165.
- [10] PALM, T., Impact resistance and residual compression strength of composite sandwich panels. *composites*, 1991.
- [11] Raju, K., et al., Impact damage resistance and tolerance of honeycomb core sandwich panels. *Journal of composite materials*, 2008. **42**(4): p. 385-412.
- [12] Guedra-Degeorges, D., P. Thevenet, and S. Maison, Damage tolerance of aeronautical sandwich structures, in *Mechanics of Sandwich Structures* 1998, Springer. p. 29-36.

- [13]Azouaoui, K., et al. Rigidité résiduelle d'un composite verre/epoxy tissu endommagé par fatigue par chocs.in CFM 2007-18ème Congrès Français de Mécanique. 2007. AFM, Maison de la Mécanique, 39/41 rue Louis Blanc-92400 Courbevoie.
- [14]Mittelman, A., Low-energy repetitive impact in carbon-epoxy composite. Journal of materials science, 1992. **27**(9): p. 2458-2462.
- [15]Azouaoui, K., Etude de l'endommagement de plaques composites en verre/epoxy soumises à la fatigue par chocs, 2004.
- [16]Miner, M.A., Cumulative damage in fatigue. 1945.
- [17]Kachanov, L., Rupture time under creep conditions. Izv. Akad. Nauk SSSR, 1958. **8**: p. 26-31.
- [18]Rabotnov, Y., Creep rupture,[in:] Proc. XII-th Int. Congr. Appl. Mech., M. HETENYI and WG VINCENTINI, 1969, Stanford, Springer, Berlin.
- [19]Lemaitre, J., et al., Mécanique des matériaux solides-3e éd2020: Dunod.
- [20]Djouabi, N., Analyse de l'endommagement de plaques composites en verre/epoxy soumises a la fatigue par chocs, 2012.
- [21]Lemaitre, J., A course on damage mechanics 2012: Springer Science & Business Media.
- [22]Mankowsky, V., Non-linear parametric creep function. Mech Compos Mater, 1982. **4**: p. 579-84.
- [23]Plackett, R.L., Discovery of the method of least squares. Biometrika, 1972. **59**: p. 239-251.
- [24]Betts, J.T., Solving the nonlinear least square problem: Application of a general method. Journal of Optimization Theory and Applications, 1976. **18**(4): p. 469-483.
- [25]Nelder, J.A. and R. Mead, A simplex method for function minimization. The computer journal, 1965. **7**(4): p. 308-313.
- [26]Lagarias, J.C., et al., Convergence properties of the Nelder--Mead simplex method in low dimensions. SIAM Journal on optimization, 1998. **9**(1): p. 112-147.
- [27]Gao, F. and L. Han, Implementing the Nelder-Mead simplex algorithm with adaptive parameters. Computational Optimization and Applications, 2012. **51**(1): p. 259-277.
- [28] Oubouzi, A., B. Keskes, and B. Vieille, Evaluation of damage within sandwich honeycomb panels subjected to impact fatigue loading. Journal of composite materials, 2021. **55**(30): p. 4563-4574.

# Influence of elevated temperatures on the bond between CFRP and concrete

ABDERRAHMANE ABDESSELAM<sup>1</sup>, ABDELGHANI MERDAS<sup>2</sup>, AHLEM REZIG<sup>2</sup>

<sup>1, 2, 3</sup> Department of Civil Engineering, University of Setif 1, Algeria.

## ABSTRACT

*The use of carbon fiber-reinforced polymer (CFRP) in conjunction with epoxy adhesives has become a popular method for the rehabilitation and strengthening of structures. However, the mechanical strength of the adhesive and the bonding of strengthened structures can be adversely affected by outdoor temperatures. As a response to these concerns, our study is aimed at investigating the bond relationship of CFRP-strengthened structures when exposed to elevated temperatures. To carry out this investigation, we employed a three-dimensional finite element model within the Abaqus software. This model was used to simulate double-lap shear tests on concrete blocks that had been reinforced with CFRP strips, following the principles of externally bonded reinforcement (EBR). The calibration of the model was performed using experimental data found in the existing literature. By comparing the numerical results with the experimental test data, we were able to quantify the relative importance of interfacial slippage at the bonded interfaces as influenced by temperature variations.*

**KEYWORDS** CFRP, FEA, Bond Behavior, temperature

## I. INTRODUCTION

Carbon fiber-reinforced polymer (CFRP) has become a prevalent choice in civil engineering for revitalizing and fortifying deteriorating structures, including buildings and bridges. This preference is attributed to its remarkable mechanical attributes, such as high strength, lightweight properties, corrosion resistance, and flexibility [1;2]. The rehabilitation process typically involves attaching CFRP to the structure's surface through the use of epoxy adhesives. The structural integrity of CFRP-strengthened components heavily relies on the effectiveness of this bonding interface. Therefore, it is crucial to conduct a thorough assessment of its performance. Earlier research conducted at room temperature unveiled the adhesive layer as the weakest link in this composite system, with

one of the primary modes of failure being the separation of CFRP from the substrate [3]. It's a well-established practice in Fiber-Reinforced Polymer (FRP) reinforcement for concrete to employ thermosetting polymers like epoxy or polyester resin as adhesives. Epoxy resin, in particular, serves a dual purpose by bonding the FRP composite to concrete and acting as the matrix for hand-laid FRP sheets. However, it's notably sensitive to variations in service temperature, and its diminishing mechanical properties at elevated temperatures carry significant implications for strengthened structures, particularly in terms of bond performance [4]. The effectiveness of externally reinforced FRP sheets significantly hinges on the characteristics of the interfaces between FRP and the adhesive, as well as between the adhesive and the concrete substrate. This study concentrates on numerical modeling to evaluate the influence of elevated temperatures on the bond behavior between concrete and CFRP strips, applied using the Externally Bonded Reinforcement (EBR) technique.

## II. METHODOLOGY

The current numerical model was established employing the commercial software Abaqus and was fine-tuned based on experimental data from a study conducted by [5].

## III. MATERIAL MODELING

### A. CONCRETE

In this study, the concrete damaged plasticity (CDP) model was employed to replicate the nonlinear behavior of concrete. This model is predicated on the assumption that the primary failure mechanisms consist of concrete crushing under compression and the formation and propagation of cracks under tension

### B. CFRP

The CFRP plates used in this study have material properties of 1500 MPa for tensile strength and 150 GPa for Young's modulus and was modeled as an orthotropic material

### C. EPOXY ADHESIVE

In this study, the concrete damaged plasticity (CDP) model was employed to replicate the nonlinear behavior of concrete. This model is predicated on the assumption that the primary failure mechanisms consist of concrete crushing under compression and the formation and propagation of cracks under tension

## IV. INTERACTION MODELING

The bond between the concrete and the NSM-CFRP strips was modeled using the cohesive zone model to account for possible separation at the concrete-FRP interface. This interaction was defined using the traction separation law as a function of temperature.

## V. RESULTS

In Figure 1, we present a detailed comparison between the numerical and experimental results, depicting the relationship between applied force and slip at the end of the bonding length for various temperature conditions. The numerical models effectively replicated the non-linear characteristics observed in the curves, including the stiffness reduction evident at failure. With rising temperatures, there was a noticeable shift in the behavior of the numerical curves. This shift was marked by a gradual transition towards linearity, aligning more closely with the patterns exhibited by the corresponding experimental data. Generally, as the temperature increased, there was a discernible reduction in both the bond strength and stiffness.

## VI. CONCLUSION

In this research, a numerical investigation was carried out to study the impact of elevated temperature on the bond between CFRP and concrete. A 3D non-linear finite element (FE) model was established with particular attention given to defining critical parameters within the model to ensure precise predictions. These parameters encompassed the constitutive models for concrete, steel, and FRP, as

well as the incorporation of a temperature-dependent bond-slip relationship between FRP and concrete. The numerical model exhibited a notable degree of accuracy in predicting the bond behavior at various temperatures.

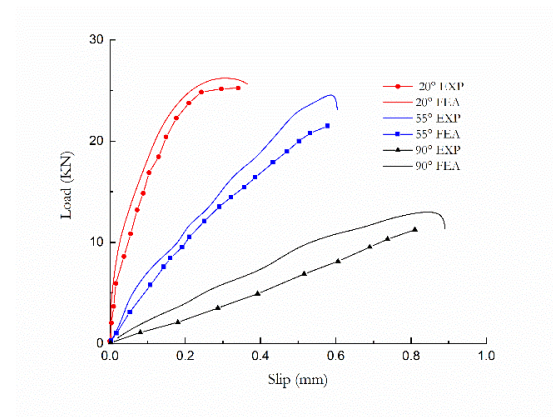


Fig. 1. Bond slip at different temperatures.

## REFERENCES

- [1] J. A. O. Barros, S. J. E. Dias, and J. L. T. Lima, "Efficacy of CFRP-based techniques for the flexural and shear strengthening of concrete beams," *Cement and Concrete Composites*, vol. 29, no. 3. Elsevier BV, pp. 203–217, Mar. 2007.
- [2] C. Mazzotti, M. Savoia, and B. Ferracuti, "An experimental study on delamination of FRP plates bonded to concrete," *Construction and Building Materials*, vol. 22, no. 7. Elsevier BV, pp. 1409–1421, Jul. 2008. doi: 10.1016/j.conbuildmat.2007.04.009.
- [3] W. Xue, L. Zeng, and Y. Tan, "Experimental studies on bond behaviour of high strength CFRP plates," *Composites Part B: Engineering*, vol. 39, no. 4. Elsevier BV, pp. 592–603, Jun. 2008.
- [4] Klamer EL, Hordijk DA, Janssen HJM. The Influence of temperature on the debonding of externally bonded CFRP. 2005. p. 1551-70
- [5] Firmo JP, Pitta D, Correia JR, Tiago C, Arruda MRT. Experimental characterization of the bond between externally bonded reinforcement (EBR) CFRP strips and concrete at elevated temperatures. *Cem Concr Compos* 2015;60:44–54.

# Title: Effect of welding current on the properties of stainless steel parts produced by the WAAM-CMT additive manufacturing technique

MOHAMED HAMIDOUCHE<sup>1,\*</sup>, FARROUK BENSALEM<sup>2</sup>, ABDELGHANI KENZOUR<sup>1</sup>, HALIM MERABTI<sup>1</sup>, KAMEL LOUCIF<sup>2</sup>, ABDESALEM KAHLOUCHE<sup>1</sup>

1. Research Center in Industrial Technologies CRTI, P.O. Box 64, Cheraga, 16014 Algiers, Algeria, \*hamidouchemohamed@yahoo.fr
2. Laboratoire des Matériaux non Métalliques, Université Ferhat Abbas Sétif, 19000 Sétif, Algeria

## ABSTRACT

*The aim of this research work is to study the influence of a very important parameter of the CMT process, namely current, on metal transfer mechanisms (melting and wire deposition) and on the microstructural and mechanical characteristics of the pieces manufactured by CMT. This parameter can be used to control the thickness of cords and pieces manufactured by CMT. The effect of heat build-up during the layer deposition process is also taken into account as a study parameter. Austenitic 316 L stainless steel is used throughout this study as a filler material for the manufacture of the workpieces.*

## KEY WORDS

Additive Manufacturing; Welding current; WAAM; CMT; 316 L stainless steel

## I. INTRODUCTION

Metal additive manufacturing is a new technology that has been fully developed in recent years with the emergence of new processes. It enables the production of three-dimensional parts, often by successive layer deposition, and thus offers new design and manufacturing freedoms compared to the conventional methods of forging, casting and machining. Furthermore, additive manufacturing makes parts lighter, saves raw materials and eliminates assembly operations. The idea of superimposing cords of molten metal with an electric arc to make pieces is not new: Ralph Baker filed a patent in 1920 in which he described a method of making decorative objects by superimposing layers of molten metal with an electric arc [1].

Technologies based on the creation of an arc between a refractory (non-melting) electrode and the surface of the parts, such as plasma or TIG (Tungsten Inert Gas) technologies, are the most precise, as the melting and

deposition of the metal in its liquid state is generally regular. On the other hand, processes based on a fusible electrode, such as the MIG (Metal Inert Gas) process, enable higher deposition speeds, but suffer from instabilities that generally produce poor surface finish of the beads. However, a recently developed variant of the MIG process, known as CMT (Cold Metal Transfer), offers improved deposit quality. It is this latter method that we have chosen to study in this work.

## II. EXPERIMENTAL

### A. MATERIALS

The material used in this work as filler wire for the manufacture of our parts is 316L austenitic stainless steel. **Table 1** shows the chemical composition of this steel.

Element	C	Si	P	S	Cr	Ni	Mn	Mo
Content %	0.03	1.0	0.045	0.03	18.5	13.0	2.0	2.5



**Fig.1.** The used 316L austenitic stainless steel wire coil.

### B. SAMPLES PREPARATION

The TPS 500i intelligent welding station is used to manufacture our parts. The movement of the welding torch on the three axes (X, Y, Z) is controlled by a CNC system. The 316 L stainless steel wire used as the electrode is melted by the electric arc produced between the electrode and the substrate.

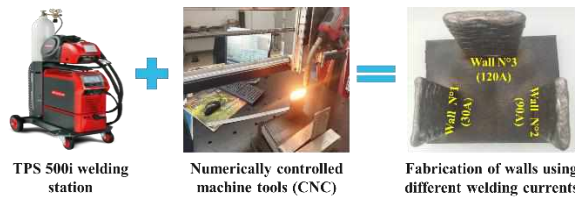


Fig.2. The used experimental setup.

The fixed and variable welding parameters used to manufacture our samples are summarized in **Table 2**.

	Current I (A)	Voltage U (V)	Torch speed TS (mm/min)	Wire speed WFS (mm/min)	Wire diameter d (mm)	Protective gas	Gas pressure (bar)
Wall 1	60	16	850	3.8	1	Argon + 2.5 %CO <sub>2</sub>	10
Wall 2	90	17.3	850	4.8	1	Argon + 2.5 %CO <sub>2</sub>	10
Wall 3	120	18.8	850	6.4	1	Argon + 2.5 %CO <sub>2</sub>	10

### C. CHARACTERIZATIONS

After the series of preparations, the parts are subjected to geometric characterization (including thickness measurement), mechanical characterization (hardness and tensile tests) and microstructural characterization by metallography.

## III. RESULTS AND DISCUSSION

Based on an analysis of the thickness as a function of the height and width of the elaborated walls. Two observations can be made. Firstly, the greater the current, the thicker the wall, hence the increase in current due to the greater quantity of molten metal. Secondly, the top of the wall is thicker than its base, which can be explained by the increasing accumulation of heat flux towards the top.

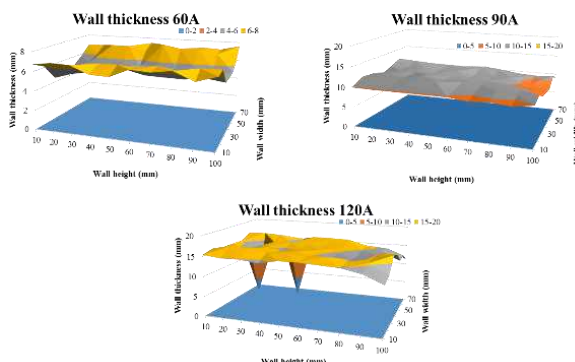


Fig.3. Variation in thickness as a function of wall width and height.

Tensile tests carried out on samples cut in the direction of the deposited cord show perfect elastoplastic behavior comparable to that of austenitic stainless steel for the three constructed walls. The second observation

concerns the superposition of tensile curves at different heights. This confirms that the material retains its properties regardless of the projected layer or cooling kinetics.

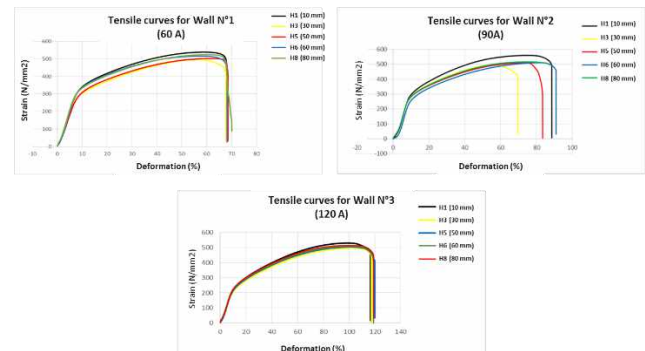


Fig.4. Tensile curves for specimens taken from elaborated walls.

Metallographic observations show a structure completely different from that of austenitic steel. For the bottom of the walls, the micrograph shows a random granular structure with wide grain boundaries and unidentified intergranular deposits. For the top of the walls, it shows a granular structure close to dendritic with compounds at the grain boundaries and with a generalized particle distribution.

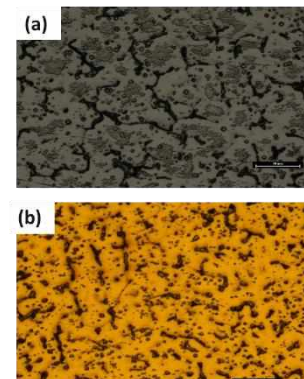


Fig.5. Optical micrograph of the bottom (a) and the top (b) of the wall processed at 120A.

## IV. CONCLUSION

The results of this study show that the welding current can be used as an effective tool to control the thickness of parts manufactured by WAAM-CMT, as it affects their thickness without influencing their mechanical and microstructural properties.

## REFERENCES

- [1] C. Bourlet, Development of wire-arc additive manufacturing for steels: microstructure and mechanical characterisations of ER100 and 316L deposits for validation of industrial parts requirements, Thèse de doctorat, Ecole nationale supérieure d'arts et métiers - ENSAM, 2019.



# Morphological, structural, and magnetic properties of the mechanically alloyed $\text{Co}_{63}\text{Cr}_{35}\text{Mo}_2$ mixture

S. DJOUADI<sup>1,\*</sup>, S. LOUIDI<sup>2</sup>, S. ALLEG<sup>1</sup>, J.J. SUNOL<sup>3</sup>

1. Laboratoire de Magnétisme et de Spectroscopie des Solides LM2S, Département de Physique. Université Badji Mokhtar Annaba, B.P. 12 Annaba 23000, Algeria.
2. Département des Sciences de la Matière, Faculté des Sciences, Université 20 Août 1955-Skikda, Algeria.
3. Dept. De Fisica, Universitat de Girona, Campus Montilivi, 17071 Girona, Spain.

## ABSTRACT

*Nanostructured  $\text{Co}_{63}\text{Cr}_{35}\text{Mo}_2$  powders were prepared by mechanical alloying, and their morphological changes, phase formation, and magnetic properties were studied by scanning electron microscope, X-ray diffraction, and vibrating sample magnetometer. The XRD diffraction pattern of the milled powders for 48 h reveals the formation of HCP, FCC, and BCC solid solutions. The saturation magnetization and coercivity values are about 16.41 emu/g and 258.39 Oe, respectively.*

## KEY WORDS

Mechanical alloying; Co-Cr-Mo alloys;  
X-ray diffraction; SEM; Magnetic properties;

## I. INTRODUCTION

Cobalt-chromium-based alloys are widely employed in the aerospace industry and biomedical domains due to their excellent high-temperature strength, good corrosion resistance, and wear resistance [1, 2]. Ternary CoCrMo alloys are commonly used in total hip and knee replacements, support structures for heart valves, and dental devices [3]. They can be also used for articular applications with metal-on-metal contact owing to their superior tribological properties in comparison to those of titanium alloys [4]. The study aims to investigate the morphological, structural, and magnetic properties of the mechanically alloyed  $\text{Co}_{63}\text{Cr}_{35}\text{Mo}_2$  powders.

## II. MATERIALS AND METHODS

$\text{Co}_{63}\text{Cr}_{35}\text{Mo}_2$  powders mixture was mechanically alloyed in a planetary ball-mill Fritsch P7 under argon atmosphere for 48 h. Morphological changes of the powder particles were followed by scanning electron microscopy. The structural and magnetic properties were

investigated using X-ray diffraction, and vibrating sample magnetometer, respectively.

## III. RESULTS AND DISCUSSION

Figure 1 shows the morphology of the mechanically alloyed  $\text{Co}_{63}\text{Cr}_{35}\text{Mo}_2$  powders with two magnifications. The presence of smaller and larger particles is due to the competition between fracturing and cold-welding phenomena during the milling process.

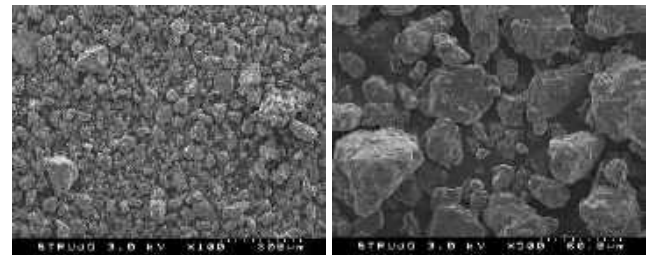


Fig. 1. SEM micrographs of the  $\text{Co}_{63}\text{Cr}_{35}\text{Mo}_2$  powder particles.

The Rietveld refinement of the XRD pattern (Fig. 2) reveals the formation of HCP, FCC, and BCC solid solutions, and their weight fractions are about 35.75%, 35.85%, and 28.40%, respectively. The crystallite sizes are about 3–9 nm.

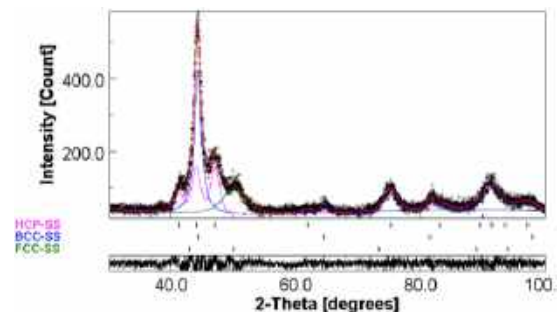
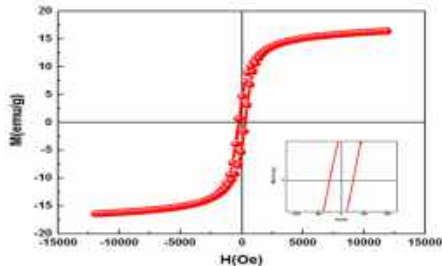


Fig. 2. Rietveld refinement of the XRD pattern.

The hysteresis loop of the mechanically alloyed powders, at room temperature, is shown in Fig. 3. The coercivity ( $H_c$ ) and saturation magnetization ( $M_s$ ) values are about 258.39 Oe and 16.42 emu/g, respectively. The decrease of  $M_s$  confirms the mixing of the elemental Cr, Co, and Mo powders at the atomic level.



**Fig. 3.** Hysteresis cycle and enlargement of the central part.

#### IV. CONCLUSION

Nanostructured  $\text{Co}_{63}\text{Cr}_{35}\text{Mo}_2$  powders were prepared by mechanical alloying. The crystal structure consists of a mixture of BCC, FCC, and HCP solid solutions. The crystallite sizes range between 3 and 9 nm. The coercivity and saturation magnetization values are about 258.39 Oe and 16.42 emu/g, respectively.

#### REFERENCES

- [1] G.J. Cui, J.R. Han, G.X. Wu, High-temperature wear behavior of self-lubricating Co matrix alloys prepared by P/M, *Wear* 346–347 (2016) 116–123.
- [2] J.A. García, C. Díaz, S. M€ and l, J. Lutz, R. Martínez, R.J. Rodríguez, Tribological improvements of plasma immersion implanted CoCr alloys, *Surf. Coating. Technol.* 204 (2010) 2928–2932.
- [3] P.E. Sinnott-Jones, J.A. Wharton, R.J.K. Wood, Micro-abrasion–corrosion of a CoCrMo alloy in simulated artificial hip joint environments, *Wear* 259, (2005) 259 898.
- [4] D. Sun, J.A. Wharton, R.J.K. Wood, L. Ma, W.M. Rainforth, Microabrasion–corrosion of cast CoCrMo alloy in simulated body fluids, *Trib. Inter.*, 42 (2009), 99–110.

# NOUVELLE APPROCHE D'ESTIMATION DE LA DUREE DE VIE RESIDUELLE DES ROULEMENTS

FEDALA SEMCHEDINE<sup>1,\*</sup>, BOUALI FAKHREDDINE<sup>2</sup>

1. Laboratoire de Mécanique de précision Appliquée (LMPA), Institut d'Optique et Mécanique de Précision, Université Sétif 1, Algérie, e-mail: fedala.semchedine@univ-setif.dz
2. Laboratoire de Mécanique de précision Appliquée (LMPA), Institut d'Optique et Mécanique de Précision, Université Sétif 1, Algérie, e-mail: bouali.f@univ-setif.dz

## RESUME

*L'approche de pronostic et de gestion de santé (Prognostics and Health Management, PHM), permet de se renseigner sur l'état de santé des différents composants des systèmes mécaniques, tels que les roulements, et d'estimer leur durée de vie utile résiduelle (Remaining Useful Life, RUL) avant la défaillance.*

*Ce travail a pour objectif de faire une étude du modèle de pronostic basé sur les données. Plus précisément, on cherche une méthode efficace pour sélectionner le meilleur indicateur de dégradation des roulements afin d'estimer leur durée de vie utile résiduelle (Remaining Useful Life, RUL) avant la défaillance.*

**MOTS CLES** Roulements, Vibrations, Surveillance, Prognostic, PHM RUL

## I. INTRODUCTION

Les roulements sont des composants très utilisés et très critiques dans diverses machines, et leurs défaillances sont l'une des principales causes de pannes des machines tournantes. Pour cela, l'objectif majeur de la surveillance est de minimiser au maximum les coûts élevés induits par les indisponibilités non planifiées et les pannes des équipements qui peuvent générer des pertes considérables.

La maintenance industrielle, qui est l'ensemble de toutes les actions techniques durant le cycle de vie d'un bien, destinées à le maintenir ou à le rétablir dans un état dans lequel il peut accomplir la fonction requise. Elle représente la solution adéquate à ces défis. Malheureusement, la maintenance traditionnelle, basée principalement sur le diagnostic après-panne, présente beaucoup d'inconvénients comme l'arrêt de la production pendant une période indéfinie, le remplacement inutile de pièces de rechange et le coût de maintenance très élevé. On peut remédier à ces

inconvénients en passant à un autre type de maintenance qui est la maintenance prédictive. Cette maintenance est basée principalement sur le pronostic qui est l'estimation du temps de fonctionnement avant défaillance d'un équipement ou d'un système.

Le pronostic (Prognostics and Health Management, PHM) permet de garantir la qualité des produits, d'effectuer la maintenance juste à temps, de réduire les temps d'arrêt des équipements et d'éviter les pannes catastrophiques. Le pronostic des systèmes industriels devient actuellement un objectif important pour les industriels, sachant que la panne, qui peut survenir soudainement, est généralement très coûteuse en termes de réparation et d'interruption de la production et est mauvaise pour la réputation. Le but principal du pronostic est d'estimer la durée de vie utile restante (Remaining Useful Life, RUL). Beaucoup de travaux dans le domaine du PHM, dont le but est d'estimer la RUL, ont montrés le besoin d'améliorer le pronostic, tel que la disponibilité et l'accès facile au service de pronostic.

Dans ce travail, nous proposons d'utiliser l'approche du pronostic guidée par les données, qui offre l'avantage de pouvoir apprendre des modèles basés sur des données empiriques et d'utiliser des méthodes de l'intelligence artificielle. Donc, les informations sur les indicateurs jouent un rôle important pour une prévision fiable. Ce travail s'intéresse essentiellement au développement de méthodes efficaces de sélection des meilleurs indicateurs de surveillance.

## PARTIE EXPERIMENTALE

### A. DESCRIPTION DU BANC D'ESSAI

La méthodologie adoptée pour ce banc d'essai consiste à accélérer la durée de vie du roulement en utilisant de fortes charges axiales et radiales à une vitesse d'arbre moyenne à élever. Le banc d'essai est conçu pour faire fonctionner jusqu'à la rupture un roulement à bille

(SKF6008-2RS1) en appliquant une charge radiale et axiale. L'entraînement est réalisé à l'aide d'un moteur électrique relié directement à l'arbre du palier d'essai par un accouplement à mâchoires qui permet un certain désalignement [1]. Il y a 4 roulements qui supportent l'arbre. De gauche à droite : Le roulement testé SKF 6008-2RS1; deux roulements radiaux de support; un roulement axial de support. Les roulements radiaux et axiaux de support sont plus résistants que le roulement testé, de sorte qu'ils ne devraient pas se casser. Une image simplifiée est présentée par la figure 1.

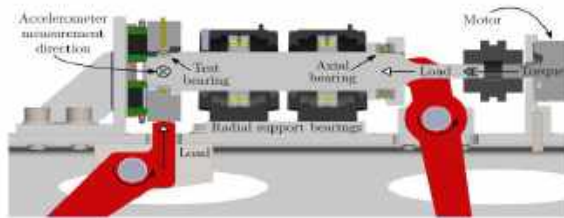


Fig. 1. Banc d'essai [1]

Cette base de données a été utilisée pour la première fois dans [2]. Ce test a nécessité environ 35 jours de fonctionnement continu jusqu'à la défaillance complète du roulement. L'arbre a tourné au total 42,7 millions de tours. Seuls les 7 derniers jours de fonctionnement sont donnés dans l'ensemble de données. Il y a des dommages à la fois sur la bague extérieure, certains éléments roulants, et aussi sur la bague intérieure. Le moteur utilisé est capable de faire tourner l'arbre à une vitesse moyenne à élever pour accélérer la durée de vie du roulement. La vitesse de l'arbre pendant la mesure dans cet ensemble de données est de 250 tr/min.

Le roulement testé de type SKF 6008-2RS1 est un roulement rigide à billes à une rangée avec joints ou flasques. Il supporte des charges radiales et axiales dans les deux sens. Il a un diamètre extérieur  $D = 68$  mm, un diamètre intérieur  $d = 40$  mm et une largeur  $B = 15$  mm.

Les fréquences de défauts sont données pour une vitesse d'arbre de 1 Hz, elles doivent donc être mises à l'échelle de la vitesse d'arbre de 250 tr/min soit une fréquence de rotation  $F_r = 4,1667$  Hz. Donc, ces fréquences caractéristiques sont des multiples de la fréquence de rotation tels que [2] :

- Fréquence de défaut de la bague extérieure :  
 $BPFO = 5.11 \times F_r = 21,29$  Hz
- Fréquence de défaut de la bague intérieure :  
 $BPFI = 6.88 \times F_r = 28,67$  Hz
- Fréquence de défaut des éléments roulants :  
 $BSF = 3.32 \times F_r = 13,83$  Hz

Il y a des dommages à la fois sur la bague extérieure,

certaines éléments roulants, et aussi sur la bague intérieure. La figure 2 montre tous les défauts dans le roulement démonté [2]



Fig. 2. Défaut des roulements à la fin de l'essai [2]

Une carte d'acquisition haute fréquence de 24 bits, compatible IEPE  $\pm 30$  V, mesure la vibration de l'accéléromètre fixé au boîtier du palier d'essai. L'accéléromètre a une sensibilité de 100 mV/g dans la plage linéaire jusqu'à 10 kHz. En outre, un capteur de proximité mesure le mouvement radial de l'arbre dans une direction. Il a une plage de mesure de 1,1 mm et une résolution de 18,5 nm, ce qui le rend capable de détecter de petits changements dans la position de l'arbre lorsque le roulement est endommagé. Pendant le test, le signal de vibration  $v(t)$  et le signal de position du codeur  $\theta(t)$  sont mesurés toutes les 30 minutes à une vitesse de référence  $\theta(\text{réf}) = 250$  tours par minute. La fréquence d'échantillonnage est de 51,2 kHz et la durée de mesure est de 24s (100 tours) [1].

## B. PRÉTRAITEMENT DES DONNÉES

### - Analyse temporelle

La figure 3 représente deux types de signaux sans et avec défauts. On peut voir clairement que l'énergie du signal du roulement défectueux est supérieure à celle du signal sans défaut.

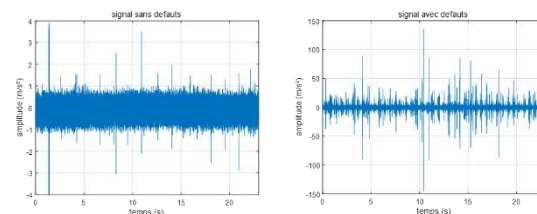


Fig. 3. Signaux temporels sans et avec défaut

### - Analyse fréquentielle

L'analyse d'enveloppe ainsi que le kurtosis spectrale sont parmi les méthodes les plus utilisées pour la détection et le diagnostic des défauts de roulements [3]. Sur le spectre d'enveloppe (Fig.4.) on distingue

clairement la présence du pic qui correspond à la fréquence de rotation en plus, des trois fréquences des différents défauts des organes du à savoir la fréquence de la bague extérieure BPFO, de la bague intérieure BPFI et des billes BSF.

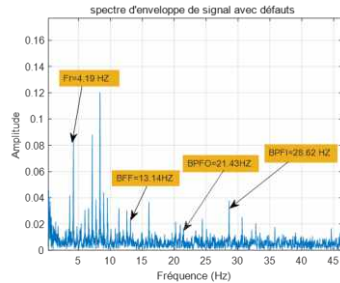


Fig. 4. Spectre d'enveloppe de signal avec défaut

La figure 5 présente le kurtogramme du signal d'un roulement défectueux. On distingue la bande optimale de largeur 0.8 kHz, centrés autour de 23.6 kHz, avec une valeur du kurtosis de 3591.3494 obtenus au 5<sup>ème</sup> niveau de filtrage.

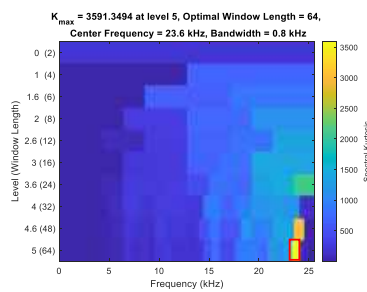


Fig. 5. Kurtogramme du signal avec défaut

### C. Estimation de la durée de vie résiduelle RUL

L'objectif de ce travail est d'étudier différentes stratégies de sélection et d'extraction d'indicateurs basées sur les techniques de traitement de signal et d'analyse de données, pour améliorer l'estimation de la durée de vie résiduelle (RUL) du roulement testé. L'organigramme de la figure 6 illustre l'approche proposée.

La première étape consiste à l'extraction des différents indicateurs temporels, fréquentiels et de kurtosis spectral à partir des signaux vibratoires enregistrés par le capteur. Ensuite, une étape de sélection et de transformation des indicateurs est réalisée dans le but de définir un indicateur de santé. A partir de ce dernier, l'algorithme de prédiction basé sur les supports vecteurs régression (Support Vector Regression SVR) est utilisé pour prédire la durée de vie résiduelle RUL du roulement testé. Cet algorithme utilise une

partie des données pour l'apprentissage et une autre pour le test. Enfin, on compare la prédiction par rapport aux données réelles.

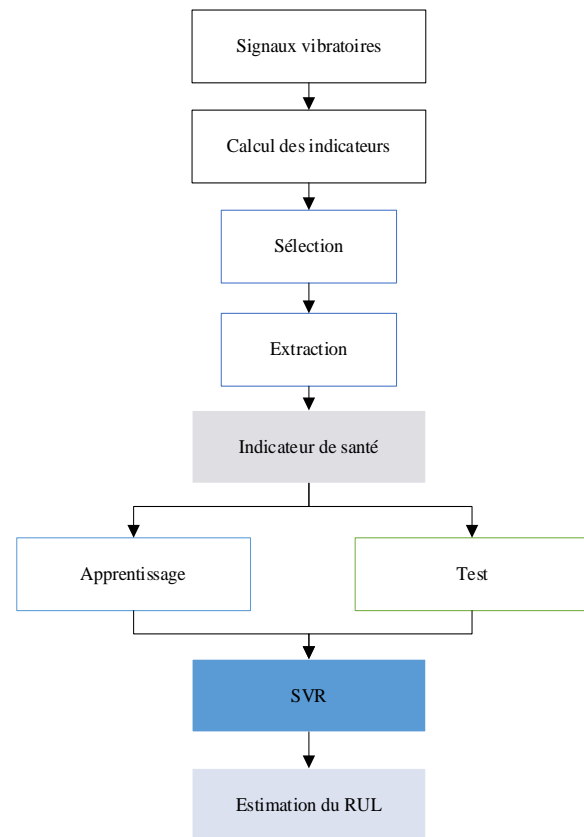


Figure 6. Organigramme représentant la démarche de prédiction

### - Signaux vibratoires

La figure 7 présente tous les différents signaux utilisés dans ce travail. D'après la forme des signaux, on distingue l'évolution de la dégradation en fonction du temps.

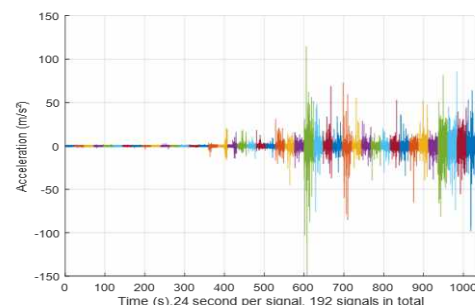


Fig. 7. Signaux vibratoires

### - Calcul d'indicateurs

Pour suivre la dégradation du roulement, nous proposons de calculer les indicateurs cités dans le tableau 1.

Numéro	Domaines	Indicateur
1	Temporel	valeur efficace
2		coefficient d'aplatissement
3		coefficient de dissymétrie
4		écart type
5		facteur de crête
6		différence Maximum-to-minimum
7		moyenne
8		Shape Factor
9		Impulse Factor (Facteur d'impulsion)
10		Facteur de marge
11		Energie
12		Facteur de clairance
13	Fréquentiel	1ere bande [0 50]
14		2ème bande [50 100]
15		3ème bande [100 150]
16		4ème bande [150 200]
17		5ème bande [200 2500]
18		Bande totale
19	kurtosis spectral SK	Moyenne de SK
20		L'écart type de SK
21		Coefficient d'asymétrie de SK
22		Coefficient d'aplatissement de SK

**Tableau 1.** les indicateurs utilisés

### - Le choix de l'indicateur de surveillance

Le choix d'indicateur de surveillance ou de santé (Heath indication) est basé sur deux étapes : la sélection et l'extraction

### - Sélection

Nous avons utilisé le critère de monotonicté (fonction Matlab monotonicity) comme méthode de sélection. La monotonicté d'une population d'indicateurs, est basée sur l'estimation de la différence moyenne entre le nombre de croissances positives et négatives pour chaque chemin : où  $n$  est le nombre de points de temps de mesure et  $m$  est le nombre de systèmes contrôlés [27]. Avec,  $m = 1$  le nombre de système surveillé,  $x$  représente le vecteur d'indicateurs et  $n=35$  le nombre de vecteurs.

$$Monotonicity = moyenne \left( \left| \frac{\text{positif}(\text{diff}(x_i)) - \text{négatif}(\text{diff}(x_i))}{n-1} \right| \right) \quad (1)$$

La figure 8 présente le potentiel de chaque indicateur à réaliser le pronostic. On peut distinguer que la Bande 5 du spectre d'enveloppe est considérée comme la meilleure caractéristique par le critère de

monotonicté. Les indicateurs dont le score d'importance est supérieur à 0,2 sont sélectionnés pour la fusion de caractéristiques dans la section suivante.

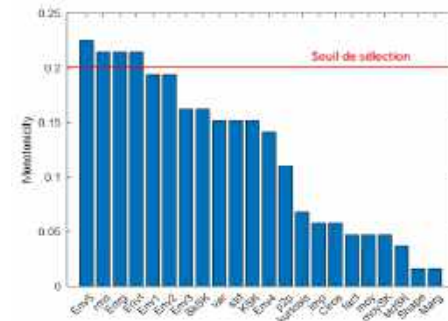


**Fig.8.** Performance des indicateurs

### - Extraction

L'analyse en composantes principales (ACP) [4] est utilisée pour la réduction de la dimension des indicateurs. La figure 9 présente la première composante principale issue de la transformation des données sélectionnées et qui sera considérée comme l'indicateur de santé (HI) du pronostic. Ce dernier est représenté dans la figure 9. On peut voir l'allure exponentielle reflète bien la dégradation progressive du roulement. La valeur maximale de cet indicateur sera considérée comme le seuil de dégradation final. On remarque que l'indicateur de santé passe par deux étapes : la première étant constante et la deuxième augmente progressivement de manière exponentielle. Donc nous allons éliminer un certain nombre d'échantillons de la partie linéaire. Le reste des vecteurs qui est représenté sur la figure 10 a été lissé en utilisant la fonction Matlab « movmean ». Ce lissage est réalisé par centrage local en calculant la moyenne de 10 points successifs ; puis soustraire cette moyenne de chaque point. La valeur maximale de l'indicateur de santé représente le seuil d'alarme et marque la fin de la durée de vie du roulement.

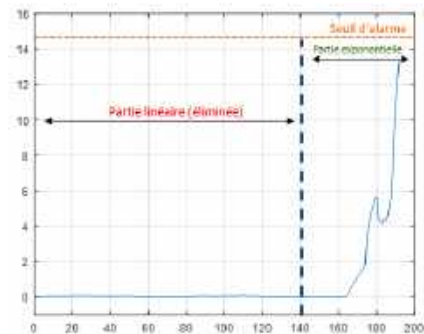


**Fig.9.** Indicateur de santé (HI)



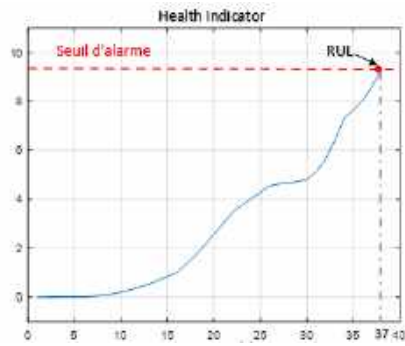


Fig.10. Indicateur de santé (HI) après l'élimination de 155 vecteurs

#### - Estimation de la RUL basée sur SVR

D'après [5], la prédiction est considérée comme correcte si la différence entre la RUL estimée et réelle appartient à l'intervalle  $[-10; +13]$ . Si elle est supérieure à +13, les prédictions sont considérées comme précoces et si elle est inférieure -10, la prédiction est considérée comme tardives.

Le tableau 2 montre l'erreur de prédiction de la durée de vie RUL du roulement en utilisant l'indicateur de santé extrait par ACP. Le nombre de vecteurs optimal, (19% soit 37 vecteurs) de la partie exponentielle (figure 10), a été déterminé de façon itérative. Trois pourcentages 40%, 50% et 60% sont utilisés pour l'apprentissage de SVR. Le reste pour le test.

Nombre de vecteurs retenus	Pourcentage des vecteurs retenus	Pourcentage d'apprentissage	Pourcentage de test	Erreur de prédiction	
				(%)	Heures
52	30	40	60	3.11	0.8
		50	50	3.64	0.94
		60	40	0.833	0.21
42	22	40	60	1.39	0.29
		50	50	2.03	0.42
		60	40	2.03	0.42
37	19	40	60	4.30	0.79
		50	50	0.28	0.05
		60	40	0.18	0.03

Tableau 2. Résultats du modèle SVR

D'après le tableau 2, la valeur la plus fiable pour l'estimation de la durée de vie résiduelle du roulement est déterminée par un pourcentage d'apprentissage de 60%. L'erreur de prédiction entre la RUL estimé et réelle est presque négligeable de 0.18% équivalente à 0.03 heures. Cette prédiction est dans l'intervalle de prédiction correcte [5].

La figure 11 représente les résultats du tableau 2, pour 37 vecteurs 60% pour l'apprentissage et 40% pour le test.

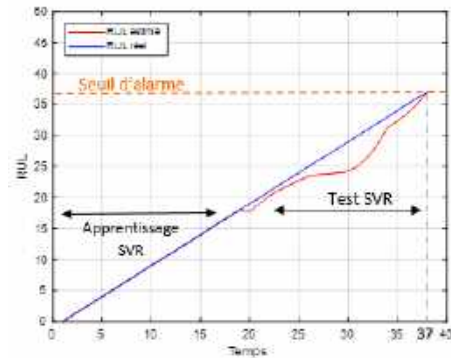


Fig. 11. RUL obtenus par le modèle SVR avec un pourcentage d'apprentissage de 60% et 40% de test

## II. CONCLUSION

Nous avons appliqué un algorithme de pronostic basé sur le modèle SVR pour estimer le RUL des roulements.

Les résultats de prédiction de la RUL pour la base de données étudiée démontrent que l'approche proposée de pronostic est capable d'estimer la RUL avec précision.

## REFERENCES

- [1] K. Andreas et al., "Accelerated Bearing Life-time Test Rig Development for Low Speed Data Acquisition", Modeling, Identification and Control, 38(3),p.143-156 (2017), doi:10.4173/mic.2017.3.4.
- [2] K. Andreas et al., "Autonomous bearing fault diagnosis method based on envelope", IFAC-PapersOnLine 50.1 (2017): 13378-13383. doi:10.1016/j.ifacol.2017.08.2262
- [3] J. Antoni et R. B. Randall, "The spectral kurtosis : application to the vibratory surveillance and diagnostics of rotating machines", Mechanical Systems and Signal Processing, 20(12), p.308-331, (2006).
- [4] I. T. Jolliffe, "Principal Component Analysis". Second ed., New York: Springer Series in Statistics, 2002.
- [5] K. Goebel et P. Bonissone, "Prognostic information fusion for constant load systems", Proceedings of the 7th Annual Conference on Information Fusion, 2 (2005).

***Session T10: Coating,  
thin films and solar  
panels***

# Spreading coefficient effect of thin films on the optical glass.

ASMA ABCHI<sup>1\*</sup>, NABIL BELKHIR<sup>1</sup>

<sup>1</sup> Laboratory of applied optics, Institute of optics and precision mechanics, Ferhat Abbas university setif1, Algeria.

\*Corresponding author: [asma\\_abchi@univ-setif.dz](mailto:asma_abchi@univ-setif.dz)

## ABSTRACT

In this context, we presented the spreading coefficient of a test liquid ( $\text{SnO}_2$ ,  $\text{TiO}_2$ , distilled water, and N-octane) to investigate the effect of several factors on the morphology, surface quality of the glasses (SL, B270, and PC). Furthermore, the adhesion phenomenon was studied via droplet technique

**KEY WORDS:** Adhesion, Spreading coefficient, glass, roughness.

## I. INTRODUCTION

Orava et al [1] are mentioned the techniques for producing thin film materials are exceptionally numerous, the nature of these materials is only multiplying: glass, insulators, semiconductors, polymers and superconductors, their applications covering several disciplines: optics, microelectronics, mechanics, chemistry, etc. In addition, the development of many surface analysis techniques, the increasingly precise control of parameters involved in the repository and a better understanding of the thin-film material growth [2-3].

## II. PRACTICAL STUDY

### A. DIGI DROP MEASUREMENT:

The measurement of the contact angle was done via the falling drop method, where a Digi Drop device was used (Krüss Easy Drop Standard). A droplet about  $2\mu\text{l}$  of the prepared sol-gel solutions: distilled water, N-octane, Tin dioxide ( $\text{SnO}_2$ ), and Titanium dioxide ( $\text{TiO}_2$ ) were deposited on the glasses substrates (SL, B270, and PC) with the Digi Drop technique.

### B. SPREADING COEFFICIENT EFFECT

In order to study the Spreading coefficient effect (S) of the deposited liquids (distilled water, N-octane, Tin dioxide ( $\text{SnO}_2$ ), Titanium dioxide ( $\text{TiO}_2$ )) on the optical materials, Soda lime glass (SL), polycarbonate (PC), and B270. The samples used were storage for 4 years in our institute (IOMP).

### C. SURFACE CHARACTERIZATION

AFM topography of some surfaces, before and after storage state are shown in Fig.1-2.

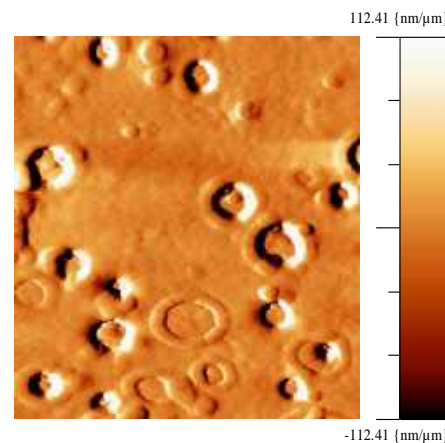


**Fig. 1.** 3D AFM of the Soda lime glass (SL) substrate Before storage (with coating).

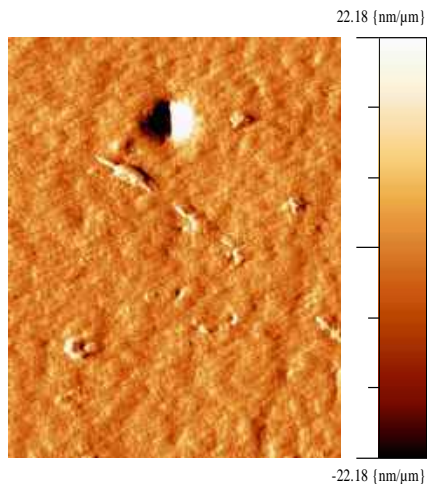


**Fig. 2.** 3D AFM of the Soda lime glass (SL) substrate  
After storage (with coating).

### III. CONCLUSION

In this work, the quality control of an existing optical glass product at the level of our institute of optics and precision mechanics. In fact, the results indicate that the increasing of the surface roughness decreases the adhesion strength. This highlights the spreading coefficient effect on the quality of the deposited solutions.

### REFERENCES

- [1] Orava J. Kohoutek T. Wagner T. Deposition techniques for chalcogenide thin Films. Woodhead. Oxford. 2014.
- [2] Seshan K. Thin-Film Deposition Processes And Techniques Principles, Methods, Equipment and Applications. 2Ed. Noyes Publications. 2002.
- [3] Kasap S. Capper P. Handbook of electronic and photonic materials. 2Ed. Springer. Switzerland .2017.

# Titre: les problèmes liés à l'exploitation des circuits de refroidissement de la Raffinerie de condensât RA2K-SONATRACH- SKIKDA

GAIDI Fayçal<sup>1, a \*</sup>, TOUKAL LINDA<sup>2, b</sup>

<sup>1</sup> Université Ferhat Abbas-Sétif, Algeria, <sup>a</sup> gaidifaycal@univ-setif.dz

<sup>2</sup> Université Ferhat Abbas-Sétif, Algeria, <sup>b</sup> toukellinda@univ-setif.dz

## ABSTRACT

*Dans ce travail, j'ai étudié l'influence de la qualité d'eau sur la production du complexe. Nous avons constaté que ce problème (la mauvaise qualité d'eau) agit directement sur le taux de marche de l'unité de production car les équipements sollicitant l'eau utilisée dans le service utilités souvent isolaient, suite au bouchage, d'où une réduction impérative de la production, afin d'améliorer la température des sous-produits vers stockage et assurer un taux de production minimale.*

*Durant notre étude nous avons révélés ce qui suit : L'eau réceptionnée à partir de l'organisme ADE est d'une mauvaise qualité.*

*L'eau de refroidissement traitée dans la section 502 (section traitement d'eau de refroidissement) ne répond pas aux exigences suite aux problèmes externes déjà*

*Parmi les inconvénients d'exploitation des tours de refroidissement du type semi- ouvert l'évaporation, les matières en suspension d'où des difficultés d'assurer une bonne qualité d'eau de refroidissement.*

## KEY WORDS

CONDENSAT, EAU DE REFROIDISSEMENT, ANALYSE, PURIFICATION, ENTARTAGE

## I. INTRODUCTION

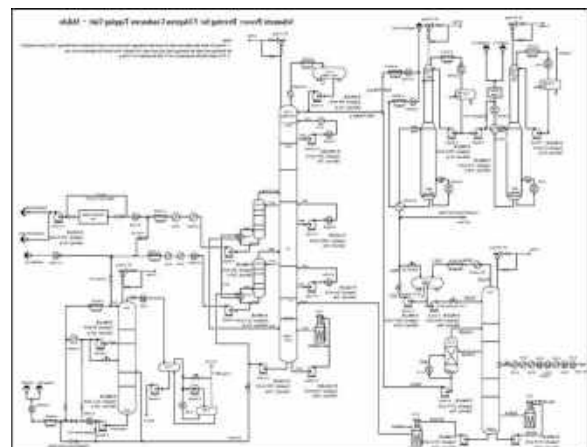
Ces dernières années, nous avons assisté à un grand développement rapide de l'industrie pétrolière ; ceci nous montre que le pétrole et le gaz de simple produit combustible sont des matières premières de choix peuvent donner d'énormes produits synthétiques

L'eau de refroidissement est devenue indispensable dans la majeure partie des procès de production et de

transformation industrielle. Les exigences vont de l'élimination de la chaleur produite par les machines de production à la nécessité de maintenir des conditions de température contrôlée, leurs composants, leurs phases de production et les locaux. Aujourd'hui la possibilité d'installer des systèmes de refroidissement spécifiquement adaptés aux applications industrielles sont des facteurs clés pour maintenir une fiabilité et une continuité de la production et ainsi optimiser les processus en réduisant les coûts.

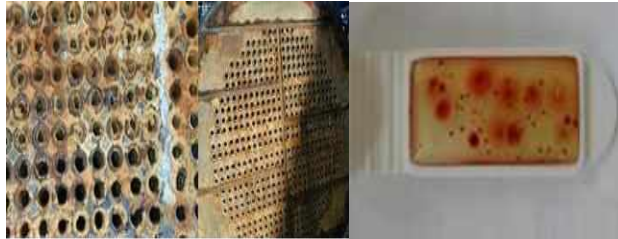
L'usage de l'eau implique l'utilisation de récipients, canalisations et mécanismes qui mettent en contact un matériau avec cette eau. Lorsqu'une paroi solide est en contact avec une eau naturelle douce ou salée, le développement d'une couche à l'interphase est couramment observé : biofilm, dépôt calco-magnésien, tartre, produit de corrosion...etc, provenant de la précipitation d'une espèce en solution et ou de la dégradation de la paroi elle-même. Tous les circuits alimentés par des eaux naturelles sont confrontés au problème de formation de dépôt calco-carbonique au niveau des parois en contact avec l'eau [1]. L'enjeu économique de ce problème est d'autant plus important qu'il touche beaucoup de secteurs

## A. DESCRIPTION DU COMPLEXE RA2K



### B. LES TROIS PHENOMENES (CORROSION, ENTARTREGE, PROLIFERATION)

Puisque les circuits de refroidissement ont pour mission de refroidir des produits ou des unités de procès par l'intermédiaire d'échangeurs de chaleur, l'on conçoit que le rendement d'échange soit un point important au niveau du rendement global des unités, donc de la production.



### C. SUIVI DE LA QUALITE D'EAU DE REFROIDISSEMENT ET INTERPRETATION DES RESULTATS

Pour éviter les différents problèmes qui peuvent être rencontrés du circuit de refroidissement, on va essayer de contrôler la qualité de l'eau d'alimentation (eau industriel) et l'eau de refroidissement et de suivre la tendance de l'eau de refroidissement. Ce chapitre a donc pour but d'exposer la tendance de l'eau suivant la valeur de l'indice de Rayznar.

#### D. ANALYSE DES INDICES DE RYZNAR

Les conditions dans lesquelles le carbonate de calcium déposera sont complexes, cela dépend de :

1. La dureté du calcium
2. L'alcalinité totale
3. La quantité totale de matières solides
4. La température
5. pH

C'est un problème qui a été étudié par :

LANGELIER et RYZNAR

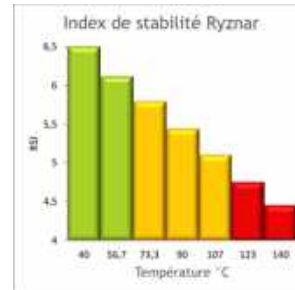


Fig. 1. Influence du chlorure Cl<sup>-</sup>

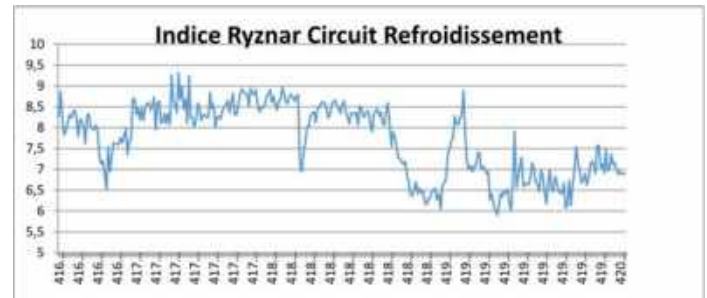


Fig. 2. évolution de l'inde de Rayznar

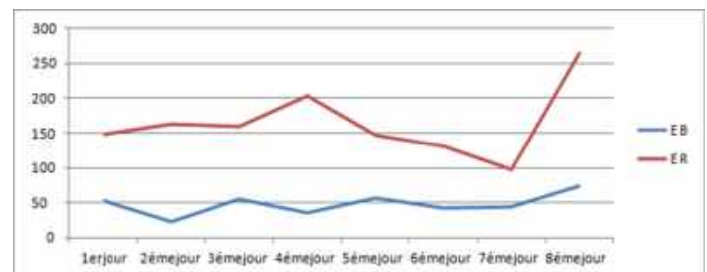


Fig. 3. Influence du chlorure Cl<sup>-</sup>

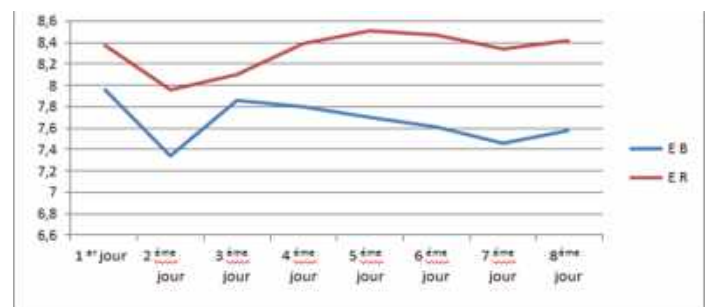


Fig. 4. Influence du pH

## II. CONCLUSION

Dans ce travail, on a choisi les circuits de refroidissement au niveau du Complexe Topping Condensat RA2K souffrant de divers problèmes en essayant de localiser les problèmes de circuit, chercher les causes contribuant à leurs apparitions et on propose des solutions.

Les analyses physico-chimiques de l'eau industrielle



et l'eau de refroidissement ont été effectuées au niveau du laboratoire de Complexe Topping Condensat de la Willaya de Skikda. L'ensemble des résultats des paramètres que nous avons analysés permet de tirer des informations sur la qualité de l'eau. Ces résultats indiquent que cette eau ne répond pas aux normes opérationnelles, donc elle est non conforme. Ainsi que cette eau est corrosive et cela est confirmé par la valeur de l'indice de Ryznar (IR) qui est supérieure à 6 pour l'eau industrielle et l'eau de refroidissement.

## REFERENCES

- [1] : Documentation, service technique RA2K Topping Condensat. [2]: Documentation, service utilité RA2K Topping Condensat.
- [3] : Documentation, RA2K Topping Condensat et ADE (Algérienne des eaux).
- [4] : R. DESJARDINS «le traitement des eaux», Ed de l'école polytechnique de Montréal, 1997.
- [5] : S. Rehamnia, Med R. Benchachemane « Caractérisation des eaux résiduaires industrielles étude analytique et statistique: cas FERTIAL » Mémoire de Master II, département de génie des procédés université Badji Mokhtar ANNABA 2011.
- [6] : F. Benachour «Caractéristique électrochimique d'inhibiteur de corrosion (Akwacure 353, Akwacure 369) et le biocide (Akwacure 395) destinés au circuit de refroidissement.» Mémoire de fin d'études- département génie des procédés• université Badji Mokhtar ANNABA 2008/2009.
- [7] : [www.developpement-durable.gouv.fr/la-reglementation-Biocide\\_37426.htm](http://www.developpement-durable.gouv.fr/la-reglementation-Biocide_37426.htm). [8]: [www.en.wikipedia.org/wiki/Dispersant](http://www.en.wikipedia.org/wiki/Dispersant).
- [9] : [www.fr.wikipedia.org/wiki/Acide\\_sulfurique](http://www.fr.wikipedia.org/wiki/Acide_sulfurique).
- [10] : L.Larbi « Etude et traitement des eaux de refroidissement de la machine à coulée continue radiale de l'aciérie à oxygène n°1 (SIDER-ANNABA) ».Mémoire de Magister, département génie des procédés, Badji Mokhtar ANNABA.2000
- [11] : Mémento technique de l'eau. Processus élémentaire du génie physico-chimique en traitement de l'eau. Tome 1, 10ème édition, Degremont, mai 2005.
- [12] : [www.fr-wikipedia.org/wiki/Tour-de\\_refroidissement](http://www.fr-wikipedia.org/wiki/Tour-de_refroidissement).
- [13] : [www.fr.wikipédia.org/wiki/Légionella](http://www.fr.wikipédia.org/wiki/Légionella).
- [14] : [www.légionellose.com/le\\_cour/traitement\\_preventifs\\_et\\_curatifs/traitement\\_courant\\_la\\_corrosion\\_et\\_l'entartrage\\_dans\\_les\\_circuits\\_de\\_refroidissement](http://www.légionellose.com/le_cour/traitement_preventifs_et_curatifs/traitement_courant_la_corrosion_et_l'entartrage_dans_les_circuits_de_refroidissement).
- [15] : Z. Bouzelifa, S.Medjani «Analyse et contrôle de la qualité de l'eau adoucie alimentant le circuit de refroidissement de l'ACOI (METAL STEEL). Mémoire de fin d'études, département génie des procédés, Université Badji Mokhtar-ANNABA 2005.
- [16] : I.Abid, «Etude analytique et impact de la qualité d'eau adoucie sur le circuit d'eau de refroidissement de l'aciérie à oxygène N°2 (Arcelor Mittal-ANNABA) ». Mémoire de Master II, département génie de procédés Université Badji Mokhtar ANNABA2013.
- [17] : Pr.Khalil Elguermai « LA CORROSION » département de BMF faculté de Médecine Dentaire de Casablanca Université HASSAN II.Ain chok.
- [18] : S. Belkahla, N.Dine «Etude et analyse de l'effet inhibiteur de corrosion dans les équipements de l'unité UAN du complexe ASMIDAL.ANNABA ».Mémoire de fin d'études Badji Mokhtar ANNABA 2004.
- [19] : Lévy Armand «Métaux et alliage dans l'industrie chimique. Aciers ordinaires et spéciaux»- Technique de l'ingénieur 14310.
- [20] : Fiaud Christan « Inhibiteur de corrosion-corrosion vieillissement »-tome 2- Technique de l'ingénieur COR1005.
- [21] : Martin Beaulieu, Ph.D, chimiste Van Hiep Nguyen, ing. «la bactérie légionnelle dans les tours de refroidissement.
- [22]-L. Duvivier, « Considérations générales relatives à l'entartrage des circuits de refroidissement industriels », Actes des Journées Information Eaux, Vol. 1, 311-3111, 18-20 septembre 1996.
- [23] : [Fr.wikipedia.org/wiki/Légionellose](http://fr.wikipedia.org/wiki/Légionellose).
- [24] : [www.powershow.com/view/29b6eb-ZDclZ/légionella\\_et\\_traitement\\_des\\_eaux.ppt](http://www.powershow.com/view/29b6eb-ZDclZ/légionella_et_traitement_des_eaux.ppt).
- [25] :Kurita Handbook ofwater treatment- second English edition

# Effect of Plasticizer Content on the Properties of Biodegradable coating based on Starch/ Microcrystalline Cellulose Blend

AOUFI DJALILA<sup>1,2,\*</sup>, BENHAOUA FAIROUZ<sup>3</sup>, AND BELLOUL NABILA<sup>2</sup>

1. Research Center In Industrial Technologies -CRTI- Echahid Mohammed ABASSI Cheraga, Algiers; Algeria.
2. Laboratory of Coatings, Materials and Environment, M'Hamed Bougara University, Boumerdes, Algeria.
3. Research Unit: Materials, Processes and Environment, M'Hamed Bougara University, Boumerdes, Algeria.

## ABSTRACT

*Our work focuses on the development of coating based on polysaccharides blend and the evaluation of the influence of the plasticizer content (Glycerol) on the behaviour of these coating. The coating was prepared by casting. The physicochemical characteristics of the coating were highlighted by different techniques (FT-IR, sorption isotherm, water vapour permeability, and mechanical properties). The presence of glycerol increases the hydrophilic nature of coating, resulting in an increase in water vapour permeability. Thus, these two properties depend on the hydration state of the coating. The increase of glycerol content caused an increase in elongation at break of each coating, coating become more flexible.*

**KEY WORDS:** Glycerol, Starch/Microcrystalline cellulose, Coating, Casting.

## I. INTRODUCTION

The development of new biodegradable packaging is a very interesting alternative to reduce the volume of waste from plastic packaging materials. Biodegradable packaging is made of biopolymers, renewable macromolecules such as polysaccharides and their mixtures (cellulose derivatives, starch derivatives, chitin and chitosan, etc.), proteins (gelatin, gluten, etc.), lipid compounds (waxes, fatty acids and derivatives, etc.) and polyesters (PLA, PHB, etc.). Starch is a promising raw material because of its annual availability from many plants [1,2]. In addition to being staple food, starch has recently gained interest as a renewable and biodegradable plastic [3,4] because of the worldwide environment and resources problems resulted from petroleum-derived plastics [5,6]. The aim of this work was the development and the characterization of coating obtained from a mixture of cornstarch and microcrystalline cellulose and the study of the influence of plasticizers on the behavior of these coating. These coating have been characterized in order

to use them as new formulations to produce coating for food packaging.

## II. RESULTS AND DISCUSSION

### A. FOURIER TRANSFORM INFRARED SPECTROSCOPY

The FTIR spectra of prepared coating are illustrated in the following figure 1.

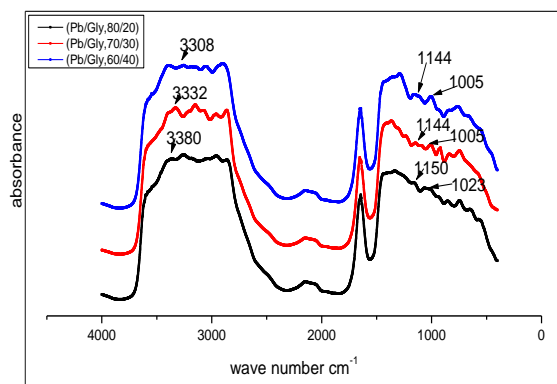


**Fig. 1.** FTIR spectra of different coating.

Figure 1 indicate the formation of hydrogen bonds between starch chains and glycerol molecules. The lowest wave number corresponds to the most stable hydrogen bonds similar observations were reported in previous studies [3, 7].

### B. WATER SORPTION ISOTHERM

The water vapor sorption isotherms of different coating are shown in Figure 2. When the relative humidity increases, the water molecules no longer react with the polymer but they aggregate together and form multilayers. The number of aggregates (multilayers) depends on the glycerol content.

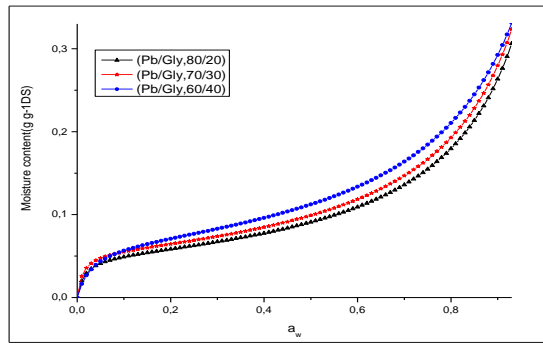


Fig. 2. Water vapor sorption isotherms of different coating

### C. WATER VAPOR PERMEABILITY

WVP values of different coating are shown in Figure 3:

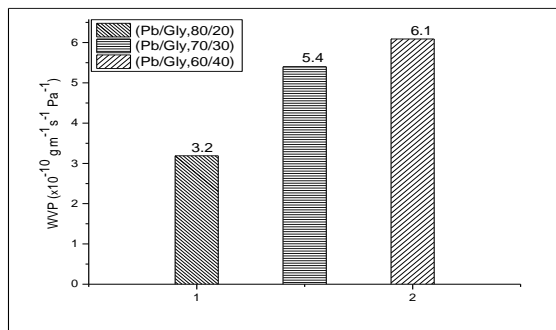


Fig.3. water vapor permeability of different coating.

The obtained results show that the variation in permeability is closely linked to the plasticizer content. The highest value of WVP was presented by the coating with 40% of glycerol.

### D. MECHANICAL PROPERTIES

Figure 4 represents the variation of the elongation at break of prepared coating under 33% and 75% RH.

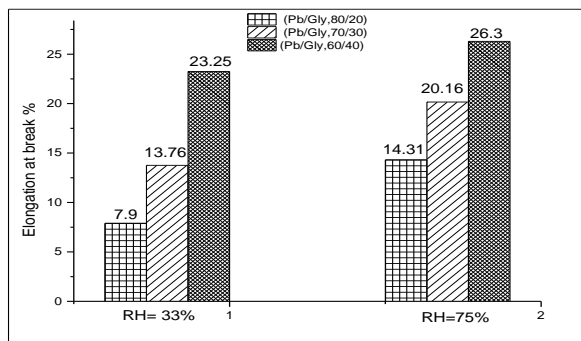


Fig.4. Elongation at break of different coating

From obtained results, we clearly notice the influence

of the plasticizer on the mechanical properties of the films: the elongation at break increases with the increase of the plasticizer content, similar observations were reported in previous studies [8-10].

### A. CONCLUSION

The obtained results highlighted the effect of glycerol on the properties of coating. Indeed, glycerol, a small hydrophilic molecule, is inserted between the polymer chains and forms hydrogen bonds with the hydroxyl groups of the starch. These bonds lead to an increase in the mobility of the polymer chains, thus increasing the flexibility of the films. On the other hand, the presence of glycerol increases the hydrophilic nature of the coating, resulting in an increase in water vapor permeability. Thus, these two properties depend on the hydration state of the coating.

### REFERENCES

- [1] Md. Hoque, et al "Properties of film from cuttlefish (*Sepia pharonis*) skin gelatin incorporated with cinnamon, clove and star anise extracts" *Food Hydrocoll.* 25,1085-1097 (2011).
- [2] T. Jiang et al "Starch-based biodegradable materials: Challenges and opportunities" *Adv. Ind. Eng. Polym.* 3, 8-18 (2020).
- [3] F. Larotonda, et al "Gonçalves M. Green edible films obtained from starch-domestic carrageenan mixtures". 2<sup>nd</sup> Mercosur congress on Chemical Engineering.
- [4] K. James Falua et al "Valorization of Starch to Biobased Materials: A Review." *Polym.* 14, 2215 (2022).
- [5] C. Muller, et al "Effect of cellulose fibers on the mechanical properties and water vapor barrier of starch-based films" *Food Hydrocoll.* 23, 1328-1333 (2009).
- [6] P. Brain Wilfer et al "Effect of starch type on the film properties of native starch based edible films" *Mater. Today: Proc.* 44, 3903-3907 (2021).
- [7] H. Dai, et al "Preparation and Properties of Starch-based Film Using N, N-bis (hydroxyethyl) formamide as a new plasticizer" *Carbohydr. Polym.* 79, 306-311 (2010).
- [8] S. Mali, et al "Water sorption and mechanical properties of cassava starch films and their relation to plasticizing effect" *Carbohydr. Polym.* 60, 283-289 (2005).
- [9] R. Arham et al "Physical and mechanical properties of agar based edible film with glycerol plasticizer" *Int. Food Res. J.* 23,1669-1675 (2016).
- [10] L. Muhammed et al "Effect of Plasticizer Type and Concentration on Tensile, Thermal and Barrier Properties of Biodegradable Films Based on Sugar Palm (*Arenga pinnata*) Starch" *Polym.* 7,1106-1124 (2015).

# Effect of barium doping on the properties of NiO thin films.

LAHCENE FELLAH<sup>1,\*</sup>, ABDALLAH DIHA<sup>2</sup>, AND MOAHAMED ZAKARIA MERAD<sup>3</sup>

1. Faculty of Hydrocarbons and Renewable Energies and Earth and Universe  
Ouargla, Algeria, fellahcene@yahoo.fr
2. Department of Mechanical Engineering, University Larbi Tébessi  
Tébessa, Algeria, diha\_a@yahoo.fr
3. Exploitation et valorisation des ressources naturelles en zones arides  
Ouargla, Algeria, meradzaki1995@gmail.com

## ABSTRACT

*This Work examines the impact of barium doping on NiO thin films. Undoped and barium-doped thin films were deposited on a glass substrate at 450°C using the spray pyrolysis technique at varying barium concentrations (0-8 at. %). XRD patterns indicate these films to be polycrystalline in nature with a preferred (111) orientation. We determined the crystal sizes of the deposited thin films for (111) orientation using the Debye-Scherrer formula. Analysis of SEM photographs revealed crystal sizes ranging from 11.95 to 33.02 nm in both cases. In the visible spectral range, the optical transmittance of NiO thin films doped with Ba decreased by a maximum of 46% when compared to undoped NiO thin films (which had a transmittance of 70%). The band gap was found to decrease within the range of 3.742 - 3.503 eV as a result of Ba doping.*

## KEY WORDS

Spray pyrolysis ; Ba doped NiO ; Thin films ; Band gap ; Grain size.

## I. INTRODUCTION

Transparent conducting oxides (TCOs) are essential in various applications like solar cells, windows, and light-emitting diodes. While most TCOs are n-type semiconductors, p-type TCOs are crucial for smart windows, optoelectronic devices, and transparent electronics. Kawazoe et al. introduced the first p-type TCO, CuAlO<sub>2</sub>, paving the way for transparent electronics [1-5]. Nickel oxide (NiO) shows promise as a p-type TCO due to its excellent properties: high chemical stability, good crystallinity, wide direct energy gap (3.6 – 4.0 eV), broad spectral transparency, and cost-effectiveness. Undoped NiO films have relatively high resistivity, but p-doped NiO with increased Ni vacancies or interstitial oxygen exhibits

improved conductivity[6,7].

## II. EXPERIMENTAL PROCEDURE

NiO: Barium-doped nickel oxide thin films, containing 0-8 (at.%) of Ba, were deposited onto glass substrates using the spray pyrolysis deposition process. We have characterized the deposited thin films by three methods: X-ray diffraction, SEM and UV-Visible spectrophotometry.

## III. RESULTS AND DISCUSSION

### A. STRUCTURAL PROPERTIES

Figure 1 displays the XRD spectra of NiO: Ba thin films, which were prepared on glass substrates, within the 2θ range of 30-85°. The diffraction peaks were indexed by comparing the obtained data with ICDD card No. 01-047-1049. The grain size (G) was determined using the Debye-Scherrer equation [7].

$$G = \frac{k\lambda}{\beta \cdot \cos\theta} \quad (1)$$

The dislocation densities (δ) were calculated through the equation presented in reference [7].

$$\delta = G^{-2} \quad (2)$$

The lattice constant can be computed from Eq. (3) [7] by considering cubic symmetry:

$$a_{hkl} = d_{hkl} \cdot \sqrt{h^2 + k^2 + l^2} \quad (3)$$

Where:  $k = 0.98$  is shape constant,  $\lambda$  is the X-ray wavelength of Cu-Kα (1.54056 Å),  $\theta$  is the diffraction angle (in radians),  $\beta$  denotes the full width at half maximum of the peak, ( $h, k, l$ ) are Miller indices, and  $d_{hkl}$  is the inter-planar spacing.

We have found that the lattice parameter was in range of [0.41949-0.41665 nm], the grain size in [11.95-33.02 nm], and dislocations density in range of [7.00-9.17 ( $10^{-3} \text{ l/nm}^2$ ).

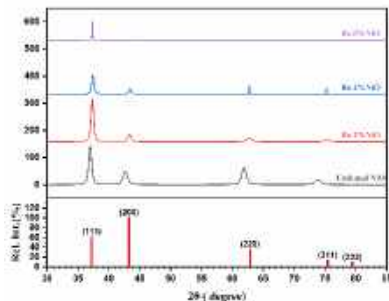


**Fig. 1.** XRD patterns of undoped NiO and Ba doped NiO thin films deposited at 450°C.

#### B. MORPHOLOGICAL CHARACTERISTICS

Figure 2 display the morphology of NiO thin films deposited with varying concentrations of Ba. The SEM images demonstrate precisely defined nanostructures and a strong likeness in morphology among the as-deposited NiO nanoparticles. These nanoparticles maintain their regular shapes, including spherical and elliptical morphologies, with clustering commonly observed.

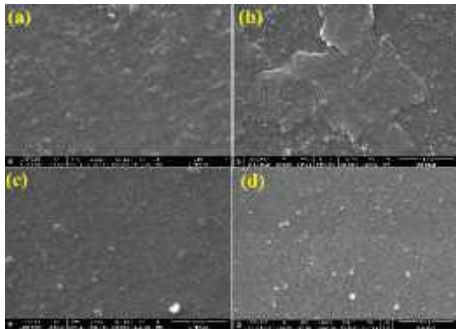


**Fig.2.** XRD patterns of undoped NiO and Ba doped NiO thin films deposited at 450°C.

#### C. OPTICAL PROPERTIES

The transmission spectra for sprayed thin films of undoped NiO and Ba-doped NiO in the 300 to 800 nm wavelength range are presented in Figure 3(a). The undoped sample has a transmission of approximately 70%, which decreases with an increase in doping concentration. The optical band gap of the films was determined (as shown in Fig. 3(b)) by using Tauc's plots [9, 10]:

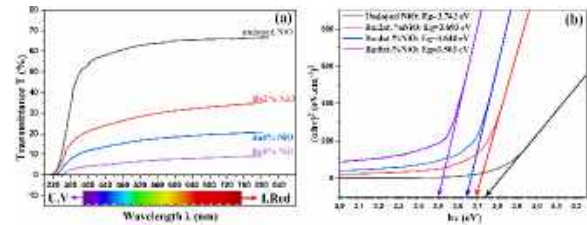


**Fig.3.** (a) Transmittance curves of all samples, (b) Plots of  $(ah\nu)^2$  as function of photon energy ( $h\nu$ ).

#### IV. CONCLUSION

This work investigates the effect of different Ba doping levels on the structural, morphological, and optical properties of NiO thin films. The films were produced using spray pyrolysis on 450°C glass substrates. The films exhibited a nanocrystalline cubic structure primarily along the (111) plane. With an increase in Ba doping percentage from 2at.% to 8at.%, there was a significant improvement in deposited thin layers' crystallinity, with crystallite size growth in the nanometric range. The films' optical band gap decreased from 3.742 eV to 3.503 eV as Ba concentration increased.

#### REFERENCES

- [1] Bädeker K., Über die elektrische Leitfähigkeit und die thermoelektrische Kraft einiger Schwermetallverbindungen, *Annalen der Physik*, 327, 749-66, (1907).
- [2] Harold A. McMaster, *Conductive coating for glass and method of application*, Libbey Owens Ford Glass Co, USA, (1947).
- [3] Lytle W.O., Junge A.E., *Electroconductive products and production thereof*, PPG Industries Inc, USA, (1951).
- [4] Mochel J.M., *Electrically conducting coatings on glass and other ceramic bodies*, Corning Inc, USA, (1951).
- [5] Kawazoe H., Yasukawa M., Hyodo H., Kurita M., Yanagi H., Hosono H., P-type electrical conduction in transparent thin films of  $\text{CuAlO}_2$ , *Nature*, 389, 939-42, (1997).
- [6] Cullity B.D., Stock S.R., *Elements of X-ray Diffraction*, 3<sup>rd</sup> ed., Prentice-Hall, New York, 2001.
- [7] Carlsson J.-O., Martin P.M., Ch.7 - Chemical Vapor Deposition, in: Martin P.M. (Ed.), *Handbook of Deposition Technologies for Films and Coatings* (Third Edition), William Andrew Publishing, Boston, 314-63, (2010).
- [8] Alagiri M., Ponnusamy S., Muthamizhchelvan C., Synthesis and characterization of NiO nanoparticles by sol-gel method, *Journal of Materials Science: Materials in Electronics*, 23, 728-32, (2012).
- [9] Çayır Taşdemirci T., Influence of annealing on properties of SILAR deposited nickel oxide films, *Vacuum*, 167, 189-94, (2019).
- [10] Boulila S., Ghamnia M., Boukhachem A., Ouhaibi A., Chakhroum M.A., Fauquet C., et al., Photocatalytic properties of NiO nanofilms doped with Ba, *Philosophical Magazine Letters*, 100, 283-93, (2020).

# Effect of graphene oxide nanosheets on the microstructure and morphology of the electrodeposited Ni-Co coatings

F.Z. MESSAGIER<sup>1,2,\*</sup>, M. HAMIDOUCHE<sup>3</sup>, AND N. KHENNAFI-BENGHALEM<sup>1,2</sup>

1. Ferhat Abbas Setif 1 University, Research Unit of Emergent Materials, Setif 19000, Algeria

2. Ferhat Abbas Setif 1 University, Institute of Optics and Precision Mechanics, Setif 19000, Algeria

3. Research Centre in Industrial Technologies (CRTI) P.O.Box 64, Cheraga 16014 Algiers, Algeria

Adresse E-mail: [messgier.zara@gmail.com](mailto:messgier.zara@gmail.com)  
[hamidouchemohamed@yahoo.fr](mailto:hamidouchemohamed@yahoo.fr)  
[n\\_khanafi@yahoo.fr](mailto:n_khanafi@yahoo.fr)

## ABSTRACT

*Graphene oxide (GO) nanosheets are commonly used to improve the performance of various bulk materials and coatings. Since changes in various properties are generally associated with microstructural and morphological changes, we thought in this work to study the effect of the incorporation of GO nanosheets on the microstructure and morphology of Ni-Co coatings commonly used in several industrial and technological sectors. To this end, Ni-Co and Ni-Co/GO coatings were deposited by ultrasound-assisted electrodeposition on StW24 mild steel. Characterizations were carried out by X-ray diffraction (XRD) and scanning electron microscopy (SEM). The results show that graphene oxide in Ni-Co coatings has a significant influence on their microstructure and morphology.*

## KEY WORDS

Ni-Co; Graphene oxide; Electrodeposition; Coating; Microstructure; Morphology

## I. INTRODUCTION

Electrodeposited Ni-Co coatings have a wide range of applications in many industrial and technological sectors, thanks to their very good magnetic, mechanical, anticorrosive and tribological properties [1]. The various good properties of Ni-Co coatings can be further enhanced by several techniques, including the incorporation of different nanofillers such as ZnO, SiO<sub>2</sub>[2], Al<sub>2</sub>O<sub>3</sub> [3], etc. Graphene oxide (GO) is one of the most widely used nanofillers for improving the performance of various coatings, thanks to its excellent thermal, electrical and mechanical properties [4]. Modifications in the various properties of coatings can generally only be achieved after structural and morphological changes. The aim of the present work

is to incorporate graphene oxide nanosheets into the matrix of a nanocrystalline Ni-Co alloy coating and to study its influence on the microstructural and morphological properties of such coatings.

## EXPERIMENTAL

### A. ELECTRODEPOSITION OF COATINGS

The ultrasonic-assisted electrodeposition technique was used to deposit Ni-Co and Ni-Co/GO coatings on StW24 mild steel substrates from two different Watts baths. The composition of the used baths and the electrodeposition parameters are summarized in **Table 1** and **Table 2**, respectively, while the applied experimental set-up is illustrated in **Figure 1**.

**Table 1:** The composition of the used Watts baths.

Bath 01	Bath 02
-Nickel sulfate (NiSO <sub>4</sub> )	-Nickel sulfate (NiSO <sub>4</sub> )
-Cobalt sulfate (CoSO <sub>4</sub> )	-Cobalt sulfate (CoSO <sub>4</sub> )
-Improving additives (Boric acid, saccharin, BD, SDS)	Improving additives (Boric acid, saccharin, BD, SDS)
	-Graphene oxide (GO)

**Table 2:** Electrodeposition parameters

pH of the bath	Time of deposition	temperature	Courant density
2-4	30 min	25°C	3 A/dm <sup>2</sup>



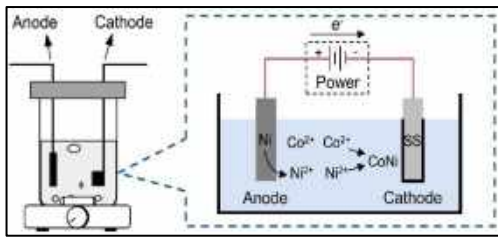


Fig. 1. The experimental setup.

### B. CHARACTERIZATION OF COATINGS

The microstructural properties of electrodeposited Ni-Co and Ni-Co/GO coatings were studied by a (Bruker Advanced D8) X-ray diffractometer (DRX), using Cu-K $\alpha$  radiation ( $\lambda = 1.54 \text{ \AA}$ ). Scanning was performed at a target voltage of 40 kV, covering the  $2\theta = 0-90^\circ$  range with a scan step of  $0.03^\circ$ .

The surface morphology of the coatings was analyzed using a (MAIA3 TESCAN) scanning electron microscope (SEM).

## II. RESULTS AND DISCUSSIONS

### A. MICROSTRUCTURAL PROPERTIES

The XRD profiles of the Ni-Co and NiCo/GO coatings are shown in Fig. 2. It is clear that only the characteristic XRD peaks corresponding to the fcc phase usual for the Ni-Co alloy can be observed in the diffraction pattern of both coatings (Ni-Co and Ni-Co/GO), which is expected due to the amorphous graphene oxide structure.

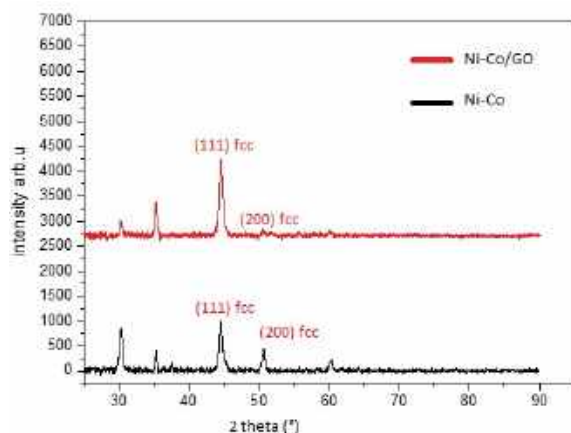


Fig. 2. X-ray diffractograms of NiCo and NiCo/GO coatings

However, changes in texture and crystallographic orientations can be clearly observed where the intensity of peaks corresponding to the (111)

orientations increases after incorporation of GO nanosheets into the Ni-Co matrix, while the intensity of peaks corresponding to the (200) orientations decreases.

### B. MORPHOLOGICAL PROPERTIES

SEM micrographs of electrodeposited Ni-Co and Ni-Co/GO are shown in Figure 3. It is clear that the incorporation of GO nanosheets into the Ni-Co matrix leads to a significant change in morphology from a rough lamellar morphology to a smooth granular morphology. The presence of the incorporated GO sheets can also be clearly observed on the surface of the Ni-Co/GO coating.

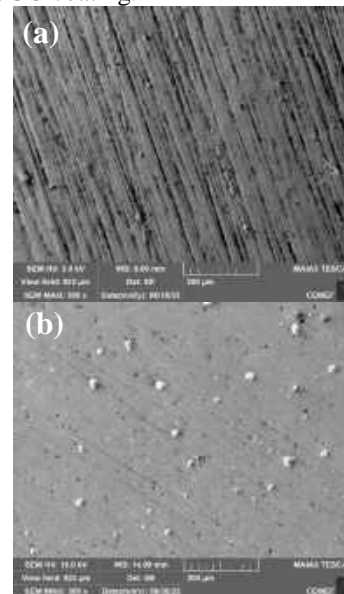


Fig. 3. (a) SEM micrographs of Ni-Co and (b) NiCo/GO coatings.

### C. CONCLUSION

In this work, the effect of incorporating GO nanosheets into the matrix of a Ni-Co coating was investigated. The results indicate that GO nanosheets incorporated into the Ni-Co matrix lead to significant microstructural and morphological changes that can have a significant influence on the properties and applications of such coatings.

### REFERENCES

- [1] M. Duch, J. Esteve, E. Gomez, R. Perez-Castillejos and E. Valles: J. Micromech. Microeng., 12, 400–405, (2002).
- [2] Yu SR, Liu Y, Li W, Liu JA, Yuan DS. The running-in tribological behavior of nano-SiO<sub>2</sub>/Ni composite coatings. Composite Part B, 43:1070-6, (2012).
- [3] Saha RK, Khan TI. Effect of applied current on the electrodeposited Ni-Al<sub>2</sub>O<sub>3</sub> composite coatings, Surf Coating Technol 205:890-5, (2010)

[4] Y.Su, V.G. Kravets, S.L. Wong, J. Waters, A.K. Geim, R.R. Nair, Impermeable barrier films and protective coatings based on reduced graphene oxide, Nat. Commun. 5.5843, (2014).

# Effet de la cémentation sur le retour élastique dans l'essai d'étirage pliage en U

IMENE ABDEDAIM<sup>1\*</sup>, ALI DEBIH<sup>2</sup>, ELHADJ OUAKDI<sup>1</sup>

1. Laboratoire de Physique et Mécanique des Matériaux Métalliques, Institut d'Optique et Mécanique de Précision, Université Ferhat Abbas Sétif 1, Algérie, abdedaim\_imene@yahoo.fr
2. Université Mohamed Boudiaf M'sila, Algérie, debihwh@yahoo.fr

## RÉSUMÉ

*Les pièces mécaniques embouties ou pliées présentent toujours des anomalies sur l'état de surface (peau d'orange) et sur le manque d'une précision dimensionnelle, causé par le retour élastique. Le retour élastique est si compliqué qu'il est difficile à simuler avec précision car il est lié à de nombreux facteurs tels que la géométrie de l'outillage, les propriétés des matériaux, le frottement et les conditions de chargement. Dans ce contexte, le retour élastique de l'essai d'étirage-pliage en U est étudié expérimentalement. Le métal étudié est un acier non allié, utilisé spécialement pour la fabrication des produits d'électroménager au niveau de l'entreprise SONARIC.*

*Des tôles d'acier C5 ont subi des traitements de cémentation effectués à 900° pendant 3h (sans trempe). Elles sont toutes testées en étirage-pliage en variant la force de serrage et la profondeur d'étirage. Ceci est nécessaire pour évaluer l'effet de la cémentation sur la qualité de formage et sur le retour élastique.*

## MOTS CLES :

Cémentation, Etirage-pliage, Frottement, Retour élastique.

## I. INTRODUCTION

Dans les industries mécaniques, les produits plats (tôles) sont largement utilisés pour réaliser diverses composantes. Bien qu'il existe une grande variété de procédés de formage par déformation plastique des métaux, L'emboutissage reste l'un des procédés les plus utilisés. Différents types de défauts peuvent impacter les propriétés mécaniques ou esthétiques des

tôles embouties et le phénomène du retour élastique en fait partie. [1]

Au cours des dernières années, les propriétés mécaniques des aciers ont été améliorées grâce à l'utilisation de la cémentation, qui est un procédé de traitement thermique des métaux par lequel les atomes de carbone se fixent aux atomes de fer. Ce processus donne aux aciers une structure très fine et homogène, ce qui contribue à améliorer leurs propriétés mécaniques.

## II. MATÉRIELS & MÉTHODES

Les essais d'étirage-pliage sont assurés par un dispositif en U adapté sur une machine de traction de type Fu 1000e (Fig.1). Un capteur de déplacement, adapté au dispositif réalisé et relié à un lecteur électronique, peut enregistrer à chaque instant la profondeur d'étirage  $h$  pour calculer le retour élastique final  $\Delta h_2$  qui est dû à l'élimination de la force de serrage par libération totale de l'éprouvette.



**Fig 1.** Dispositif d'étirage-pliage en V adapté sur la machine de traction

### A. LA CÉMENTATION

D'une manière pratique, les pièces sont placées dans des caisses en acier convenablement espacées les unes des autres et recouvertes d'une couche de ciment de 3 mm d'épaisseur (Fig. 2). Une fois pleine, la caisse est fermée par un couvercle et portée dans un four de température de cémentation (900°C) pendant 3 heures. Les pièces cémentées restent dans le four jusqu'au refroidissement totale.

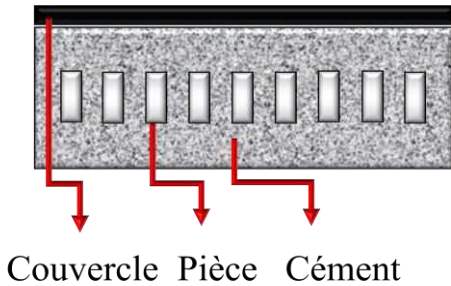


Fig 2. Caisse de cémentation

## III. RÉSULTATS ET DISCUSSIONS

### A. L'ESSAI DE TRACTION

Les résultats de l'essai de traction de la figure 3, présente des courbes de traction très proches de l'acier C5 et l'acier C5 cémenté (sans trempe). Une légère diminution de résistance pour ce dernier est observée suite à un recuit sans production d'une structure martensitique.

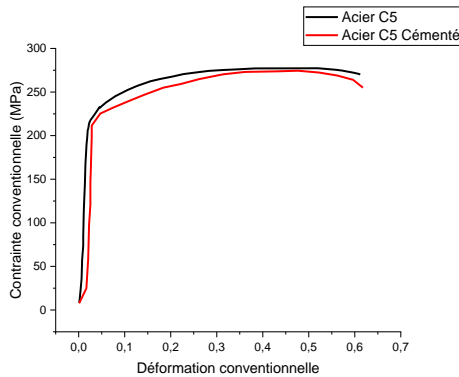
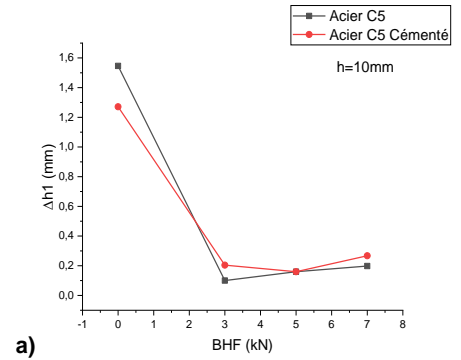


Fig. 3. Courbes conventionnelles de traction des éprouvettes utilisées.

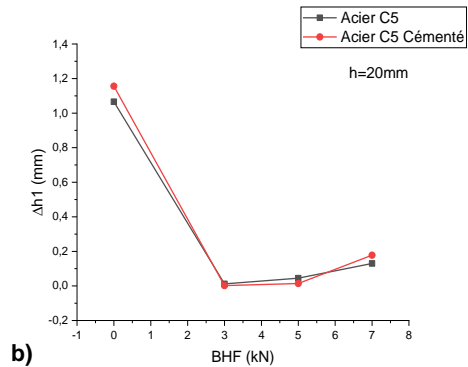
### B. ESSAI D'ÉTIRAGE-PLIAGE EN U

Les échantillons cémentés préalablement à température 900° pendant 3 heures, sans trempe, sont passé en essais d'étirage-pliage en U, en variant la force de serrage et la profondeur d'étirage.

En faisant une analyse des résultats obtenus, on observe en premier lieu un rapprochement des valeurs du retour RE des éprouvettes traitées (cimentées) et des éprouvettes non traitées, particulièrement dans le cas du retour élastique primaire (Fig. 4)



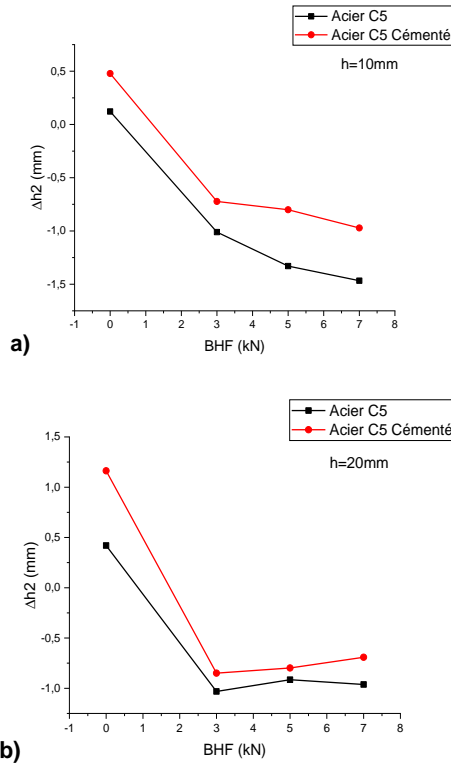
a)



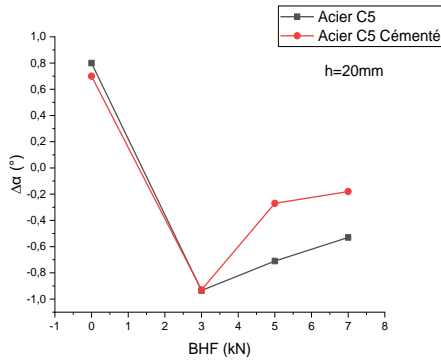
b)

Fig. 4. Variation du retour élastique primaire ( $\Delta h_1$ ) avec la force de serrage pour acier cémenté d'essai d'étirage-pliage en U.

Le retour élastique final, représenté par ( $\Delta h_2$  et  $\Delta \alpha$ ), apparaît plus élevé dans le cas des éprouvettes traitées par rapport à celles non traitées, figures 5 et 6. Cela est dû au fait qu'il y'a un changement des propriétés et du comportement mécanique de la couche externe des éprouvettes par un traitement de cémentation. D'après [2], Gupta a étudié l'investigation des comportements mécaniques d'aciers doux cémentés à différentes plages de température de 850, 900 et 950 °C et il a constaté que le simple traitement thermique améliore considérablement la dureté, la résistance à la traction des aciers doux.



**Fig. 5.** Variation du retour élastique final ( $\Delta h_2$ ) avec la force de serrage pour acier cémenté d'essai d'étirage-plier en U.



**Fig. 6.** Variation du retour élastique final aux extrémités ( $\Delta \alpha$ ) avec la force de serrage pour acier cémenté d'essai d'étirage-plier en U.

#### IV. CONCLUSION

Les traitements de surfaces modifient les propriétés mécaniques du substrat durant l'écoulement plastique et jouent le rôle d'un lubrifiant durant la mise en forme.

Le traitement par cémentation produit un retour élastique plus élevé par rapport aux éprouvettes nus

Une augmentation de BHF réduit le glissement de la feuille entre la matrice et le serre-flan et réduit le retour élastique en augmentant la tension d'étirage. Le retour élastique, en angle et en profondeur, est plus petit pour une petite profondeur d'étirage. L'effet combiné d'un fort serrage et d'une grande profondeur d'étirage réduit énormément le R.E. à des valeurs négatives.

#### REFERENCES

- [1] I. Abdedaim et al., "Effects of coating, holding force, stretching height, yield stress, and surface roughness on springback of steel in the V-stretch bending test", *Mechanical Testing*, 64(5): 678–689, (2022).
- [2] M. K. Alsaadi, "Bending Characteristics of Carburized Low Carbon Steel Experimental and Numerically Study", *Engineering Sciences*, 25(2), 761–773, (2017).

# Study of efficiency of the heterogeneous cell CdTe/ CdS/ SnS

WAHIBA SLIMANI

University Mohamed El Bachir El Ibrahimi of Bordj Bou Arreridj  
Algeria, wahiba.slimani@univ-bba.dz

## ABSTRACT

*Heterogeneous Solar cells are made from different semiconductor materials. This allows their properties to be optimized for increased efficiency and durability. It can be designed to operate in extreme weather conditions or to produce a specific amount of energy. We have made an optimization on the category of CdTe/Cds heterojunction solar cells by studying the effect of the SnS layer on its performance. The best efficiency obtained was for a CdTe layer thickness of 2000 nm, 50 nm of CdS and 20 nm of SnS, these performances are deduced by the AMPS 1D software, where the yield has achieved 23.140 %.*

## KEY WORDS

Simulation by AMPS-1D, Heterogeneous solar cell, CdTe, Cds, SnS.

## I. INTRODUCTION

Heterogeneous solar cells are a fast developing technology that offers significant potential for solar energy production [1]. They are more efficient, less expensive and more customizable than homogeneous solar cells [2]. CdTe/CdS solar cells are a promising technology for solar energy production. They are relatively cheap and easy to make [3].

Our optimization involves adding materials that can increase their yields. SnS, as a semiconductor with: high potential, inexpensive, broad absorption spectrum, and high electrical conductivity, seems a promising candidate, for which its use is proposed in the structure of the CdTe/CdS cell.

This study aimed to deduce the impact of SnS layer in efficiency of the CdTe/CdS cell.

## II. PRESENTATION OF THE CDTE/CDS-BASED CELL:

The electrical performances of the heterogeneous cell is simulated by the AMPS 1D software. The following figure illustrates its structure:

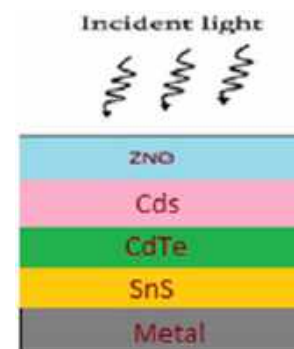


Fig. 1. CdTe/Cds-based cell.

## III. SIMULATION OF SNS THICKNESS VARIATION BY AMPS 1D

Table [1] show the electrical properties of each layer used in the heterogeneous cell structure.

**Tab1.** The parameters for the CdTe CdS-based solar cell at 300K [4, 5].

Parameters	ZnO	CdS	CdTe	SnS
Thickness (nm)	50	20	2000	Variable
Dielectric constant $\epsilon_{PS}$	9	10	9.4	9.4
Electron mobility ( $\text{cm}^2\text{V}^{-1}\text{s}^{-1}$ ) $\mu_{N}$	100	100	500	200
Hole mobility ( $\text{cm}^2\text{V}^{-1}\text{s}^{-1}$ ) $\mu_{P}$	25	25	60	30
Effective conduction band density ( $\text{cm}^{-3}$ ) $N_C$	$2.22 \times 10^{18}$	$1.78 \times 10^{18}$	$8 \times 10^{17}$	$2.2 \times 10^{18}$
Effective valence band density ( $\text{cm}^{-3}$ ) $N_V$	$1.78 \times 10^{19}$	$1.78 \times 10^{18}$	$1.8 \times 10^{19}$	$1.8 \times 10^{19}$
Acceptor concentration ( $\text{cm}^{-3}$ ) $N_A$	0	0	$2 \times 10^{14}$	$2 \times 10^{11}$
Donor concentration ( $\text{cm}^{-3}$ ) $N_D$	$1 \times 10^{18}$	$2 \times 10^{17}$	0	0
Band gap (eV) $E_g$	3.3	2.4	1.5	1.4
Electron affinity (eV) $\chi$	4.4	4.25	4.28	4
Absorption ( $\text{cm}^{-1}$ )	Scaps 2.5	Scaps 2.5	Scaps 2.5	Scaps 2.5

The performances of the proposed cell are simulated by AMPS 1D, which gave an efficiency reaching 23.140% for a thickness of 20 nm of SnS; Their graphs are illustrated by the following figure:



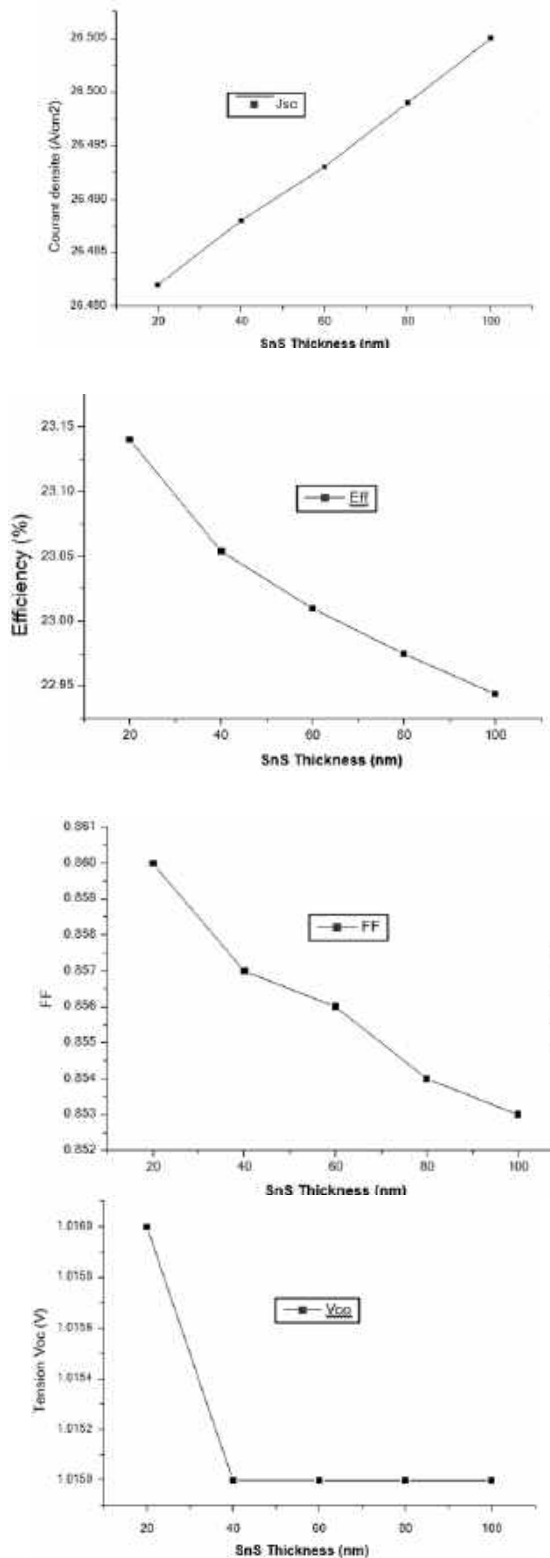


Fig. 2. Variation of: Jsc, Eff, FF and Voc in relation of the SnS thickness.

#### IV. DISCUSSION:

The simulated: Jsc, Eff, FF and Voc characteristics, showed by figure (2) are realized with illumination conditions AM1.5 (1000mW/cm<sup>2</sup>, 300°K), by AMPS 1D software. The results indicate that the solar cell with 20 nm of SnS thickness has given the high efficiency of 23.140%.

#### V. CONCLUSION

By our result, we confirm that SnS is a very promising material for heterojunction solar cells. It has a wide band gap, which allows it to absorb a broad range of wavelengths of light. It is also a good conductor of electricity, which helps to efficiently transport electrons. SnS is also relatively inexpensive and easy to produce, which could make it a cost-effective option for heterogeneous solar cell manufacturing.

#### REFERENCES

- [1] Tölgyesi, C., Bátor, et al. (2023). Ecovoltaics: Framework and future research directions to reconcile land-based solar power development with ecosystem conservation. *Biological Conservation*, 285, 110242.
- [2] Raising Rathod, D., Suresh Karkal, S., Jamadar, A. S., Hashem, A. M., Suresh, P. V., Mamatha, S. S., & Kudre, T. G. (2023). Prospects of novel heterogeneous base catalysts and nanocatalysts in achieving sustainable biodiesel production. *International Journal of Green Energy*, 1-26.
- [3] Adeyinka, A. M., Mbelu, O. V., Adediji, Y. B., & Yahya, D. I. (2023). A review of current trends in thin film solar cell technologies. *International Journal of Energy and Power Engineering*, 17(1), 1-10.
- [4] Sadao Adachi, Properties of Group-IV, III-V and II-VI Semiconductors, Department of Electronic Engineering Gunma University Japan ,2005.
- [5] Fukuda R, Nishimura T, Yamada A. Experimental and theoretical EBIC analysis for grain boundary and CdS/Cu (In, Ga)Se<sub>2</sub> heterointerface in Cu (In, Ga)Se<sub>2</sub> solarcells. *Prog Photovolt Res Appl*. 2023; 31(7):678-689.

# Numerical optimization of (FTO/ZnO/Cs<sub>2</sub>AgBiBr<sub>6</sub>/P3HT/MO) perovskite solar cell

LEILA BECHANE<sup>1\*</sup>, WAHIBA SLIMANI<sup>2</sup>

1. 1 Laboratory of Materials Physics and its Applications, Faculty of technology, PO Box 166 Ichebilia, University of M'sila 28000, Algeria, [Leila.bechane@univ-msila.dz](mailto:Leila.bechane@univ-msila.dz)

2 University Mohamed El Bachir El Ibrahimi, of Bordj Bou Arréridj 34000, Algeria, [wahiba.slimani@univ-bba.dz](mailto:wahiba.slimani@univ-bba.dz)

## ABSTRACT

*A non-toxic, lead-free double-perovskite solar cell (Cs<sub>2</sub>AgBiBr<sub>6</sub>) is simulated using the one-dimensional computer code AMPS-1D. The aim of the present contribution is to study the effect of active layer thickness (Cs<sub>2</sub>AgBiBr<sub>6</sub>) on solar cell performance, namely: short-circuit current (JSC), open-circuit voltage (VOC), form factor (FF) and efficiency (Eff). We also seek to determine the structural parameters characterizing of each layer making up the cell. The best active layer thickness for the solar cell is between 600 and 800 nm. Our optimization gave an optimum thickness of 600 nm, where: Voc= 0.857V, Jsc = 15.983mA/cm<sup>2</sup> and FF= 0.772, which correspond to an efficiency of Eff = 10.567%.*

**KEY WORDS:** AMPS-1D; Cs<sub>2</sub>AgBiBr<sub>6</sub> solar cells; Active layer; Efficiency of perovskite cells.

## I. INTRODUCTION

A new generation of perovskite materials such as Cs<sub>2</sub>AgBiBr<sub>6</sub> has been proposed [1, 2], these materials are inorganic, stable and non-toxic. Moreover, they are considered useful materials for photovoltaic applications since they have been successfully synthesized [3]. Perovskite solar cells based on Cs<sub>2</sub>AgBiBr<sub>6</sub> film have reported efficiency of 2.43% [4].

In this work, we present a numerical study of the non-toxic organic and inorganic double halide perovskite (Cs<sub>2</sub>AgBiBr<sub>6</sub>) photovoltaic cell, using AMPS-1D software, with standard illumination (AM1.5G, 100 mW/cm<sup>2</sup>, 300K). The effect of the thickness of the absorber layer (Cs<sub>2</sub>AgBiBr<sub>6</sub>) on performance (short-circuit current density: Jsc, open-circuit voltage: Voc, form factor FF, conversion efficiency  $\eta$ ) and the J-V

characteristic are deduced.

## II. DESCRIPTION OF THE STRUCTURE

The structure of our solar cell based on the perovskite compound consists of:

- a Layer of zinc oxide (ZnO) (n) used as an electron-transporting material.
- b Double perovskite (Cs<sub>2</sub>AgBiBr<sub>6</sub>) (n) used as an absorbing material.
- c P3HT (poly (3-hexylthiophene)) (p) as a hole-transporting material (see Figure .1).

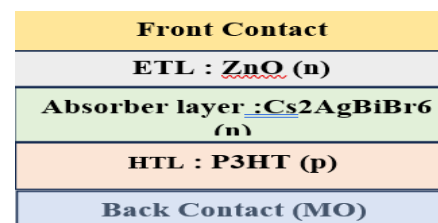


Fig. 1. The solar cell structure.

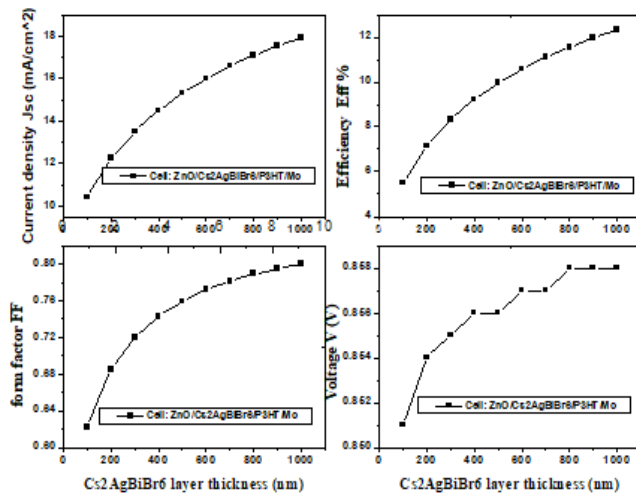
## III. SIMULATION OF INPUT STRUCTURE AND PARAMETERS

All the parameters described in this paragraph and others, used in the simulation are summarized in Table 1[5-9].

**Tab. 1.** Electrical parameter of cell layers

Parameters	ZnO	Cs2AgBiBr6	P3HT
Thickness (nm) <b>L</b>	100	variable	40
Dielectric constant <b>EPS</b>	9	5.8	3.4
Electron mobility ( $\text{cm}^2\text{V}^{-1}\text{s}^{-1}$ ) <b>MUN</b>	100	11.81	$10^{-4}$
Hole mobility ( $\text{cm}^2\text{V}^{-1}\text{s}^{-1}$ ) <b>MUP</b>	25	0.49	$10^{-4}$
Effective conduction band density ( $\text{cm}^{-3}$ ) <b>NC</b>	$2.22 \times 10^{18}$	$1 \times 10^{19}$	$1 \times 10^{20}$
Effective valence band density ( $\text{cm}^{-3}$ ) <b>Nv</b>	$1.78 \times 10^{19}$	$1 \times 10^{19}$	$1 \times 10^{20}$
Acceptor concentration ( $\text{cm}^{-3}$ ) <b>NA</b>	0	0	$6 \times 10^{16}$
Donor concentration ( $\text{cm}^{-3}$ ) <b>ND</b>	$1 \times 10^{18}$	$1 \times 10^{18}$	0
Band gap (eV) <b>Eg</b>	3.4	2.05	2
Electron affinity (eV) <b>CHI</b>	4.3	4.19	3.8
Band tail density of states ( $\text{cm}^{-3}\text{eV}^{-1}$ ) <b>GAO,GDO</b>	$1 \times 10^{14}$	$1 \times 10^{14}$	$1 \times 10^{14}$
Gaussian density of states ( $\text{cm}^{-3}$ ) <b>NDG, NAG</b>	$1 \times 10^{17}$	$1 \times 10^{15}$	$1 \times 10^{13}$
Absorption ( $\text{cm}^{-1}$ )	Scaps2.5	[10]	wxAMPS

#### IV. RESULT GRAPHS

**Fig.2.** Variation of ( $J_{sc}$ ,  $\eta$ , FF and  $V_{oc}$ ) in relation of Cs2AgBiBr6 absorber layer thickness.

#### V. DISCUSSION

The thickness optimization of Cs2AgBiBr6 absorber layer is done from 100nm to 1000nm. The electrical parameters ( $J_{sc}$ ,  $V_{oc}$ , FF and  $\eta$ ) plotted in function of this variation show that, increasing the thickness of the Cs2AgBiBr6 layer lead to increase all photovoltaic parameters.

#### VI. CONCLUSION

By AMPS1-D we have carried out a simulation study and optimization of a non-toxic organic and inorganic double halide perovskite cell. Cs2AgBiBr6 was the absorber layer, P3HT was the HTL, ZnO was the ETL, and Mo was the back contact. The study revealed that for an optimum absorber thickness of 600 nm we have achieved a maximum yield of 10.567%.

#### REFERENCES

1. Zhang, Z., et al., Improvement of Cs2AgBiBr6 double perovskite solar cell by rubidium doping. Organic Electronics, 74: p. 204-210, (2019).
2. Fu, R., et al., Pressure-induced structural transition and band gap evolution of double perovskite Cs2AgBiBr6 nanocrystals. Nanoscale, 11(36): p. 17004-17009, (2019).
3. García-Espejo, G., et al., Mechanochemical synthesis of three double perovskites: Cs2AgBiBr6, (CH3NH3)2TlBiBr6 and Cs2AgSbBr6. Nanoscale, 11(35): p. 16650-16657, (2019).
4. Greul, E., et al., Highly stable, phase pure Cs2AgBiBr6 double perovskite thin films for optoelectronic applications. Journal of Materials Chemistry A, 5(37): p. 19972-19981, (2017).
5. I. Alam, R. Mollick, M.A. Ashraf, Numerical simulation of Cs2AgBiBr6-based perovskite solar cell with, ZnO nanorod and P3HT as the charge transport layers, Phys. B Condens. Matter. 618 ,413187, (2021).
6. J. Zhou, Z. Xia, M.S. Molokeev, X. Zhang, D. Peng, Q. Liu, Composition design, optical gap and stability investigations of lead-free halide double perovskite Cs2AgInCl6, J. Mater. Chem. A. 5 ,15031–15037, (2017).
7. X. Yang, Y. Chen, P. Liu, H. Xiang, W. Wang, R. Ran, W. Zhou, Z. Shao, Simultaneous Power Conversion Efficiency and Stability Enhancement of Cs2AgBiBr6 Lead-Free Inorganic Perovskite Solar Cell through Adopting a Multifunctional Dye Interlayer, Adv. Funct. Mater. 30 ,2001557, (2020).
8. Z. Zhang et al., "Potential Applications of Halide Double Perovskite Cs2AgInX6 (X = Cl, Br) in Flexible Optoelectronics: Unusual Effects of Uniaxial Strains," J Phys Chem Lett, vol. 10, no. 5, pp. 1120–1125, (2019).
9. Hend I, A., M Mottakin, Md Mosaddek ,H.,Md Akhtaruzzaman and Mohammad Junaebur, R. , Design and defect study of Cs2AgBiBr6 double perovskite solar cell using suitable charge transport layers, Semicond. Sci. Technol. 38 ,015005 (11pp), (2023).
10. A. Menedjhi , N. Bouarissa , S. Saib , M. Boucenna and F. Mezrag, Band Structure and Optical Spectra of Double Perovskite Cs2AgBiBr6 for Solar Cells Performance, ACTA PHYSICA POLONICA A, Vol. 137 (2020).

# Synthèse de couches minces d'oxyde de cuivre par sol gel

LAMECHE NORELHOUDA<sup>1,\*</sup>, MELIA HAMICI<sup>2</sup>, HAMMACI CYLIA<sup>1</sup>

1. Affiliation (1): Institut d'Optique et de Mécanique de Précision, université Sétif é-mail :norelhouda\_1@yahoo.fr
2. Affiliation (2): université Sétif département de physique

## ABSTRACT

*Dans ce travail nous avons élaboré des couches minces de CuO par voie Sol-Ge par deux méthodes. La caractérisation structurale et morphologique des couches minces obtenues ont été faites par la diffraction des rayons X (DRX) et par la microscopie électronique à balayage (MEB), la caractérisation optique a été faite par l'UV Visible. La DRX a permis de confirmer l'état cristallin de nos couches minces ainsi que la formation de la phase de CuO pour les deux méthodes d'élaboration. La caractérisation par MEB a montré l'état de surface des couches élaborées. Enfin, l'UV-Visible nous a permis de mesurer la transmission des couches minces à base de CuO, le gap optique est trouvé d'environ 1,76 eV et 1,65 eV.*

**KEY WORDS** (CuO, Sol-Gel, couche mince, Dip Coating.)

## I. INTRODUCTION

Ces dernières années, les oxydes métalliques ont suscité un intérêt considérable en raison de leurs applications différentes telles que les cellules photovoltaïques, les capteurs à gaz, biotechnologie, photo catalyse, capteur biologique, pile à combustible, etc. Parmi tous les oxydes métalliques, les oxydes de cuivre avec ces deux formes stables à savoir: la cuprite (Cu<sub>2</sub>O) et la ténorite (CuO) ont suscité un grand intérêt auprès de la communauté scientifique en raison de leurs propriétés uniques. Ces oxydes présentent des caractéristiques uniques telles que la non toxicité, l'abondance sur terre, faible coût, grande stabilité, disponibilité et son absorption optique importante dans le domaine du visible et de l'ultraviolet. Dans ce travail nous présentons deux protocoles expérimentaux pour élaborer les couches minces CuO.

### A. PREPARATION DES SOLUTIONS

#### 1. SOLUTION DE L'OXYDE DE CUIVRE PURE (SOL -1)

Pour élaborer les couches minces de CuO, on a utilisé l'acetate de cuivre (C<sub>4</sub>H<sub>6</sub>CuO<sub>4</sub>-H<sub>2</sub>O) comme précurseur de base (Cu), le solvant utilisé est isopropanol 2. Dans un bécher on a pesé 0.84g de dé (0.21 M) de masse molaire M = 199.93g/mol, cette masse est dissoute dans 10 ml d'isopropanol, la solution résultante est agitée pendant 5 minutes à la température ambiante pour homogénéiser la solution, puis on a versé 5 gouttes de la Diéthanolamine dans la solution comme stabilisant. La solution obtenue est de couleur bleu est portée à une température de 60°C pendant 2h avec agitation. Avant l'usage, la solution a été préservée pendant 24 heures. Les couches de Sol 1 ont été déposées par dip-coating sur des substrats en verre et un recuit de 500°C pour 1 heure.

#### 2. SOLUTION DE L'OXYDE DE CUIVRE PURE (SOL -2)

Dans un bécher de 50ml, on dissout 1,0041 g d'acétate de cuivre (C<sub>4</sub>H<sub>6</sub>CuO<sub>4</sub>-H<sub>2</sub>O) dans 40 ml d'éthanol à 96% de pureté, 5 ml de DEA ont été ajoutés. On laisse agiter, jusqu'à obtenir une solution homogène, ensuite on rajoute 0,5 ml de polyéthylène glycol et on laisse agiter pendant 3h à 50°C. La solution est maintenue sous agitation à température ambiante jusqu'à l'obtention d'une solution homogène. La solution est laissée 24h avant usage bien couverte. Les couches de Sol 2 ont été déposées par dip-coating sur des substrats en verre et un recuit de 500°C pour 1 heure.

## II. RÉSULTATS ET DISCUSSION

### II.1. CARACTÉRISATION STRUCTURALE

A partir des spectres des rayons X, on peut déterminer la phase de l'oxyde de cuivre synthétisé, ce dernier peut être cristallin, poly-cristallin, monocristallin ou bien amorphe selon les conditions expérimentales utilisées au cours de la préparation

des échantillons. Une analyse par DRX a été effectuée pour étudier les propriétés structurales du CuO pur obtenu par deux solutions différentes, La figure 3.12 montre les diffractogrammes de DRX des couches minces de CuO (Sol-1) et (Sol-2) balayés dans l'intervalle de  $10^\circ$  à  $80^\circ$ , montre que la phase obtenue est bien celle du CuO pour les deux échantillons obtenus par (Sol-1 et Sol-2), cette phase diffracte selon ses pics caractéristiques situés à  $2\theta$  :  $32,35^\circ$ ,  $35,50^\circ$ ,  $38,57^\circ$ ,  $48,46^\circ$ ,  $52,84^\circ$ ,  $57,26^\circ$ ,  $60,82^\circ$ ,  $64,98^\circ$ , et  $65,52^\circ$  chacun correspondant aux plans (100), (002), (111), (-202), (020), (202), (113), (-311), (220) respectivement correspond à la structure pure monoclinique (ténorite) de CuO selon la fiche du CuO (JCPDS numéro de carte 96-901-5823).

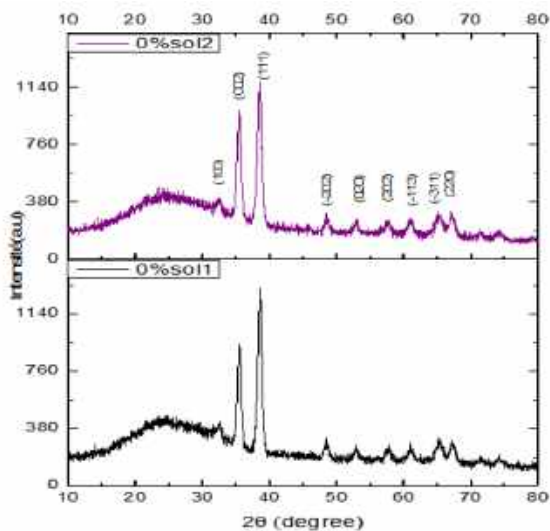


Fig. 1. Spectres du DRX de CuO obtenus pour sol -1 et Sol-2.

## II.2. CARACTERISATION OPTIQUE

L'analyse par UV-visible permet d'étudier les propriétés optiques de couches minces CuO déposés sur des substrats en verre, La Figure 2 montre les spectres de CuO obtenus par les deux méthodes déjà cités Sol-1 et Sol-2 qui ont été enregistrés dans une plage de longueur d'onde allant de 300 nm à 1100 nm, respectivement. Notons que la transmittance est d'environ 45 % pour l'échantillon préparé selon Sol-2 et d'environ 25% pour l'échantillon préparé selon Sol-1. La détermination du gap optique est basée sur le modèle proposé par Tauc, où  $E_g$  est relié au coefficient d'absorption  $\alpha$ . Comme le montre la figure 3, les gaps des échantillons Sol-2 et Sol-1 sont 1,76 eV et 1,65 eV respectivement.

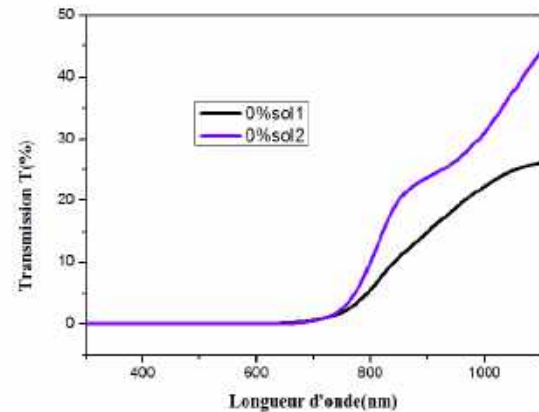


Fig. 2. Spectres de transmittance des échantillons obtenus selon Sol-1 et Sol-2

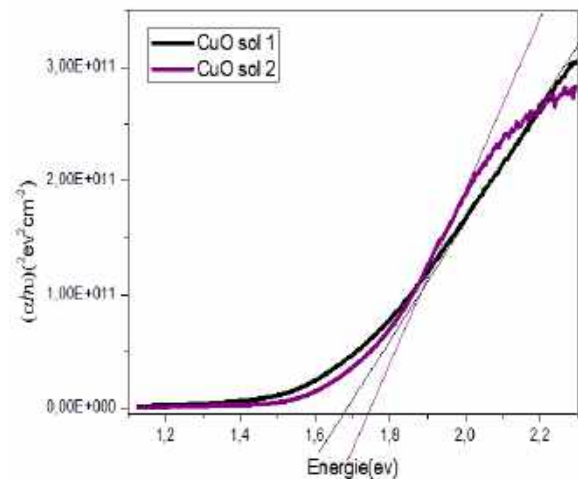
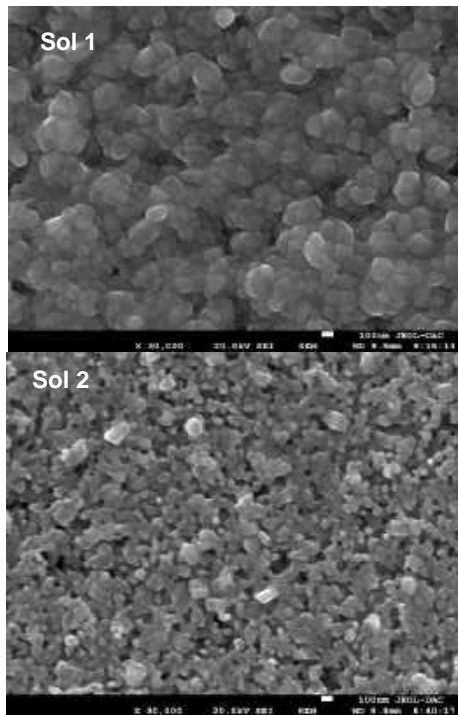


Fig. 3. Gap optique obtenus pour sol -1 et Sol-2.

## II.3. CARACTERISATION MORPHOLOGIQUE

Afin de compléter l'étude sur la microstructure, une étude par microscopie électronique à balayage (MEB), a été réalisée pour les deux couches de CuO. Les images sont prises avec un agrandissement de 30 000 X. Les images MEB nous ont permis d'observer la texture et l'état de surface de nos couches de CuO élaborées par la méthode Sol-Gel. A partir de ces images on peut observer que sa morphologie est nanostructure avec la présence d'amas de formes différentes, de l'ordre de quelques centaines de nanomètres, qui sont distribués aléatoirement dans une matrice lisse mais pas vraiment uniforme. Le Zoom nous montre que chaque cercle est formé d'un grand nombre de cristaux en germination.



**Fig. 4.** Images MEB pour sol -1 et Sol-2.

## I. CONCLUSION

Dans ce travail nous avons réussi à élaborer des couches minces CuO par deux méthodes de synthèse par sol gel, D'après les résultats obtenus par la DRX, l'oxyde CuO obtenu pour les deux sol est polycristallins. L'absence de phase hydroxyde Cu(OH)<sub>2</sub> ou de toute autre phase d'impureté à l'exception de CuO indique l'excellente pureté du CuO, les images MEB montrent une différence dans la taille des grains pour les deux sol, L'UV-Visible nous a donné des résultats de transmittances et absorption avec quoi on a pu calculer le gap optique.

## REFERENCES

- [1] R.A. Zargar, M. Arora, R.A. Bhat, J. Appl. Phys. A 124, 36 (2018).
- [2] R.M. Mohamed, F.A. Harraz, A. Shawky, Ceram. Int. 40, 2127 (2014).
- [3] R.A. Zargar, M.M. Hassan, N. Boora, I. Ahmed, S. Ahmed, K.U. Nissa, S. Kumari, A.K. Hafiz, Int. J. Ceram. Eng. Sci. 2, 169 (2020).



# Investigations of the structural, magnetic and electrical properties of thermally evaporated $\text{Ni}_x\text{Fe}_{1-x}$ thin films

Lamine TABERKANI<sup>1\*</sup>, Ahmed KHARMOUCHE<sup>1\*\*</sup>

<sup>1</sup> Laboratory of surfaces and Interfaces Studies of Solid Materials (LESIMS), Ferhat ABBAS Setif1 University

\*Email [tabrkanilamine@gmail.com](mailto:tabrkanilamine@gmail.com)

\*\* Email [kharmouche\\_ahmed@univ-setif.dz](mailto:kharmouche_ahmed@univ-setif.dz)

## ABSTRACT

*Using thermal evaporation under vacuum, we elaborated polycrystalline  $\text{Fe}_x\text{Ni}_{1-x}$  thin films,  $x$  ranging from 0.2 to 0.45. We used Rutherford Backscattering Spectrometry, X-ray diffraction, atomic force microscopy, Hall Effect measurement system (HMS-5300) and Vibrating Sample Magnetometer tools, to study their structure, microstructure, surface morphology, chemical compositions, electrical and magnetic properties. It was found that X-ray diffraction spectra exhibited face centered cubic structure with  $\langle 111 \rangle$  preferred orientation, the crystallite size and lattice parameter increasing with increasing iron content. Electrical resistivity and magnetoresistance decrease with increasing film thickness, but mobility increases. curves infer an in-plane easy axis without any preferential direction. It is also found that the saturation magnetization  $M_s$  increases and the coercive field  $H_c$  decreases with iron content.*

**KEYWORDS:**RBS;XRD;VSM;ELECTRICAL RESISTIVITY

## I. INTRODUCTION

Ni, Fe and Co are by far the most studied transition metals, during years, for their very wide uses in various magnetic equipment, spintronic, anisotropic and giant magnetoresistances, medical applications [1-7]. It is well established that FeNi thin films display excellent ferromagnetic properties, particularly a reduced coercivity and magnetostriction, high permeability and low magnetic anisotropy. FeNi films are used in various applications in the magnetic recording technology, as free layer of Anisotropic Magnetoresistance (AMR), Giant Magnetoresistance (GMR) and Tunnel Magnetoresistance (TMR) sensors for Hard Disc Drive (HDD)...

## II. RESULTS AND DISCUSSIONS

### A. RBS ANALYSIS

The RBS technique is a very powerful tool widely used to obtain the elemental compositions in depth of many materials. All the RBS spectra show the same profile. Specimen of RBS spectra are displayed in Fig. 1. The plateau of the curve, characterizing the silicon substrate and located to the left of the spectrum, falling abruptly to zero at the level of channel 200, is plainly separated from the large energetic peak relating to FeNi. This corroborates the absence of interdiffusion between the magnetic layer and the substrate. The analysis of all the RBS spectra made it possible to quantify our films, with an estimated thickness of 45 nm and compositions  $x = 0.2; 0.24; 0.30; 0.32; 0.40; 0.45$ ,  $x$  being the atomic percentage of iron, with an accuracy less than 3%.

### A. XRD ANALYSIS

We performed X-ray diffraction measurements on  $\text{Fe}_x\text{Ni}_{1-x}$  samples. The analysis of the spectra makes it possible to estimate the position and intensity of the Bragg peaks, once the impact of the instrumental contribution and  $K\alpha_2$  line are stripped analytically. Fig. 2 illustrates the diffraction patterns of our films. Next, we make use of the experimental spectra to obtain the identification and the crystallinity of the FeNi/Si(111) phases, using the X' Pert High Score Plus software from Philips, the Origin 2019 software from OriginLab, and, by composition, the data from the ICDD (International Center for Diffraction Data) sheets for the processing of the experimental spectra.

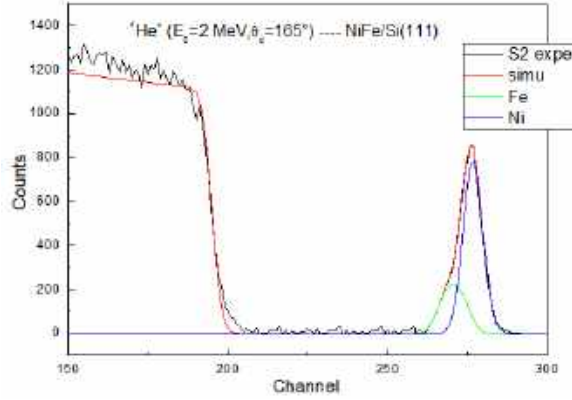


Fig. 1. A specimen of experimental simulated RBS spectra example of  $\text{Ni}_x\text{Fe}_{1-x}$  thin films onto Si (111) substrate.

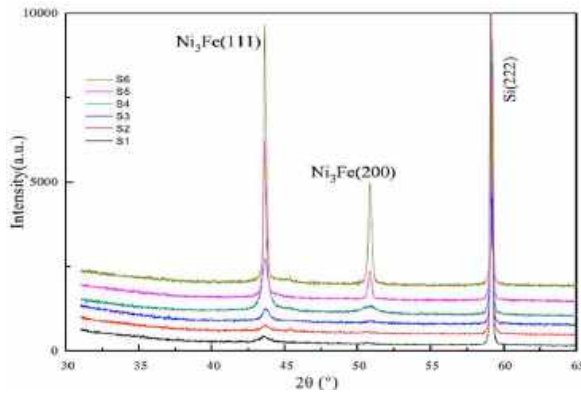


Fig. 2. XRD patterns of  $\text{Fe}_x\text{Ni}_{1-x}$  thin films.

### B. ELECTRICAL PROPERTIES

The measurements of electrical resistivity as well as magnetoresistance and mobility of the films were carried out using the Hall effect measurement system (HMS-5300), based upon the Van der Pauw method. Fig. 3 presents the evolution of the electrical resistivity  $\rho$  versus iron content

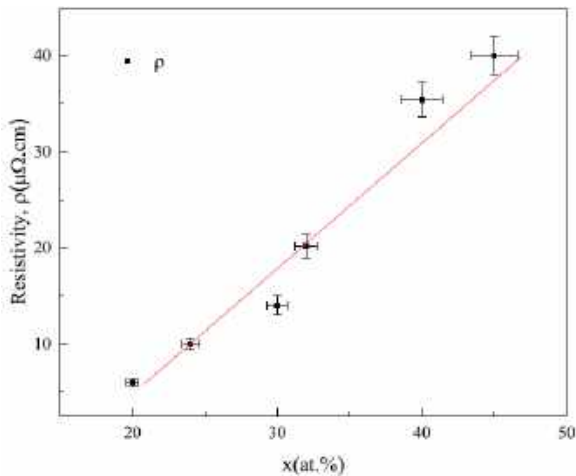


Fig. 3. Electrical resistivity  $\rho$  as a function of iron content  $x$ . The bold squares are experimental points.

### C. MAGNETIC PROPERTIES

The magnetic properties were probed by analyzing the magnetization curves recorded at room temperature, using a vibrating sample magnetometer (VSM), and applying a magnetic field up to 20 kOe, in the longitudinal configuration. The values of several parameters, namely the magnetic moment, the saturation magnetization  $M_s$ , the squareness ratio SQR, and the coercive field  $H_c$  are extracted from the hysteresis loops. In Fig. 4 we plot the variations of the saturation magnetization  $M_s$  as a function of iron content  $x$ .

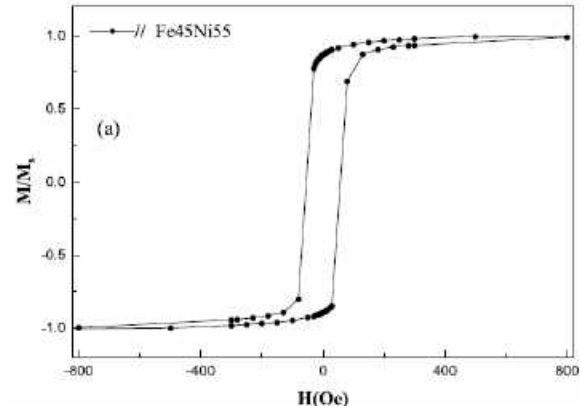


Fig. 4. Specimen of magnetization curves in the longitudinal configuration

### III. CONCLUSION

In this work, we elaborated  $\text{Fe}_x\text{Ni}_{1-x}$  thin films, using the physical vapor deposition technique under vacuum. We investigated the effect of iron content  $x$  on their properties. These polycrystalline thin films exhibit face-centered cubic  $\text{Ni}_3\text{Fe}$  structure, with a  $\langle 111 \rangle$  texture. The addition of iron produced an increase in the crystallite size and in the lattice parameter, together with an increase in microstrains, inferring that the films are under a tensile stress, probably due to the mismatch of lattice parameters between  $\text{Fe}_x\text{Ni}_{1-x}$  thin film and Si(111) substrate. Both the electrical resistivity and the magnetoresistance increase with the addition of iron atoms, considered as impurities in the first matrix containing a majority of nickel atoms. The saturation magnetization  $M_s$  increase with  $x$  increase, following Slater-Pauling curve, whereas the coercive field  $H_c$  decreases, due probably to the evolution of the crystallite size as well as to the shape anisotropy of the  $\text{Fe}_x\text{Ni}_{1-x}$  thin films.

**REFERENCES**

- [1] M. Zhang, C. Deng, J. Mater. Sci. Mater. Electron. **32** (2021) 4949–4960.
- [2] A. Melloul, A. Kharmouche, J. Mater. Sci. Mater. Electron. **30** (2019) 13144–13150.
- [3] M. Tinouche, A. Kharmouche, B. Aktas, F. Yildiz, A.N. Koçbay, J. Supercond. Nov. Magnetism **28** (2015) 921–925.
- [4] S.M. Chérif, Y. Roussigné, A. Kharmouche, T. Chauveau, D. Billet, Eur. Phys. J. B **45** (2005) 305–309.
- [5] A. Kharmouche, J. Nanosci. Nanotechnol. **11** (2011) 4757–4764.
- [6] N. Guechi, A. Bourzami, A. Guittoum, A. Kharmouche, S. Colis, N. Meni, Physica B **441** (2014) 47–53.
- [7] A. Kharmouche, I. Djouada, Appl. Surf. Sci. **254** (2008) 5732–5735.

# Simulation d'une jonction ZnO/NiO par Scaps 1D pour application photovoltaïque

LOUCIF MAROUA<sup>1,\*</sup>, HAMICI MELIA<sup>2</sup>, AND DERAFA ACHOUR<sup>2</sup>

1.Department of Physics Faculty of Science, URME, University Ferhat Abbas Sétif 1  
Algeria, [\\*maroualoucif198@gmail.com](mailto:maroualoucif198@gmail.com)

2.Department of Physics Faculty of Science, DAC, University Ferhat Abbas Sétif  
Algeria

## ABSTRACT

Dans ce travail, nous avons simulé la caractéristique I-V à l'aide du logiciel « SCAPS 1D », une jonction composée d'une couche fenêtre ZnO et d'une couche absorbante NiO. Notre objectif était d'optimiser quelques paramètres pour améliorer le rendement de la jonction.

En faisant varier les épaisseurs et les bandes interdites de chaque oxyde avec des valeurs tirées de la bibliographie [1,2], nous avons constaté après plusieurs tentatives que les meilleurs paramètres qui donnent de bonnes performances sont : une épaisseur de 2950 nm et une énergie de gap de 1,75 eV, et une épaisseur de 375 nm et une énergie de gap de 3,1 eV pour NiO et ZnO respectivement.

Avec ces valeurs testées, nous avons trouvé que la jonction ZnO/NiO répond avec une bonne caractérisation I-V.

Les meilleures valeurs simulées concernant la photo courant, le rendement photovoltaïque  $\eta$  et le nombre d'électrons photo générés de cette hétérostructure sont : 33,91 mA/cm<sup>2</sup>, 16,88%  $2,10^{19}$  ev respectivement.

**MOTS CLÉS** Scaps 1d, ZnO, NiO, le rendement photovoltaïque.

## I. INTRODUCTION

Les nouvelles recherches technologiques avancées sont basées sur l'élaboration de nanomatériaux qui ont été au cœur de nombreuses études à cause de leurs propriétés intéressantes qui ne peuvent être trouvées dans les matériaux massifs. Les nanomatériaux sont largement utilisés dans différentes applications telles que les capteurs de gaz, les cellules solaires, la photocatalyse, etc et parmi ces matériaux TiO<sub>2</sub>, SiO<sub>2</sub>, SnO<sub>2</sub>, NiO, ZnO etc et dans ce travail on s'intéresse aux couches minces de ZnO et NiO en raison de leur disponibilité, faible coût, non toxicité. L'intérêt de ce travail consiste à simuler la caractéristique I-V d'une jonction hétérogène réalisée à partir de deux oxydes ZnO et NiO, on utilisant le logiciel « SCAPS 1D » destiné pour la conception des cellules solaires. Cette étude nous a permis de trouver une bonne caractéristique courant/tension ( $I=f(V)$ ) et un bon rendement.

## II. RESULTATS ET DISCUSSIONS

Après exécution du logiciel, une fenêtre de résultat affiche le tracé de la caractéristique I-V et le rendement  $\eta$  (16.88%), par contre le nombre d'électrons photogénérés  $n_e$  a été calculé et affiché à partir du courant de court-circuit  $J_{sc}$ , il a été trouvé dans l'ordre de  $2.10^{19}$ . Le rendement de la jonction est lié à l'épaisseur du NiO cela indique que plus la couche est épaisse plus elle pourrait absorber de photons qui à leur tour génèrent un excès en porteurs de charge voir la Fig. 1 et le Tabl .1.

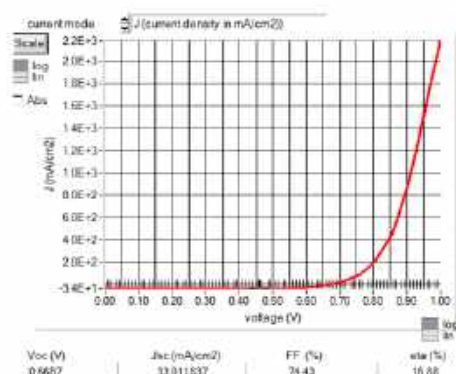


Fig. 1. La caractéristique courant- tension (I-V) avec le rendement photovoltaïque.

Epaisseur de ZnO (nm)	Epaisseur de NiO(nm)	le nombre d'électrons(ev)	$\eta$ (%)
375	2950	$2,10^{19}$	16,88

Tabl. 1. Les résultats de la simulations.

### III. CONCLUSION

Nous avons utilisé logiciel « SCAPS 1D » pour simuler les caractéristiques d'une jonction ZnO/NiO.

Le rendement de la jonction est lié à l'épaisseur du NiO (couche absorbante) trouvée dans l'ordre e 2950 nm.

L'épaisseur de la couche fenêtre de ZnO doit être comprise entre 300nm-400nm pour avoir de bonnes performances de la jonction

Plus le rendement est meilleur plus le photo-courant est amélioré.

D'après l'exploitation de ces résultats, la jonction ZnO/NiO peut être réalisable autant que cellule photovoltaïque en pratique.

### REFERENCES

[1] F. Baig, Numerical Analysis for Efficiency Enhancement of Thin Film Solar Cells, Politècnica de València, 2019;

[2] S.H. Zyoud, A.H. Zyoud, N.M. Ahmed, A.F.I. Abdelkader, Numerical Modeling Analysis for Carrier Concentration Level Optimization of CdTe Hetero-junction Thin Film-Based Solar Cell with Different Non-Toxic Metal Chalcogenide Buffer Layers Replacement: Using SCAPS-1D Software. Crystals 2021, 11, 145, Crystals 2021,

# ***Session T11: Additive manufacturing***



# PROTHESES PAR FABRICATION ADDITIVE (IMPRESSION 3D)

BOUCHAREB SAMIR <sup>1,2\*</sup>

1. Research Center in Industrial Technologies CRTI, P.O. Box 64 Cheraga 16014, Algiers, Algeria;
2. Unité de Recherche des Matériaux Emergents –Sétif–URMES, Equipe de Valorisation des Polymères, Université Ferhat ABBAS Setif-1, Algérie;

## ABSTRACT

*La fabrication additive, également connue sous le nom d'impression 3D, a réalisé des avancées significatives dans divers domaines, y compris la production de dispositifs prothétiques. En Algérie la fabrication additive pour les dispositifs prothétiques est un sujet très jeune, donc il est nécessaire, en priori, à désigner un plans théorique bien précise afin de minimiser les inconvénients des méthodes conventionnelles de fabrication, ainsi que l'optimisation du rapport performance / coût.*

## KEY WORDS

Impression 3D, Fabrication additive, Prothèses, Physique médicale.

## I. INTRODUCTION

La fabrication additive, Il s'agit d'une technologie qui consiste à créer des objets tridimensionnels en ajoutant du matériau couche par couche. On parle souvent d'impression 3D. La fabrication additive a diverses applications, notamment dans le domaine des prothèses [1]. La Fabrication de prothèses : Les prothèses, ou prothèses, sont des dispositifs artificiels qui remplacent les parties manquantes du corps, telles que des membres ou des dents. Ceux-ci peuvent être fabriqués à l'aide de diverses techniques, notamment des méthodes traditionnelles comme le moulage et la coulée ou des méthodes plus modernes comme la fabrication additive (impression 3D).

## II. LES INCONVENIENTS DES PROTHESES FABRIQUEES PAR LES METHODES CONVENTIONNELLE (MOULAGE/THERMOFORMAGE)

- ✓ Une fonctionnalité médiocre
- ✓ Aspect peu esthétique.
- ✓ Durabilité limitée.
- ✓ Besoins en entretien fréquent.
- ✓ Coût élevé.
- ✓ Augmentation de la température de la peau sous le dispositif [2].

Donc la nécessité de les développer sera souhaitable.

## III. LA VALEUR AJOUTÉE DE LA FABRICATION ADDITIVE

- ✓ **Personnalisation** : La fabrication additive permet de créer des prothèses sur mesure pour chaque patient. Les prothèses peuvent être adaptées aux besoins spécifiques de l'individu en termes de taille, de forme et de fonctionnalité.
- ✓ **Conception complexe** : Avec la fabrication additive, il est possible de créer des designs complexes et organiques qui seraient difficiles, voire impossibles, à réaliser avec des méthodes conventionnelles. Cela permet de concevoir des prothèses plus légères, ergonomiques et esthétiques.
- ✓ **Réduction des déchets** : Contrairement aux

méthodes traditionnelles de fabrication, qui peuvent générer beaucoup de déchets, la fabrication additive est plus économe en matières premières, car elle ajoute de la matière couche par couche, réduisant ainsi le gaspillage.

- ✓ **Temps de production réduit :** La fabrication additive peut souvent être plus rapide que les méthodes traditionnelles, car elle évite certaines étapes de fabrication, telles que l'usinage ou le moulage. Cela permet de fournir des prothèses plus rapidement aux patients.
- ✓ **Amélioration de la fonctionnalité :** Les prothèses fabriquées par impression 3D peuvent intégrer des fonctionnalités avancées, telles que des mécanismes articulés complexes ou des composants internes personnalisés pour améliorer la mobilité et le confort du patient.
- ✓ **Réduction des coûts de main-d'œuvre :** Dans certains cas, la fabrication additive peut réduire les coûts de main-d'œuvre, car elle nécessite moins d'interventions manuelles que les méthodes traditionnelles. Cela peut se traduire par des coûts de fabrication plus bas.
- ✓ **Matériaux innovants :** La fabrication additive permet l'utilisation de matériaux avancés, tels que des polymères spéciaux, des composites et même des biomatériaux, offrant ainsi des options plus diversifiées pour les prothèses.
- ✓ **Réduction des coûts à long terme :** Bien que la fabrication additive puisse avoir des coûts initiaux plus élevés en raison de l'équipement spécialisé, elle peut réduire les coûts à long terme en minimisant les besoins de réparation et d'entretien des prothèses grâce à une meilleure adaptation initiale et à une durabilité accrue.

#### IV. **LES ÉTAPES CLES DE LA PRODUCTION D'UNE PROTHESE EN FABRICATION ADDITIVE (PROTHESE D'UNE MAIN COMME EXEMPLE)**

##### **Étape 1 : Recherche et Conception**

- ✓ **Identifier les Besoins de l'Utilisateur :** Comprendre les besoins spécifiques de la personne qui utilisera la main prothétique. Prendre en compte des facteurs tels que le niveau d'amputation, les fonctionnalités désirées et l'esthétique.
- ✓ **Prendre les mesures :** Prendre des mesures exactes et avec précision et s'assurer que la conception est ajustable et personnalisable pour s'adapter à différentes tailles de main et exigences fonctionnelles de la personne en besoin.

##### **Étape 2 : Sélection du Matériau**

- ✓ **Choisir le Matériau d'Impression :** Sélectionner un matériau approprié pour l'impression 3D. Les matériaux couramment utilisés pour les prothèses comprennent le PLA (Acide Polylactique) et l'ABS (Styrène-Acrylonitrile-Butadiène).
- ✓ **Considérer la Force de Préhension :** S'assurer que le matériau choisi peut fournir la force de préhension et la durabilité requises pour l'utilisation prévue.

##### **Étape 3 : Impression**

- ✓ Imprimer les différentes pièces de la conception.

##### **Étape 4 : Assemblage et Intégration**

- ✓ Assembler les différentes pièces imprimées.

##### **Étape 5 : Tests et Ajustements**

- ✓ **Ajustement et Confort :** Tester la main prothétique sur l'utilisateur prévu. S'assurer qu'elle s'adapte confortablement et ne provoque pas d'inconfort ou de douleur.
- ✓ **Fonctionnalité :** Tester la fonctionnalité de la main, telle que la préhension d'objets de différentes tailles et formes. Effectuer des ajustements si nécessaire pour améliorer les performances.

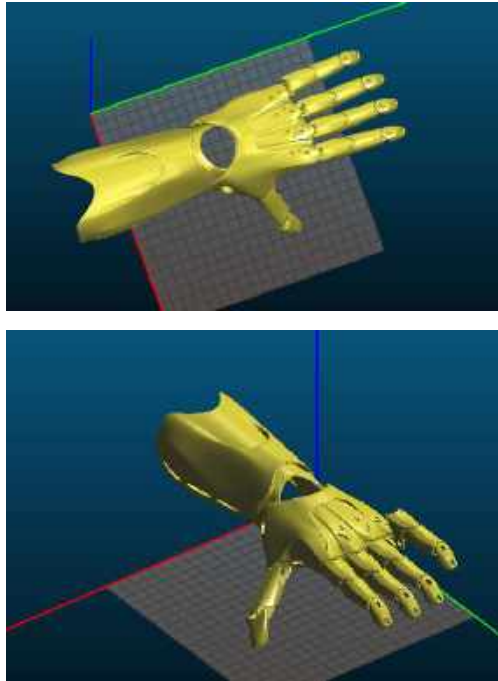


**Fig. 1.** Photos d'un modèle d'une prothèse d'une main à imprimer en 3D.

## V. CONCLUSION

La planification et la préparation théorique d'un projet en fabrication additive pour les prothèses est une étape clé qui vise à fixer les grandes lignes de la conception, la production et les performances des dispositifs prothétiques imprimés en 3D, ce qui contribue finalement à améliorer la qualité de vie des personnes qui en dépendent.

## REFERENCES

- [1] Kaufui V. Wong, Aldo Hernandez, "A Review of Additive Manufacturing", International Scholarly Research Notices, vol. 2012, Article ID 208760, 10 pages, 2012. <https://doi.org/10.5402/2012/208760>
- [2] Biddiss, Elaine, Dorcas Beaton, and Tom Chau. 2007. Consumer design priorities for upper limb prosthetics. Disability and Rehabilitation: Assistive Technology 2 (6): 346-57.

# The effect of the Geometry and Material Type of Heat Sink on the Cooling of the Electronic Chip

CHADI KAMEL<sup>1\*</sup>, LAIDOUDI FAROUK<sup>1</sup>, AZZOUZ EL AMIN<sup>2</sup> AND BENCID ABDESLAM<sup>1</sup>

<sup>1</sup>Research Center in Industrial Technologies CRTI, P.O. Box 64, Cheraga, 16014, Algiers, Algeria.

[chadikamel\\_dz@yahoo.fr](mailto:chadikamel_dz@yahoo.fr)

<sup>2</sup>University of Science and Technology of Oran, 1505 El M'nouar, Oran, Algeria

## ABSTRACT

*This work aims to study the effect of the shape and type of heat sink material on the cooling of the electronic chip. For this purpose, we chose three models or geometric shapes of the heat sink to study. We also chose three different types of materials according to their thermo-physical properties of the heat sink. The heat flow of electronic chips is constant. The results showed that Model No. 3 is the most suitable for the chip cooling process. The results also showed that the copper material helps reduce the temperature of the electronic chip, followed by the aluminum material, while the steel material does not give ideal cooling of the chip.*

## KEY WORDS

Material type; electronic chip; heat sink; temperature

## I. INTRODUCTION

The problem of overheating electronic components is considered one of the most important problems that researchers have addressed. Excessive heat makes the electronic component not work well and its performance decreases over time. In addition, an excessive temperature rise of electronic chips will increase packaging and cooling costs [1]. Several studies that have addressed this topic, including: Song et al. [2] have cooled the electronic chip with air and using a miniature atomization. Singh et al.[3] have studied the thermo-hydraulic performance of cooling electronic chips with high heat flux through microchannel heat sinks with fins. Aly et al. [4] conducted an experimental study on the performance of solar cells coupled to a heat sink. They have also studied the effect of using a heat sink cooling system on the performance of solar cells.

## II. GEOMETRICAL SYSTEM

The figure below (Fig.1) shows three models of heat sinks chosen according to their shape to cool an electronic chip with the dimensions (35×35 mm<sup>2</sup>) placed below the heat sink:

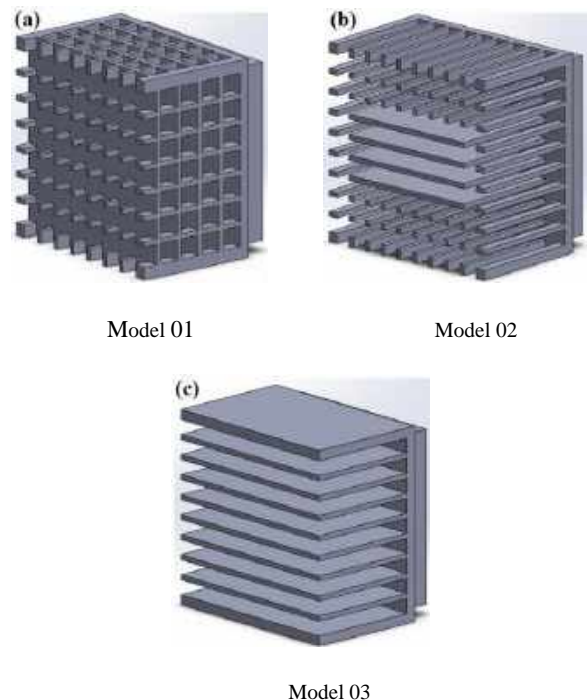


Fig. 1. Geometric shape of three models studied

## III. INDEPENDENT OF THE RESULTS

Fig. 2 represents the temperature distribution for three models of the heat sink at a constant airspeed. We note that model No. 3 helps dissipate heat from the electronic chip, and this is due to the ease with which the fins of the heat sink obtain proper ventilation.

Fig. 3 shows the variation of the average temperature of the electronic chip for three models as a function of time. It has been found that the average

temperature of the chip rises over time and then changes by small values after some time for three models due to heat dissipation from the heat sink. We also note that heat sink No. 3 is the best in the process of cooling the electronic chip.

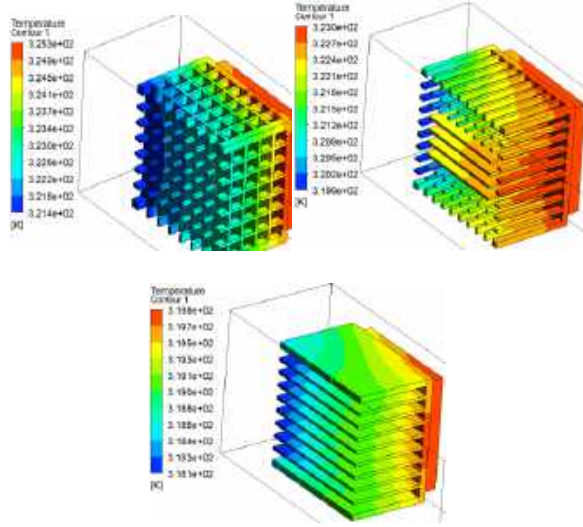


Fig. 2. Temperature distribution for the three models studied

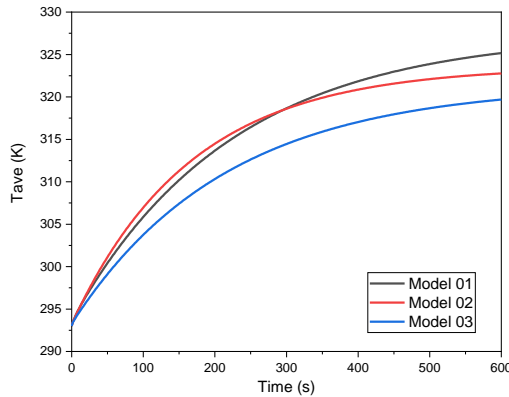


Fig. 3. Distribution of  $T_{ave}$  for three models as a function of time

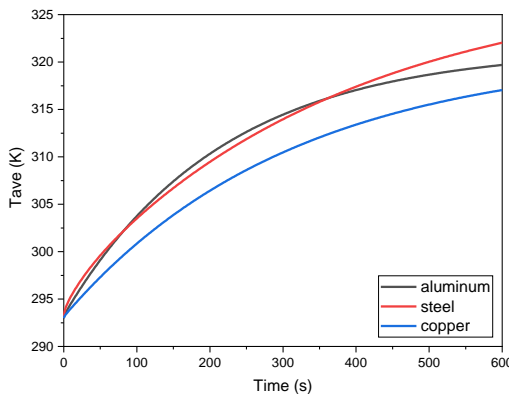


Fig. 4. Distribution of  $T_{ave}$  for model 03 as a function of the material type

Figures 4 and 5 represent the variation of the average temperature of the electronic chip as a function of the material type of model 03 and model 02, respectively. We note that the heat sink material contributes to reducing the average temperature of the chip and accelerating the cooling process. According to the results, we find that copper is suitable and the best material in the cooling process compared to aluminum and steel. This is due to the thermo-physical composition of the metal. We also notice according to the results that steel does not perform the cooling process better for the chip compared to aluminum.

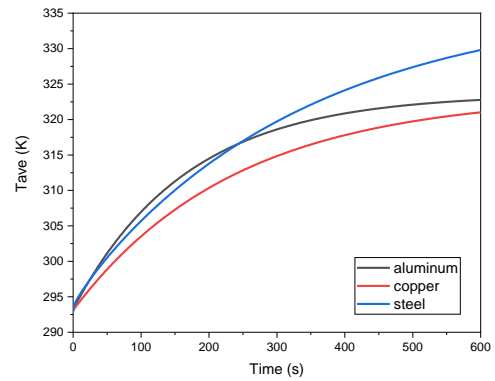


Fig. 5. Distribution of  $T_{ave}$  for model 02 as a function of the material type

#### IV. CONCLUSION

In this work, we studied the effect of the geometry of three heat sink models and their material type on the electronic chip cooling process. According to the results obtained, Model No. 3 helps dissipate heat from the electronic chip and is considered the best in the process of cooling the electronic chip. Copper also increases the efficiency of the heat sink compared to aluminum and steel.

#### REFERENCES

- [1] K. Skadron et al., "Temperature-aware micro-architecture," ACM SIGARCH Computer Architecture News. 31, (2) 2-13 (2003).
- [2] C. Song et al., "A miniature atomization-air-cooled heat sink for electronic chips," International Journal of Thermal Sciences .190, 108305 (2023).
- [3] V. Singh et al., "Thermo-Hydraulic Performance of High Heat Flux Electronic Chip Cooling Through Microchannel Heat Sinks with Fins on Base Plate," Energy Storage Systems. 385-413 (2022).
- [4] M.A. S. Aly et al., "An experimental study of the performance of the solar cell with heat sink cooling system," Energy Procedia.162, 127-135 (2019).

# Impact of the Diameter Dimension of Multi-Channel Cooler on the Flow and Temperature Distribution

CHADI KAMEL<sup>1\*</sup>, BELFENNACHE DJAMEL<sup>1</sup>, AZZOUZ EL AMIN<sup>2</sup>, LAIDOUDI FAROUK<sup>1</sup> AND FOURAR ISSAM<sup>1</sup>

<sup>1</sup>Research Center in Industrial Technologies CRTI, P.O. Box 64, Cheraga, 16014, Algiers, Algeria.

[chadikamel\\_dz@yahoo.fr](mailto:chadikamel_dz@yahoo.fr)

<sup>2</sup>University of Science and Technology of Oran, 1505 El M'nouar, Oran, Algeria

## ABSTRACT

*The aim of this work is to study the effect of the diameter dimension of multi-channel cooler on the flow and temperature distribution. For this reason, three cases of diameter have been considered, case1  $d=6\text{mm}$ , case2  $d=9\text{mm}$ , and case 3  $d=12\text{mm}$ . The air inlet velocity is constant for all cases. The governing equations of the physical phenomenon were solved by the finite volume method. According to the results obtained from this study, it was noted that when the diameter of the channel is increased with a constant velocity, high levels of vorticity are recorded at the outlet which decreased with the increased channel diameter. At different temperature distribution according to the diameter of the channel, increasing in the channel diameter causes a decreasing of the hot source temperature.*

## KEY WORDS

Muti-channel; diameter; cooler; flow; temperature

## I. INTRODUCTION

Cooling by channels is considered one of the best methods of cooling, as we find some researchers used it in the field of heat exchange. Song *et al* [1] showed that the multi-channel design can effectively enhance the heat transfer effect of the cooling plate and reduce the pressure drop. The local serpentine channel design can increase the fluidity of the coolant, avoid local backflow, make the temperature distribution more uniform and avoid local temperature rise. Yin *et al.* [2] designed a novel kilowatt-scale air cooled PEMFC stack based on graphite plate. Their experimental results prove that the stack with edge channel design shows better performance than the conventional stack without edge channels. Xing *et al.* [3] found controlling the cooling water flow rate and stack inlet cooling water temperature could effectively satisfy the thermal management constraints template.

## II. GEOMETRICAL SYSTEM

The Fig.1a represents a multi-channel cooler with dimensions'  $L=W=2H$ ,  $H=50\text{mm}$  to cool a heat source located at the top. The cooler has a symmetrical shape that can be studied on the field shown in the figure Fig.1b

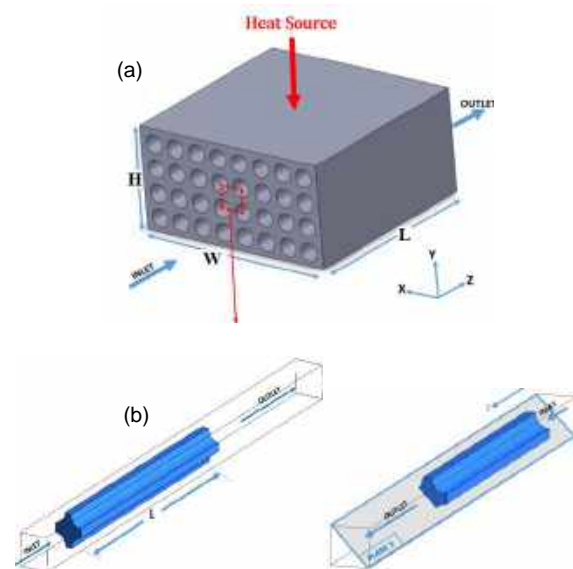


Fig. 1. A) multi-channel cooler b) domain study

## III. RESULTS

This section will present the results for the three cases under consideration in the form of streamlines, velocity and temperature distribution. Fig. 2 represents streamlines for three cases. We note that the diameter of the channel has an effect on the air flow at the channel exit. As the channel diameter increases, the vortexes size decrease, and the air velocity inside the channel decreases as shown in Fig.3. This is due to the



principle of momentum conservation. The channel section decreases lead to the increasing in the flow velocity and vice versa.



Fig. 2. Stream line distribution for the three cases studied

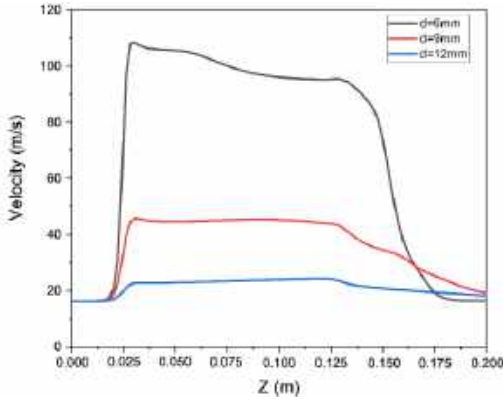


Fig. 3. Distribution of velocity at plane 1 for different channel diameter

Fig.4 represents the distribution of the surface temperature of the cooler for the two cases, case 1 - diameter  $d=6\text{mm}$  and case 2  $d=9\text{mm}$ , under the influence of a heat source placed at the top of the cooler with a constant value and the same value of the air entry speed in both cases. We notice that the temperature distribution on the surface of the cooler is different for the two cases, due to The effect of the diameter of the channel, we find that when the diameter of the channel increases, the temperature of the heat source decreases, i.e. in the first case, it is equal to  $345\text{K}$ . When the diameter is increased, the maximum temperature becomes equal to  $335\text{K}$ , and this is due to the increase in the contact area between the surfaces of the coolant channels and the cold air. We also find that the temperature of the upper surface of the cooler decreases with the increase in the diameter of the channel, which is shown in Fig.5.

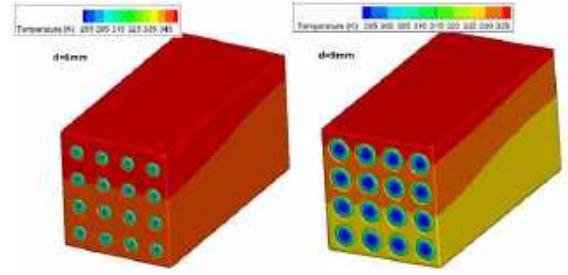


Fig. 4. Temperature distribution for case 1 ( $d = 6\text{ mm}$ ) and case 2 ( $d = 9\text{ mm}$ )

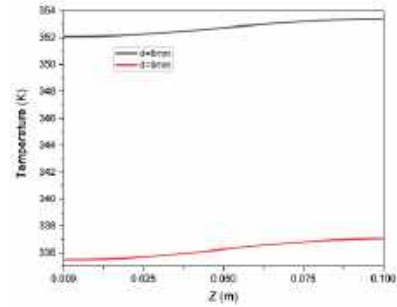


Fig.5. Temperature variation of the upper surface of the cooler For  $d=6\text{mm}$  (case 01) and  $d=9\text{mm}$  (case 02)

#### IV. CONCLUSION

In this work, we have shown the effect of the channel diameter of the cooler on the air flow and the temperature distribution at the same value of the air inlet velocity. This led us to conclude that the channel diameter of the cooler affects the flow of air at the exit of the channel. When the diameter increases, the flow velocity decreases and the vortices size decreases. Besides, the maximum temperature of the heat source decreases, and vice versa.

#### REFERENCES

- [1] J. Song et al., "Design and numerical investigation of multi-channel cooling plate for proton exchange membrane fuel cell," Energy Rep. 8, 6058-6067 (2022).
- [2] C. Yin et al., "Design and numerical analysis of air-cooled proton exchange membrane fuel cell stack for performance optimization," Energy Convers. Manage. 245, 114604 (2021).
- [3] L. Xing et al., "Thermal analysis and management of proton exchange membrane fuel cell stacks for automotive vehicle," Int. J. Hydrogen Energy. 46, 32665-32675 (2021).

# Effect of printing direction on 3D printed 3 DM ABS black reins specimens by Stereolithography SLA

LEILA LAMIRI<sup>1,2\*</sup>, MOHAMED HAMIDOUCHE<sup>1</sup>, HASSAN HAMMOUCHI<sup>1</sup>, ABDELGHANI KENZOUR<sup>1</sup>, CHIBANI ATEF<sup>1</sup>, BOUSSAHA BOUCHOUL<sup>1</sup>, OUAFIA BELGHERBI<sup>1</sup>, SAMAH BOUDOUR<sup>1</sup>, ASSIA TOUNSI<sup>1,2</sup>, LASMI SOFIANE<sup>1</sup>, KATIB HAMLAOUI<sup>1</sup>, MERABET SAFIA<sup>1</sup>, RADHIA KHOUATRA<sup>1</sup>

1. Research Center in Industrial Technologies CRTI, P.O. Box 64, Cheraga 16014, Algiers, Algeria
2. Laboratoire d'Electrochimie et Matériaux, Département de Génie des Procédés, Faculté de Technologie, Université Ferhat Abbas Sétif, Sétif 19000, Algérie

E-mail address l.lamiri@crti.dz lamiri.lila@yahoo.fr

## ABSTRACT

*In this present work, a specimens based on black 3DM ABS resin mixed with ZnO nanoparticles has been fabricated via stereolithography (SLA) at different direction. The ultimate tensile strength and elastic modulus of printed 3DM ABS - ZnO samples were studied. Tensile testing of 3D printed ABS specimens showed that the printing vertically direction give a stress stronger at a printing horizontally*

## KEY WORDS

3DM ABS resin; ZnO nanoparticles; stereolithography SLA

## I. INTRODUCTION

The fabrication of new materials and the synthesis of new products are currently key drivers for innovative and alternative technologies. One of the leading technologies in this decade is 3-D printing, due to unique multidimensional functionality, allow as reducing cost and increasing efficiency. It is poised to reshape manufacturing; and has the potential to make marked industrial, economic, and societal impacts. These features are attractive for applications in virtually all areas of science and engineering, including load-carrying parts in the automobile, aerospace industries, personalized prosthetics, tissue engineering, electronic, mechanical, optics, biomedical, energy, and bioengineering [1-3]

Additive manufacturing (AM), commonly known as three-dimensional (3D) printing, is an

innovative technology group that enables structures with complex geometries or prototype by printing 3D parts layer-by-layer using computer-aided design (CAD) model data [4]. Three-dimensional printing technology is categorized into different techniques; these include fused deposition modelling (FDM), Stereolithography (SLA) and Selective Laser Sintering (SLS) (Figure.) Among these printing technologies for 3D printing polymeric materials is Stereolithography (SLA), SLA method, which is considered as the beginning of AM methods, is still preferred widely. Rapid printing, high resolution, and low cost advantages are the most outstanding features of this approach [5,6]. Photosensitive epoxy resin is used as the starting material in the SLA method. This application increases the printing resolution up to 100 times compared to other methods using solid polymer filaments.

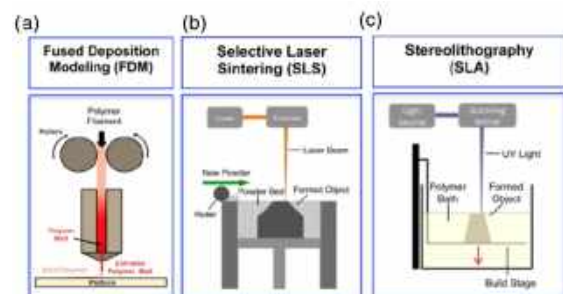


Fig. 1. Schematics depicting 3D printing techniques: FDM (a), SLS (b) and SLA (c)

## II. EXPERIMENTAL

Five specimens were printed using the Resin (3DM-ABS BLACK) polymeric material by the DLP Station 5-405 method. SOLIDWORKS software (version 2018) was utilized to build designed models; to slice the 3D file for layer-by-layer material deposition and set the various parameters during printing then which has been save it in STL extension and imported by the 3D printer software (Operator Station). ZnO nanoparticles, figure 2 show the specimen printed in different directions.

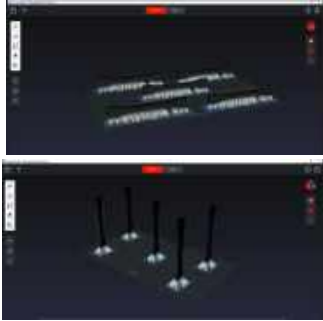


Fig. 2. Specimen printed in different directions

### III. RESULTS AND DISCUSSION

#### A. MORPHOLOGICAL ANALYSIS

The metallographic microscope of the 3D printed resin pure and resin -ZnO structures are given in Figure. 3 Agglomerations white were observed on the surfaces of resin in the form of circles. The ZnO nanoparticles were well dispersed in the resin chains, and the ZnO was fixed on the chains by chemical interactions.

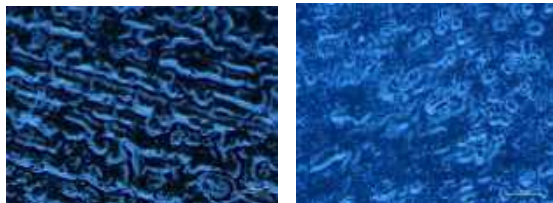


Fig. 3. Optical microscopy image of resin pure and resin-ZnO

#### B. MECHANICAL PROPERTIES

The tensile tests were carried out on five specimens at each printing direction until failure using Zwick Roell Z 100 (Figure 3) loading machine with a capacity of 10KN. The 3D printed 3DM ABS pure and 3DM ABS-ZnO composite specimens were tested under displacement control of 5 mm/min loading rate,

figure 3 illustrates the testing setup.

The tensile tests were carried out on the five specimens at each printing direction. Figure 4 shows the effect of adding ZnO particles of the specimen, printing direction (horizontal or vertical). The results of the tensile tests are illustrated in table 1. It was observed that the 3DM ABS-ZnO specimens printed vertical give a stress at rupture (47.15 MPa) greater than those printed horizontal (22.82 MPa).



Fig. 4. The Zwick Roell Z 100 testing machine

Printing Orientation	Ultimate Tensile Strength (MPa)
Horizontal	47.14
Vertical	22,82

### IV. CONCLUSION

Five 3DM ABS - ZnO specimens had been printed by the DLP Station 5-405 method, we are fauced on the effect of printing direction. The obtained results demonstrated that the specimens printed vertical give a stress at rupture strong than those printed horizontal

### REFERENCES

- [1] Wu, P.; Wang, J.; Wang, X. A Critical Review of the Use of 3-D Printing in the Construction Industry. *Autom. Constr.* 2016, 68,21–31.
- [2] Kroll, E.; Artzi, D. Enhancing Aerospace Engineering Students' Learning with 3D PrintingWind-Tunnel Models. *Rapid Prototyp. J.*2011, 17, 393–402.
- [3] Stansbury, J.W.; Idacavage, M.J. 3D Printing with Polymers: Challenges among Expanding Options and Opportunities. *Dent. Mater.* 2016, 32, 54–64.
- [4] Ligon, S.C.;Liska, R.;Stampfl, J.;Gurr, M.;Mülhaupt, R. Polymers for 3D printing and customized additive manufacturing. *Chem. Rev.* 2017, 117, 10212–10290
- [5] M. Guvendiren, J. Molde, R. M. D. Soares, J. Kohn, *ACS Biomater Sci. Eng.* 2016, 2, 1679.
- [6] S. C. Ligon, R. Liska, J. Stampfl, M. Gurr, R. Mülhaupt, *Chem.Rev.* 2017, 117, 10212.

# A numerical analysis of the mixing effect caused by internal helical fins inside an additively manufactured tube.

FOURAR ISSAM<sup>\*,1</sup>, FAROUK AIDOUDE<sup>1</sup>, ATEF CHIBANI<sup>1</sup>, AZZOUZ EL AMIN<sup>2</sup>

1. Research Center in Industrial Technologies, CRTI, P.O.Box 64, Cheraga 16014 Algiers, Algeria  
[ifourar1992@gmail.com](mailto:ifourar1992@gmail.com)

2. University of Science and Technology of Oran, 1505 El M'nouar, Oran, Algeria

## ABSTRACT

*In this study, we investigated the impact of employing internal fins within a tube to enhance the mixing effect by introducing turbulence inside the tube. The material used for the work is PA-12, which is utilized in a 3D printer for various fin pitches. The results show that by employing helical fins, we can increase the mixing effect and decrease the overall length needed to reach the same temperature.*

## KEY WORDS

Computational fluid dynamics; Additive manufacturing; Heat transfer.

## I. INTRODUCTION

Enhancing the heat transfer for a tube heat exchanger is commonly done with external fins, however, it is possible to improve the heat transfer by adding internal fins.

A numerical heat transfer analysis was conducted by S. Padmanabhan et al. [1] for a double tube heat exchanger with helical inserts. The authors conclude that using twisted tape inserts is a cost-efficient and easy way to maximize heat transfer. The increase in the coefficient of heat transfer can reach up to 63.91% for helical insert due to the turbulence occurring in the transportation. P. Promvong et al. [2] conducted an experimental study to improve heat transfer in a helical-ribbed tube with double-twisted tape inserts. The results show that for the same condition, the tube with double twisted tape inserts provides better heat transfer. The authors also proposed correlations for both the Nusselt number and friction factor. An Experimental investigation was performed by M.R. Salem et al. [3] to study the hydrothermal performance of a double-pipe heat exchanger using helical tape insert. They have found that we can increase the heat transfer significantly by installing a continuous HTI around the outer surface of the inner pipe of DFHE.

In this study, we will examine the effect of the internal fins on the mixing process. The parameters

investigated in this case are the pitch of the fins with two fluids at different temperatures. The material used for the fins is PA-12, a polymer-based material with low thermal conductivity.

## II. MODEL DESCRIPTION

The model under study is a tube with a diameter  $d$  of 20 mm and a length of 300 mm (Fig. 1.). The fins are made from a polymer (PA-12) with a thermal conductivity of 0.5 w/m.K. The fins have the same length as the tube with a height  $h$  of 10 mm while the pitch of the fins  $P$  is 300, 60, and 30 mm. This model has two inlets where water enters with different temperatures of 300 and 350 K. For the boundary condition, we used a wall condition where  $Q = 0 \text{ w/m}^2$  (isolation), velocity inlet (3 m/s) for the entrances, and pressure outlet for the exit (Fig. 2.).

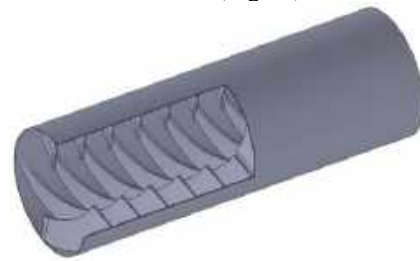


Fig.1. Tube with internal helical fins (not to scale).

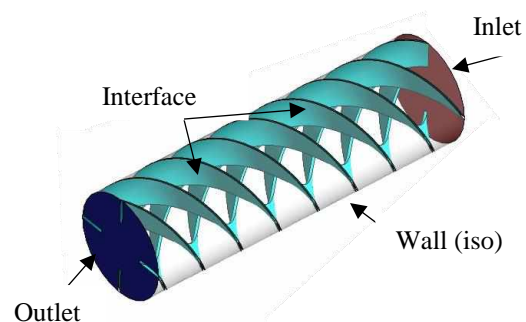


Fig. 2. Boundary conditions (not to scale).



### III. RESULTS

In this case, we conducted a 3D simulation for a tube without the fins and with 4 internal fins. The height of the fins is always the same (10 mm) while the pitch  $P$  changes from 300, 60, and 30 mm. Fig. 3. shows the variation between the maximum and the minimum temperatures in the outlet.

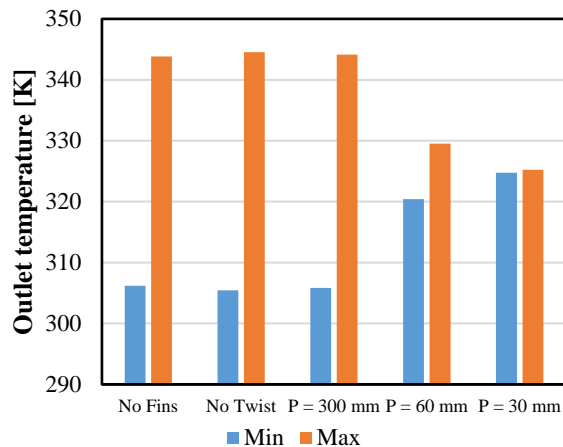


Fig. 3. The variation between the maximum and the minimum temperatures in the outlet for different configurations.

The results show that using straight fins has low to no effect on the temperature variation in the outlet. However, with the presence of the twisted fins, the temperature variation decreases due to the introduction of the turbulence created by the fins (Fig. 4.).

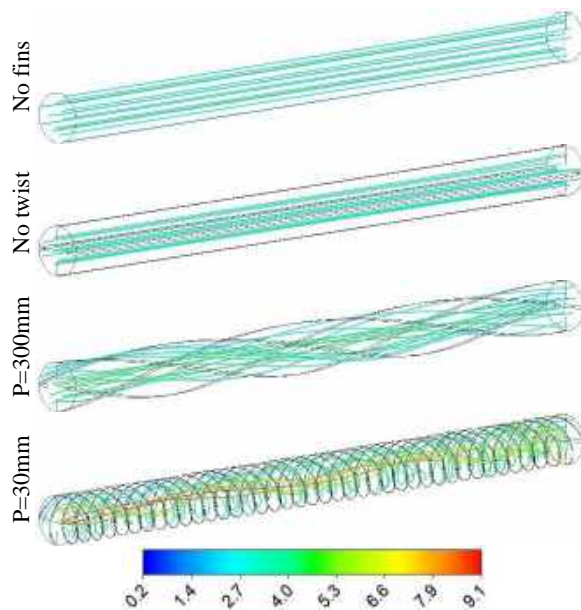


Fig. 4. Velocity streamline for different confederations [m/s]

The results also show that, as the pitch decreases the

variation in the temperature decreases to a point where it can be negligible (less than 1 [K]).

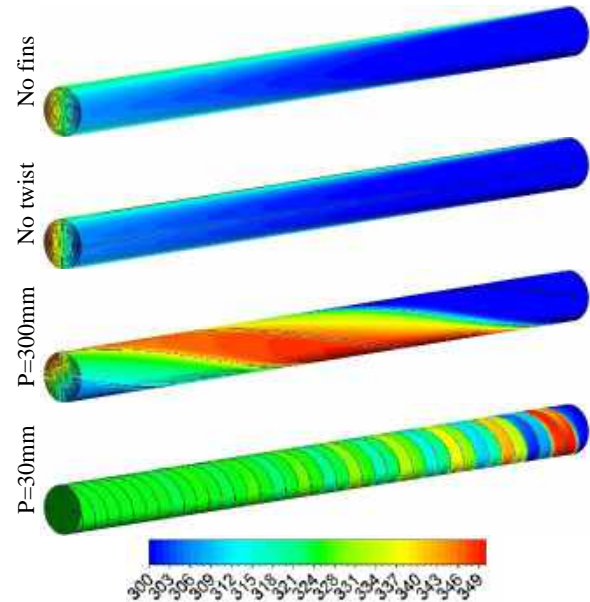


Fig. 5. Temperature contour for the different geometries [K].

Fig. 5. shows that in the case with a low pitch ( $P = 30$  mm), the overall length of the tube can be reduced to less than half for a temperature variation of less than 1 K.

### IV. CONCLUSION

Based on this study, we can determine that helical fins significantly improve the mixing process. Also, as the pitch decreases the overall length of the tube needed to achieve the same temperature decreases.

### REFERENCES

- [1] S. Padmanabhan et al., "Heat transfer analysis of double tube heat exchanger with helical inserts." *Materials Today: Proceedings*. 46, 3588-3595 (2021).
- [2] P. Promvong et al., "Heat transfer augmentation in a helical-ribbed tube with double twisted tape inserts." *International Communications in Heat and Mass Transfer*. 39, 953-959 (2012).
- [3] M.R. Salem et al., "Experimental investigation on the hydrothermal performance of a double-pipe heat exchanger using helical tape insert." *International Journal of Thermal Sciences*. 124, 496-507 (2018).

# Effect of pores geometry on the heat transfer for longitudinal pores.

FOURAR ISSAM<sup>\*,1</sup>, BELFENNACHE DJAMEL<sup>1</sup>, AZZOUZ EL AMIN<sup>2</sup> AND CHADI KAMEL<sup>1</sup>

1. Research Center in Industrial Technologies, CRTI, P.O.Box 64, Cheraga 16014 Algiers, Algeria  
[ifourar1992@gmail.com](mailto:ifourar1992@gmail.com)
2. University of Science and Technology of Oran, 1505 El M'nouar, Oran, Algeria

## ABSTRACT

*In this work, we investigated the effect of pore geometry (circular, square, and polygonal) on heat transfer in porous media. The goal is to aid in the creation of porous models through additive manufacturing, specifically 3D printing. The study reveals that pore geometry has minimal to no impact on heat transfer for the same pore entrance surface and inlet velocity.*

## KEY WORDS

Porous media; Additive manufacturing; Heat transfer

## I. INTRODUCTION

Porous media flow has extensive engineering applications, including air, fuel, and oil filtration, heat transfer, energy storage, and other applications.

Kundu et al. [1] examined the hydrodynamics of fluid flow through a structured array of circular cylinders by comparing two strategies, transient LES and RANS. The flow fields and turbulent Kinetic energy were affected by the porosity and Reynolds number, as shown by their findings. Kuwahara et al. [2] conducted a numerical simulation of turbulent flow over porous media using an LES model. Their study demonstrates that turbulence can occur in the porous media with low Reynolds numbers. Nakayama and Kuwahara [3] employed a two-equation turbulence model to analyze flow and heat transfer in porous media. The authors discovered that the results obtained with a large-scale microscopic computation are in agreement with the streamwise variations of turbulent kinetic energy and its dissipation rate. Rabeah et al. [4] Found that it is possible to predict the dynamic of heat convection for a forced convection in a porous medium with an unsteady flow and low Reynolds numbers.

In this study, we will examine how pore geometry impacts heat transfer in a porous medium at various inlet velocities and temperatures. The pore geometry

that is examined in the work is square, polygonal, and circular.

## II. MODEL DESCRIPTION

The model under study is a porous media cube-shaped with dimensions of 100 mm by 100 mm by 100 mm, as shown in Fig. 1. This study examines circular, square, and polygon pores with a surface area of 64 mm<sup>2</sup>. The velocity values studied in this work are 4.8 and 6.4 m/s, and the temperature variation is 50 and 100 °C. To reduce calculations time, a portion of the original model is analyzed where a symmetry condition is applied, as shown in Fig. 2, with other boundary conditions.

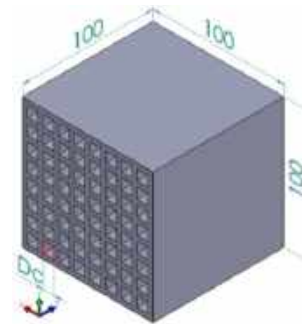


Fig.1. Porous media with rectangular pores.

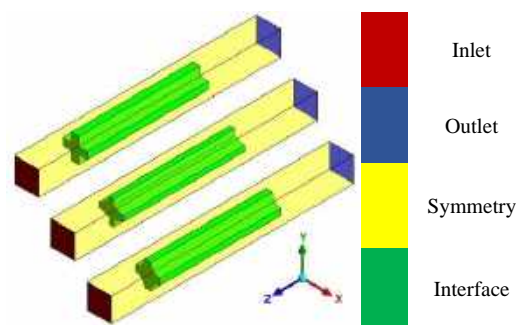


Fig. 2. Boundary conditions (not to scale).



### III. RESULTS

In this study, we performed a 3D simulation of the different pore geometries for a velocity inlet of 1.82 and 18.26 m/s. The porous medium is kept at a constant temperature of 350 K 400 K, and the inlet temperature is 300 K. The heat flux between the inlet and the outlet is shown in Fig. 3.

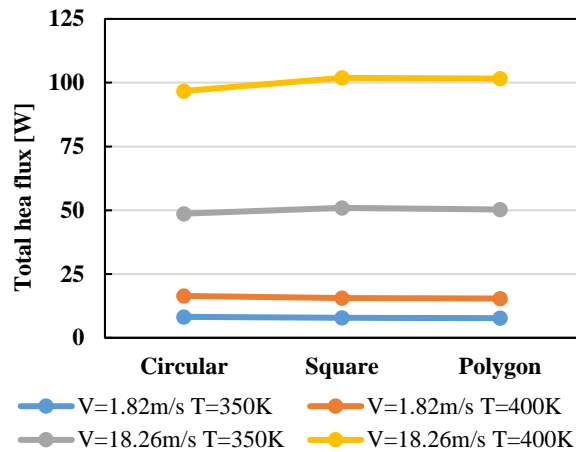


Fig. 3. Variation of the total heat flux for the different geometries, temperatures, and inlet velocity.

In most cases, the difference in total heat flux between different geometries is very small or negligible, as we can see from Fig. 3. Fig. 4 shows that the recirculation zone after the porous medium is the same due to the equal surface entrance and exit for all geometries.

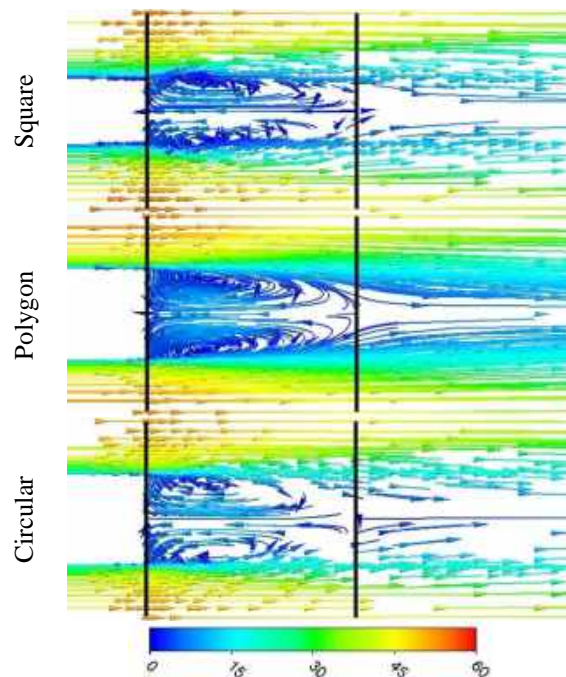


Fig. 4. Velocity streamlines for the different geometries, temperatures, and inlet velocity.

### IV. CONCLUSION

Based on this study, we can determine that the pore geometry does not affect heat transfer, while the entrance surface remains constant for the same inlet velocity. This study can be beneficial for designing porous media that considers heat transfer, particularly in additive manufacturing (3D printing).

### REFERENCES

- [1] P. Kundu et al., "Numerical simulation and analysis of fluid flow hydrodynamics through a structured array of circular cylinders forming porous medium." *Appl. Math. Model.* 40 (23-24), 9848-9871 (2016).
- [2] F. Kuwahara et al., "Large eddy simulation of turbulent flow in porous media." *Int. Commun. Heat Mass. Transf.* 33.4, 411-418 (2006).
- [3] A. Nakayama, and F. Kuwahara., "A macroscopic turbulence model for flow in a porous medium." *J. Fluid Eng.* 427-433 (1999).
- [4] H. Rabeeah et al., "A pore-scale assessment of the dynamic response of forced convection in porous media to inlet flow modulations." *Int. J. Heat Mass Transf.* 153, 119657 (2020).

# Study the effect of 3D printing parameters on the cross-linking rate of stereolithography.

KATIB HAMLAOUI<sup>1,2\*</sup>, BOUSSAHA BOUCHOUL<sup>1</sup>, LEÏLAMIRI<sup>1</sup>, RADHIA KHOUATRA<sup>1</sup>

1. Research Center in Industrial Technologies CRTI, B.P.64, Cheraga 16014 Algiers, Algeria,
2. Badji Mokhtar University -Annaba- B.P.12, Annaba, 23000 Algeria.

## ABSTRACT

*Additive manufacturing or 3D printing is a process of making three-dimensional solid objects from a digital file with complex shapes and unique properties. The kinetics of photo-polymerisation (solidification) of photosensitive polymer resins have an impact on the conversion rate of photosensitive polymer resins, which influences the final properties of the product. SLA method, which is considered as the beginning of Additive manufacturing methods, is still preferred widely. Rapid printing, high resolution, and low cost advantages are the most outstanding features of this approach. The aim of this work is to develop a numerical model to study the effect of 3D printing parameters (radiation power, wavelength, layer thickness, etc.) on the mechanical, thermal and physico-chemical properties and kinetics of photopolymérisation*

**Keywords:** Stereolithography SLA, 3D printing, photopolymerization, photosensitive polymer.

## I. INTRODUCTION

Besides these existing technologies, very sophisticated techniques have recently been developed for generating 3D objects. These techniques have been integrated into a new technology known as Additive Manufacturing processes, comprising different techniques using different materials as indicated in Figs. 1.2 and 1.3 However, all of these different techniques use the same principle, i.e. the transformation of a geometric CAD model into a physical model produced layer by layer. The main advantage of these processes is that they build a part, even a complex part, in one-step without requiring planning of process sequences or specific equipment for handling materials

## A. STEREOLITHOGRAPHY PROCESSES:

SLA is part of a family of additive manufacturing technologies known as vat light curing. All these machines are built with the same principle: using a light source – a laser or a UV projector to solidify a liquid resin and transform it into solid plastic. The main physical difference is in the layout of the main components, such as the light source, build platform, and resin tank. The machine uses for this research called: stereolithography (SLA) reversed (upside-down), the process is carried out in the other direction. This method uses a tank with a transparent bottom and a non-adhesive surface, which provides a substrate on which the resin hardens and which allows the newly formed layers to be gently peeled off. The build platform lowers leaving a space at the bottom of the resin tank equal to the height of one layer [1,2].

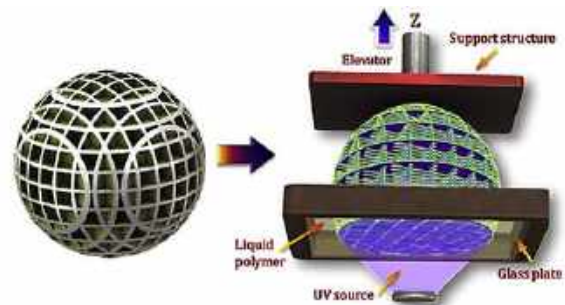


**Fig. 2 :** Stereolithographic Processes SLA [2].

The photopolymerization refers to the transformation of a reactive liquid resin into a solid material under the action of UV irradiation. The component of the formulation that will allow this change of state is the photoinitiator. It will absorb the radiation and initiate the crosslinking by reacting with the functional groups of the oligomers and monomers. In order to achieve cross-linking, several compounds are needed in the formulation of UV products [3].

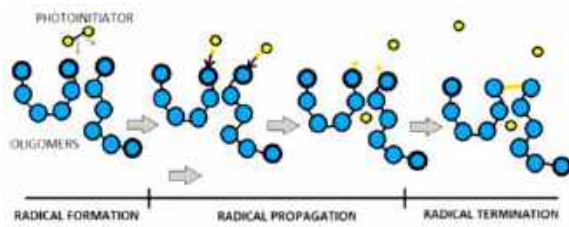


**Fig. 3:** Processes de photopolymérisation

#### B. CURING DEPTH :

The curing depth determines the minimum layer thickness suitable for stereolithography fabrication and curing time per layer to optimize the printing process. This will also minimize the chances of delamination between each layer since there is a slight overlap of curing between the previous cured layer and the next layer, which is illustrated in Figure 5. The purpose is to ensure that the layer thickness set on the printing system is always smaller than the lowest curing depth achievable.

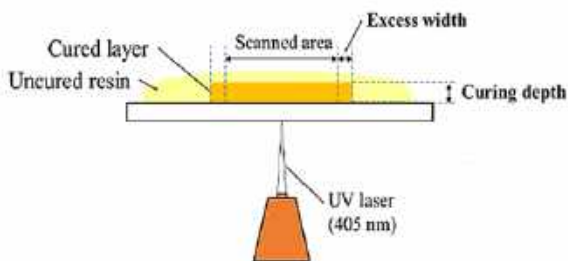


**Fig.5:** Schematic illustration of curing depth between layers.

#### 4.1. Calculation condition:

- Isotropic materials: Any part printed on an SLA machine is isotropic (no change in physical and mechanical properties during printing).
- The print is vertically movable in both directions along the Z axis (depending on the printing process).
- A high power ultraviolet light for rapid solidification during laser contact with photosensitive polymer resins.

**Synthesis parameters:** parameter indicated in table 1:

**Table1:** Print settings:

Resin type	Polyurethane acrylate
Polymérisation	Radical
Transfert de chaleur	Exothermique
Layer thickness	0,05 - 0,2 mm
Wavelength	365-445 nm
UV power	4 à 12 mw/cm <sup>2</sup>
Température	Ambiant (25 -31) °C
Vitesse d'imprimant	22.5 mm/h

The illustration in figure 6 shows the curing process is faster and the final conversion becomes higher. The degree of conversion is lower in the upper layers than in the lower layers. Thinner layer thickness leads to higher conversion and smaller conversion difference between neighboring layers, which means better homogeneity.

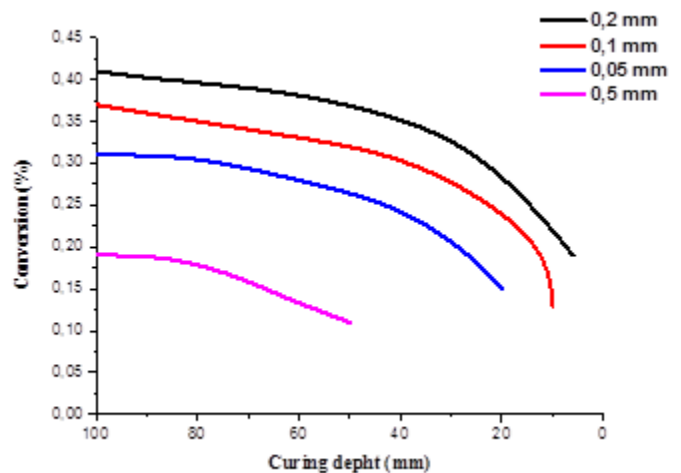


**Fig.7:** Conversion rate as a function of curing depth.

## II. CONCLUSION

We followed in this research, the main parameters of the coatings of the photopolymerization under UV radiation. The purpose of this work is to produce a numerical model for optimizing certain parameters of photopolymerization by UV radiation, and to study the influence of the rate of crosslinking on the thickness of deposit, speed of polymerization, transition temperature  $T_g$  of the material formed by radical polymerization and on the mechanical, thermal and chemical properties of the substrate studied.

**REFERENCES**

- [1] S. LAURENT, Développement et études de l'influence des procédés d'application et de réticulation de vernis acrylates photopolymérisables, Matériaux, INSA de Lyon-France, PP 21-29-30, 2015.
- [2] A. KAFLE, E.LUIS, 3D/4D Printing of Polymers: Fused Deposition Modelling (FDM), Selective Laser Sintering (SLS), and Stereolithography (SLA), *Polymers* 2021, *13*(18), 3101
- [3] W. HAMADOUCHE, Effets des agents réticulant sur la photopolymérisation, Université Abou-Bekr Belkaid – Tlemcen -Algérie, PP 3-4,2018

# Title: Reduce Porosity in CMTed Aluminium Parts (Walls and Massive Parts)

BOUHANK ANTAR<sup>1\*</sup>, BELLAL YUCEF<sup>1</sup>, AND ABABSA Abdelmadjid<sup>2</sup>

1. Research Center in Industrial Technologies - CRTI P.O.Box 64, Cheraga 16014 Algiers, Algeria,  
 antarbouhank@yahoo.fr

## ABSTRACT

*In this paper, Cold metal transfer (CMT) technique has been used to manufacture aluminium parts of AlMg5Cr(A). The latter is widely used according to its good features like its lightweight and good corrosion resistance. However, the presence of some parts defects as the porosity, cracking and the Rapid oxidation of the surface due to the quick solidification of aluminium, presents a drawback in the additive manufacturing and parts qualities. The purpose of the present paper is an attempt to reduce porosity inside walls and ensure a good wetting between cords in the case of massive parts. To this end, by optimizing of printing parameters as torch Travel Speed (from 0.35 to 1.4m/min), the current (35 to 70A) and so on, a reduction in porosity has been noticed from the naked eye to micro meter scale. Furthermore, a good wetting between beads inside massive parts was found by the use of different strategy of filling (zigzag and grid).*

**KEY WORDS** CMT; porosity; parts defect; filling strategy

## I. INTRODUCTION

Metal additive manufacturing, in particular the (CMT) technique, is attracting a great deal of attention from manufacturers especially in the automobile industry [1] aeronautical, industry of nuclear energy [2], and so on. This technique is enables to product parts have highly complex shapes, with a good degree of precision that is certainly impossible to achieve using conventional methods. CMT also is suitable for 3D print the aluminium which was once considered limited because of the problems occurred like such as reduction of the metal strength and heat affected zone produced by the high energy input[3]. Moreover, CMT is a suitable option for joining thin sheets [4]. In this work we have manufactured parts with Aluminium alloys (AlMg5Cr(A)). The latter is widely and increasingly used because of their light weight and high corrosion resistance [5]. Conventional methods, for printing,

need high energy input. The CMT method has a short-circuit transfer process with lower thermal heat input. Therefore, its uses are thus necessary in the welding and additive manufacturing field.

## II. MATERIAL AND METHODS

For the porosity and inter-beads wetting inside walls and massive parts investigation, different CMT parameters have been used as torch travel speed (from 0.35 to 1.4m/min), gas flow rates from 8 to 12 L/min, and the current (from 35 to 70 A). All experiments were carried out with (AlMg5Cr(A)) wire with a wire diameter of 1.0 mm on plates substrate of Aluminium. the printing operation has been done with Fronius welding device (TPS 500i) and computer-numerical control CNC table.



**Fig.1.**CMT equipment and printing

## III. RESULTS AND DISCUSSION

The fig.2.shows a mechanical cutting of CMTed parts wherein the porosity and Interspace are seen with the naked eyes for walls and massive parts.

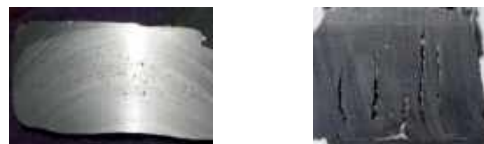


**Fig. 2.** Porosity and Interspace in wall and massive CMTed part

After optimizations, we were able to reduce porosity and interspace. However, we a metallographic



characterization, the porosity was still existed. With other optimizations, the porosity is reduces to micrometers scale (see figure3). After that, we can't reduce anything because the latter is inherent for aluminium parts due to the rapid solidification when the bubble can't escape.

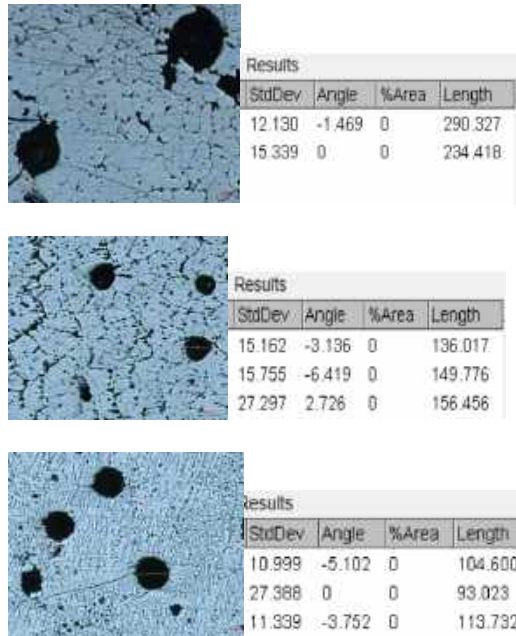


Fig. 2. Reduction of the porosity in CMTed part.

Although, the porosity is reduces, the shape of the latter is very important to know the parts state. According to the shape of the gas bubble, we were able to figure out the parts state i.e. w if we have a non-spherical pore that means a collapsed manufactured parts occurs where the matter was melts (see Figure 4) and the density is increased. Hence, the parts weights increase.

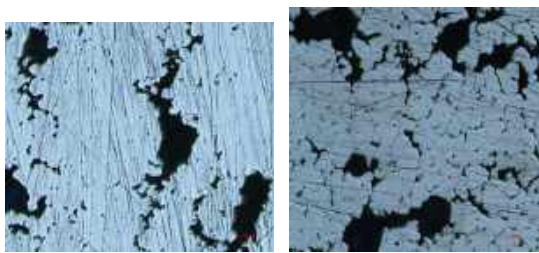


Fig. 4. Pores deformation (Collapsed parts).

In order to reduce the interspace between beads to improve the parts quality, two filling strategies have been followed zigzag and grid (see Fig.5)



Fig. 5. Filling strategies for massive parts

By changing CMT parameters, the inter pass was reduced with the two filling strategies. However, the grid reached the filling with only in 40A, whereas the zigzag in 70A .

#### IV. CONCLUSION

From the outcome of our study it is possible to conclude that we can reduce the porosity inside aluminium parts additively manufactured (Cold metal transfer) by optimizing parameters such as torch travel speed, gas flow and current. Some porosity is left and seen by metallographic investigation. The latter are in micrometers scale. However, we could reduce this drawback from the mean of pore diameter ( $D=260\text{ }\mu\text{m}$  to  $100\text{ }\mu\text{m}$ ). Besides the porosity, the problem of non-wetting between beads was investigated. The grid filling was reached with low current, in contrary, the filling zigzag needs high current.

#### REFERENCES

- [1] JK .Larsson "Overview of joining technologies in the automotive industry". WeldRes Abroad;49(6/7):29–45(2003).
- [2] K.S. Derekar "A review of wire arc additive manufacturing and advances in wire arc additive manufacturing of aluminium" Mater. Sci. Technol. 34, 895–916. (2018)
- [3] P.Wang ,et al., "Characterization the contribution and limitation of the characteristic processing parameters in cold metal transfer deposition of an Al alloy" Journal of Materials Processing Technology, 245, 122-133(2017).
- [4] M. R.Ahsan, et al., "Porosity formation mechanisms in cold metal transfer (CMT) gas metal arc welding (GMAW) of zinc coated steels" Science and Technology of Welding and Joining, 21(3), 209-215. (2016)
- [5]R. Kaibyshev, et al., "Superplastic behavior of an Al–Mg alloy at elevated temperatures" Mater. Sci. Eng.: A 342 169–177(2003)



# Effect of the Free Quenching Residual Stresses on the Thermophysical and Morphological Properties of Acrylonitrile-Butadiene-Styrene (ABS).

BENCID ABDESLAM<sup>\*1</sup>, MERABET SAFIA<sup>1</sup>, FARID ROUABAH<sup>2</sup>, MAGALIS FOIS<sup>3</sup>, CHADI KAMEL<sup>1</sup>.

1. Research Center in Industrial Technologies (CRTI), P.O. Box 64 Cheraga 16014, Algiers, Algeria, abdeslambencid@yahoo.com; safiamerabet@yahoo.fr; f\_rouabah2002@yahoo.fr; chadikamel\_dz@yahoo.fr
2. Université Paris-Est Créteil Val de Marne, CERTES, 61 Av. du Général de Gaulle, 94010 Créteil Cedex France, fois@u-pec.fr
3. Laboratoire de Physico-chimie des Hauts Polymères, Université Ferhat Abbas Sétif -1, Sétif 19000, Alegria, brahim\_barkat@yahoo.fr

## ABSTRACT

*The present work aims to study and recognize the influence of thermal annealing and quenching residual stress on the thermophysical, Thermal, morphological and thermomechanical properties of acrylonitrile butadiene styrene (ABS). A study of secondary relaxations in DMA highlighted a secondary relaxation mode at -10 ° C in ABS. Observations by scanning electron microscopy revealed the existence of porosities close to the surface for samples quenched at the lowest temperatures. These porous materials have a direct influence on the evolution of the density and thermal conductivity of ABS.*

**KEY WORDS:** Acrylonitrile Butadiene Styrene (ABS), Annealing, Quenching, Residual Stresses, Thermal Conductivity.

## I. INTRODUCTION

A thermal conductivity of polymer can replace other materials for heat sensitive applications. They are being used increasingly in various heat-sink applications such as electronics, housings or in automotive parts. The use of thermally conductive plastics, which are injection molded, leads to maximum design freedom for constructing parts. Furthermore, thermal conductivity of polymers has a lower density and can be much lighter than equivalent components. Though bulk amorphous polymers are typically regarded as thermal insulators due to their low thermal conductivities (0.1–1W/mK) [1-2], also single polymer chains and highly aligned polymer fibers can have much higher thermal conductivity than their amorphous counterparts [2–7]. In addition, the heat treatments and in particular on the quenching conditions which they undergo during their transformation due to the low thermal conductivity of polymers, quenching results in the appearance of temperature gradients, which can become significant

in the case of rapid quenching; this leads to the formation of residual stresses (CR) [8-10]. Residual stresses are exactly the internal stresses that exist within a material even in the absence of external loads or thermal gradients. They occur in metals, ceramics, and also in polymers. Residual stresses are induced to thermoplastic polymers during processing, such as injection molding, extrusion, grinding, polishing, and other post-processing operation [4], [11-14]. Residual stresses can have both beneficial and detrimental effects on the performance and behavior of materials and structures [13]. Understanding and managing residual stresses is important in many engineering applications to ensure the integrity, reliability, and durability of components. In this work also, we present the results obtained on the effect of the quenching temperature on the thermomechanical, thermophysical, thermal and morphological properties of ABS. The results are compared to an annealed sample which was taken as a reference sample.

## II – EXPERIMENTAL

### a. Materials

The polymer used in this study is a commercial Acrylonitrile butadiene styrene (ABS), Starex ® 0520, supplied by Samsung (Korea), with a melt flow index at 220 °C of 15 g/10 min and a glass transition temperature of about 95 °C.

### b. Thermal treatment

#### b.1. Free quenching procedure

Thermal treatments are heating operations followed by cooling. They are done in order to give a material

with adequate mechanical resistance and ductility. Pellets were oven dried at 80°C during 24 hours, then put in a mould and pressed at 2,5 bars for 15 minutes at 170°C. Then, the samples were immediately quenched in air for 15 minutes. These specimens were heated again in an oven at 110°C ( $T_g + 15^\circ\text{C}$ ) for 3 h and were immediately quenched in an antifreeze cooling liquid bath at -15, -5 °C and in water bath at 0, 20, 40 and 60°C for 15 min. Annealing was performed on samples considered as reference. Specimens were prepared using samples first quenched in air, heated again at 110°C for 2 h and finally slowly cooled in the oven until room temperature at a rate of about  $0.5^\circ\text{C}.\text{min}^{-1}$ . These samples were named annealed samples.

#### FIGURES

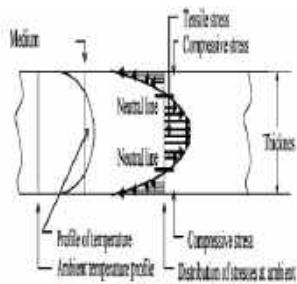


**Fig.1:** Temperature and stress distribution in a plastic resulting from cooling

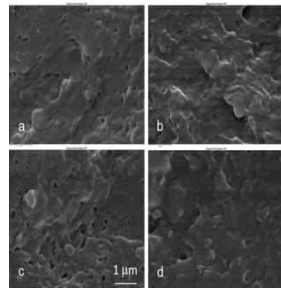


**Fig.2:** SEM micrograph of fracture surface of notched Izod impact test, sample of 3 mm thickness; annealed (a) close to the edge, (b) depth 1 mm; and quenched at -5°C (c) close to the edge, (d) depth 1 mm.

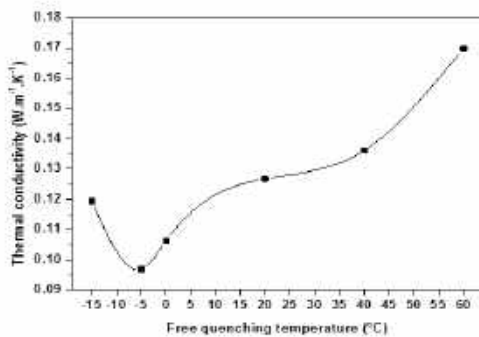


**Fig.3:** Thermal conductivity of acrylonitrile butadiene styrene (ABS) as a function of the free quenching temperature (annealed sample,  $k = 0.18 \pm 0.004 \text{ W.m}^{-1}.\text{K}^{-1}$ ).

#### III- CONCLUSION

The results presented in this paper have shown the influence of quenching on the thermophysical, and morphological properties of ABS. overall, and as long as the quenching temperature remains greater than or equal to -5 °c, the more the quenching temperature decreases the more the density, the thermal conductivity decrease. these variations were linked to the presence of porosities, to the evolution of free volume, to the molecular mobility, to the chain alignment and to the generation of residual stresses associated with quenching. this work has shown that the use of the free quenching process is an interesting means for significantly reduces the thermophysical properties of ABS.

#### IV. REFERENCES

- David, D.J., Misra, A., 2001. Relating materials properties to structure: Handbook and software for polymer calculations and materials properties, Relating Materials Properties to Structure: Handbook and Software for Polymer Calculations and Materials Properties.
- Zhang, T., Luo, T., 2012. Morphology-influenced thermal conductivity of polyethylene single chains and crystalline fibers. Journal of Applied Physics 112, 1–5.
- Luo, T., Esfarjani, K., Shiomi, J., Henry, A., Chen, G., 2011. Molecular dynamics simulation of thermal energy transport in polydimethylsiloxane, in: Journal of Applied Physics.
- Turnbull, A., Maxwell, A.S., Pillai, S., 1999. Residual stress in polymers - evaluation of measurement techniques. Journal of Materials Science 34, 451–459.
- Henry, A., Chen, G., Plimpton, S.J., Thompson, A., 2010. 1D-to-3D transition of phonon heat conduction in polyethylene using molecular dynamics simulations. Physical Review B -

- Condensed Matter and Materials Physics 82.
6. Ebadi-Dehaghani, H., Nazempour, M., 2012. Thermal Conductivity of Nanoparticles Filled Polymers. *Smart Nanoparticles Technology*.
  7. Henry, A., Chen, G., 2009. Anomalous heat conduction in polyethylene chains: Theory and molecular dynamics simulations. *Physical Review B - Condensed Matter and Materials Physics* 79.
  8. Bencid, A., Rouabah, F., Fois, M., Djidjelli, H., 2017. Effect of the Free Quenching on Mechanical and Thermomechanical Properties of ABS. *Russian Journal of Applied Chemistry* 90.
  9. Rouabah, F., Fois, M., Ibos, L., Boudenne, A., Picard, C., Dadache, D., Haddaoui, N., 2008. Mechanical and thermal properties of polycarbonate, part 1: Influence of free quenching. *Journal of Applied Polymer Science*
  10. Barka, B., Rouabah, F., Zouaoui, F., Fois, M., Nouar, Y., Bencid, A., 2022. Thermophysical Behavior of Polycarbonate: Effect of Free Quenching above and below the Glass Transition Temperature. *Advanced Materials Research* 1174 Barka, 123–136.
  11. Deveci, S., Eryigit, B., Nestelberger, S., 2021. Re-distribution of residual stress in polymer extrusion: An eccentric approach. *Polymer Testing* 93, 106971. Hornberger, L.E., Devries, K.L., 1987. The effects of residual stress on the mechanical properties of glassy polymers. *Polymer Engineering & Science* 27, 1473–1478.
  12. Huskić, M., Kusić, D., Pulko, I., Nardin, B., 2022. Determination of residual stresses in amorphous thermoplastic polymers by DMA. *Journal of Applied Polymer Science* 139, 1–8.
  13. Kandil, F.A., Lord, J.D., Fry, A.T., Grant, P. V., n.d. Matc4. A Review of Residual Stress Measurement Methods-A Guide to Technique Selection.
  14. Rasouli Yazdi, S., Retraint, D., Lu, J., 2000. Experimental Study of Residual Stress Distributions in Quenched Parts by the Incremental Large Hole Drilling Method and by the Neutron Diffraction Method. *Journal of Testing and Evaluation*.

# The Effect of Micro-channels Geometry on the Fluid Flow Characteristics

CHADI KAMEL<sup>1\*</sup>, LAIDOUDI FAROUK<sup>1</sup>, AZZOUZ EL AMIN<sup>2</sup>

<sup>1</sup>Research Center in Industrial Technologies CRTI, P.O. Box 64, Cheraga, 16014, Algiers, Algeria.  
[chadikamel\\_dz@yahoo.fr](mailto:chadikamel_dz@yahoo.fr)

<sup>2</sup>Univrsity of Science and Technology of Oran, 1505 El M'nouar, Oran, Algeria

## ABSTRACT

*The effect of micro channel geometry was studied using CFD to understand fluid flow characteristics of microchannels with rectangular in the sidewalls and different shaped ribs in the center core flow. Two different rib configurations (non-hollow and hollow) are considered including a rectangular. The goal was to optimize the microchannels structure, thus enhancing heat transfer and reducing flow resistance and pressure drop. The results indicate that the overall performance can be significantly improved by adding holes to the ribs, which helps to form vortices, and increase flow turbulence in the fluid flow area.*

## KEY WORDS

Fluid flow; microchannel; ribs; CFD.

## I. INTRODUCTION

The field of studying the characteristics of fluid flow on microchannels is considered one of the most important areas that many researchers address in order to improve the performance of structures of microchannel. Among the studies that dealt with this topic we find the study of Jianwei et al. [1]. They analysed the properties of fluid flow and heat transfer numerically for a Reynolds number (Re) ranging from 157 to 668 on the geometry of microchannels with small pin fins. The results indicate that the oval-shaped pin fins in the microchannel have effective performance. Pistoresi et al. [2] studied experimentally the fluid flow characteristics of a multi-scale fluid network consisting of a number of elementary stairs. They relied on computational fluid dynamics (CFD) to conduct the simulation. Kaushik et al. [3] conducted a comparative study of the flow characteristics of nanofluids over geometric channels. They also compared their results experimentally and numerically. The results showed that nanofluids contribute to increasing the performance of channels, unlike basic fluids such as water.

## II. GEOMETRICAL SYSTEM

The figure below (Fig.1) shows three geometric of microchannels chosen according to their shape to understand the fluid flow characteristics of the microchannels. In this study we chose: (a) a rectangular microchannel without ribs, (b) a microchannel with ribs, and (c) a microchannel that has hollow ribs.

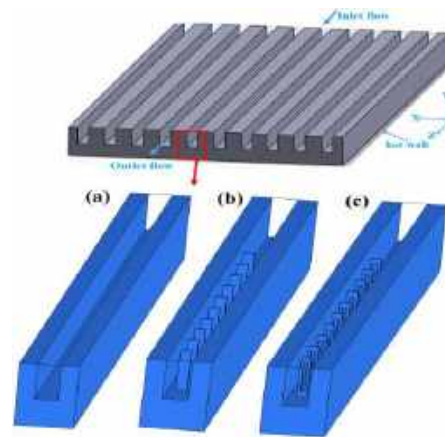
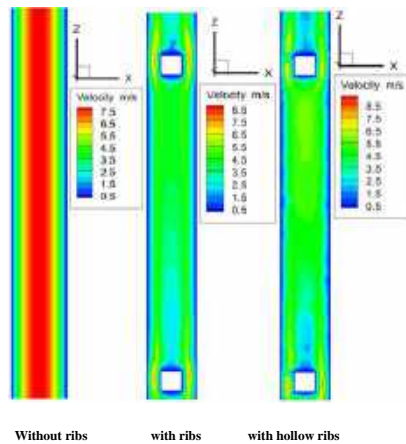


Fig. 1. three geometric shapes of microchannels.

## III. INDEPENDENT OF THE RESULTS

Figures 2 and 3 represent contour plots of the fluid velocity in the micro channels in the flow direction at  $Y = 0.25\text{mm}$  and in the transverse direction at  $Z = 0.01$ ,  $0.005$  and  $Z = 0.00025\text{m}$ , respectively. We note that the shape of streamlines in the microchannel without ribs parallel sides to each other. We also note that in the microchannel with ribs, the liquid is separated into two parts by the ribs, and enters the grooves at high speeds, and the areas of flow stagnation are formed. However, in the microchannel with hollow ribs, the flow speed is somewhat moderate and the flow shape is turbulent,

which helps to mix the hot liquid of the vortex with cold liquid.



**Fig. 2.** The velocity distribution along the horizontal plane ( $y=0.25$  mm)

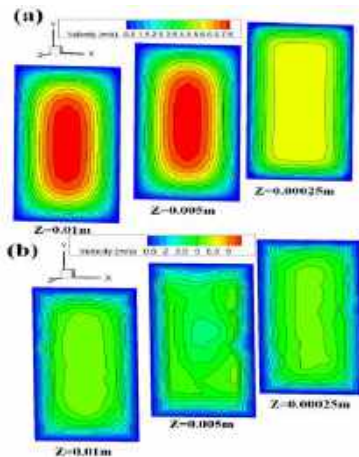


**Fig. 3.** The velocity distribution in the transverse direction (a) without ribs; (b) with ribs

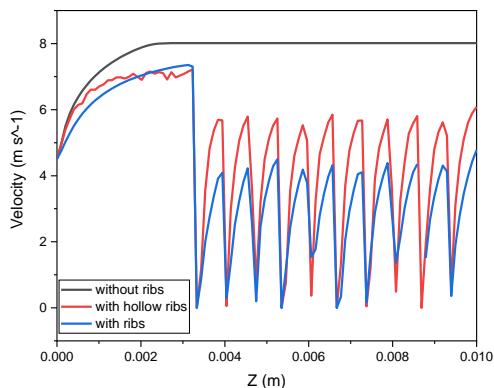


**Fig. 4.** The velocity distribution along the horizontal plane ( $y=0.25$  mm),

Fig. 4 represents the variation of the fluid flow velocity at  $Y=0.25$ mm. We notice from the figure that the micro

channel with hollow and non-hollow ribs significantly affects the flow of the liquid, and the fluid velocity rises at the inlet of the microchannel and continues to rise until  $Z=0.002$ m from the channel entrance for all microchannels. It decreases then at the location of the ribs in the channel with hollow ribs or without hollow ribs. As for the microchannel that does not contain ribs, the flow speed remains constant until the channel outlet. Fig. 5 represents the temperature changes at the bottom wall of the microchannels studied vs  $Z$ . We notice that the temperature has low values in the microchannel with hollow ribs. We also find that the microchannel with ribs has slightly higher temperature values than the microchannel with hollow ribs, and this is due to the effectiveness of the hollow ribs in transferring heat. As for the microchannel without ribs, the temperature of its lower wall is high compared to the microchannels studied.

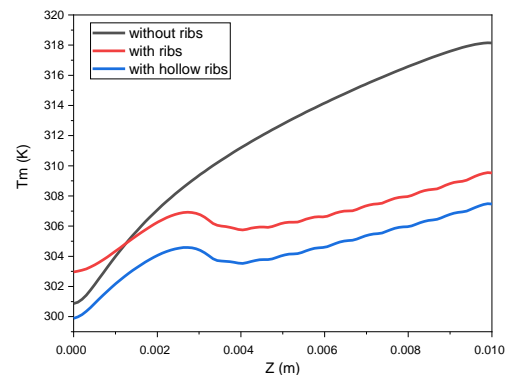


**Fig. 5.** Temperature distribution on the heated bottom wall

#### IV. CONCLUSION

In this work, we studied the geometry of microchannels on the flow characteristics of liquids to improve their effectiveness. According to the results obtained, the microchannels with hollow ribs have good performance, and the type of flow in them is turbulent. This is due to the effect of the holes in the ribs, on the other hand. We find that microchannels with ribs are more effective compared to those without ribs.

#### REFERENCES

- [1] H. Jianwei et al., "Heat Transfer and Fluid Flow Characteristics of Microchannel with Oval-Shaped Micro Pin Fins," *Entropy*. 23(11), 1482 (2021).
- [2] C. Pistoresi et al., "Fluid flow characteristics of a multi-scale fluidic network," *Chemical Engineering and Processing - Process Intensification*. 123, 67-81 (2018).
- [3] S. Kaushik et al., "Comparative analysis of fluid flow in mini channel with nano fluids and base fluid," *Materials: Proceedings*. Available online 8 June 2023.

# Caractérisation microstructurale et mécanique d'une couronne élaborée par fabrication additive

KAHLOUCHE ABDESALEM<sup>1</sup>, BOUKEBAL HADJER<sup>2</sup>, DEBBACHE SAMI<sup>1</sup>, KENZOUR ABDELGHANI<sup>1</sup>,  
HAMIDOUCHE MOUHAMED<sup>1</sup>, MERABTI HALIM<sup>1</sup>, FATMI HAKIM<sup>1</sup>, LOUCIF KAMEL<sup>2</sup>

1. Research Center in Industrial Technologies - CRTI P.O.Box 64, Cheraga 16014 Algiers, Algeria.  
a.kahlouche@crti.dz
2. Laboratoire Des Matériaux Non Métalliques institut D'optique Et De Mécanique De Précision Université  
Ferhat Abbas Sétif1 k\_loucif19@yahoo.fr

## RÉSUMÉ:

*Cet article analyse les propriétés microstructurales et mécaniques des couronnes d'aluminium produits par CMT (cold Metal Transfert). La stratégie adoptée dans la fabrication des couronnes à l'aide d'une table CNC liée à une torche du poste à souder MIG-MAG Fornius (TPS 500i). Ensuite, la caractérisation mécanique et l'observation métallographique réalisée à partir des échantillons des couronnes, suivant la base ou la tête de ces couronnes (début et la fin des couronnes). Les résultats représentent la différence des propriétés entre la base et la tête des couronnes. L'observation microscopique montre une microstructure fine et autre poreuse avec la présence des précipités. La dureté des échantillons coupés transversales augmente de la base vers la tête des couronnes, et la traction indirecte des couronnes donne des résultats proches pour les trois hauteurs. Enfin, une étude comparative entre une pièce réalisée par la fabrication additive et l'autre réalisée par le tour conventionnel. La hauteur influencée sur les caractéristiques et les propriétés des couronnes par l'effet de la chaleur et le temps de refroidissement, il y a un recuit des pièces durant la fabrication de ces couronnes.*

**MOTS CLÉ:** Fabrication additive, CMT (cold metal transfert), Aluminium,

## I. INTRODUCTION

Les alliages d'aluminium à haute résistance sont largement utilisés pour fabriquer des pièces structurales d'avions, par exemple la peau, les ailes et les poutres nervurées en raison de leur résistance spécifique élevée, de leur rigidité spécifique élevée, de leur excellente résistance à la fatigue et de leur résistance à la corrosion [1-2]. Cependant, les techniques de fabrication conventionnelles ne peuvent pas produire des composants répondant aux exigences de performances globales élevées, de faible coût et de développement environnemental vert [3-4]. La technologie de fabrication additive (FA) devrait résoudre ce problème en s'appuyant sur l'intégration de la conception et de la fabrication, ainsi que de la structure et de la fonction [5-6]. Parmi les différents procédés de la fabrication additive métallique, la fabrication additive arc-fil (WAAM) utilisant le soudage CMT (Cold Metal

Transfert) est retenue pour notre étude grâce à son taux de dépôt important, faible coût des équipements et peu de perte de matière par projection lors de la fabrication. Pour les composants structurels à grande échelle des alliages d'aluminium, l'arc métallique AM (WAAM) a montré des avantages significatifs tels qu'un faible rapport achat-vol, un faible coût d'équipement, un cycle de production court et un taux de dépôt élevé. De plus, CMT ce procédé a été développé pour le soudage de l'aluminium. Le WAAM à base de CMT est caractérisé par moins d'apport de chaleur et de faibles projections en raison de la transition de court-circuit [7]. Néanmoins, une application plus large de CMT-base WAAM est limitée par sa qualité de formation et ses propriétés, qui sont contrôlées par des défauts internes et la qualité de surface.

## II. MATÉRIAUX ET TECHNIQUE EXPERIMENTALES

a. **MATERIAUX :** Les échantillons ont été élaborés par la technique CMT universel au niveau d'unité de recherche en fabrication additive URFA-CRTI. Le procédé est constitué d'un générateur de courant de type Fronius (TPS 500i) et d'une table à commande numérique. Le générateur permet de générer et de contrôler l'arc électrique, d'une bobine de fil métallique (Al5356 dans le cadre de la présente étude), d'un réservoir de gaz de protection (l'argon) pour éviter l'oxydation du métal et d'une torche de soudage. Nous avons élaboré trois séries de couronnes de même diamètre intérieur (50mm), diamètre extérieur (54mm) et de hauteurs différentes : 10, 15 et 20mm. Nous avons gardé les mêmes paramètres de CMT. La fiche technique indique que : AlMg5Cr(A) de la Série d'aluminium : 5356, Diamètre du fil : 1mm. Courant : 95A, Tension : 14,5V, Vitesse de dévidage : 9m/mn. Les échantillons ont été élaborés par la technique CMT universel au niveau d'unité de recherche en fabrication additive URFA-CRTI. Le procédé est constitué d'un générateur de courant de type Fronius et d'une table à commande numérique. Le générateur permet de générer et de contrôler l'arc électrique, d'une bobine de fil métallique (Al5356 dans le cadre de la présente étude), d'un réservoir de gaz de protection (l'argon) pour éviter l'oxydation du



métal et d'une torche de soudage

### b. Méthodes de caractérisation

1. Essais de dureté : La mesure de dureté a été effectuée par des essais Vickers sur un Duromètre de type Qness 30M. L'essai normal est exécuté avec un pénétrateur pyramidal à base carrée en diamant sous une charge appliquée de 0,5N pendant 15 secondes.
2. Traction : Les essais de traction indirecte et de compression ont été effectués sur une machine de traction universelle de type Zwick/Roell Z100,
3. Observation microscopique : été effectuées par un microscope métallographique de type OXION euromex.

## III. RESULTATS ET DISCUSSION

**Dureté:** La fig.2 présente la variation de la dureté Vickers en fonction de la hauteur vraie et normée respectivement des couronnes pour les trois séries (10, 15 et 20 mm). La diminution de la dureté quand la hauteur de la couronne augmente, peut être expliquée le refroidissement lent du matériau. Le matériau qui se trempe à l'air présente une dureté importante, mais le matériau qui se refroidit lentement subit à ce qui ressemble à un recuit et par conséquent il présente une dureté inférieure.

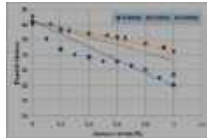


Fig. 2. Variation de la dureté en fonction de la hauteur normée des différentes couronnes.

**Traction indirecte :** La figure 3 représente la forme finale des couronnes après la traction indirecte. Les courbes de la traction indirecte (Fig.4) présente le même comportement pour les trois couronnes : une variation linéaire suivie d'une déformation plastique permanente. Ce comportement traduit la cohésion satisfaisante des couronnes élaborées par CMT. La traction indirecte sur une couronne usinée d'un lingot et ayant les mêmes dimensions que la couronne de hauteur 20mm. On enregistre le même comportement que celui des couronnes élaborées par CMT par contre, la force nécessaire pour avoir une même déformation est plus grande.



Fig. 3. Formes des couronnes après l'essai brésilien.

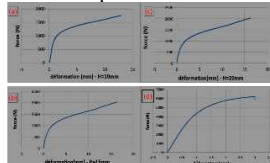


Fig. 4. Courbes force déformation en traction indirecte des couronnes (a) 10mm (b) 15mm (c) 20mm et (d) pour d'une couronne usinée à partir d'un lingot AU4G.

**Microstructures:** La fig.2 présente les micrographies optiques des surfaces transversales de couronnes fabriquées par CMT avec différentes hauteurs et même conditions. On remarque que la microstructure des couronnes évolue d'une structure moyenne ou fine vers une structure grossière en allant du bas vers le haut des couronnes. La première est signe d'une structure de recuit. Alors que la seconde est une structure de coulée.

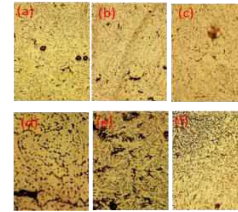


Fig. 2. Observation métallographiques transversales des couronnes ((a), (b) et (c) la base des couronnes (d), (e) et (f) la tête de couronne) pour les hauteurs 20mm, 15mm et 10mm respectivement

### a. CONCLUSION

En conclusion à notre travail, on peut soulever les points suivants :

- L'épaisseur de la couronne augmente au fur et à mesure que la hauteur augmente. Cette augmentation offre à la couronne une forme légèrement conique.
- La dureté au niveau du bas de couronne est plus élevée qu'en hauteur. Cette diminution est expliquée par la cinétique de refroidissement de la couche.
- Le comportement mécanique des couronnes de CMT, en compression ou en traction indirecte, est similaire à celui des couronnes élaborées par usinage cependant sa résistance mécanique prouve une certaine insuffisance.
- De point de vue microstructure, le bas des couronnes présente une structure plus fine que celle du haut.

## REFERENCES

- [1] Dursun T, Soutis C. Recent developments in advanced aircraft aluminium alloys. *Mater Des*;56:862e71, (2014)
- [2] Tawfik MM, Nemat-Alla MM, Dewidar MM. Enhancing the properties of aluminum alloys fabricated using wire þ arc additive manufacturing technique - a review. *J Mater Res Technol*;13:754e68 (2021).
- [3] Heinz A, et al. Recent development in aluminium alloys for aerospace applications. *Mater Sci Eng* (2000).
- [4] Cong B, Cai X, Qi Z, Qi B, Zhang Y, Zhang R, et al. The effects of ultrasonic frequency pulsed arc on wire þ arc additively manufactured high strength aluminum alloys. *Addit Manuf*;51:102617 (2022).
- [5] Gu J, Gao M, et al. Pore formation and evolution in wire + arc additively manufactured 2319 Al alloy. *Addit Manuf*;30:100900. (2019)
- [6] Colorado HA, et al. Sustainability of additive manufacturing: the circular economy of materials and environmental perspectives. *J Mater Res Technol* ; 9 (4):8221e34. (2020)
- [7] Zhang X, et al. Additive manufacturing of cellular ceramic structures: from structure to structureefunction integration. *Mater Des*;215:110470. (2022).

# Étude des propriétés mécaniques des composites à base d'une résine photosensible/TiO<sub>2</sub> pour l'impression 3D par DLP

**B. BOUCHOUL<sup>1\*</sup>, L. LAMIRI<sup>1</sup>, H. HAMOUCHI<sup>1</sup>, M. HAMIDOUCHE<sup>1</sup>, A. KENZOUR<sup>1</sup>, S. LASMI<sup>1</sup>, M. T. BENANIBA<sup>2</sup>, K. HAMLAOUI<sup>1</sup> AND O. BELGHERBI<sup>1</sup>**

1. Research Center in Industrial Technologies CRTI, B.P.64, Cheraga 16014 Algiers, Algeria,  
B\_Bouchoul@yahoo.com/B.Bouchoul@crti.dz

2. Laboratory of Multiphase Polymeric Materials (LMPMP), Faculty of Technology, Setif-1 University, 19000 Setif, Algeria.

## ABSTRACT

*Les propriétés mécaniques des objets imprimés en 3D par technique de la stéréolithographie (SLA) dépendent de la composition des résines photosensibles, des paramètres du procédé d'impression et du post-traitement des pièces. Dans cette étude, des éprouvettes sont imprimées à partir d'une résine commerciale à base de polymère photosensible chargée par différents taux de TiO<sub>2</sub>, le sens de l'orientation des éprouvettes et le post-traitement par UV ont été étudiés. Pour mieux comprendre l'effet du TiO<sub>2</sub>, l'orientation de l'impression et le durcissement UV, les éprouvettes imprimées en 3D ont été caractérisées par le test de traction, en étudiant l'évolution de la contrainte à la rupture, l'allongement à la rupture et le module d'Young. Le test de traction montre que l'augmentation du taux de charge, le sens d'impression où il est horizontal par rapport à l'axe de l'éprouvette, ainsi que le durcissement UV complémentaire après l'impression améliorent très significativement les différentes propriétés mécaniques.*

## KEY WORDS

Fabrication Additive (FA), Stéréolithographie (SLA), Photopolymérisation, Dioxyde de Titane (TiO<sub>2</sub>).

## I. INTRODUCTION

La stéréolithographie implique l'utilisation d'un faisceau laser pour balayer la surface d'une résine photosensible à l'état liquide [1]. Selon le motif 2D issu de l'étape de tranchage, la polymérisation de la structure se produit à l'endroit ciblé par le faisceau laser. La résolution élevée accessible pour la stéréolithographie se fait au prix d'un long processus en raison de la grande numérisation du parcours d'outil. Le traitement numérique de la lumière (DLP) est une autre voie d'impression qui partage le même raisonnement que la stéréolithographie mais résout le

problème du balayage à long terme en utilisant un écran numérique qui projette une image de la couche en construction. Par conséquent, le procédé DLP a la capacité de polymériser une couche entière au lieu d'un seul point [2]. Dans ce travail, Nous étudions l'effet de l'ajout du dioxyde de titane (TiO<sub>2</sub>) comme charge de différents taux pour la résine photosensible commerciale de type 3DM-ABS Black, ainsi que l'étude de l'effet du sens d'impression des éprouvettes et le durcissement complémentaire dans la chambre UV sur les différentes performances des résines composites élaborées. Des éprouvettes normalisées ont été conçues et imprimées par l'imprimante 3D d'une technologie (Digital Light Processing DLP) avec les différentes formulations des composites élaborés, puis elles sont caractérisées par le test de traction, afin d'évaluer les différentes caractéristiques mécaniques.

## II. TRAVAIL EXPÉRIMENTAL

### A. MATÉRIAUX UTILISÉS

La résine photosensible utilisée est de type 3DM-ABS BLACK.

Le dioxyde de Titane utilisé est de type A-198 de taille micrométrique.

### B. PRÉPARATION ET IMPRESSION

Les poudres de TiO<sub>2</sub> et la résine photosensible à base d'ABS ont été mélangés pour obtenir une homogénéité optimale en termes de viscosité et de dispersion. Pour assurer le bon mélange de la charge inorganique dans la résine, les particules de TiO<sub>2</sub> sont dissoutes dans une quantité optimale de résine satisfaisante pour une impression. Les formulations des résines composites ABS/TiO<sub>2</sub> ont été préparées avec différents taux (c'est-à-dire 0,25, 0,5, 1 % en poids et mélangées dans un bain ultrason.

Les éprouvettes de traction avec des dimensions normalisées sont conçues par SOLIDWORKS 2018 (Fig.1).

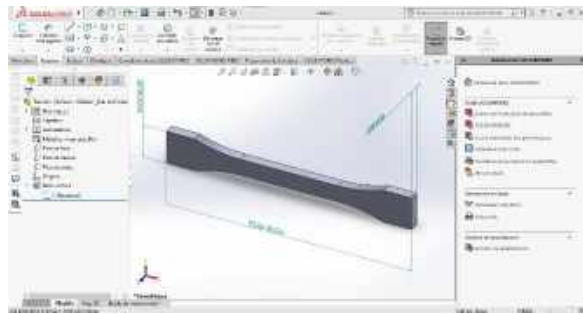


**Fig. 1.** Conception d'une éprouvette de traction par SOLIDWORKS.

Le fichier numérique des éprouvettes conçues par SOLIDWORKS doit être enregistré sous l'extension STL et importé par le logiciel de l'imprimante 3D (Fig.2).

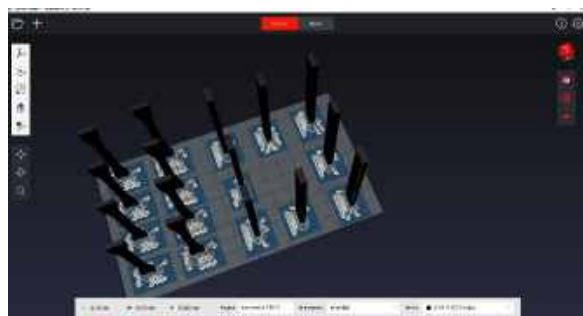
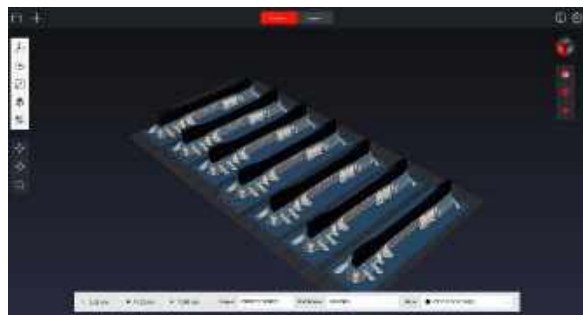


**Fig. 2.** Préparation numérique de l'impression par Operator Station.

Après la préparation numérique, fichier numérique est exporté vers la machine, la formulation préparée est ajoutée pour l'impression 3D par Stéréolithographie.

Une fois l'impression est terminée, une partie des éprouvettes ont été caractérisés et l'autre partie ont été passés à la chambre UV pour compléter ledurcissement comme le montre la figure 3.



**Fig. 3** Durcissement UV complémentaire .

### C. ESSAI DE TRACTION

Les éprouvettes de traction ont été testées selon les recommandations de la norme ISO 527-2 type d'éprouvette 5A à une vitesse de 5mm/min sur une machine de traction de type Zwick Roell Z 100 équipée d'une cellule de 10 kN et d'un extensomètre d'une longueur nominale de 25 mm, les essais sont répétés 3 fois pour chaque formulation et les résultats ont été obtenus à l'aide d'un logiciel de l'appareil.

### D. RÉSULTATS ET DISCUSSIONS

**TAB.I.** résultats de test de traction

<i>F</i>		<i>IMP. H</i>			<i>IMP. V.</i>		
		$\Sigma_R$	$\epsilon_r$	<i>E</i>	$\Sigma_R$	$\epsilon_r$	<i>E</i>
0%	N	14,05	22,89	5,54	9,12	16,00	2,86
	D	22,82	1,04	26,20	47,15	3,28	25,86
0,25%	N	12,57	15,83	5,58	9,38	13,53	3,85
	D	34,31	3,33	21,23	27,83	1,78	20,61
0,5%	N	13,24	14,87	5,80	7,87	12,74	3,12
	D	33,86	3,42	18,79	21,52	1,75	16,81
1%	N	13,70	20,87	4,87	8,78	11,92	3,53
	D	24,01	2,09	19,72	19,12	1,91	14,70

Les valeurs de la contrainte à la rupture, l'allongement à la rupture et le module d'élasticité en fonction du taux de charge, de l'orientation de l'impression et de durcissement UV sont regroupés dans le tableau 1.

#### *EFFET DU $TiO_2$*

En tant que le module est le rapport entre la contrainte et la déformation, donc il y a une concurrence dans le rôle du  $TiO_2$  dans la résine, d'un côté joue le rôle d'une charge renforçante qui diminue la flexibilité, mais d'un autre côté il absorbe la lumière UV où le taux de solidification des éprouvettes lors de l'impression est diminué, ce qui diminue les propriétés mécaniques comme la contrainte et le module[3].

#### *EFFET DE L'ORIENTATION DE L'IMPRESSION*

les valeurs de la contrainte à la rupture, de la déformation à la rupture et du module d'Young (Voir le tableau 1) dans l'impression horizontale (c'est-à-dire les couches sont parallèles au sens de l'essai de traction) sont supérieures aux celles dans l'impression verticale (les couches sont perpendiculaires à la direction de l'essai de traction), quel que soit le taux de charge ou bien le durcissement ou non, sauf dans le cas de 0% les éprouvettes non durcis imprimés verticalement donne une contrainte à la rupture (47.15 MPa) plus grande que de celle sont imprimés horizontalement (22.82 MPa). Cela confirme, l'anisotropie générée lors de l'impression par la technique de la stéréolithographie (SLA) couche par couche [4-6].

#### *EFFET DE DURCISSEMENT DANS LA CHAMBRE UV*

on trouve que les éprouvettes durcis donnent des valeurs de contraintes à la rupture et du module d'Young plus élevés que celles des éprouvettes non durcis. Par contre, l'allongement à la rupture des éprouvettes non-durcis est plus grande que les valeurs de la déformation des éprouvettes subissent au durcissement. Cela due au taux de réticulation élevé obtenu après l'exposition aux rayons UV dans la chambre de durcissement [7-9].

### **III. CONCLUSION**

On peut déduire que les propriétés mécaniques des objets imprimés par SLA, sont affectés par la nature la composition de la résine, les paramètres d'impression et le post-traitement des pièces imprimées.

L'incorporation des particules inorganiques de  $TiO_2$  dans la résine diminue la contrainte à la rupture, la

déformation à la rupture et le module d'Young ainsi, la rigidité des matériaux, cette diminution est due à l'absorption de la lumière UV par les microparticules de la charge.

L'impression des éprouvettes dans le sens horizontal donne des valeurs de contrainte à la rupture, de déformation à la rupture et de module d'Young supérieures à ceux dans l'impression verticale.

Le durcissement dans la chambre UV améliore les propriétés mécaniques des éprouvettes imprimées.

### **REFERENCES**

- [1] Huang, J., Qin, Q., & Wang, J. "A review of stereolithography: Processes and systems. Processes", 8(9), 1138 (2020).
- [2] Guessasma, S., Belhabib, S., Benmahiddine, F., Hamami, A. E. A., & Durand, S. "Synthesis of a Starchy Photosensitive Material for Additive Manufacturing of Composites Using Digital Light Processing. Molecules", 27(17), 5375 (2022).
- [3] Cazan, C., Enesca, A., & Andronic, L. "Synergic effect of  $TiO_2$  filler on the mechanical properties of polymer nanocomposites". Polymers, 13(12), (2021).
- [4] Steyrer, B., Neubauer, P., Liska, R., & Stampfl, J. "Visible light photoinitiator for 3D printing of tough methacrylate resins". Materials, 10(12), 1445, (2017).
- [5] Aznarte, E., Ayranci, C., & Qureshi, A. J. "Digital light processing (DLP): Anisotropic tensile considerations". In 2017 International Solid Freeform Fabrication Symposium. University of Texas at Austin, (2017).
- [6] KEBLER, A., Hickel, R., & Ilie, N. "In vitro investigation of the influence of printing direction on the flexural strength, flexural modulus and fractographic analysis of 3D-printed temporary materials". Dental Materials Journal, 40(3), 641-649, (2021).
- [7] Taneva, I., & Uzunov, T. "Influence of post-polymerization processing on the mechanical characteristics of 3D-printed occlusal splints". In Journal of Physics: Conference Series (Vol. 1492, No. 1, p. 012018). IOP Publishing (2020).
- [8] Zguris, Z. "How mechanical properties of stereolithography 3D prints are affected by UV curing". Formlabs White Paper, 1-11, (2016).
- [9] Ahmad, K. W., Mohamad, Z., Othman, N., Man, S. H. C., & Jusoh, M. "The Mechanical Properties of Photopolymer Prepared Via 3D Stereolithography Printing: The Effect of UV Curing Time and Anisotropy". CET Journal-Chemical Engineering Transactions, 78, (2020).

# L'étude de l'effet de la forme et du taux de remplissage sur les propriétés mécaniques des pièces réalisées avec l'impression 3D

YASMINE NASRI<sup>2,\*</sup>, BOUBEKEUR MOHAMMED BILAL MERTANI<sup>2</sup>, FAROUK BENALI<sup>2</sup>

Institut d'optique et mécanique de précision, Université de Ferhat Abbas Sétif 1

## ABSTRACT

*This thesis presents the study of the effect of the shape and the filling rate on the mechanical properties of parts made with 3D printing with PLA filament. Different patterns and filling rates were generated using a script implemented in the ABAQUS software and then a finite element simulation of quasi-static compression was performed on cylindrical samples with a height of 15 mm and a diameter of 25 mm. The results obtained from the critical force have been validated with experimental tests, they show that the pattern, the filling rate and the materials used have a major impact on the mechanical resistance of the part.*

## KEY WORDS

3D printing; PLA; compression; fill pattern

## I. INTRODUCTION

L'impression 3D offre une grande flexibilité géométrique par rapport aux méthodes conventionnelles [1]. La fabrication par filament fondu (FFF) est l'une des méthodes d'impression 3D les plus utilisées. Pour le matériau, le polylactide (PLA) est l'un des matériaux de choix pour fabriquer les pièces. Ces propriétés mécaniques sont caractérisées par les modules et les résistances en traction et en compression qui constitue un aspect important pour l'utilisation des pièces dans les applications d'ingénierie [2].

L'objectif du présent travail a donc été de faire une étude expérimentale et numérique du effet de la forme et du taux de remplissage sur les propriétés mécaniques des pièces en PLA réalisées avec l'impression 3D (FFF).

Dans notre travail une étude numérique par éléments finis en utilisant les codes de calcul Abaqus a été réalisée pour prédire le comportement mécanique en compression statique des éprouvettes dans les domaines élastiques et plastiques pour différentes formes et taux de remplissage. Afin de faire une comparaison, une étude expérimentale a été réalisée en parallèle sur les mêmes échantillons.

## II. MODELISATION ET SIMULATION DU COMPORTEMENT MECANIQUE

Différent motifs (ligne, triangle, carré et nid d'abeille) et taux de remplissage (33%, 43%, 53% et 63%) ont été générés en utilisant un script implémenté dans le logiciel ABAQUS.

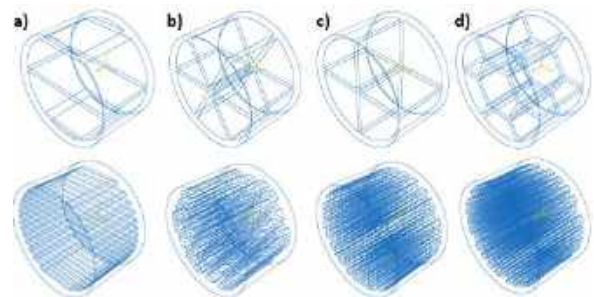


Fig. 1. Modèles 3D des échantillons a) ligne, b) triangle, c) carré, d) nid d'abeille C3D10.

### A. RESULTATS DE MODELISATION

Les résultats graphiques obtenus de déformation sont présentés dans la figure suivante :

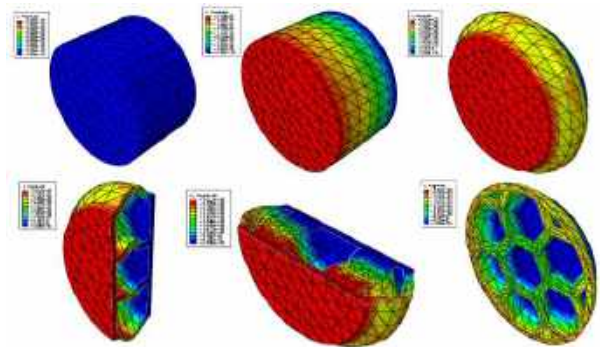


Fig. 3. Résultats graphiques avec la découpe selon le plan x,y et z.



## B. SYNTHÈSE DES RÉSULTATS

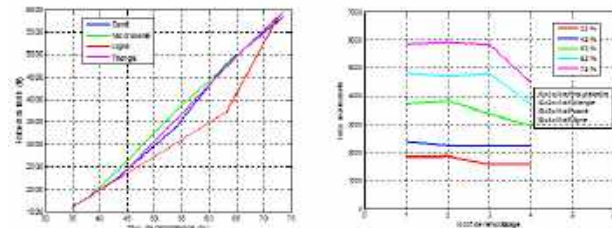


Fig. 4. Courbe de force maximale en fonction de a) motif de remplissage, b) taux de remplissage pour les différents échantillons.

## III. IMPRESSION 3D

Dans cette partie on a réalisé des essais de compressions sur les échantillons décrits dans la partie de simulation qui ont été réalisés grâce à l'impression 3D en utilisant le filament PLA.

L'objectif de cette partie de l'étude est de voir l'influence du motif et du taux de remplissage sur le comportement expérimental en compression des échantillons utilisés.

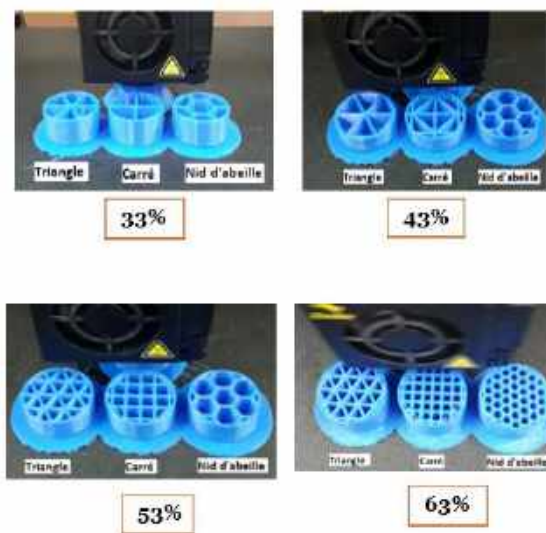


Fig. 5. Impression 3D (FDM) des 16 échantillons.

## A. RESULTATS DE COMPRESSION

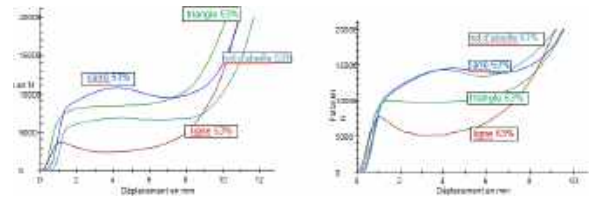
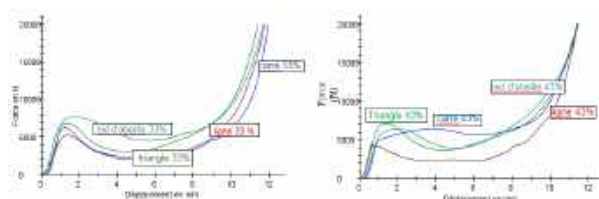


Fig. 6. L'évaluation de la force maximale en fonction de déplacement de 16 échantillons.

## IV. COMPARAISON ENTRE LES RESULTATS DE SIMULATION ET EXPERIMENTALE

De point de vue qualitatif on remarque que les deux courbes sont très proche, mais par contre de point de vu quantitatif on voit qu'il ya une grande différence qui peuvent être expliqué par le procédé de fabrication d'éprouvette 3D.

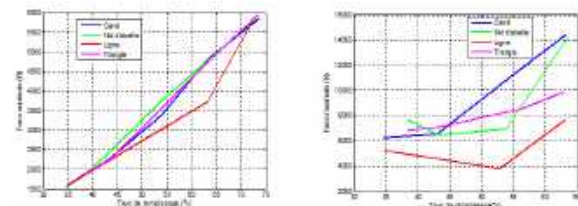


Fig. 7. Courbe de force maximale en fonction de taux de remplissage pour les différents motifs.

## V. CONCLUSION

- D'abord, concernant l'impression 3D on a conclue que plus le taux sera élevé rend la pièce hautement résistante.
- Le choix du motif est essentiel à la bonne tenue et résistance de la pièce 3D suivant les besoins et le matériau utilisé.
- D'après l'étude expérimentale sur l'effet de compression, plus le taux de remplissage est important plus l'éprouvette résiste à une forte charge.

## REFERENCES

- [1] C. B. Lubombo, « La performance mécanique des pièces en PLA allégées produites par impression 3D », 2018, Consulté le: 24 octobre 2023. [En ligne]. Disponible sur: <https://savoirs.usherbrooke.ca/handle/11143/13430>
- [2] « Acide polylactique (PLA) », Techniques de l'Ingénieur. Consulté le: 24 octobre 2023. [En ligne]. Disponible sur: <https://www.techniques-ingenieur.fr/base-documentaire/materiaux-th11/plastiques-et-environnement-42657210/acide-polylactique-pla-am3317/>



# Study Of The Influence Of Infill Patterns And Orientation On Mechanical Properties Of Z-ULTRAT Material

AMMAR HABOUSSI<sup>1,2</sup>, FARID BETTINE<sup>3,4</sup>, FAYÇAL BOUZID<sup>1</sup>, BOUCHOUL BOUSSAHA<sup>1</sup>, RAFIK MAHDAOUI<sup>5</sup>, AND FAYSSAL BOUFELGHA<sup>1</sup>

1. Research Center in Industrial Technologies CRTI, P.O. Box 64, Cheraga 16014 Algiers, Algeria
2. Laboratory of Automation and Manufacturing, University of Batna2, Algeria
3. Institute of Optics and Precision Mechanics, University Ferhat Abbas Sétif 1, Sétif 19000, Algeria
4. Laboratory of Nonmetallic Materials, Sétif, Algeria
5. Laboratory of Knowledge Engineering and Computer Security, University of Khenchela, Algeria

## ABSTRACT

*Additive manufacturing is a technology that is developing rapidly in various fields because it allows the manufacture of parts with complex shapes that are difficult to achieve by traditional manufacturing methods. The aim of this work is to examine the effect of the infill pattern orientation on the quality of 3D printed samples in order to improve our understanding of the anisotropic behaviour at higher resolution. Thus, in order to analyse the mechanical properties and evaluate the tensile strength, we tested four sample printing models: linear, grid, honeycomb and octagonal using Z-ULTRAT (ABS plastic blend) filament, which were printed with 50% infill density in different orientations (0°, 30°, 45°, 60° and 90°), using the Zortrax M300-plus printer.*

*It has been found that the internal arrangement of the infill pattern significantly affects the mechanical properties of parts printed in Z-ULTRAT material. Additionally, we noticed that the combination of different infill patterns and layer stacking sequences affect the tensile strength of the FDM (Fused Deposition Modelling) printed parts. The obtained results are of great importance for engineers and designers who want to take into account the anisotropy of their prints and highlight the importance of taking infill patterns and orientation into account when optimizing the mechanical properties of parts made of Z-ULTRAT plastic in 3D-printing.*

## KEY WORDS

Additive manufacturing; fused deposition modelling; 3D-printing; tensile test; Z-ULTRAT; infill patterns

## I. INTRODUCTION

Fused Deposition Modelling (FDM) is a 3D-printing technology that involves the extrusion of molten thermoplastic material through a nozzle to create objects layer by layer. It is a form of additive manufacturing that has applications in various fields

such as medical, engineering, military, construction, aerospace, architecture, fashion, computer industry, etc [1].

This innovative technology is gradually supplanting the conventional approach to manufacturing, owing to its remarkable flexibility in comparison to traditional manufacturing techniques. The vast majority of contemporary technologies necessitate materials exhibiting a distinct blend of characteristics inherent in conventional materials [2].

FDM printing can be carried out on irregular or non-horizontal surfaces and even in zero-gravity environments, such as in vehicles, aircraft, and boats [3]. The process involves a control system that includes an upper control part for slicing processing and data transmission, and a lower processing control part for executing the printing operation [4]. FDM printing of hollow structures can be achieved by dividing the model into sub-modules, printing them separately, and then splicing them together, eliminating the need for supporting structures [5]. FDM printing can utilize co-polycarbonate as a support material, which exhibits stability at high temperatures and can be used in conjunction with other materials like polyester, polyamide, and PC/polyester blends [6]. In this work, we have study the influence of various process parameters on the mechanical properties of Z-ULTRAT specimens in FDM. Recently, the influence of raster orientation and infill pattern on the mechanical properties of Z-ULTRAT material specimens has been studied in several papers. Martín et al. conducted a comparative evaluation of the tensile strength behaviours of parts obtained by fused filament fabrication (FFF) using different infill patterns, including zig-zag, concentric, and different orientation lines [7]. Lorenzo-Bañuelos et al. investigated the influence of raster orientation on fracture parameters for thin polymer components and found that optimizing the raster orientation is

important for preserving the structural integrity of the components [8]. Kain et al. evaluated the influence of various infill orientations on the tensile strength, compressive strength, impact strength, and heat deflection temperature of FDM processed test specimens and found a direct interaction between infill orientation and mechanical performance [9]. Parpala et al. investigated experimentally the influence of infill density and infill line width on the vibrations of 3D-printed specimens and developed a parametric finite element model for predicting eigen frequencies [11]. The influence of infill patterns and orientation on the mechanical properties of Z-ULTRAT specimens in FDM has been extensively studied. Different infill patterns, such as grid, linear, Octagonal and Honeycomb with raster orientations of 0°, 30°, 45°, 60° and 90°, have been investigated. It has been found that the internal arrangement of the infill pattern significantly affects the mechanical properties of Z-ULTRAT material printed parts, even when similar printing parameters are used [12]. These patterns have been found to affect the mechanical behavior of FDM printed parts, including their tensile strength, elastic modulus, and ductility [13].

## II. MATERIALS AND METHODS

In this study we used the Z-ULTRAT highly durable 3D printing filament. This material, which is made by Zortrax company, is a mixture of ABS plastic and PC (polycarbonate). Z-ULTRAT exhibits excellent impact resistance and produces a consistent surface texture. This versatile material is suitable for 3D printing durable components, including end-use parts that maintain their shape over time.

In table 1, we have cited some key features and properties of Z-ULTRAT.

Table 1: some key features and properties of Z-ULTRAT filament

Mechanical properties	Metric	Test method
Tensile strength	32.60 MPa	ISO 527:1998
Breaking stress	30.70MPa	ISO 527:1998
Elongation at max tensile stress	3.78%	ISO 527:1998
Elongation at break	4.87%	ISO 527:1998
Bending stress	54.00MPa	ISO 178:2011
Flexural modulus	1.85GPa	ISO 178:2011
Izod Impact, Notched	5.26KJ/m <sup>2</sup>	ISO 180:2004

### A. SPECIMEN PREPARATION AND EQUIPMENT

In this work, tensile specimens are designed with

SolidWorks computer aided design (CAD) software according to ASTM E8/E8M-13a (Figure 1.), and STL format of specimen 3D model was created for Zortrax M300 Plus.

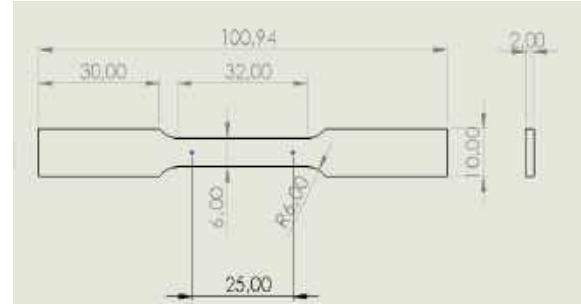


Fig. 1. Dimensions of the tensile test specimen in (mm).

The orientation and type of the infill pattern of test specimens was controlled by rotating the specimen relative to the axes of the printer's build platform. To generate additional test specimens, this base model was copied and rotated around the X, Y, and Z-axes. Figure 2 (a) shows specimens with 30°, 45°, 60°, and 90-degrees rotations about the x-y-axis as show in fig.2

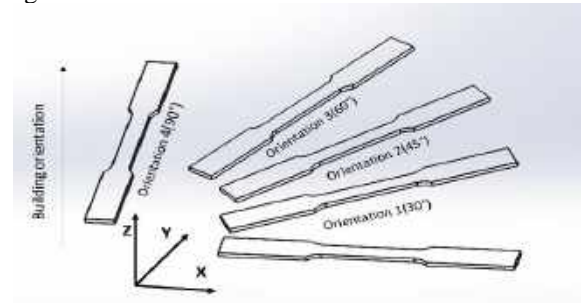


Fig.2. Test specimens orientations.

Figure 3 represents typical printing patterns: linear, grid, honeycomb, and octagon used in this study

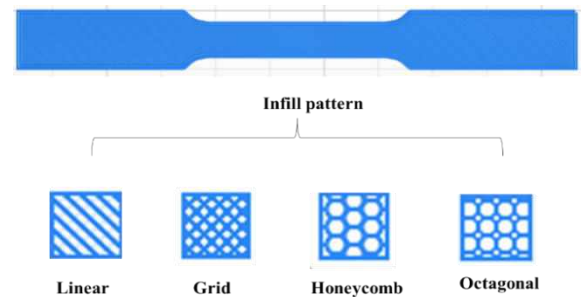


Fig.3. Infill pattern modes.

### B. MECHANICAL TESTS TABLES

The tensile testing was approved out using a **Zwick Z050** Tensile Testing Machine with a load cell of 50 KN. The crosshead speed was 10 mm/min according to the standard as shown in figure4 (a-d) represents a tensile test result of a Z-ULTRAT printed specimens to printing mode.

### III. RESULTS

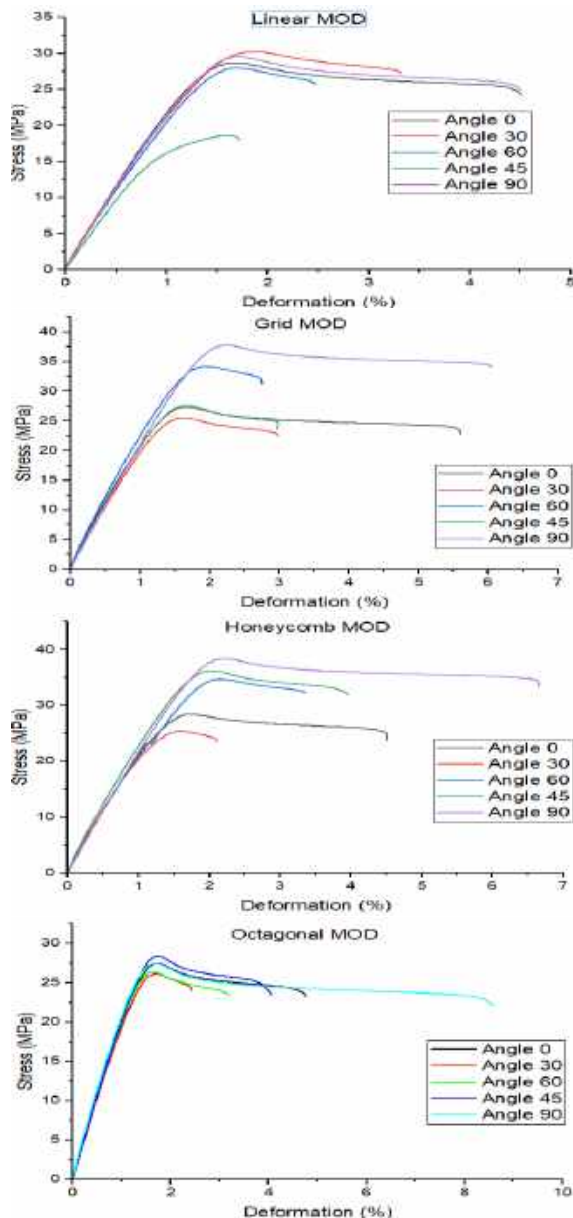


Fig.4 Tensile test result according to printing mode

### IV. CONCLUSION

In this study, we have tested and analysed the tensile mechanical properties of FDM printed Z-ULTRAT plastic specimens. 20 specimens were printed with a different infill

pattern and orientation types relative to the printer's build platform, and were exposed to tensile weight tests. Load and strain data composed during the test was analysed to calculate the elastic modulus, yield strength, and ultimate strength of each specimen. Test results showed that specimen orientation and infill pattern have a significant effect on the strength and stiffness of the specimen, as expected. Different sizes like micro and nano-metrology serving for sustainable improvements.

### REFERENCES

- [1] Martín, M. J., Auñón, J. A., & Martín, F. (2021). Influence of infill pattern on mechanical behavior of polymeric and composites specimens manufactured using fused filament fabrication technology. *Polymers*, 13(17), 2934.
- [2] Callister Jr, W. D., & Rethwisch, D. G. (2020). *Fundamentals of materials science and engineering: an integrated approach*. John Wiley & Sons.
- [3] A. Luis and L. L. Sánchez-Soto, "Probability distributions for the phase difference," *Phys. Rev. A* 53, 495 (1996).
- [4] Cano, S., Lube, T., Huber, P., Gallego, A., Naranjo, J. A., Berges, C., ... & Gonzalez-Gutierrez, J. (2020). Influence of the infill orientation on the properties of zirconia parts produced by fused filament fabrication. *Materials*, 13(14), 3158.
- [5] Lorenzo-Bañuelos, M., Díaz, A., & Cuesta, I. I. (2020). Influence of raster orientation on the determination of fracture properties of polypropylene thin components produced by additive manufacturing. *Theoretical and Applied Fracture Mechanics*, 107, 102536.
- [6] Kain, S., Ecker, J. V., Haider, A., Musso, M., & Petutschnigg, A. (2020). Effects of the infill pattern on mechanical properties of fused layer modeling (FLM) 3D printed wood/poly(lactic acid) (PLA) composites. *European journal of wood and wood products*, 78, 65-74.
- [7] Muammal, M., Hanon, József, Dobos, László, Zsidai. (2021). The influence of 3D printing process parameters on the mechanical performance of PLA polymer and its correlation with hardness. *Procedia Manufacturing*, doi: 10.1016/J.PROMFG.2021.07.038
- [8] Manickam, Ramesh, L., Rajeshkumar, D., Balaji. (2021). Influence of Process Parameters on the Properties of Additively Manufactured Fiber-Reinforced Polymer Composite Materials: A Review. *Journal of Materials Engineering and Performance*, doi: 10.1007/S11665-021-05832-y
- [9] S., Raam, Kumar, Supriya, Sridhar, R., Venkatraman, Manigandan, Venkatesan. (2021). Polymer additive manufacturing of ASA structure: Influence of printing parameters on mechanical properties. *Materials Today: Proceedings*, doi: 10.1016/J.MATPR.2020.04.500
- [10] Muhammad, Salman, Chaudhry, Aleksander, Czekanski. (2020). Evaluating FDM Process Parameter Sensitive Mechanical Performance of Elastomers at Various

Strain Rates of Loading. Materials, doi:  
10.3390/MA13143202

[10] Jayant, Giri., Anagha, Chiwande., Yash, Gupta., Chetan, Mahatme., Pallavi, Giri. (2021). Effect of process parameters on mechanical properties of 3d printed samples using FDM process. Materials Today: Proceedings, doi: 10.1016/J.MATPR.2021.04.283

[11] J., Bonada., M.M., Pastor., Irene, Buj-Corral. (2021). Influence of infill pattern on the elastic mechanical properties of Fused Filament Fabrication (FFF) parts through experimental tests and numerical analyses. Materials, 14(18):5459-. doi: 10.3390/MA14185459

[12] Gurmaheshinder, Singh, Sandhu., Kamaljit, Singh, Boparai., Kawaljit, Singh, Sandhu. (2021). Influence of slicing parameters on selected mechanical properties of fused deposition modeling prints. Materials Today: Proceedings, doi: 10.1016/J.MATPR.2021.09.118

# Mechanical behavior of 3D printed bamboo-inspired cellular structures

AKRAM ZEGADI<sup>1,2,\*</sup>, ILYAS BENSALAM<sup>1,3</sup>

1. Emerging Materials Research Unit, Ferhat Abbas University of Setif 1, Algeria
2. Institute of Optics and Precision Mechanics, Ferhat Abbas University of Setif 1, Algeria
3. Mechanics of Structures and Materials Laboratory, University of Batna 2, Algeria

## ABSTRACT

*This study examines a bamboo plant-modeled structure using SolidWorks and three-dimensional printing. The study reveals that the strength of the structure can be modified by varying the number of reinforcements. The best structure is found with six doubled ribs, while the highest plateau stress is 11.25 MPa for the sample with twelve doubled ribs. These findings align with previous scientific research on cellular materials and their role in energy absorption and densification.*

## KEY WORDS

3D printing, densification, Plateau, energy absorption, quasi-static, bio-inspired, bamboo,

## I. INTRODUCTION

Cellular materials are present in a large number of industrial applications and in everyday life.[1] Cellular materials are widely used in various engineering applications due to their exceptional and excellent properties, and have become an important subject of modern research. [2]

Cellular solids offer unique properties that enable the design of lightweight, rigid components, reliable insulation, and energy absorption. Their low density allows for lightweight structures, floating objects, and high compression pressures. Researchers are studying biological structures to optimize their energy absorption capabilities, inspired by the high energy absorption capacities found in plants and animals, which can inspire new structures with superior energy absorption capabilities.

In this work, we conducted compression tests on our manufactured parts to assess their mechanical strength, varying the number of reinforcements. These tests allow us to understand how these structures behave and can be used in the field of reinforcement, improving their strength.

## II. DESIGN AND 3D PRINTING

### A. DESIGN

The software SolidWorks conducted the design of cellular structures with different reinforcement numbers (Fig.1).

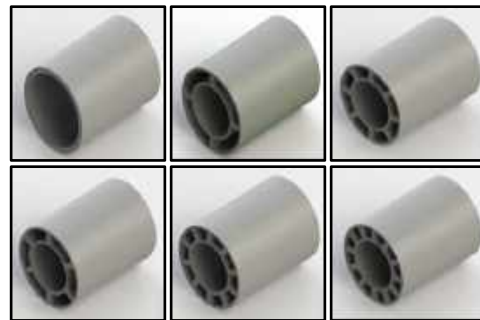


Fig. 1. Designed cellular structures with different reinforcements.

The printer used in this work is of the brand “Creality 3D” model “Ender-3 Pro”. The printing was carried out at the level of the university incubator setif-1.

### B. MECHANICAL BEHAVIOR

Uni axial compression tests were carried out at the non-metallic materials laboratory at Ferhat Abbas Sétif University, on a Zwick/Roell Z050 universal traction machine with a maximum load of 50 KN, driven by a real-time computer that allows the data to be acquired and processed quickly using a software called “testXpert version12.0.”

During this test, the machine plate (136.20 mm in diameter) is put in contact with the samples. They are

then crushed at a speed of 10 mm/min. The recording of the exhaust begins with a precharge of 0.5 N.

### III. RESULT AND DISCUSSION

Typical stress-strain curve was captured for all proposed structures. The mechanical behavior can be divided into 3 major domains:

- Stage 1: This is the elastic zone, in this initial stage we notice that the tube undergoes a compression without undergoing permanent deformation. it is a linear elasticity of 13 MPa.
- Stage 2: This is the area called plateau. In this area, it is noteworthy that there is a sharp collapse of constraints, followed by instability of the constraint during this stage. This is caused by the appearance of folds and their collapse. This is shown in the figure above. The plateau tension at this stage is 5.87 MPa.
- Stage 3: This is the area of densification, the tube undergoes a major plastic deformation. The pressure applied continues to increase during this phase from d (70.97%), while the permanent deformation accumulates. The cells collapse enough to cause contact between the edges and the opposite walls of the room.

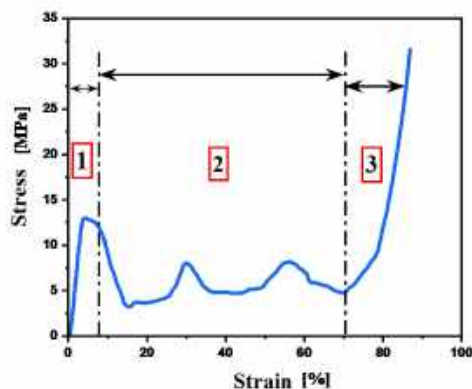


Fig. 1. Typical stress-strain curve of empty tube.

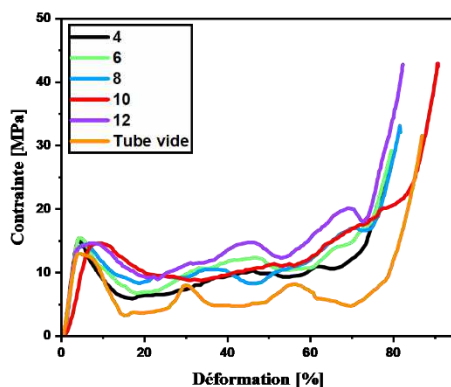


Fig. 1. Stress-strain curves for all printed structures

Table 1. Energy absorption parameters.

Number of reinforcement	4	6	8	10	12
$\sigma_{\text{seuil}}$ [MPa]	12,384	12,692	13,131	12,769	14
$\sigma_{\text{pl}}$ [MPa]	4,4687	5,4613	7,4452	7,8917	8,5755
$\epsilon_d$	66,6975	69,0993	66,882	65,588	72,240

### IV. CONCLUSION

The study of compression mechanical behavior confirms that reinforcement number affects strength and energy absorption in structures. A higher plate level promotes better dissipation of mechanical energy during shocks. When strain exceeds elastic limit, structures undergo plastic collapse, leading to densification and elimination of initial porosity.

### REFERENCES

- [1] L. B. Louise, « Description multi-échelles du comportement mécanique d'un matériau cellulaire composite sous sollicitations sévères - Application aux agglomérés de liège pour l'aéronautique - », École Nationale Supérieure d'Arts et Métiers, 2020.
- [2] I. Bensalem et A. Benhizia, « Novel design of irregular closed-cell foams structures based on spherical particle inflation and evaluation of its compressive performance », *Thin-Walled Struct.*, vol. 181, p. 109991, déc. 2022, doi: 10.1016/j.tws.2022.109991.
- [3] L. J. Gibson et M. F. Ashby, *Cellular solids: structure and properties*, 2. ed., 1. paperback ed. (with corr.), Transferred to digital printing. in Cambridge solid state science series. Cambridge: Cambridge Univ. Press, 2001.
- [4] N. S. Ha et G. Lu, « A review of recent research on bio-inspired structures and materials for energy absorption applications », *Compos. Part B Eng.*, vol. 181, p. 107496, janv. 2020, doi: 10.1016/j.compositesb.2019.107496.
- [5] S. GUÉVELOU, « Caractérisation des propriétés thermo-radiatives de mousses à structure numériquement contrôlée : vers le design d'absorbeurs solaires », Thèse de Doctorat, Nantes Angers Le Mans, France, 2015.



# Micromechanical behavior study of delta phase in 316L stainless steel elaborated by Additive Manufacturing

SALIMA ABERKANE<sup>1,\*</sup>, ABDELBASSET BERRIAH<sup>1</sup>, MOHAMED ZIANE BOUTEBINA<sup>1</sup>, BRAHIM MEHDI<sup>1</sup> AND RIAD BADJI<sup>2</sup>

1. Materials Physics Laboratory, Faculty of Physics, University of Science and Technology Houari Boumediene USTHB, Bab-Ezzouar, Algiers, Algeria.
2. Research Center in Industrial Technologies CRTI, Cheraga, Algiers, Algeria.

## ABSTRACT

*This research aims to investigate the micromechanical behavior of the different delta ferrite morphologies obtained in the 316L as-built state of wire arc additive manufacturing WAAM. The microhardness, young's modulus, initial yield stress  $\sigma_y$  and strain hardening exponent  $n$  were obtained for the three typical morphologies. The results show that  $H$  and  $E$  values are close,  $\sigma_y$  and  $n$  remain constant with different loads in the three morphologies and  $n$  is inversely correlated with  $\sigma_y$ .*

## KEY WORDS

WAAM ; 316L ; micromechanical behavior.

## I. INTRODUCTION

Additive manufacturing (AM) is a modern method of creating products by continuously adding material based on a computer-aided design model [1]. Wire Arc Additive Manufacturing (WAAM) is one specific technique within AM, which falls under the Directed Energy Deposition (DED) category of metal additive manufacturing. The micromechanical properties resulting from this process are still poorly known, particularly for 316L alloy as the most important austenitic steels investigated with WAAM process [2]. This research aims to fill this knowledge gap of the as-built state of the additive manufacturing process.

## II. EXPERIMENTAL METHODOLOGY

The wall was deposited by Fronius TPS 500i power source which is an advanced version of the GMAW machine based on short-circuit transfer,

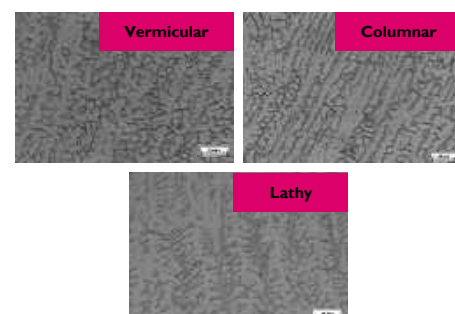
and the mode CMT was adopted. The feedstock was a 1 mm diameter commercial 316LSi stainless steel wire.

Fig. 1. Schematic diagram of deposition process

## III. EXPERIMENTAL RESULTS

### A. MICROSTRUCTURE

Figure 2 shows the microstructure of 316L steel showing the ferrite  $\delta$  phase obtained after WAAM treatment. We present the three morphologies: vermicular, columnar and lathy forms.



**Fig. 2.** Microstructures of the as build 316L alloy showing the different morphologies of  $\delta$ -ferrite.

### B. MICROMECHANICAL PROPERTIES

Figures 3-5 show the variation of the microhardness, the Young's modulus and the work hardening coefficients respectively of the three morphologies obtained. We show that microhardness and Young's modulus drop sharply with increasing applied load. This proves the variation in the concentration of dislocations from the surface layer having undergone the treatment.

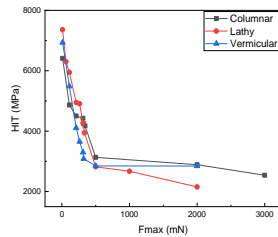


**Fig. 3.** Microhardness H of three typical morphologies

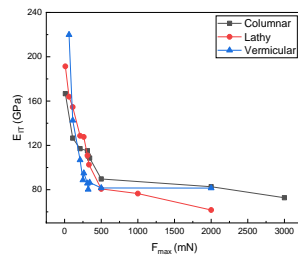


**Fig. 4.** Young modulus E of three typical morphologies

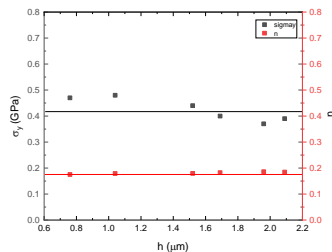


**Fig. 5.** Values of  $\sigma_y$  and  $n$  at different indentation depth of Vermicular  $\delta$ -ferrite

For the work hardening coefficients, we determine  $n=0,2$  and  $\sigma_y=400\text{MPa}$ . Which proves that the three morphologies have the same coefficients and consequently these steels will have the same plastic flow.

### IV. CONCLUSION

- H of three typical morphologies evidently decreases with the increase of h.
- E of three typical morphologies decrease with the increase of h as a whole, which can be

interpreted by increasing damage caused by accumulated dislocation.

- $\sigma_y$  and  $n$  remain constant with different loads in four morphologies.  $n$  is inversely correlated with  $\sigma_y$ .

### REFERENCES

- [1] "Standard Terminology for Additive Manufacturing—General Principles—Terminology," ISO/ASTM, 2015.
- [2] W. Jin et al., "Wire Arc Additive Manufacturing of Stainless Steels: A Review applied sciences Wire Arc Additive Manufacturing of Stainless Steels" Appl. Sci. 10, 5 (2020)